Aerothermodynamics of Impingement and Film Cooling in a Gas Turbine Blade

BY

Sean Christopher Underwood

B.S. Aerospace Engineering, Georgia Institute of Technology, 2005
B.S. Mathematics, Georgia Southwestern State University, 2005
M.S. Aerospace Engineering, University of Kansas, 2008

Submitted to the graduate degree program in the Department of Aerospace Engineering and the Graduate Faculty of the University of Kansas in partial fulfillment of the requirements for the degree of Doctor of Philosophy.

_____

Dr. Ray Taghavi, Committee Co-Chair

_____

Dr. Saeed Farokhi, Committee Co-Chair

_____

Dr. Shawn Keshmiri, Committee Member

_____

Dr. Mario Medina, Committee Member

_____

Dr. Huixuan Wu, Committee Member

_____

Date Defended

The Dissertation Committee for Sean Christopher Underwood certifies that this is the approved version of the following thesis:

Aerothermodynamics of Impingement and Film Cooling in a Gas Turbine Blade

_____

Dr. Ray Taghavi, Committee Co-Chair

_____

Dr. Saeed Farokhi, Committee Co-Chair

Date Approved:

Abstract

The service life of gas turbine engine turbine blades depends on the blade's material, service temperature and total stress. In high-performance gas turbines, film cooling is widely used to reduce the blade service temperature. Often impingement cooling is also employed to target the stagnation point heat transfer for internally-cooled gas turbine blades. A novel thermal wind tunnel was designed to study the combined effect of the impingement and film cooling on blunt airfoils. The hot exhaust plume of a micro-jet is used as the source of high-temperature gas flow in the thermal wind tunnel. An ejector nozzle was designed and integrated with the hot jet to provide a thermally controlled test section environment in the research facility. Measurements of freestream parameters such as gas speed, turbulence intensity and gas temperature were made. An airfoil that utilizes leading-edge (internal) impingement as well as film cooling holes on its suction surface was designed and fabricated. A cooling sleeve is used inside the airfoil to guide the impingement jets on the leading edge and to supply the coolant to the film holes. The surface temperature distribution is measured by an array of eight thermocouples flush-mounted on the airfoil surface downstream of the film holes. The initial ranges of blowing parameters (Mb) investigated were between 5 and 6. Numerical simulation using a commercially available Reynolds-Averaged Navier-Stokes (RANS) software was used and validated by the experimental measurements. The numerical simulations for the airfoil consisted of two thermal wall boundary conditions, the adiabatic and conjugate heat transfer (CHT) models. The adiabatic model focuses on the effect of film cooling on an adiabatic wall. The conjugate heat transfer model represents the solid and fluid heat transfer exchange, conduction and convection. Verification and validation was completed to ensure accurate aerothermodynamic simulations. The experimental and numerical data showed a close comparison for the suction surface temperatures and cooling effectiveness. A broader range of characteristic parameters (blowing parameter, turbulence intensity (Tu) and density ratio) were studied to show their impact on film cooling effectiveness parameter.

The effects from the blowing parameter are reported for different M_b of 0.53 to 5.95 with two turbulent intensities, 5% and 20%. The adiabatic film effectiveness parameter showed two unique trends: low M_b with low Tu or high M_b with high Tu both exhibited improved film cooling effectiveness. Jet detachment is also detected at $M_b \sim 1.5$ for the current film cooling set up. The study of turbulence intensity effects was completed in the range of 5% to 25 % for two density ratios of 1.65 and 1.99. The turbulence intensity study showed that higher Tu caused the adiabatic film effectiveness to decrease by an average 18%. The density ratio (DR) in the film cooling is studied to explore the real turbine environment. The velocity ratio and turbulence intensity is held at a constant of 0.64 and 20%, respectively, for a range of the density ratio: 1.49 to 1.99. The results show that coolant density would cause the adiabatic film effectiveness to increase an average of 12% from the baseline (DR: 1.65) to the representative engine condition (DR: 1.99).

Acknowledgement

To my longtime advisor, Dr. Ray Taghavi, I cannot express my gratitude for his commitment to me and my family. He has been with me since the first phone call in 2005 and supported all my educational goals. He is a true friend and mentor. Dr. Saeed Farokhi has also been there since the start of my graduate career, from his GTA in Fundamentals of Aerodynamics to Fundamentals of Jet Propulsion. I am deeply honored by having him as my co-advisor, his contribution in guiding and preparing me is tremendous to my growth. Dr. Ray Taghavi and Dr. Saeed Farokhi are an unbelievable resource to me and my family. They will always be a part of me and my future, thank you for your unwavering support.

I would like to express gratitude to Dr. Hixuan Wu and Mr. Xingtian Tao for their efforts in performing the particle image velocimetry. Their contribution was critical to the validation of the freestream velocity and turbulence intensity. In addition, it is an honor to have Dr. Hixuan Wu to serve on my committee with his background in experimental fluids research. Thanks goes to Dr. Shawn Keshmiri for aiding my manufacturing of the test article with a 3D printer and being a part of the committee. Dr. Shawn Kashmiri's directions and advice outside of academia has been a wonderful benefit to my career goals. Many thanks to Dr. Mario Medina, his knowledge in thermodynamics gave me a different understanding into my own work. Dr. Mario Medina brings an outside point of view to my committee that is welcomed and appreciated by me.

Special thanks to Dr. Z. J. Wang for acquiring Star- CCM+ and KU high performance computing (HPC) resources for the simulation component of this research. Also, special thanks go to Mr. Wes Ellison, Mr. James Newkirk and Mr. Grant Godfrey for assisting in testing and CAD modeling. Their service was instrumental in completing this research. Furthermore, I would like to thank Mr. Sunayan Mullick for his advice in meshing the CFD models.

Finally, I must give thanks to all my family members, without their support this could never happen. My wife, Diana, and my mother, Marie, have been my support system throughout my life. Their love and devotion has been the greatest thing in my life. My daughter, Sofia, who is the light of my life and holder of my heart, was there to brighten up my spirit when a difficult obstacle was confronted.

This research is supported by the Aerospace Engineering Department at The University of Kansas and is dedicated to my wife, daughter and our future son.

Table of Contents

Table of Tables

Table of Figures

Nomenclature

Latin	Definition	Unit
A	Area	ft^2
a	Augmentation factor	--
c	Airfoil chord length	in
C	Absolute flow speed	ft/s
c_p	Specific heat at constant pressure	BTU/lbm·°F
D_{le}	Diameter of leading-edge	ft
d	film hole diameter	in
D	impingement hole diameter	in
DR	Density Ratio	--
E	Total Energy	BTU
F	Force	lbf
h	heat transfer coefficient	BTU/s·ft^2·°F
I	Momentum Flux Ratio	--
k	Thermal conductivity	BTU/(hr·ft·°F)
L	length	in
M_b	Blowing Parameter	--
$\dot{m}_f$	Fuel mass flow rate	lbm/s
Nu	Nusselt number	--
Off	Cooling Off	--
On	Cooling On	--
p	Pressure	psi
P	Film hole spacing or pitch	in
Pr	Prandtl number	--
q	Dynamic Pressure	psi
q	Heat flux	BTU/s·ft^2, lbm/s^3
Q_R	Fuel (lower) heating value	BTU/lbm
r	Recovery factor	--
R	Gas constant	BTU/lbm·°R
r_t	Leading-edge radius	in
t	Thickness	in
T	Temperature	°F/°R
Tu	Turbulence intensity (%)	--
U	Velocity	ft/s
u, v, w	Velocity components in 3 spatial directions	ft/s
v	Velocity component normal to the wall	ft/s
V	Voltage	volts
VR	Velocity ratio	--
w	Velocity component in z-direction	ft/s
x	Streamwise/curvilinear coordinate	in
y	Vertical/normal distance	in
y^+	Dimensionless wall distance	--
y_t	Ordinate of point on the surface of a symmetrical airfoil section	in
z	Spanwise direction/distance	in

Greek	Definition	Unit
∇	Vector differential operator (Del)	1/ft
α	Inclination/Injection angle	degrees
β	Compound/Orientation angle	degrees
δ	Boundary layer thickness	in
Δ	Change (Delta)	--
η_0	Overall efficiency	--
η_f	Film cooling effectiveness	--
η_p	Propulsive efficiency	--
η_{th}	Thermal efficiency	--
θ	Normalization temperature	--
μ	Coefficient of dynamic viscosity	$lbf \cdot s/ft^2$
ν	Kinematic viscosity	ft^2/s
ρ	Fluid density	$slug/ft^3$
τ	Shear Stress on a surface	lbf/ ft^2
Φ	Angle measured from the airfoil leading-edge stagnation point	degrees
ϕ	Overall cooling effectiveness	--

Subscripts	Description
#	number
∞	Mainstream or Freestream
aw	Adiabatic wall
b	Blowing Parameter
c	Internal coolant
ce	Coolant exit
f	Film
g	Gas side on freestream
le	Leading Edge
m	Mean
off	without cooling
on	with cooling
r	Ratio
rms	Root mean square
t	Total or Stagnation
w	Wall
x, y, z	3 spatial directions (streamwise, normal and lateral/spanwise)

Superscripts	Description
$\bar{}$	Average conditions
$\tilde{}$	Approximately

1 Introduction

Gas turbine engines are one of the most important inventions in modern engineering history. The development of the gas turbine engine started with Sir Frank Whittle and Hans-Joachim Pabst von Ohain in the 1930's, (see Farokhi [2014]). The gas turbine engine has been used in many different applications from aircrafts to power generators. The fundamental components of the gas turbine are shown in Figure 1.1.

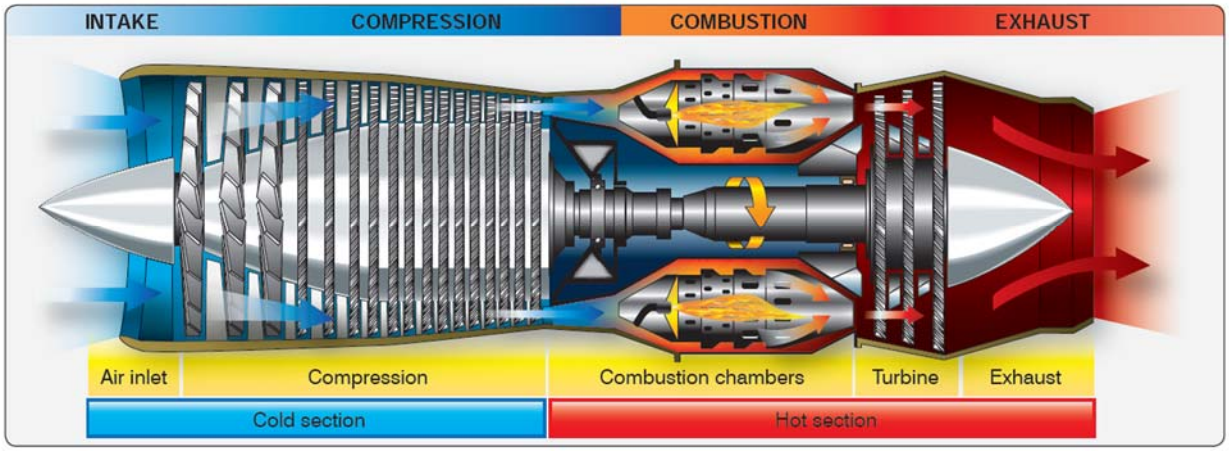

Figure 1.1: Gas turbine components with station numbers, FAA [2016]

One of the major components in the gas turbine engine is the turbine. The turbine is divided up into high and low pressure sections in 2-spool configurations. The turbine's main purpose is to convert thermal energy, from the hot gas flow, into mechanical work for the compressor and fan. The high pressure turbine (HPT spool) is located immediately downstream of the combustor, which is subjected to several thermal and stress environments. A modern combustor generates gas temperatures high enough to exceed the turbine blade's material temperature limits (known as service temperature). The reliability of gas turbine blades is a function of the blade's thermal and stress environments and physical properties such as material type and thermal barrier coatings (TBC). The constant exposure to the hot gases, centrifugal and vibrations

stresses will contribute to the total stress on the turbine rotor. The downtime of an engine for replacing blades is costly and impacts the operation of major airlines. The high temperature of the combustor is the result of improving the engine's overall efficiency (eq 1.1) as derived in Farokhi [2014] and Oates [1997].

$$\eta_0 = \eta_{th}.\eta_p = \frac{F \cdot V_0}{\dot{m}_f Q_R} \tag{1.1}$$

Engine development efforts are concentrated on increasing the engine's overall efficiency; however, the turbine material (single-crystal superalloy: nickel-based alloys) cannot withstand these high temperatures. The only practical solution is to provide continuous cooling to the turbine blade at the appropriate stages. The turbine blade (without cooling) would closely equal the hot gas total temperature. This parameter is known as adiabatic wall temperature and is expressed in equation 1.2 for a stationary blade from Hill & Peterson [1992] and Farokhi [2014].

$$T_{aw} = T_g + r\frac{C^2}{2c_p} \tag{1.2}$$

The coolant is bled from the high or low pressure compressor of the gas turbine engine, which typically reduces the working fluid in that compressor stage and impact engine performance. It is thus an important balance between percent coolant and engine performance.

1.1 Turbine Blade Cooling

The combustion chamber design of gas turbine engines is constantly advancing to improve overall engine performance. The results are causing the combustor exit temperatures or turbine entry temperatures (TET) to be higher than before. Flow around the airfoil causes pronounced hot spots to form on the turbine airfoil, which are the leading edge and transition location. Azad et al. [2000], Farokhi [2014], and Suo [1985] presented a heat transfer coefficient map around an

uncooled turbine blade. The leading edge, i.e., the stagnation point, will show the highest heat flux, due to the stagnation condition on the hot gas side. There is a second peak in the heat flux or heat transfer coefficient caused by the flow transitioning from laminar to turbulent boundary layer. Figure 1.2 shows a turbine temperature map and heat flux distribution for a gas turbine engine, from Farokhi [2014].

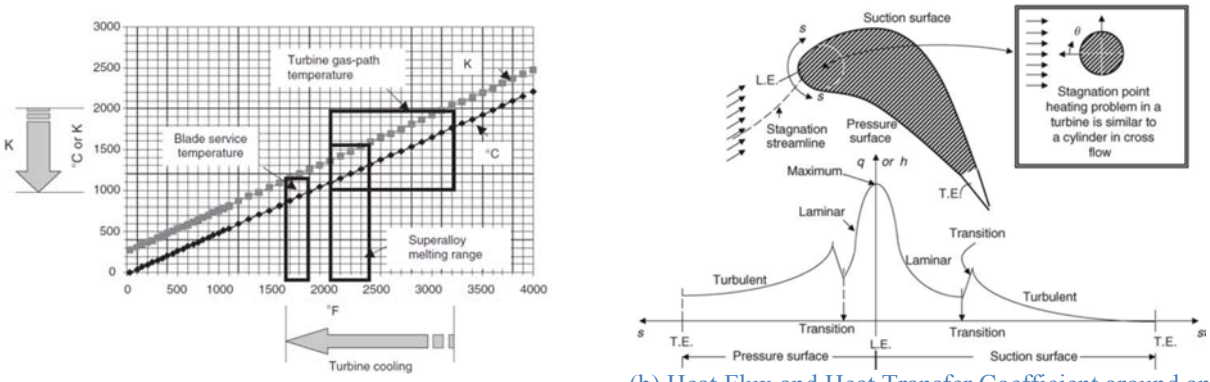

(a) Turbine temperature map

(b) Heat Flux and Heat Transfer Coefficient around an airfoil

Figure 1.2: Diagram of a Turbine Environment, Farokhi [2014]

The turbine blades are thus subjected to this heat flux and requiredcooling techniques are developed to minimize the coolant fraction for a desired blade service temperature. The cooling of a turbine blade can be categorized into two methods, i.e., passive and active cooling. The active cooling methods are divided into internal and external cooling. Table 1.1 shows the classifications of some cooling schemes, Farokhi [2014] and Suo [1985].

Table 1.1: Turbine Cooling Categories

	Passive	Active	
		Internal	***External***
Convective Cooling		X	
Impingement Cooling		X	
Film Cooling			X
Thermal Barrier Coating	X		

These cooling schemes have allowed the TET to be higher than the blade material capabilities. Figure 1.3 shows the inlet temperature for the turbine against the cooling strategies at the entry in service and the forecast to the year 2030.

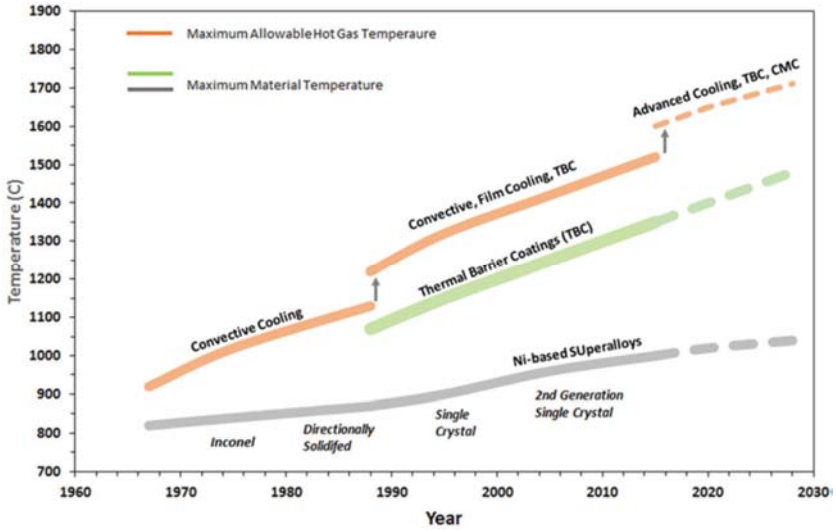

Figure 1.3: TET and Cooling Technology from Naik [2017]

1.1.1 Convective Cooling

Convective cooling has been successfully applied since the 1960's and is the fundamental method for cooling the turbine blade. As the word convective suggest it is the process of using heat transfer due to convection for a fluid and solid surface interface. This forced convection is governed by Newton's Law of Cooling shown in eq. 1.3 from Farokhi [2014] and Moran and Shapiro [2008].

$$q \equiv \frac{\dot{Q}_c}{A} = h \cdot \Delta T \tag{1.3}$$

Coolant is transported through internal passages from the root or tip and is ejected at the rotor tip or nozzle root or trailing edge slots as noted by Suo [1985]. Some internal cooling passages are fabricated with turbulent promoters from pin fin arrays, dimpled surfaces, rib turbulators and swirl chambers, reported in Ligrani [2013] and Farokhi [2014]. These turbulent promoters,

shown in Figure 1.4, establish a turbulent flow fluctuation for higher heat transfer rate. Han et al. [1984] showed the heat transfer and pressure drop in convective cooling passages with these turbulent flow promoters.

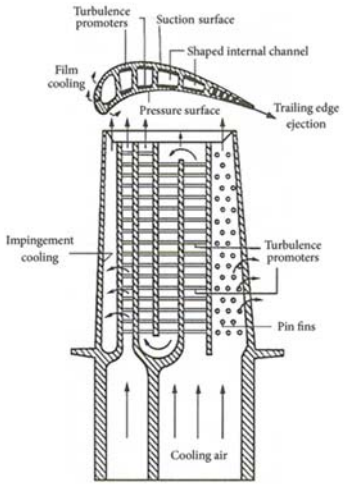

Figure 1.4: Internal Cooling Turbine Blade, Han et al. [1984]

A form of convective cooling is an often an integral part of all active cooling technologies. The main interest of this investigation is the combination of two active cooling schemes, namely impingement and film cooling.

1.1.2 Impingement Cooling

Impingement cooling is one of the most utilized cooling techniques in heat transfer engineering, due to its superior local heat transfer coefficient of the active schemes, according to Han, Dutta & Ekkad [2013]. The heat transfer coefficient is high due to the stagnation region that is formed at the wall. Impingement cooling can be divided up into two strategies, leading edge and midchord cooling, according to Suo [1985]. One of the best applications of jet impingement is on the leading edge of an airfoil or turbine blade where the highest heat flux is encountered. This approach is seen on an aircraft from wing anti-ice to turbine cooling. Often, impingement cooling is employed to target the stagnation point heat transfer for internally-

cooled gas turbine blades. Amano and Sunden [2014] compiled and edited research works on impingement jet cooling in gas turbines, including a chapter on design, applications and limitations from Bunker et al. [2014]. Figure 1.5 (a) demonstrates a simple diagram of a leading edge impingement cooling technique.

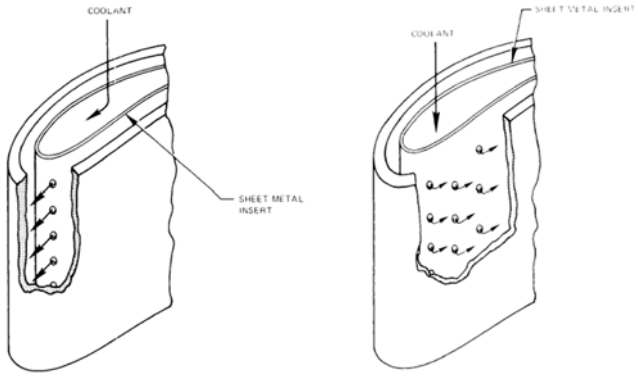

(a) Leading Edge (b) Midchord

Figure 1.5: Impingement cooling, Suo [1985]

Midchord impingement cooling, Figure 1.5 (b), is used for turbine nozzles or stators, which are stationary and may be bulkier than a rotor blade. The thicker wall in the nozzle is needed to handle the thermal stresses caused by the high cooling effect of the impingement jet. There are many parameters that impact the effectiveness of the impingement jet. These parameters include the wall surface topology (flat, concave or convex in 2D and 3D), jet nozzle diameter/spacing, wall to jet distance and Reynolds number based on the jet diameter as noted by Hadier [2015]. Figure 1.6 shows a diagram of important geometric parameters related to impingement cooling.

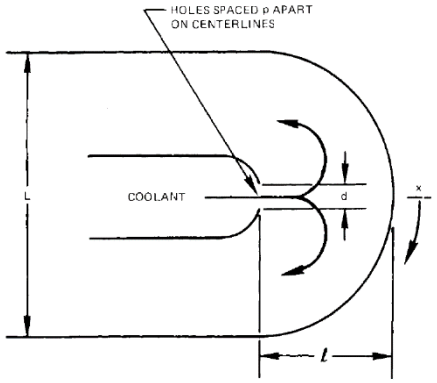

Figure 1.6: Definition sketch for the Impingement Cooling on the Airfoil Leading Edge, Chupp et al. [1969]

There have been extensive studies of impingement on flat plate from Goldstein and Timmer [1982], Ekkad et al. [1999],Ingole and Sundaram [2016], Zhou et al. [2016], Lee et al. [2014&2015] and Bergman et al. [2011]. The focus of the current research is on a concave wall which forms the internal leading edge of an airfoil.

Chupp [1969] and Metzeger [1969 & 1972] did some early pioneering study on the effect of leading edge curvature and heat transfer with impingement cooling. They showed that a flat plate impingement is less efficient than a corresponding concave wall. Colladay [1975] reported the heat transfer coefficient correlation to the leading edge on a cylinder in a cross-flow. The correlation is for a laminar boundary layer with an augmentation factor introduced for the turbulent boundary layer. Kreith & Bohn [2001] conveyed that the heat transfer coefficient for the cylinder in cross flow can be found from the Nusselt number (Nu) shown by Squire [1950]. Squire [1950] equation for Nu is shown in eq. 1.4 and Colladay [1975] modified formula for the convection heat transfer coefficient is displayed in eq. 1.5.

$$Nu(\theta) = \frac{h_c(\Phi)D}{k} = 1.14\left(\frac{\rho U_\infty D}{\mu}\right)^{0.5} Pr^{0.4}\left[1-\left(\frac{\Phi}{90}\right)^3\right] \tag{1.4}$$

$$h_{g,le} = a\left[1.14\frac{k_g}{D}\left(\frac{\rho_g U_g D}{\mu}\right)^{0.5} Pr^{0.4}\left[1-\left(\frac{\Phi}{90}\right)^3\right]\right] \tag{1.5}$$

Hadier [2015], Martin [2011], Azimi et al. [2015], Andreini et al. [2015], Liu and Feng [2011] and Yang et al. [2011] furthered the study of impingement cooling on concave surfaces. Hadier [2015] simulated the effects of jet H/D with different jet diameters, which showed that the larger diameter had the highest Nusselt number for x/ D (curvilinear distance to diameter) from 0 to 15. Martin [2011] conducted experiments for (pitch-diameter ratio) P/D and H/D, of 2, 4 and 8, and reported that lower P/D with lower H/D had the highest average stagnation Nusselt Number. Azimi et al. [2015] tested and simulated the effects of H/D on the curvature of a concave surface, and reported the Nu_θ for a curvature angle measured from the stagnation point. Azimi et al. [2015] showed that lower H/D produces a high Nusselt number along the curved surface. Suo [1985] and Kerrelbrock [1992] reported that that Chupp et al. [1969] research produced the same conclusion but reported in a format of the Nusselt number divided by the stagnation Nusselt number. Han et al. [2013] and Naik [2017] also produce the same result for the higher and lower H/D effects on the Nusselt number. Liu and Feng [2011] and Liu et al. [2018] performed Computational Fluid Dynamics (CFD) simulations on an airfoil leading edge with different impingement jet locations from the center of the concave wall. The jet to wall distance affects the Nusselt number due to the entrainment of the surrounding air, as shown in Figure 1.7. The farther away from the jet inlet, there is higher mixing and entrainment that would occur on the jet, from Capone et al. [2013].

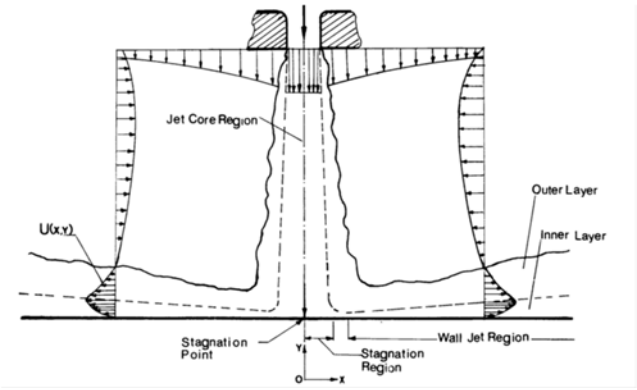

Figure 1.7: Impingement Jet Flow, Kayansayan [1978]

1.1.3 Film Cooling

The film cooling promotes the creation of a cool boundary layer shield or blanket on the suction or pressure surface as external cooling. A coolant is ejected through the film holes into the boundary layer to lower the heat transfer to the wall. This interaction between the film jet and the hot gas causes a pressure loss by disrupting the natural boundary layer, according to Kerrebrock [1992]. Film cooling is thus a balance between the aerodynamics, structure and thermodynamic tradeoffs, which may be negative or positive. The diameters of the film holes are larger than the boundary layer thickness; therefore, the momentum of the freestream and jet determine the detachment and reattachment of the film jets to the surface, Kerrebrock [1992]. There are four key non-dimensional parameters used to determine the cooling jet versus the freestream flow: blowing parameter, momentum flux ratio, velocity ratio and density ratio. The blowing parameter is defined in eq. (1.6) from Hill and Peterson [1992] and Farokhi [2014].

$$M_b = \frac{\rho_{ce} U_{ce}}{\rho_g U_g} \tag{1.6}$$

Kodzwa and Eaton [2005] expressed that the typical blowing parameter is in the range of 0 to 5. The momentum flux ratio is defined by eq. (1.7), acquired from Bogard and Thole [2006] and Mattingly et al. [2002].

$$I = \frac{\rho_{ce} U_{ce}^2}{\rho_g U_g^2} \tag{1.7}$$

The velocity ratio describes the coolant velocity to the velocity of the freestream flow, and is defined in equation 1.8 from Bogard and Thole [2006].

$$VR = \frac{U_{ce}}{U_g} \tag{1.8}$$

The density ratio is based on the temperature and pressure of the freestream and coolant flow and is defined by equation 1.9 based on perfect gas law.

$$DR = \frac{\rho_{ce}}{\rho_g} = \frac{p_{ce} T_g R_g}{p_g T_{ce} R_{ce}} \tag{1.9}$$

The typical DR is around 2.0 for the gas turbine engine according to Bogard and Thole [2006]. These non-dimensional parameters are dependent on the density and velocity of the coolant to the freestream ratio. Figure 1.8 shows a simple diagram of the hot gas (freestream) and coolant gas.

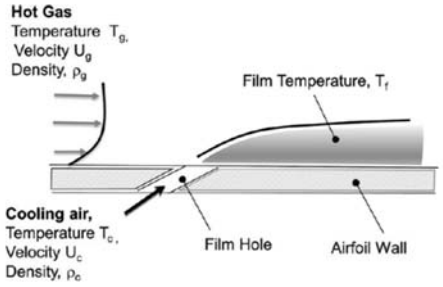

Figure 1.8: Cooling air and hot gas film cooling diagram, Naik [2017]

One should note that the evaluation of film cooling is based on normalizing the temperatures by the temperature differential between the gas and the coolant. The standard normalized equation is defined in equation 1.10.

$$\theta = \frac{T_g - T}{T_g - T_{ce}} \tag{1.10}$$

Using the normalized equation, the local film cooling effectiveness (η) is defined as eq. (1.11) from Suo [1985],

$$\eta_f = \frac{T_g - T_f}{T_g - T_{ce}} \tag{1.11}$$

If the wall is insulated, i.e., adiabatic wall, then it is called the adiabatic film cooling effectiveness. The second evaluation parameter is the overall cooling effectiveness, which accounts for the internal and external cooling of the system. The overall cooling effectiveness is defined in eq. (1.12) from Williams et al. [2013], where the coolant temperature is at the entrance of the system.

$$\phi = \frac{T_g - T_w}{T_g - T_c} \tag{1.12}$$

Note the coolant temperature for the adiabatic film cooling effectiveness is the same as the overall film cooling effectiveness. Film cooling performance is dominated by turbulence intensity, density/velocity ratio, geometry of the hole and geometry of the airfoil according to Bogard [2006]. The geometry of the hole is defined as the shape of the hole, L/d, P/d, inclination (α) and compound (β) angle. The geometry of the airfoil consisted of hole locations, surface curvature and roughness, Bogard [2006]. Figure 1.9 shows the geometry of a film hole and design margins.

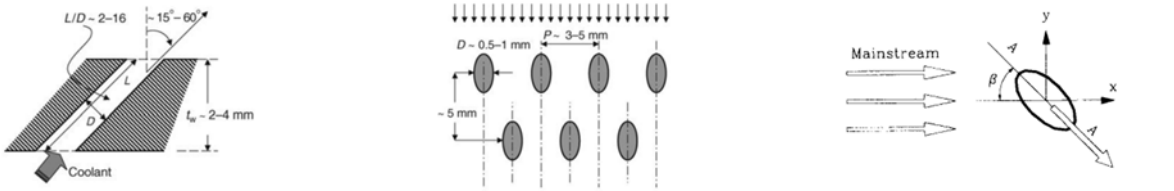

(a) Cross-section, Farokhi [2014] (b) Row Spacing, Farokhi [2014] (c) Compound Angle, Cho et al. [2001]

Figure 1.9: Geometry of a typical film cooling system

Film cooling research has a long history in gas turbine engines; therefore, Bogard and Thole [2006] and Kodzwa and Eaton [2005] summarized the history of film cooling in their works. Airfoils represented the characteristics of a turbine blade, and the majority of the reported research focused on a flat plate test article. Jung and Lee [1999] operated an open-circuit

subsonic wind tunnel with a plate resting on the bottom wall. The adiabatic film cooling effectiveness was studied with a velocity ratio of 0.5, 1.0 and 2.0. The Jung and Lee [1999] experiment showed that a lower velocity ratio had better performance over the higher velocity ratios. As the first part of Leylek's research, Walters and Leylek [1997] presented an experimental and numerical approach to the flat plate film cooling investigation. An L/d of 3.5 with an inclination of 35 deg was recorded for the centerline local film cooling effectiveness of a blowing parameter of 0.5 and 1.0. Walters and Leyleck [1997] reported the experiment for M_b of 0.5 showed a high effectiveness and 1.0 displayed a small detachment at the injection point. Dees et al. [2013] and Dees [2010] reported airfoil research for the momentum and blowing parameter from I = 0.34 to 1.41 or M_b = 0.65 to 1.3. The results showed the overall and film cooling effectiveness at different locations for the momentum flux ratios. Following Dees [2010], Williams et al. [2013] results are collected for a range of I = 0.18 to 5.0 with the overall and film cooling effectiveness being calculated at multiple positions. Dees [2010] and Williams et al. [2013] used a single row of film holes on the airfoil to show the higher cooling effect for a lower momentum flux ratio jet.

The combustor is a highly turbulent environment, where the turbulence and temperatures are significantly higher than the other components of the gas turbine engine. The turbulence intensity entering the 1st stage of the nozzle guide vane is roughly 10-25%, according to Farokhi [2014]. The equation for turbulent intensity follows the standard definition shown in equations 1.13 and 1.14, e.g., Schetz and Bowersox [2011].

$$Tu = \frac{u_{rms}}{U_m} \tag{1.13}$$

$$u_{rms} = \sqrt{\frac{1}{3}\left(u_x^2 + u_y^2 + u_z^2\right)} \tag{1.14}$$

Repko et al. [2016] simulated a high blowing ratio of 2.0 on a flat plate and showed the turbulent intensity effects (5%, 10% and 20%) on the film cooling jet. Repko et al. [2016] showed the lateral spreading effect of the adiabatic film effectiveness. Cutbirth and Bogard [2002], Dees et al. [2013], Williams et al. [2013], and Waye and Bogard [2006] collected data for the turbulent intensity of 0.5 to 21 percent at the University of Texas at Austin, showing that a high Tu would cause high lateral spreading of the jet. Further data support the findings of the Bogard research team, which include Tu of 0.5 to 12.5% from Burd et al. [1998], Mayhew et al. [2004], Islami and Jubran [2012], Al-Hamadi et al. [1998], Wu et al. [2014] and Wright et al. [2011].

The geometry of the hole and wall is important because it determines the injection (hydrodynamic) characteristics of the jet. The film hole length to diameter is dependent on the inclination angle and the thickness of the wall. Gritsch et al. [2001] tested multiple α values, causing a range of L/d of 3 to 6, which showed the discharge coefficient for 30, 45 and 90 deg. The 30 and 45 degrees showed similar a trend, while 90 degrees had a lower discharge coefficient. Song et al. [2017] showed flow field visualization of different inclination angles of 20 to 40 degrees for blowing parameters of 0.5 to 1.5. These flow visualizations showed detached and attached jet flows.

In addition, Gritsch et al. [2001], McGovern and Leylek [1997], and Brittingham and Leylek [1997] examined the orientation/compound angle effects to the film cooling jet. McGovern and Brittingham reported simulations showing that a symmetric counter rotating vortex would form and become asymmetric as the compound angle increased. McGovern and Brittingham found that compounding increases the lateral distribution for the film cooling effectiveness. Brittingham and Leyleck [1997], further researched the shaped of the hole exit

following Hyams and Leylek [1997] and Goldstein et al. [1974], and showed the shape of the holes would expand the jet and spread the jet laterally increasing the covered surface area.

1.1.4 Other Cooling Technologies

One of the passive ways to improve the cooling of an airfoil is to reduce the thermal conductivity or increase the resistance to heating. Thermal barrier coating (TBC) is a method in which a thin layer (~0.015 in) of highly resistance (low thermal conductivity) material is coated on the surface of the blade, according to Suo [1985] and Clarke et al. [2012]. Furthermore, changing the nozzle airfoil from Nickel-base alloy to a ceramic matrix composite (CMC), a high thermally resistance (low thermal conductivity) material. Ceramic matrix composites have been researched for a long time, but now CMCs are being introduced to the hot section of the gas turbine engine and combustor liners, Zok [2016]. Takeshi et al. [2014] shows a vane compiled of Al_2O_3 and SiC (silicon carbide), which was tested for a life-cycle and real environment assessment, and showed excellent results. The big three aircraft engine companies (General Electric, Pratt & Whitney and Rolls-Royce) have increased their research in CMC for turbine applications due to the potential for higher TET, according to Gardiner [2015]

Other active cooling technologies include transpiration and end wall cooling. Transpiration cooling is highly effective due to the porous structure shown in Wang, et al. [2004] and Moskowitz and Lombardo [1971] under ideal circumstances. The porous structure however comes with structural, manufacturing and clogging issues. Henderson [1969] reported a loss in pressure around a porous cylinder compared to a solid cylinder. At this time, the problems with transpiration cooling outweigh the beneficial cooling effects for turbine blades.

As TET increases, there has been a need for end wall cooling (tip cooling) for the turbine blade. End wall cooling is based on impingement and film cooling at the blade tips and shroud. Naik [2017] described key parameters and tip designs for cooling the end wall. Understanding the aerothermodynamics of the turbine blade tip region is a complicated subject. Taskeishi, et al. [2012] experiments showed the heat transfer effects of swirling flow on the endwall of a first stage nozzle.

1.2 Objectives

The major contribution of this research is the development and testing of the thermal wind tunnel with an integrated impingement and film cooling scheme. A combination of impingement leading edge and suction surface film cooling was investigated to provide an understanding of the thermal gradient on a blunt airfoil. The leading edge impingement cooling incorporates an arrangement of jets producing internal stagnation points on the opposing side of the freestream stagnation line. The internal coolant is expelled to the suction surface of the airfoil through film holes. The film cooling promotes a cool boundary layer shield on the suction surface for external cooling. The experiments focused on the film cooling effects on the airfoil. The film cooling boundary layer is measured with arranged surface thermocouples. Numerical research will show the complete cooling scheme from adiabatic and conjugate heat transfer CFD models. This dissertation will report the experimental and numerical findings of the combined cooling scheme.

2 Experimental Investigation

The experiments in the thermal wind tunnel facility were conducted at the Mal Harned Propulsion Laboratory of the University of Kansas. The laboratory is located at the University of

Kansas facility at the Lawrence Municipal Airport, which is inside a 3,840 square foot hangar, Figure 2.1. The thermal wind tunnel was design to be a subsonic open-circuit tunnel and mount to a portable test stand. Testing was completed in an open atmospheric engine test chamber with the dimensions of 24x12x10.5 feet. The test chamber is constructed of 6 to 12 inch thick reinforced concrete, which was designed to handle multiple engine tests.

(a) Propulsion and Fabrication Hangar

(b) Propulsion test camber

Figure 2.1: University of Kansas Facilities

2.1 Apparatus and Equipment

Additional images of the experiment and setup can be obtained in Appendix A.

2.1.1 Heat and Flow Source

The heat source for the experimental facility came from a small gas turbine (GT) for a radio-controlled aircraft. The GT engine is an Olympus HP engine produced by AMT Netherlands, shown in Figure 2.2. The operation of the GT was done by following the Olympus HP manual from AMT Netherlands, van de Goor [2017]. Key engine parameters, EGT, RPM and throttle, were monitored via AMT Netherlands telemetry software. The engine control unit (ECU) monitors and sends the data to the telemetry software to monitor the turbine performance. The engine can reach an exhaust gas temperature (EGT) of 1382 °F and max thrust of 51 lbs. In this study, the engine is maintained at idle (35,500 rpm) to protect the engine and the tunnel. The EGT stayed at a constant temperature of 842 °F. The Olympus HP runs on Jet A with a 22 to

1 turbine oil fuel mixture. The tunnel gas flow components are the combustion gases from the micro-jet and the ambient air that is entrained through an ejector nozzle.

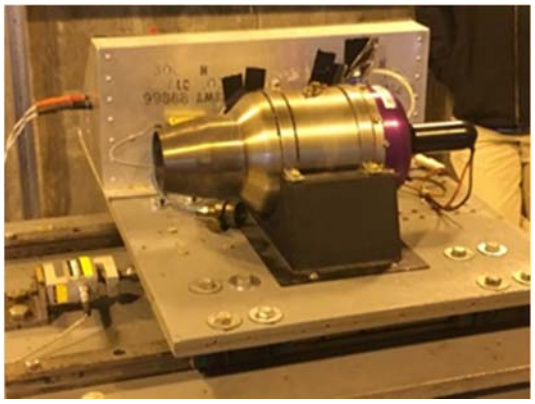

Figure 2.2: AMT Netherlands Olympus HP engine

2.1.2 Thermal Wind Tunnel

The tunnel is constructed from 1/32nd inch thick sheet metal riveted together by 1/32nd inch thick custom flanges. The tunnel is comprised of three separate sections: inlet, ejector/mixer and the test section. Figure 2.3 shows the constructed/assembled tunnel that features an 8 in. x 8 in. test section.

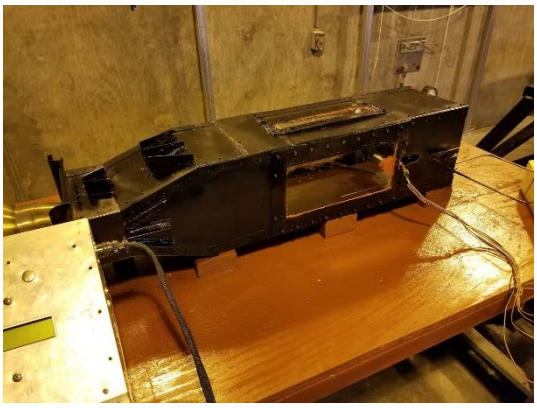

(a) Side View

(b) Rear View

Figure 2.3: Thermal Wind Tunnel

The inlet's cross sectional dimension is 8 in. x 4 in. with a length of 3 inches. One of the major components of the inlet section is the bell mouth construction for the ejector nozzle. The curved inlet lip aids with a smooth entrainment flow and efficient mixing with the exhaust plume of the

engine. The tunnel temperature is controlled through the ejector nozzle entrainment. After passing through the inlet, the flow enters an expansion/mixer section of 6 inches of length, where the flow is diffused in an expansion duct with an area ratio of 2. This diffuser is designed with three sets of splitter vanes, two vertical sets and one horizontal for efficient mixing. The expansion duct with splitter plates is designed to prevent flow separation, promote mixing and uniformity in the test section. The test section has an 8 in. x 8 in. cross section and a length of 26.5 inches.

A symmetric NACA 0024 airfoil with a 6 inch chord is installed at a zero angle of attack with the leading edge 11.7 inches from the rear of the test section. Two 14 in. x 5.5 in. glass windows were molded into the sides of the test section to allow for optical access and flow measurement. A 14 in. x 2 in. section was cut from the top of the test section for a laser to illuminate the flow for greater visibility. The length before the airfoil is sized to provide spatial mixing and uniformity in the test section. A NX (CAD) model was generated of the tunnel and test article, shown in Figure 2.4 and Appendix B.

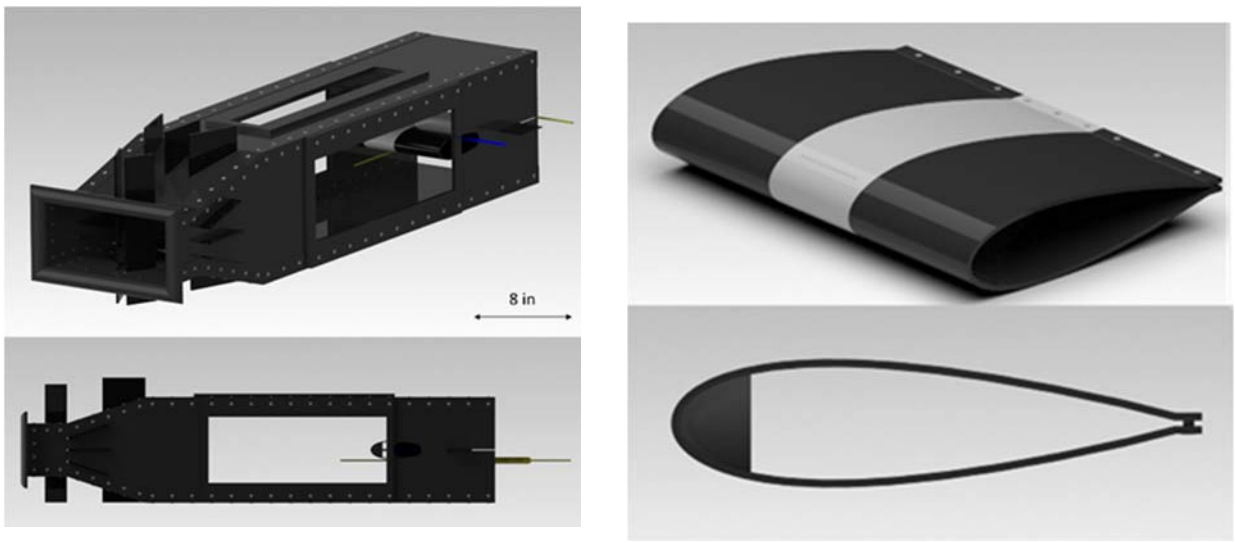

(a) Thermal Wind Tunnel Designed and Fabricated for Gas Turbine Heat Transfer Research

(b) Test Article

Figure 2.4: CAD Models

2.1.3 Thick-Airfoil Selection for Heat Transfer Research

The test article is a NACA 0024 airfoil scaled to a chord length of 6 inches, shown in Figure 2.5.

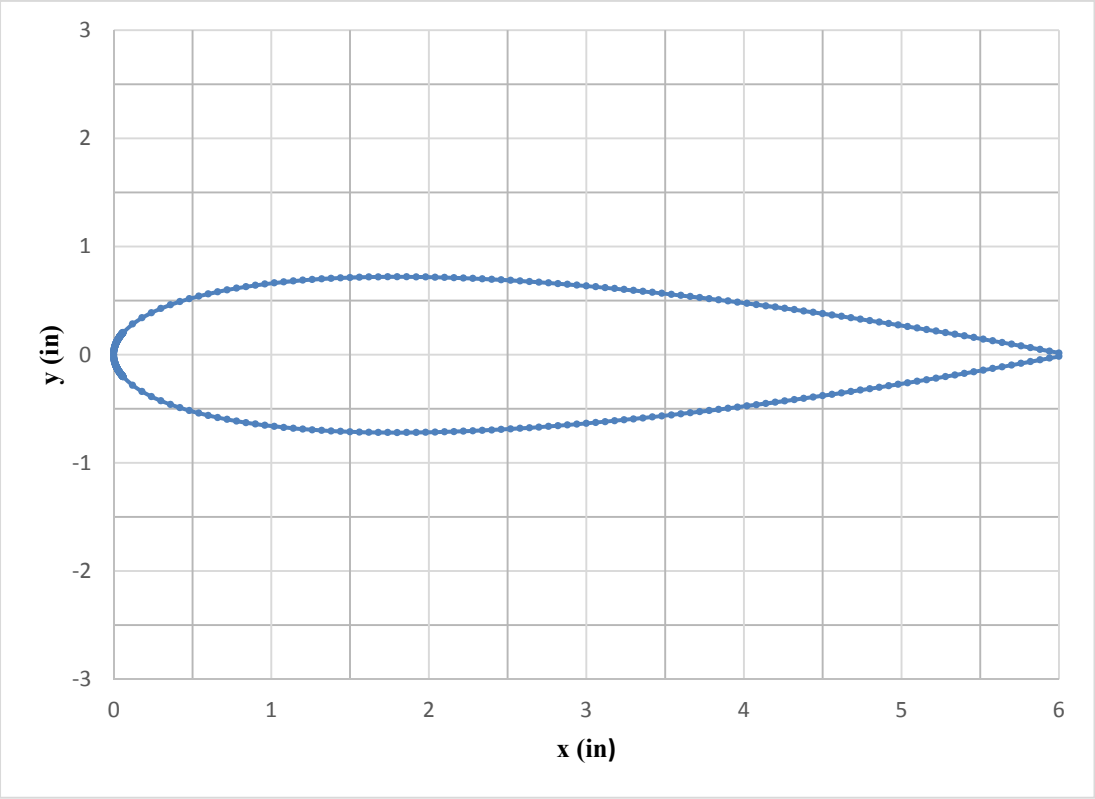

Figure 2.5: NACA 0024 airfoil section scaled to a chord length of 6 inches

NACA 0024 is a four-digit section, where the thickness distribution is determined by equation 2.1 and the leading edge radius is given by equation 2.2, from Abbott [1959].

$$y_t = \frac{t}{0.20}\left(0.29690\sqrt{x} - 0.12600x - 0.35160x^2 + 0.28430x^3 - 0.10150x^4\right) \quad (2.1)$$

$$r_t = 1.1019t^2 \quad (2.2)$$

The model is molded out of an aluminum 6061 sheet with a wall thickness of 0.09 inches. The sheet metal was heated and shaped to a NACA 0024 3D printed mold, shown in Figure 2.6.

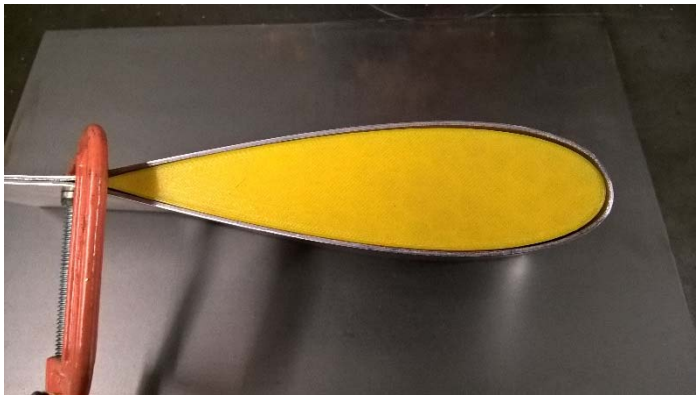

Figure 2.6: NACA 0024 molding

The airfoil has an 8 inch span with a 2 inch test section span in the center (Figure 2.7). The surface roughness inside and outside of the airfoil was sanded with a 1000 grit emery cloth to create a smooth surface. The walls adjacent to the cooling passage are insulated with silicone and fiberglass insulation to simulate an adiabatic wall condition. Thermal conductivity for aluminum 6061 was obtained from Department of Defense [2003].

Figure 2.7: Test Article

2.1.4 Cooling System

A single cylinder air compressor is used to provide coolant for the airfoil. The compressor was sized to ensure a constant pressure for the cooling ejector. The compressor is connected to three regulators to hold a cooling ejector pressure of 0.5 psig. The first regulator was held at 80 psig to keep a high reservoir pressure. The second regulator was held at 25 psig

for a flow regulator. The third digital regulator used the static pressure of the flow regulator to maintain the low pressure for the ejector. The cooling ejector diameter is 5/64th inch, which is blowing off center onto the impingement showerhead holes, displayed in Figure 2.8.

Figure 2.8: Cooling ejector

2.1.4.1 Impingement Cooling

The impingement cooling at the leading edge is done by a sheet metal insert with 8 holes with a diameter of 1/16th inch equally spaced of 3/16th inch, Figure 2.9. The shower plate is positioned to impinge cooling air onto the leading edge of the airfoil from a distance of 1/8th inch.

Figure 2.9: Sleeve insert with impingement cooling holes

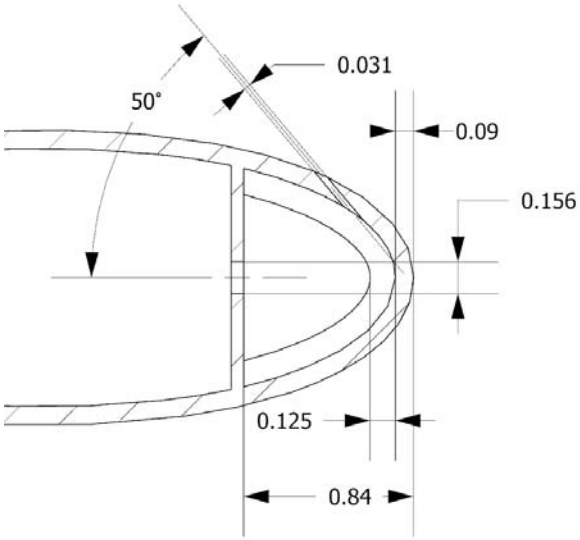

Figure 2.10: Diagram of the Test article at the center plane (inches)

The H/D for the impingement cooling system is 2 (Figure 2.10) and typical H/D is in a range of 1 to 3, Han et al. [2013].

2.1.4.2 Film Cooling

There are fifteen cylindrical film holes with a diameter of 1/32nd inch (tolerance: -0 to +1/64 in) and spacing of 3/32nd inch, Figure 2.11(a). The film inclination angle of the holes is ~ 50 degrees and ~40 degree tilt angle, Figure 2.11(b), causing a length-to-diameter ratio (L/d) of ~3.76 with a compound angle of 0 degree, equation 2.3.

$$\frac{L}{d} = \frac{\left({}^{t_w}/_{\sin\alpha}\right)}{d} \tag{2.3}$$

(a) Spacing

(b) Tilt Angle

Figure 2.11: Machined film cooling holes on the instrumented blade

Film holes machining are normally accomplished by laser (LBM), electron-beam (EBM) or electro discharge (EDM) machining, Farokhi [2014] and Bogard & Thole [2006]. The film holes in the test article are drilled with a Dremel 3000 at 35000 rpm with end mill bits. The holes are drilled ~0.60 inches downstream of the airfoil stagnation point for experimental research purposes. These dimensions are correlated with Farokhi [2014] and Suo [1985] and are shown in Table 2.1.

Table 2.1 Guidelines for film hole design in inches, Farokhi [2014]

	Typical Design	Article Design
Diameter (in)	3/128 to 5/128	1/32
Length to Diameter	2 to 16	3.76
Tilt Angle (deg)	15 to 60	40±5
Wall Thickness (in)	5/64 to 5/32	0.09
Pitch/Spacing (in)	15/128 to 25/128	3/32
Pitch to Diameter	3 to 10	3

The film cooling blowing ratio was set to 5.75, which correlates to a momentum flux ratio of 28.44.

2.1.5 Instrumentation

The static and total pressures are measured by two independent pressure instrumentations for error reduction. The Honeywell 143PC01D is used to collect the bulk differential pressure data of the thermal wind tunnel at a sample rate of 100 samples per second. The differential pressure information is cross referenced with the Dwyer – Series 477 Digital Manometer. In addition, the Series 477 is used to collect the static pressure data of the tunnel at the Pitot tube and the airfoil. The Pitot tube has five static ports that are six diameters downstream of the stagnation port. This is shown in Figure 2.12(a). The location of the Pitot tube is placed three inches ahead of the airfoil, as shown in Figure 2.12(b). The pressure data has an error of 2% for both pressure transducers.

(a) Ports locations

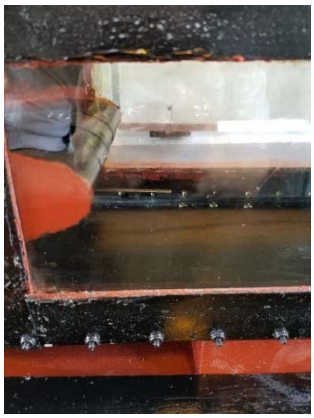

(b) Pitot placement

Figure 2.12: Pitot - static tube

The calibration of the Honeywell pressure transducer is performed in house, shown in Figure 2.13. The signals from the pressure transducer are sent to a Labview program, which converts the voltage to psig utilizing the calibration. The Dwyer manometer is calibrated at the Dwyer institute.

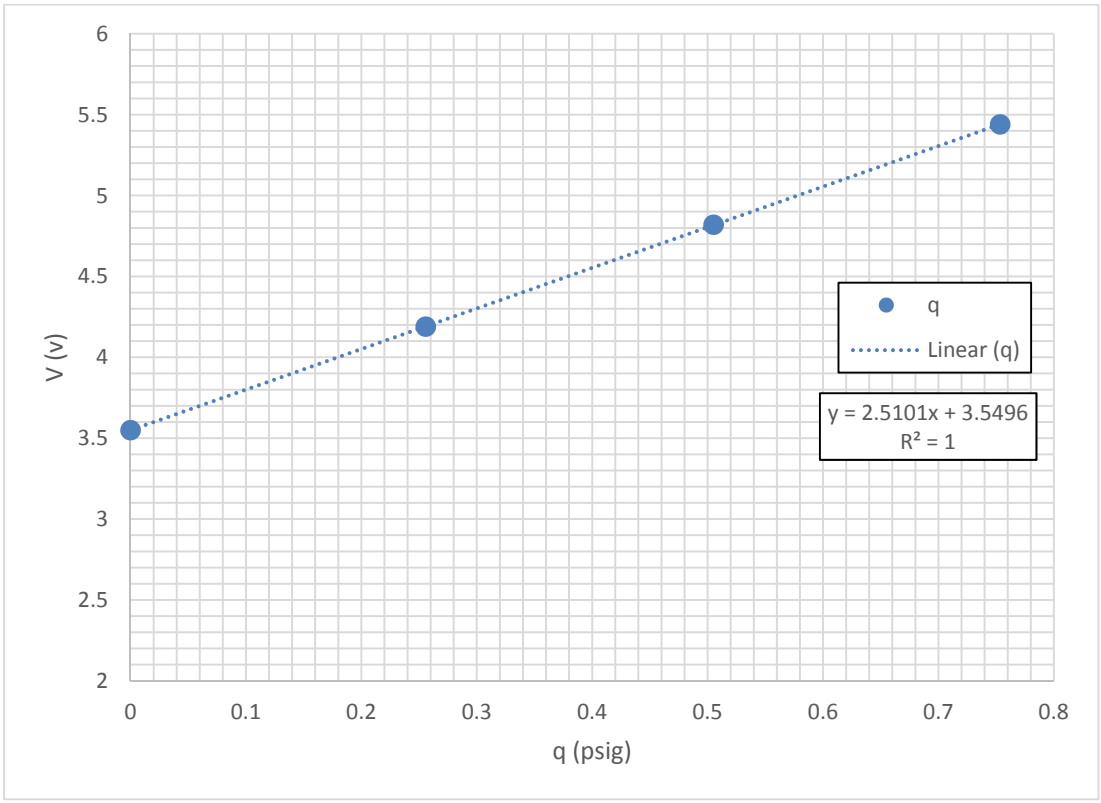

Figure 2.13: Honeywell 143PC01D Pressure Transducer Calibration

The freestream temperature is recorded by the Omega HH85 and a Type K thermocouple probe throughout the test. The temperatures on the surface of the airfoil are measured using the National Instruments SCXI-1112 board with eight Omega Type K thermocouples. The thermocouple signals are sent to a second Labview program, which converts the signals into °F at a sample rate of 100 samples per second per thermocouple. The thermocouple locations are shown in Figure 2.14 and Table 2.2. They are secured in place with a high temperature epoxy at a height range of ~1/64th inch above the surface. The thermal accuracy has an error of 1 to 2 percent.

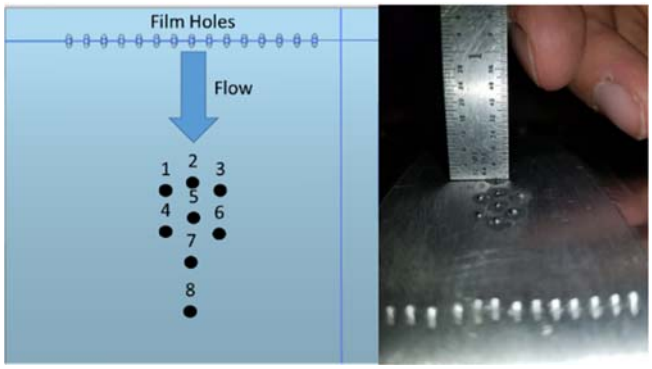

Figure 2.14: Surface Thermocouples

Table 2.2: Thermocouple Location from Centerline Stagnation Point

#	x (in)	y (in)	z (in)
1	1.15	0.785	-0.14
2	1.11	0.780	0.00
3	1.15	0.785	0.14
4	1.35	0.805	-0.13
5	1.27	0.799	0.00
6	1.35	0.805	0.13
7	1.48	0.817	0.00
8	1.71	0.821	0.00

The calibration of the Omega HH85 is carried out by the Omega calibration department. Each surface thermocouple for the SCXI-1112 is calibrated to the Omega HH85 by adding an offset to the Labview program before each test session.

2.1.6 Particle Image Velocimetry

In addition to the standard instrumentation, particle image velocimetry is used to determine the velocity and turbulence intensity of the freestream. The system is shown in Figure 2.15.

Figure 2.15: Particle Image Velocimetry Setup in the Thermal Wind Tunnel

The laser beam used in the setup is a blue 450 nm with a maximum output of 4.5 Watts. The beam is shot from an elevated position on a reflected mirror into the top of the tunnel. A 9:1 (mineral to olive oil) mixture is used to create the smoke particles for illumination. These smoke/seeding particles are tracked by a NAC HX7 camera at 6000 frames per second. The camera calibration at this focus is 0.1064 mm/pixel, which is used in the determination of freestream velocity (equation 2.4) and turbulent intensity of 19.08 ft/s and ~13.5 percent, respectively. An in house Matlab code with LaVision software is used to find the pixel per frame (Figure 2.16).

$$U_\infty = v\frac{pixel}{frame} * 0.1064\frac{mm}{pixel} * 6000\frac{frame}{sec} \tag{2.4}$$

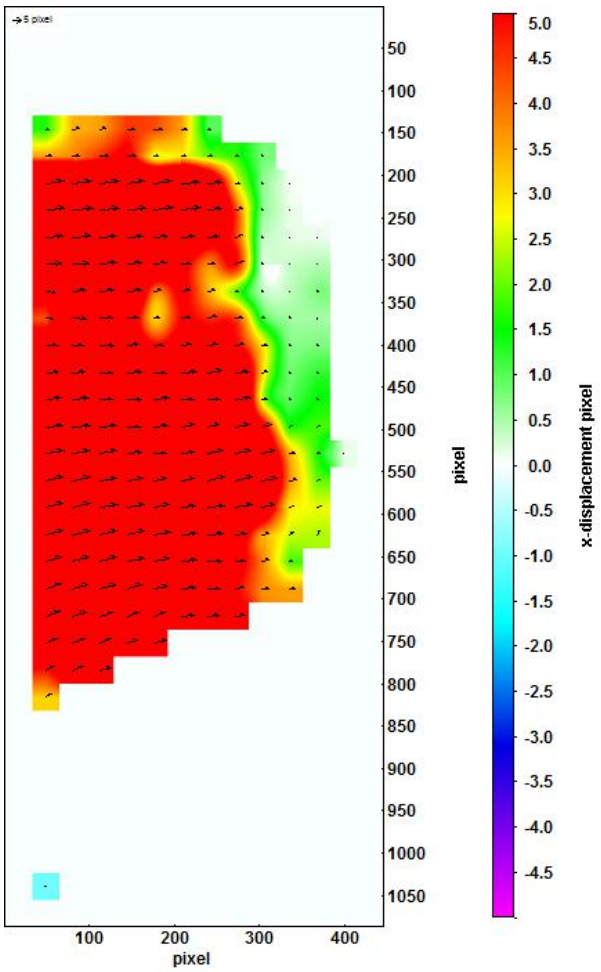

Figure 2.16: Particles displacement in x-direction from PIV

3 Experimental Results

The test chamber is opened to ambient conditions, which is measured during testing. The ambient temperature and pressure are 38.80 °F and 30.03 in.Hg (14.75psia), respectively. This session involved three ground tests for a duration of 30 to 40 minutes. The test duration is based on the thermodynamics of the steady state operation in the system. Steady state is defined as one degree change per minute.

An important parameter needed from this test is the freestream temperature measurement. This temperature remained constant throughout numerous test sessions within 400 to 415 °F.

The measurements are made 3 inches upstream of the airfoil at different lateral positions, seen in Figure 3.1. The freestream temperature is determined to be 408°F from the average of the average of the freestream temperature measurements.

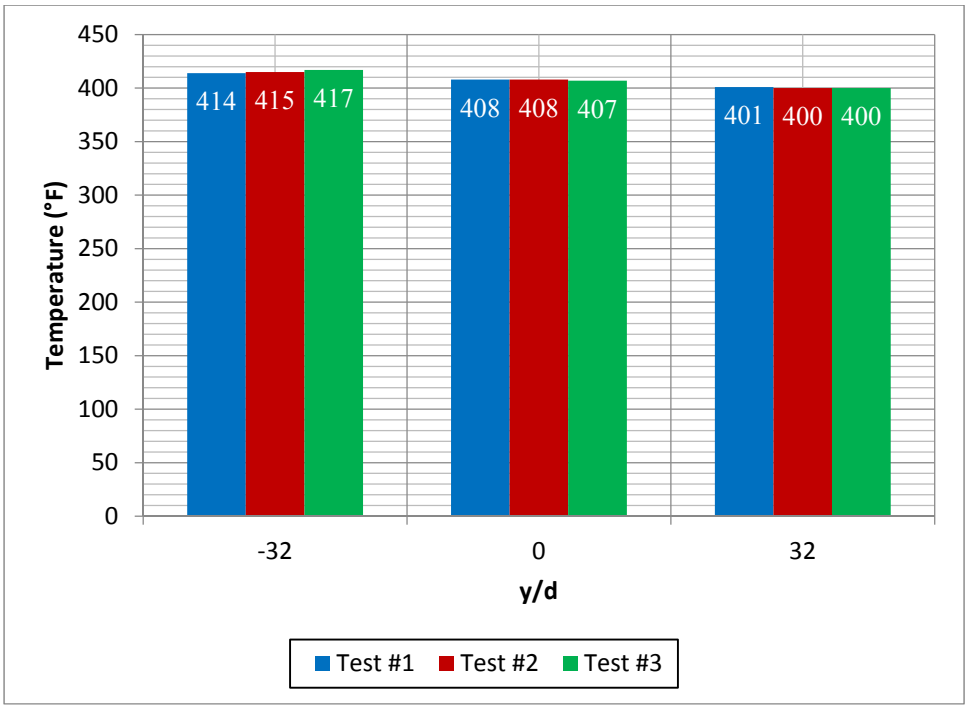

Figure 3.1: Lateral Temperatures for the Freestream Flow at 3 inches upstream

The second freestream parameter collected is the test section gas speed. The velocity in the test section is calculated by the total and static pressures from the Pitot-static tube (Prandtl Tube) using Bernoulli's equation (eq 2.5) and the equation of state (eq 2.6), Anderson Jr. [2011].

$$p_\infty + q = p_\infty + \frac{1}{2}\rho U^2 = p_t \tag{2.5}$$

$$p = \rho RT \tag{2.6}$$

The pressure data for three tests are shown in Figure 3.2 & 3.3, where the average differential and static pressures are 0.00168 psig and -.00131 psig, respectively.

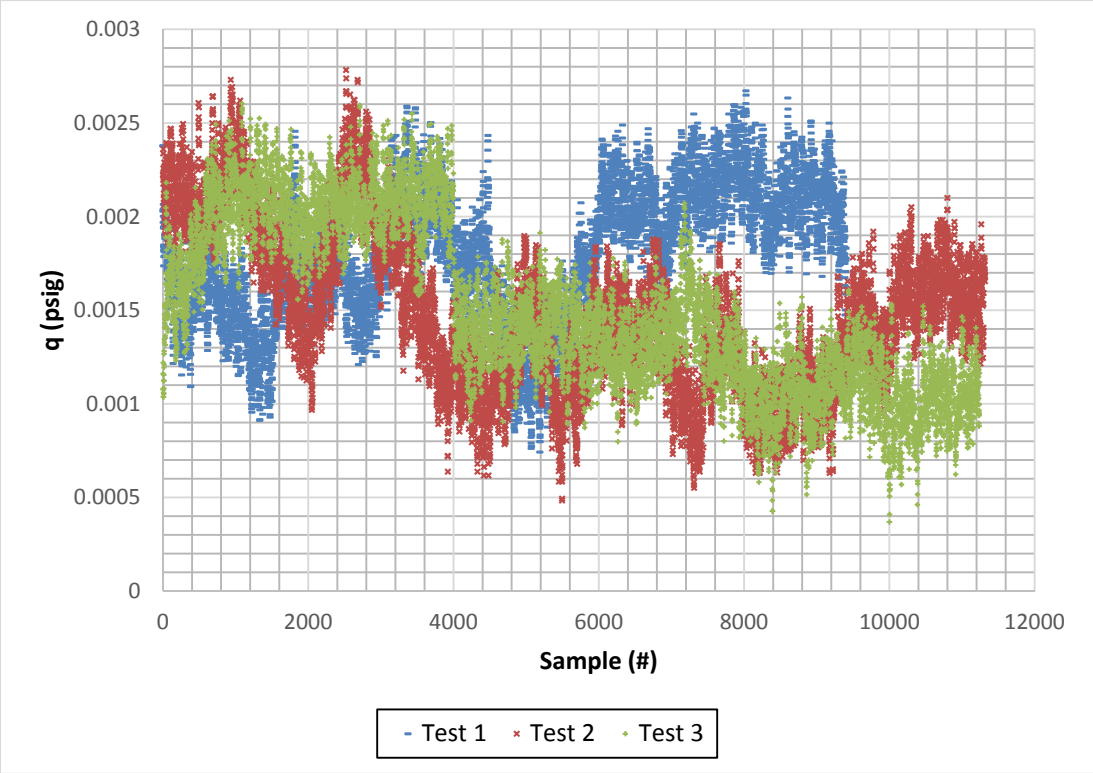

Figure 3.2: Honeywell Pressure Data

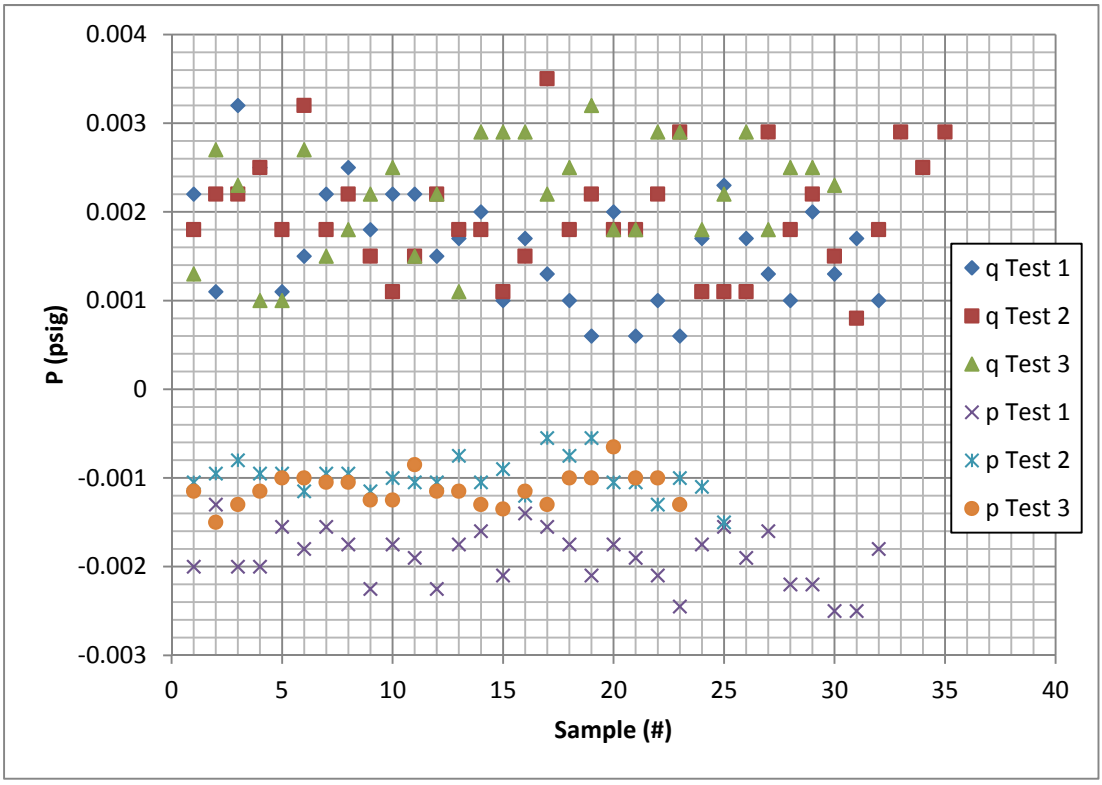

Figure 3.3: Dwyer Pressure Data

The velocity of the freestream, 18.47 ft/s (5.63 m/s), is calculated from the pressure data. This velocity closely matches the PIV measurement of 19.08 ft/s (5.81 m/s). The average surface temperatures show a cooling trend of 15 to 20 °F when the cooling system is turned on and has achieved a steady-state condition, this is shown in Table 3.1, Figure 3.4 and Appendix C.

Table 3.1: Thermocouple Temperatures

	T_1 (°F)	T_2 (°F)	T_3 (°F)	T_4 (°F)	T_5 (°F)	T_6 (°F)	T_7 (°F)	T_8 (°F)
OFF	374.67	374.09	370.94	374.48	372.27	370.57	370.01	371.21
ON	354.18	351.44	350.52	357.02	354.34	352.13	353.25	355.45
ΔT	20.50	22.65	20.42	17.46	17.94	18.44	16.77	15.76

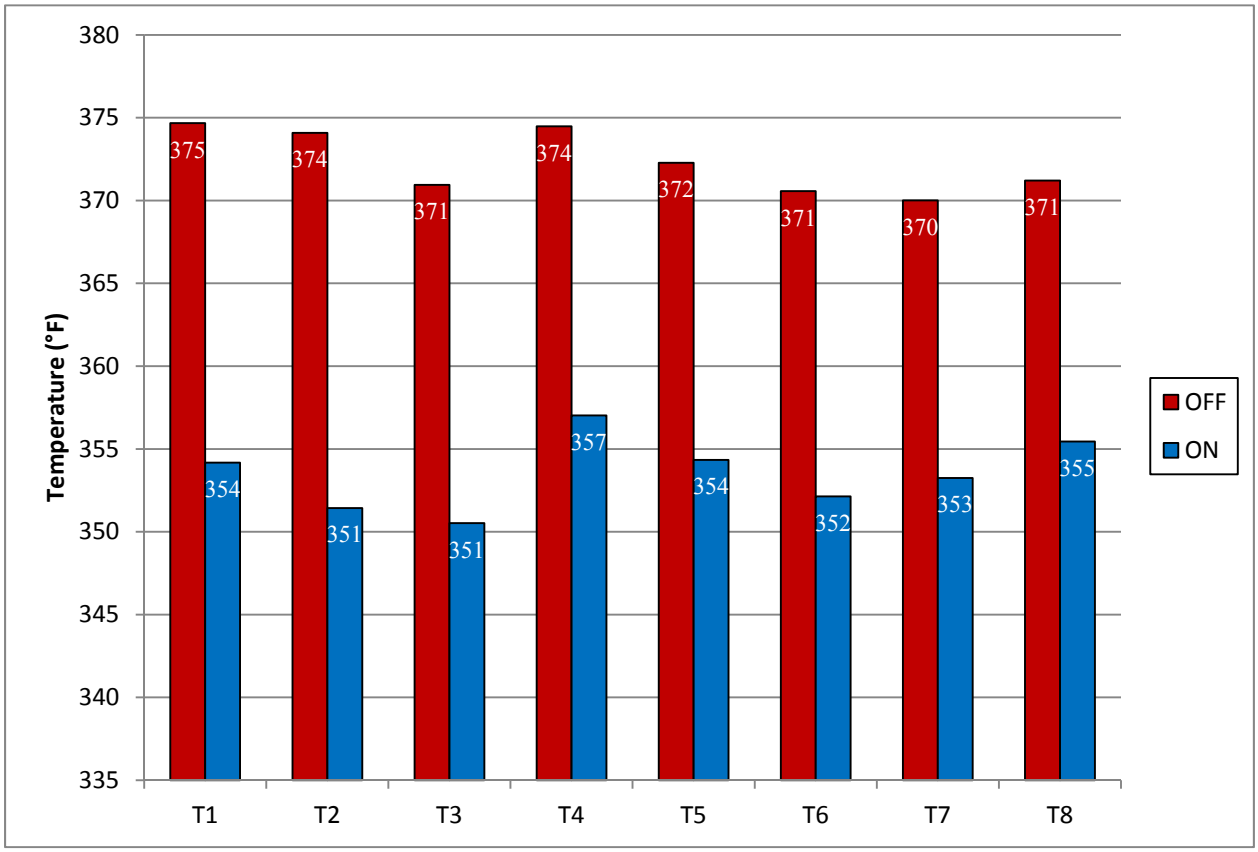

Figure 3.4: Thermocouple Temperatures with and without Cooling

The local film and overall cooling effectiveness of the thermocouples are calculated by using eq. 1.11& 1.12 and are reported in Figures 3.5 and 3.6.

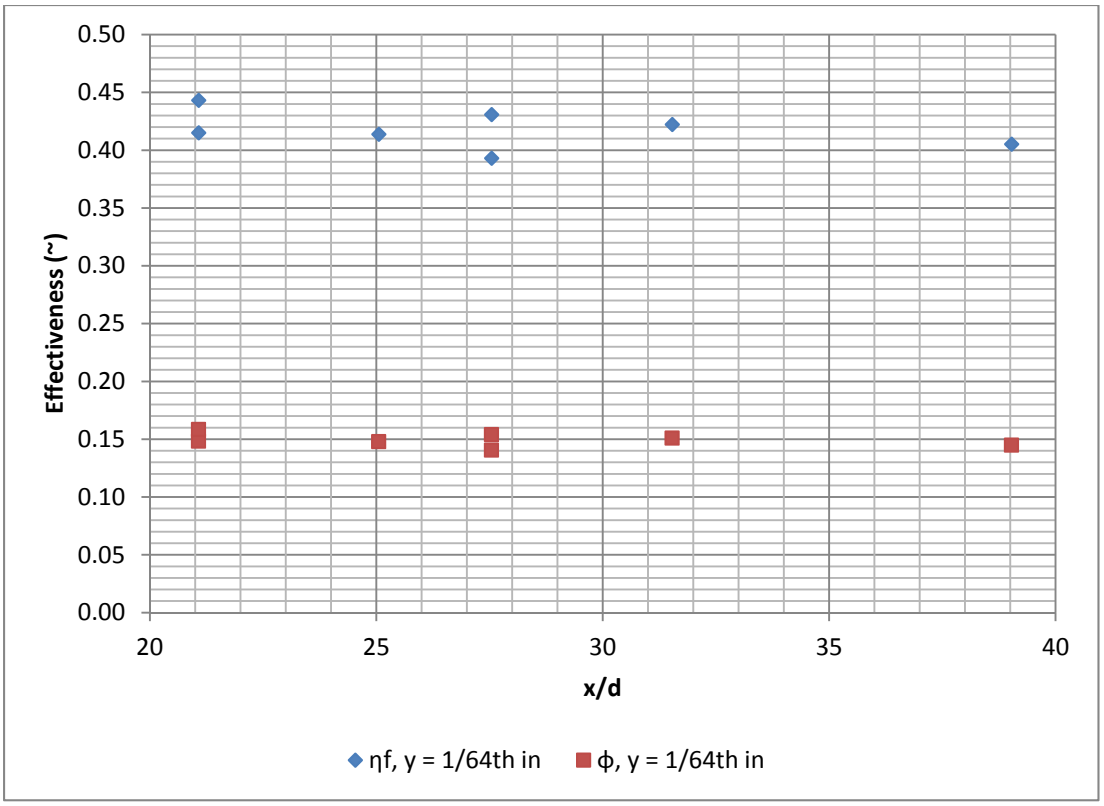

Figure 3.5: Streamwise Local Film and Overall Cooling Effectiveness

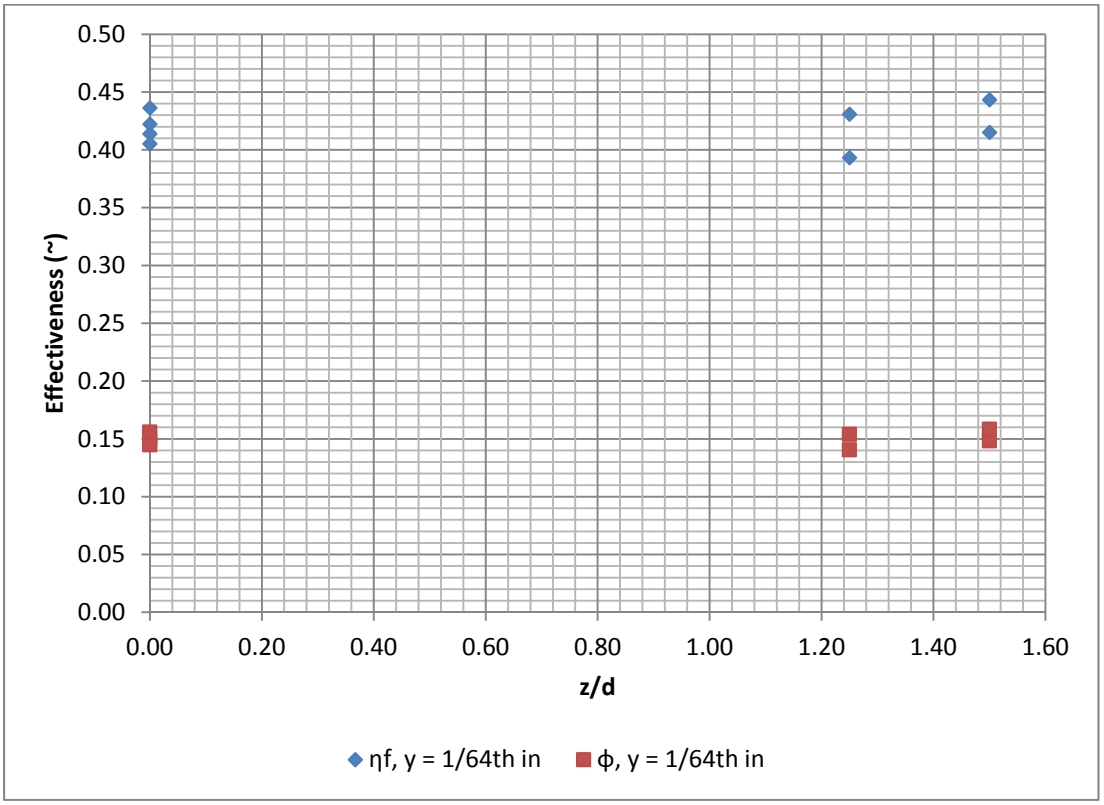

Figure 3.6: Spanwise Local Film and Overall Cooling Effectiveness

4 Numerical Simulation

4.1 Software

There were two commercial software packages that were available to the author for the numerical investigation, ANSYS-Fluent and STAR CCM+. Siemens CD-Adapco STAR CCM+ was selected to perform the numerical investigation because of the compatibility to Siemens NX CAD software. STAR CCM+ v12.04.011-R8 is a commercial software that is used to perform the Reynolds-Averaged Navier-Stokes (RANS) numerical simulation to compute the flowfield and the surface temperatures on a stationary airfoil. The experimental article was created in the NX CAD software and imported into STAR CCM+, Figure 4.1.

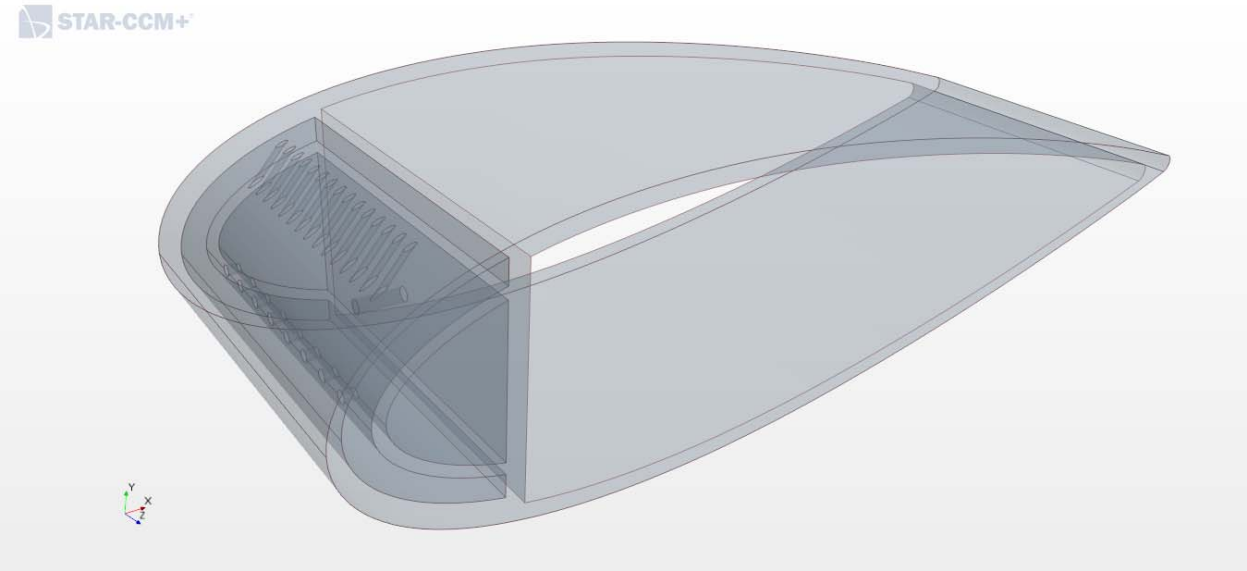

Figure 4.1: Airfoil CAD used in the CFD Simulation Showing the Leading-Edge Chamber & the Internal Sleeve

4.2 Solver

The governing equations (continuity and momentum) are solved sequentially in the segregated flow solver, which is also demonstrated in Dobrowolski [2009], Lin et al. [2011] and Elebiary [2010 & 2012] for subsonic turbine cooling. Continuity is the conservation of mass in a fluid.

The mass flux into to a volume must equal the mass flux coming out of the same volume. The continuity equation can be seen in equation 4.1, Anderson [2011], Young et al [2011] and Siemens [2017].

$$\frac{\partial \rho}{\partial t} + \nabla \cdot (\rho \boldsymbol{V}) = 0 \tag{4.1}$$

For steady flow; equation 4.1 becomes;

$$\nabla \cdot (\rho \boldsymbol{V}) = 0 \tag{4.2}$$

$$\frac{\partial (\rho u)}{\partial x} + \frac{\partial (\rho v)}{\partial y} + \frac{\partial (\rho w)}{\partial z} = 0 \tag{4.3}$$

The momentum equations come from Newton's second law of motion, where the time rate of change of momentum of a body is equal to the sum of the external forces acting on the body, equation 4.4.

$$\sum \boldsymbol{F} = \frac{d}{dt}(m\boldsymbol{V}) \tag{4.4}$$

The forces on the left hand side come from two sources, the body and surface forces. These forces can influence the time rate of change of fluid momentum. The viscous differential form of the momentum equation produces equation 4.5, Anderson [2011], Tu et al. [2013], and Siemens [2017].

$$\rho \frac{D\boldsymbol{V}}{Dt} = -\nabla p + \rho \boldsymbol{f} + \boldsymbol{F}_{\boldsymbol{viscous}} \tag{4.5}$$

The local derivative in the momentum will become zero in the steady state limit. The segregated flow solver also adds two additional solvers for velocity and pressure. The energy equation can be solved by using three different models: Enthalpy, Temperature or Isothermal (Siemens

[2017]). The segregated fluid temperature model was selected to solve the temperature as a variable in the total energy equation and enthalpy was calculated from the equation of state, Siemens [2017]. The temperature model is preferred for the current simulation because the temperature is changing due to coolant interactions. The energy equation from the first law of thermodynamics for a system is shown in equation 4.6, Anderson [2011], Munson et al [2013], and Zikanov [2010].

$$\rho \frac{DE}{Dt} = \rho \dot{q} - \nabla \cdot (p\boldsymbol{V}) + \rho(\boldsymbol{f} \cdot \boldsymbol{V}) + \dot{Q}_{Viscous} \tag{4.6}$$

The segregated flow and energy model is based on pressure and is used for incompressible flows, where the coupled approach is based on density. The coupled flow and energy model are used for compressible flow and natural convection, Siemens [2017]. Both models were evaluated and showed similar simulations; therefore, the segregated model was selected for effective computational resources.

The flow was assumed to be turbulent to represent the turbine environment. Bogard and Thole [2006] summarized that the two-equation eddy-viscosity models k-epsilon and k-omega with wall treatment were used for the majority of turbine cooling research. Dobrowolski [2009] researched the accuracy of turbulence model simulations for adiabatic effectiveness and heat transfer coefficients and found that RKE 2L is better suited to meet the experimental results. Dobrowolski [2009] included studies from Harrison and Bogard [2008], Laskowski et al. [2008], Luo and Razinski [2006], and Medic and Durbin [2002]. Harrison and Bogard [2008] showed that the RKE model simulated centerline adiabatic effectiveness the best from SKW, but showed worst lateral results at x/d of 0 to 15 and good results downstream. In the end, both SKW and RKE showed good results for lateral averaged adiabatic effectiveness. Harrison and Bogard

[2008] conducted their simulation on a flat plate, which agrees with Silieti et al. [2004] and Zhang and Hassan [2006]. There are many turbulence model comparison studies on flat plate, but Walters and Leylek [1997] simulated turbulence model with turbine airfoil and found overall RKE and RSM models to improve predictions and validations with the experimental results. Early works of Walters and Leylek [1997] show that SKE 2LWT was also an excellent predictor. Silieti et al. [2009] compared three turbulence models (the realizable k-ε, the SST k-ω and v^2-f) in an adiabatic and CHT models, and found that the RKE model performed the best of the three. Bogard and Thole [2006] reported that Sinha et al. [1991], Pedersen et al. [1977] and Schmidt et al. [1996] conducted a similar simulation for the k-epsilon and predicted decent comparisons to the experimental values. Tu et al. [2013] compared four turbulence models (Standard k-ε, Realizable k-ε, Standard k-ω and SST k-ω) on a NACA-16 series airfoil for a case test. Tu et al. [2013] showed that Standard k-ε, Standard k-ω (Wilcox's) and SST k-ω (Menter's) over-predict the boundary-layer thickness to the experimental data. Realizable k-ε showed a close comparison to the experimental boundary layer and surface pressure coefficient, Tu et al. [2013]. However, Hoda and Acharya [1999] reported that k-epsilon and k-omega turbulence models did not predict the flow accurately for their research. In the end, the decision for the best turbulence model is left to the researcher's determination based on the application.

The turbulence model selected was the Realizable K-Epsilon Two-layer (RKE 2L) model, which is a form of k-ε is used in Dobrowolski [2009], Silieti et al. [2009], Walters and Leylek [1997], Harrison and Bogard [2008], Brittingham and Leylek [1997], Kohli and Thole [1998], Martin and Thole [1997], Cho et al. [2001], Islami and Jubran [2012] and Hyams and Leylek [1997]. There are countless studies on turbine cooling with k-ε giving a solid foundation for the current work. SST k-ω is also used many times in turbine cooling research shown in

Repko [2016], Chandran and Prasad [2015], Panda and Prasad [2014], Hadier [2015], Martin [2011], Dyson et al. [2012] and Williams et al. [2013]. The Shear Stress Transport k-ω was considered but showed higher error in the simulations for the benchmark validation when compared to RKE 2L. Using Waye and Bogard [2006] data for the blowing parameter, Mb of 1.2 with a similar airfoil shape, RKE 2L showed a 5 to 10% relative error. This relative error is consistent with the Dobrowolski [2009] review. The comparison is reported in Figure 4.2.

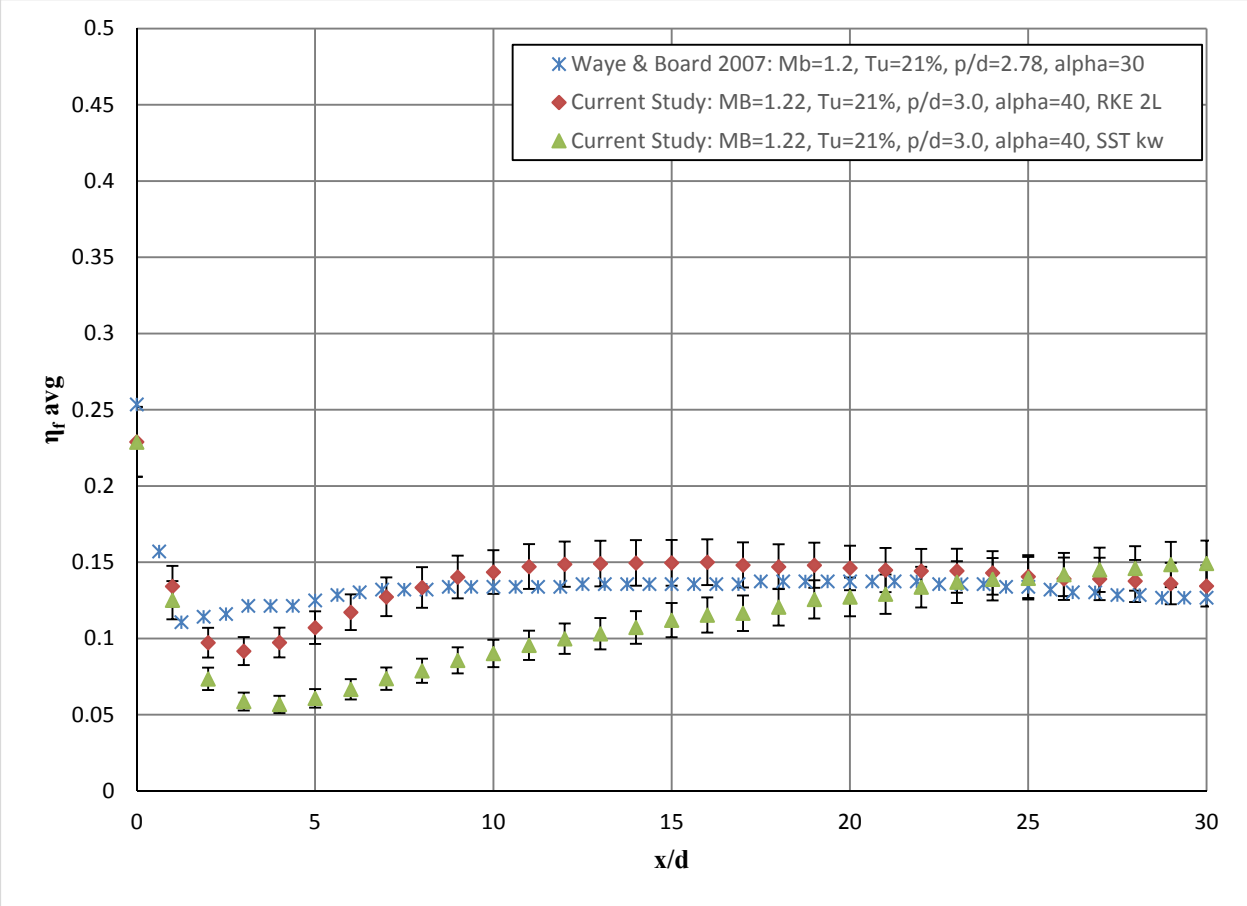

Figure 4.2: Adiabatic Turbulence Model Comparison to Capture Film Cooling Effectiveness

Realizable k-epsilon was first shown in 1994 from the Institute for Computational Mechanics in Propulsion and Center for Modeling of Turbulence and Transition at the NASA-Lewis Research Center in Cleveland, Ohio: Shih et al. [1994]. The RKE model is based on the SKE model and

the transport equations for the kinetic energy and turbulent dissipation rate are shown in equations (4.7) and (4.8), Siemens [2017] and Tannehill et al. [1997].

$$\frac{\partial}{\partial t}(\rho k) + \nabla \cdot (\rho k \bar{V}) = \nabla \cdot \left[\left(\mu + \frac{\mu_t}{\sigma_k}\right)\nabla k\right] + P_k - \rho(\varepsilon - \varepsilon_0) + S_k \tag{4.7}$$

$$\frac{\partial}{\partial t}(\rho \varepsilon) + \nabla \cdot (\rho \varepsilon \overline{\boldsymbol{V}}) = \nabla \cdot \left[\left(\mu + \frac{\mu_t}{\sigma_\varepsilon}\right)\nabla \varepsilon\right] + \frac{1}{T_e} C_{\varepsilon 1} P_\varepsilon - C_{\epsilon 2} f_2 \rho \left(\frac{\varepsilon}{T_e} - \frac{\varepsilon_0}{T_0}\right) + S_\varepsilon \tag{4.8}$$

The turbulent eddy viscosity is defined in equation 4.9.

$$\mu_t = \rho C_\mu f_\mu k T \tag{4.9}$$

RKE model adjusted the model coefficient (Cμ) to a function (eq. 4.10) of the mean flow and turbulence properties, which was a constant of 0.09 in the SKE model.

$$C_\mu = \frac{1}{A_0 + A_S \frac{kU^*}{\varepsilon}} \tag{4.10}$$

The model coefficient (Cμ) is consistent with the experimental boundary layer's data and constraints the normal stresses; hence, the term realizable, Tu et al. [2013] and Siemens [2017].

A two-layer approach is added with the RKE model to predict the turbulence near the wall, because RKE has a limitation of high Re regions without it. This approach allows the computations for the viscous sub-layer and the buffer layer for meshes with $y^+ \sim 1$ and $y^+ > 30$. The two-equation turbulence models and two-layer approach provided an acceptable accurate means of simulating the free shear layer mixing and reattachment, which describes the flow environment of the film-cooled blade in the experiment.

4.3 Wall Models (Thermal Boundary Conditions)

The numerical simulations consist of two wall models, the adiabatic model (the fluid study with the airfoil surface treated as adiabatic) and the conjugate heat transfer (CHT) model that accounts for the fluid and solid interface. The adiabatic model focuses on the fluid interaction of the hot and cold flows, which establishes the fluid convection environment. Demonstrating a pure film cooling effectiveness (without wall heat transfer) is comparable to other studies with the adiabatic wall. The CHT simulation represents the aerothermodynamics of the solid and fluid heat transfer with conduction and convection. Accuracy of the CHT model is comparable to the experiment, since it reveals the impingement cooling effectiveness from the interaction between the two (inner and outer) stagnation conditions.

The adiabatic and CHT models are based on a three dimensional steady state RANS simulation with ideal gas properties as the working fluid. The flow velocities in this study are as follows: 166 ft/s for the cooling ejector and 18.77 ft/s for the freestream, which are treated as incompressible flow.

4.4 Mesh Generation

The computational mesh was created by using STAR CCM+ polyhedral, surface and prism layer mesher. The volume mesh is an unstructured polyhedral generated arrangement of cells with a slow growth rate of 1.2, presented in Figures 4.3 and 4.4.

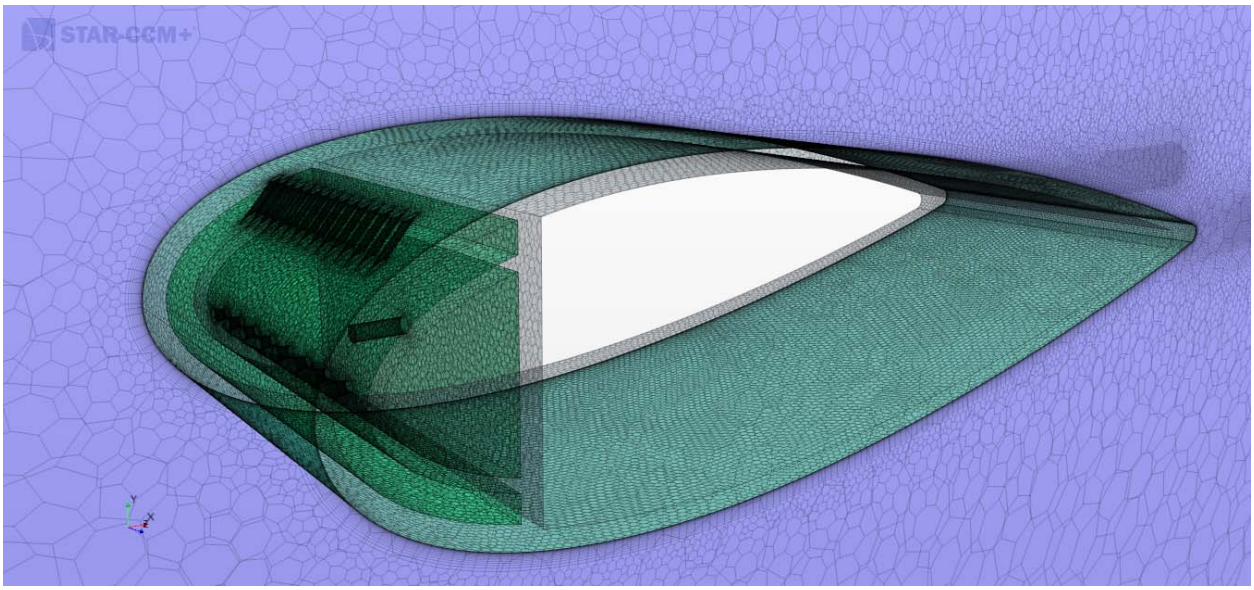

Figure 4.3: Computational Mesh used in the Airfoil Simulation

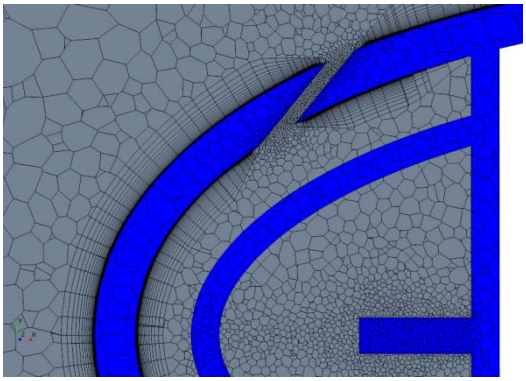

(a) Center Plane of the Inner/Outer Chamber

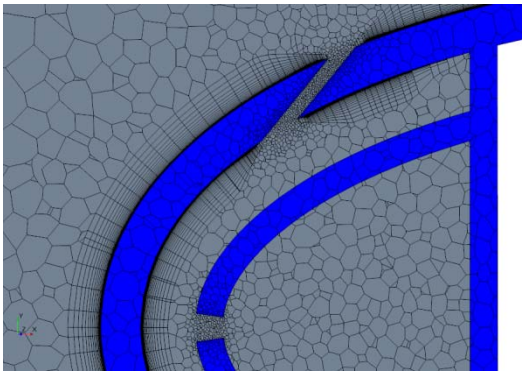

(b) Off Centered (1/10 in.) Section of the Inner/Outer Chamber

Figure 4.4: Planar Cut of the Computational Mesh

The mesh quality is important in calculating an accurate and stable solution. Poor quality volume mesh will impact the simulation of convective and diffusive fluxes for fluid, Siemens [2017]. There are metrics that aids in determining good quality: Face Validity, Cell Quality, Volume Change, Cell Skewness Angle, Cell Warpage Quality, Chevron Quality Indicator and Least Squares Quality. Each metric has value for determining good or poor cells. Table 4.1 shows the mesh diagnostic results to STAR CCM+ quality matrix, values are compared to the poor criteria limits.

Table 4.1: Metric for Grid Quality

	Poor Values	# Cell
Face Validity	< 0.51	0
Cell Quality	< 1.0E-8	0
Volume Change	< 0.01	0
Cell Skewness Angle	> 85	0
Chevron Quality Indicator	1	0
Least Squares Quality	< 0.001	0
Cell Warpage Quality	< 0.15	0

There are four zones in the turbulent boundary layer for incompressible flow, which are shown in Figure 4.5.

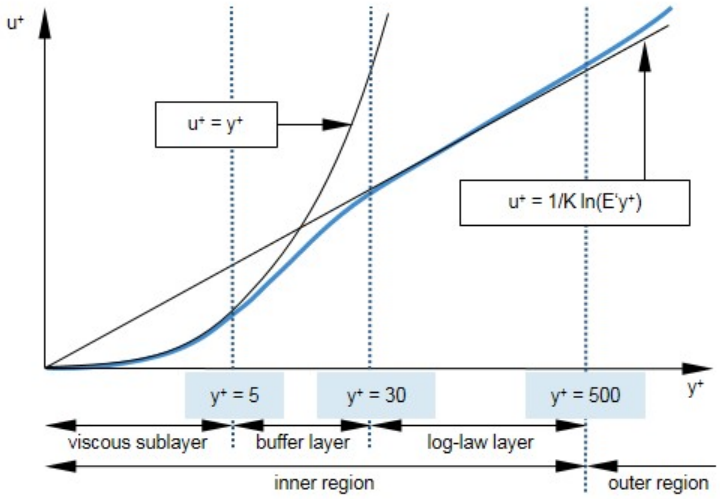

Figure 4.5: Zones in the turbulent boundary layer, Siemens [2017].

The viscous sublayer is desired to model the heat transfer and the viscous effects correctly. The prism layer mesh was added at the surface of the airfoil to capture the viscous sublayer of the inner region with y+<1 for the suction surface, Figure 4.6.

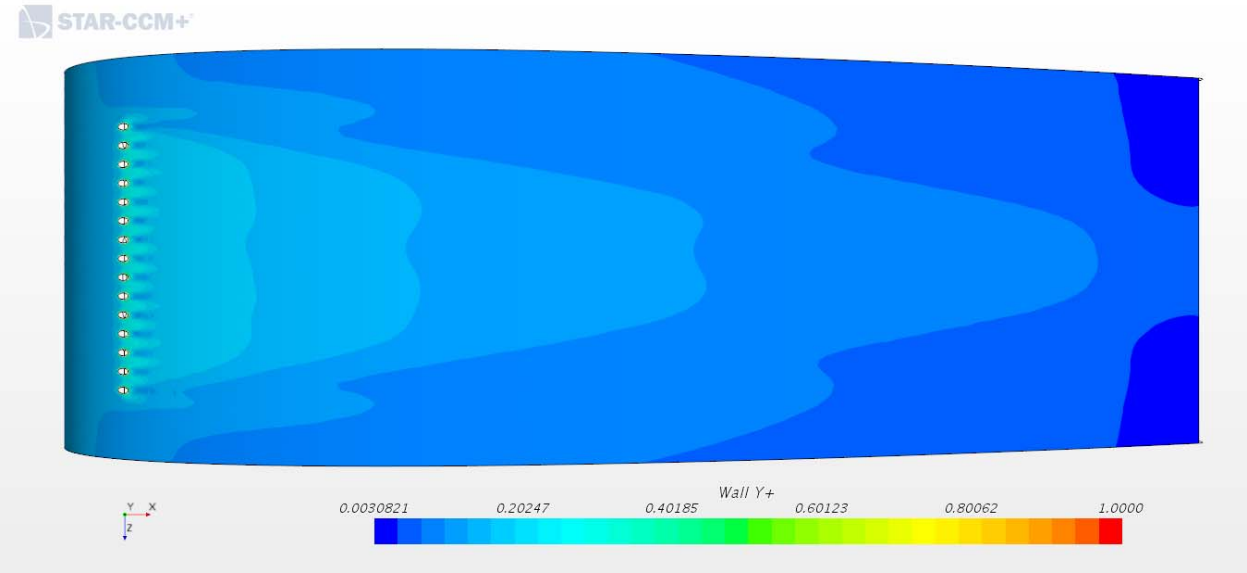

Figure 4.6: y+ values on the Suction Surface

The low y+ values ensure the capture of the heat transfer interaction at the viscous sub-layer of the airfoil surface. The prism layer profile consisted of 20 prism layers with a near wall thickness of 4.0×10^{-4} inches. The law of the wall was used to estimate the near wall thickness then modified to reduce the y+ values, equation 4.11, Cummings [2015] and Tannehill [1997].

$$y^+ = \frac{y\left(\frac{|\tau_w|}{\rho_w}\right)^{1/2}}{\upsilon_w} \tag{4.11}$$

For turbulent flow the boundary layer thickness is defined for a flat plate as equation 4.12, and used to approximate a starting total thickness for the prism.

$$\delta \approx \frac{0.37x}{Re^{1/5}} \tag{4.12}$$

The Reynolds number for the system is defined in equation 4.13 and reported in Table 4.2.

$$Re_c = \frac{\rho_\infty V_\infty c}{\mu_\infty} = \frac{V_\infty c}{\nu_\infty} \tag{4.13}$$

Table 4.2: Reynolds Number for the Experiment

		Reynolds Number
Airfoil	Re_c	24174.81
Ejector	Re_{DE}	7409.07
Impingement	Re_{DI}	3845.03

Overall, the adiabatic and CHT models have a mesh size of 1 million and 1.5 million cells, respectively. The domain is modeled as a box where the inlet upstream of the airfoil is a velocity inlet and the outlet downstream of the airfoil is a pressure outlet, Figure 4.7. The remaining surfaces are slip walls or symmetry planes. The inlet is 4 airfoil chords upstream with a temperature of 408 °F with a velocity of 18.77 ft/s and ~13.5% turbulence intensity. The outlet is 6 airfoil chords downstream and is set to the ambient initial reference pressure. The spanwise and vertical dimensions are 2 in x 32 in for a corresponding area match of the test section area, 64 in^2.

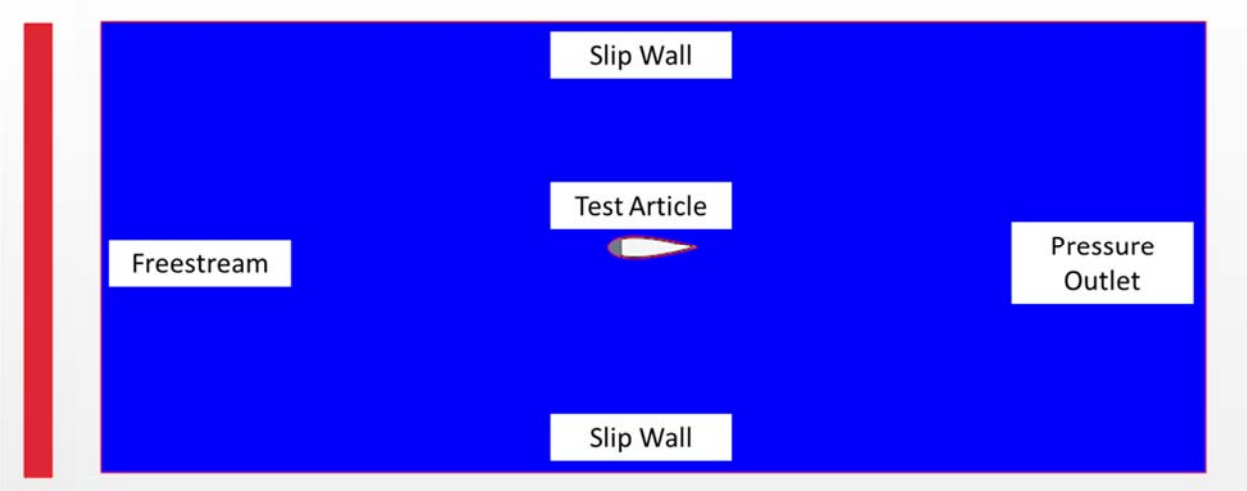

Figure 4.7: Domain with Boundary Conditions

The cooling ejector is set to a stagnation inlet, where the pressure is held to 0.5 psig at 45 °F. The coolant is injected inside a showerhead passage, where the flow impinges on the leading edge and exits through the film holes causing a blowing parameter for the models.

4.5 Verification

The simulations were considered to have converged once the continuity, momentum, energy, turbulence kinetic energy (TKE) and turbulence dissipation rate (TDR) residuals were under or at 10^{-5}, Figures 4.8 and 4.9.

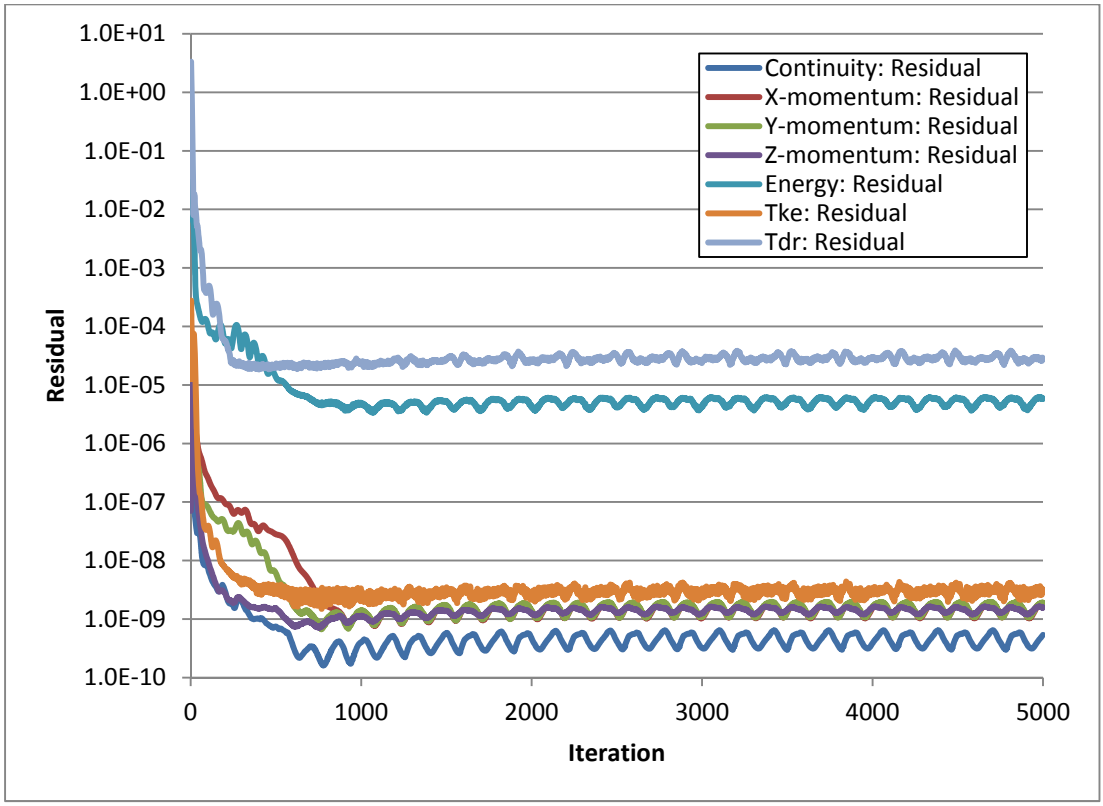

Figure 4.8: Residuals of the CHT Model

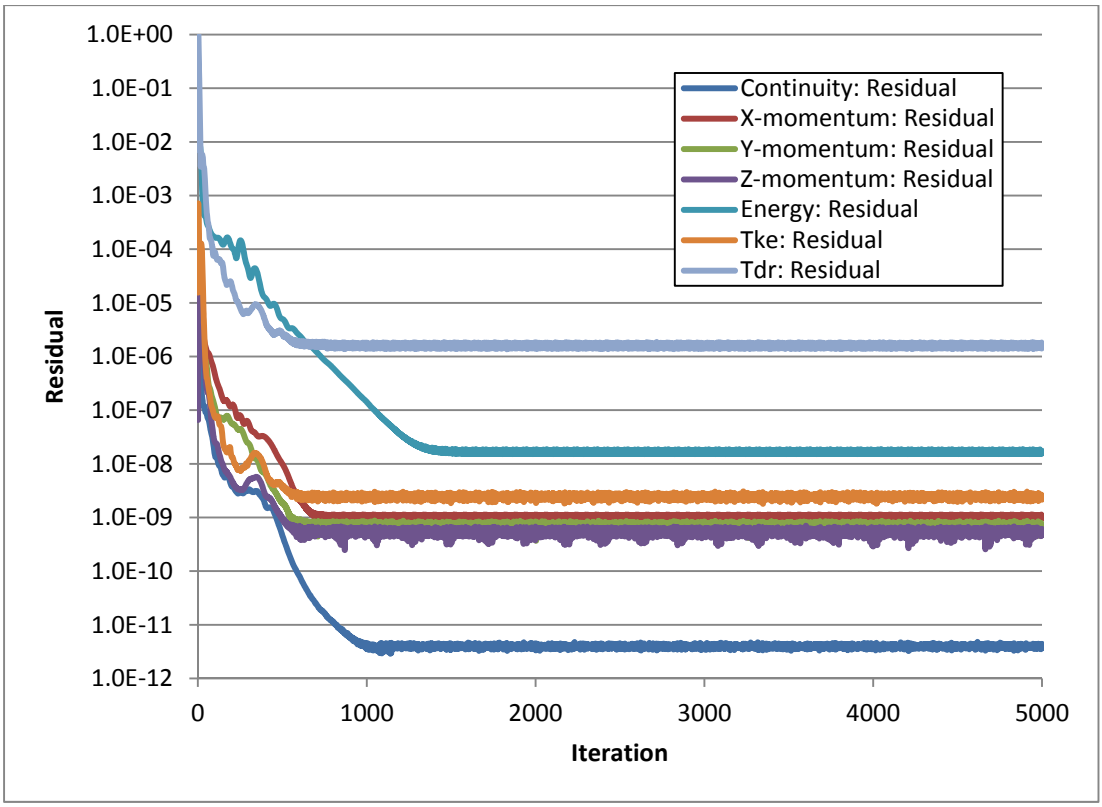

Figure 4.9: Residuals of the Adiabatic Model

The simulation was monitored for convergence with the film cooling lateral average effectiveness at six (x/d) locations: 0, 10, 20, 30, 40 and 50. The $\bar{\eta}_f$ converged at around 2500 iterations for the CHT model and at about 1500 iterations for the adiabatic model, Figures 4.10 and 4.11. The average change rate for the last 4000 iteration is 1.64×10^{-6} and an average difference of 4.7×10^{-4} between iteration 5000 and 3000 for the film cooling lateral average effectiveness.

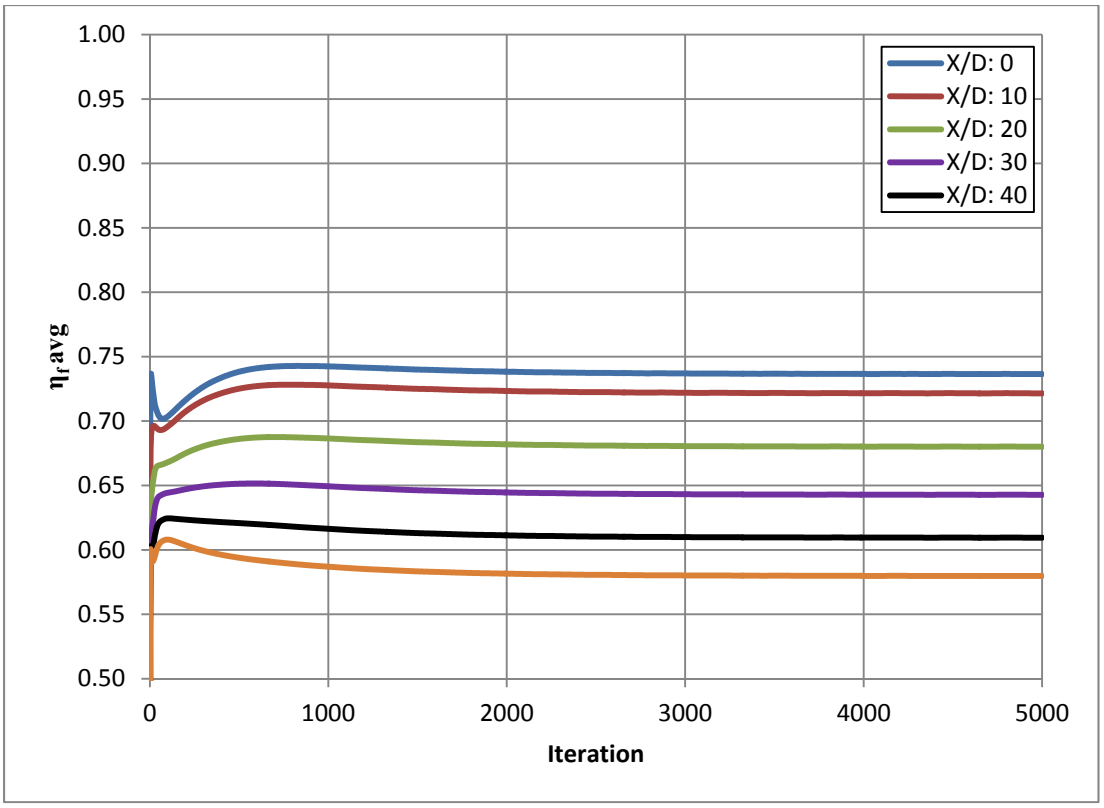

Figure 4.10: CHT Model - Film Cooling (Lateral Average) Effectiveness for convergence

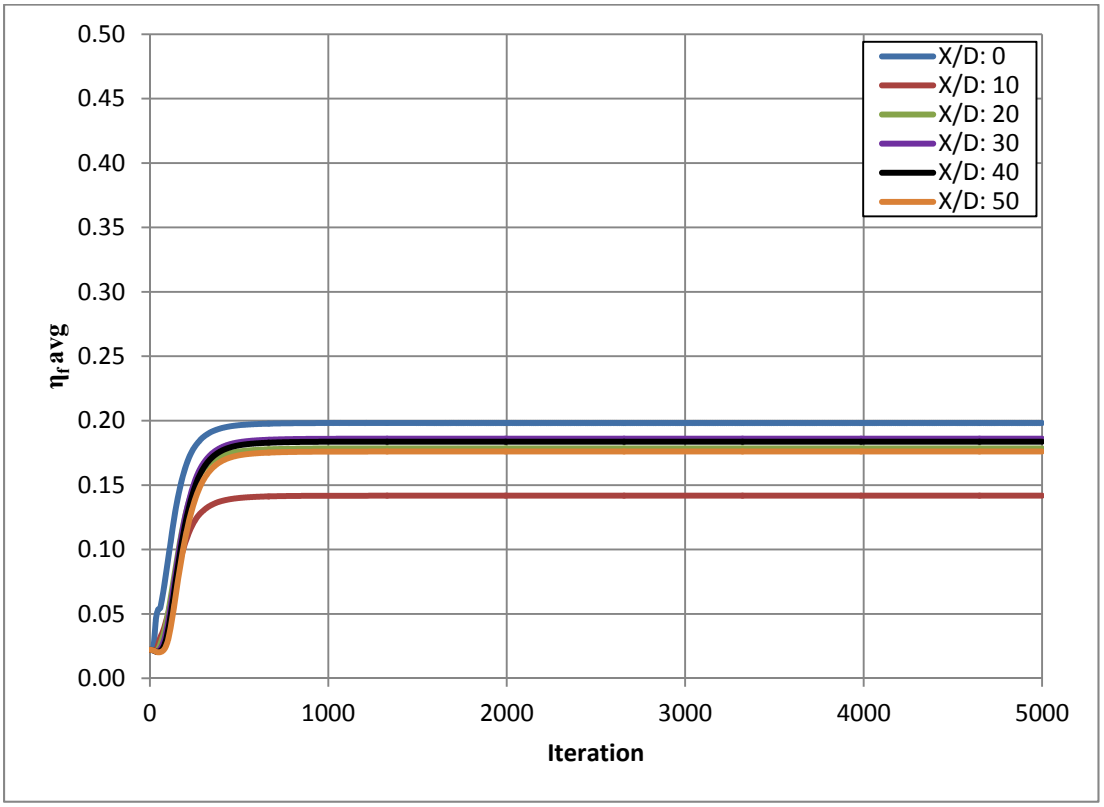

Figure 4.11: Adiabatic Model - Film Cooling (Lateral Average) Effectiveness for convergence

A grid independence study was carried out for each model with three base sizes: 0.75 in., 0.5 in. and 0.25 in. The cell counts for the base sizes are listed in Table 4.3.

Table 4.3: Grid Independence Study for each Model

	Conjugate Heat Transfer			Adiabatic		
Base Size (in)	0.75	0.5	0.25	0.75	0.5	0.25
Cells (in Millions)	1.50	2.60	8.80	0.89	1.80	7.90

Grid independence is demonstrated for the film cooling (lateral average) effectiveness with a blowing parameter of 5.75 for CHT and 6.21 for adiabatic, see Figure 4.12.

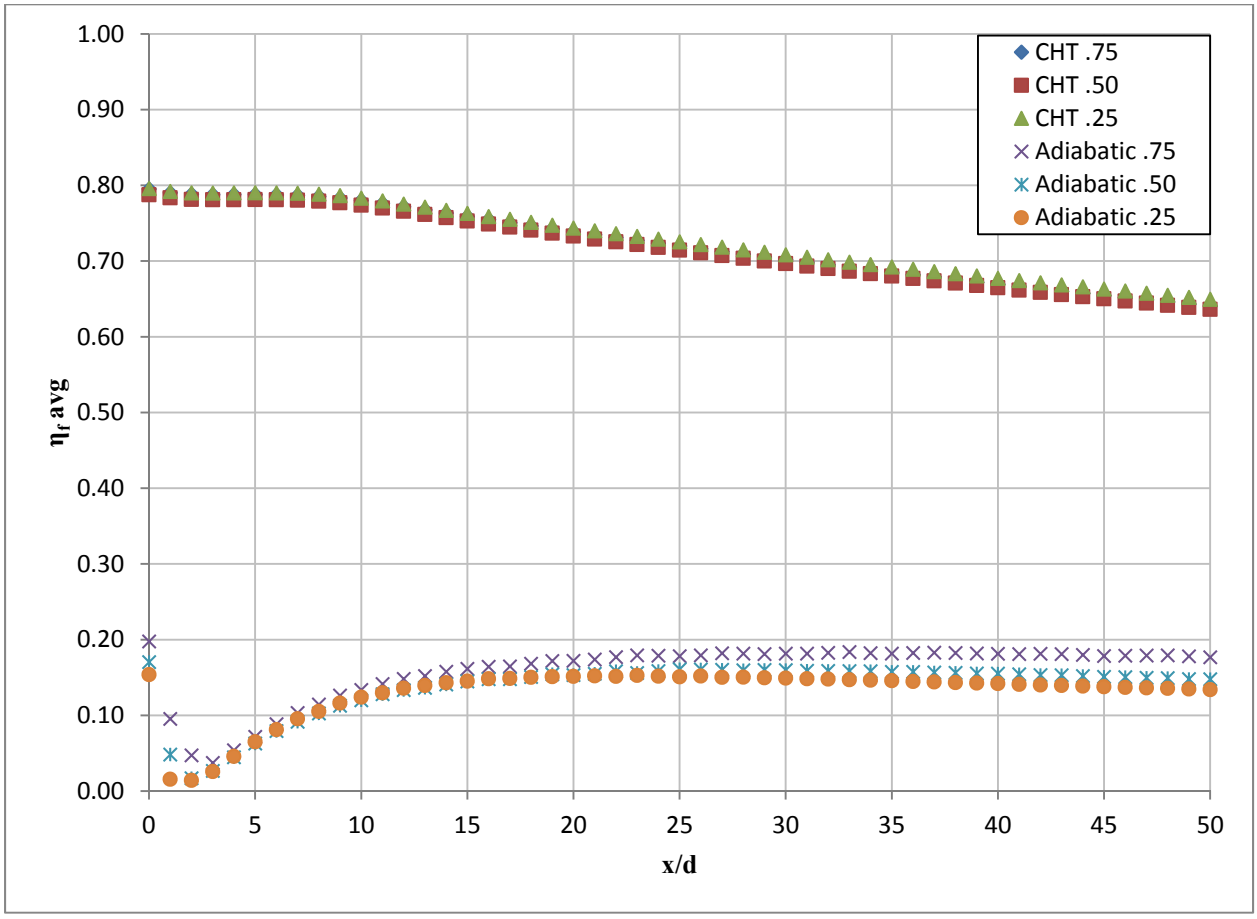

Figure 4.12: Film Cooling (Lateral Average) Effectiveness for Grid Independence

The CHT model showed a relative error of less than 1% corresponding to the base size of 0.25 in. The adiabatic model displayed a relative error of less than 2% for the same base size. Grid independence is thus established with these relative errors.

5 Numerical Results

5.1 Numerical/Experimental Validation

The surface temperature measurements and the corresponding numerical simulation results are shown in Table and Figure 5.1. Each simulated probe exhibits less than 10 °F difference when compared to the thermocouple measurements, which validates the accuracy of the CHT numerical simulation.

Table 5.1: Temperature Comparison

	T_1	T_2	T_3	T_4	T_5	T_6	T_7	T_8
ON	(°F)	(°F)	(°F)	(°F)	(°F)	(°F)	(°F)	(°F)
EXP	354.18	351.44	350.52	357.02	354.34	352.13	353.25	355.45
CHT	358.08	357.24	357.62	357.32	356.09	356.7	355.51	349.1
ΔT	3.91	5.81	7.09	0.30	1.76	4.57	2.26	6.39

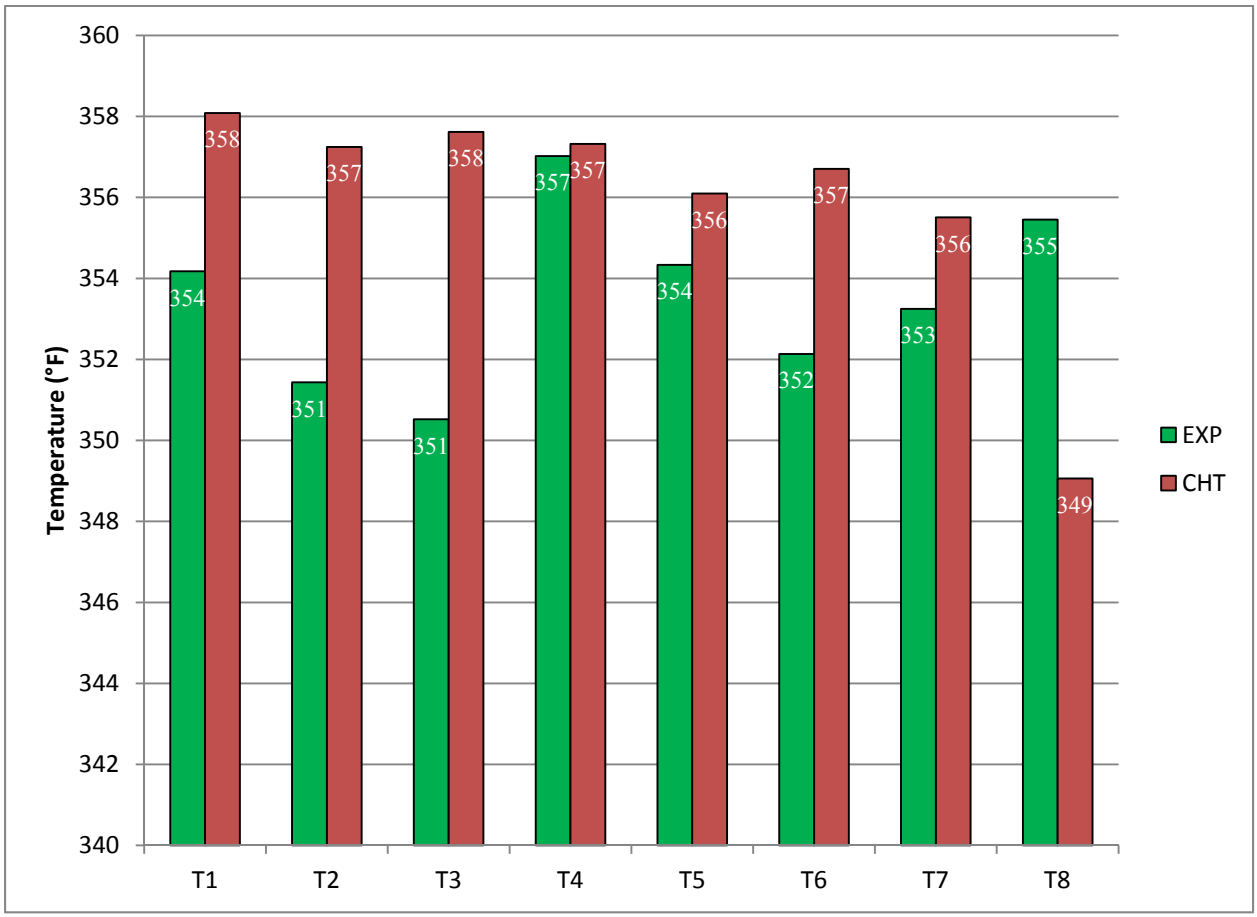

Figure 5.1: Thermocouple Temperatures for Experimental and Numerical

The local film effectiveness for the experiment and simulation matches the trend of Bogard and Thole [2006] for a high blowing parameter on a convex wall at y/d of 0.5, which is reported in Table 5.2.

Table 5.2: Film Cooling Effectiveness Comparison

	T_1	T_2	T_3	T_4	T_5	T_6	T_7	T_8
x/d	21.08	19.84	21.08	27.55	25.05	27.55	31.54	39.03
z/d	-1.50	0.00	1.50	-1.25	0.00	1.25	0.00	0.00
EXP: η_f	0.42	0.44	0.44	0.39	0.41	0.43	0.42	0.41
CHT: η_f	0.38	0.39	0.39	0.39	0.40	0.40	0.40	0.45

5.2 Numerical/Experimental Simulations

The simulated velocity field in the inner/outer chambers of the airfoil leading edge is shown in Figures 5.2 & 5.3. The computed velocities demonstrated a blowing ratio of 5.75, which is a non-dimensional design parameter in film cooling.

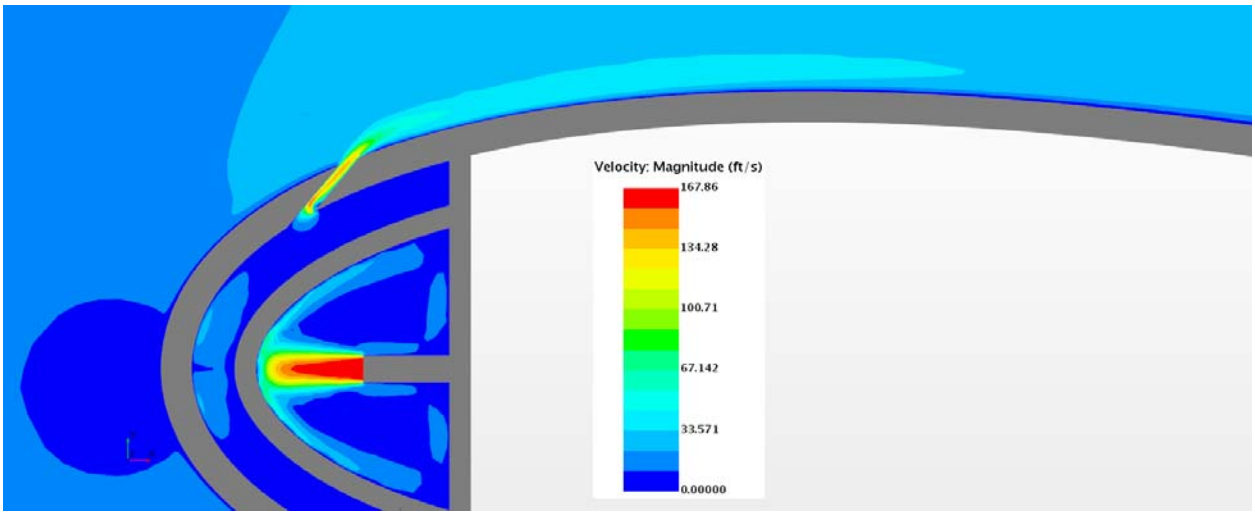

Figure 5.2: CHT Model - Center Plane of the Inner/Outer Chamber Velocity Field

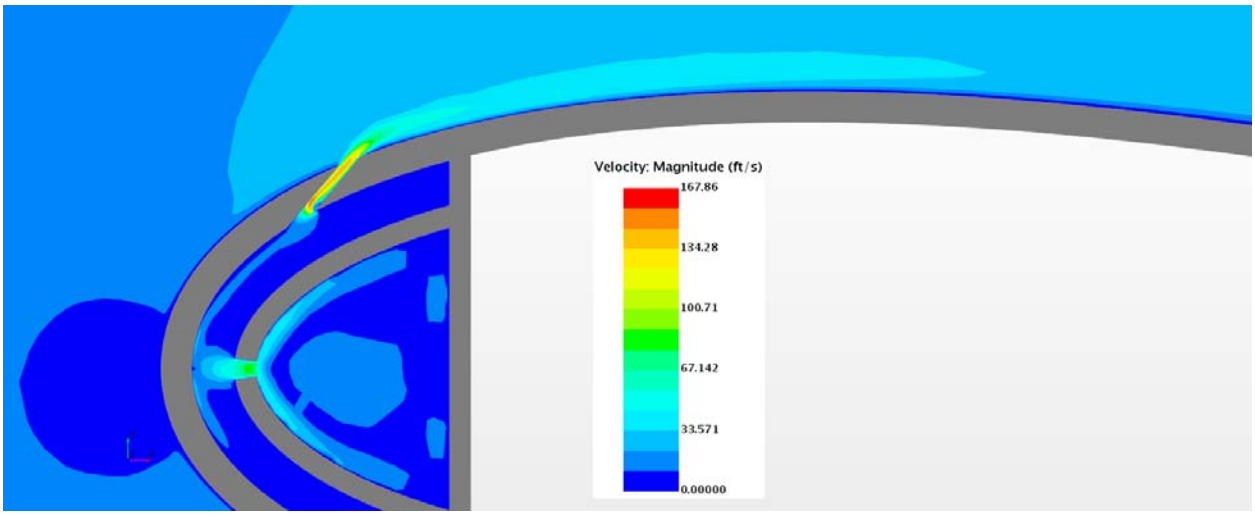

Figure 5.3: CHT Model - Off Centered (1/10 in.) Section of the Inner/Outer Chamber Velocity Field

The non-dimensional parameters for film cooling of the adiabatic and conjugate heat transfer models are shown in Table 5.3.

Table 5.3: Non-Dimensional Parameters for the Numerical Experimental Simulations

	Supplied Pressure (psig)	M_b (~)	DR (~)	VR (~)	I (~)
Adiabatic	0.5	6.21	1.70	3.66	22.75
Conjugate Heat Transfer	0.5	5.75	1.16	4.94	28.44

There are differences in adiabatic and CHT parameters with the same supply pressure, which is due to the heat transfer interaction with the solid model. The internal thermal parameters change due to the coolant absorbing the heat of the leading edge.

Figure 5.4 shows the velocity vector interaction of the freestream and film jet along streamwise locations.

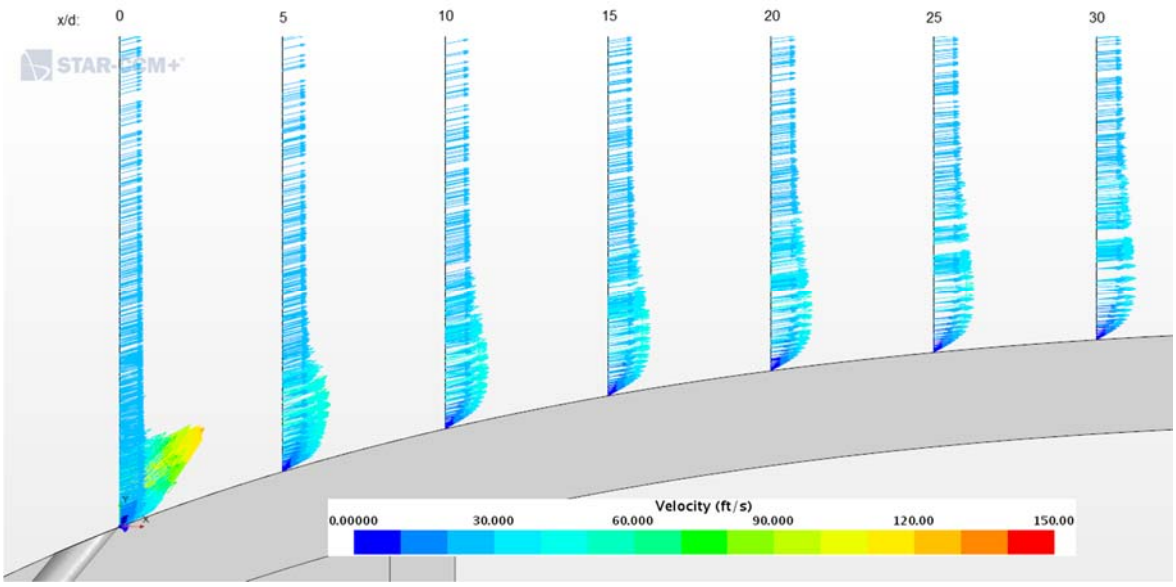

Figure 5.4: Velocity Vector for Suction Surface

Thermal probes were placed in the same location as in the experimental investigation, shown in Table 2.2. The temperatures from the probes and suction surface temperature distribution are presented in Figure 5.5 and in Table 5.4.

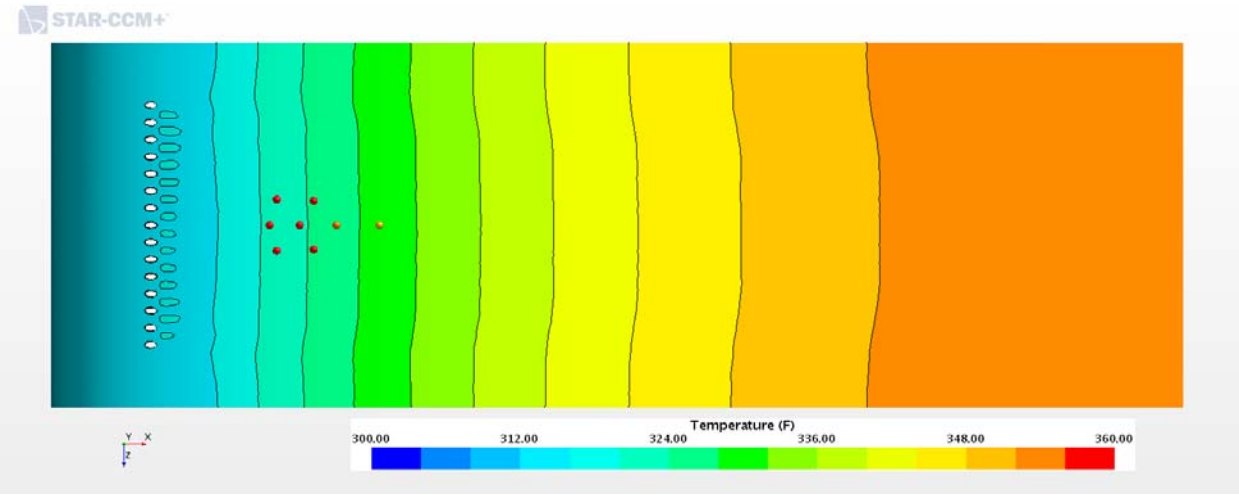

Figure 5.5: CHT Model - Temperature Distribution on the Airfoil Suction Surface with Thermal Probes

Table 5.4 shows that the adiabatic wall is an inaccurate model for the experiment; however, it shows the film-gas interaction in the absence of wall heat transfer.

Table 5.4: Thermal Probes Tabulation

	T_1	T_2	T_3	T_4	T_5	T_6	T_7	T_8
ON	(°F)	(°F)	(°F)	(°F)	(°F)	(°F)	(°F)	(°F)
CHT	358.08	357.24	357.62	357.32	356.09	356.70	355.51	349.06
Adiabatic	293.53	295.01	295.37	296.90	295.54	297.33	298.32	301.18
ΔT	64.56	62.23	62.24	60.43	60.56	59.37	57.19	47.88

The local film cooling effectiveness data was calculated on the centerline and the spanwise locations from the film hole positions (with film-hole diameter of 1/32nd inch). Table 5.5 shows the spatial distribution of the film cooling effectiveness, as produced by the numerical simulation.

Table 5.5: Simulated Local Film Cooling Effectiveness at Probes Locations

	T_1	T_2	T_3	T_4	T_5	T_6	T_7	T_8
x/d	21.08	19.84	21.08	27.55	25.05	27.55	31.54	39.03
z/d	-1.50	0.00	1.50	-1.25	0.00	1.25	0.00	0.00
CHT η_f	0.42	0.44	0.44	0.39	0.41	0.43	0.42	0.41
Adiabatic η_f	0.32	0.31	0.31	0.31	0.31	0.30	0.30	0.29

Figures 5.6 and 5.7 display detached jets that spreads and reattaches downstream of the injection point at x/d of ~6. The detachment is also observed in Figure 5.8 between 2 and 4 x/d. The effects of the airfoil convex curvature and freestream momentum produced a normal pressure gradient (or force), which turns the jet towards the airfoil surface. Bogard and Thole [2006] showed from Ito [1978] that blowing parameters lower than one would produce higher film cooling effectiveness than higher blowing parameters. However, the film cooling effectiveness downstream of the injection would gradually increase for higher blowing parameters. Naturally, the peak film cooling effectiveness, η_f, is achieved at the film hole, and the lower η_f will be registered in the freestream gas flow, as shown in Figures 5.6 and 5.7.

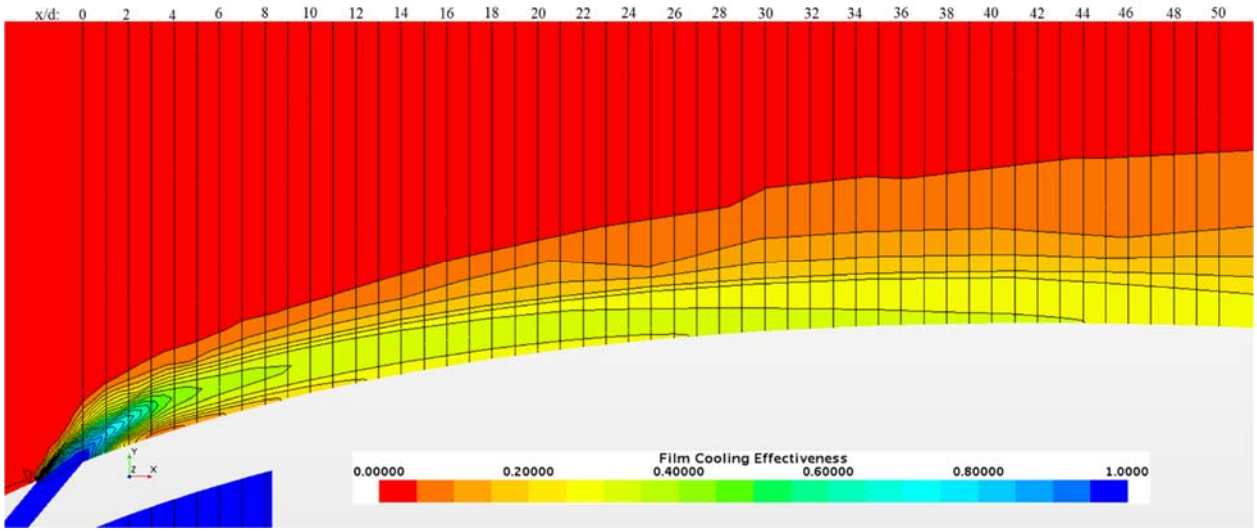

Figure 5.6: Adiabatic Film Cooling Effectiveness profile for centerline jet

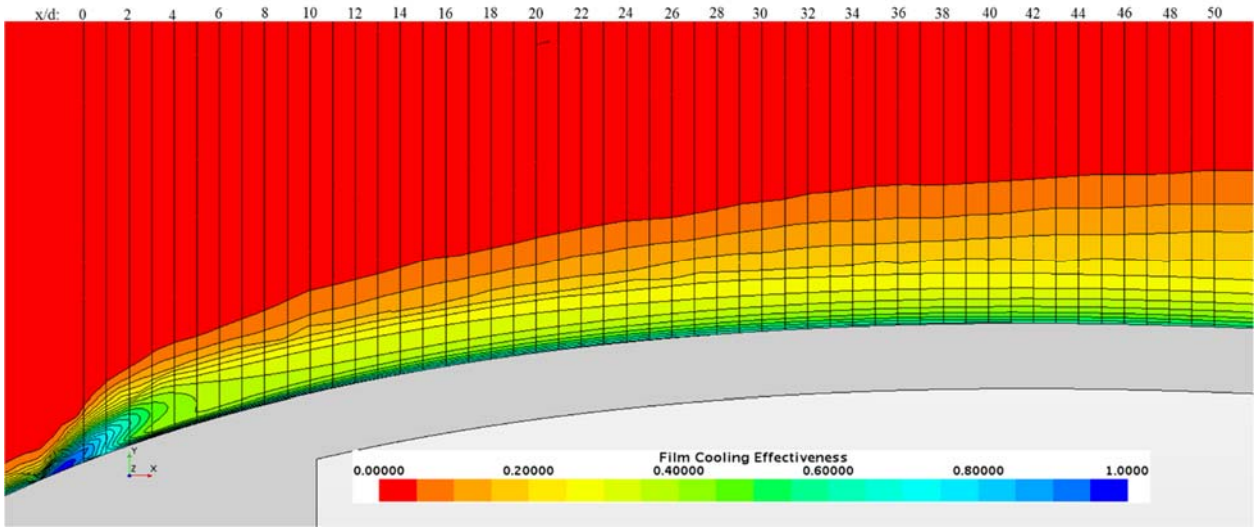

Figure 5.7: Film Cooling Effectiveness profile for CHT Model center plane

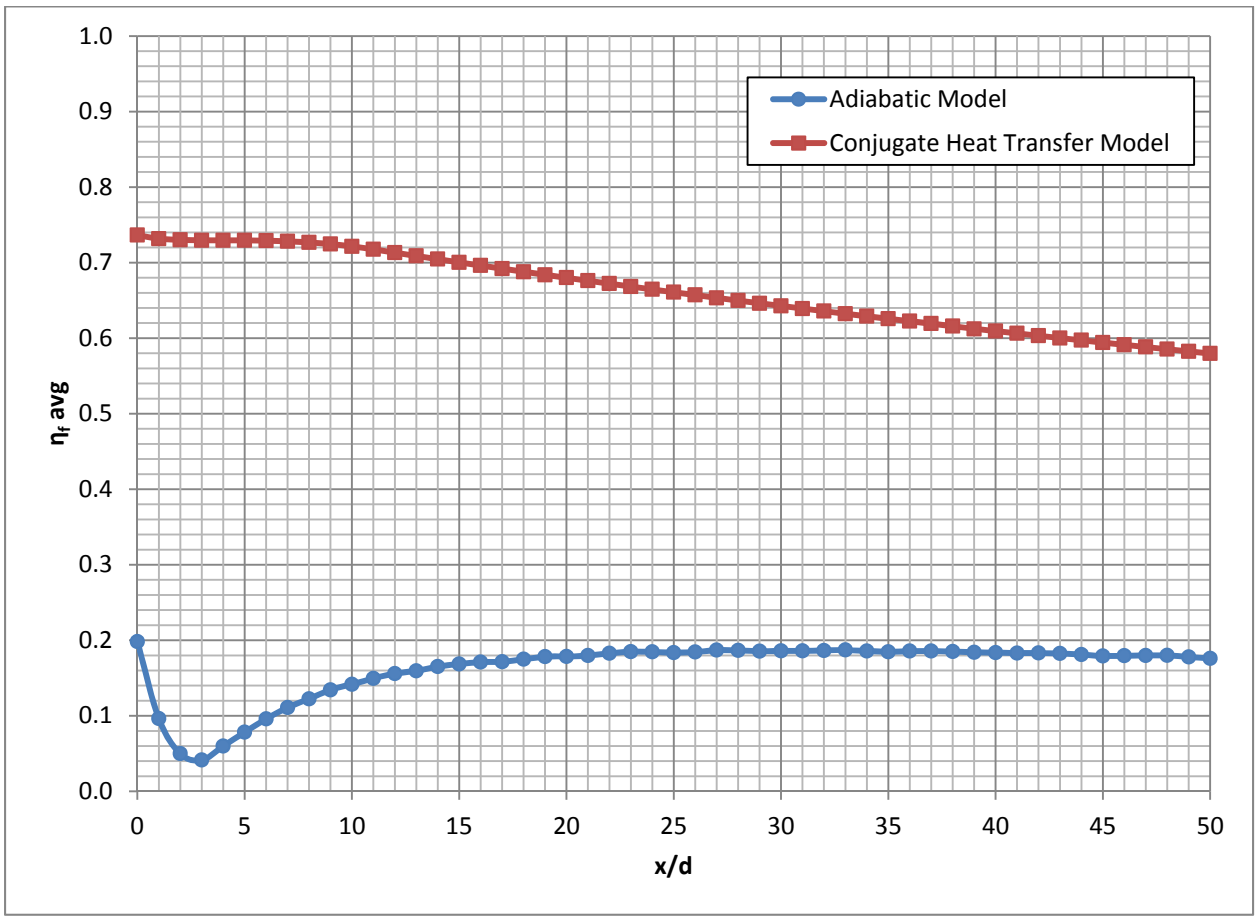

Figure 5.8: Laterally averaged film effectiveness for a convex wall

The single row of film cooling jets acts like a fence on the surface of the airfoil. When the freestream flow reaches the film jet, the flow has two paths, entrain with the jet or move around the jet, Figure 5.9.

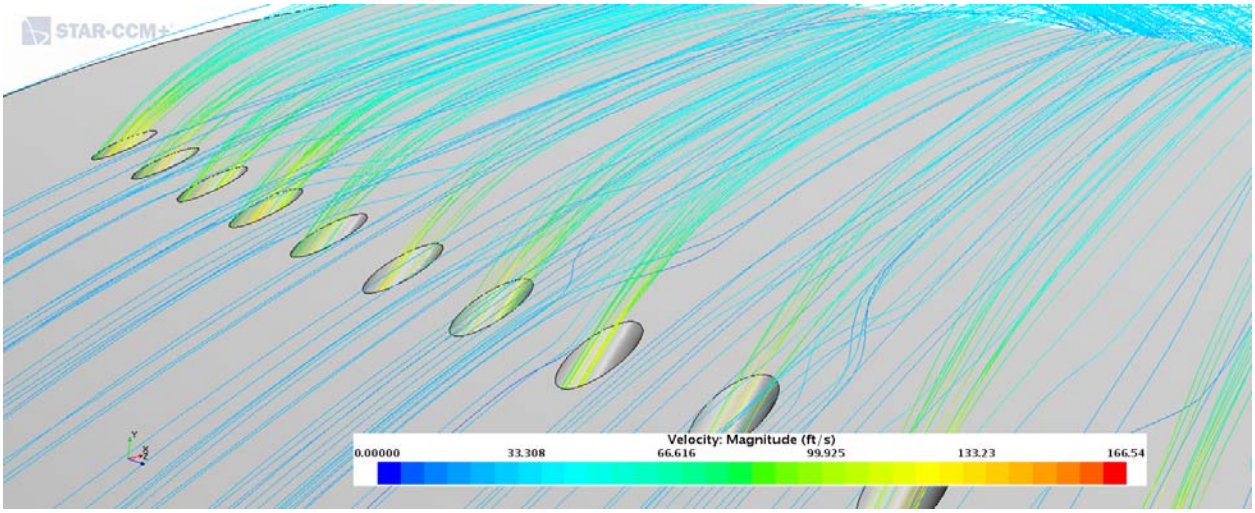

Figure 5.9: Streamlines showing interaction of the freestream and the cooling jets that emerge from discrete film holes

The detached jet creates a three-dimensional static pressure footprint on the surface surrounding the detached bubble. Fluid dynamics of the freestream at the surface is influenced by the spacing-diameter ratio, P/d and the bubble pressure. A hot spot or "blister" is created by the detached bubble, as seen in Figures 5.6 & 5.7. The entrainment flow from the jet will cause mixing/diffusion of the cool jet and the rate of diffusion is influenced by the freestream turbulence intensity and blowing parameter. The effect of freestream turbulence is to promote mixing and enhanced entrainment with the film jet. The spatial distribution of the coolant downstream of the injection point is shown in Figures 5.10 and 5.11.

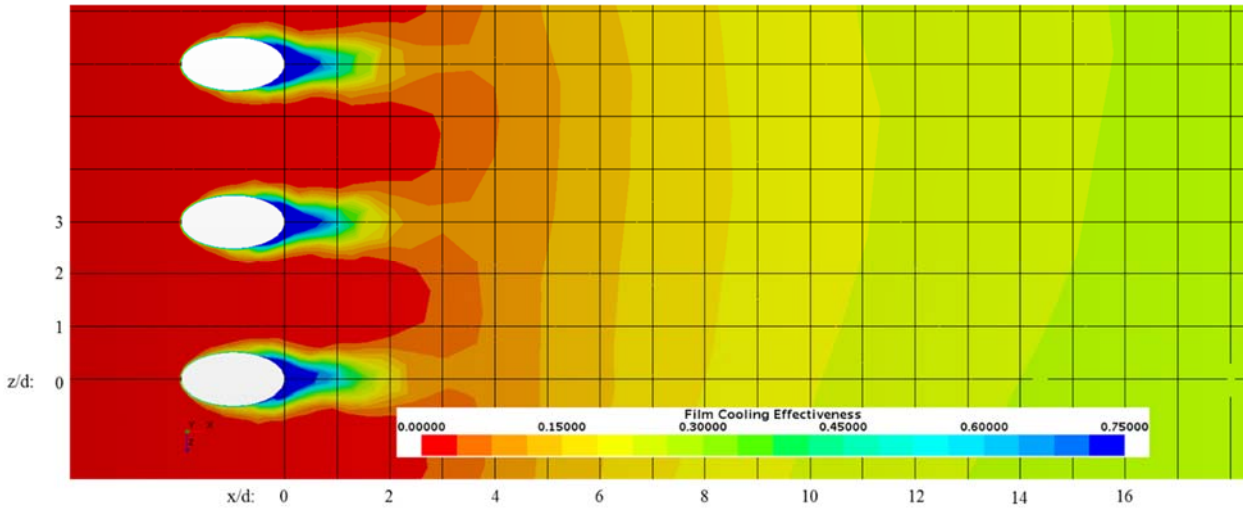

Figure 5.10: Spatial distribution of film effectiveness: Adiabatic Model

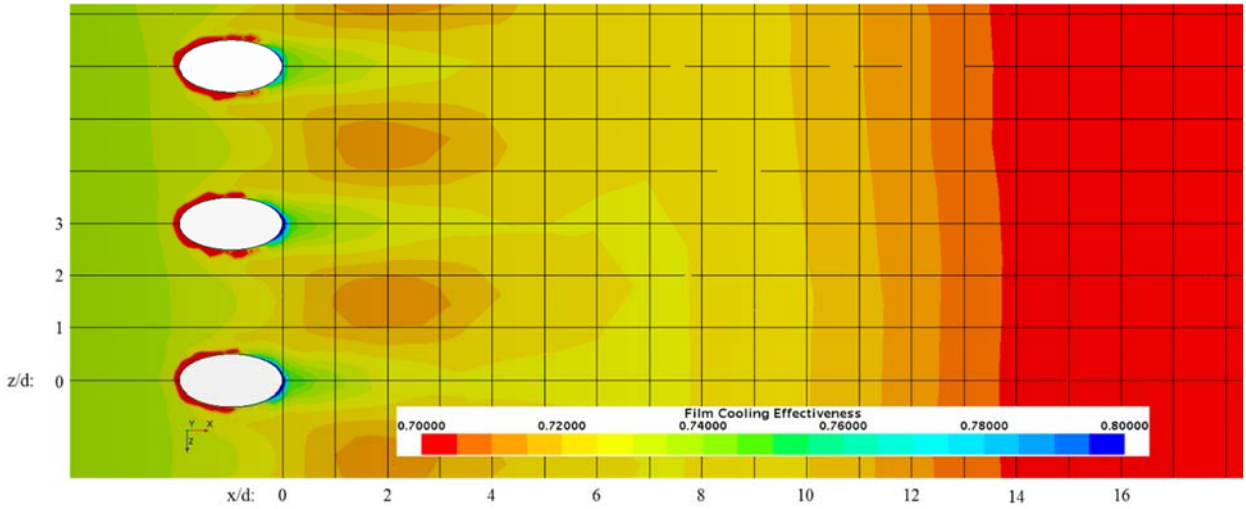

Figure 5.11: Spatial distribution of film effectiveness: CHT Model

The overall film effectiveness was investigated to explore the conduction and convective effects on the model from the internal and external cooling. Overall film effectiveness can only be evaluated with the CHT model, which is shown in Table 5.6 and Figures 5.12 – 5.14.

Table 5.6: CHT Model - Simulated Local Overall Cooling Effectiveness at Probes Locations

	T_1	T_2	T_3	T_4	T_5	T_6	T_7	T_8
X/D	21.08	19.84	21.08	27.55	25.05	27.55	31.54	39.03
Z/D	-1.50	0.00	1.50	-1.25	0.00	1.25	0.00	0.00
CHT ϕ	0.14	0.14	0.14	0.14	0.14	0.14	0.14	0.16

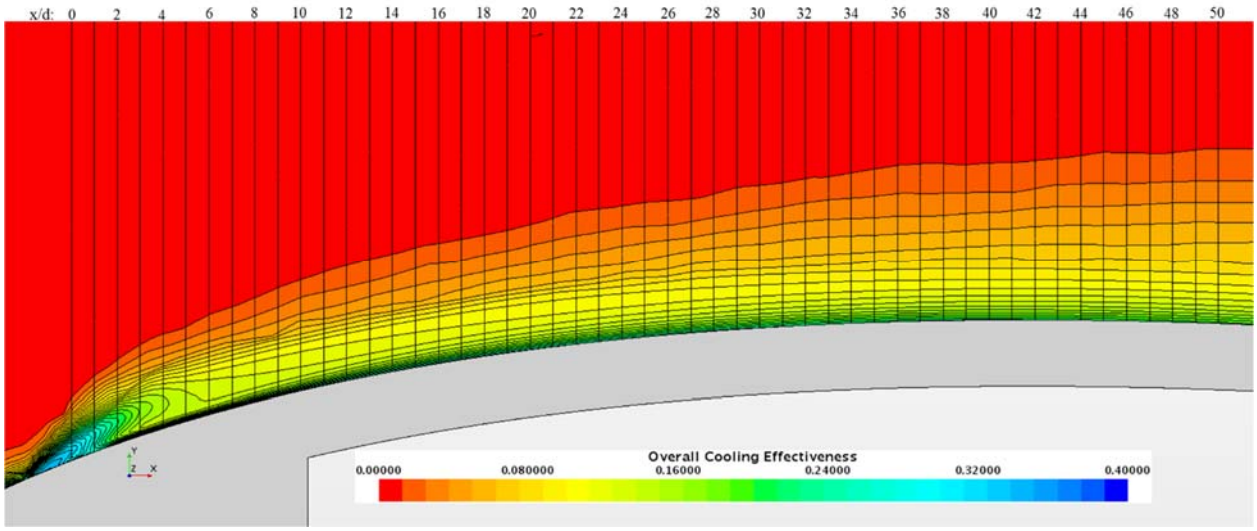

Figure 5.12: Overall Cooling Effectiveness profile for CHT Model center plane

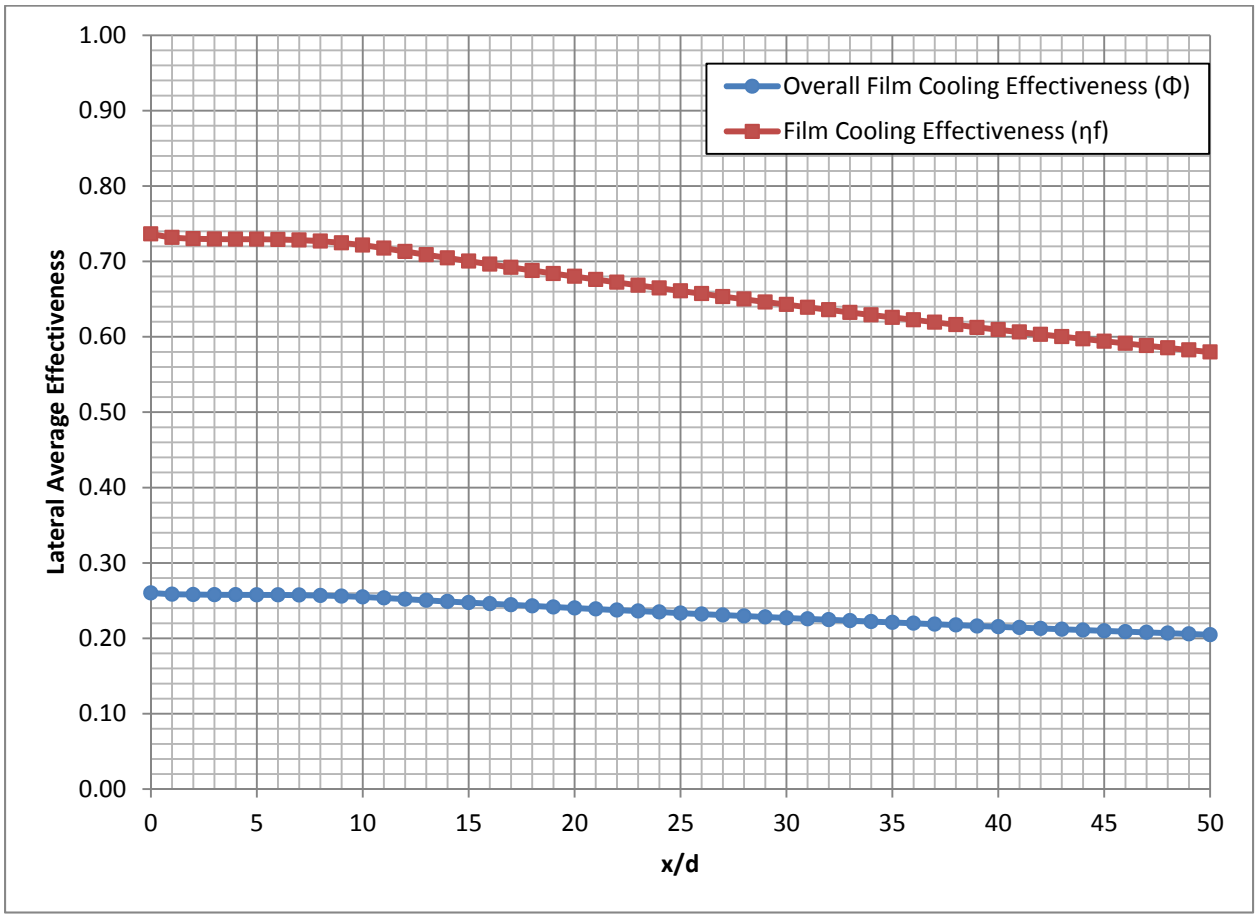

Figure 5.13: Overall averaged film effectiveness comparison for a convex wall

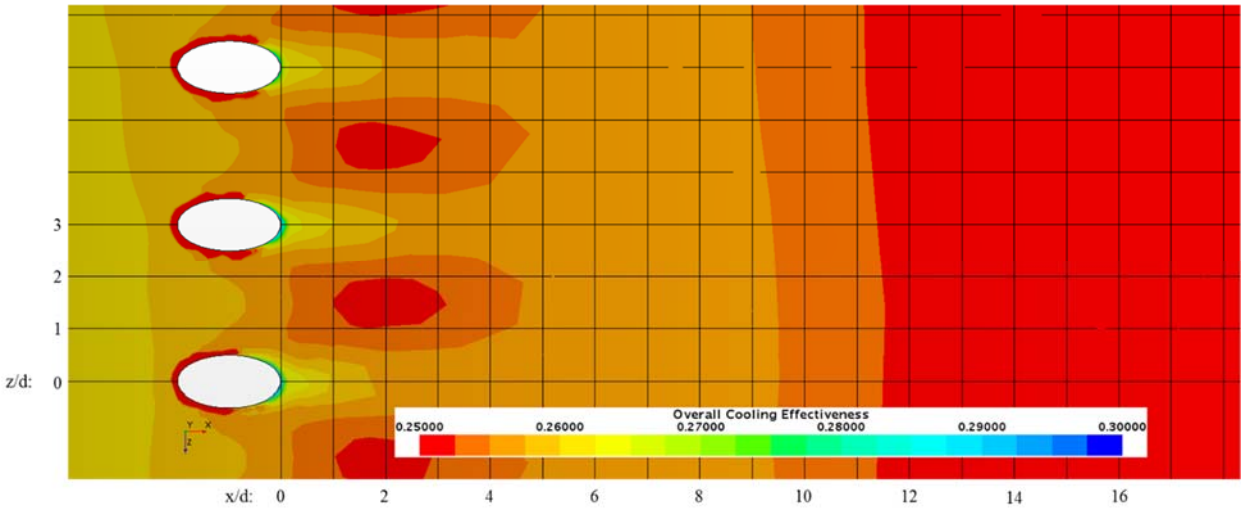

Figure 5.14: Spatial distribution of overall effectiveness for CHT Model

Overall film effectiveness is lower than the film cooling effectiveness of the CHT model due to the system entry temperature and film injection temperature. This is seen in Figure 5.13 for the CHT model and in equations 1.11 and 1.12.

The impingement effectiveness is evaluated using the Nusselt number, which is defined in equation 5.1.

$$Nu = \frac{hL}{k} = \frac{Convective\ Heat\ Transfer}{Conductive\ Heat\ Transfer} \tag{5.1}$$

The Nusselt number at the impingement stagnation point is used to develop an Impingement Nusselt Stagnation Ratio, which is shown in Figure 5.15 at surface curvilinear distance from the stagnation point.

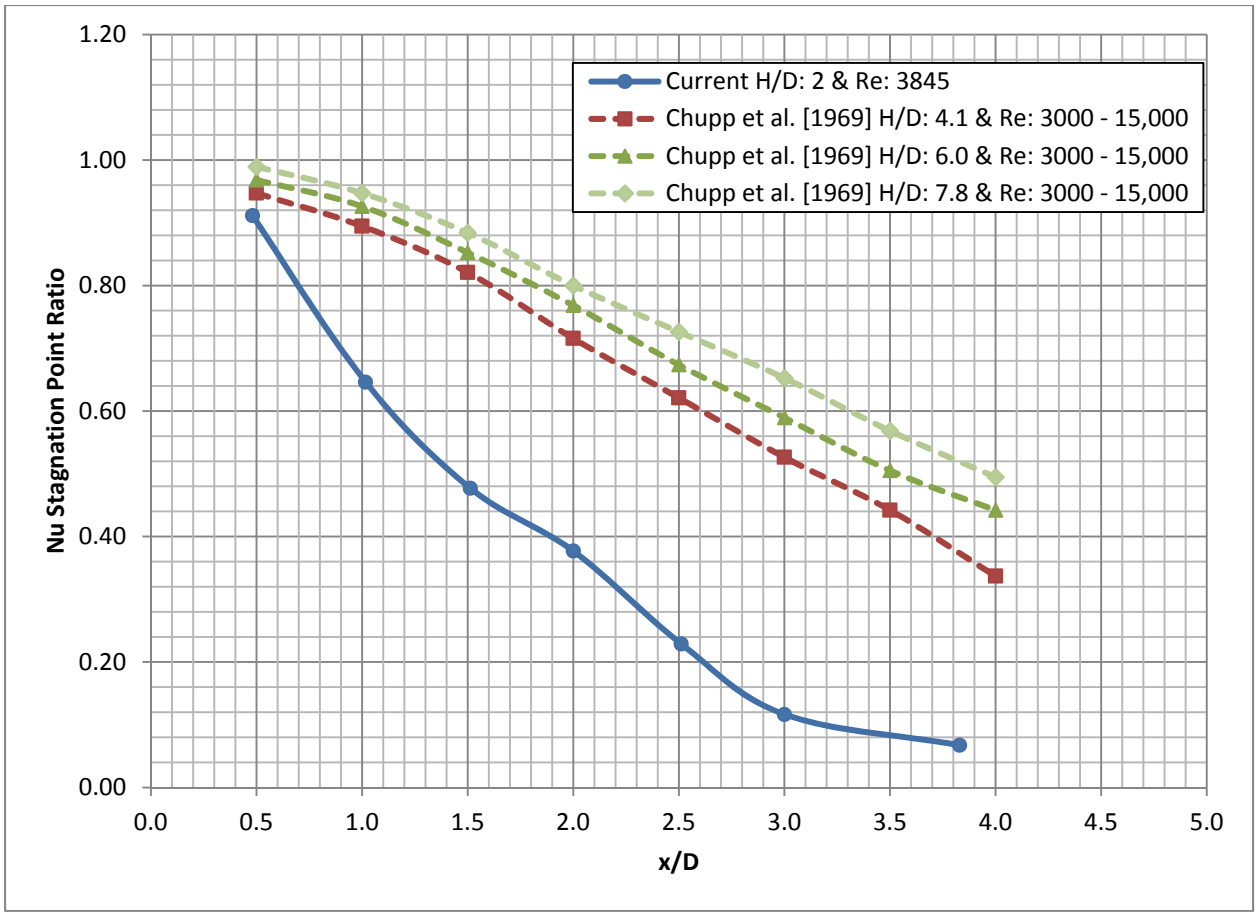

Figure 5.15: Nusselt Stagnation Ratio for the Impingement Cooling

The current study followed a similar trend of Chupp et al. [1969], which was reported in Kerrebrock [1992], Suo [1985] and Liu et al. [2018]. As H/D decrease so does the Nusselt Stagnation Ratio and further from the impingement stagnation point. Figure 5.16 shows the Nusselt number contour on the internal leading edge. Note: Appendix D and E report more material for the adiabatic and CHT simulation of the experiment.

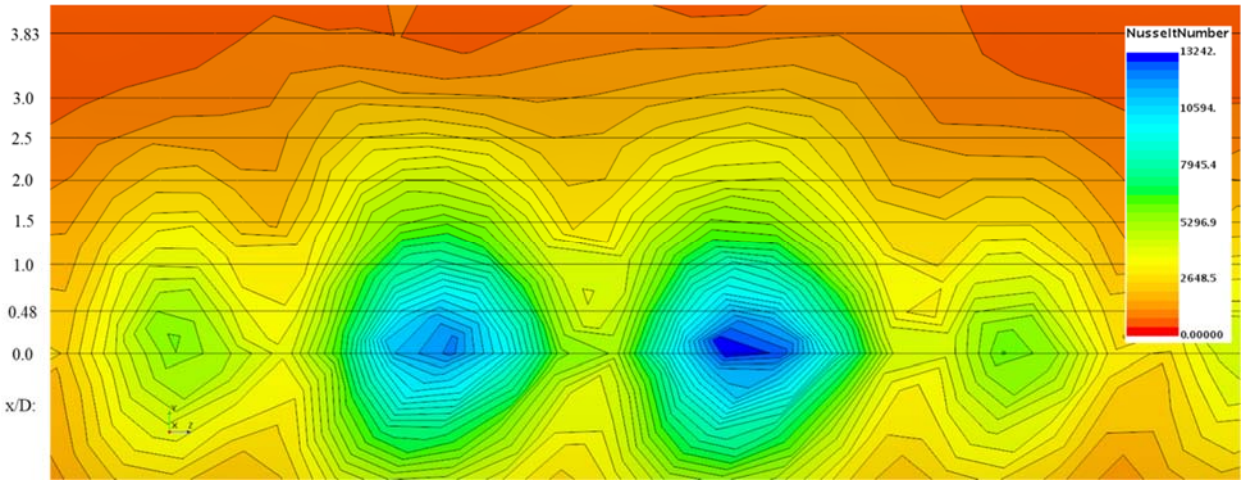

Figure 5.16: Nusselt Number on the Internal Leading Edge

5.3 Parametric Studies on Blowing Parameter, Turbulence Intensity and Density Ratio

A parametric study was conducted on the blowing parameter, turbulence intensity and density ratio. The study matrix is shown in Table 5.7. Case study #1 and #25 are the pivot cases for the investigation, where Case #1 is based on the experiment and Case #25 is based on real engine's density ratio.

Table 5.7: Matrix of the parametric study

Mb	TU: 5%	TU: 10%	TU: 15%	TU: 20%	TU: 25%	DR
0.53	2			11		1.65
0.77	3			12		1.65
0.97				27		1.49
0.98	4	19	20	1	21	1.65
1.10				28		1.72
1.26	22	23	24	25	26	1.99
1.51	5			13		1.65
2.13	6			14		1.65
2.96	7			15		1.65
4.08	8			16		1.65
5.04	9			17		1.65
5.95	10			18		1.65

A detail description of the non-dimensional parameters for film cooling is shown in Table 5.8 for this parametric study.

Table 5.8: Non-dimensional parameters for the parametric study

Supplied Pressure (psig)	Mb (~)	DR (~)	VR (~)	I (~)
0.0025	0.53	1.56	0.34	0.18
0.00625	0.77	1.63	0.47	0.36
0.0125	0.98	1.65	0.59	0.58
0.025	1.51	1.68	0.90	1.35
0.05	2.13	1.69	1.26	2.67
0.1	2.96	1.70	1.75	5.17
0.2	4.08	1.70	2.40	9.80
0.325	5.04	1.70	2.97	14.98
0.475	5.95	1.70	3.51	20.90

5.3.1 Effect of Blowing Parameter on Film Cooling Effectiveness Parameter

A literature study is simulated to compare the trend and laterally average adiabatic effectiveness of the current model blowing parameters. Baldauf et al. [2002] is used for the comparison at multiples blowing parameters and at constant injection angle (α: 30°), turbulence intensity (Tu=1.5%) and density ratio (DR=1.8). Baldauf et al. [2002] was an experiment on a flat plate, where the current study is based on a NACA 0024 airfoil shape. Figure 5.17 shows a comparison of blowing parameter range of 0.5 to 1.51 for both models and the detachment of the jet. The flat plate shows a detached jet at the blowing parameter of 1.0 and the NACA 0024 airfoil shows the detachment at around 1.51.

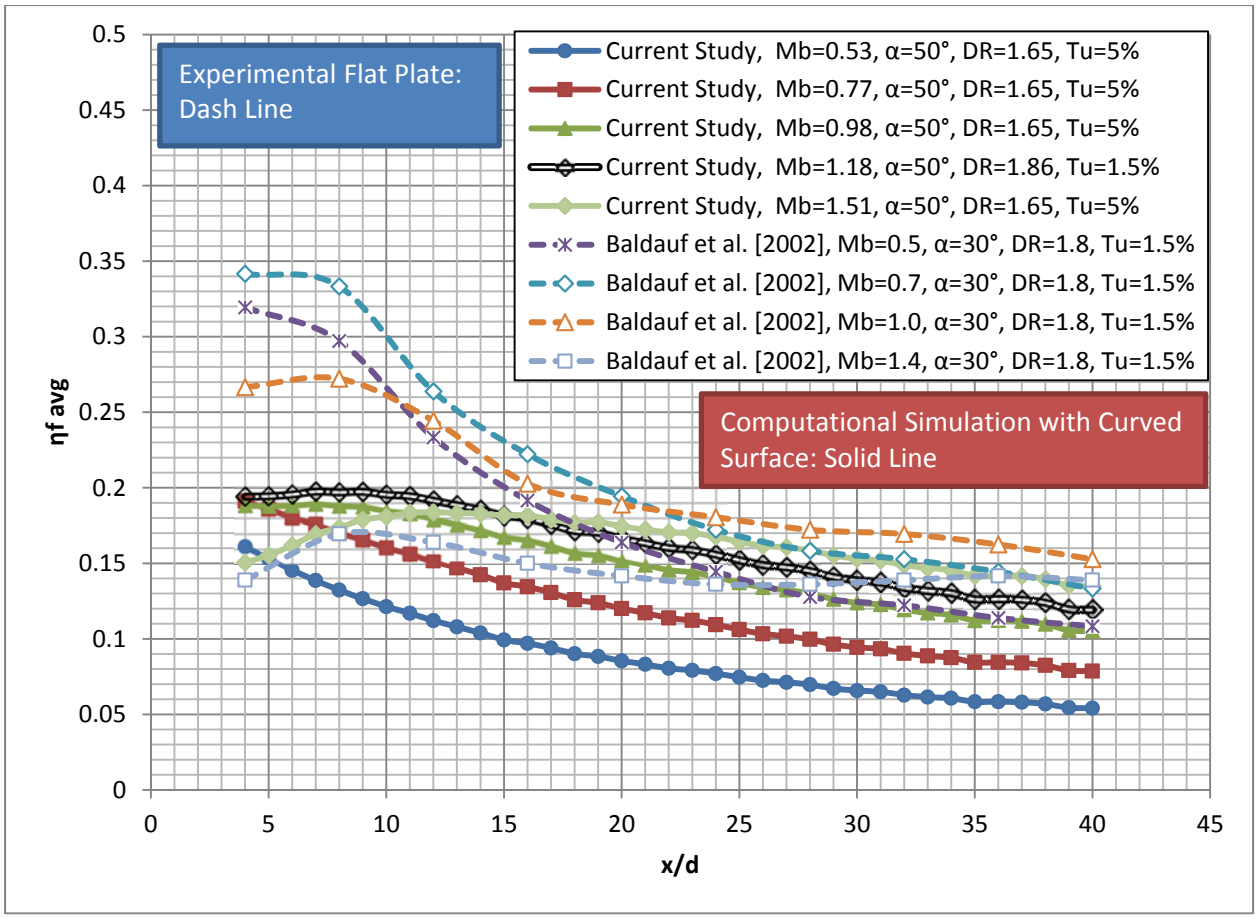

Figure 5.17: Blowing Parameter Comparison between a convex surface and flat plate literature results

The current study shows a good correlation/trend to the flat plate; but the convex curvature, which is one of Bogard [2006] performance factors, explains the discrepancies in the data. In addition, the injection angles have a 20 degree difference, which will induce a 10 to 30% decrease in film effectiveness on flat plates, which is summarized in Bogard and Thole [2006].

Numerical simulations for blowing ratios in the range of 0.5-6.0 are studied. These blowing ratios are simulated at Tu of 5% and 20% with a DR of 1.65. The laterally averaged and local centerline adiabatic effectiveness is reported in Figures 5.18 to 5.21 at various streamwise locations. The turbulence intensity of 20% is modeled to represent realistic of a gas turbine engine flow environment. The case of 5% is shown to relate the current study to other studies in literature. In Figure 5.18 the results for high turbulence intensity of 20% are shown. Figure 5.19

displays the results for low turbulence intensity at 5%. Figures 5.20 and 5.21 are the centerline adiabatic effectiveness at 20% and 5% turbulence intensities, respectively.

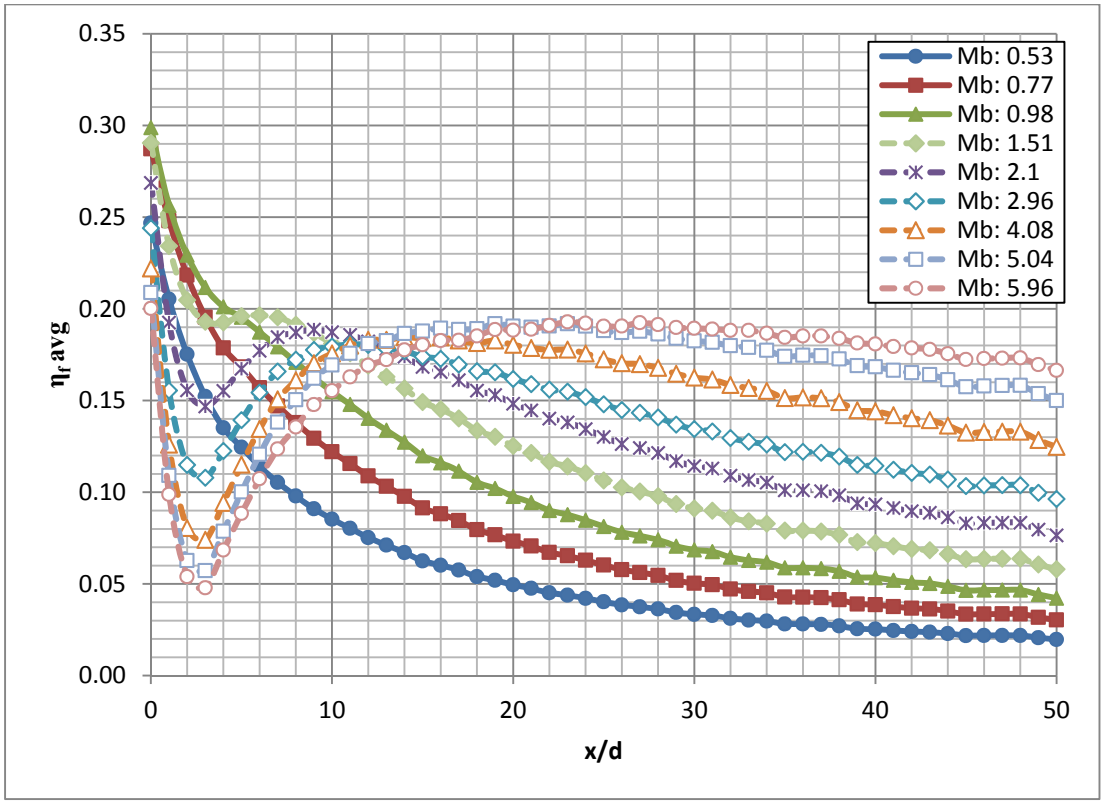

Figure 5.18: Laterally averaged adiabatic effectiveness for various Blowing Parameters, Tu = 20%

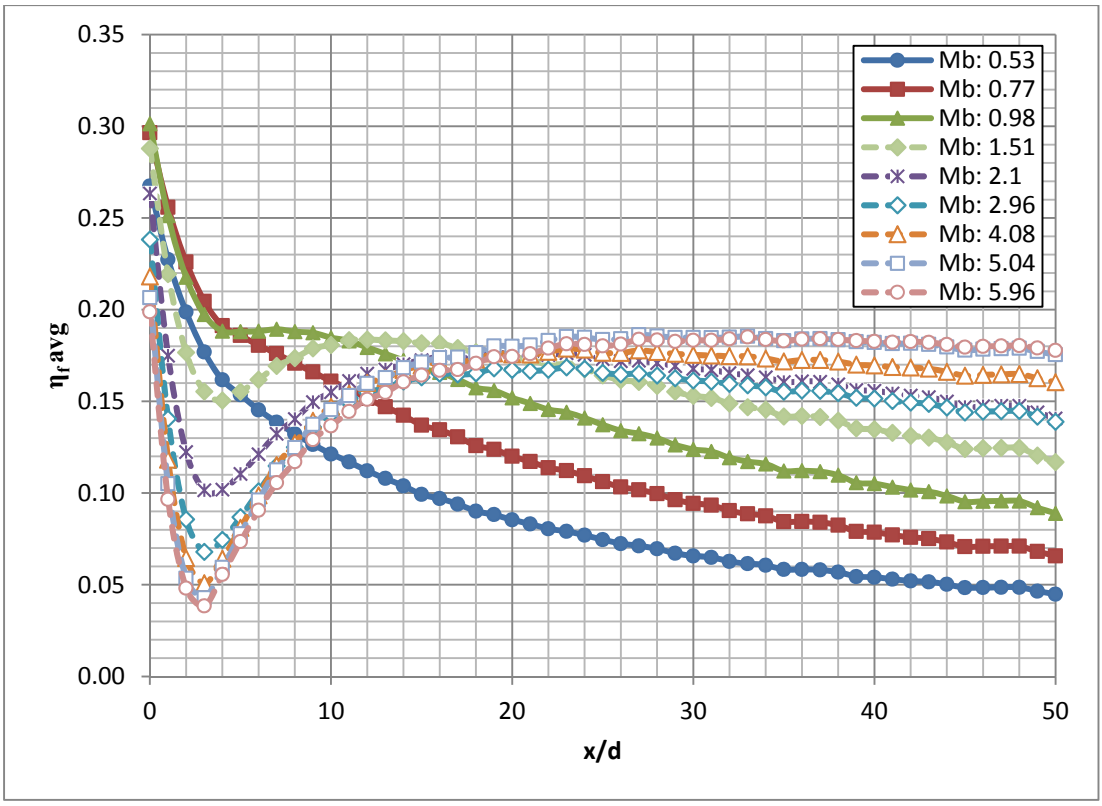

Figure 5.19: Laterally averaged adiabatic effectiveness for various Blowing Parameters, Tu = 5%

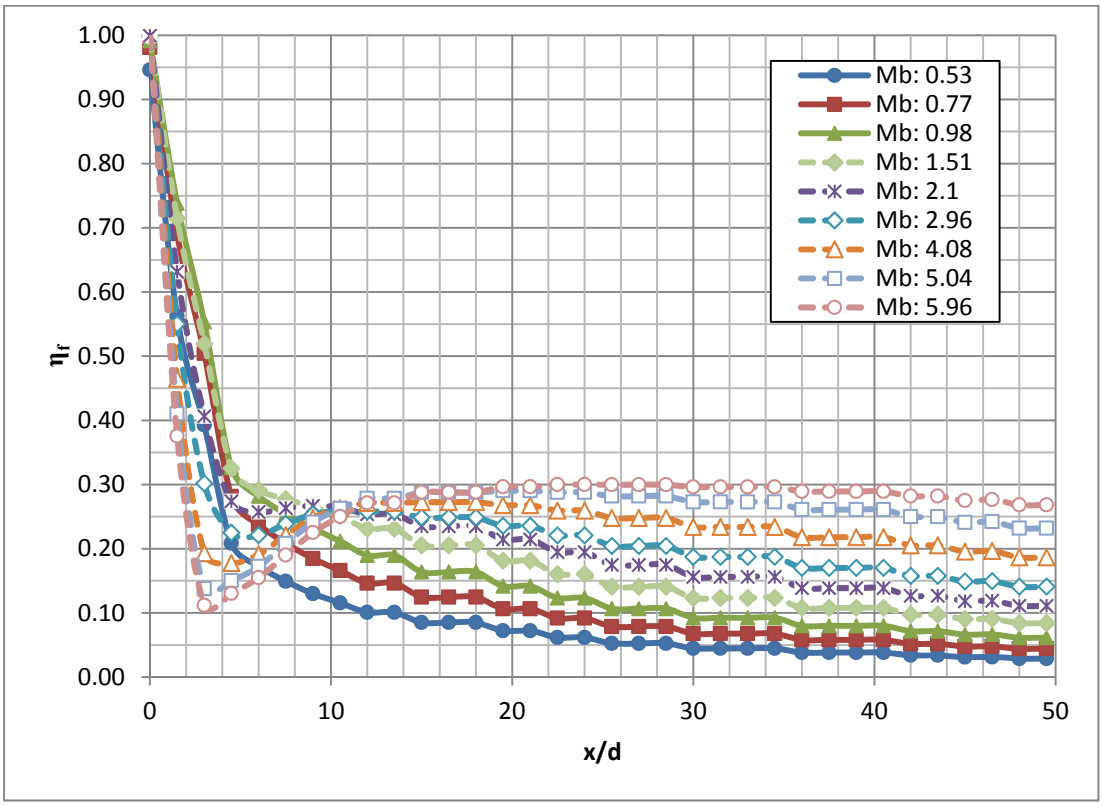

Figure 5.20: Centerline adiabatic effectiveness for various Blowing Parameters, Tu = 20%

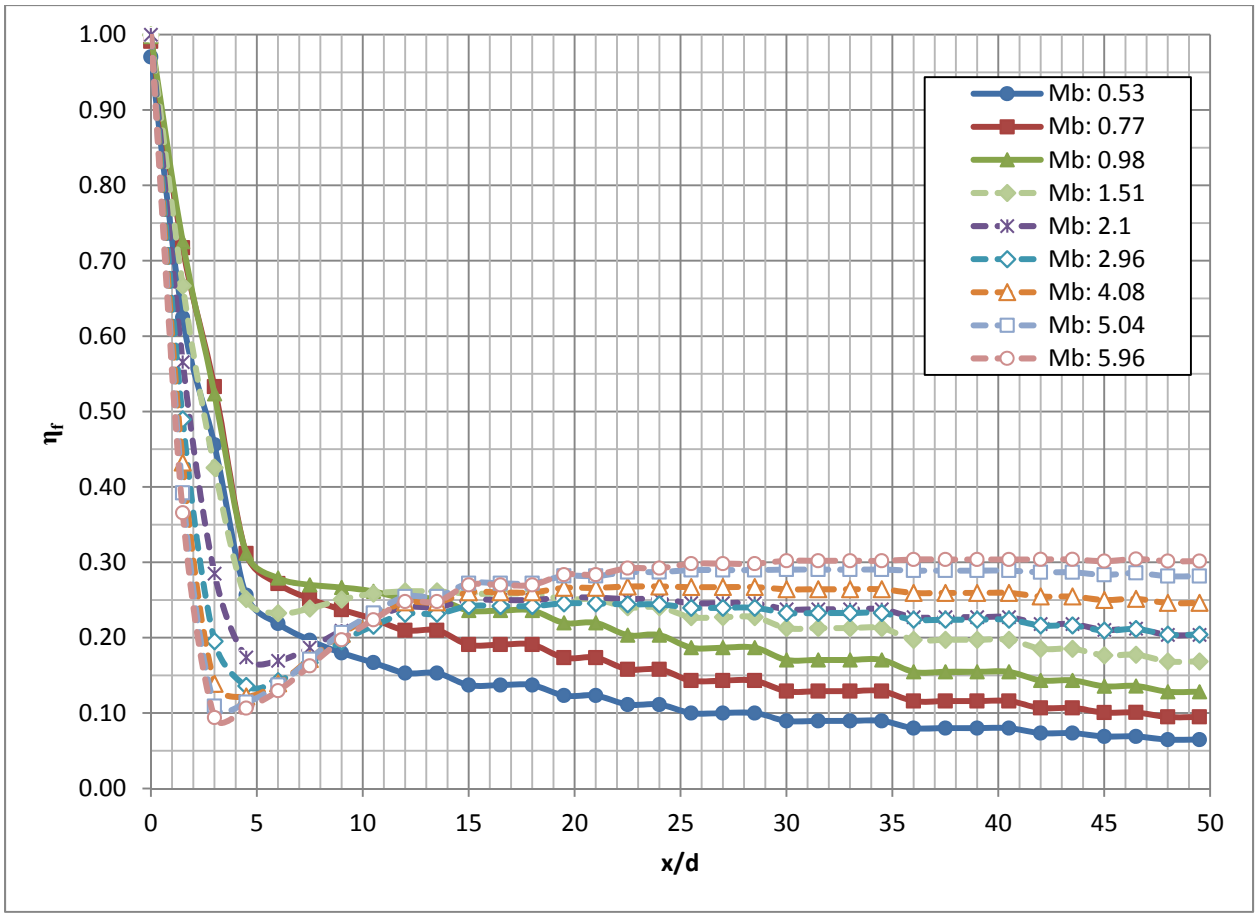

Figure 5.21: Centerline adiabatic effectiveness for various Blowing Parameters, Tu = 5%

Low blowing parameters are considered to be below 1.0 and anything above is classified to be moderate to high. Low blowing parameters yield high lateral averaged adiabatic effectiveness from 0 to 10 x/d, but farther downstream from the film holes, the high blowing parameters show higher effectiveness. The low blowing parameters attach and spread on the wall immediately after the coolant is injected. These results are correlated to other blowing parameters studies; Baldauf et al. [2002], Ito et al. [1978] and Waye and Bogard [2006]. As the blowing parameter increases from 0.53 to 0.98, the film cooling effectiveness is increased along with the blowing parameter. This is caused by the increasing mass flow of the coolant, while remaining attached to the wall. Once the blowing parameter reaches the value of 1.51, the jet shows the onset of separation; therefore, the transition from attached to detached is between 1.0

and 1.5 for this configuration. At higher blowing parameter, the film cooling effectiveness drops due to the detachment from the surface, but reattaches downstream to increase the lateral averaged adiabatic film effectiveness. The blowing parameter's impact on attachment and detachment can be seen in Figure 5.22 – 5.39. Blowing parameters from 0.53 to 0.98 showed attached flow and higher blowing parameters demonstrate a detached jet from the surface, which is shown in Figures 5.22 to 5.30 for Tu of 20% and Figures 5.40 to 5.39 for Tu of 5%. Additional data is tabulated in Appendix F and G for the blowing parameter cases.

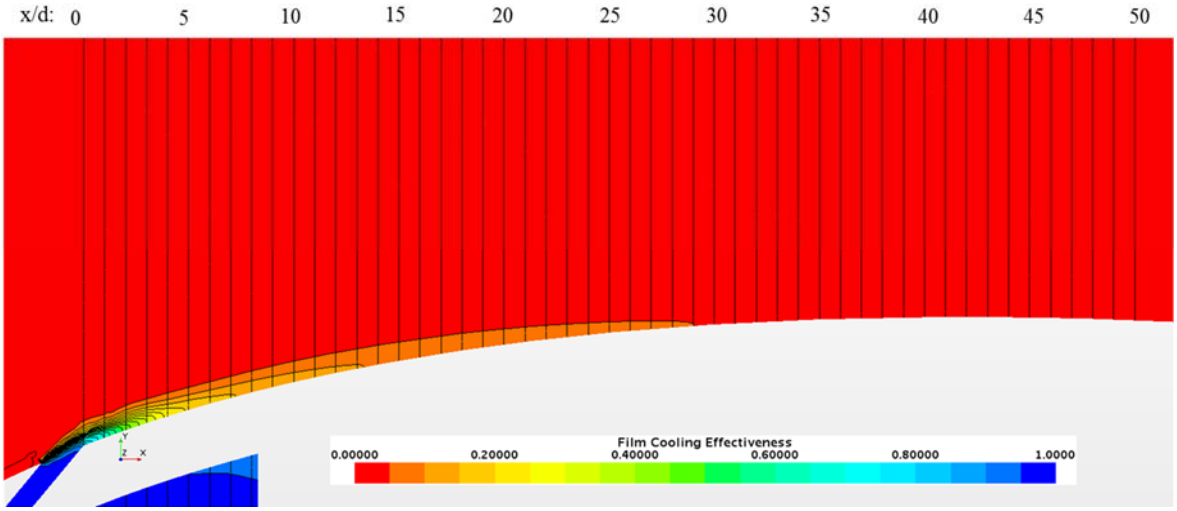

Figure 5.22: Adiabatic Film Cooling Effectiveness profile for centerline: Mb = 0.53, Tu = 20%

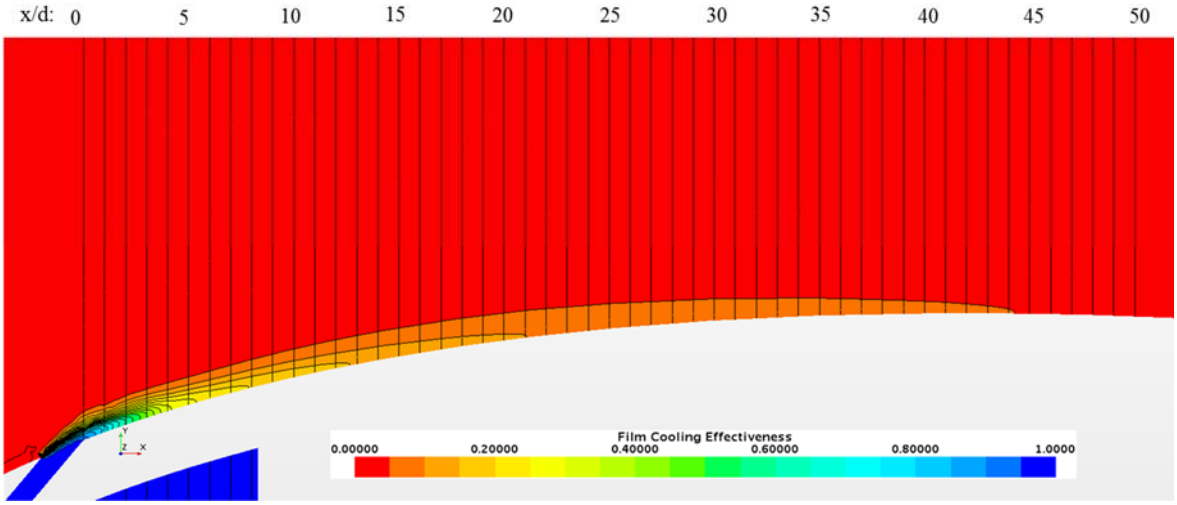

Figure 5.23: Adiabatic Film Cooling Effectiveness profile for centerline: Mb = 0.77, Tu = 20%

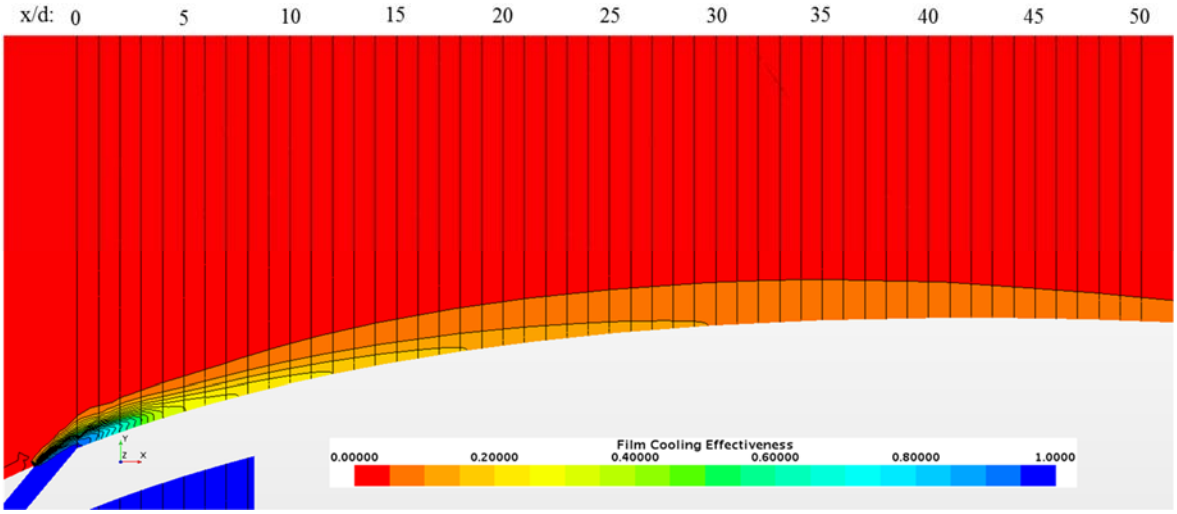

Figure 5.24: Adiabatic Film Cooling Effectiveness profile for centerline: Mb = 0.98, Tu = 20%

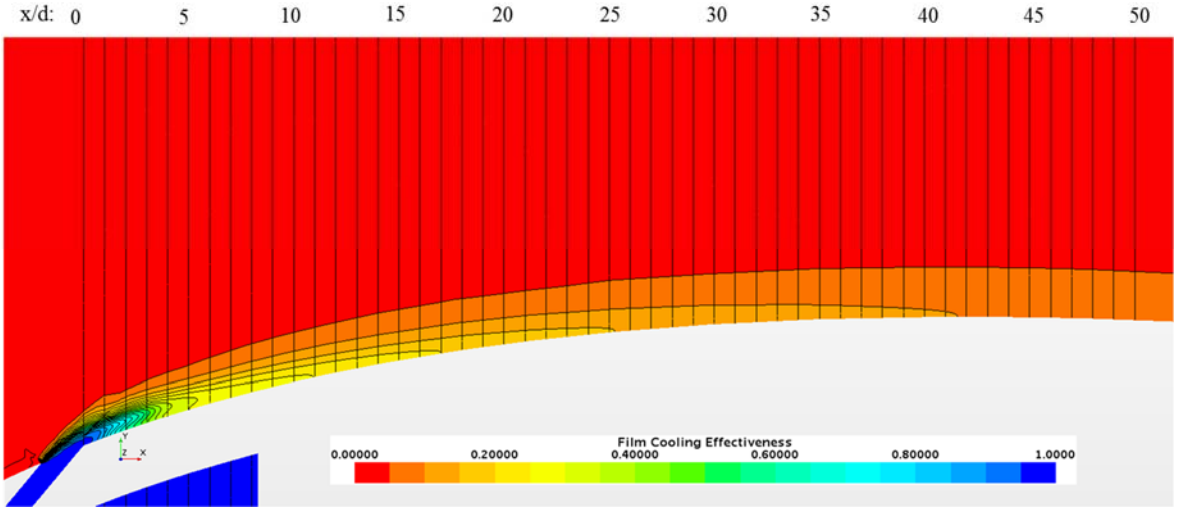

Figure 5.25: Adiabatic Film Cooling Effectiveness profile for centerline: Mb = 1.51, Tu = 20%

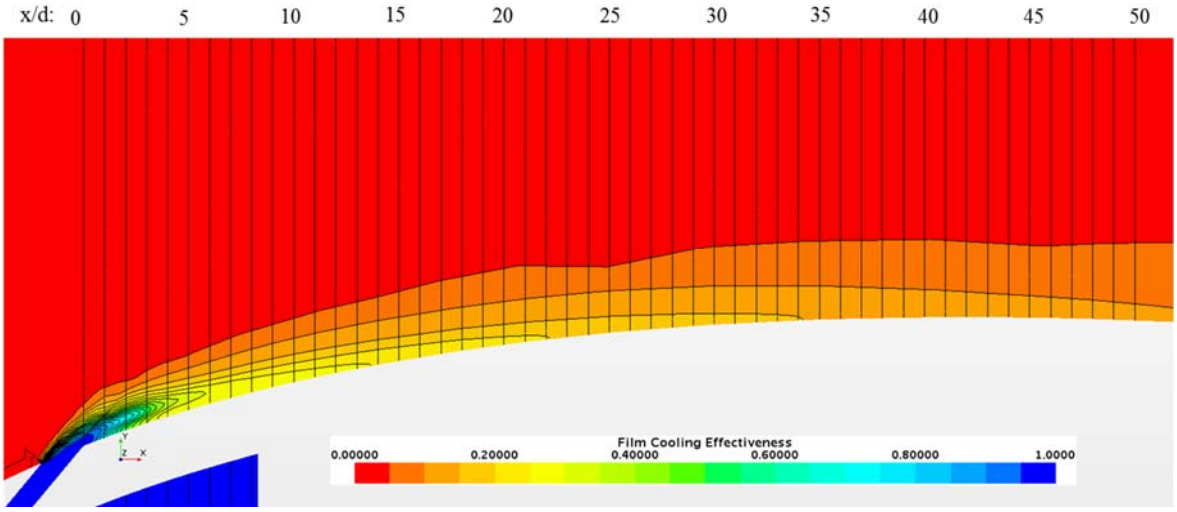

Figure 5.26: Adiabatic Film Cooling Effectiveness profile for centerline: Mb = 2.13, Tu = 20%

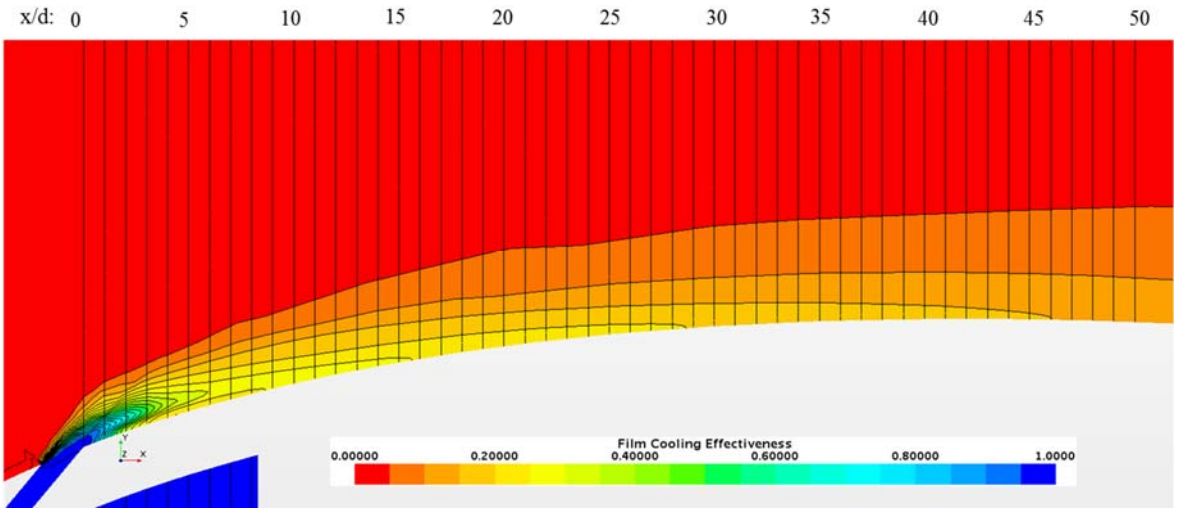

Figure 5.27: Adiabatic Film Cooling Effectiveness profile for centerline: Mb = 2.96, Tu = 20%

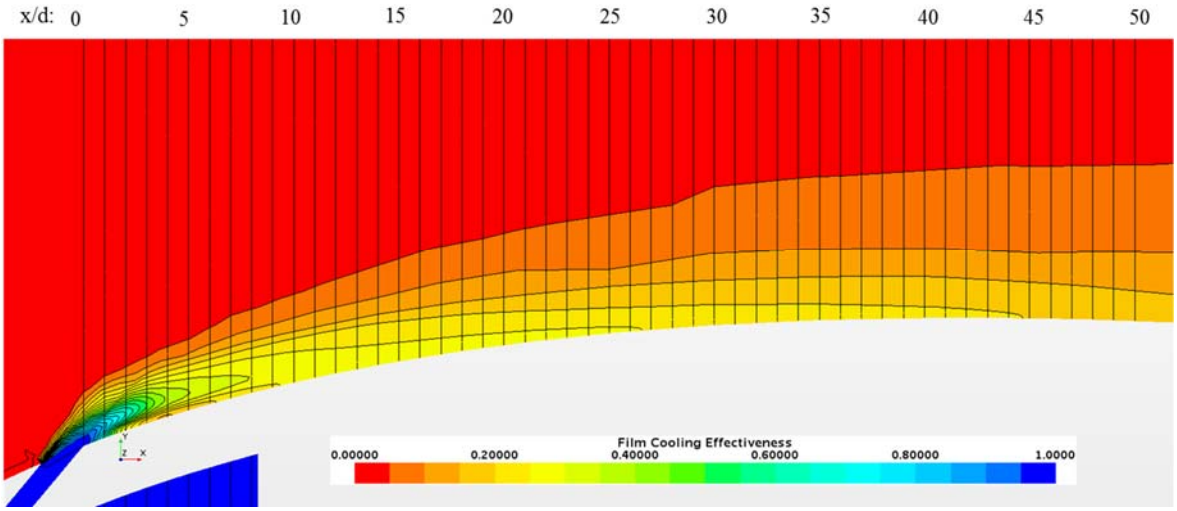

Figure 5.28: Adiabatic Film Cooling Effectiveness profile for centerline: Mb = 4.08, Tu = 20%

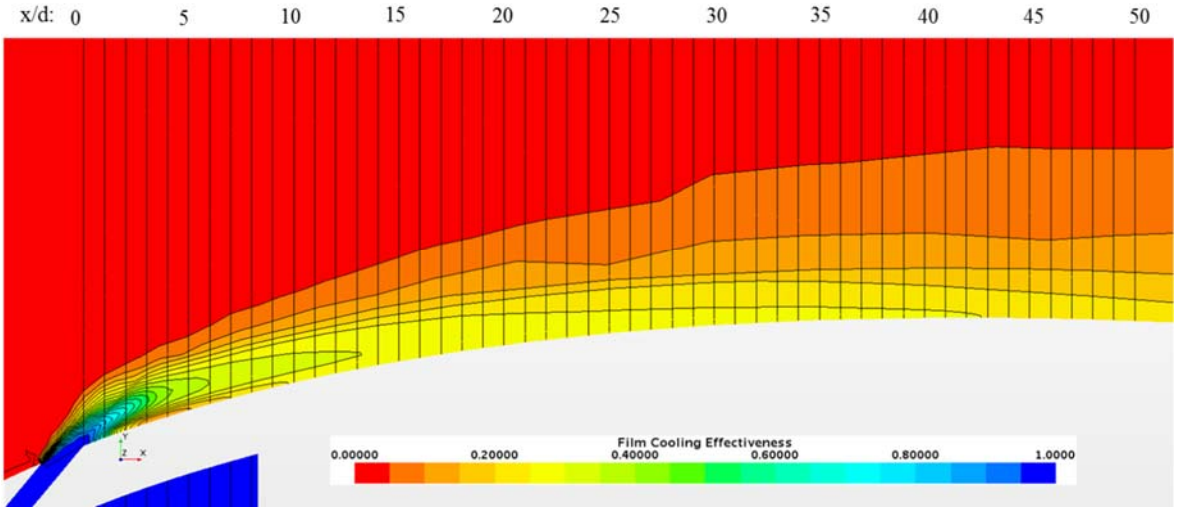

Figure 5.29: Adiabatic Film Cooling Effectiveness profile for centerline: Mb =5.04, Tu = 20%

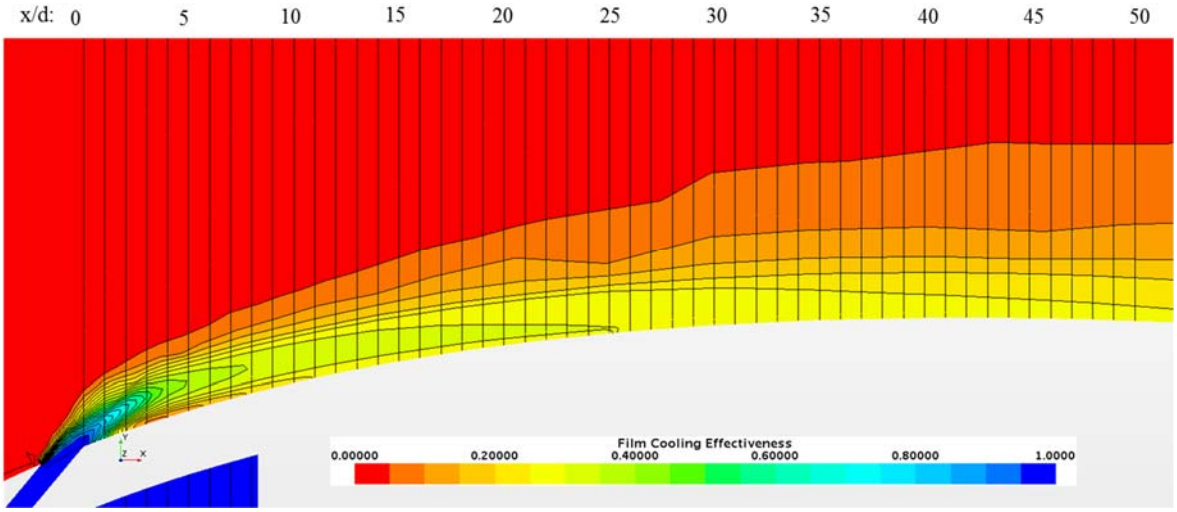

Figure 5.30: Adiabatic Film Cooling Effectiveness profile for centerline: Mb =5.95, Tu = 20%

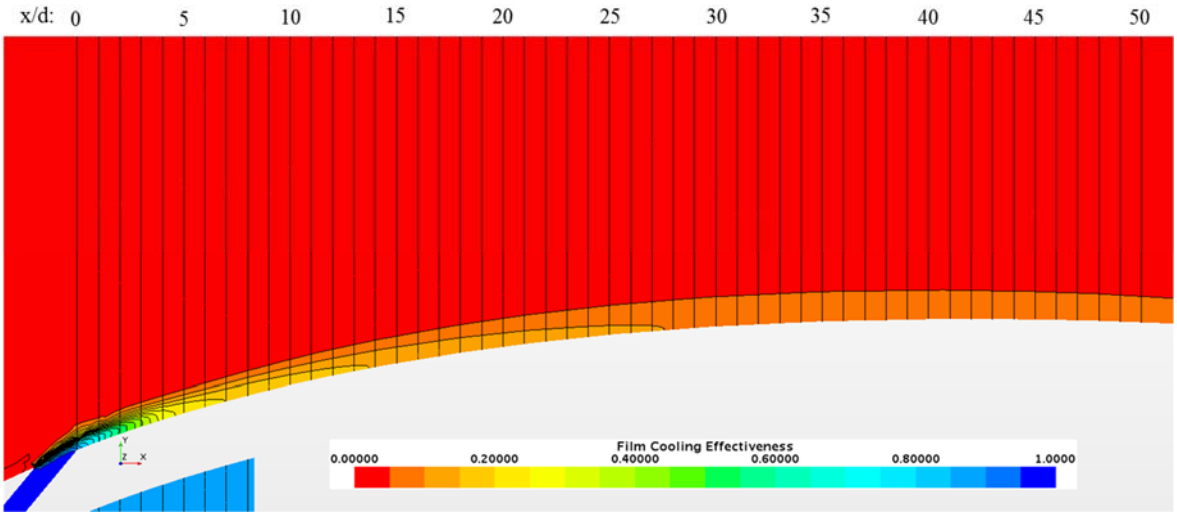

Figure 5.31: Adiabatic Film Cooling Effectiveness profile for centerline: Mb =0.53, Tu = 5%

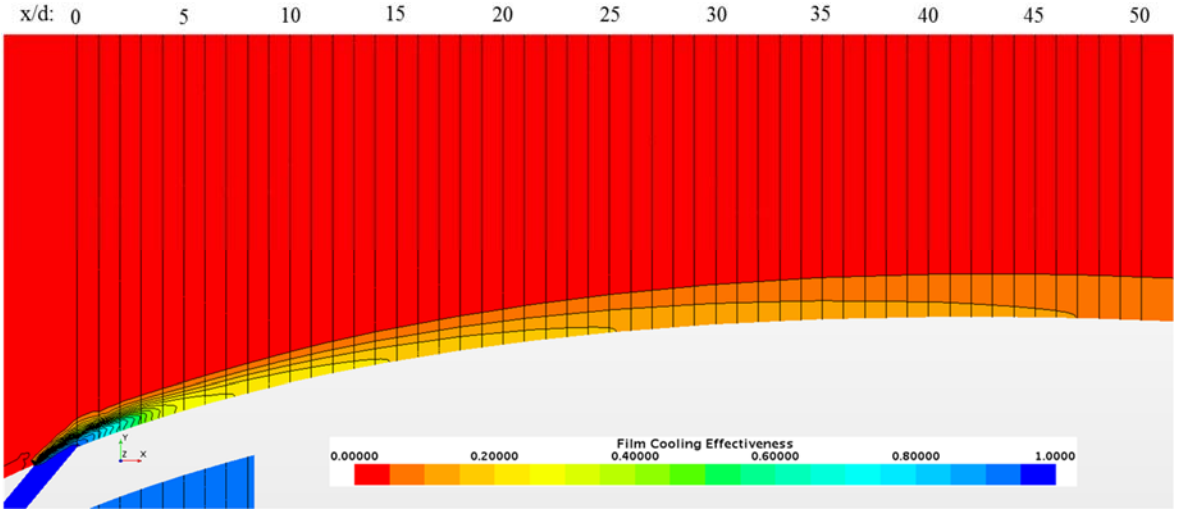

Figure 5.32: Adiabatic Film Cooling Effectiveness profile for centerline: Mb =0.77, Tu = 5%

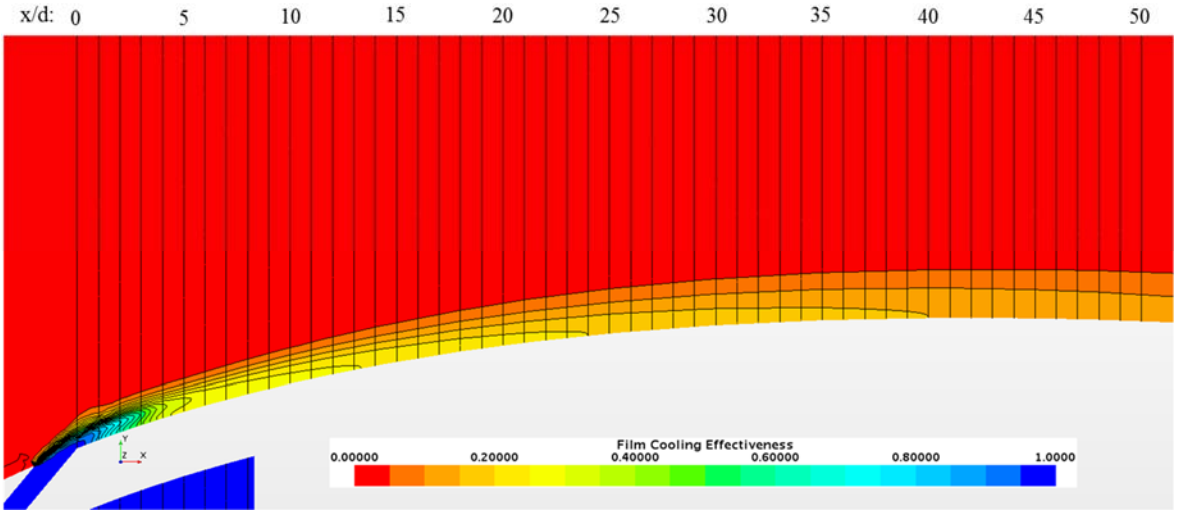

Figure 5.33: Adiabatic Film Cooling Effectiveness profile for centerline: Mb =0.98, Tu = 5%

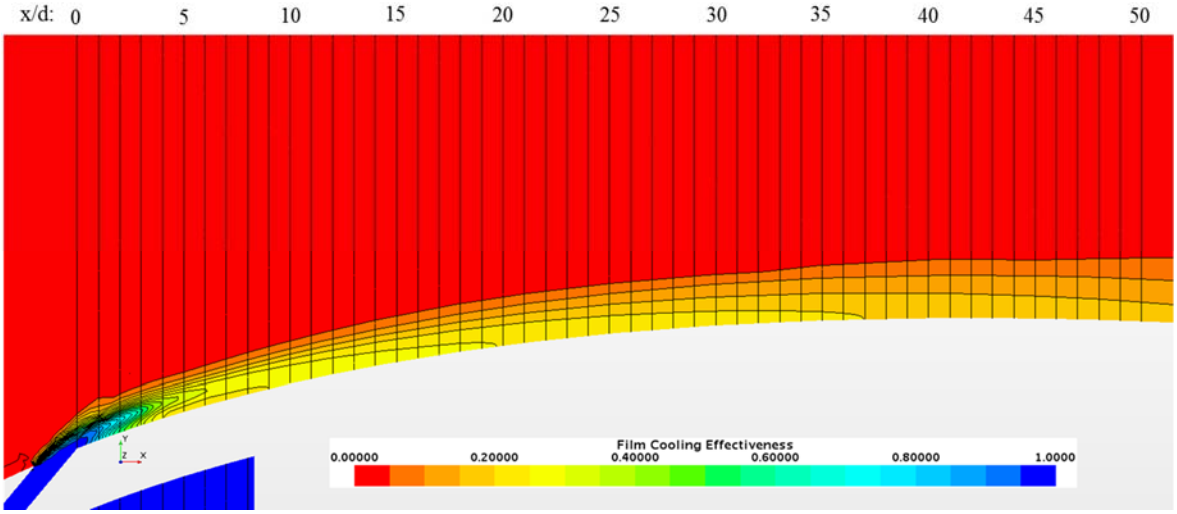

Figure 5.34: Adiabatic Film Cooling Effectiveness profile for centerline: Mb =1.51, Tu = 5%

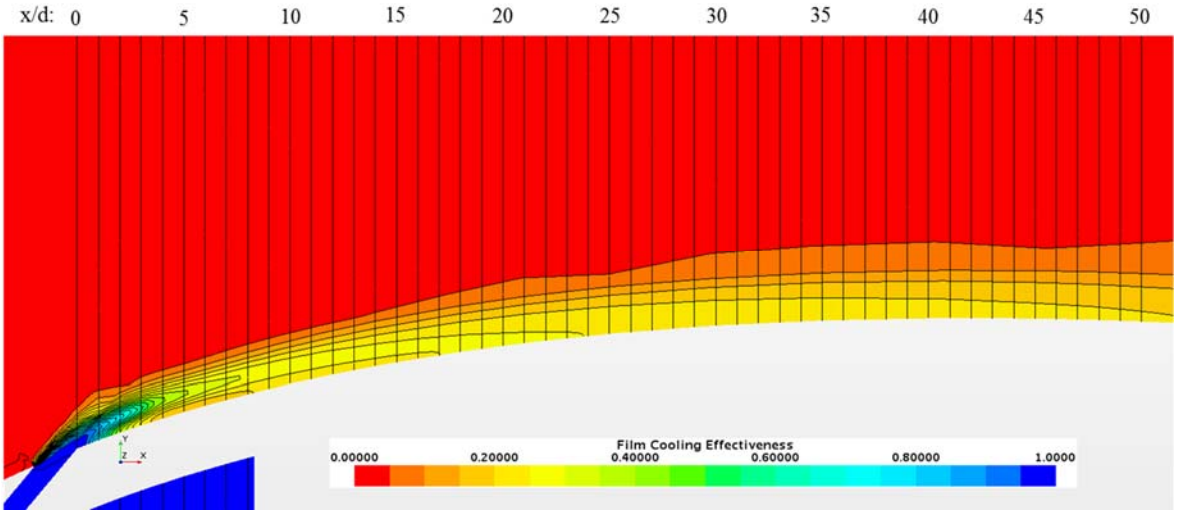

Figure 5.35: Adiabatic Film Cooling Effectiveness profile for centerline: Mb =2.13, Tu = 5%

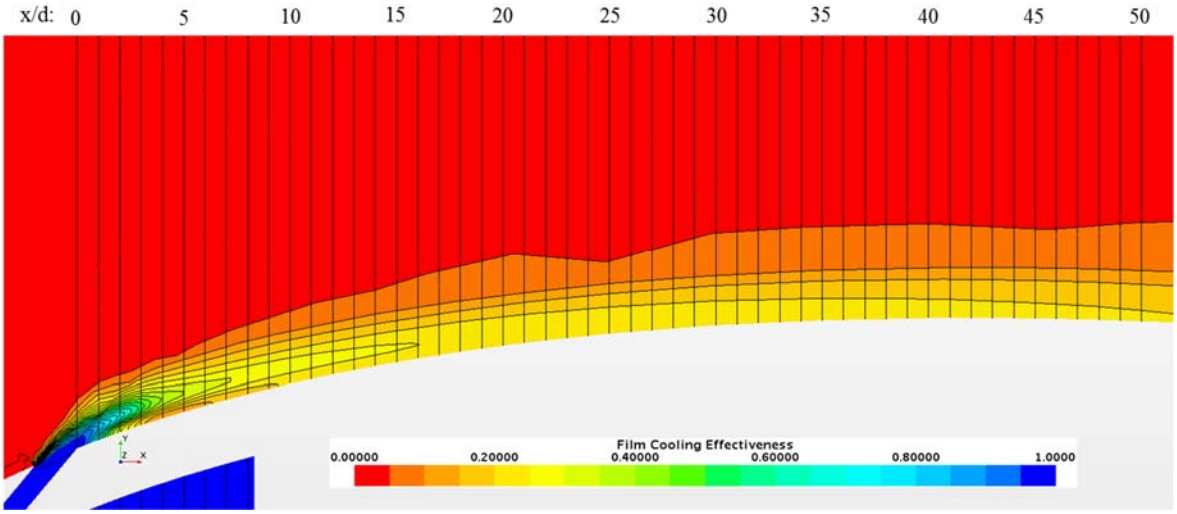

Figure 5.36: Adiabatic Film Cooling Effectiveness profile for centerline: Mb =2.96, Tu = 5%

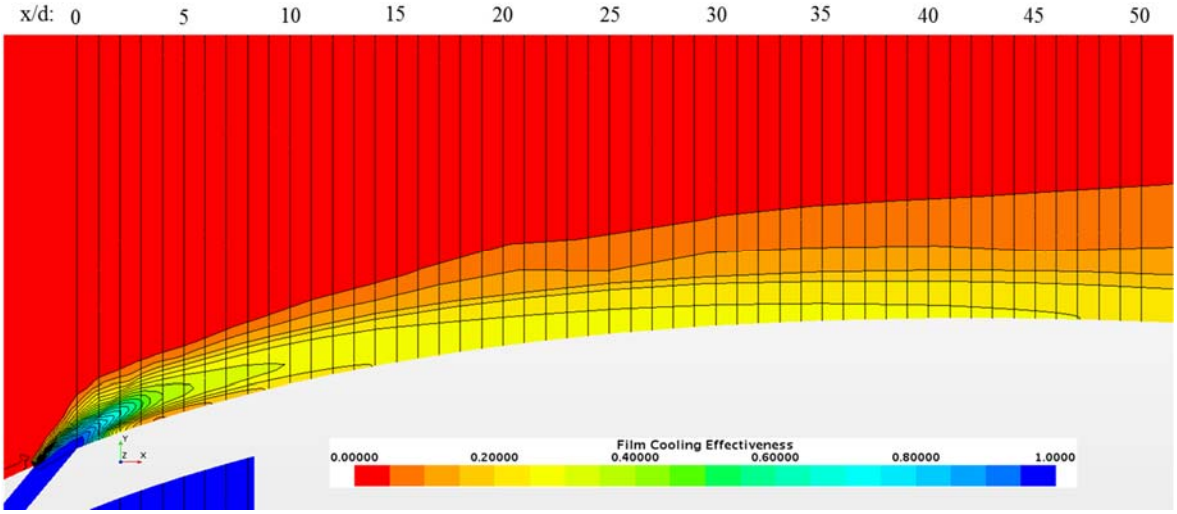

Figure 5.37: Adiabatic Film Cooling Effectiveness profile for centerline: Mb =4.08, Tu = 5%

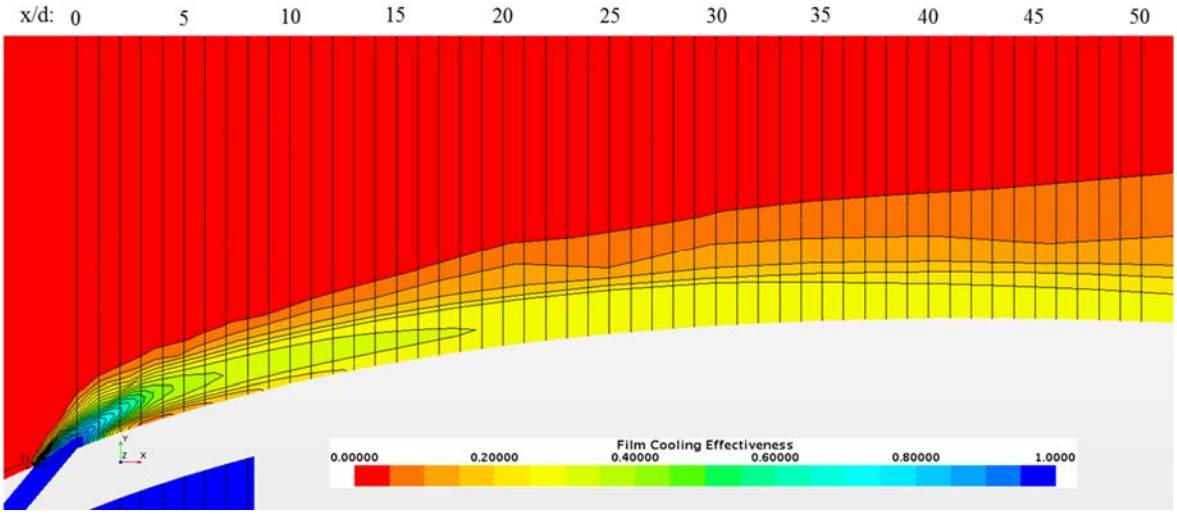

Figure 5.38: Adiabatic Film Cooling Effectiveness profile for centerline: Mb =5.04, Tu = 5%

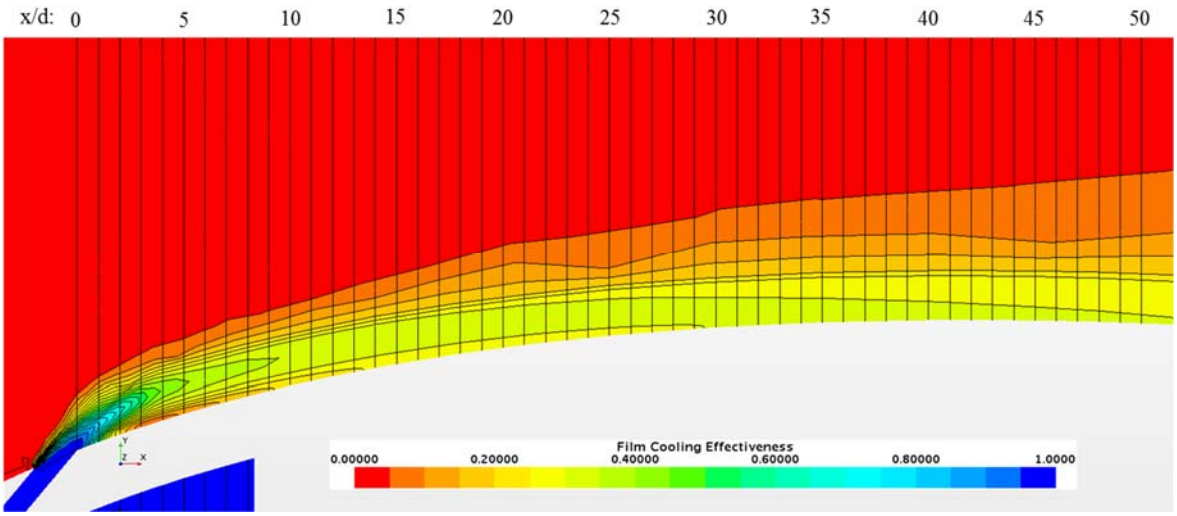

Figure 5.39: Adiabatic Film Cooling Effectiveness profile for centerline: Mb =5.95, Tu = 5%

Figures 5.40 - 5.57 display the suction surface distribution for the adiabatic film cooling effectiveness. The distribution shows the detachment and the adiabatic film cooling effectiveness spreading downstream by the blowing parameter and turbulence intensity.

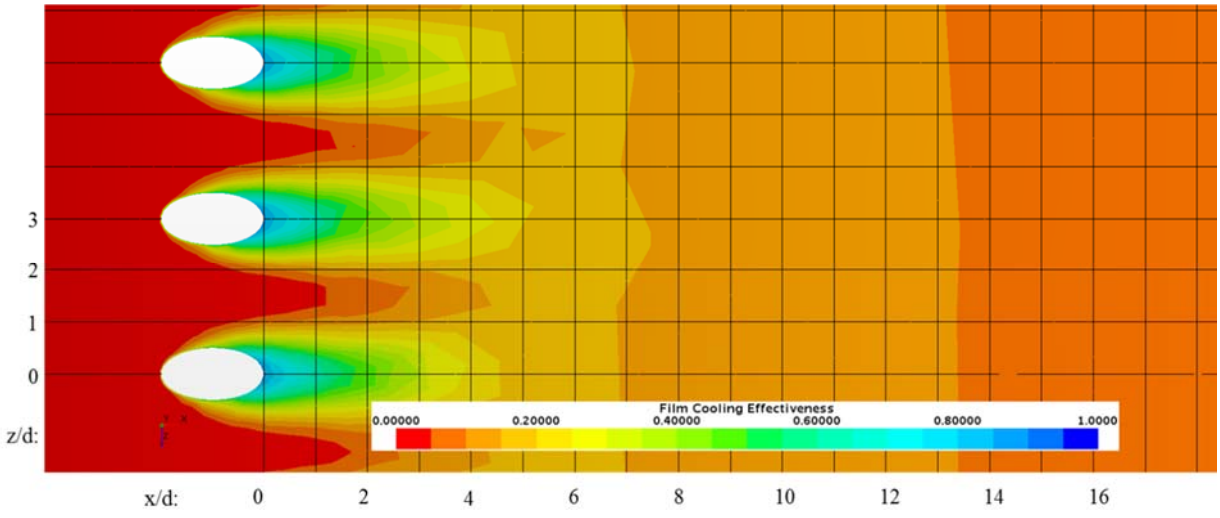

Figure 5.40: Adiabatic Effectiveness distribution for Suction Surface: Mb = 0.53, Tu = 20%

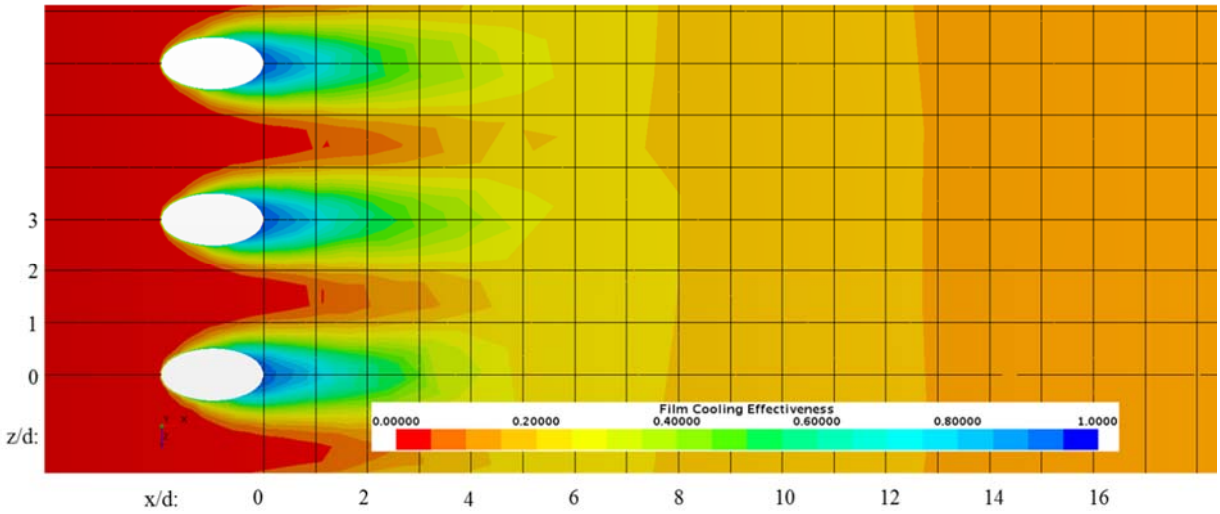

Figure 5.41: Adiabatic Effectiveness distribution for Suction Surface: Mb = 0.77, Tu = 20%

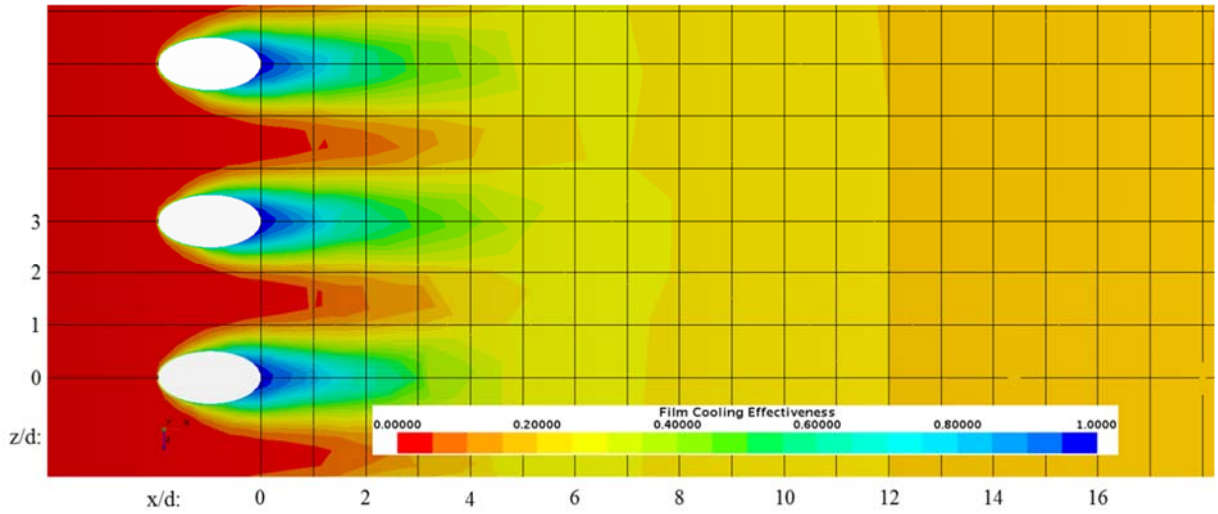

Figure 5.42: Adiabatic Effectiveness distribution for Suction Surface: Mb = 0.98, Tu = 20%

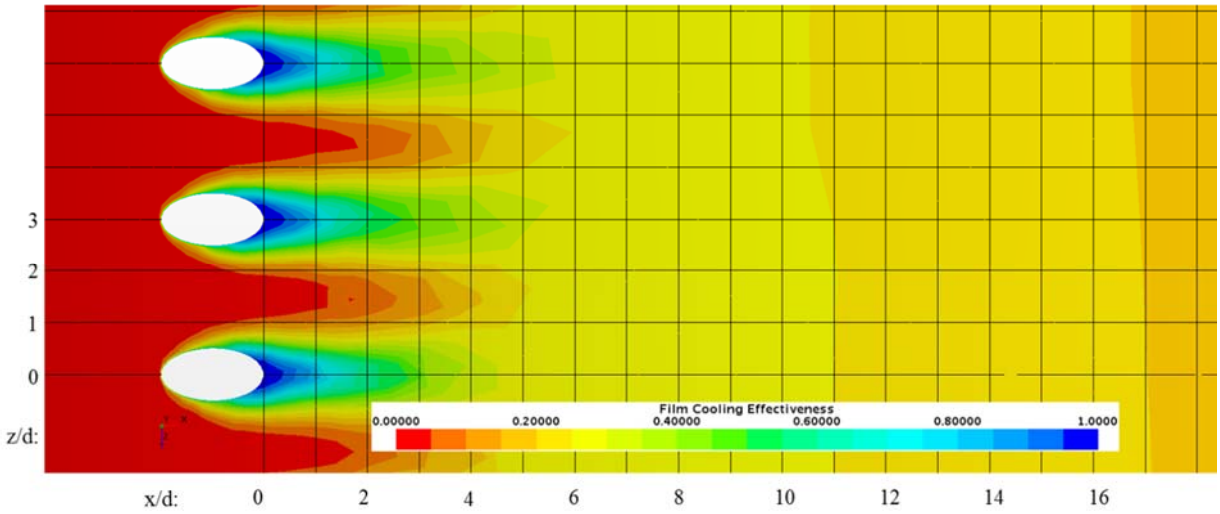

Figure 5.43: Adiabatic Effectiveness distribution for Suction Surface: Mb = 1.51, Tu = 20%

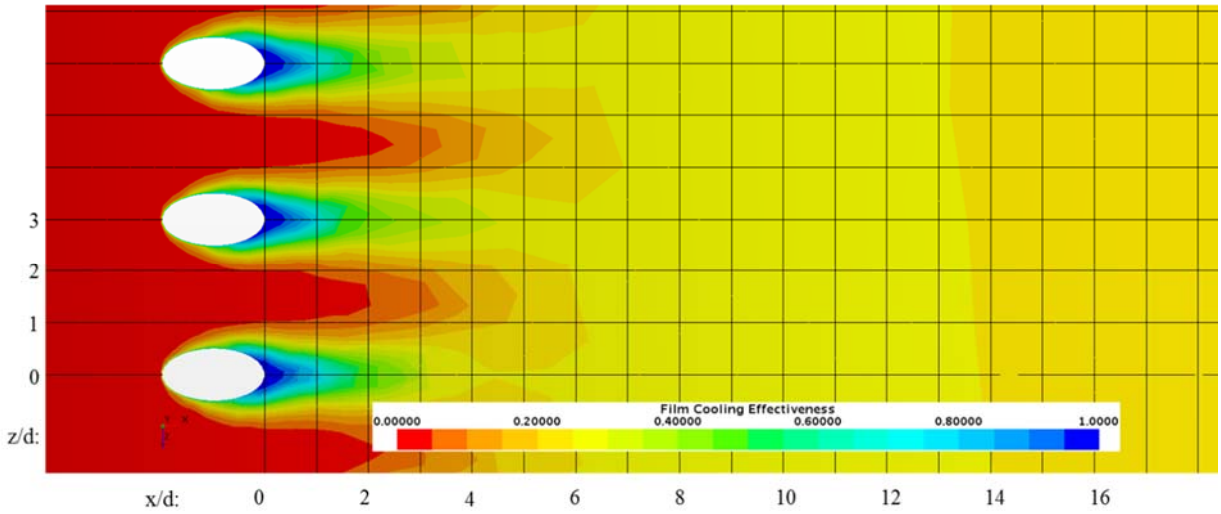

Figure 5.44: Adiabatic Effectiveness distribution for Suction Surface: Mb = 2.13, Tu = 20%

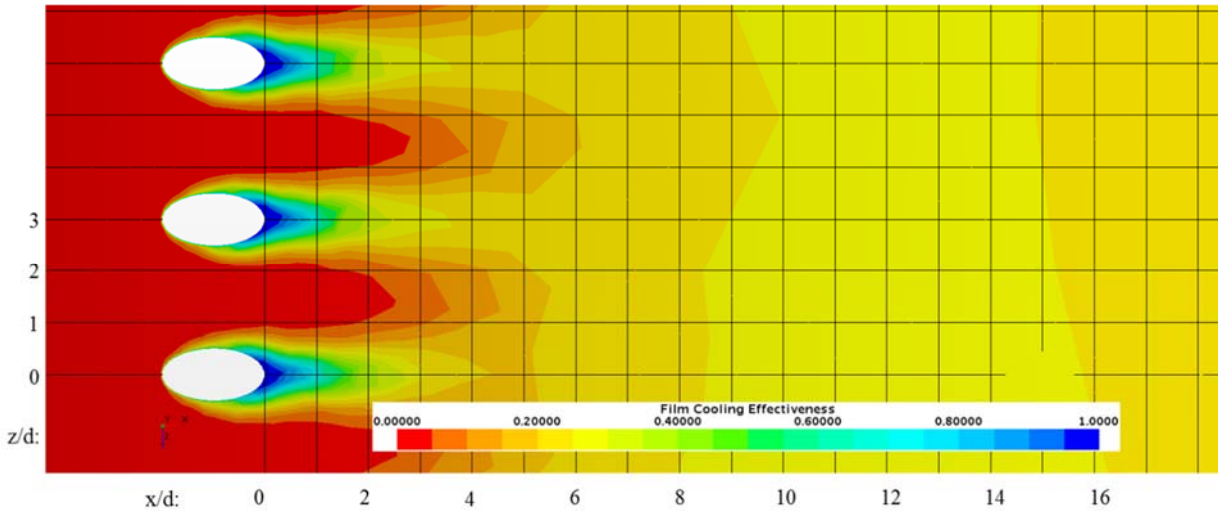

Figure 5.45: Adiabatic Effectiveness distribution for Suction Surface: Mb = 2.96, Tu = 20%

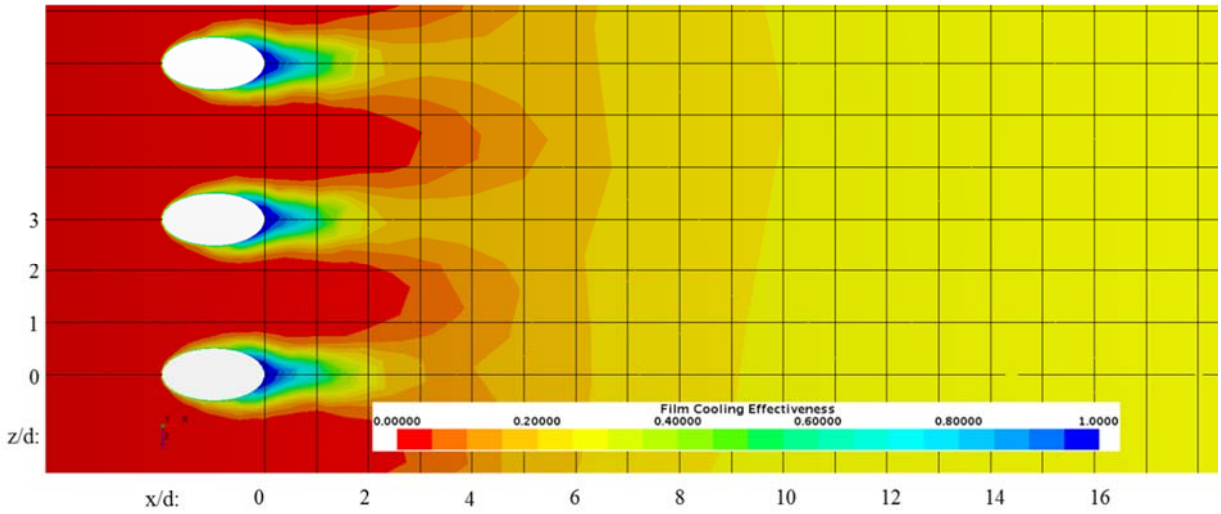

Figure 5.46: Adiabatic Effectiveness distribution for Suction Surface: Mb = 4.08, Tu = 20%

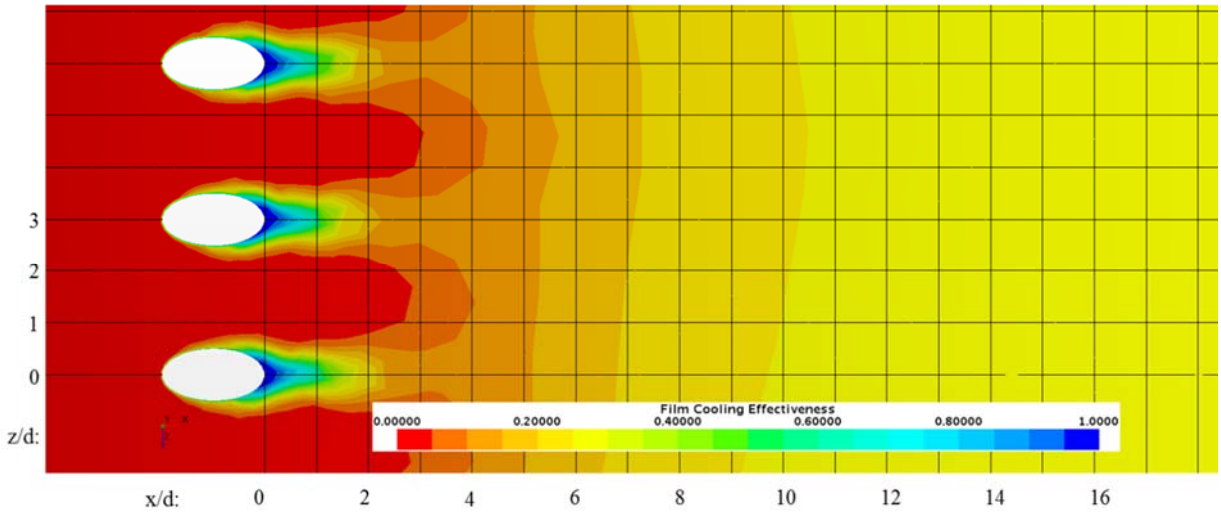

Figure 5.47: Adiabatic Effectiveness distribution for Suction Surface: Mb =5.04, Tu = 20%

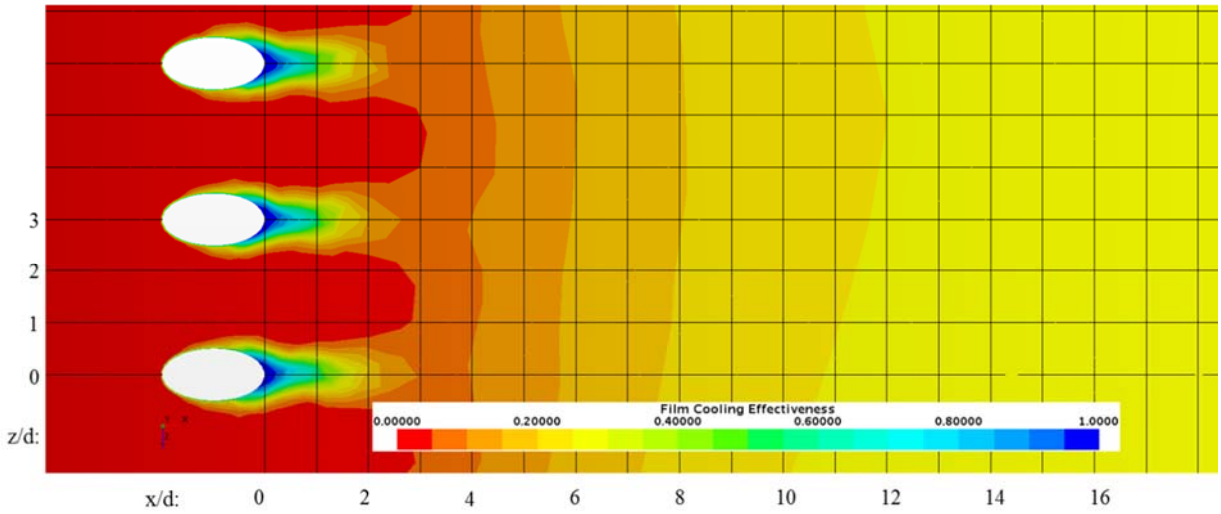

Figure 5.48: Adiabatic Effectiveness distribution for Suction Surface: Mb =5.95, Tu = 20%

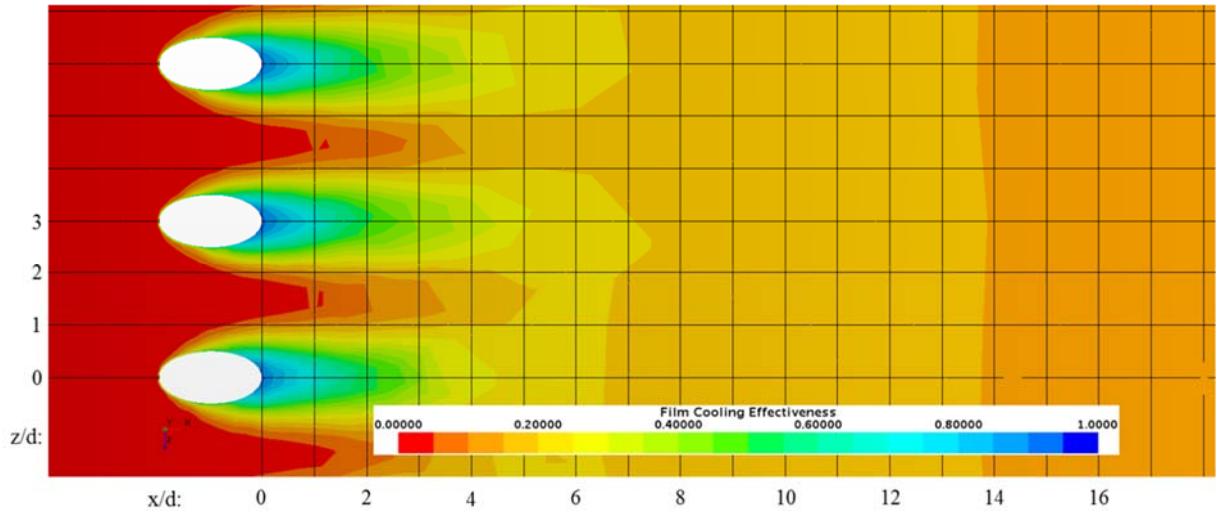

Figure 5.49: Adiabatic Effectiveness distribution for Suction Surface: Mb =0.53, Tu = 5%

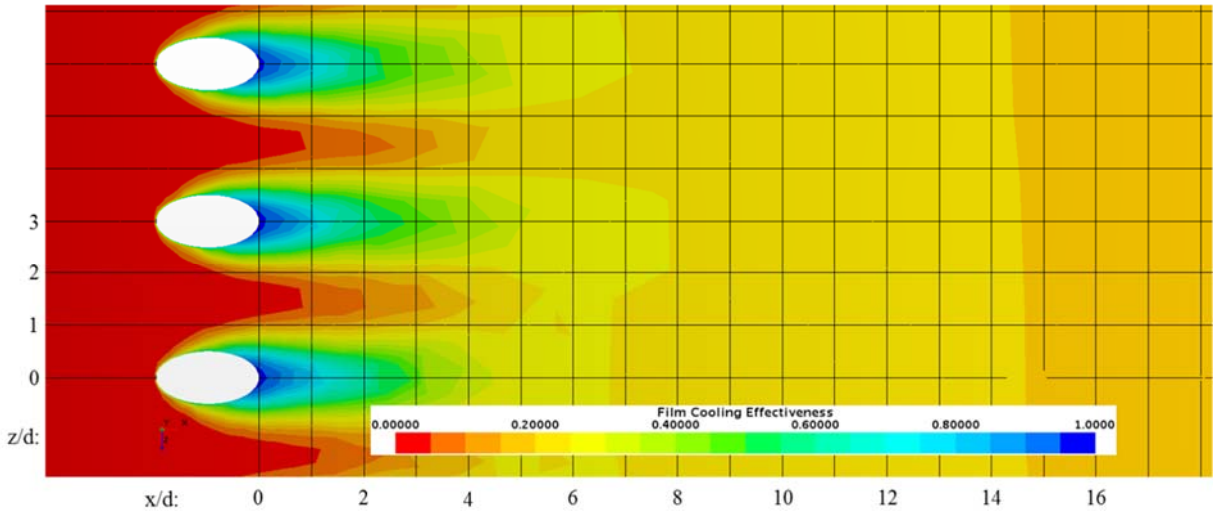

Figure 5.50: Adiabatic Effectiveness distribution for Suction Surface: Mb =0.77, Tu = 5%

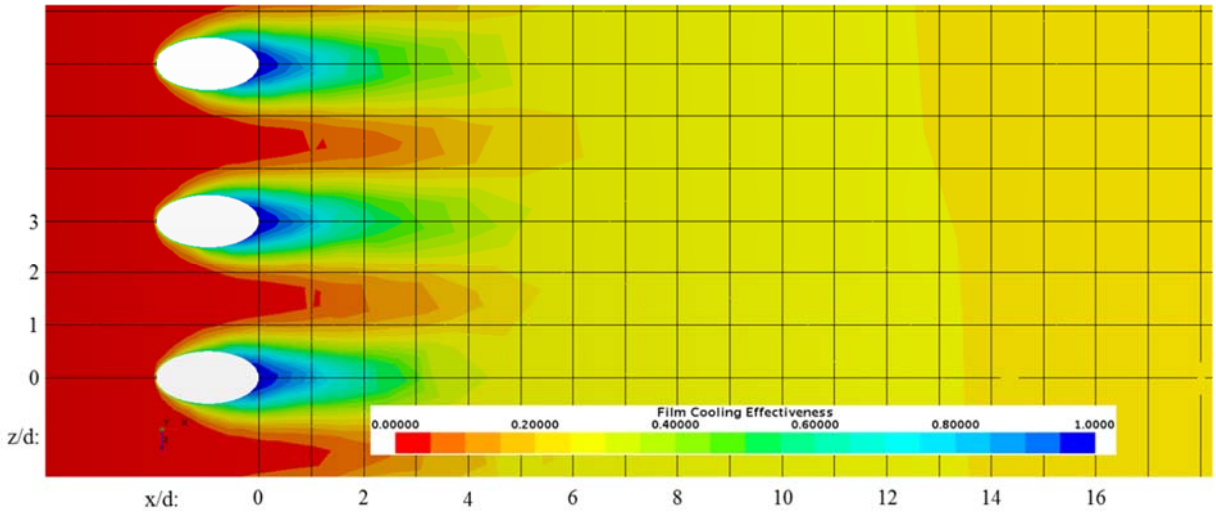

Figure 5.51: Adiabatic Effectiveness distribution for Suction Surface: Mb =0.98, Tu = 5%

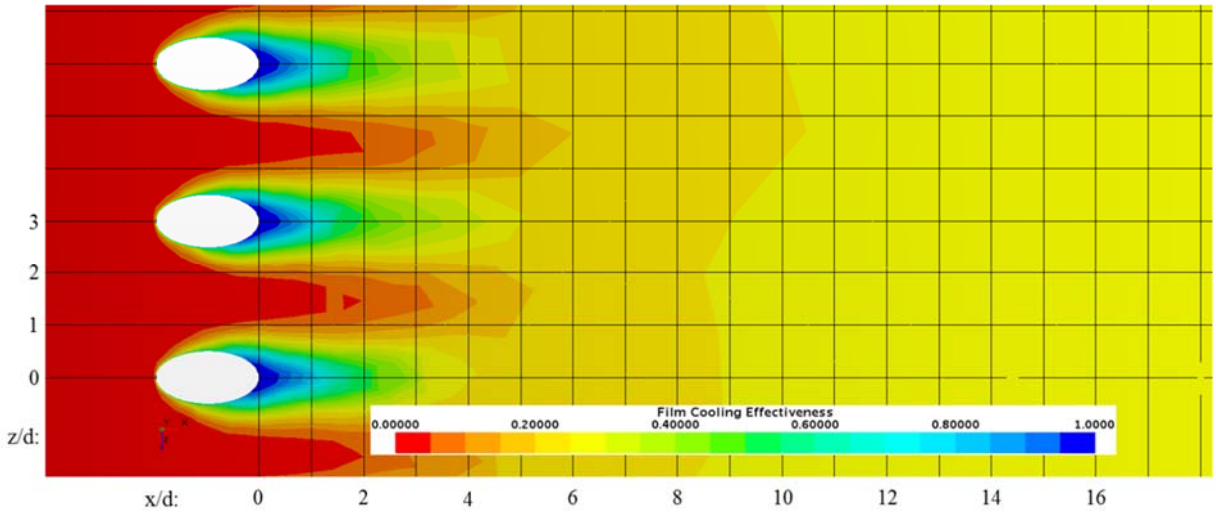

Figure 5.52: Adiabatic Effectiveness distribution for Suction Surface: Mb =1.51, Tu = 5%

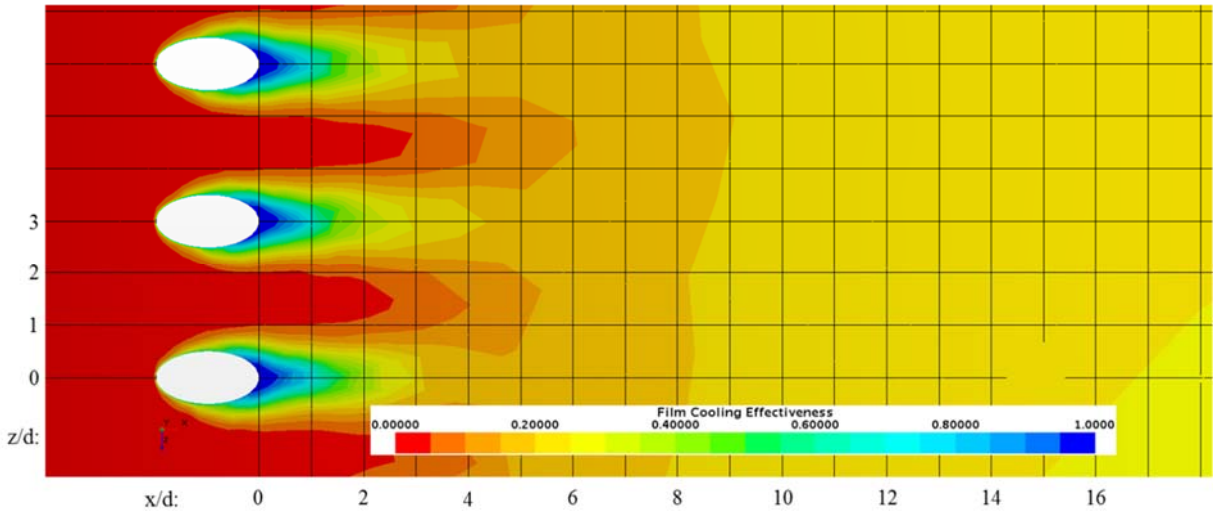

Figure 5.53: Adiabatic Effectiveness distribution for Suction Surface: Mb =2.13, Tu = 5%

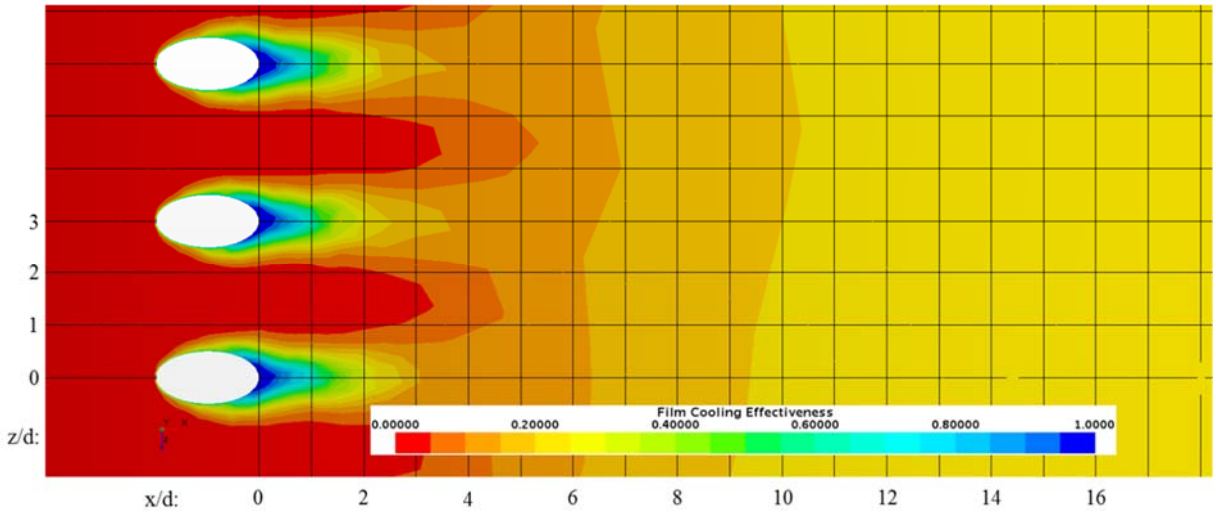

Figure 5.54: Adiabatic Effectiveness distribution for Suction Surface: Mb =2.96, Tu = 5%

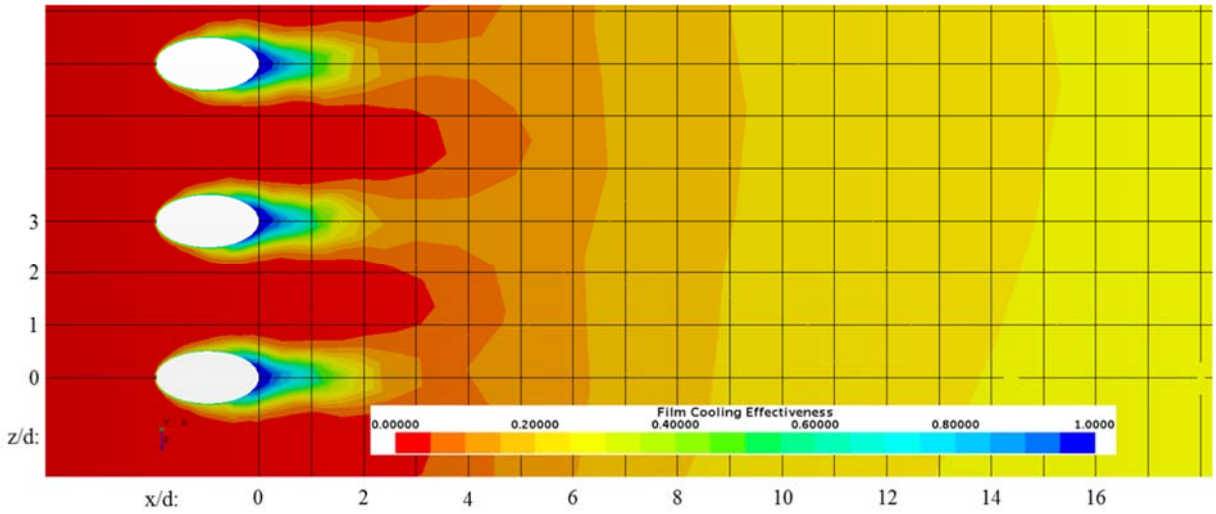

Figure 5.55: Adiabatic Effectiveness distribution for Suction Surface: Mb =4.08, Tu = 5%

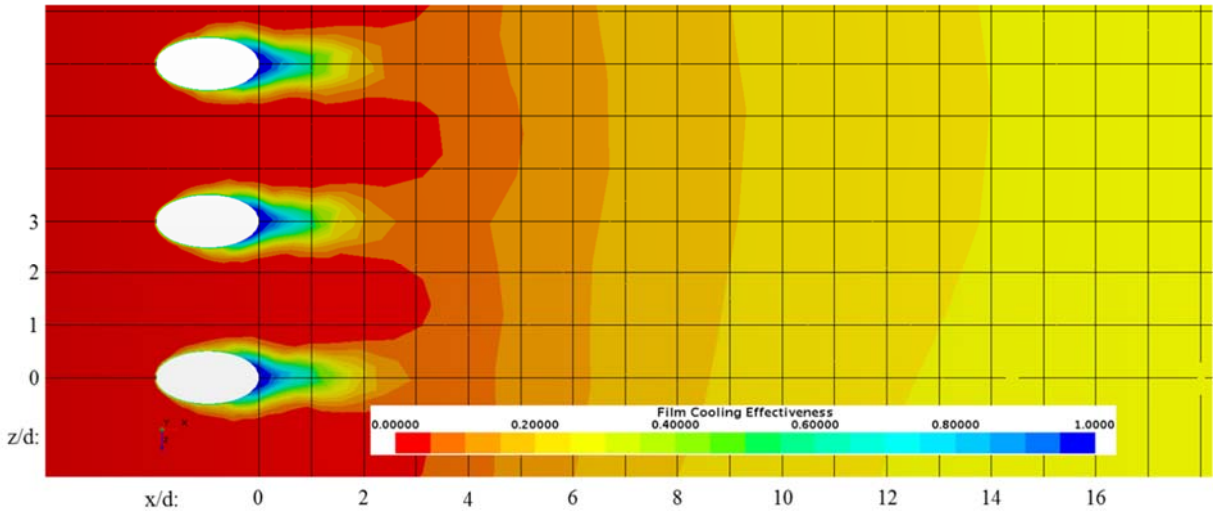

Figure 5.56: Adiabatic Effectiveness distribution for Suction Surface: Mb =5.04, Tu = 5%

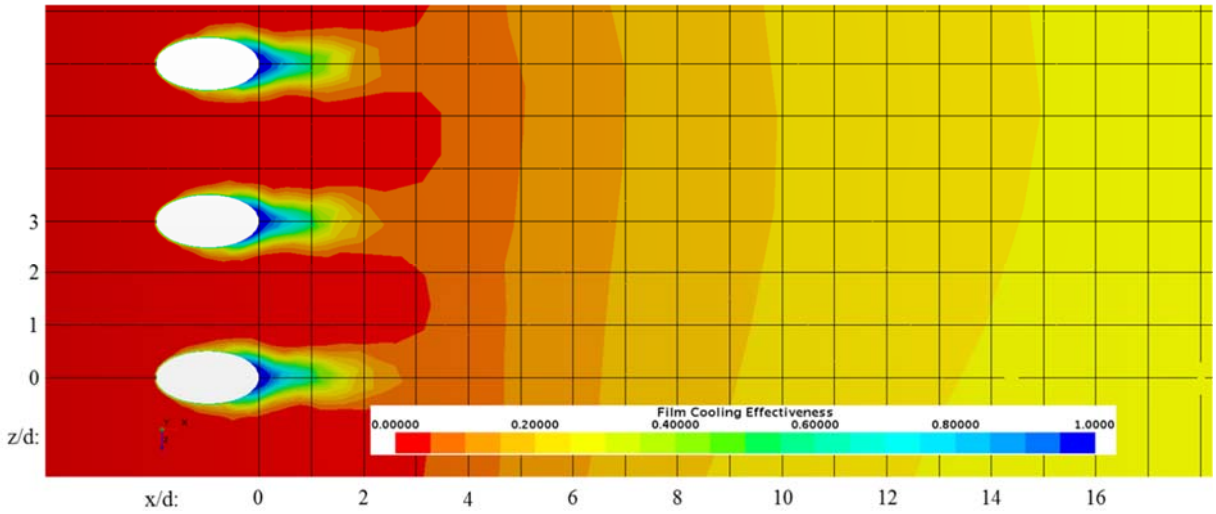

Figure 5.57: Adiabatic Effectiveness distribution for Suction Surface: Mb =5.95, Tu = 5%

5.3.2 Effect of Turbulence Intensity on Film Cooling Effectiveness Parameter

Turbulence intensity is considered to be a dominant parameter on film cooling effectiveness. Turbulence intensity comparison from Mayhew et al. [2003], Bons et al. [1994], and Schmidt and Bogard [1996] is shown in Figure 5.58 for Tu of 10%. Figure 5.58 displays the local centerline adiabatic film cooling effectiveness of the current study and its comparison to the literature.

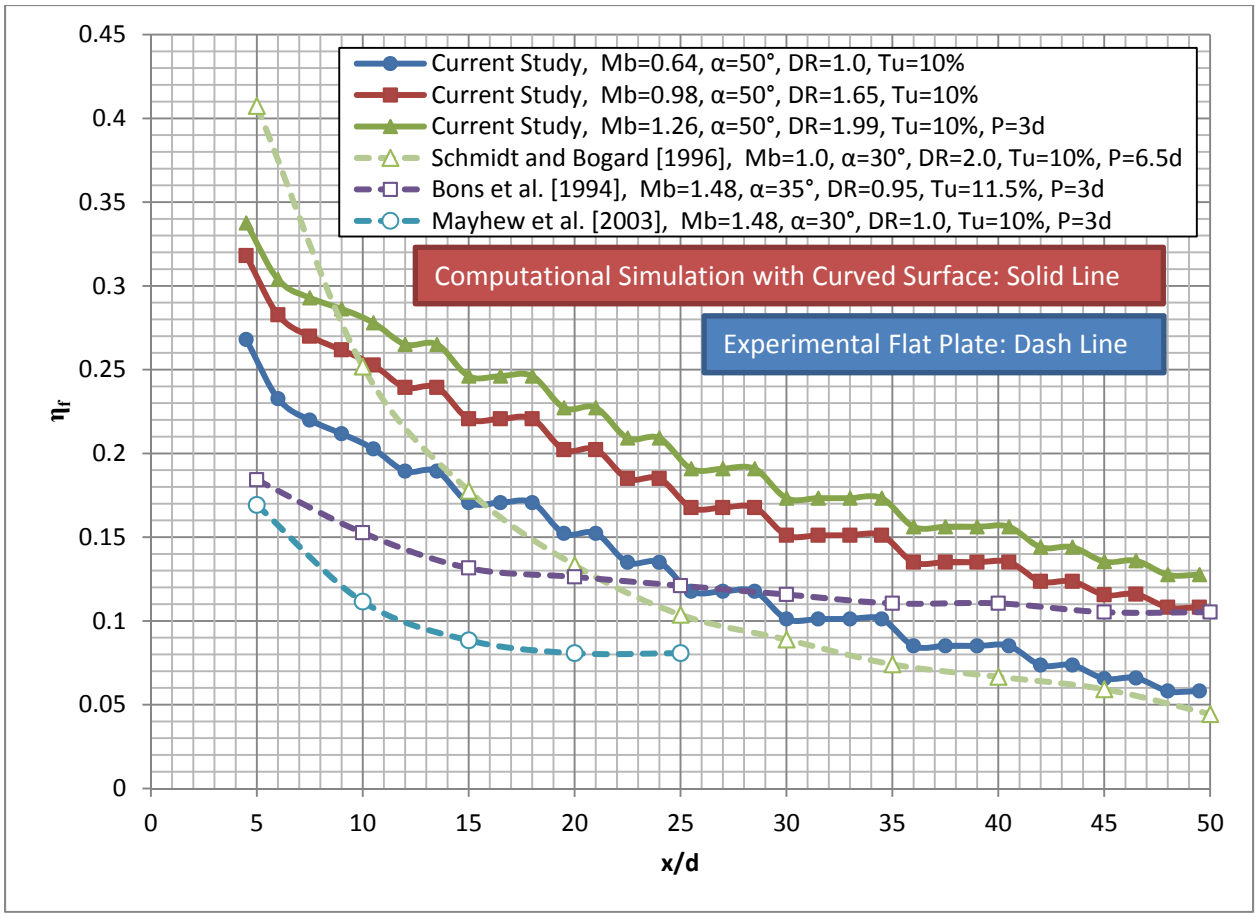

Figure 5.58: Turbulence Intensity Comparison with the results in the literature

Again, there are discrepancies is in the curvature, injection angle and density ratio, but the result follow the similar path of the literature studies

Furthermore, Figures 5.18 to 5.21 show an important effect of turbulence intensity on the blowing parameter. Mayhew et al. [2003], Bons et al. [1994], and Schmidt and Bogard [1996] showed that low blowing parameters have lower film cooling effectiveness as the freestream turbulence intensity increased. Conversely, a high blowing parameter showed improved film cooling effectiveness as the freestream turbulence intensity increased. The current study agrees with the conclusions of Mayhew et al. [2003], Bons et al. [1994], and Schmidt and Bogard [1996] in Figure 5.59.

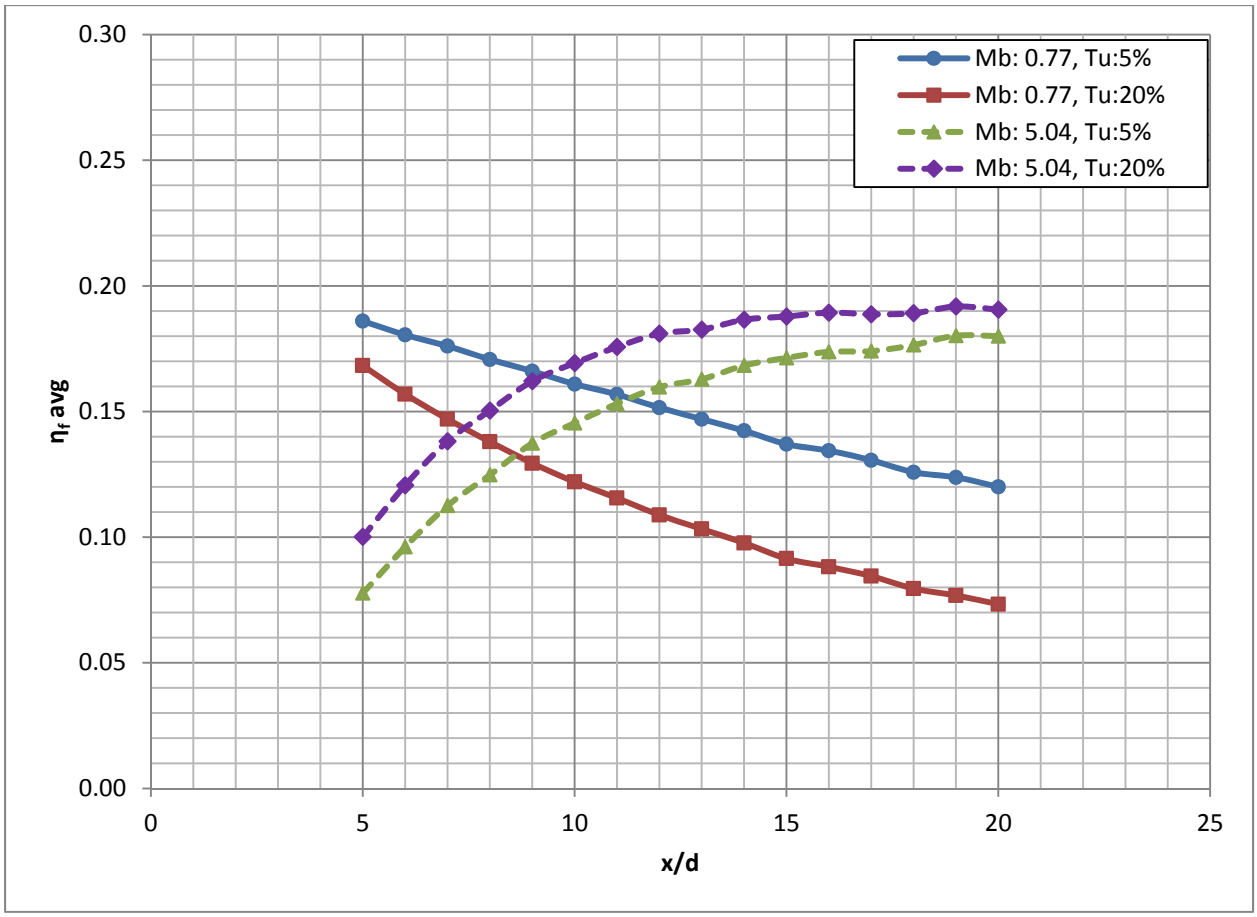

Figure 5.59: Low and High Blowing Parameter with Low and High Turbulence Intensity

Figure 5.59 shows two blowing parameters of 0.77 (low) and 5.04 (high) at 5% and 20% turbulence intensity. Low turbulence intensities are not found in the real engine environment, where in a gas turbine engine the turbulence intensity is high. Turbulence intensity of 20% is considered to be the incoming flow from the combustor. Low turbulence intensity studies are excellent in validating the simulation studies, where it is difficult in creating the engine environment. The current study is validated by these low Tu studies in the literature.

Numerical simulations for different turbulence intensities from 5% to 25% are performed to study the effects of turbulence intensity on a blowing parameter of 0.98 at two density ratios. The simulations are reported in Figures 5.60 – 5.63, where laterally averaged and local centerline adiabatic effectiveness is shown against the streamwise locations.

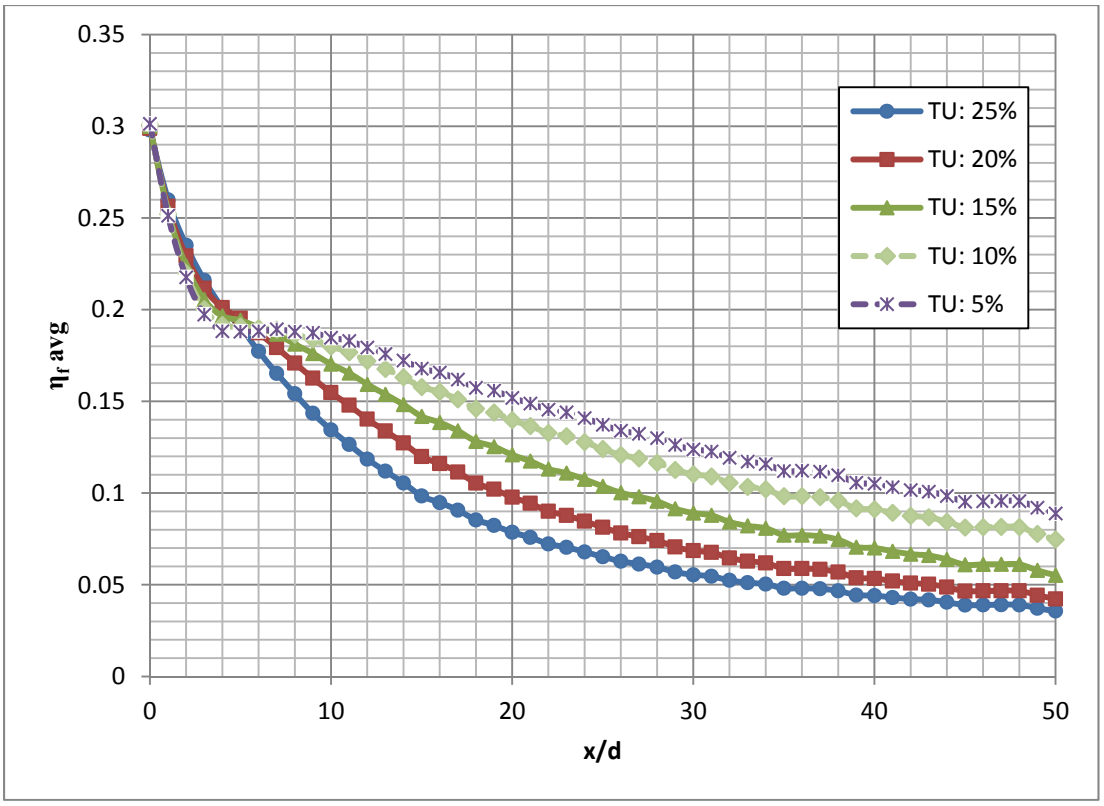

Figure 5.60: Laterally averaged adiabatic effectiveness for various Turbulence Intensities, DR = 1.65

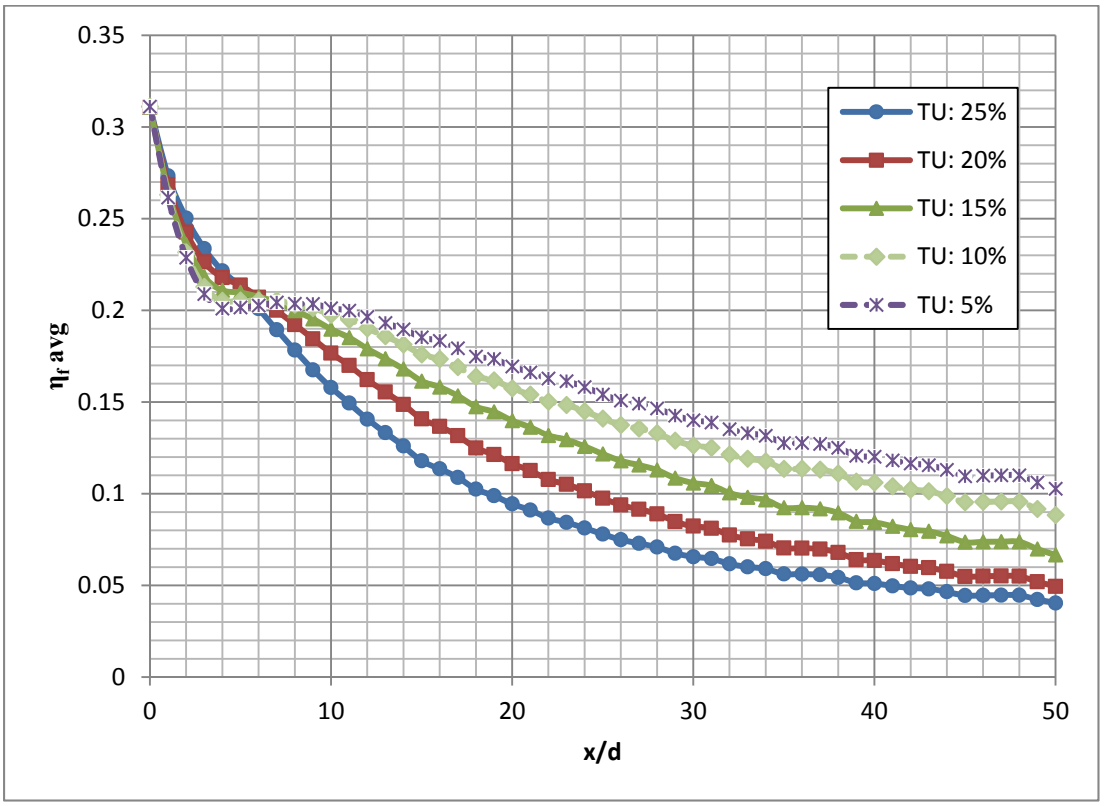

Figure 5.61: Laterally averaged adiabatic effectiveness for various Turbulence Intensities, DR = 1.99

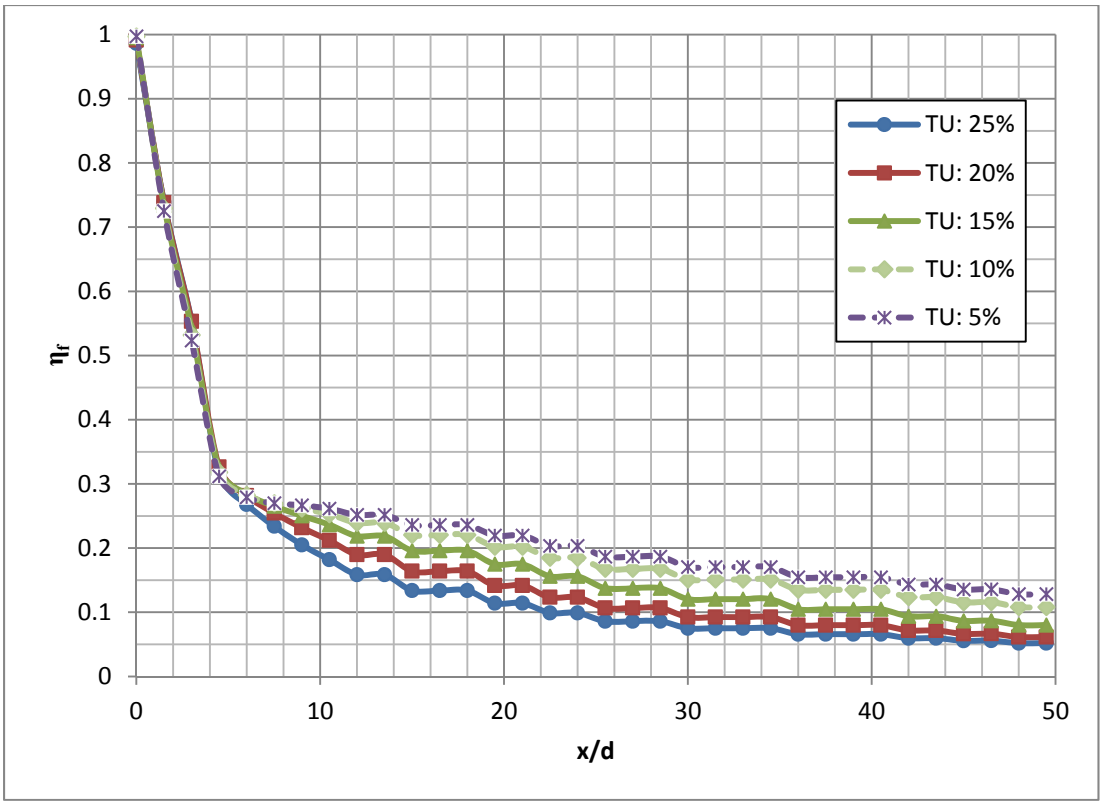

Figure 5.62: Centerline adiabatic effectiveness for various Turbulence Intensities, DR = 1.65

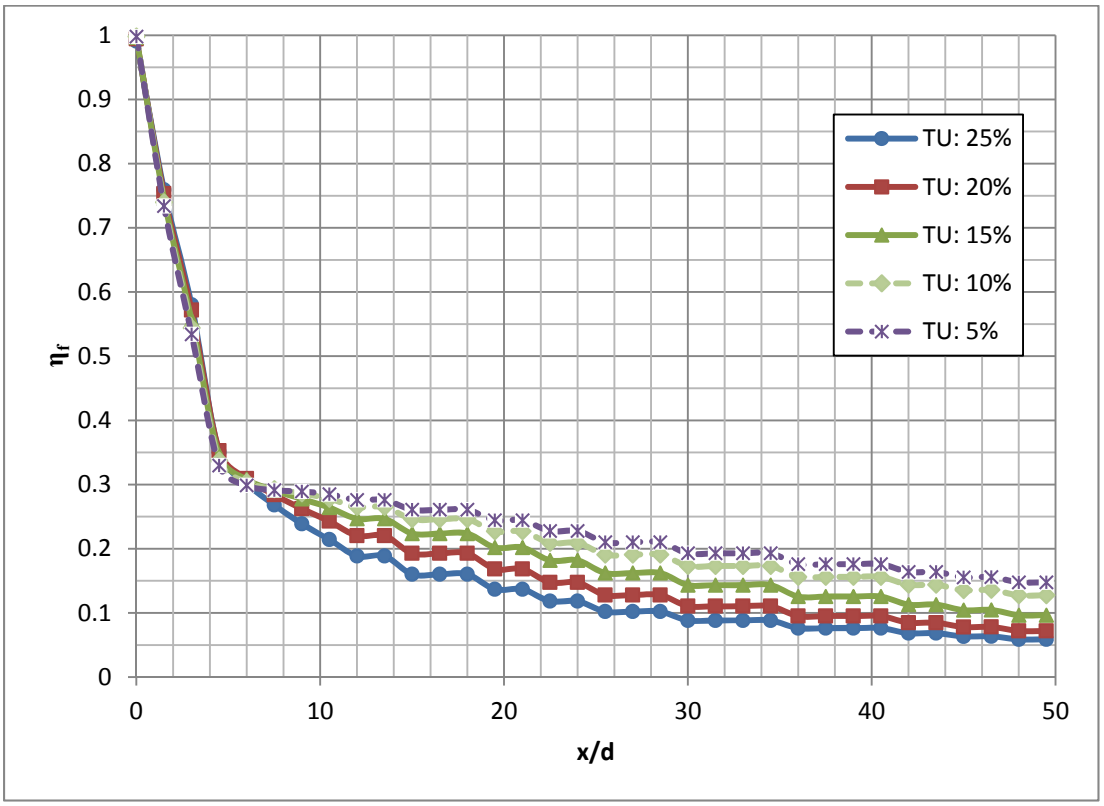

Figure 5.63: Centerline adiabatic effectiveness for various Turbulence Intensities, DR = 1.99

Figures 5.60 to 5.63 demonstrate that turbulence intensity has the potential to effect film cooling effectiveness by nearly 200% downstream of the hole. Figures 5.60 and 5.61 show that there is a ~0.07 difference in effectiveness for turbulence intensity of 20% and 5% between location of 10<x/d<50. One of the differences is the spreading and mixing of coolant on the surface. Higher Tu mixes and spreads the coolant at a faster rate than a lower Tu. This is shown in Figures 5.64 – 5.73 for turbulence intensity cases for z/d and y/d.

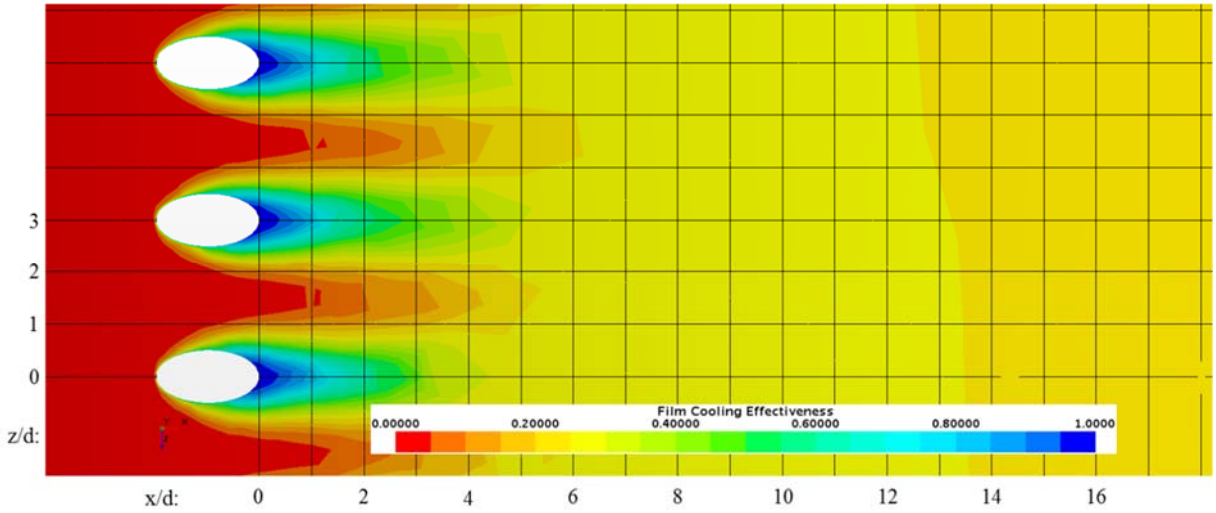

Figure 5.64: Adiabatic Effectiveness distribution for Suction Surface (Mb: 0.98, Tu: 5%, DR: 1.65)

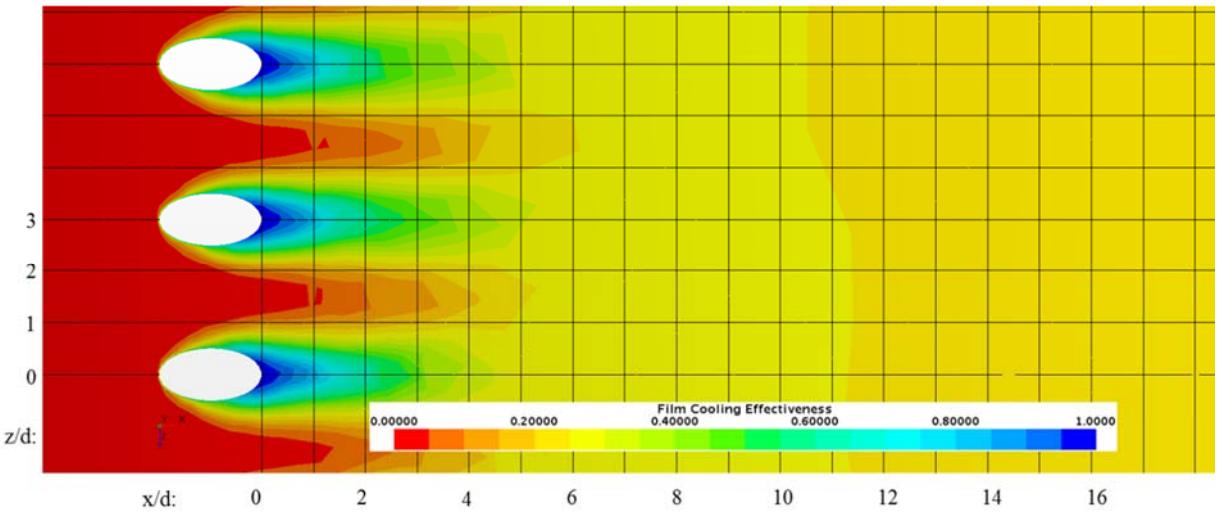

Figure 5.65: Adiabatic Effectiveness distribution for Suction Surface (Mb: 0.98, Tu: 10%, DR: 1.65)

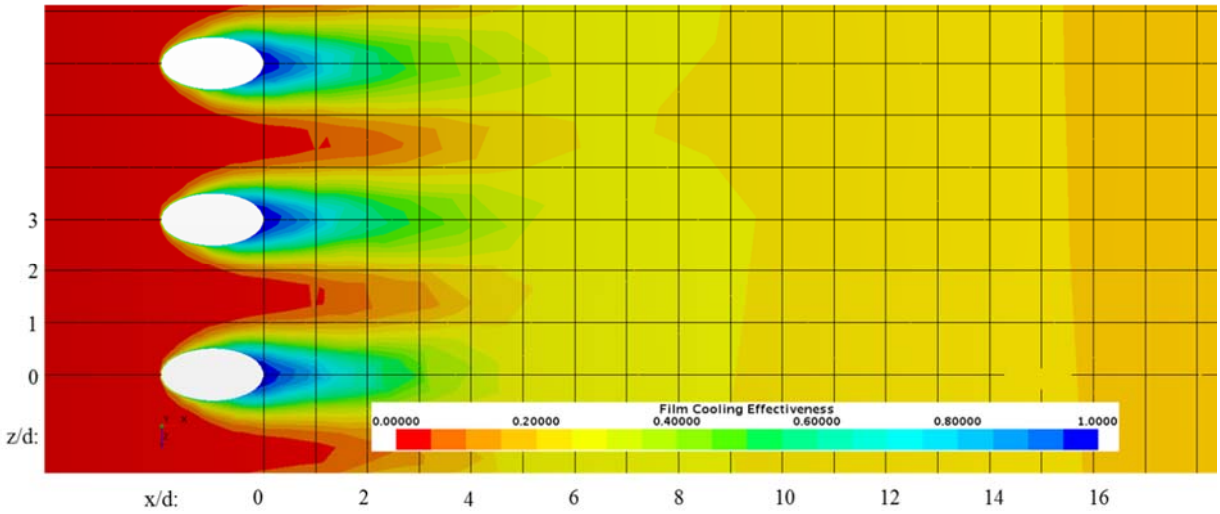

Figure 5.66: Adiabatic Effectiveness distribution for Suction Surface (Mb: 0.98, Tu: 15%, DR: 1.65)

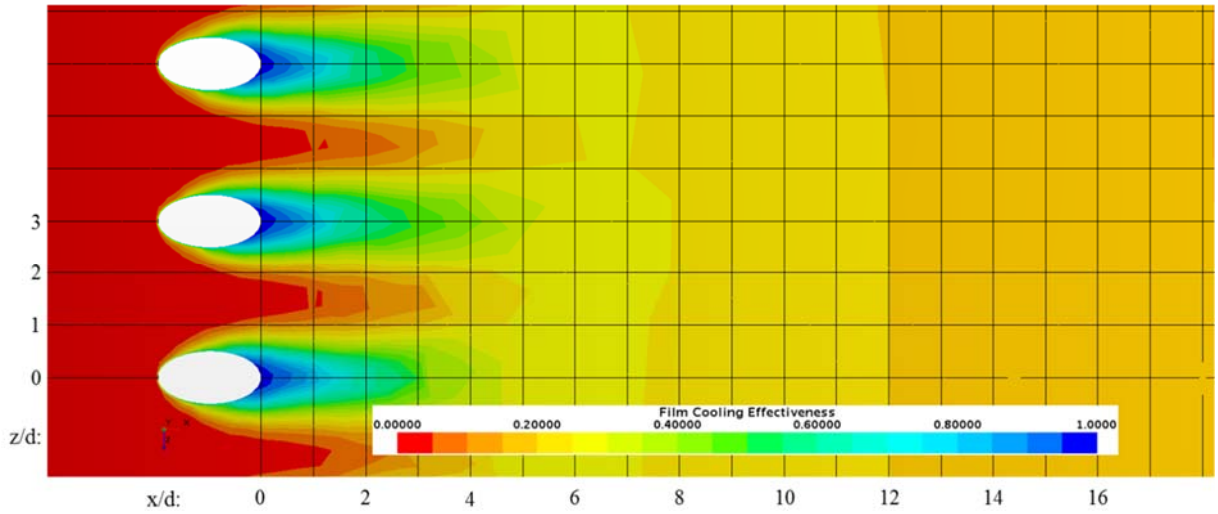

Figure 5.67: Adiabatic Effectiveness distribution for Suction Surface (Mb: 0.98, Tu: 20%, DR: 1.65)

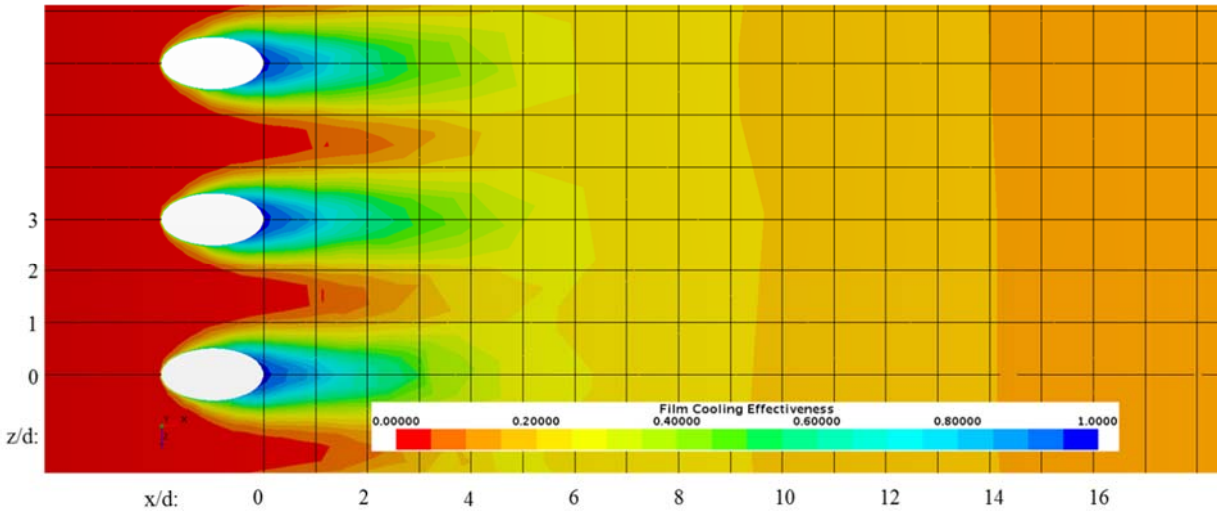

Figure 5.68: Adiabatic Effectiveness distribution for Suction Surface (Mb: 0.98, Tu: 25%, DR: 1.65)

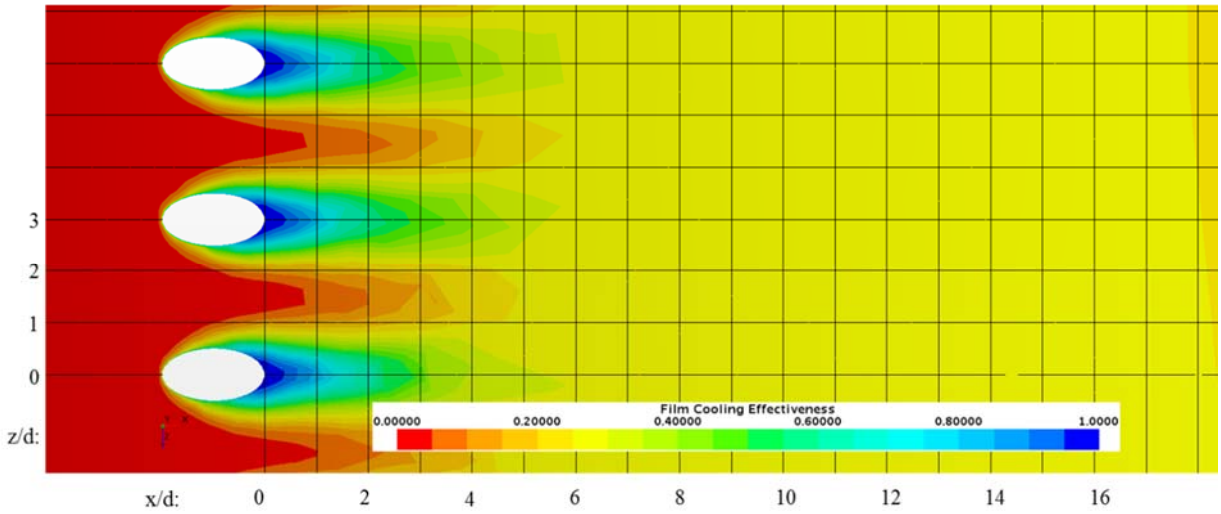

Figure 5.69: Adiabatic Effectiveness distribution for Suction Surface (Mb: 1.26, Tu: 5%, DR: 1.99)

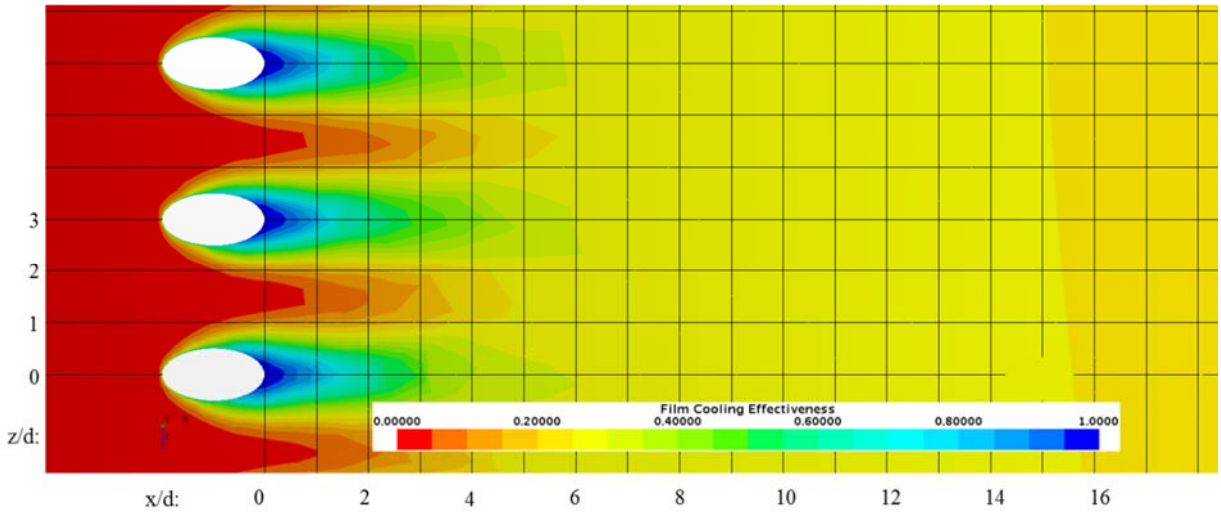

Figure 5.70: Adiabatic Effectiveness distribution for Suction Surface (Mb: 1.26, Tu: 10%, DR: 1.99)

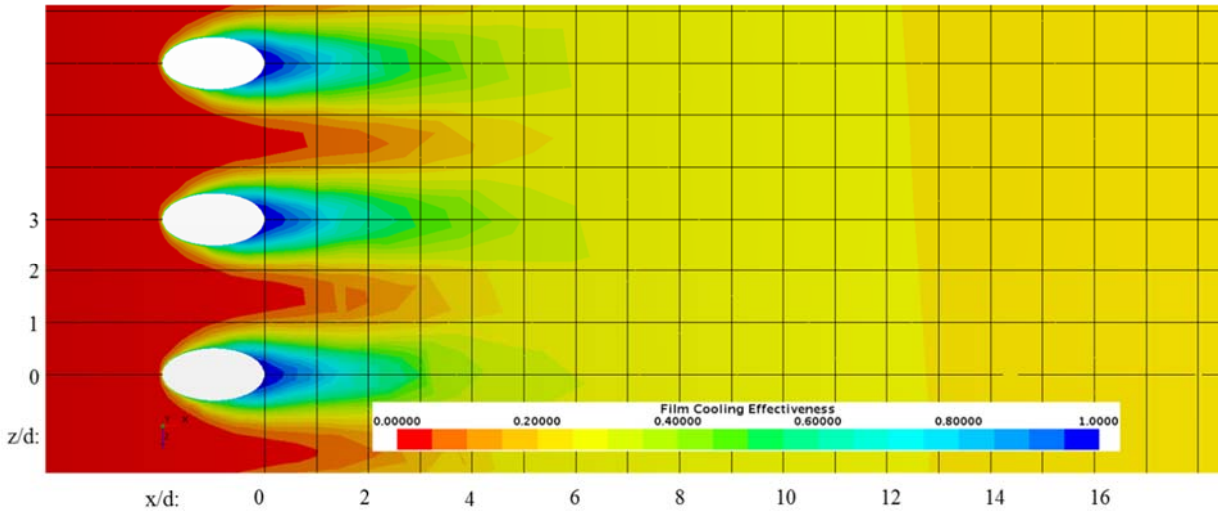

Figure 5.71: Adiabatic Effectiveness distribution for Suction Surface (Mb: 1.26, Tu: 15%, DR: 1.99)

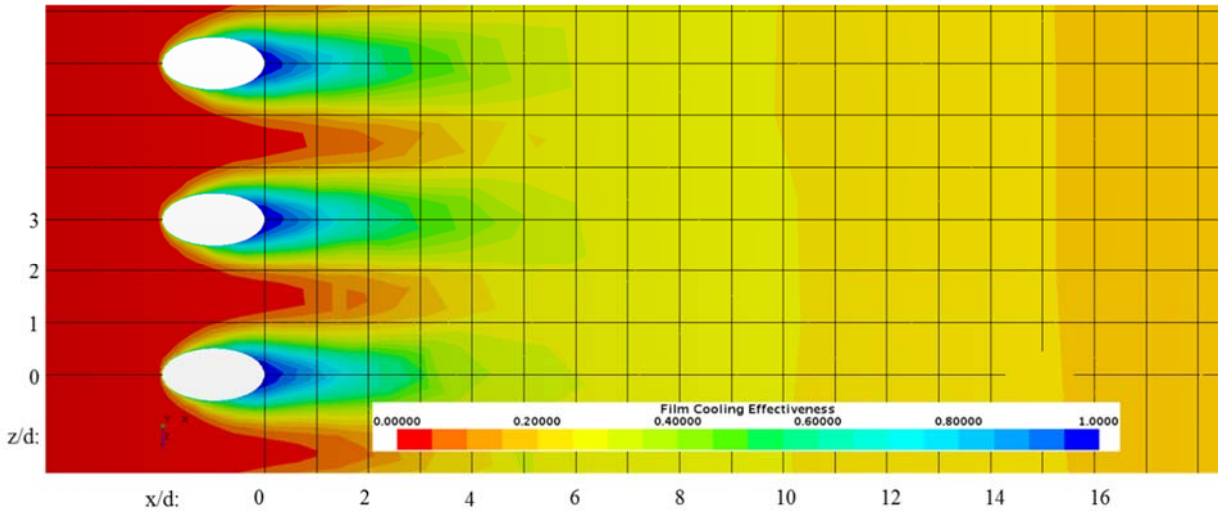

Figure 5.72: Adiabatic Effectiveness distribution for Suction Surface (Mb: 1.26, Tu: 20%, DR: 1.99)

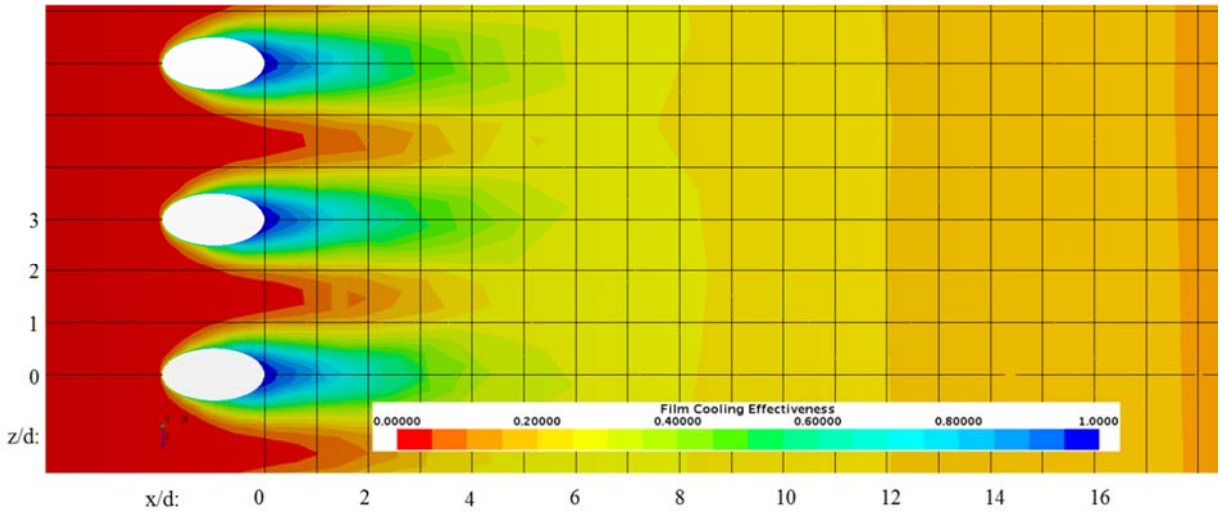

Figure 5.73: Adiabatic Effectiveness distribution for Suction Surface (Mb: 1.26, Tu: 25%, DR: 1.99)

As seen in Figures 5.74 - 5.83, the centerline profile of the adiabatic film cooling effectiveness is diminished as the Tu increases. This is based on the M_b of one, which corresponds to the blowing parameter results. The momentum of the film jet is not strong enough to withstand the high turbulence freestream, but is affected at low turbulence intensity.

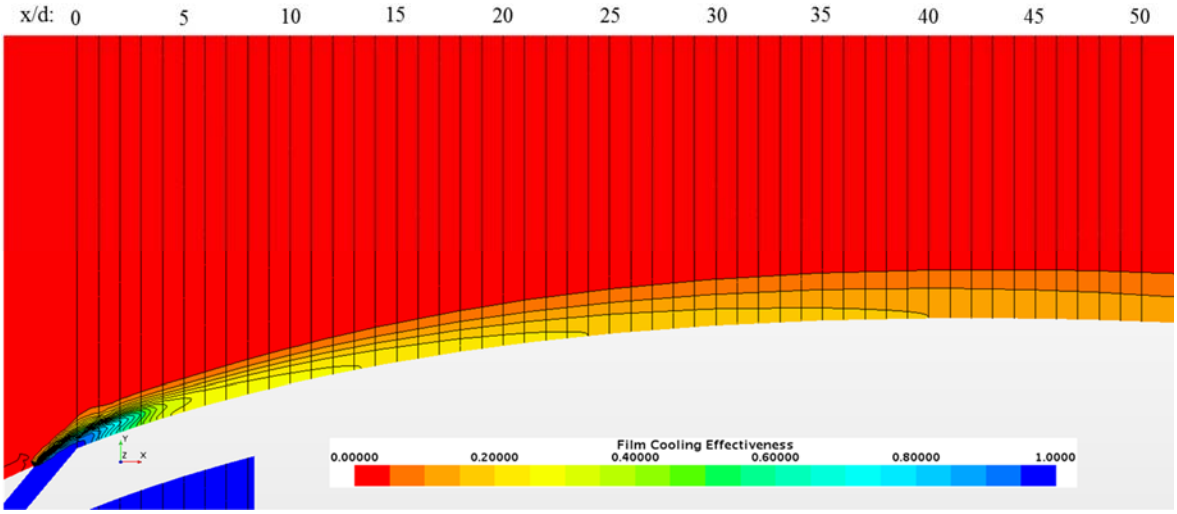

Figure 5.74: Adiabatic Effectiveness profile for centerline (Mb: 0.98 Tu: 5% DR: 1.65)

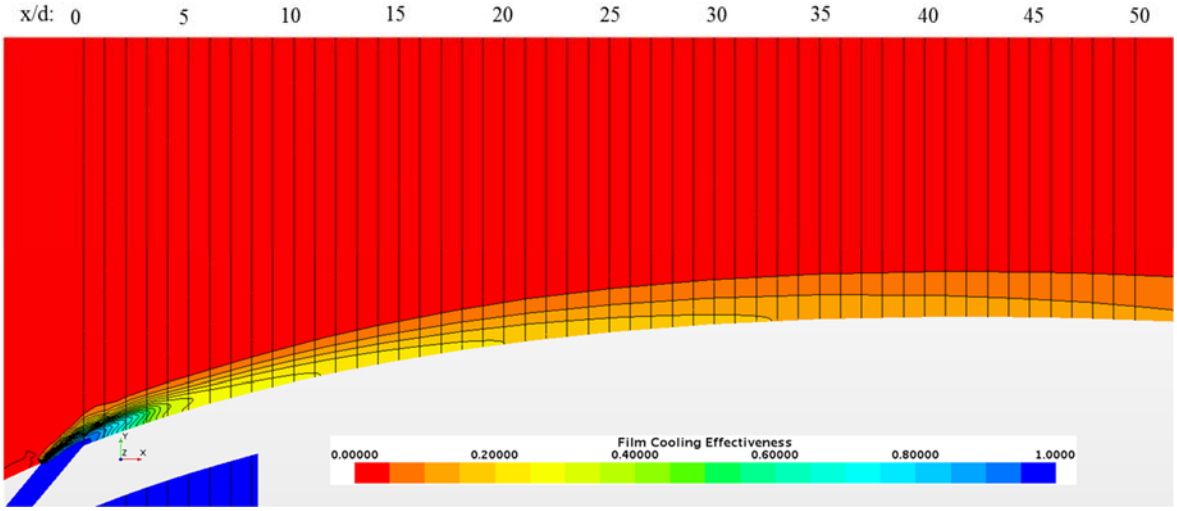

Figure 5.75: Adiabatic Effectiveness profile for centerline (Mb: 0.98 Tu: 10% DR: 1.65)

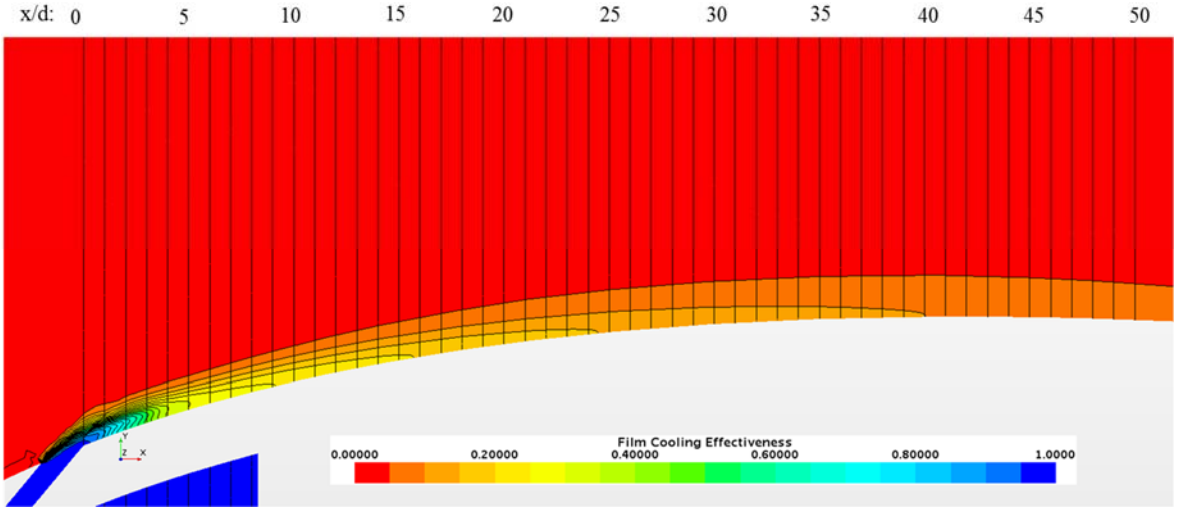

Figure 5.76: Adiabatic Effectiveness profile for centerline (Mb: 0.98 Tu: 15% DR: 1.65)

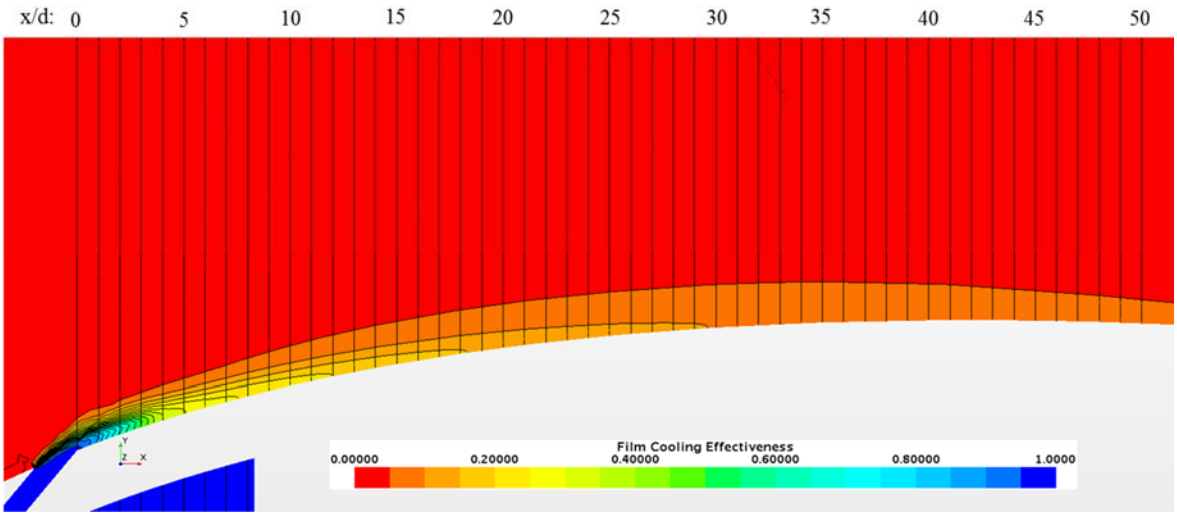

Figure 5.77: Adiabatic Effectiveness profile for centerline (Mb: 0.98 Tu: 20% DR: 1.65)

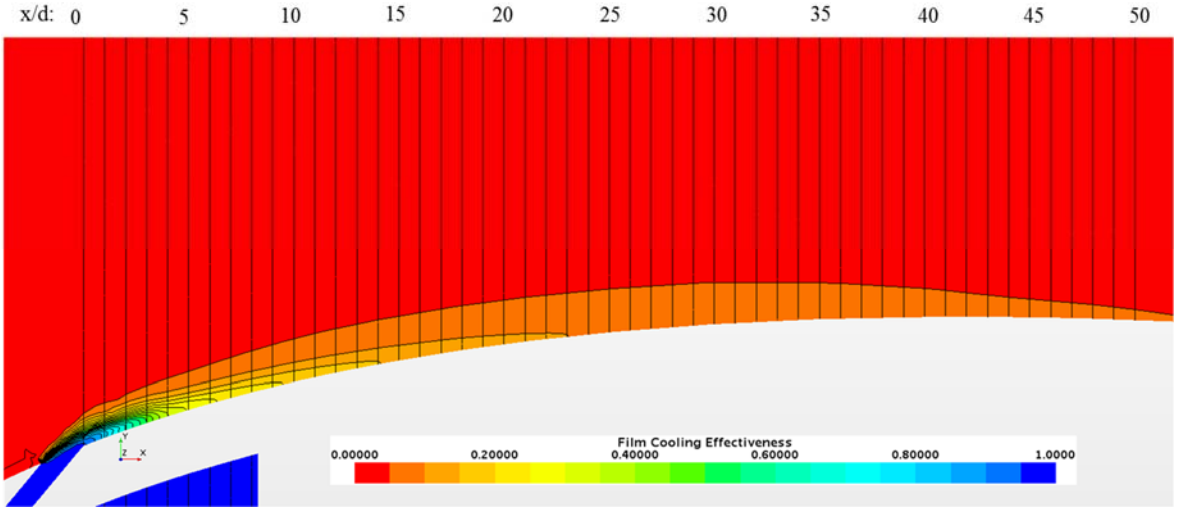

Figure 5.78: Adiabatic Effectiveness profile for centerline (Mb: 0.98 Tu: 25% DR: 1.65)

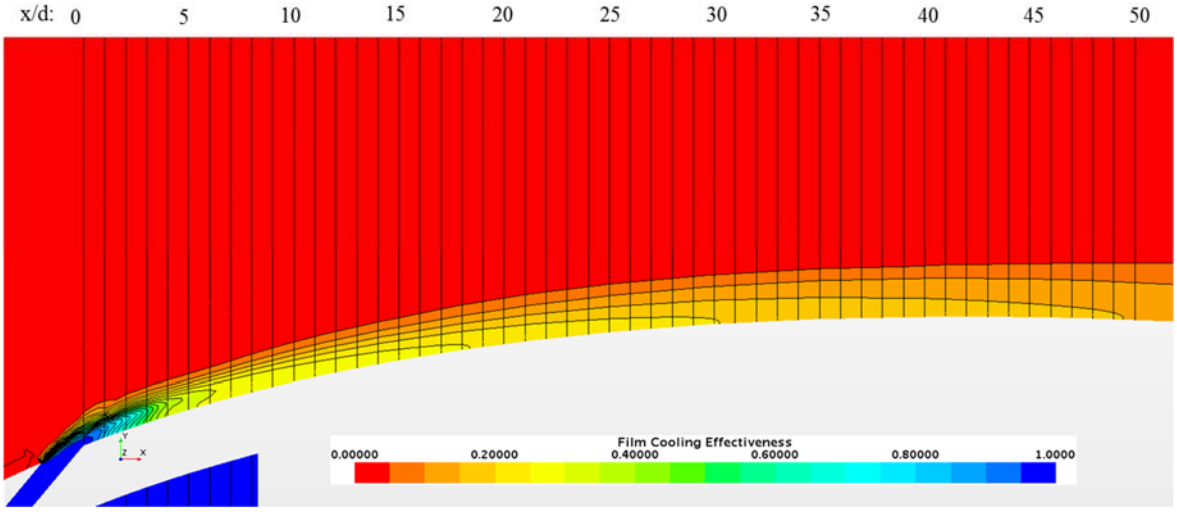

Figure 5.79: Adiabatic Effectiveness profile for centerline (Mb: 1.26 Tu: 5% DR: 1.99)

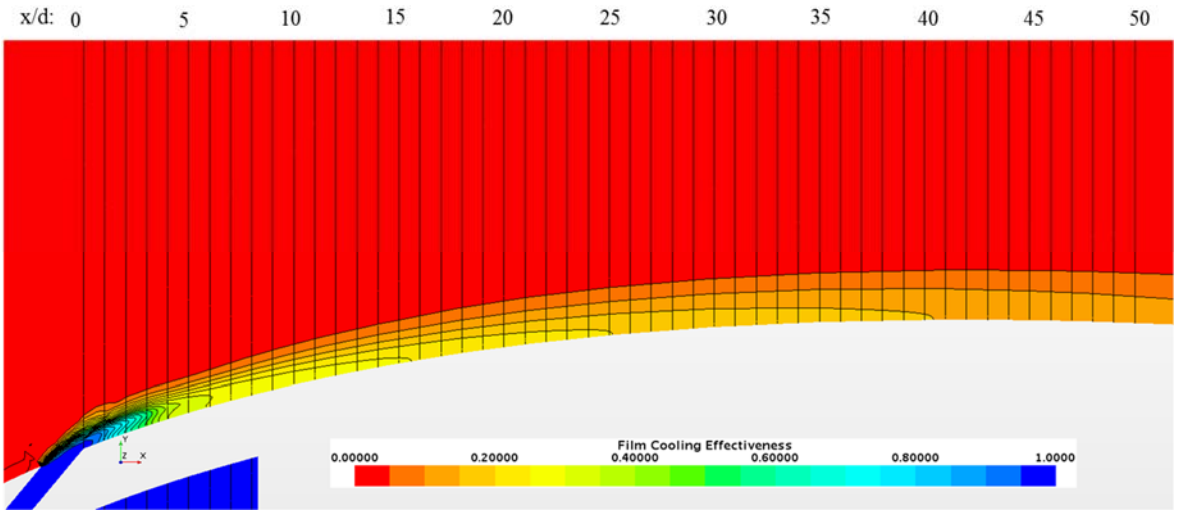

Figure 5.80: Adiabatic Effectiveness profile for centerline (Mb: 1.26 Tu: 10% DR: 1.99)

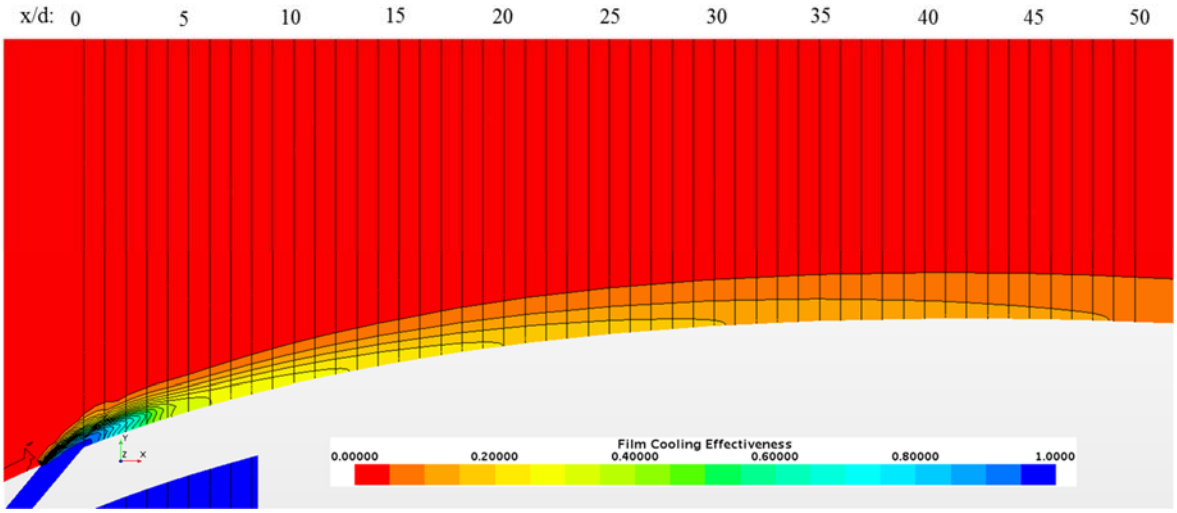

Figure 5.81: Adiabatic Effectiveness profile for centerline (Mb: 1.26 Tu: 15% DR: 1.99)

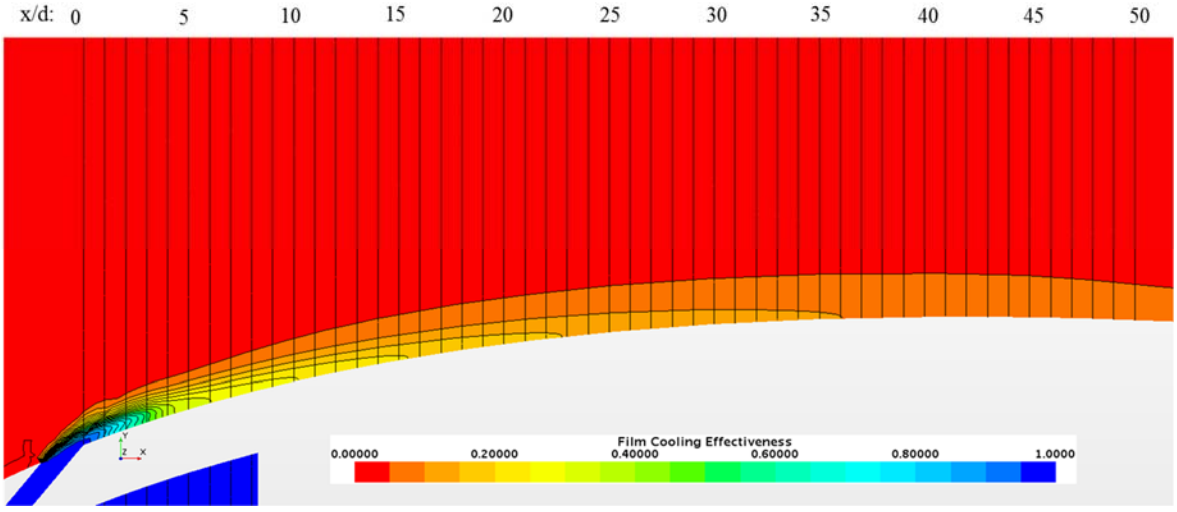

Figure 5.82: Adiabatic Effectiveness profile for centerline (Mb: 1.26 Tu: 20% DR: 1.99)

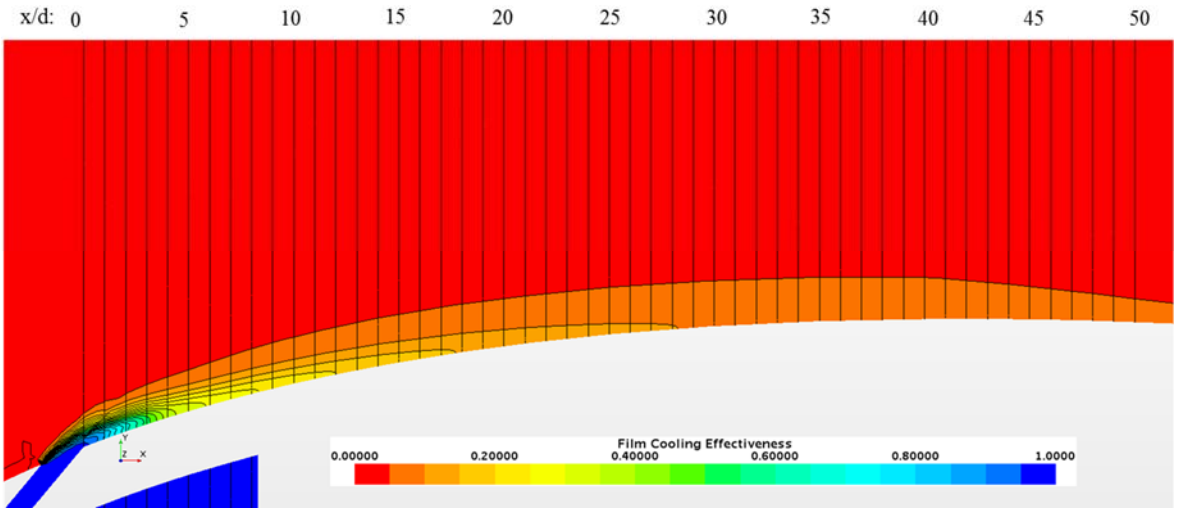

Figure 5.83: Adiabatic Effectiveness profile for centerline (Mb: 1.26 Tu: 25% DR: 1.99)

5.3.3 Effect of Density Ratio on Film Cooling Effectiveness Parameter

The effect of density ratio come from equations 1.6 and 1.7, the density of the gas and coolant change the blowing parameter or momentum flux ratio. The realistic density ratio of a gas turbine engine is approximately 2.0, according to Bogard and Thole [2006]. In the current experiment, the DR was 1.65 but couldbe increased by changing the temperature of the gas turbine engine. This experimental simulation was not conducted due to the safety and hazard limitations placed on the experiment.

The literature study results for density ratio are collected and compared to the current study. Figure 5.84 shows the data for the current study, Foster and Lampard [1980], Pedersen et al. [1977] and Baldauf et al. [2002] at a DR ~ 2.0 for a M_b of 1.0. Figure 5.85 reports the results of Pedersen et al. [1977], Baldaurf et al. [2002], and Drost et al. [1997] against the current study at $M_b = 1.0$ and DR ~ 1.5.

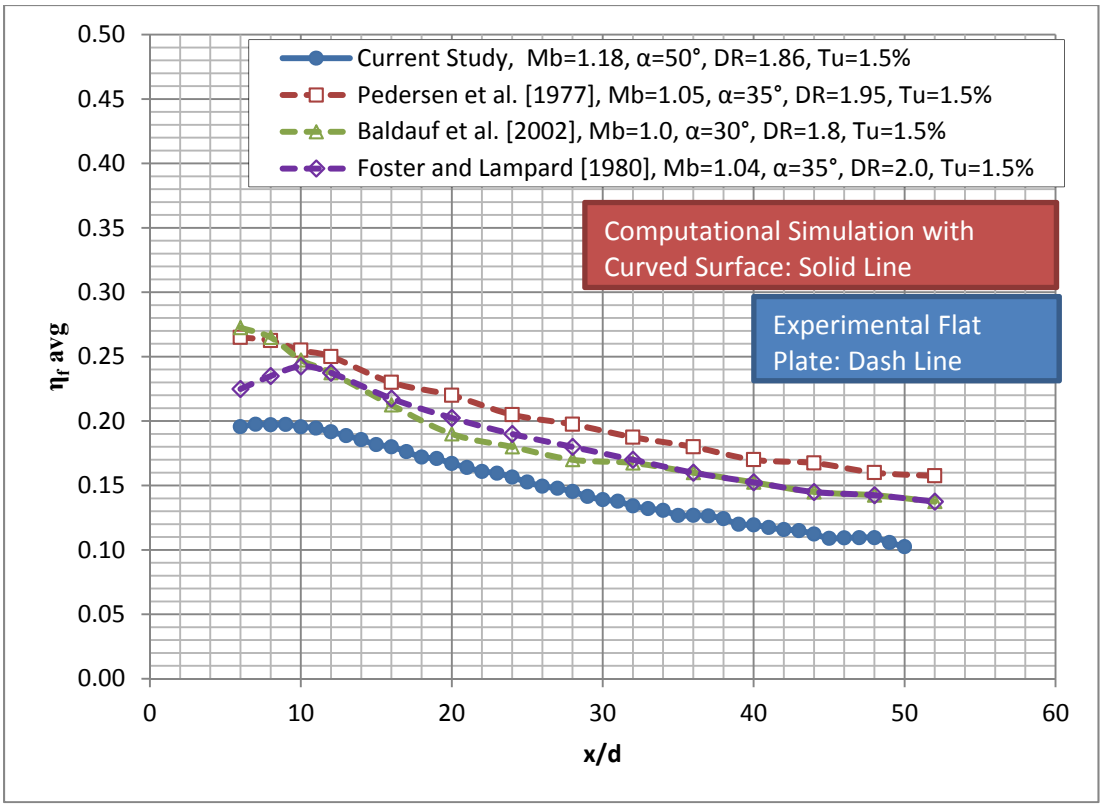

Figure 5.84: Density Ratio Comparison with literature results: Mb~1.0 & DR~2.0

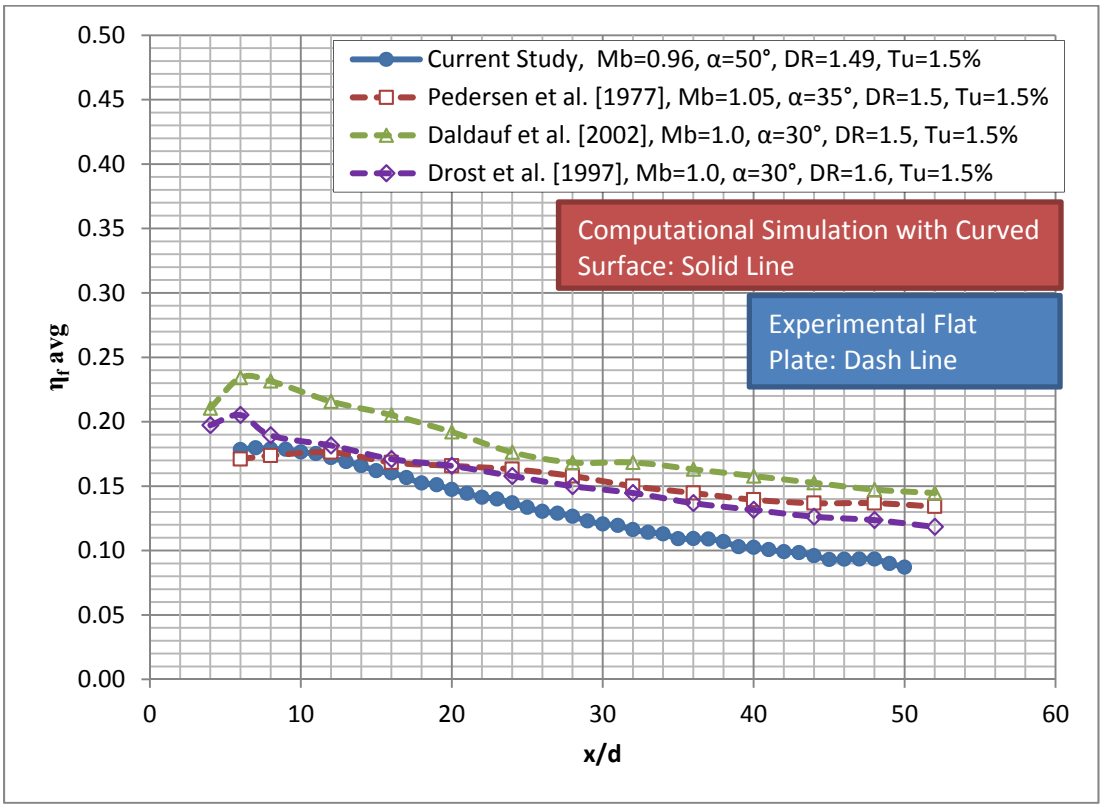

Figure 5.85: Density Ratio Comparison with literature results: Mb~1.0 & DR~1.5

The comparison to literature shows an excellent correlation even when we consider differences in the curvature and injection angle. The study shows a direct comparison of the varying density ratio for a constant velocity ratio. Holding the velocity ratio constant ensures that only the density effects are introduced in the blowing parameter or momentum flux ratio. Table 5.9 shows the non-dimensional parameters for the density ratio case study with a constant VR.

Table 5.9: Non-dimensional Parameters for different Density Ratio

DR	VR	Mb	I
1.99	0.64	1.26	0.80
1.72	0.64	1.10	0.71
1.49	0.64	0.97	0.63

Figure 5.86 and 5.87 display the effects of Table 5.9 for the laterally averaged and local centerline adiabatic effectiveness.

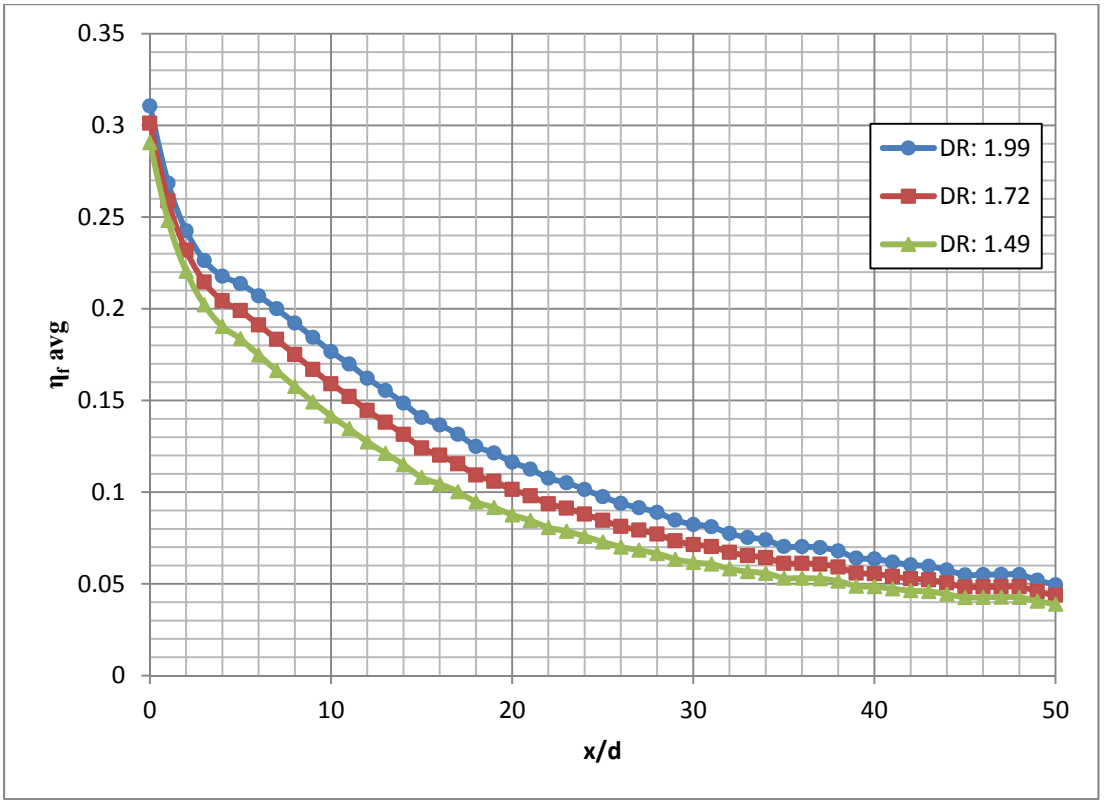

Figure 5.86: Laterally averaged adiabatic effectiveness for various density ratios

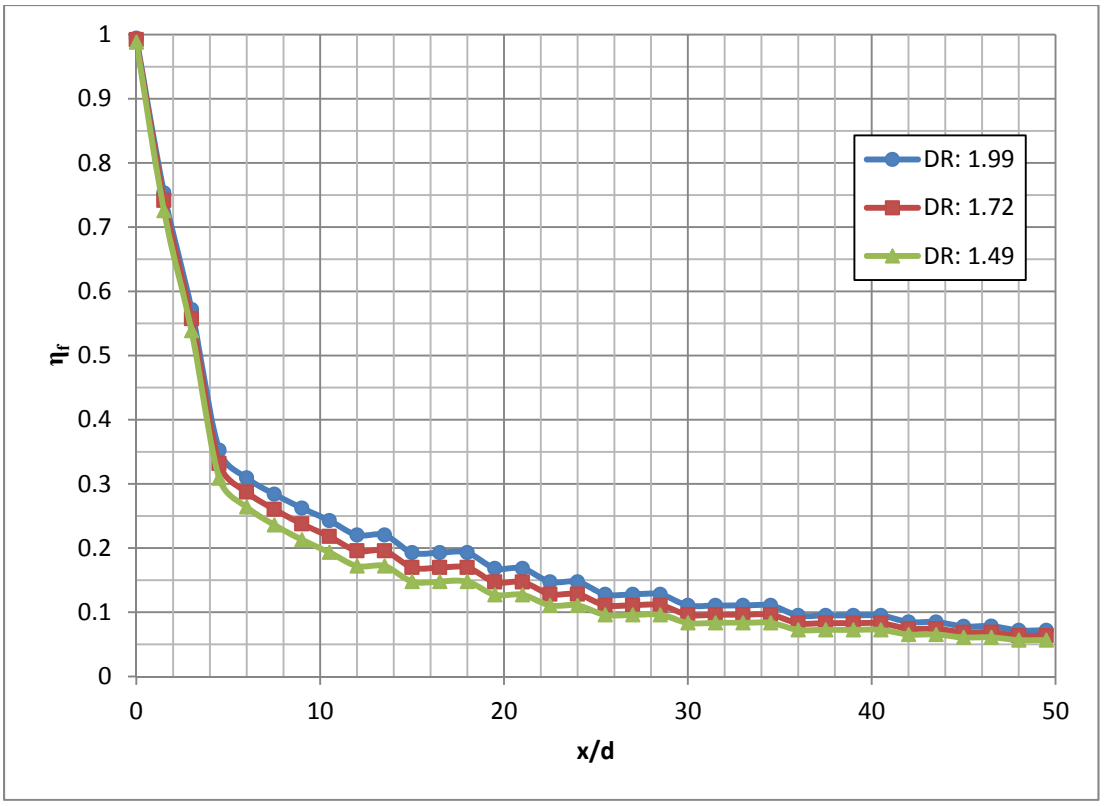

Figure 5.87: Centerline adiabatic effectiveness for various density ratios

Figure 5.86 shows a constant average of 0.0232 adiabatic effectiveness differences between DR of 2.0 and 1.5. The effect of density ratio is important in simulating realistic gas turbine engine effectiveness.

Density Ratio affects the blowing parameter by increasing or decreasing the mass flux. Figures 5.88 to 5.90 show the centerline performance as the DR is increased, but there was no detachment at these blowing parameters. The suction surface distribution for change in DR is shown in Figures5.91 to 5.93. These figures show how mixing and spreading of the coolant for a constant Tu is affected by the changing of DR. The jet persisted longer for higher DR than a lower DR. DR of 1.99 persisted until 6 x/d (Figure 5.93), whereas, a DR of 1.72 disintegrated at 5 x/d (Figure 5.92).

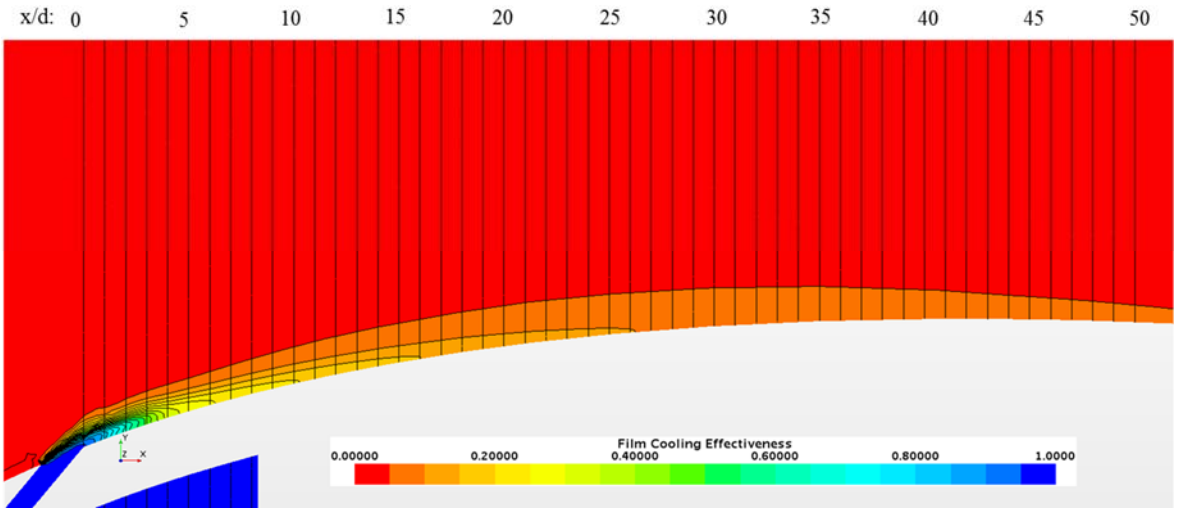

Figure 5.88: Adiabatic Effectiveness profile for centerline (VR: 0.64 Tu: 20% DR: 1.49)

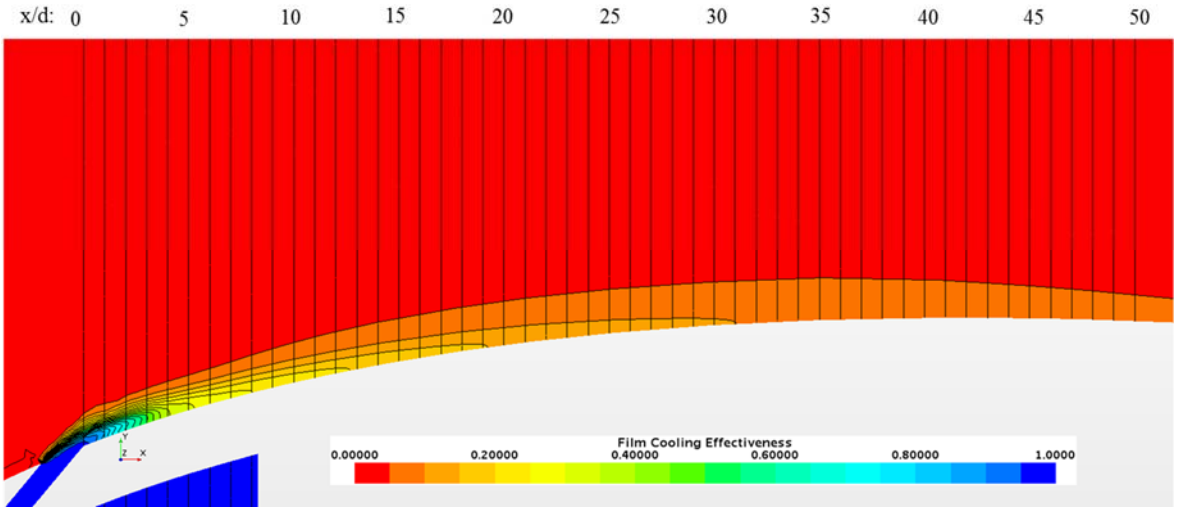

Figure 5.89: Adiabatic Effectiveness profile for centerline (VR: 0.64 Tu: 20% DR: 1.72)

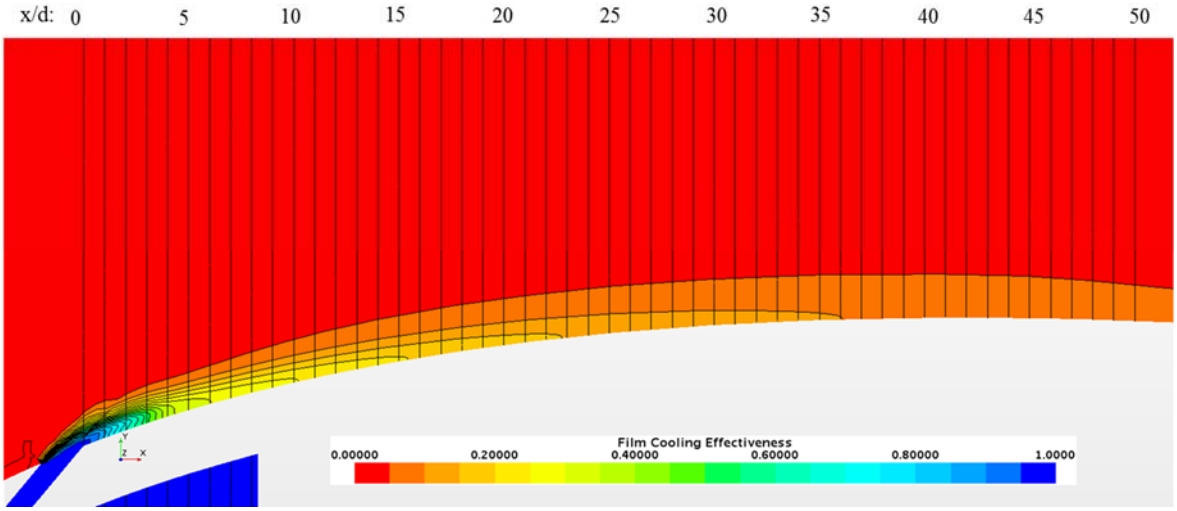

Figure 5.90: Adiabatic Effectiveness profile for centerline (VR: 0.64 Tu: 20% DR: 1.99)

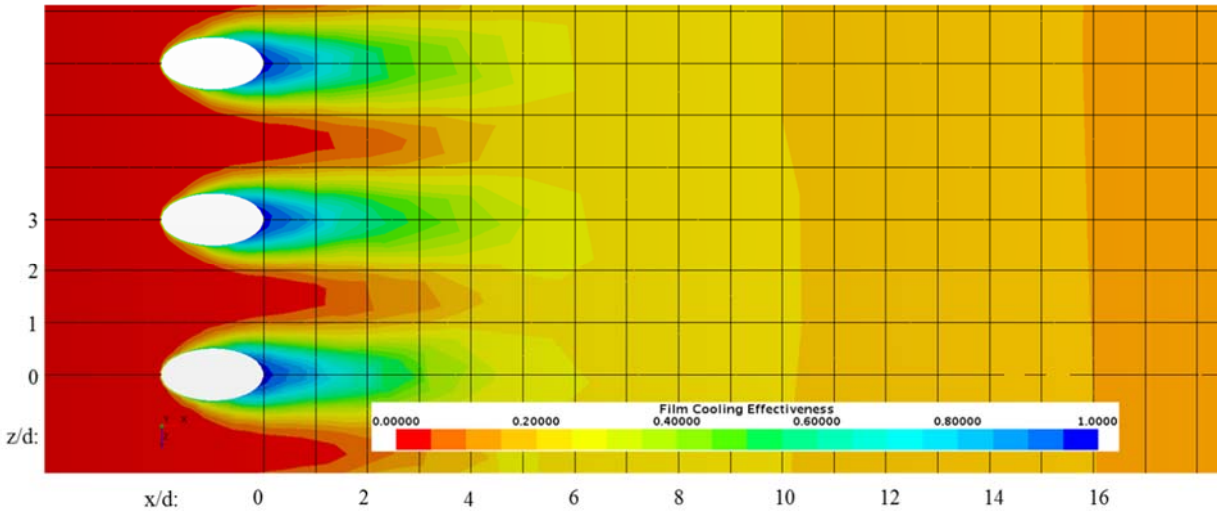

Figure 5.91: Adiabatic Effectiveness distribution for Suction Surface (VR: 0.64, Tu: 20%, DR: 1.49)

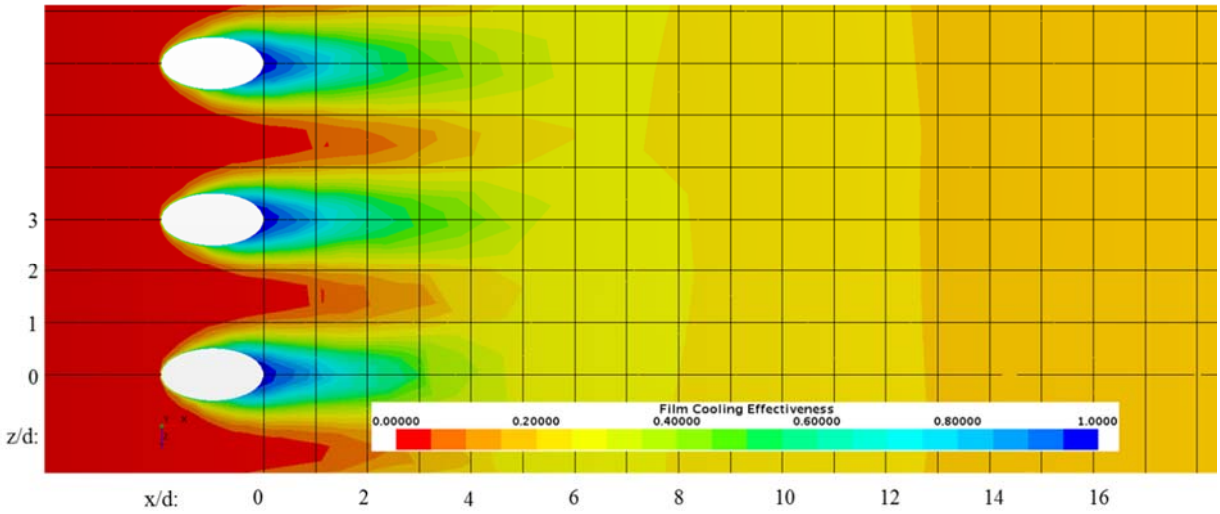

Figure 5.92: Adiabatic Effectiveness distribution for Suction Surface (VR: 0.64, Tu: 20%, DR: 1.72)

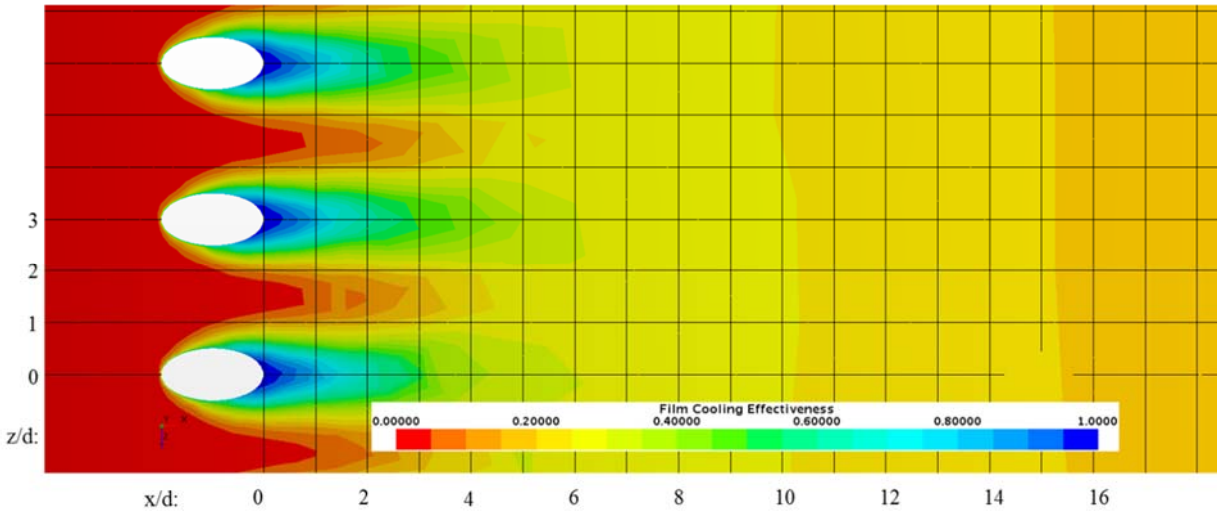

Figure 5.93: Adiabatic Effectiveness distribution for Suction Surface (VR: 0.64, Tu: 20%, DR: 1.99)

5.3.4 Three-Parameter Comparative Study

It is instructive to define a baseline case, e.g., M_b=0.98, DR=1.65 and Tu=20%, and compare the film effectiveness parameter between different blowing ratios, density ratios and turbulence intensities. The highest percent change in film cooling effectiveness was produced in Case #10 (M_b = 5.95, DR = 1.65 and Tu = 5%) at 300 % or 3 times the baseline adiabatic film cooling effectiveness at x/d of 50. This is mainly caused from the high blowing parameter effect and low turbulence intensity, which shows higher effectiveness farther downstream of the film injection. Figure 5.94 shows the aggregate of all the cases studied in three parameters, M_b, DR and Tu intensity.

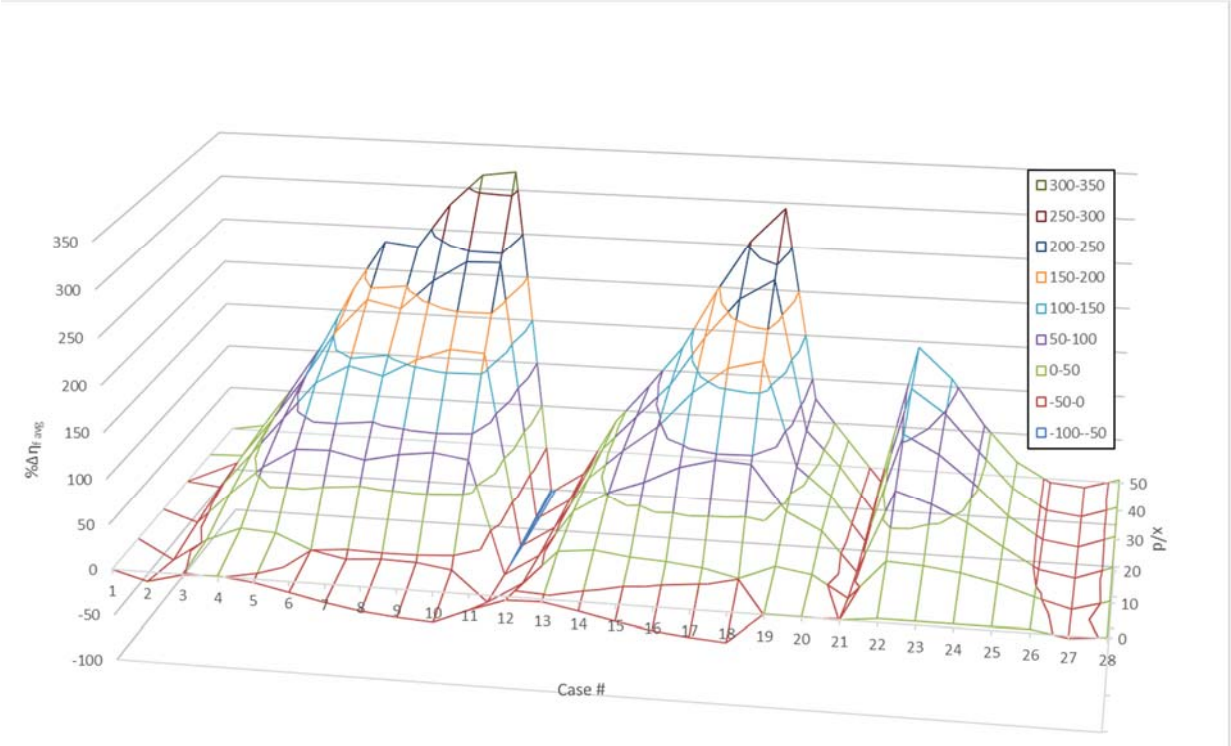

Figure 5.94: The Change of Adiabatic Film Cooling Effectiveness (in %) for all Cases

The change in film cooling effectiveness caused by the blowing parameter alone is summarized in Table 5.10. Cases #11 and #12 show a decrease in film cooling effectiveness due to the low blowing parameter. As the blowing parameter increases, detachment and

reattachment is introduced between 0 and 10 x/d causing a drop in film cooling effectiveness. The higher blowing parameters show a better adiabatic film cooling effectiveness downstream of the film holes due to the high turbulence intensity effects.

Table 5.10: Percent Change for Blowing Parameter

	x/d	0	10	20	30	40	50
Case #	Case	$\%\Delta\eta_f$ avg	$\%\Delta\eta_f$ avg	$\%\Delta\eta_f$ avg	$\%\Delta\eta_f$ avg	$\%\Delta\eta_f$ avg	$\%\Delta\eta_f$ avg
11	Mb: 0.53, Tu: 20%, DR: 1.65	-17.42	-44.88	-49.31	-51.34	-52.52	-53.35
12	Mb: 0.77, Tu: 20%, DR: 1.65	-3.90	-21.16	-24.98	-26.64	-27.58	-28.24
1	Mb: 0.98, Tu: 20%, DR: 1.65	0.00	0.00	0.00	0.00	0.00	0.00
13	Mb: 1.51, Tu: 20%, DR: 1.65	-2.82	16.99	28.23	32.93	35.46	37.26
14	Mb: 2.13, Tu: 20%, DR: 1.65	-10.07	21.04	51.78	66.67	74.94	80.99
15	Mb: 2.96, Tu: 20%, DR: 1.65	-18.35	15.94	65.55	95.99	114.11	127.90
16	Mb: 4.08, Tu: 20%, DR: 1.65	-25.71	13.56	84.65	136.98	169.87	195.08
17	Mb: 5.04, Tu: 20%, DR: 1.65	-30.10	9.40	95.05	166.10	215.18	254.83
18	Mb: 5.95, Tu: 20%, DR: 1.65	-33.01	0.43	92.75	176.13	238.58	293.78

The percent change in film cooling effectiveness due to turbulence intensity is summarized in Table 5.11, which shows the trend of a low blowing parameter with high and low turbulence intensity. A higher Tu creates lower effectiveness for a low blowing parameter and a low Tu improves cooling performance.

Table 5.11: Percent Change for Turbulence Intensity

	x/d	0	10	20	30	40	50
Case #	Case	$\%\Delta\eta_f$ avg	$\%\Delta\eta_f$ avg	$\%\Delta\eta_f$ avg	$\%\Delta\eta_f$ avg	$\%\Delta\eta_f$ avg	$\%\Delta\eta_f$ avg
4	Mb: 0.98, Tu: 5%, DR: 1.65	0.84	19.37	55.50	80.53	96.80	110.36
19	Mb: 0.98, Tu: 10%, DR: 1.65	0.63	16.24	43.03	60.74	70.70	76.61
20	Mb: 0.98, Tu: 15%, DR: 1.65	0.36	10.04	23.69	29.86	31.18	30.44
1	Mb: 0.98, Tu: 20%, DR: 1.65	0.00	0.00	0.00	0.00	0.00	0.00
21	Mb: 0.98, Tu: 25%, DR: 1.65	-0.30	-13.13	-19.52	-19.21	-17.47	-15.62

The density ratio shows the same trend as the blowing parameter study, but without the detachment in Table 5.12. The comparison of realistic engine condition shows a 20% change in adiabatic film cooling effectiveness with respect to the baseline.

Table 5.12: Percent Change for Density Ratio

	x/d	0	10	20	30	40	50
Case #	Case	$\%\Delta\eta_f$ avg	$\%\Delta\eta_f$ avg	$\%\Delta\eta_f$ avg	$\%\Delta\eta_f$ avg	$\%\Delta\eta_f$ avg	$\%\Delta\eta_f$ avg
27	VR: 0.64, Tu: 20%, DR: 1.49	-2.74	-8.57	-10.32	-10.10	-9.21	-7.99
1	VR: 0.64, Tu: 20%, DR: 1.65	0.00	0.00	0.00	0.00	0.00	0.00
28	VR: 0.64, Tu: 20%, DR: 1.72	0.80	2.78	3.83	4.07	3.90	3.54
25	VR: 0.64, Tu: 20%, DR: 1.99	3.95	14.15	19.12	20.08	19.06	17.04

6 Conclusions

The main objective of this research was to perform both experimental and numerical simulations for the impingement and film cooling in a gas turbine. An effective thermal wind tunnel was designed and fabricated that incorporates the exhaust plume of a micro-jet and the entrainment of an ejector nozzle. Impingement and film cooling were combined to create a leading edge and mid-chord heat transfer/cooling flux from a single cooling ejector. Validation of the numerical simulations with experimental results is an important element in our research. Based on the results, an excellent correlation with surface temperature distribution was demonstrated. The CHT model was identified to provide more accurate overall cooling simulations (impingement and film cooling) than the adiabatic wall model. The adiabatic model was used to study the pure film cooling effects in the absence of wall heat transfer. Therefore, an adiabatic parametric study was simulated and showed the effect of blowing parameter, turbulence intensity and density ratio for the film cooling system. Real engine non-dimensional parameters were also simulated and analyzed to assess the differences between realistic parameters and the experimental model. The results obtained from the experiment and numerical investigations were compared with heat transfer data available in the literature, which showed a favorable trend for the non-dimensional parameters, e.g., film cooling effectiveness studied.

The broad variation in the blowing parameter is considered in this research. The blowing parameter is classified as low, moderate and high categories, which can affect the film cooling effectiveness downstream of the coolant injection. Low blowing parameters are attached to the surface of the airfoil, but mix and spread quickly downstream. The higher blowing parameters would detach from the surface and reattach downstream. These detachments develop a hot spot

behind the film hole, which can cause thermal stresses on the blade. Therefore, attached blowing parameters before detachment show the best cooling performance.

The turbulence intensity study data shows two trends that affect the blowing parameter. Low blowing parameter and high turbulence will cause a decrease in film cooling performance, due to the jet lower momentum and thus faster mixing rate, or dissipation. In general, higher blowing parameter and high turbulence intensity show an increase in adiabatic film effectiveness.

The density ratio study shows that increasing coolant density would increase the blowing parameter. The effect is small compared to the other film cooling factors, but the density ratio could detach the jet if the blowing parameter is in the detachment transition zone.

In conclusion, the major research objectives of the thermal wind tunnel design, construction, instrumentation and testing was accomplished. The goal of computational simulation to study the complex heat transfer problem of impingement and film cooling is accomplished. A broad investigation of blowing coefficient, density ratio and turbulence intensity was conducted and major conclusions drawn.

There are many more research goals to be accomplished beyond the current research reported in this dissertation. A brief summary of those goals are outlined in the next section.

7 Recommendations for Future Research

As noted, the objective of this study was to develop a thermal wind tunnel to test an impingement and film cooling airfoil in a gas turbine engine exhaust plume. The work lays a foundation for continuing research for experimental and numerical investigations. The recommendations for future work are as follows:

1. Geometric Effects:
    a. A study of different surface curvature effects on the film cooling performance. This would result in several airfoils contours.
    b. A matrix of inclination angles (α) should be simulated to show the effects of this angle on the adiabatic film cooling effectiveness.
    c. Film hole shaping, i.e., non-circular, non-elliptic film holes
2. Angle of Attack: Different AoA should be investigated based on the airfoil's and flow characteristics.
3. Rotation: The simulation of rotation should be added for the effect of rotating observer. There has been very little experimental study on rotation, due to the complexities and expenses. Therefore rotation simulation should be validated by experiments and for different film cooling parameters.
4. IR Camera: Temperature readings can be improved by inducing an IR camera for flow visualization and mapping of the temperatures on the suction/pressure surfaces of turbine blade. This will give a real world detail contour of the temperature and film cooling effectiveness.
5. The effect of Mach number in transonic turbine on blade cooling

8 References

[1] Abbott, I. H., " Families of Wing Sections "*in Theory of Wing Sections*, Dover Publications, INC., New York, 1959, pp. 111-123

[2] Al-Hamadi, A.K., Jubran, B.A., and Theodoridis, G., "Turbulence Intensity Effects on Film Cooling and Heat Transfer from Compound Angle Holes with Particular Application to Gas Turbine Blades," Energy Convers. Mgmt, 1998 Vol. 39, No. 14, pp. 1449-1457

[3] Amano, R.S., Sunden, B., *Impingement Jet Cooling in Gas Turbines*, WIT Press, Billerica, MA, 2014

[4] Anderson Jr., J. D., "Fundamentals of Inviscid, Incompressible Flow," in *Fundamentals of Aerodynamics*, 5th ed., McGraw Hill, New York, 2011, pp. 203-309

[5] Andreini, A., Burberi, E., Cocchi, L., Facchini, B., Massini, D., Pievaroli, M., "Heat Transfer Investigation on an Internal Cooling System of a Gas Turbine Leading Edge Model," Energy Procedia, Volume 82, 2015, Pages 222-229

[6] Azad GS, Han J, Teng S, Boyle RJ. "Heat Transfer and Pressure Distributions on a Gas Turbine Blade Tip," ASME. J. Turbomach. 2000; 122 (4):717-724.

[7] Azimi, A., Ashjaee, M., Razi, P., "Slot jet impingement cooling of a concave surface in an annulus," Experimental Thermal and Fluid Science, Volume 68, 2015, Pages 300-309

[8] Baldauf SS, Scheurlen MM, Schulz AA and Wittig SS, "Correlation of Film-Cooling Effectiveness From Thermographic Measurements at Engine like Conditions," ASME. J. Turbomach. 2002;124(4):686-698

[9] Bergman, T. L., Lavine, A. S., Incropera, F. P., and Dewitt, D. P., "External Flow," in *Fundamentals of Heat and Mass Transfer*, Seventh Edition, John Wiley and Sons, Ltd., Hoboken, NJ, 2011, pp. 433-486

[10] Bogard, D. G., "Airfoil Film Cooling," in *The Gas Turbine Handbook*, National Energy Technology Laboratory, Department of Energy, Morgantown, WV, Sect. 4.2.2.1., 2006

[11] Bogard, D. G., and Thole, K. A., "Gas Turbine Film Cooling," Journal of Propulsion and Power, Vol. 22, No. 2 March – April 2006, pp. 249-270

[12] Bons JP, MacArthur CD and Rivir RB, "The Effect of High Free-Stream Turbulence on Film Cooling Effectiveness," ASME. Turbo Expo: Power for Land, Sea, and Air, Volume 4: Heat Transfer; Electric Power; Industrial and Cogeneration:V004T09A011. doi:10.1115/94-GT-051. 1994

[13] Brittingham RA, Leylek JH. "A Detailed Analysis of Film Cooling Physics: Part IV — Compound–Angle Injection With Shaped Holes," ASME. Turbo Expo: Power for Land, Sea, and Air, Volume 3: Heat Transfer; Electric Power; Industrial and Cogeneration, V003T09A055. 97-GT-272., 1997

[14] Bunker, R.S., Dees, J.E., and Palafox, P., "Impingement Cooling in Gas Turbines: Design, Applications, and Limitations," *in Impingement Jet Cooling in Gas Turbines*, WIT Press, Billerica, MA, 2014, pp. 1-28

[15] Burd, S.W., Kaszeta, R.W., and Simon, T.W., "Measurements in Film Cooling Flows: Hole LID and Turbulence Intensity Effects," ASME, Journal of Turbomachinery, Vol. 120, 1998, pp 791-798

[16] Capone, A., Soldati, A., Romano, G.P., "Mixing and entrainment in the near field of turbulent round jets," Springer-Verlag, Experiments in Fluids 54: 1434.,2013, pp. 1-14

[17] Chandran, D., and Prasad, B., "Conjugate Heat Transfer Study of Combined Impingement and Showerhead Film Cooling Near NGV Leading Edge," Hindawi Publishing Corporation, International Journal of Rotating Machinery, Volume 2015, Article ID 315036, pp. 1-13

[18] Cho, H.H., Rhee, D.H., and Kim, B.G., "Enhancement of Film cooling Performance Using a Shaped Film Cooling Hole with Compound Angle Injection," *JSME International Journal*, Vol. 44, No. 1, 2001, pp. 99-110

[19] Chupp, R. E., Helms, H. E., McFadden, R. W., and Brown, T. R., "Evaluation of Internal Heat Transfer Coefficients for Impingement Cooled Turbine Airfoils," *Journal of Aircraft,* Vol. 16, May-June 1969, pp. 203-208.*

[20] Chupp, R. E., Helms, H. E., McFadden, R. W., and Brown, T. R., "Evaluation of Internal Heat Transfer Coefficients for Impingement Cooled Turbine Airfoils," *Journal of Aircraft,* Vol. 16, May-June 1969*

[21] Clarke, D., Oechsner, M., & Padture, N. (2012), "Thermal-barrier coatings for more efficient gas-turbine engines," MRS Bulletin, 37(10), 2012 pp. 891-898. doi:10.1557/mrs.2012.232

[22] Colladay, R.S., "Turbine Cooling," in Turbine Design and Applications, Glassman, A.J. (Ed.), NASA SP-290, Washington, DC, 1975.

[23] Cummings, R.M., Mason, W.H., Morton, S.A., and McDaniel, D.R., "Geometry and Grids: Key Considerations in Computational Aerodynamics," in *Applied Computational Aerodynamics A Modern Engineering Approach*, Cambridge University Press, New York, NY, 2015, pp. 641-761

[24] Cutbirth J, Bogard DG. Thermal Field and Flow Visualization within the Stagnation Region of a Film-Cooled Turbine Vane. *ASME. J. Turbomachinery,* 2002;124(2):200-206

[25] Dees JE, Bogard DG, Ledezma GA, Laskowski GM. Overall and Adiabatic Effectiveness Values on a Scaled Up, Simulated Gas Turbine Vane. *ASME. J. Turbomachinery* 2013;135(5):051017-051017-10.

[26] Dees, J.E., "Experimental Measurements of Conjugate Heat Transfer on a Scaled up Gas Turbine Airfoil with Realistic Cooling Configuration," Dissertation, The University of Texas at Austin, May 2010

[27] Department of Defense, "Aluminum," in *Metallic Materials and Elements for Aerospace Vehicle Structures*, Department of Defense and Federal Aviation Administration, MIL-HDBK-5J, 2003, pp. 3-1 to 3-525

[28] Dobrowolski, L. D., "Numerical Simulation of a Film Cooled Turbine Blade Leading Edge Including Heat Transfer Effects," M.S. Thesis, The University of Texas at Austin, 2009

[29] Dobrowolski, L.D., Bogard, D.G., Piggush, and J., Kohli, A., "Numerical simulation of a simulated film cooled turbine blade leading edge including conjugate heat transfer effects," In: ASME International Mechanical Engineering Congress & Exposition, IMECE2009-11670, Lake Buena Vista, USA, 2009.*

[30] Drost, U., Bolcs, A., and Hoffs, A., 1997, ''Utilization of the Transient Liquid Crystal Technique for Film Cooling Effectiveness and Heat Transfer Investigations on a Flat Plate and a Turbine Airfoil,'' ASME Paper 97-GT-26.

[31] Dyson TE, Bogard DG, Bradshaw SD. "Evaluation of CFD Simulations of Film Cooling Performance on a Turbine Vane Including Conjugate Heat Transfer Effects," ASME. Turbo Expo: Power for Land, Sea, and Air, Volume 4: Heat Transfer, Parts A and B ():1527-1535. doi:10.1115/GT2012-69107.

[32] Ekkad, S. V., Huang, Y., and Han, J., "Impingement Heat Transfer on a Target Plate with Film Cooling Holes," *Journal of Thermophysics and Heat Transfer*, Vol. 13, No. 4 (1999), pp. 522-528.

[33] Elebiary KK, Taslim ME. Experimental/Numerical Crossover Jet Impingement in an Airfoil Leading-Edge Cooling Channel. *ASME. J. Turbomachinery*, 2012; 135(1):011037-011037-12.

[34] Elebiary, K., "Numerical Investigation of Impingement Cooling in an Airfoil Leading-Edge Cooling Channel," MS Thesis, Northeastern University, Boston, Massachusetts, January 2010

[35] FAA, "Transition to Turbopropeller-Powered Airplanes" in *Airplane Flying Handbook*, FAA-H-8083-3B, U.S. Department of Transportation, Federal Aviation Administration, 2016

[36] Farokhi, S., "Aerothermodynamics of Gas Turbines," in *Aircraft Propulsion*, 2nd ed., John Wiley and Sons, Ltd., West Sussex (UK), 2014, pp. 718-732.

[37] Farokhi, S., "Airbreathing Engine Performance Parameters," in *Aircraft Propulsion*, 2nd ed., John Wiley and Sons, Ltd., West Sussex (UK), 2014, pp. 113-150.

[38] Foster, N. W., and Lampard, D., 1980, "The Flow and Film Cooling Effectiveness Following Injection Through a Row of Holes," ASME J. Eng. Power, 102, pp. 584–588.

[39] Gardiner, G., "Aeroenine Composites, Part 1: The CMC invasion," Composites World, https://www.compositesworld.com/articles/aeroengine-composites-part-1-the-cmc-invasion, 2015

[40] Goldstein, R.J., Eckert, E.R.G., and Burggraf, F, "Effects of hole geometry and density on three-dimensional film cooling," *International Journal of Heat and Mass Transfer*, Volume 17, Issue 5, 1974, Pages 595-607*

[41] Goldstein, R.J., Timmer, J.F. "Visualization of heat transfer from arrays of impinging jets," *Int. J. Heat Mass Transfer*, Vol. 25, 1982, pp. 1857- 1868.*

[42] Gritsch M, Schulz A, Wittig S. Effect of Crossflows on the Discharge Coefficient of Film Cooling Holes With Varying Angles of Inclination and Orientation. *ASME. J. Turbomachinery,* 2001;123(4):781-787

[43] Hadier, S.A., "Jet Diameter Effect on Impingement Jet Cooling on the Leading Edge of a Turbine Blade," MS Thesis, Southern Illinois University Edwardsville, 2015

[44] Han, J. C., Dutta, S., & Ekkad, S., "Turbine Internal Cooling," in *Gas Turbine Heat Transfer and Cooling Technology,* 2nd Edition Taylor & Francis, New York, 2013, pp. 329-525

[45] Han, J. C., Park, J. S., and Lie, C. K., "Heat Transfer and Pressure Drop in Blade Cooling Channels with Turbulence Promoters," NASA CR-3837, 1984

[46] Harrison KL, Bogard DG. Comparison of RANS Turbulence Models for Prediction of Film Cooling Performance. ASME. Turbo Expo: Power for Land, Sea, and Air, Volume 4: Heat Transfer, Parts A and B ():1187-1196. doi:10.1115/GT2008-51423.

[47] Harrison KL, Bogard DG. Use of the Adiabatic Wall Temperature in Film Cooling to Predict Wall Heat Flux and Temperature. ASME. Turbo Expo: Power for Land, Sea, and Air, Volume 4: Heat Transfer, Parts A and B: 1197-1207. doi:10.1115/GT2008-51424.

[48] Henderson, R.E., "The Temperature. Pressure and Flow Distribution Characteristics Around a Transpiration Cooled Cylinder in Cross Flow," M.S. Thesis, The Ohio State University, 1969*

[49] Hill, P. and Peterson, C., "Axial Turbines," in *Mechanics and Thermodynamics of Propulsion*, 2nd ed., Addison-Wesley Longman, Massachusetts, 1992, pp. 393-400.

[50] Hoda, A. and Acharya, S., 1999, "Predictions of a film coolant jet in crossflow with different turbulence models," ASME Paper 99-GT-124.*

[51] Hyams DG, Leylek JH. "A Detailed Analysis of Film Cooling Physics: Part III — Streamwise Injection With Shaped Holes," ASME. Turbo Expo: Power for Land, Sea, and Air, Volume 3: Heat Transfer; Electric Power; Industrial and Cogeneration V003T09A054, 97-GT-271, 1997

[52] Ingole, S.B., Sundaram, K.K., "Experimental average Nusselt number characteristics with inclined non-confined jet impingement of air for cooling application," Experimental Thermal and Fluid Science, Volume 77, 2016, Pages 124-131

[53] Islami, S.B., and Jubran, B.A., "The effect of turbulence intensity on film cooling of gas turbine blade from trenched shaped holes," Springer-Verlag, Heat Mass Transfer, 2012, 48:831–840

[54] Ito, S., Goldstein, R., and Eckert, E., "Film Cooling of a Gas Turbine Blade," *Journal of Engineering for Power*, Vol. 100, No. 3, pp. 476-481, 1978

[55] Jung I, Lee J. Effects of Orientation Angles on Film Cooling Over a Flat Plate: Boundary Layer Temperature Distributions and Adiabatic Film Cooling Effectiveness. *ASME. J. Turbomachinery,* 1999; 122(1):153-160.

[56] Kayansayan, N., "An Experimental Study of Two Dimensional Impingement Cooling," Dissertation, The Ohio State University, 1978

[57] Kerrebrock, J. L., "Turbines," in *Aircraft Engines and Gas Turbines*, 2nd edition, Massachusetts Institute of Technology, Massachusetts, 1992 pp. 283-313

[58] Kodzwa, P.M., and Eaton, J.K., "Measurements of Film cooling Performance in a Transonic Single Passage Model," Report No. TF 93, Stanford University, Stanford, CA, June 2005

[59] Kohli AA, Thole KA. Entrance Effects on Diffused Film-Cooling Holes. ASME. Turbo Expo: Power for Land, Sea, and Air, Volume 4: Heat Transfer; Electric Power; Industrial and Cogeneration ():V004T09A070. doi:10.1115/98-GT-402.

[60] Kohli, A., and Bogard, D. G., 1997, ''Adiabatic Effectiveness, Thermal Fields, and Velocity Fields for Film Cooling With Large Angle Ejection,'' ASME J. Turbomach., 119, pp. 352–358.

[61] Kreith, F. and Bohn, M., "Forced Convection Over Exterior Surfaces" in *Principles of Heat Transfer,* 6th ed. Brooks/Cole, Pacific Grove, CA, 2001, pp. 421-483

[62] Laskowski, G. M., Ledezma, G. A., Tolpadi, A. K., and Ostrowski, M. C., "CFD Simulations and Conjugate Heat Transfer Analysis of a High Pressure Turbine Vane Utilizing different Cooling Configurations," 20065 presented at ISROMAC, 2008*

[63] Lee, J., Ren, Z., Ligrani, P., Fox, M.D., Moon, H.K., "Cross-flow effects on impingement array heat transfer with varying jet-to-target plate distance and hole spacing," International Journal of Heat and Mass Transfer, Volume 75, 2014, Pages 534-544

[64] Lee, J., Ren, Z., Ligrani, P., Fox, M.D., Moon, H.K., "Crossflows from jet array impingement cooling: Hole spacing, target plate distance," Reynolds number effects, *International Journal of Thermal Sciences*, Volume 88, 2015, Pages 7-18

[65] Ligrani, Phil, "Heat Transfer Augmentation Technologies for Internal Cooling of Turbine Components of Gas Turbine Engines," *International Journal of Rotating Machinery*, Volume 2013, January 2013

[66] Lin, C.X., Holder, R.J., Sekar, B., Zelina, J., Polanka, M. D., Thornburg, H.J., and Briones, A.M., "Heat Release in Turbine Cooling II: Numerical Details of Secondary Combustion Surrounding Shaped Holes", Journal of Propulsion and Power, Vol. 27, No. 2 (2011), pp. 269-281

[67] Liu, L., Zhu, X., Liu, H., and Du, Z. Effect of tangential jet impingement on blade leading edge impingement heat transfer, *Applied Thermal Engineering*, Volume 130, 2018, Pages 1380-1390,

[68] Liu, Z., and Feng, Z. Numerical simulation on the effect of jet nozzle position on impingement cooling of gas turbine blade leading edge, *International Journal of Heat and Mass Transfer*, Volume 54, Issues 23–24, 2011, Pages 4949-4959,

[69] Luo, L., and Razinski E. H., "Conjugate Heat Transfer Analysis of a Cooled turbine vane using the V2F Turbulence Model," *Journal of Turbomachinery*, Vol. 129, No. 4, pp. 773-781, 2006*

[70] Martin CA, Thole KA. A CFD Benchmark Study: Leading Edge Film-Cooling With Compound Angle Injection. ASME. Turbo Expo: Power for Land, Sea, and Air, Volume 3: Heat Transfer; Electric Power; Industrial and Cogeneration ():V003T09A059. doi:10.1115/97-GT-297

[71] Martin, E.L., "Experimental and Numerical Investigation of High Temperature Jet Impingement for Turbine Cooling Applications," MS Thesis, Baylor University, 2011

[72] Mattingly, J., Heiser, W., and Pratt, D., "Engine Component Design: Combustion Systems," in *Aircraft Engine Design*, 2nd ed., AIAA, Reston, Virginia, 2002, pp. 350-351

[73] Mayhew J.E., Baughn J. W., and Byerley A. R., The effect of freestream turbulence on film cooling adiabatic effectiveness, International Journal of Heat and Fluid Flow, Volume 24, Issue 5, 2003, Pages 669-679,

[74] Mayhew JE, Baughn JW, Byerley AR. Adiabatic Effectiveness of Film Cooling with Compound Angle Holes-The Effect of Blowing Ratio and Freestream Turbulence. ASME. *J. Heat Transfer.* 1904;126(4):501. 2004 doi:10.1115/1.1811720.

[75] McGovern KT, Leylek JH. A Detailed Analysis of Film Cooling Physics: Part II—Compound-Angle Injection With Cylindrical Holes. *ASME. J. Turbomachinery*, 1997;122(1):113-121.

[76] Medic G., and Durbin P. A., "Towards improved -prediction of heat transfer in turbine blades," Journal of Turbomachinery, , Vol. 124, No. 4, pp. 187-192, 2002*

[77] Metzger, D. E., Baltzer, R. T., and Jenkins, C. W., "Impingement Cooling Performance in Gas Turbine Airfoils Including Effects of Leading Edge Sharpness," *Journal of Engineering for Power*, Transactions of ASME, Ser. A, Vol. 94, July 1972*

[78] Metzger, D.E., Yamashiata, T., and Jenkins, G.W., "Impingement Cooling of Concave Surfaces with Lines of Circular Air Jets," *Journal of Engineering for Power*, Transactions ASME, Series H, Vol. 91, No. 3, January 1969*

[79] Moran, M.J., and Shapiro, H.N., "Energy and the First Law of Thermodynamics" in *Fundamentals of Engineering Thermodynamics*, John Wiley & Sons, Inc., Hoboken, NJ, 2008, pp. 31-79

[80] Moskowitz, S. L. and Lombardo, S., "2750 Degree F Engine Test of a Transpiration Air-Cooled Turbine," *Journal of Engineering for Power*, Transactions of ASME, Ser. A, Vol. 93, April 1971*

[81] Munson, B. R., Okiishi, T.H., Huebsch, W.W., and Rothmayer, A.P., "Finite Control Volume Analysis," in *Fundamentals of Fluid Mechanics,* John Wiley & Sons, Inc., 2013, pp.199-255

[82] Naik, Shailendra, "Basic Aspects of Gas Turbine Heat Transfer," in *Heat Exchangers – Design, Experiment and Simulation*, Murshed, S. M. S., and Lopes, M. M., Editor, InTech, Rijeka, Croatia, 2017, pp. 111- 142

[83] Oates, G. C., "Ideal Cycle Analysis," in *Aerothermodynamics of Gas Turbine and Rocket Propulsion,* Third Edition, AIAA, Reston, Virginia, 1997, pp. 121-188

[84] Panda R. K., and Prasad, B. V. S. S. S., "Conjugate Heat Transfer from an Impingement and Film-Cooled Flat Plate," *Journal of Thermophysics and Heat Transfer*, Vol. 28, No. 4 (2014), pp. 647-666.

[85] Pedersen, D. R, " Effect of Density Ratio on Film Cooling Effectiveness for Injection through a Row of Holes and for a Porous Slot," PhD Thesis, The University of Minnesota, 1972

[86] Pedersen, D. R., Eckert, E., and Goldstein, R., "Film Cooling with Large Density Differences Between the Mainstream and the Secondary Fluid Measured by the Heat-Mass Transfer Analogy," *Journal of Heat Transfer*, Vol. 99, 1977, pp. 620–627 *

[87] Repko TW, Nix AC, Uysal C, Heidmann JD. Numerical Study on the Effects of Freestream Turbulence on Anti-vortex Film Cooling Design at High Blowing Ratio. *ASME. J. Thermal Sci. Eng. Appl*. 2016; 9(1):011013-011013-12

[88] Schetz, J. A., and Bowersox, R. D. W., "Introduction to Viscous Flows" in *Boundary Layer Analysis*, Second Edition, AIAA, Inc., Reston, Virginia, 2011, pp. 1-32

[89] Schmidt DL and Bogard DG. "Effects of Free-Stream Turbulence and Surface Roughness on Film Cooling," ASME. Turbo Expo: Power for Land, Sea, and Air, Volume 4: Heat Transfer; Electric Power; Industrial and Cogeneration: V004T09A049. 1996

[90] Schmidt, D., Sen, B., and Bogard, D., "Film Cooling with Compound Angle Holes: Adiabatic Effectiveness," *Journal of Turbomachinery*, Vol. 118, 1996, pp. 807–813.*

[91] Shih, T.H., Liou, W.W., Shabbir, A., Yang, Z., and Zhu, J., "A New k-ε Eddy Viscosity Model for High Reynolds Number Turbulent Flows – Model Development and Validation,: NASA, Technical Memorandum 016721, August 1994

[92] Siemens, "STAR CCM+ User Guide," Munich, Germany, 2017

[93] Silieti, M., Divo,E., and Kassab, A.J, 2004, "Numerical investigation of adiabatic and conjugate film cooling effectiveness on a single cylindrical film-cooling hole," ASME Paper IMECE2004-62196.*

[94] Silieti, M., Kassab, A.J., and Divo,E., "Film cooling effectiveness: Comparison of adiabatic and conjugate heat transfer CFD models," *International Journal of Thermal Sciences,* Volume 48, Issue 12, 2009, Pages 2237-2248, ISSN 1290-0729,

[95] Sinha, A., Bogard, D., and Crawford, M., "Film Cooling Effectiveness Downstream of a Single Row of Holes with Variable Density Ratio," *Journal of Turbomachinery*, Vol. 113, 1991, pp. 442–449.*

[96] Song, L., Zhang, C., Song, Y., Li, J. and Feng, Z. "Experimental investigations on the effects of inclination angle and blowing ratio on the flat-plate film cooling enhancement using the vortex generator downstream," *Applied Thermal Engineering*, Volume 119, 2017, Pages 573-584

[97] Squire, H. B., *Modern Developments in Fluid Dynamics*, 3rd ed., Vol. 2, Clarendon, Oxford, 1950*

[98] Suo, M., "Turbine Cooling," in *Aerothermodynamics of Aircraft Engine Components*, Oates, G. C., Editor, AIAA, New York, 1985, pp. 275-328.

[99] Takeishi, K., Oda, Y., and Kondo, S., "An experimental study of a film cooling with swirling flow on the endwall of a high loaded 1st nozzle," WIT Transactions on Engineering Sciences, WIT Press, Vol 75, 2012, pp 85-96

[100] Takeshi, N., Takashi, O., Kuniuuki, I., Ken-ichi, S., and Masato, I., "Development of CMC Turbine Parts for Aero Engines," *IHI Engineering Review*, Vol. 47 No. 1, 2014, pp. 29-32

[101] Tannebill, J. C., Anderson, D. A., and Pletcher, R. H., "Governing Equations of Fluid Mechanics and Heat Transfer," in *Computational Fluid Mechanics and Heat Transfer*, 2nd Edition Taylor & Francis, 1997, pp 249-350

[102] Tu, J., Yeoh, G., and Liu, C., "Practical Guidelines for CFD Simulation and Analysis," in *Computational Fluid Dynamics A Practical Approach*, 2nd Edition, Elsevier, 2013,

[103] van de Goor, B. J. J., “Manual & Engine Log Olympus HP”, AMT Netherlands, v2.17, 2017

[104] Walters DK, Leylek JH. A Detailed Analysis of Film-Cooling Physics: Part I—Streamwise Injection With Cylindrical Holes. *ASME. J. Turbomachinery,* 1997;122(1):102-112.

[105] Wang, J.H., Messner, J., and Stetter, H., “An Experimental Investigation on Transpiration Cooling Part II: Comparison of Cooling Methods and Media, “ *International Journal of Rotating Machinery*, Vol. 10, No. 5, 2004

[106] Waye SK, Bogard DG. High-Resolution Film Cooling Effectiveness Comparison of Axial and Compound Angle Holes on the Suction Side of a Turbine Vane. *ASME. J. Turbomachinery,* 2006; 129(2):202-211.

[107] Williams RP, Dyson TE, Bogard DG, Bradshaw SD. “Sensitivity of the Overall Effectiveness to Film Cooling and Internal Cooling on a Turbine Vane Suction Side,” *ASME. J. Turbomachinery,* 2013; 136(3):031006-031006-7.

[108] Wright LM, McClain ST, Clemenson MD. Effect of Freestream Turbulence Intensity on Film Cooling Jet Structure and Surface Effectiveness Using PIV and PSP. *ASME. J. Turbomachinery*, 2011; 133(4):041023-041023-12.

[109] Wu, P.S., Tsai, S.T., and Jhuo, Y. H., “Effect of Turbulence Intensity on Cross-Injection Film Cooling at a Stepped or Smooth Endwall of a Gas Turbine Vane Passage,” Hindawi, *The Scientific World Journal*, Vol. 2014, Article ID 256136, 2014, pp. 1-14

[110] Yang, Y.T., Wei, T.C., Wang, Y.H., “Numerical study of turbulent slot jet impingement cooling on a semi-circular concave surface,” *International Journal of Heat and Mass Transfer,* Volume 54, Issues 1–3, 2011, Pages 482-489

[111] Young, D.F., Munson, B.R., Okiishi, T.H., and Huebsch, W.W., " Finite Control Volume Analysis" in *A Brief Introduction to Fluid Mechanics*, fifth edition, John Wiley & Sons, Inc., 2011, pp. 125-166

[112] Zhang, X. Z. and Hassan, I., 2006, "Numerical Investigation of Heat Transfer on Film Cooling with Shaped Holes," *International Journal of Numerical Methods for Fluid Flow*, Vol. 16, n 8, p 848-869.

[113] Zhou, T., Xu, D., Chen, J., Cao, C., Ye, T., "Numerical analysis of turbulent round jet impingement heat transfer at high temperature difference," *Applied Thermal Engineering*, Volume 100, 2016, Pages 55-61

[114] Zikanov, O., "Governing Equations of Fluid Dynamics and Heat Transfer," in *Essential Computational Fluid Dynamics*, John Wiley & Sons, Inc., Hoboken, New Jersey, 2010, pp. 11-30

[115] Zok, F. W., "Ceramic-matrix composites enable revolutionary gains in turbine engine efficiency," *American Ceramic Society Bulletin*, Vol. 95, No. 5, 2016, pp. 22-28

9 Research Publications to Date:

[1] Underwood, S., Taghavi, R., and Farokhi, S., "Design of a Thermal Wind Tunnel for Impingement and Film Cooling Research", Paper 2941606 to be presented at the AIAA Propulsion and Energy Forum and Exposition, in Cincinnati, Ohio 2018

[2] Underwood, S., Taghavi, R., and Farokhi, S., "Experimental and Numerical Investigation of an Airfoil using Impingement and Film Cooling in a Gas Turbine Engine Exhaust Plume", Paper 2941698 to be presented at the AIAA Propulsion and Energy Forum and Exposition, in Cincinnati, Ohio 2018

[3] Underwood, S., Taghavi, R., and Farokhi, S., "Research on Impingement and Film Cooling," paper to be presented at 2019 AIAA SciTech and Forum, January 7-11, 2019, San Diego, California

10 Appendix A: Experiment Images

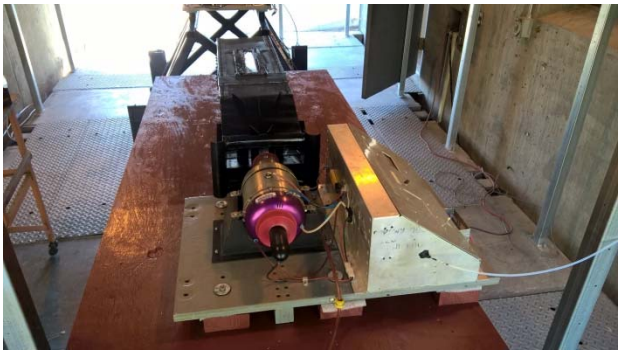

Figure 10.1: Front View of the Thermal Wind Tunnel

Figure 10.2: Rear View of the Thermal Wind Tunnel

Figure 10.3: Port View of the Thermal Wind Tunnel

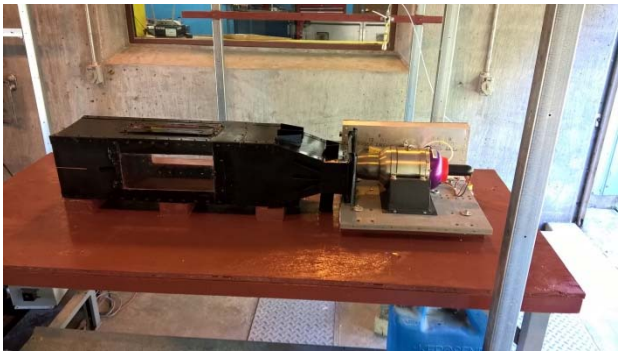

Figure 10.4:Starboard View of the Thermal Wind Tunnel

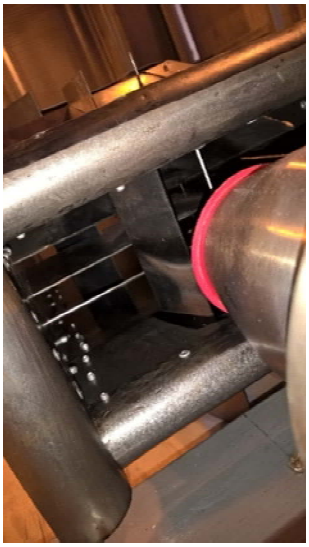

Figure 10.5: Splitter Diffuser Vanes of the Thermal Wind Tunnel

Figure 10.6: Laser Window of the Thermal Wind Tunnel

Figure 10.7: Pitot Tube

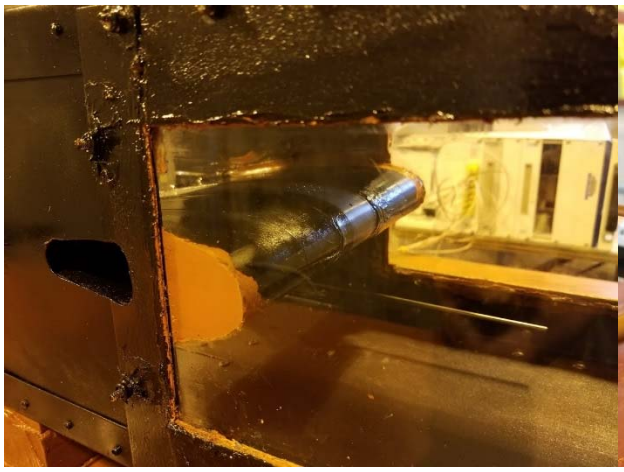

Figure 10.8: Installed Pitot Tube Side View

Figure 10.9: Installed Pitot Tube Rear View

Figure 10.10: Installed Pitot tube and Pressure Transducer

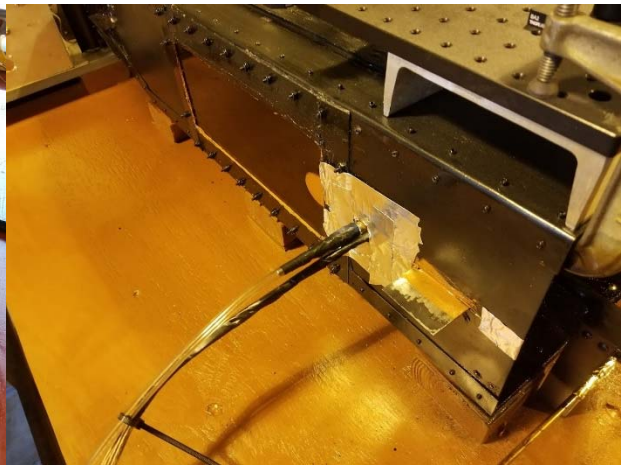

Figure 10.11: Coolant Supply Line with Thermocouples Wires Entrance Point

Figure 10.12: Freestream Thermocouple Entrance Point

Figure 10.13: Experiment Front View

Figure 10.14: Experiment Rear Port View

Figure 10.15: Experiment Rear Starboard View

11 Appendix B: Experimental Apparatus Schematics

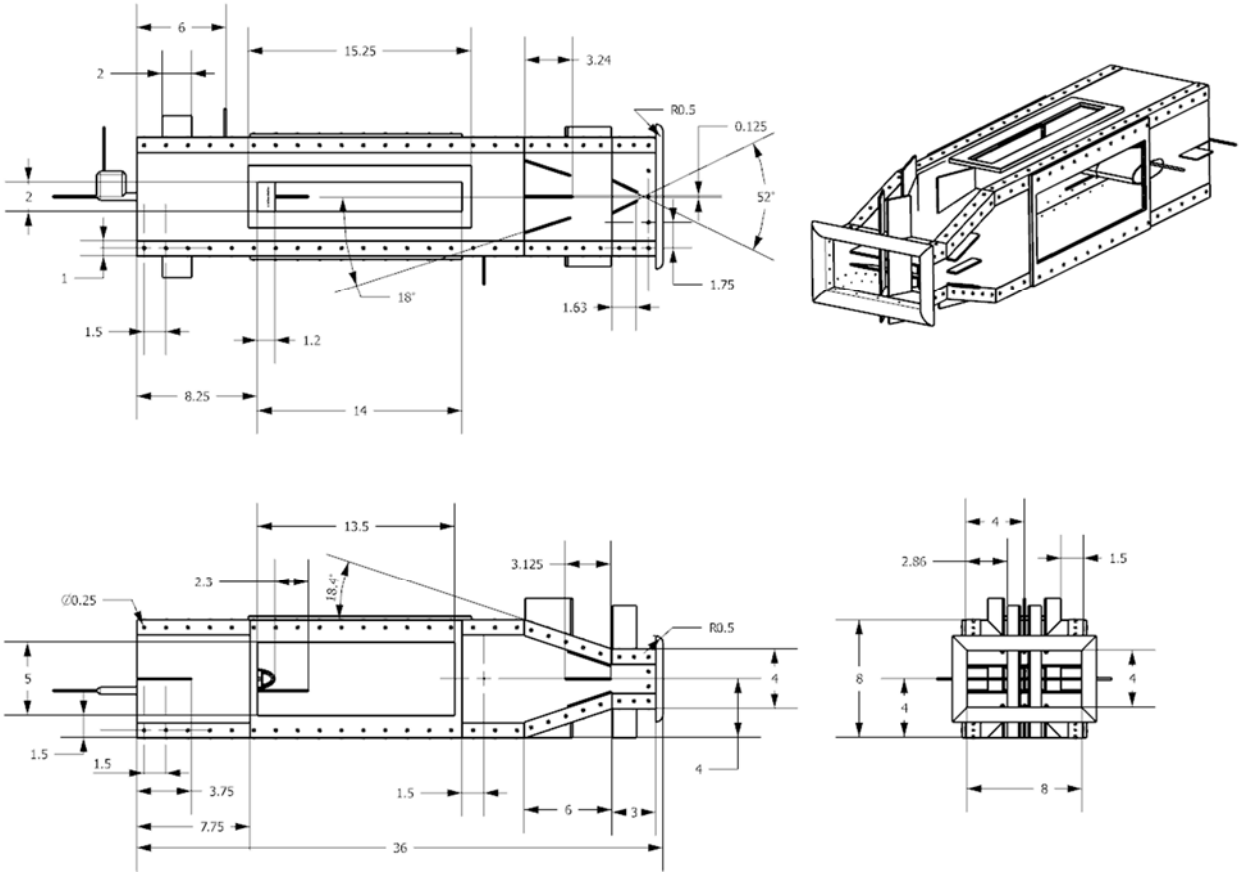

Figure 11.1: Schematic of the thermal wind tunnel (inches)

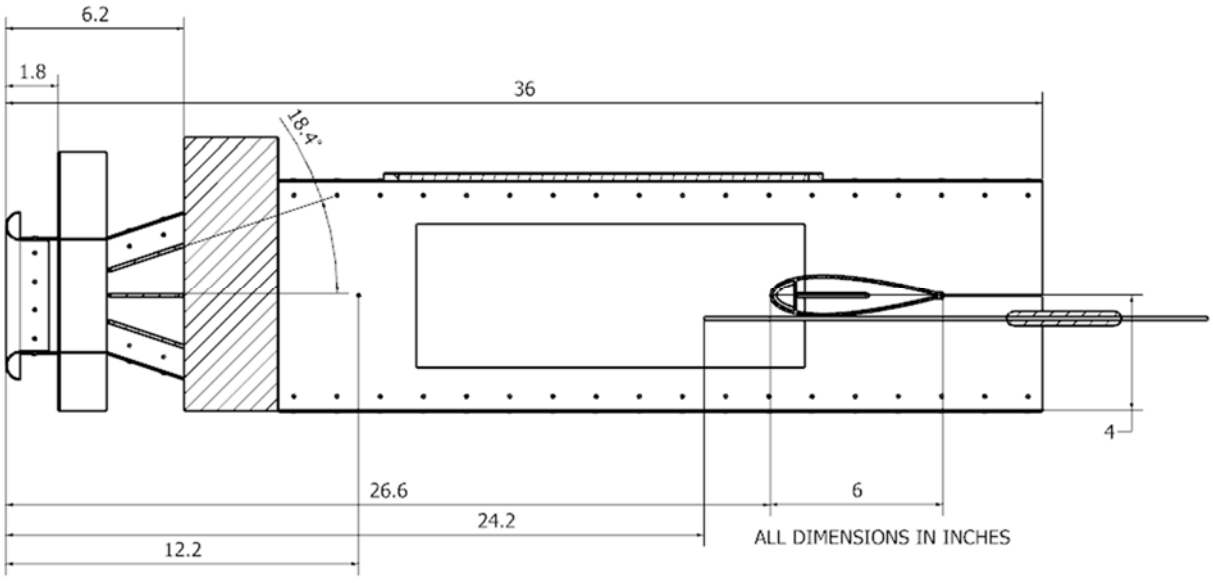

Figure 11.2: Side View Center Plane Schematic of the thermal wind tunnel (inches)

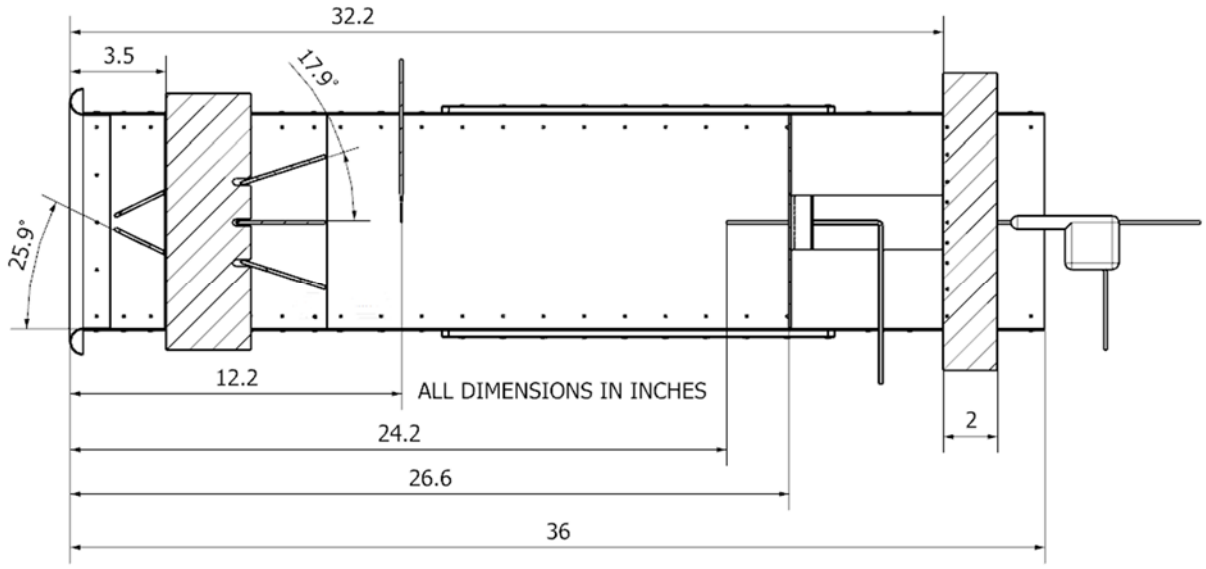

Figure 11.3: Top View Center Plane Schematic of the thermal wind tunnel (inches)

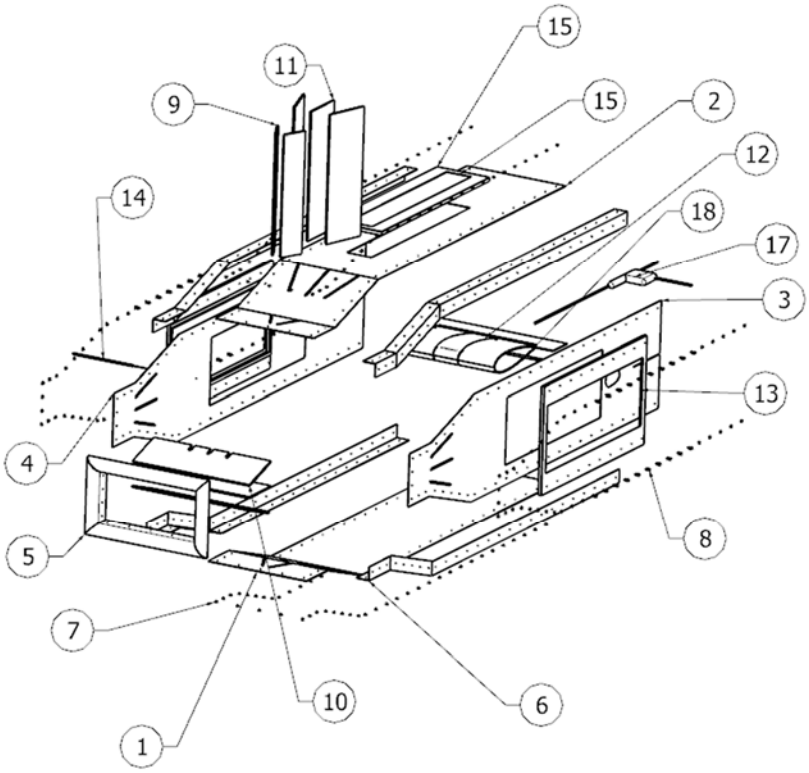

#	PART NAME	QTY
18	COMPRESSOR TUBE	1
17	PITOT TUBE	1
16	TOP GLASS	1
15	TOP GLASS FRAME	1
14	THERMAL COUPLER	1
13	SIDE GLASS	2
12	AIRFOIL ASSEMBLY	1
11	DIFFUSER 3	3
10	DIFFUSER 2	3
9	DIFFUSER 1	2
8	LONG RIVETS	40
7	RIVETS	192
6	FLANGE	4
5	INLET	1
4	LEFT SIDE	1
3	RIGHT SIDE	1
2	TOP SIDE	1
1	BOTTOM SIDE	1

Figure 11.4: Exploded View of the thermal wind tunnel

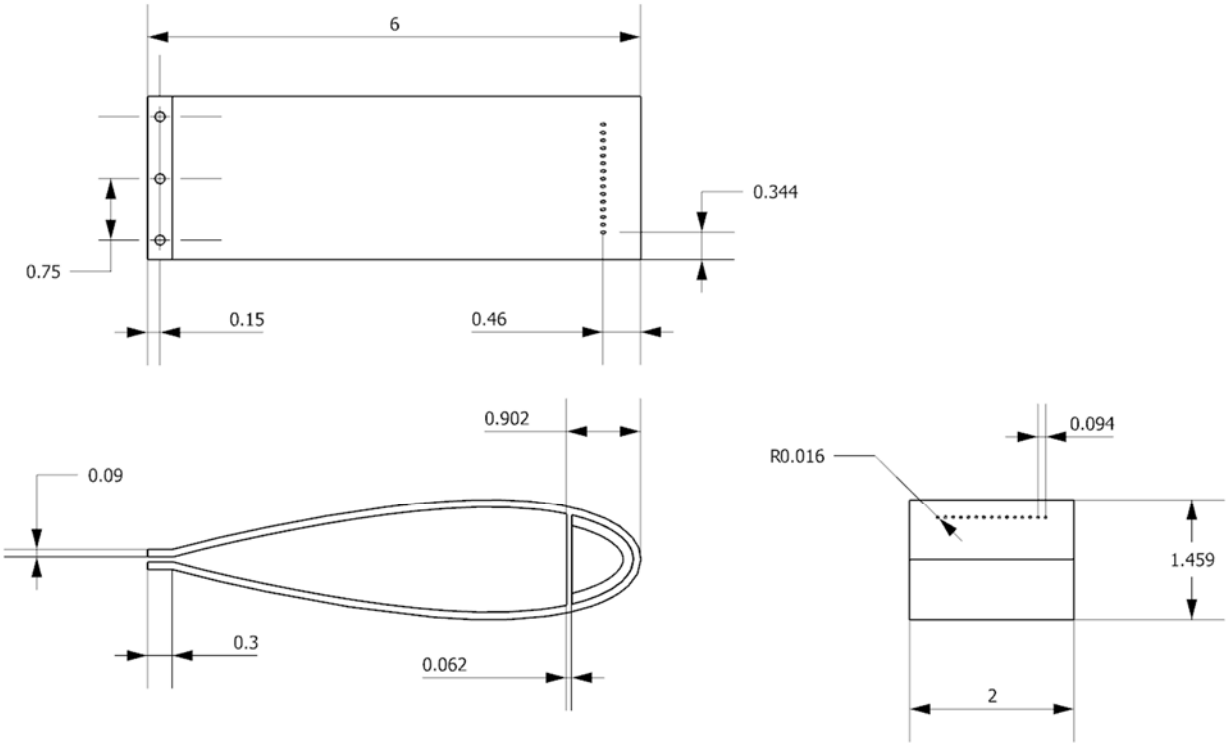

Figure 11.5: Schematic of the test article (inches)

12 Appendix C: Experiment Thermocouples Raw Data

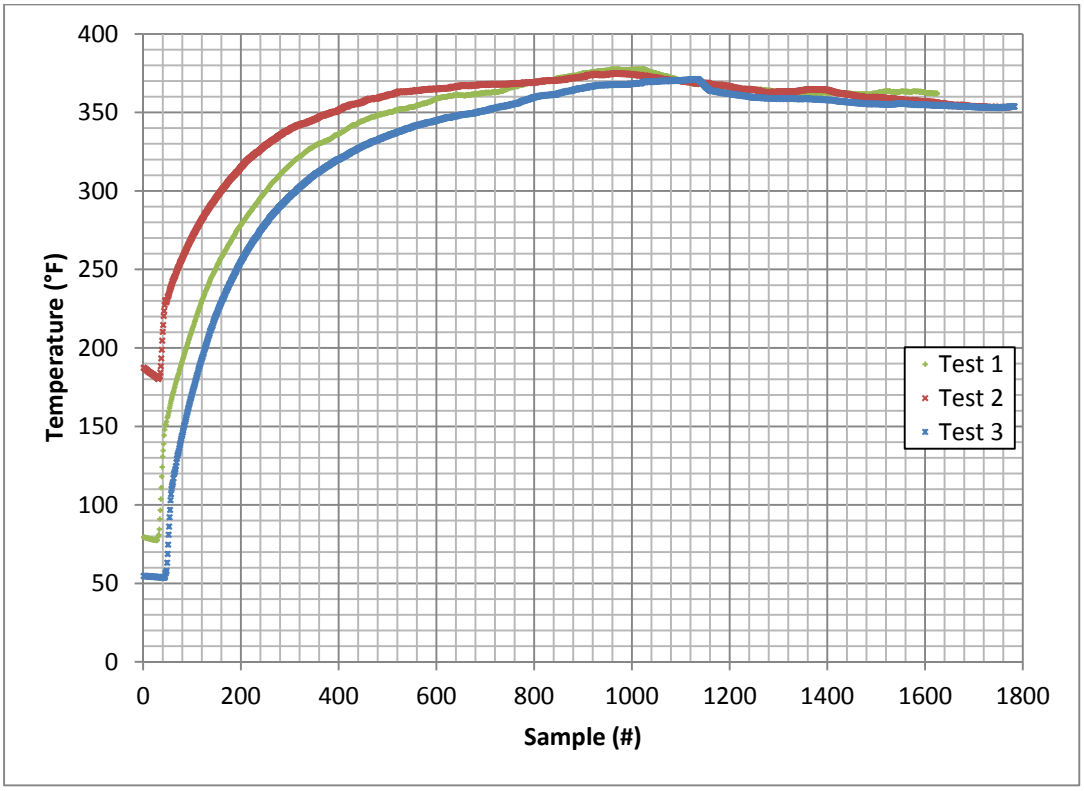

Figure 12.1: Raw Data of Thermocouple #1

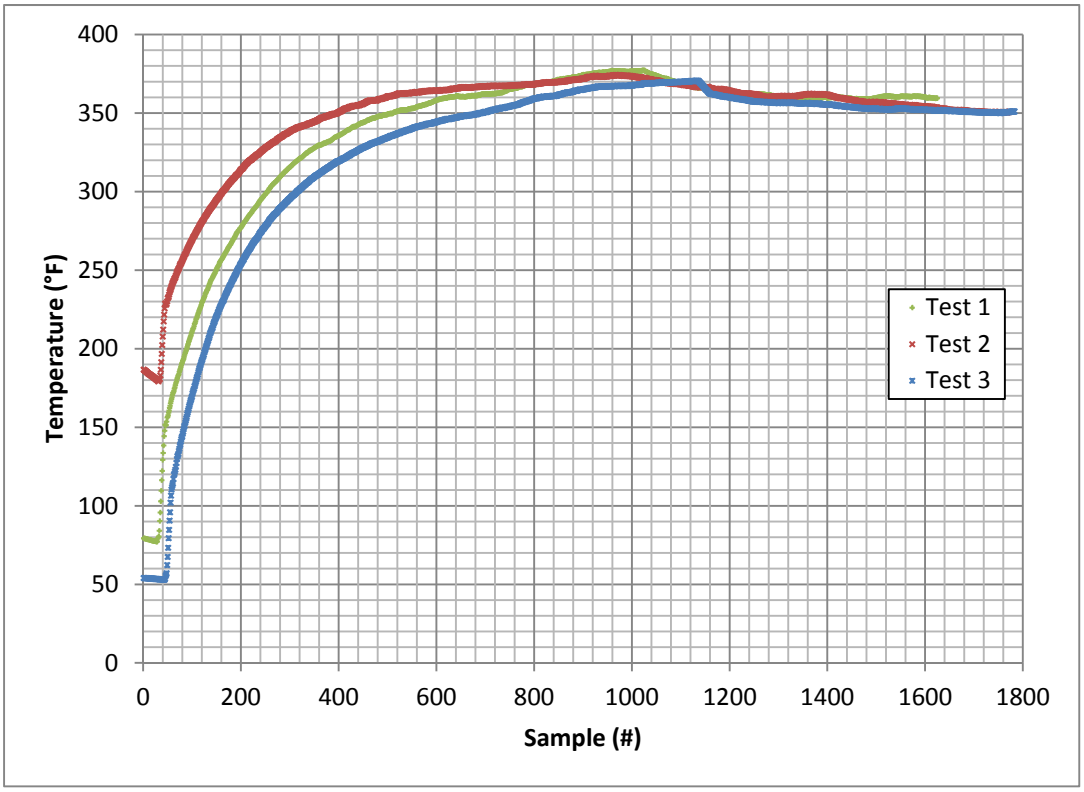

Figure 12.2: Raw Data of Thermocouple #2

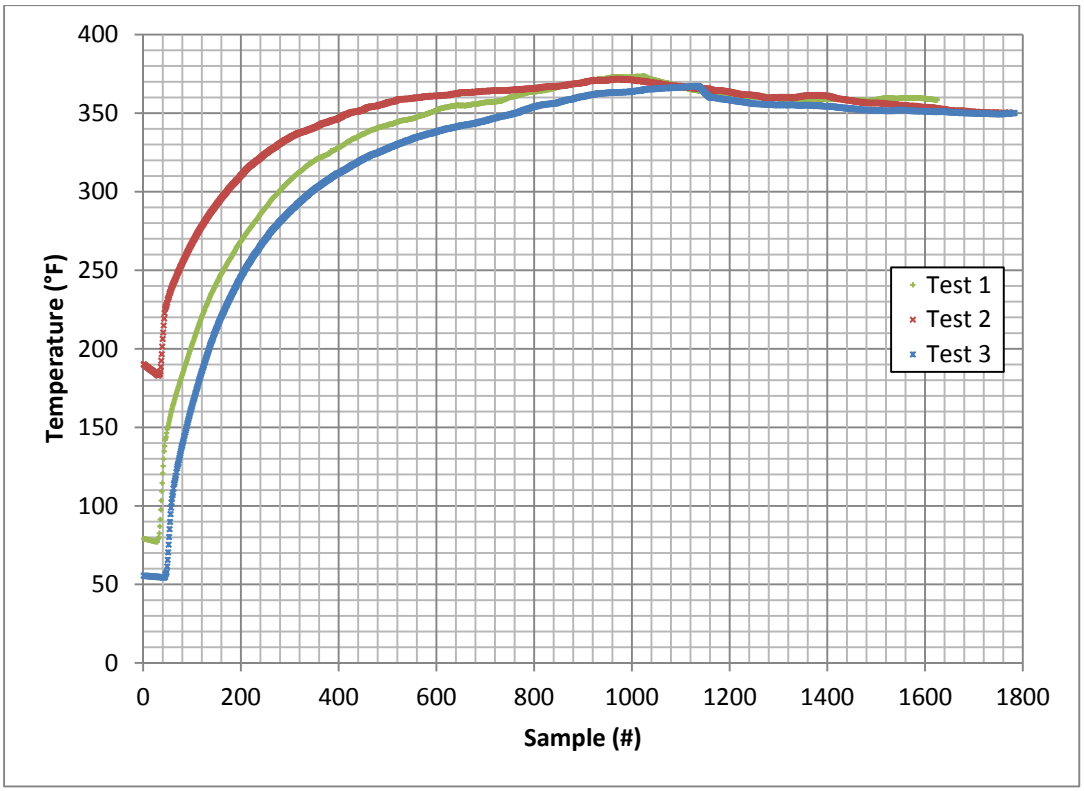

Figure 12.3: Raw Data of Thermocouple #3

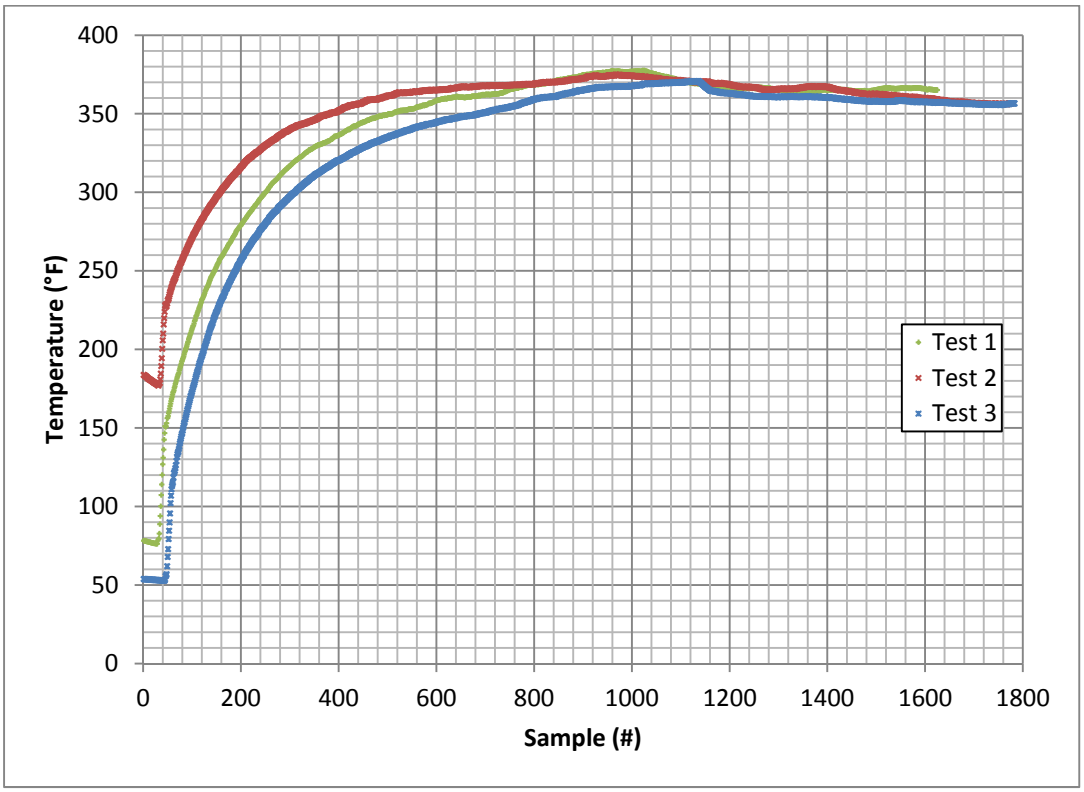

Figure 12.4: Raw Data of Thermocouple #4

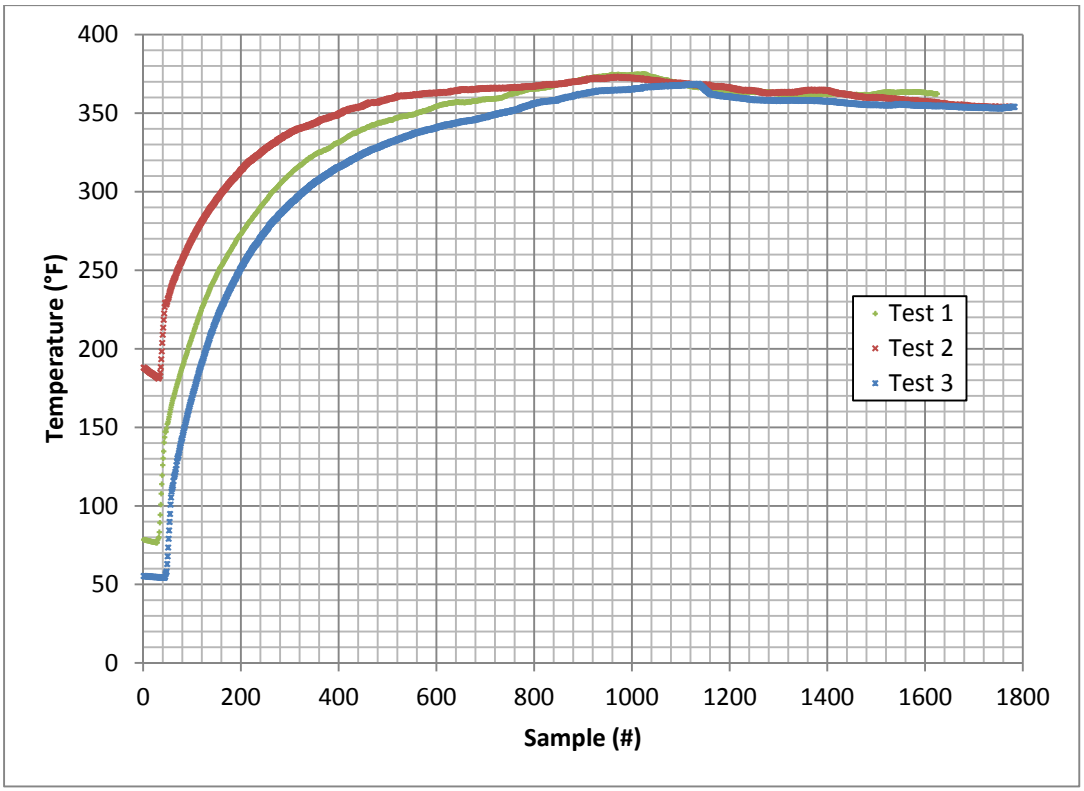

Figure 12.5: Raw Data of Thermocouple #5

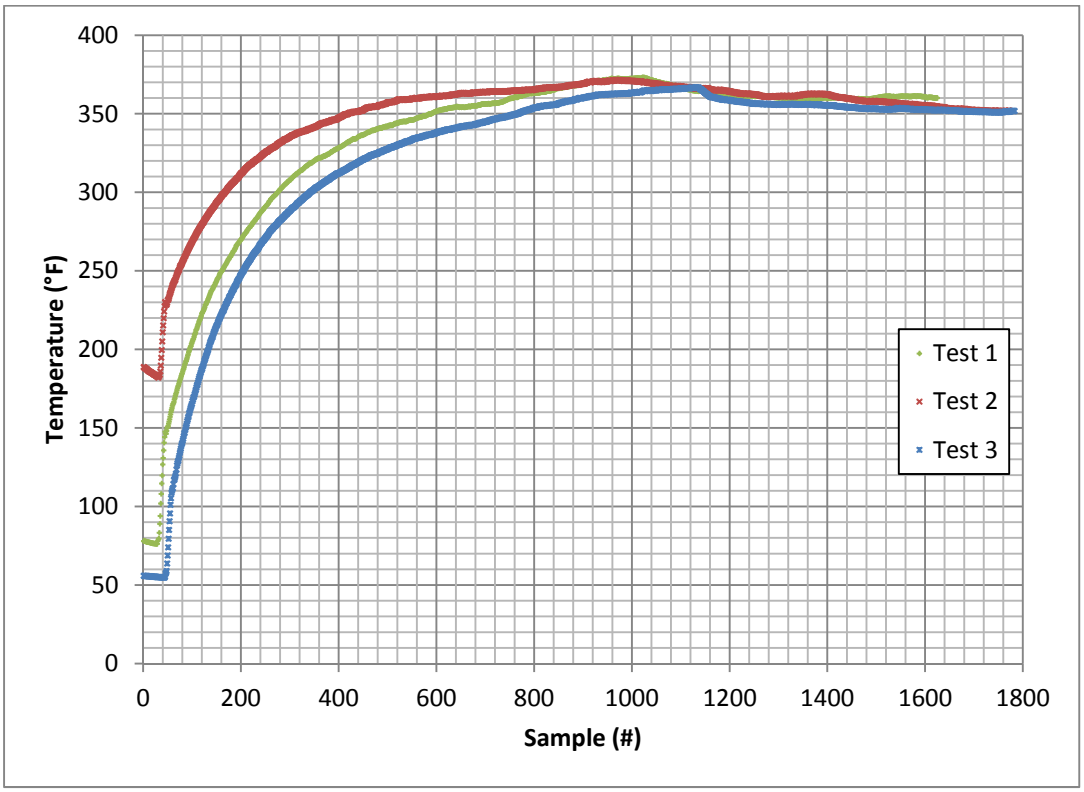

Figure 12.6: Raw Data of Thermocouple #6

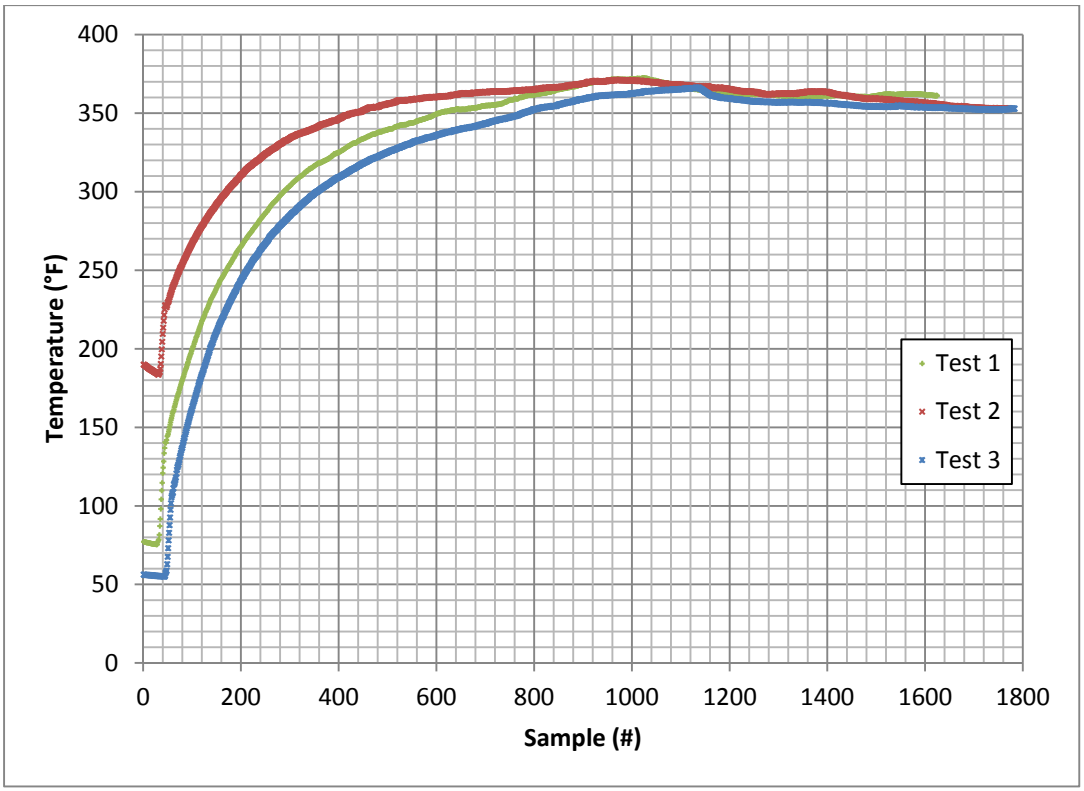

Figure 12.7: Raw Data of Thermocouple #7

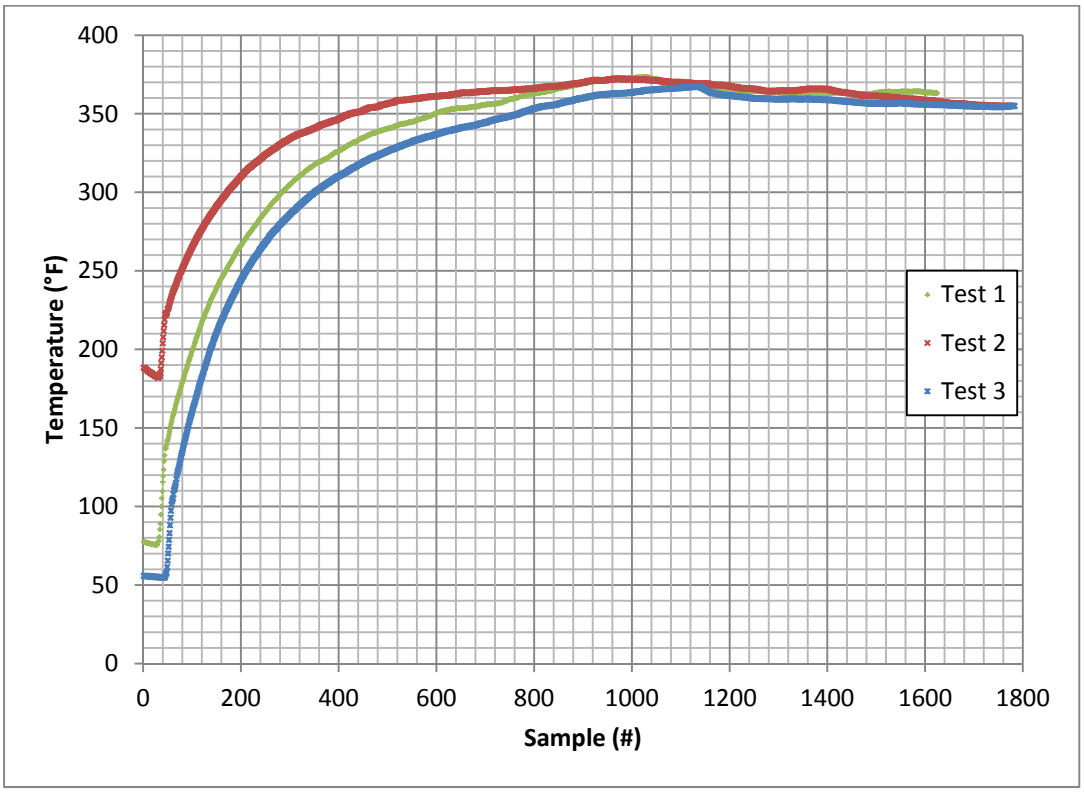

Figure 12.8: Raw Data of Thermocouple #8

13 Appendix D: Adiabatic Simulation of the Experiment

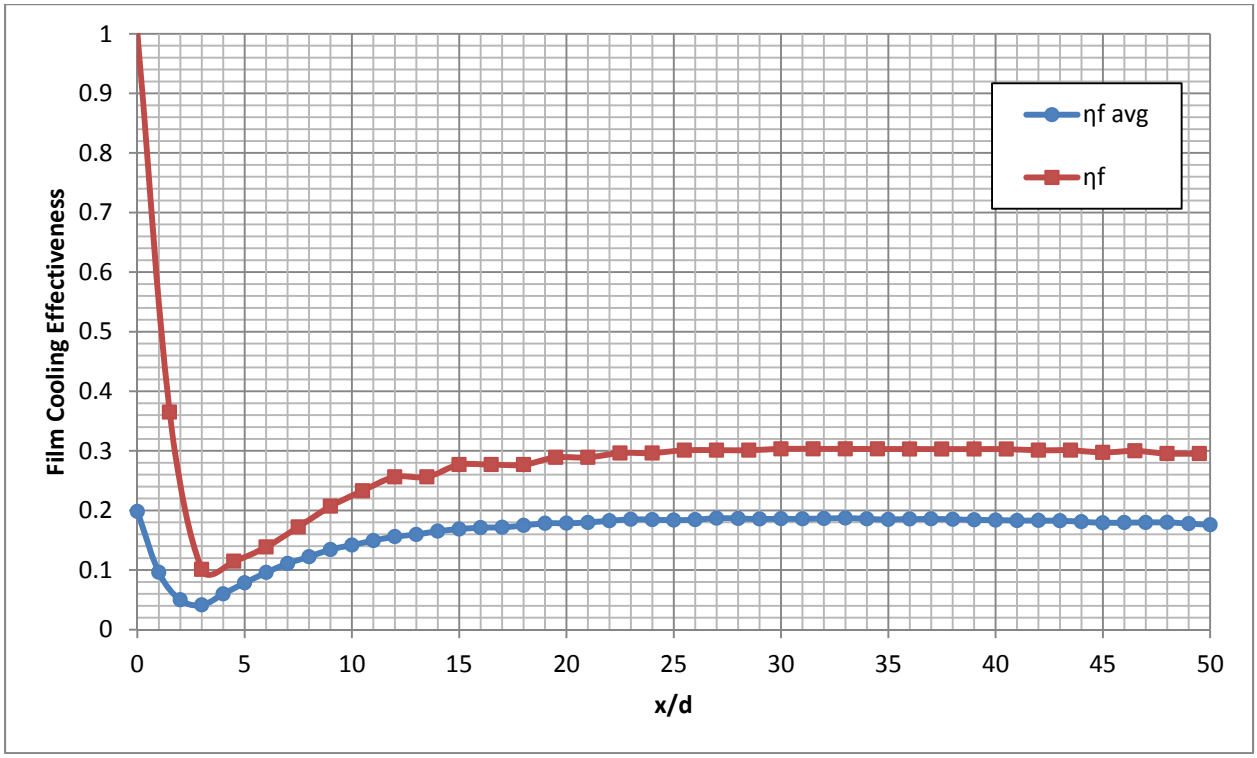

Figure 13.1: Laterally averaged and Centerline adiabatic film cooling effectiveness

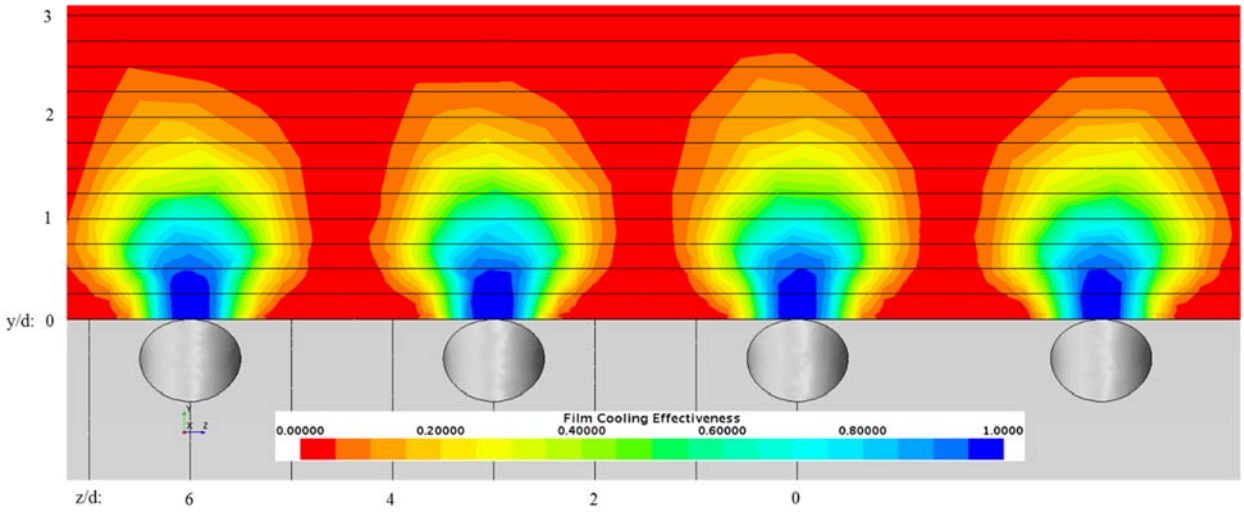

Figure 13.2: Spatial distribution of adiabatic film cooling effectiveness at x/d: 0

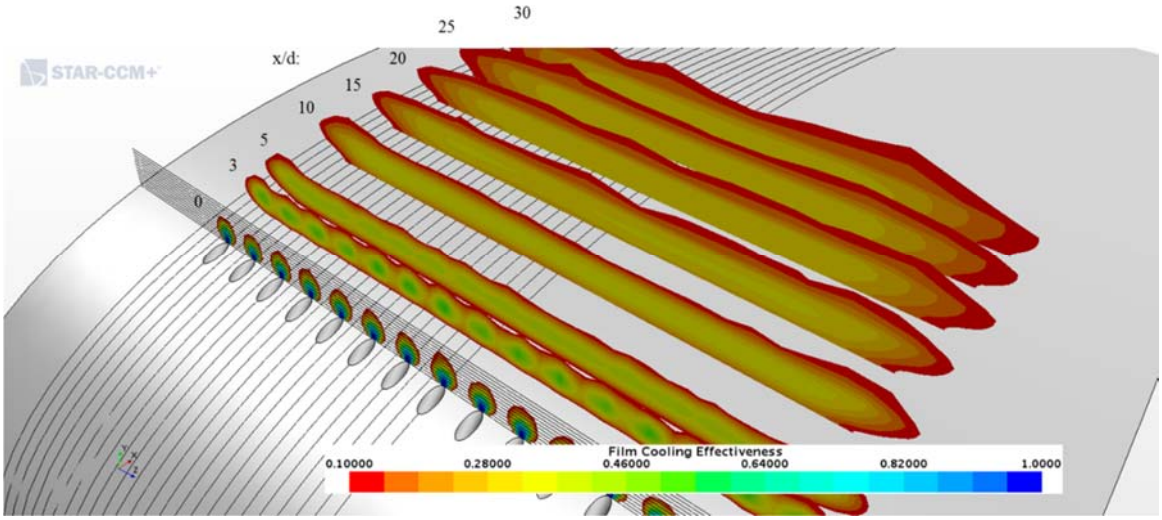

Figure 13.3: Streamwise spatial distribution of adiabatic film cooling effectiveness

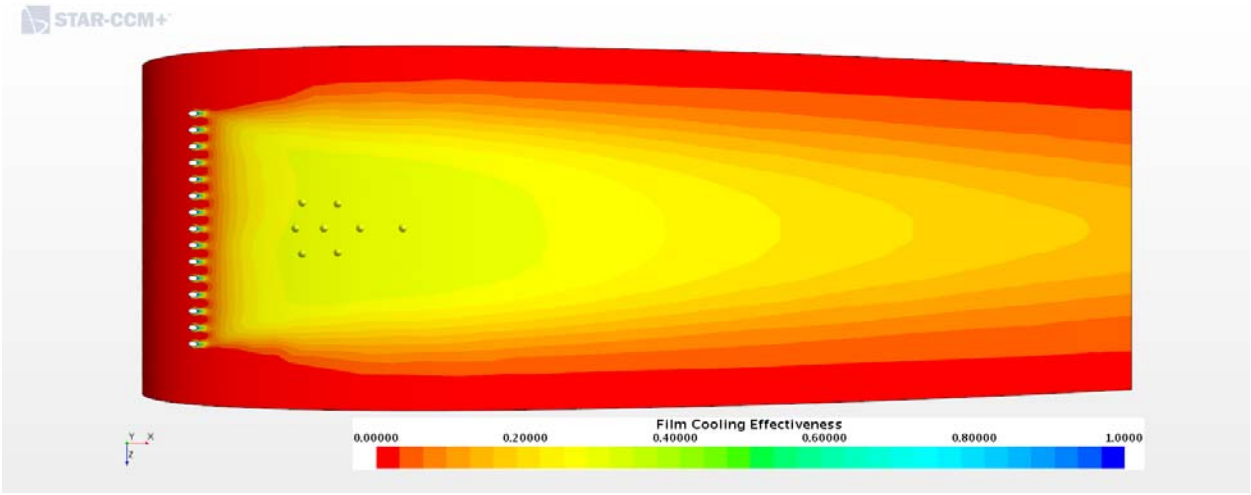

Figure 13.4: Adiabatic Film Cooling Effectiveness on the Suction Surface

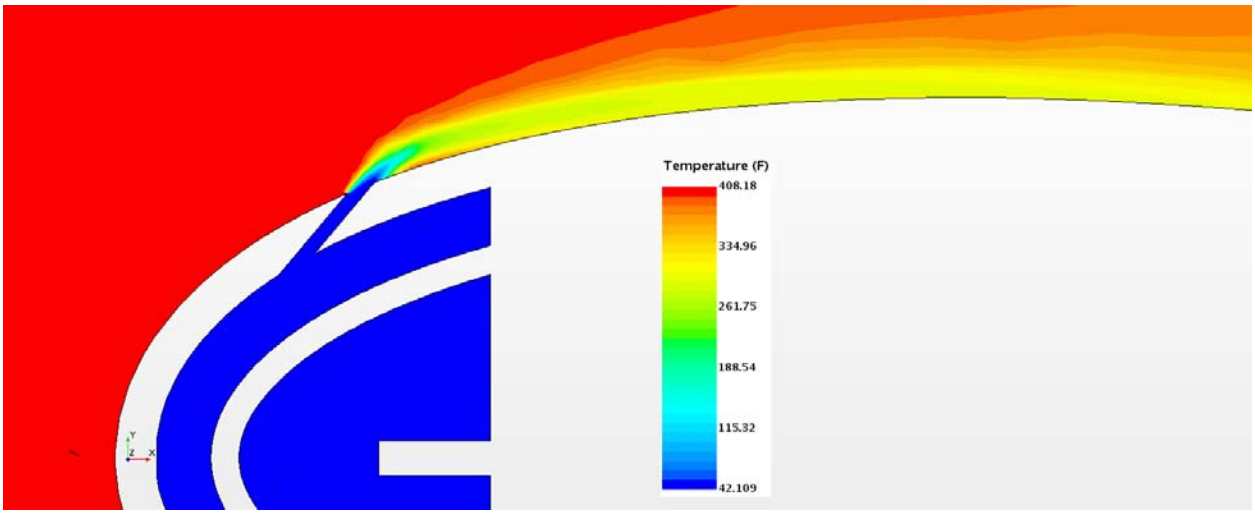

Figure 13.5: Adiabatic Temperature profile for center plane

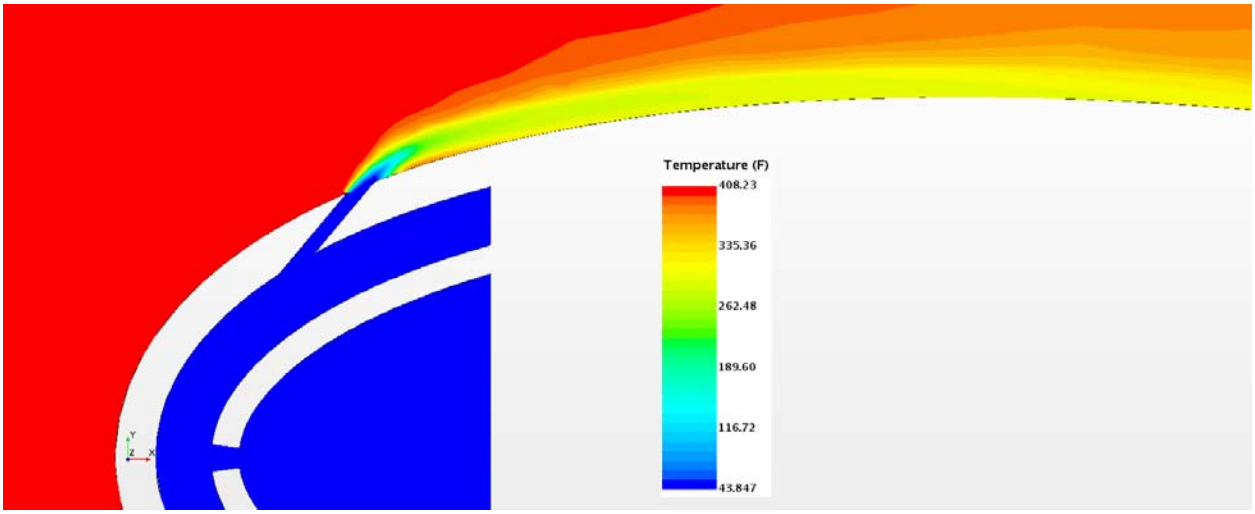

Figure 13.6: Adiabatic Temperature profile for off-center plane

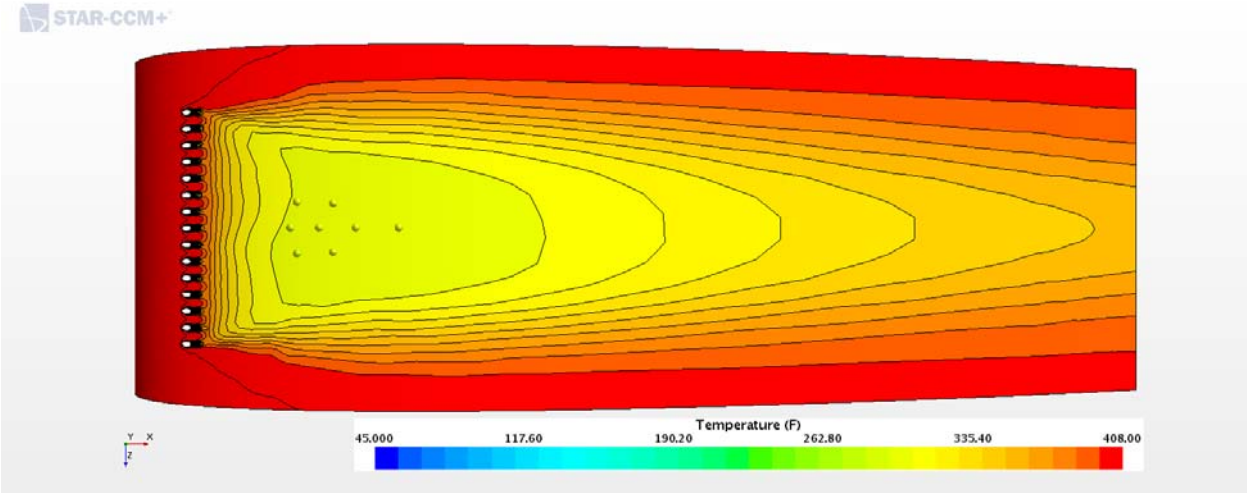

Figure 13.7: Adiabatic Temperature Distribution for Suction Surface

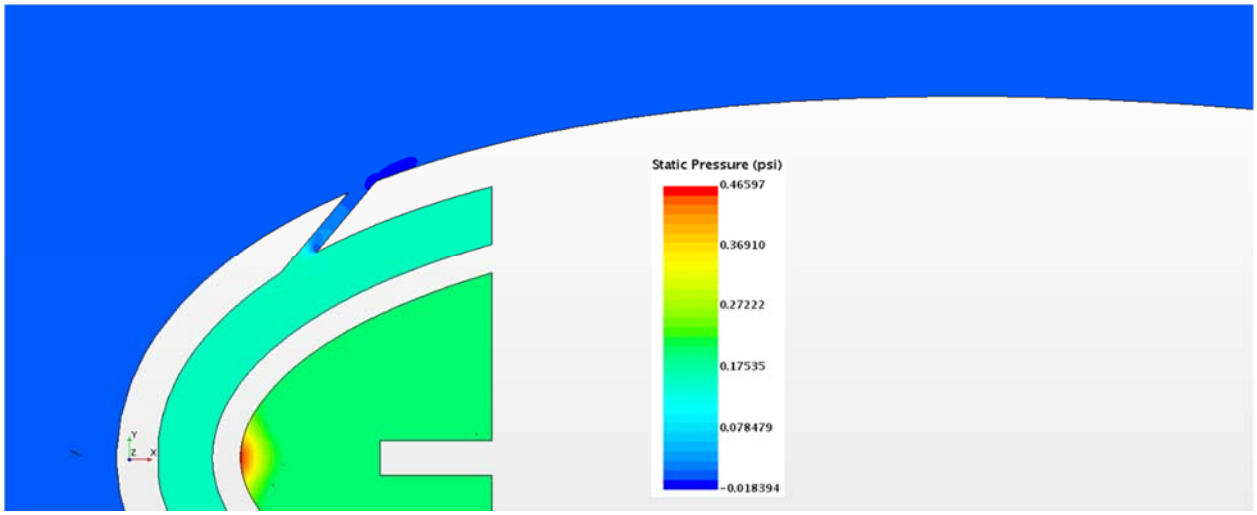

Figure 13.8: Static Pressure profile for center plane of Adiabatic Model

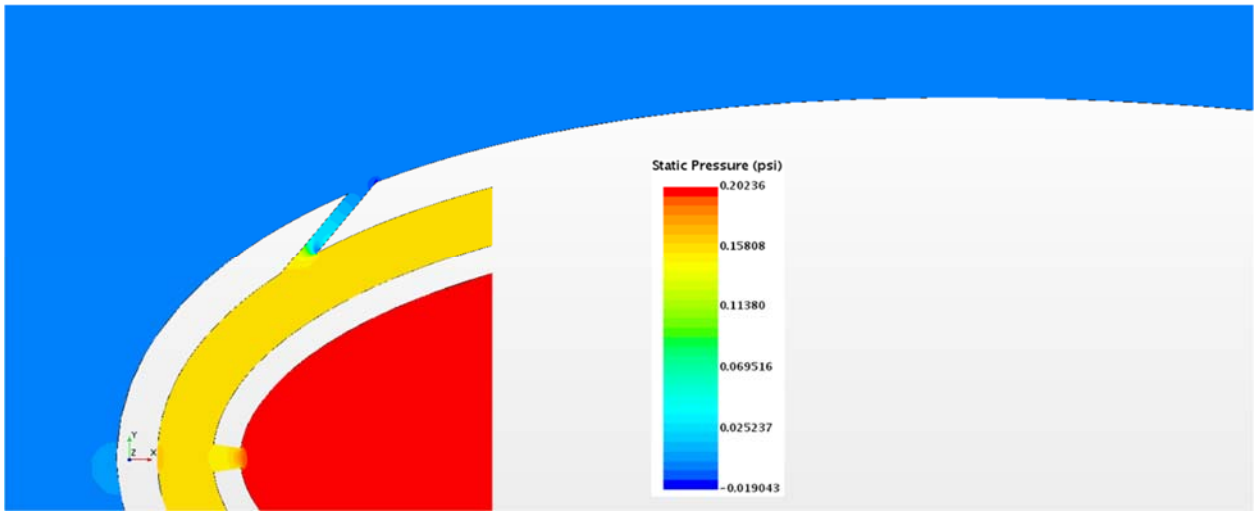

Figure 13.9: Static Pressure profile for off-center plane of Adiabatic Model

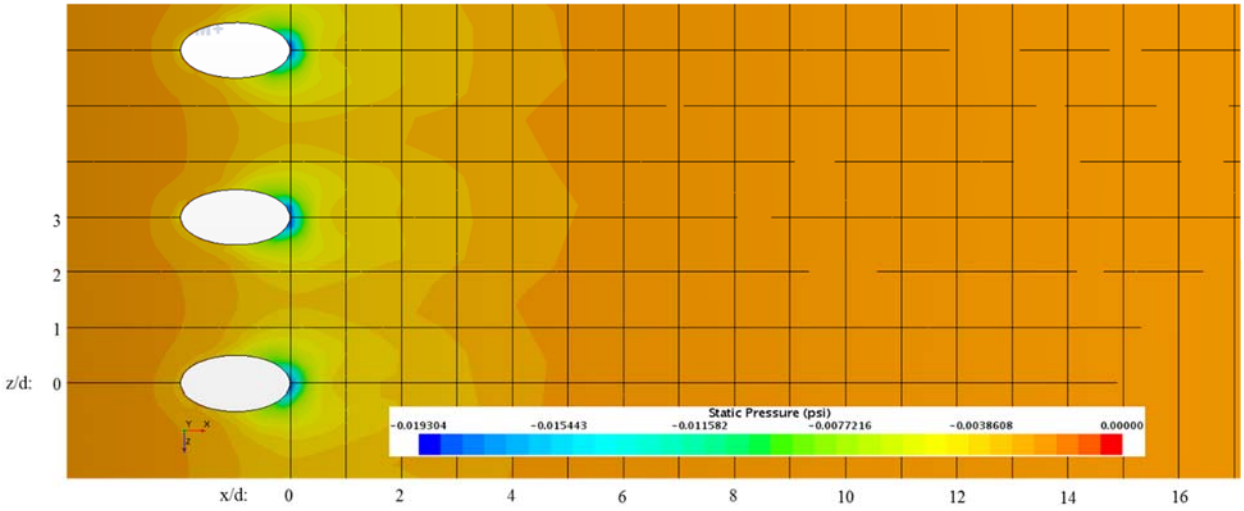

Figure 13.10: 3D Pressure distribution for Adiabatic Model

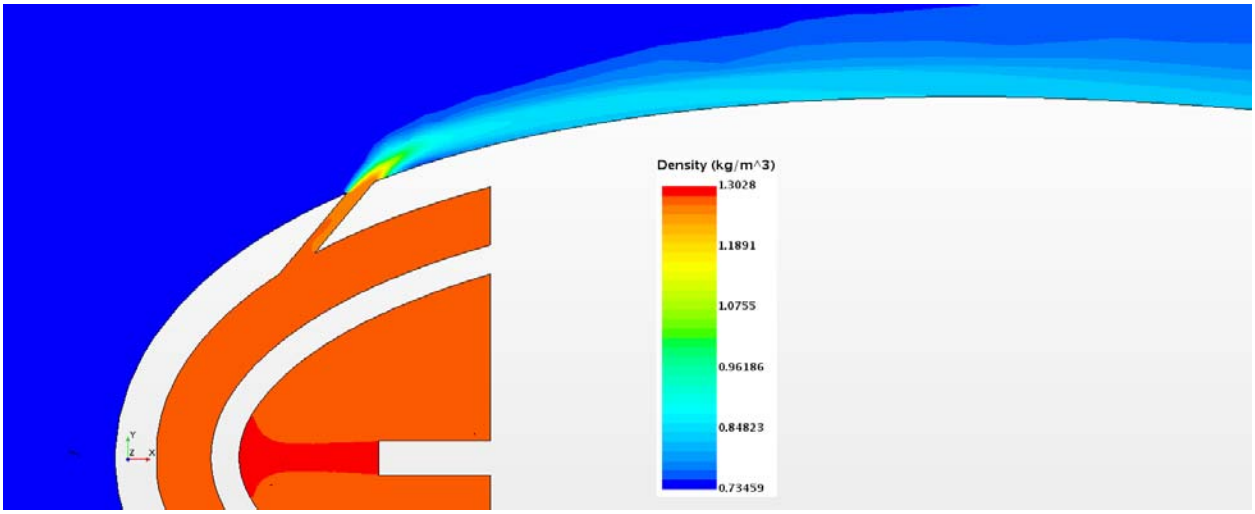

Figure 13.11: Density profile for center plane of Adiabatic Model

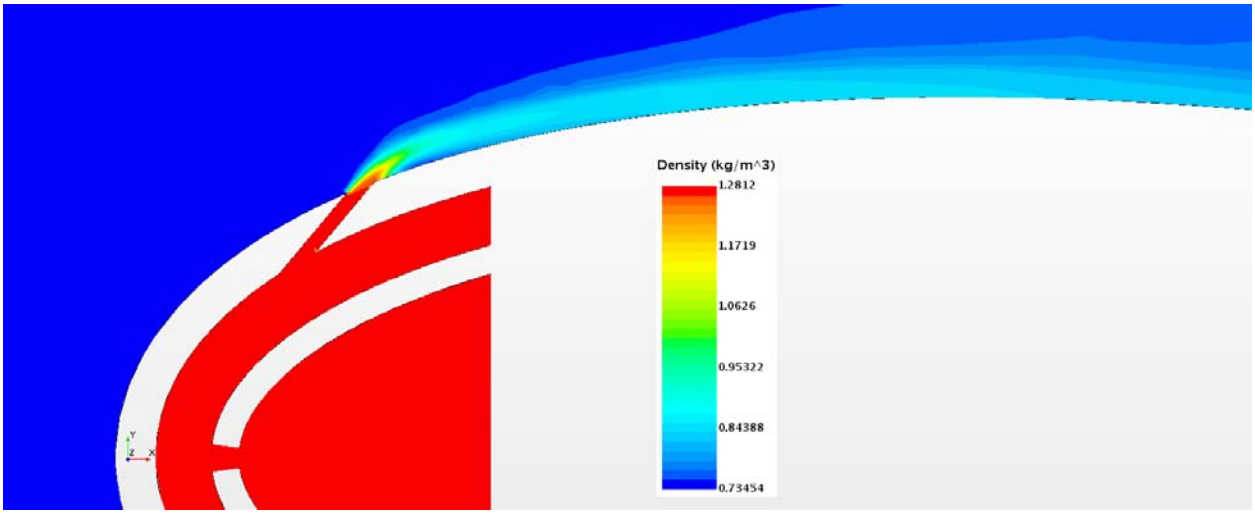

Figure 13.12: Density profile for off-center plane of Adiabatic Model

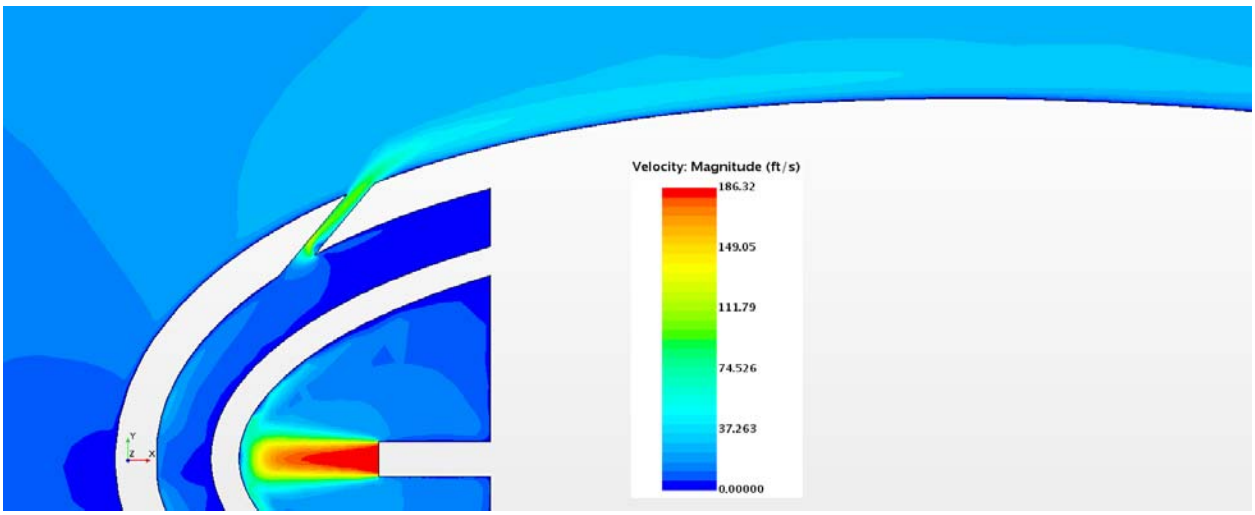

Figure 13.13: Velocity profile for center plane of Adiabatic Model

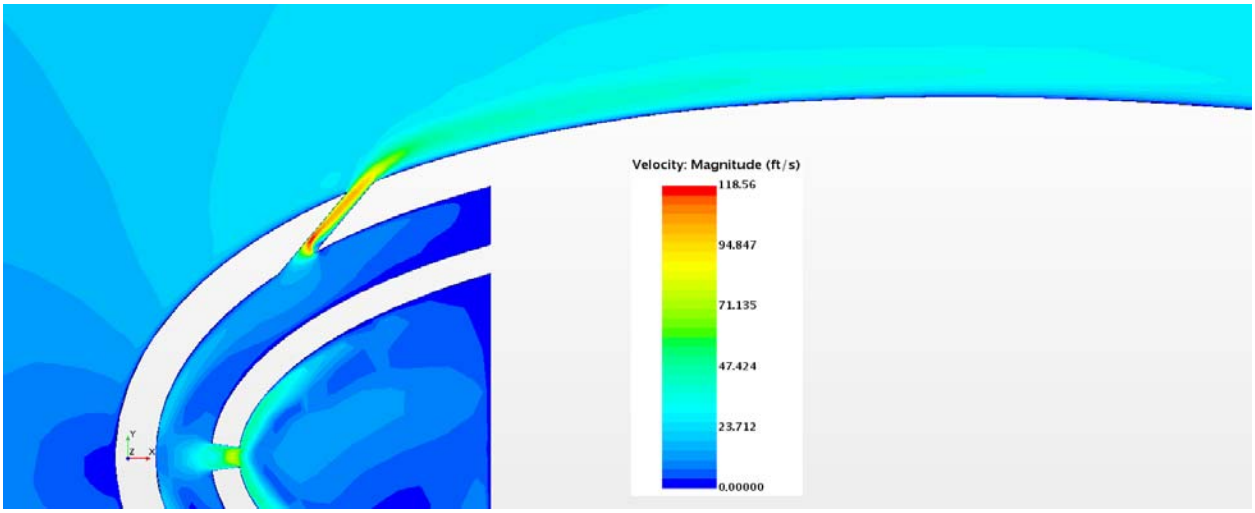

Figure 13.14: Velocity profile for off-center plane of Adiabatic Model

14 Appendix E: Conjugate Heat Transfer Simulation of the Experiment

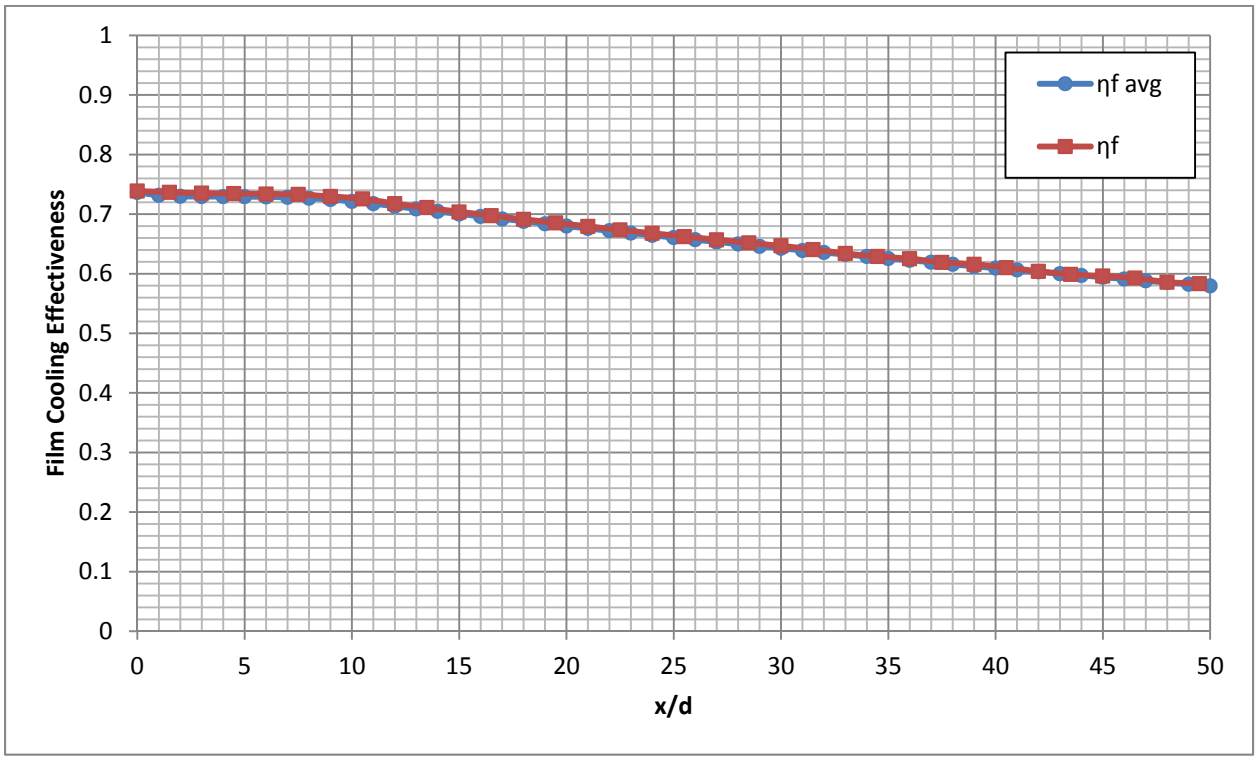

Figure 14.1: Laterally averaged and Centerline film cooling effectiveness

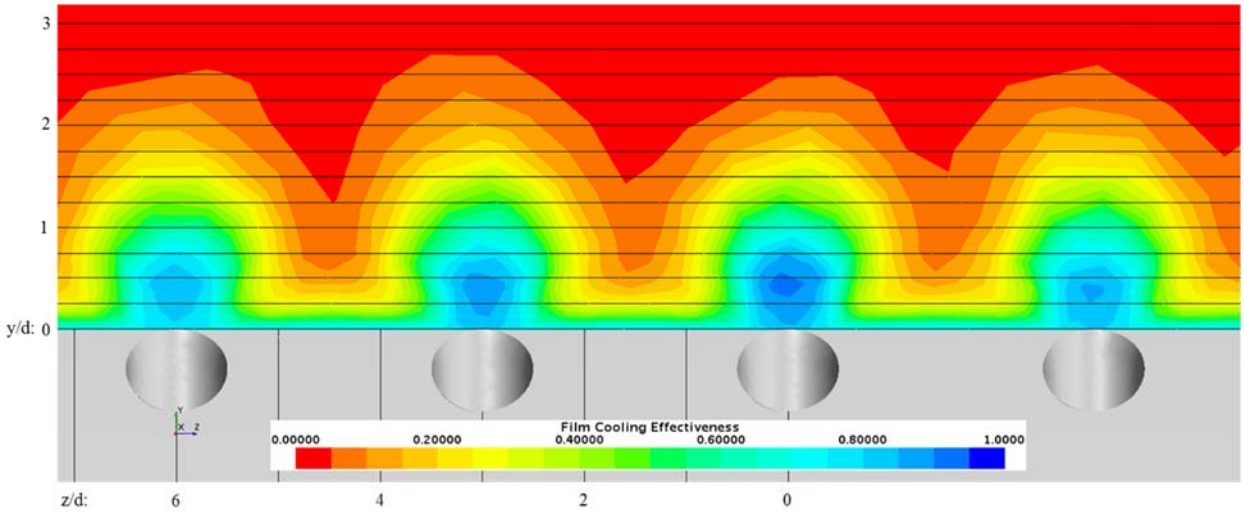

Figure 14.2: Spatial distribution of CHT film cooling effectiveness at x/d: 0

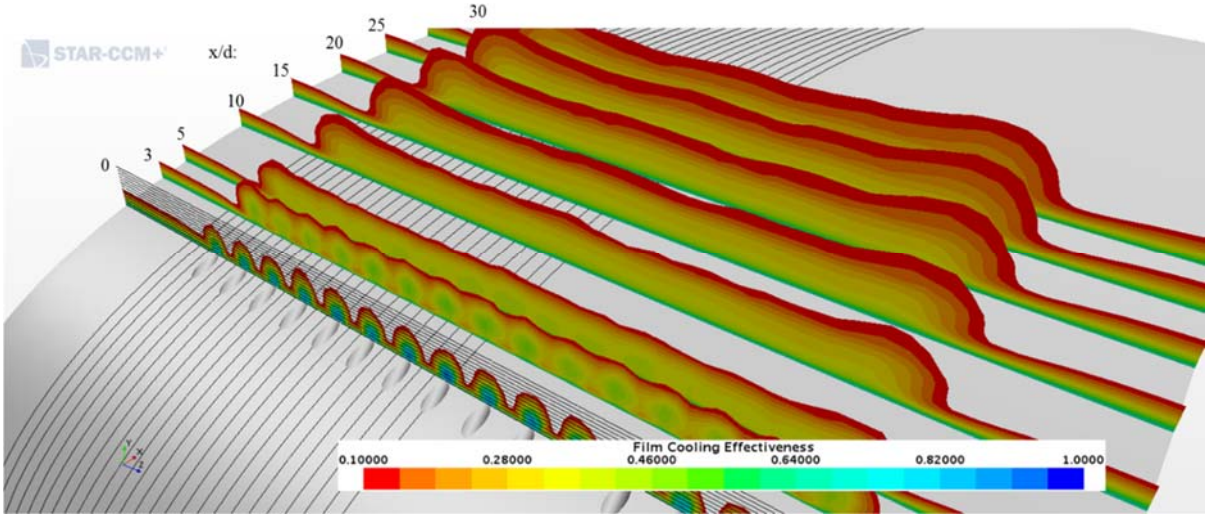

Figure 14.3: Streamwise spatial distribution of CHT film cooling effectiveness

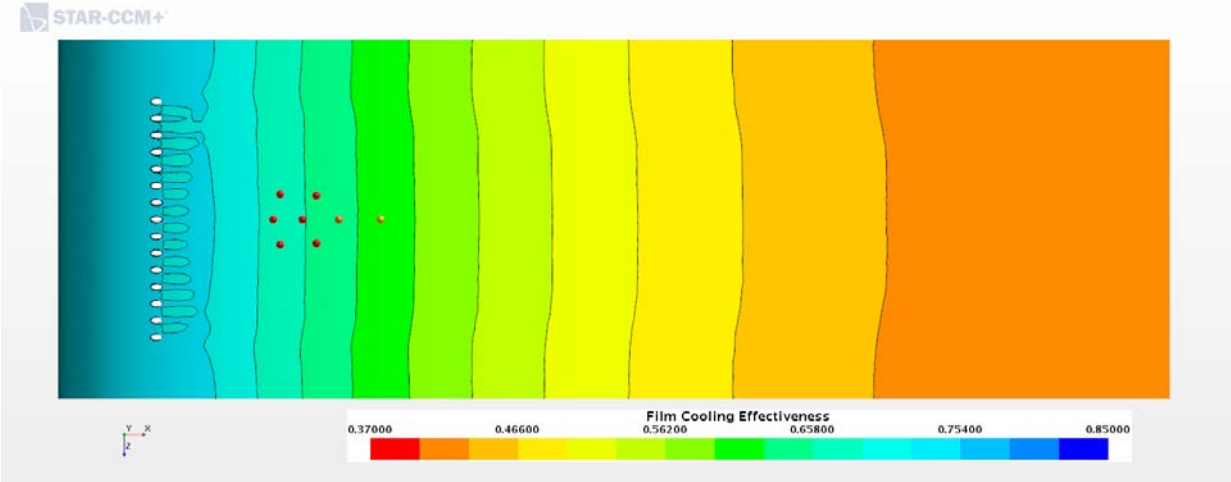

Figure 14.4: CHT Film Cooling Effectiveness on the Suction Surface

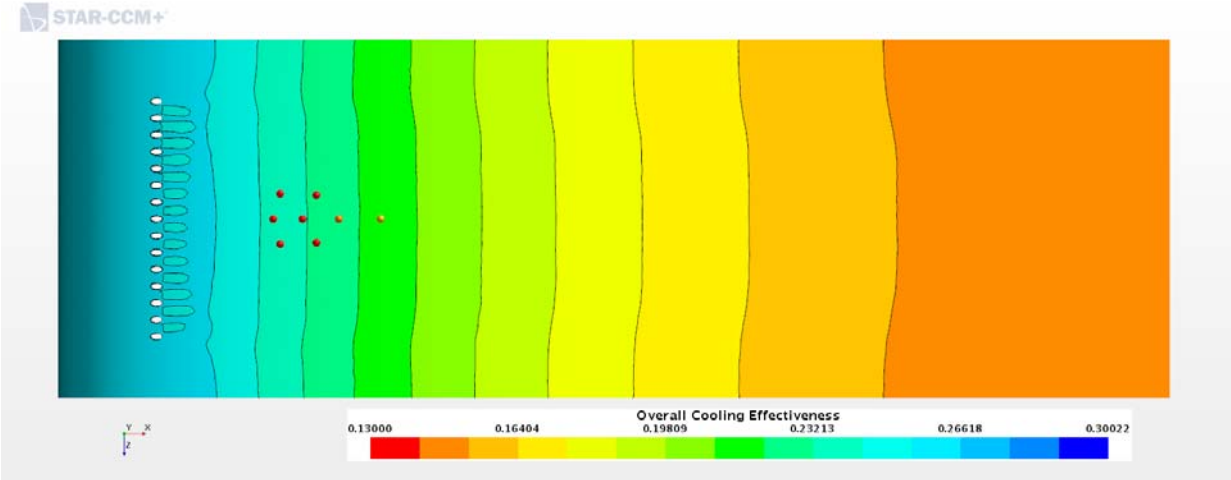

Figure 14.5: CHT Overall Cooling Effectiveness on the Suction Surface

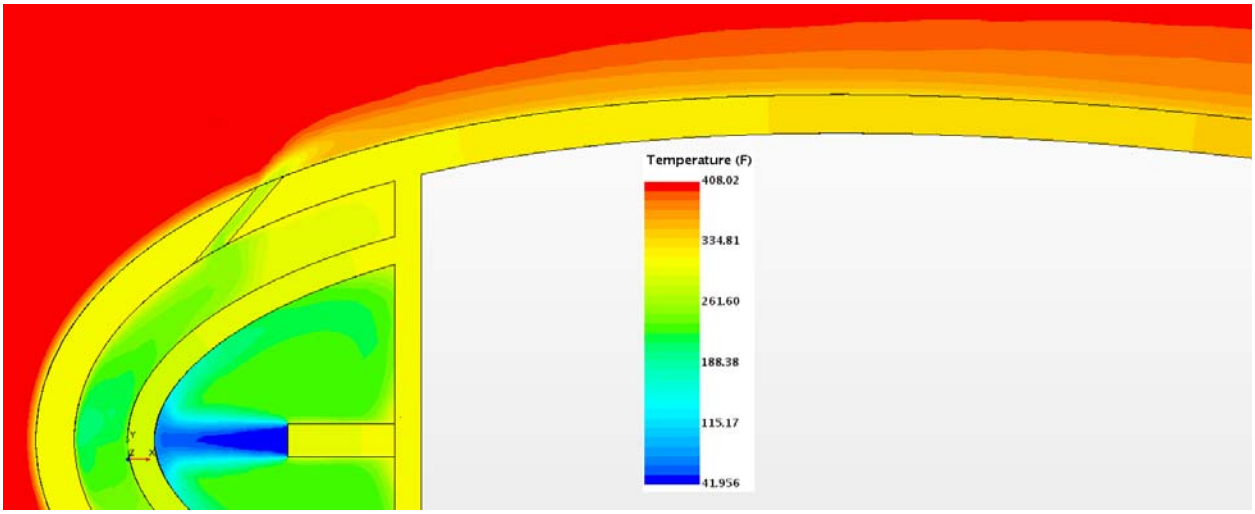

Figure 14.6: CHT Temperature profile for center plane

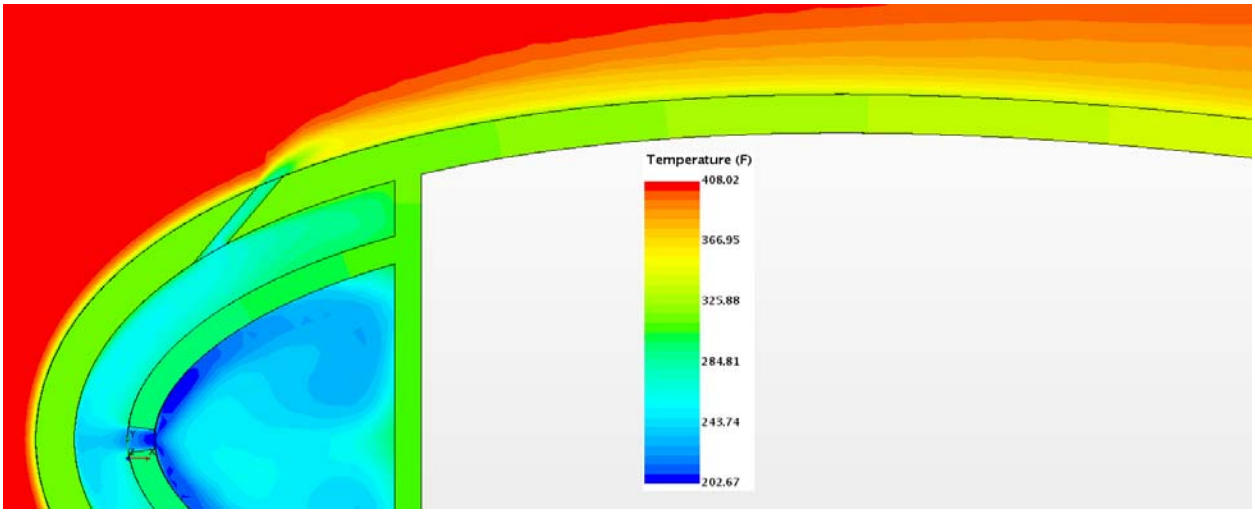

Figure 14.7: CHT Temperature profile for off-center plane

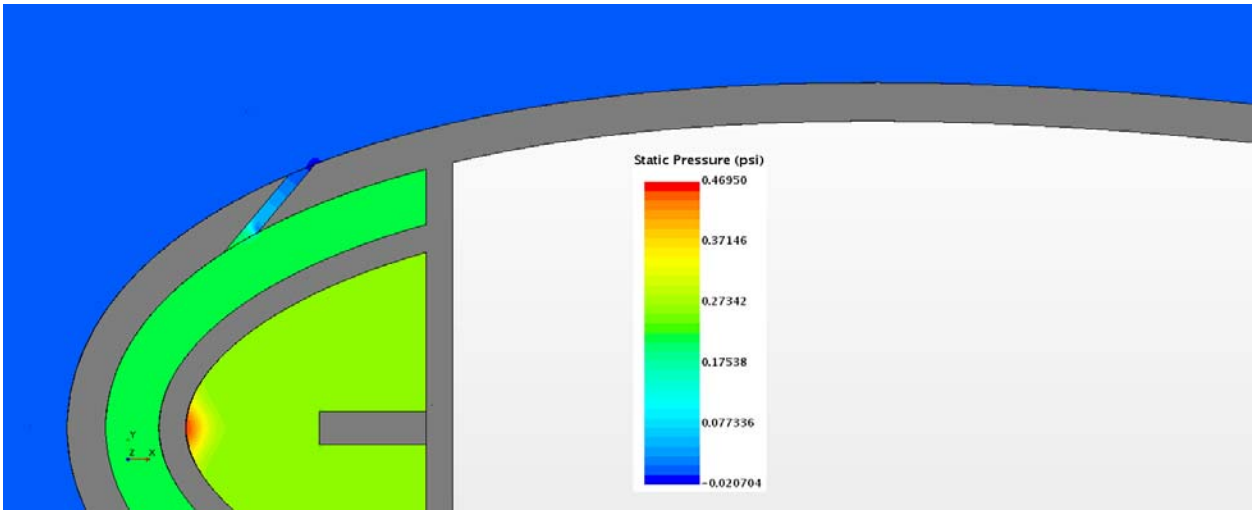

Figure 14.8: Static Pressure profile for center plane of CHT Model

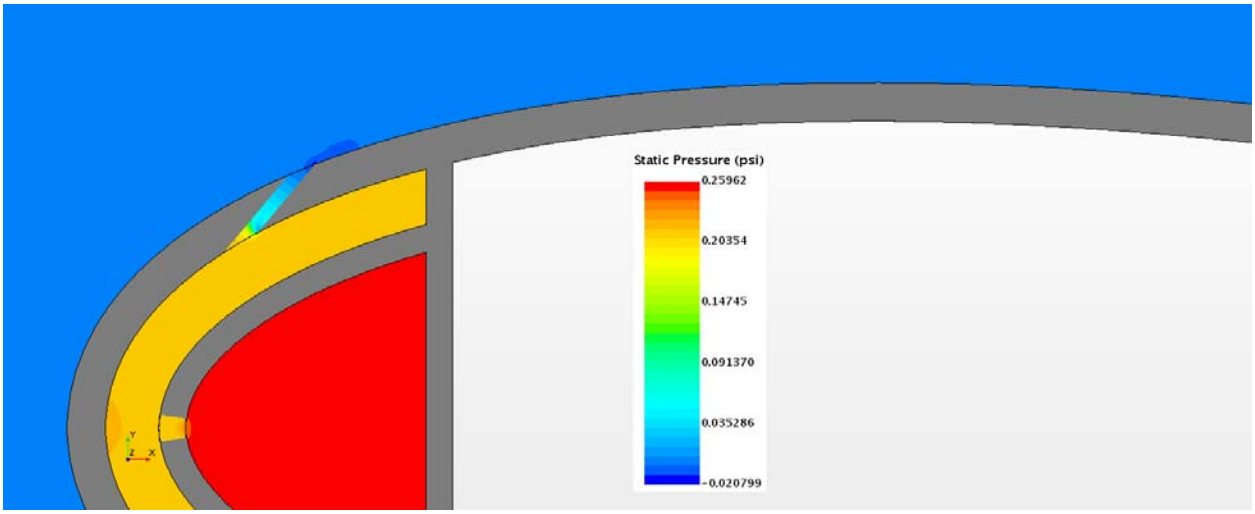

Figure 14.9: Static Pressure profile for off-center plane of CHT Model

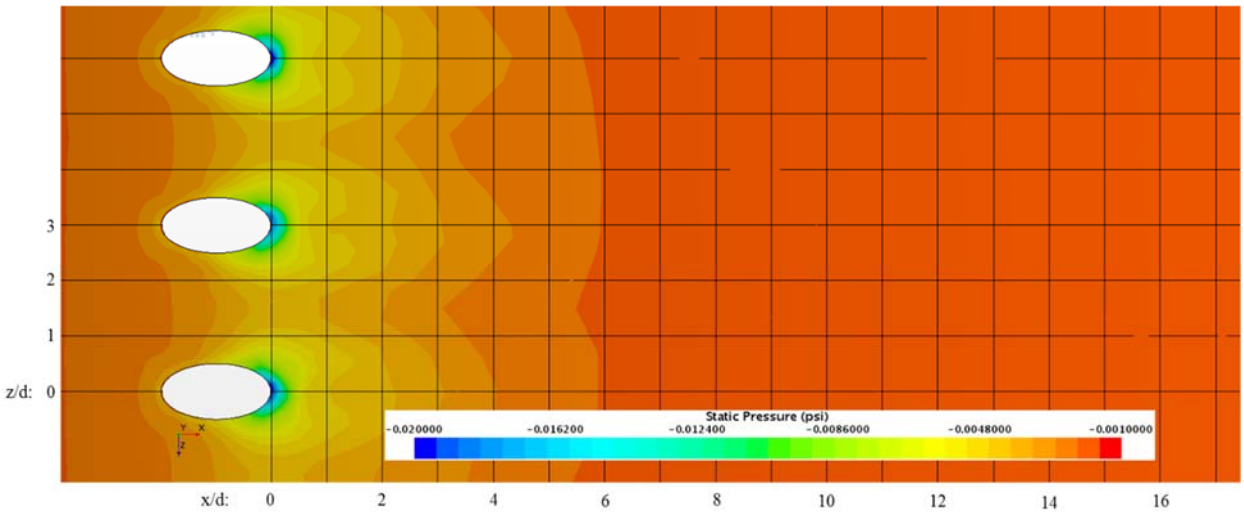

Figure 14.10: 3D Pressure distribution for CHT Model

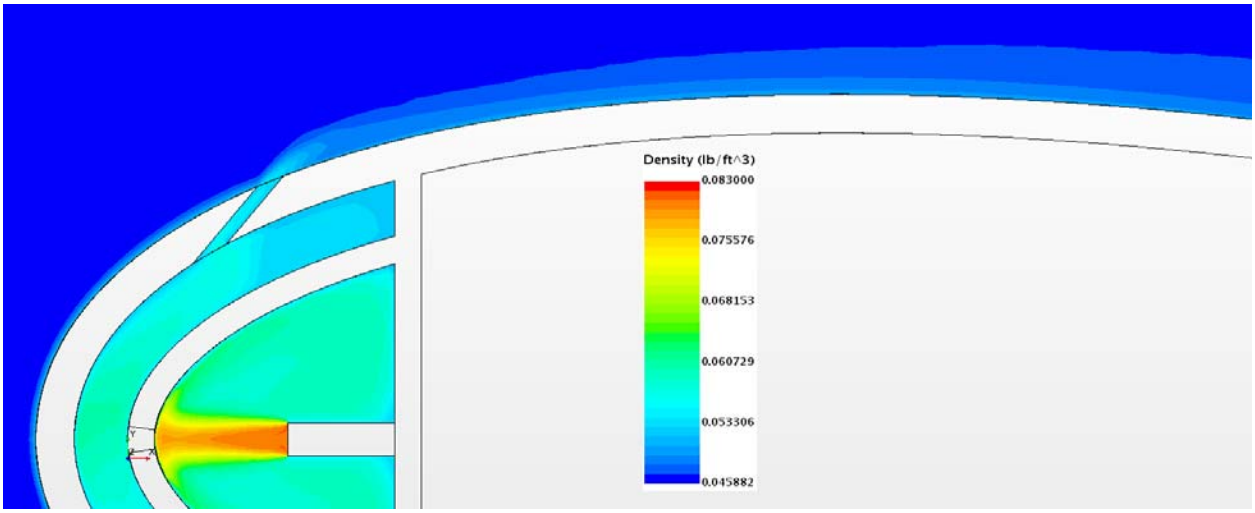

Figure 14.11: CHT Density profile for center plane

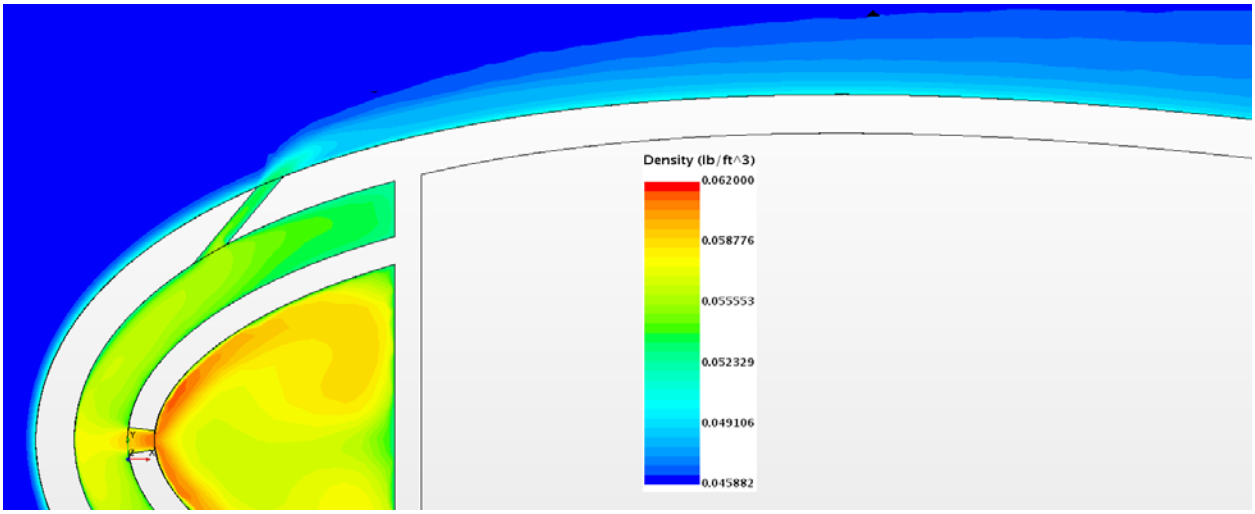

Figure 14.12: CHT Density profile for off-center plane

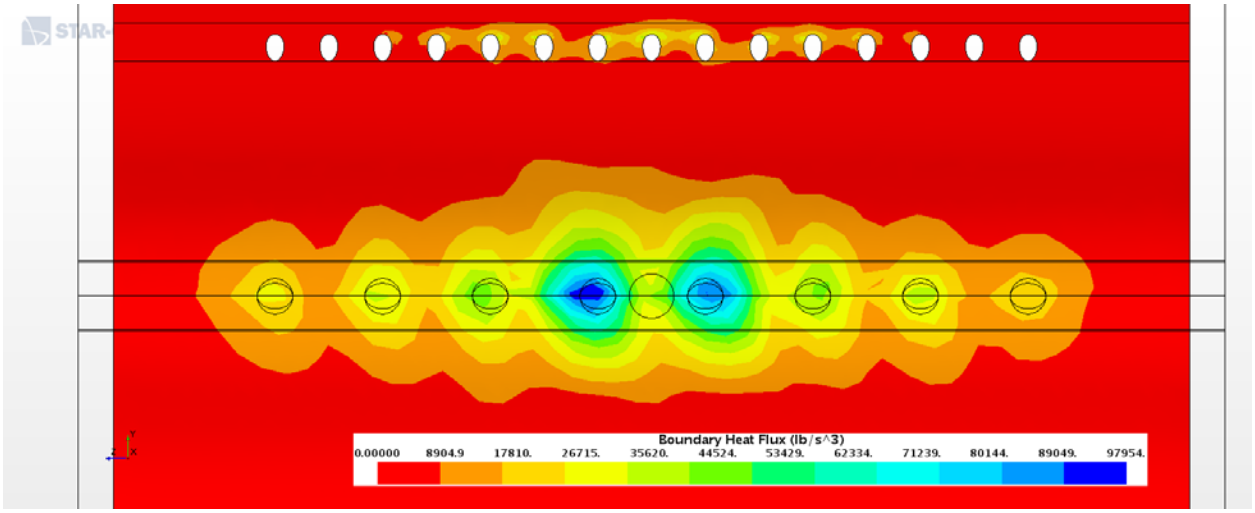

Figure 14.13: Heat Flux of Impingement on Leading Edge – Internal Cooling

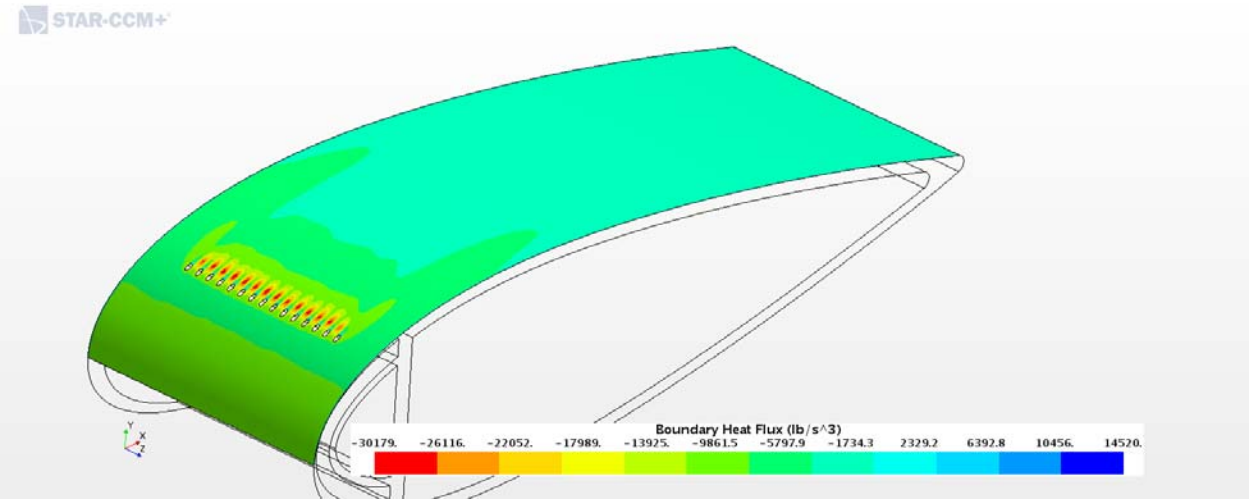

Figure 14.14: Heat Flux of Impingement on Suction Surface – External Cooling

15 Appendix F: Tabulated Case Study Data

Table 15.1: Percent Change based on Mb: 0.98, Tu: 20%, DR: 1.65

	x/d	0	10	20	30	40	50
#	Case	$\%\Delta\eta_{f\,avg}$	$\%\Delta\eta_{f\,avg}$	$\%\Delta\eta_{f\,avg}$	$\%\Delta\eta_{f\,avg}$	$\%\Delta\eta_{f\,avg}$	$\%\Delta\eta_{f\,avg}$
1	Mb: 0.98, Tu: 20%, DR: 1.65	0.00	0.00	0.00	0.00	0.00	0.00
2	Mb: 0.53, Tu: 5%, DR: 1.65	-10.51	-21.62	-12.60	-4.22	1.33	6.06
3	Mb: 0.77, Tu: 5%, DR: 1.65	-0.78	3.98	22.86	37.53	47.23	55.46
4	Mb: 0.98, Tu: 5%, DR: 1.65	0.84	19.37	55.50	80.53	96.80	110.36
5	Mb: 1.51, Tu: 5%, DR: 1.65	-3.67	16.82	78.59	123.05	152.44	176.69
6	Mb: 2.13, Tu: 5%, DR: 1.65	-11.85	0.20	79.67	144.64	191.78	232.90
7	Mb: 2.96, Tu: 5%, DR: 1.65	-20.26	-7.66	71.11	135.32	183.72	228.68
8	Mb: 4.08, Tu: 5%, DR: 1.65	-27.00	-4.94	79.71	155.66	217.58	279.56
9	Mb: 5.04, Tu: 5%, DR: 1.65	-30.90	-6.03	84.26	169.43	240.91	315.18
10	Mb: 5.95, Tu: 5%, DR: 1.65	-33.48	-11.70	78.63	167.28	242.07	320.60
11	Mb: 0.53, Tu: 20%, DR: 1.65	-17.42	-44.88	-49.31	-51.34	-52.52	-53.35
12	Mb: 0.77, Tu: 20%, DR: 1.65	-3.90	-21.16	-24.98	-26.64	-27.58	-28.24
13	Mb: 1.51, Tu: 20%, DR: 1.65	-2.82	16.99	28.23	32.93	35.46	37.26
14	Mb: 2.13, Tu: 20%, DR: 1.65	-10.07	21.04	51.78	66.67	74.94	80.99
15	Mb: 2.96, Tu: 20%, DR: 1.65	-18.35	15.94	65.55	95.99	114.11	127.90
16	Mb: 4.08, Tu: 20%, DR: 1.65	-25.71	13.56	84.65	136.98	169.87	195.08
17	Mb: 5.04, Tu: 20%, DR: 1.65	-30.10	9.40	95.05	166.10	215.18	254.83
18	Mb: 5.95, Tu: 20%, DR: 1.65	-33.01	0.43	92.75	176.13	238.58	293.78
19	Mb: 0.98, Tu: 10%, DR: 1.65	0.63	16.24	43.03	60.74	70.70	76.61
20	Mb: 0.98, Tu: 15%, DR: 1.65	0.36	10.04	23.69	29.86	31.18	30.44
21	Mb: 0.98, Tu: 25%, DR: 1.65	-0.30	-13.13	-19.52	-19.21	-17.47	-15.62
22	Mb: 1.26, Tu: 5%, DR: 1.99	4.10	29.99	73.35	104.24	125.03	143.18
23	Mb: 1.26, Tu: 10%, DR: 1.99	4.11	27.65	61.12	84.17	98.51	109.03
24	Mb: 1.26, Tu: 15%, DR: 1.99	4.03	22.59	43.15	54.29	57.95	57.54
25	Mb: 1.26, Tu: 20%, DR: 1.99	3.95	14.15	19.12	20.08	19.06	17.04
26	Mb: 1.26, Tu: 25%, DR: 1.99	4.04	2.02	-3.35	-4.40	-4.43	-4.41
27	Mb: 0.97, Tu: 20%, DR: 1.49	-2.74	-8.57	-10.32	-10.10	-9.21	-7.99
28	Mb: 1.10, Tu: 20%, DR: 1.72	0.80	2.78	3.83	4.07	3.90	3.54

Table 15.2: Adiabatic Lateral Average Film Cooling Effectiveness for TU: 20% and DR: 1.65

	Mb: 0.53	Mb: 0.77	Mb: 0.98	Mb: 1.51	Mb: 2.1	Mb: 2.96	Mb: 4.08	Mb: 5.04	Mb: 5.96
x/d	$\eta_{f\,avg}$	$\eta_{f\,avg}$	$\eta_{f\,avg}$	$\eta_{f\,avg}$	$\eta_{f\,avg}$	$\eta_{f\,avg}$	$\eta_{f\,avg}$	$\eta_{f\,avg}$	$\eta_{f\,avg}$
0	0.2468	0.2872	0.2988	0.2904	0.2687	0.2440	0.2220	0.2089	0.2002
1	0.2053	0.2481	0.2564	0.2343	0.1925	0.1555	0.1260	0.1091	0.0989
2	0.1753	0.2184	0.2293	0.2048	0.1556	0.1149	0.0806	0.0627	0.0540
3	0.1522	0.1954	0.2117	0.1930	0.1468	0.1080	0.0741	0.0572	0.0479
4	0.1351	0.1787	0.2011	0.1926	0.1553	0.1225	0.0942	0.0787	0.0685
5	0.1246	0.1683	0.1954	0.1960	0.1674	0.1393	0.1151	0.1001	0.0885
6	0.1141	0.1569	0.1873	0.1965	0.1772	0.1543	0.1345	0.1207	0.1074
7	0.1054	0.1470	0.1793	0.1954	0.1846	0.1659	0.1506	0.1382	0.1236
8	0.0979	0.1380	0.1709	0.1914	0.1872	0.1723	0.1611	0.1504	0.1356
9	0.0910	0.1294	0.1626	0.1869	0.1888	0.1776	0.1704	0.1621	0.1478
10	0.0853	0.1220	0.1548	0.1811	0.1873	0.1794	0.1758	0.1693	0.1554
11	0.0803	0.1156	0.1479	0.1758	0.1858	0.1807	0.1801	0.1757	0.1629
12	0.0753	0.1089	0.1403	0.1691	0.1822	0.1803	0.1831	0.1810	0.1693
13	0.0712	0.1033	0.1338	0.1630	0.1782	0.1784	0.1831	0.1826	0.1723
14	0.0671	0.0977	0.1273	0.1566	0.1740	0.1770	0.1846	0.1866	0.1777
15	0.0626	0.0915	0.1199	0.1492	0.1684	0.1740	0.1840	0.1879	0.1804
16	0.0602	0.0882	0.1160	0.1453	0.1656	0.1728	0.1844	0.1894	0.1827
17	0.0576	0.0845	0.1115	0.1403	0.1611	0.1696	0.1828	0.1888	0.1829
18	0.0540	0.0796	0.1054	0.1337	0.1555	0.1660	0.1814	0.1892	0.1852
19	0.0520	0.0768	0.1021	0.1303	0.1530	0.1654	0.1828	0.1918	0.1887
20	0.0495	0.0733	0.0977	0.1253	0.1483	0.1618	0.1804	0.1906	0.1883
21	0.0477	0.0706	0.0944	0.1215	0.1447	0.1590	0.1787	0.1900	0.1889
22	0.0452	0.0672	0.0901	0.1166	0.1402	0.1560	0.1777	0.1907	0.1910
23	0.0439	0.0653	0.0878	0.1141	0.1381	0.1548	0.1778	0.1918	0.1929
24	0.0421	0.0629	0.0847	0.1105	0.1344	0.1519	0.1757	0.1905	0.1922
25	0.0403	0.0603	0.0813	0.1064	0.1302	0.1480	0.1725	0.1881	0.1905
26	0.0386	0.0578	0.0782	0.1027	0.1264	0.1448	0.1704	0.1871	0.1906
27	0.0375	0.0562	0.0762	0.1004	0.1242	0.1433	0.1699	0.1878	0.1924
28	0.0363	0.0546	0.0741	0.0978	0.1214	0.1408	0.1678	0.1862	0.1914
29	0.0344	0.0519	0.0706	0.0936	0.1170	0.1369	0.1646	0.1839	0.1898
30	0.0334	0.0503	0.0686	0.0912	0.1143	0.1344	0.1626	0.1825	0.1894
31	0.0328	0.0495	0.0676	0.0899	0.1130	0.1332	0.1615	0.1818	0.1890
32	0.0312	0.0472	0.0646	0.0863	0.1090	0.1296	0.1585	0.1799	0.1883
33	0.0303	0.0459	0.0629	0.0842	0.1067	0.1275	0.1569	0.1790	0.1883
34	0.0298	0.0451	0.0618	0.0829	0.1053	0.1261	0.1553	0.1774	0.1867
35	0.0282	0.0428	0.0588	0.0791	0.1011	0.1219	0.1513	0.1741	0.1844
36	0.0282	0.0428	0.0588	0.0791	0.1011	0.1221	0.1517	0.1747	0.1853

37	0.0279	0.0425	0.0584	0.0786	0.1006	0.1216	0.1513	0.1744	0.1852
38	0.0272	0.0413	0.0569	0.0767	0.0984	0.1194	0.1492	0.1727	0.1839
39	0.0255	0.0390	0.0538	0.0728	0.0940	0.1149	0.1448	0.1690	0.1814
40	0.0254	0.0387	0.0534	0.0724	0.0934	0.1144	0.1441	0.1683	0.1808
41	0.0246	0.0376	0.0520	0.0706	0.0914	0.1123	0.1420	0.1665	0.1794
42	0.0240	0.0368	0.0509	0.0691	0.0897	0.1106	0.1403	0.1651	0.1787
43	0.0238	0.0363	0.0503	0.0684	0.0888	0.1096	0.1393	0.1641	0.1779
44	0.0229	0.0351	0.0487	0.0663	0.0864	0.1070	0.1364	0.1613	0.1756
45	0.0219	0.0335	0.0465	0.0635	0.0831	0.1034	0.1325	0.1575	0.1724
46	0.0219	0.0336	0.0466	0.0637	0.0833	0.1037	0.1329	0.1580	0.1729
47	0.0219	0.0336	0.0467	0.0638	0.0834	0.1039	0.1331	0.1582	0.1731
48	0.0219	0.0336	0.0467	0.0637	0.0834	0.1038	0.1331	0.1582	0.1733
49	0.0207	0.0318	0.0442	0.0606	0.0796	0.0997	0.1285	0.1537	0.1696
50	0.0197	0.0303	0.0423	0.0580	0.0765	0.0963	0.1247	0.1500	0.1665

Table 15.3: Centerline Adiabatic Film Cooling Effectiveness for TU: 20% and DR: 1.65

	Mb: 0.53	Mb: 0.77	Mb: 0.98	Mb: 1.51	Mb: 2.1	Mb: 2.96	Mb: 4.08	Mb: 5.04	Mb: 5.96
X/D	η_f	η_f	η_f	η_f	η_f	η_f	η_f	η_f	η_f
0	0.9460	0.9808	0.9915	0.9966	0.9994	1.0001	1.0003	1.0006	1.0010
1.5	0.5623	0.6909	0.7383	0.7145	0.6317	0.5500	0.4648	0.4103	0.3756
3	0.3927	0.5043	0.5532	0.5191	0.4066	0.3019	0.1931	0.1378	0.1119
4.5	0.2087	0.2815	0.3264	0.3253	0.2742	0.2250	0.1776	0.1504	0.1304
6	0.1732	0.2375	0.2817	0.2914	0.2575	0.2213	0.1912	0.1724	0.1550
7.5	0.1492	0.2085	0.2546	0.2775	0.2633	0.2388	0.2213	0.2080	0.1901
9	0.1300	0.1847	0.2316	0.2653	0.2670	0.2538	0.2481	0.2413	0.2252
10.5	0.1156	0.1660	0.2119	0.2510	0.2644	0.2592	0.2632	0.2628	0.2503
12	0.1009	0.1464	0.1897	0.2313	0.2539	0.2579	0.2714	0.2784	0.2713
13.5	0.1009	0.1464	0.1897	0.2313	0.2539	0.2579	0.2714	0.2784	0.2713
15	0.0851	0.1246	0.1639	0.2054	0.2350	0.2487	0.2726	0.2879	0.2880
16.5	0.0851	0.1246	0.1639	0.2054	0.2350	0.2487	0.2726	0.2879	0.2880
18	0.0851	0.1246	0.1639	0.2054	0.2350	0.2487	0.2726	0.2879	0.2880
19.5	0.0721	0.1065	0.1417	0.1814	0.2146	0.2357	0.2679	0.2903	0.2966
21	0.0721	0.1065	0.1417	0.1814	0.2146	0.2357	0.2679	0.2903	0.2966
22.5	0.0618	0.0918	0.1233	0.1604	0.1947	0.2209	0.2595	0.2879	0.3000
24	0.0618	0.0918	0.1233	0.1604	0.1947	0.2209	0.2595	0.2879	0.3000
25.5	0.0526	0.0787	0.1067	0.1408	0.1748	0.2043	0.2480	0.2820	0.2998
27	0.0526	0.0787	0.1067	0.1408	0.1748	0.2043	0.2480	0.2820	0.2998
28.5	0.0526	0.0787	0.1067	0.1408	0.1748	0.2043	0.2480	0.2820	0.2998
30	0.0448	0.0677	0.0924	0.1234	0.1562	0.1874	0.2340	0.2730	0.2963
31.5	0.0448	0.0677	0.0924	0.1234	0.1562	0.1874	0.2340	0.2730	0.2963
33	0.0448	0.0677	0.0924	0.1234	0.1562	0.1874	0.2340	0.2730	0.2963
34.5	0.0448	0.0677	0.0924	0.1234	0.1562	0.1874	0.2340	0.2730	0.2963
36	0.0382	0.0580	0.0799	0.1078	0.1388	0.1702	0.2181	0.2610	0.2894
37.5	0.0382	0.0580	0.0799	0.1078	0.1388	0.1702	0.2181	0.2610	0.2894
39	0.0382	0.0580	0.0799	0.1078	0.1388	0.1702	0.2181	0.2610	0.2894
40.5	0.0382	0.0580	0.0799	0.1078	0.1388	0.1702	0.2181	0.2610	0.2894
42	0.0340	0.0518	0.0716	0.0974	0.1267	0.1577	0.2053	0.2500	0.2820
43.5	0.0340	0.0518	0.0716	0.0974	0.1267	0.1577	0.2053	0.2500	0.2820
45	0.0312	0.0477	0.0662	0.0904	0.1185	0.1489	0.1957	0.2409	0.2751
46.5	0.0313	0.0479	0.0665	0.0908	0.1190	0.1496	0.1965	0.2422	0.2767
48	0.0288	0.0442	0.0615	0.0842	0.1111	0.1409	0.1867	0.2321	0.2683
49.5	0.0288	0.0442	0.0615	0.0842	0.1111	0.1409	0.1867	0.2321	0.2683

Table 15.4: Adiabatic Lateral Average Film Cooling Effectiveness for TU: 5% and DR: 1.65

Mb	Mb: 0.53	Mb: 0.77	Mb: 0.98	Mb: 1.51	Mb: 2.1	Mb: 2.96	Mb: 4.08	Mb: 5.04	Mb: 5.96
X/D	$\eta_{f\,avg}$	$\eta_{f\,avg}$	$\eta_{f\,avg}$	$\eta_{f\,avg}$	$\eta_{f\,avg}$	$\eta_{f\,avg}$	$\eta_{f\,avg}$	$\eta_{f\,avg}$	$\eta_{f\,avg}$
0	0.2674	0.2965	0.3014	0.2879	0.2634	0.2383	0.2182	0.2065	0.1988
1	0.2274	0.2558	0.2513	0.2195	0.1749	0.1406	0.1182	0.1050	0.0966
2	0.1988	0.2260	0.2177	0.1767	0.1224	0.0856	0.0646	0.0535	0.0482
3	0.1770	0.2046	0.1973	0.1554	0.1016	0.0680	0.0508	0.0429	0.0384
4	0.1617	0.1913	0.1883	0.1505	0.1019	0.0745	0.0642	0.0594	0.0556
5	0.1536	0.1860	0.1880	0.1553	0.1105	0.0869	0.0810	0.0777	0.0735
6	0.1454	0.1805	0.1883	0.1619	0.1212	0.1010	0.0988	0.0961	0.0907
7	0.1386	0.1760	0.1893	0.1693	0.1323	0.1148	0.1152	0.1126	0.1057
8	0.1323	0.1707	0.1880	0.1736	0.1403	0.1250	0.1272	0.1248	0.1171
9	0.1265	0.1661	0.1874	0.1789	0.1496	0.1360	0.1394	0.1374	0.1292
10	0.1213	0.1609	0.1848	0.1808	0.1551	0.1429	0.1471	0.1454	0.1367
11	0.1170	0.1568	0.1830	0.1834	0.1611	0.1497	0.1543	0.1531	0.1445
12	0.1121	0.1516	0.1794	0.1838	0.1652	0.1548	0.1601	0.1598	0.1511
13	0.1080	0.1470	0.1759	0.1833	0.1674	0.1573	0.1626	0.1629	0.1549
14	0.1039	0.1424	0.1723	0.1829	0.1703	0.1609	0.1671	0.1683	0.1606
15	0.0993	0.1370	0.1678	0.1818	0.1725	0.1632	0.1695	0.1714	0.1643
16	0.0970	0.1344	0.1658	0.1817	0.1744	0.1651	0.1716	0.1738	0.1669
17	0.0940	0.1306	0.1620	0.1791	0.1737	0.1647	0.1715	0.1741	0.1673
18	0.0901	0.1258	0.1574	0.1768	0.1740	0.1653	0.1728	0.1765	0.1708
19	0.0883	0.1238	0.1559	0.1773	0.1765	0.1680	0.1761	0.1802	0.1744
20	0.0854	0.1200	0.1519	0.1745	0.1756	0.1672	0.1756	0.1800	0.1745
21	0.0832	0.1171	0.1489	0.1723	0.1748	0.1666	0.1755	0.1807	0.1760
22	0.0805	0.1138	0.1455	0.1705	0.1753	0.1673	0.1770	0.1832	0.1791
23	0.0792	0.1122	0.1440	0.1700	0.1763	0.1685	0.1787	0.1853	0.1814
24	0.0770	0.1094	0.1409	0.1676	0.1754	0.1677	0.1782	0.1849	0.1811
25	0.0746	0.1062	0.1372	0.1642	0.1731	0.1656	0.1766	0.1837	0.1803
26	0.0725	0.1033	0.1340	0.1617	0.1720	0.1647	0.1764	0.1841	0.1812
27	0.0712	0.1017	0.1324	0.1607	0.1723	0.1653	0.1778	0.1862	0.1839
28	0.0697	0.0997	0.1300	0.1585	0.1709	0.1641	0.1769	0.1856	0.1835
29	0.0672	0.0964	0.1262	0.1553	0.1693	0.1626	0.1760	0.1848	0.1827
30	0.0657	0.0943	0.1238	0.1530	0.1678	0.1614	0.1754	0.1848	0.1833
31	0.0650	0.0933	0.1227	0.1519	0.1671	0.1608	0.1751	0.1847	0.1833
32	0.0628	0.0904	0.1192	0.1488	0.1654	0.1596	0.1747	0.1849	0.1841
33	0.0615	0.0887	0.1172	0.1469	0.1643	0.1588	0.1746	0.1855	0.1851
34	0.0607	0.0876	0.1158	0.1455	0.1632	0.1577	0.1734	0.1842	0.1837
35	0.0584	0.0844	0.1121	0.1418	0.1605	0.1553	0.1718	0.1831	0.1830
36	0.0584	0.0845	0.1122	0.1420	0.1610	0.1559	0.1726	0.1841	0.1840

37	0.0581	0.0841	0.1117	0.1416	0.1608	0.1557	0.1726	0.1842	0.1842
38	0.0569	0.0824	0.1097	0.1396	0.1593	0.1545	0.1717	0.1836	0.1837
39	0.0544	0.0790	0.1056	0.1354	0.1563	0.1520	0.1700	0.1825	0.1831
40	0.0541	0.0786	0.1051	0.1348	0.1559	0.1515	0.1696	0.1821	0.1827
41	0.0530	0.0771	0.1033	0.1329	0.1544	0.1503	0.1687	0.1815	0.1822
42	0.0521	0.0758	0.1017	0.1313	0.1532	0.1494	0.1684	0.1816	0.1826
43	0.0516	0.0751	0.1008	0.1303	0.1523	0.1487	0.1678	0.1811	0.1822
44	0.0502	0.0733	0.0984	0.1276	0.1500	0.1466	0.1662	0.1797	0.1810
45	0.0484	0.0707	0.0953	0.1241	0.1469	0.1440	0.1640	0.1779	0.1795
46	0.0485	0.0709	0.0955	0.1245	0.1474	0.1444	0.1645	0.1784	0.1800
47	0.0486	0.0710	0.0957	0.1247	0.1476	0.1447	0.1648	0.1787	0.1802
48	0.0486	0.0710	0.0956	0.1246	0.1476	0.1447	0.1649	0.1789	0.1805
49	0.0465	0.0681	0.0920	0.1205	0.1440	0.1417	0.1626	0.1772	0.1791
50	0.0448	0.0657	0.0889	0.1170	0.1407	0.1389	0.1604	0.1755	0.1778

Table 15.5: Centerline Adiabatic Film Cooling Effectiveness for TU: 5% and DR: 1.65

Mb	Mb: 0.53	Mb: 0.77	Mb: 0.98	Mb: 1.51	Mb: 2.1	Mb: 2.96	Mb: 4.08	Mb: 5.04	Mb: 5.96
X/D	η_f	η_f	η_f	η_f	η_f	η_f	η_f	η_f	η_f
0	0.9704	0.9911	0.9974	0.9995	0.9999	1.0001	1.0003	1.0006	1.0010
1.5	0.6246	0.7172	0.7252	0.6669	0.5656	0.4896	0.4323	0.3921	0.3657
3	0.4560	0.5330	0.5235	0.4257	0.2850	0.1953	0.1388	0.1092	0.0941
4.5	0.2564	0.3115	0.3119	0.2513	0.1739	0.1360	0.1220	0.1144	0.1066
6	0.2188	0.2716	0.2791	0.2326	0.1694	0.1423	0.1395	0.1370	0.1296
7.5	0.1965	0.2516	0.2701	0.2388	0.1868	0.1671	0.1717	0.1713	0.1626
9	0.1797	0.2372	0.2666	0.2506	0.2093	0.1953	0.2051	0.2067	0.1971
10.5	0.1670	0.2248	0.2615	0.2586	0.2267	0.2158	0.2286	0.2326	0.2238
12	0.1530	0.2097	0.2517	0.2615	0.2405	0.2317	0.2469	0.2544	0.2479
13.5	0.1530	0.2097	0.2517	0.2615	0.2405	0.2317	0.2469	0.2544	0.2479
15	0.1371	0.1908	0.2360	0.2585	0.2500	0.2420	0.2601	0.2722	0.2701
16.5	0.1371	0.1908	0.2360	0.2585	0.2500	0.2420	0.2601	0.2722	0.2701
18	0.1371	0.1908	0.2360	0.2585	0.2500	0.2420	0.2601	0.2722	0.2701
19.5	0.1232	0.1734	0.2196	0.2510	0.2533	0.2456	0.2661	0.2818	0.2837
21	0.1232	0.1734	0.2196	0.2510	0.2533	0.2456	0.2661	0.2818	0.2837
22.5	0.1113	0.1580	0.2034	0.2405	0.2514	0.2442	0.2680	0.2870	0.2922
24	0.1113	0.1580	0.2034	0.2405	0.2514	0.2442	0.2680	0.2870	0.2922
25.5	0.1000	0.1430	0.1868	0.2273	0.2459	0.2397	0.2671	0.2898	0.2983
27	0.1000	0.1430	0.1868	0.2273	0.2459	0.2397	0.2671	0.2898	0.2983
28.5	0.1000	0.1430	0.1868	0.2273	0.2459	0.2397	0.2671	0.2898	0.2983
30	0.0896	0.1291	0.1705	0.2128	0.2378	0.2328	0.2643	0.2904	0.3021
31.5	0.0896	0.1291	0.1705	0.2128	0.2378	0.2328	0.2643	0.2904	0.3021
33	0.0896	0.1291	0.1705	0.2128	0.2378	0.2328	0.2643	0.2904	0.3021
34.5	0.0896	0.1291	0.1705	0.2128	0.2378	0.2328	0.2643	0.2904	0.3021
36	0.0800	0.1159	0.1547	0.1973	0.2273	0.2239	0.2594	0.2890	0.3038
37.5	0.0800	0.1159	0.1547	0.1973	0.2273	0.2239	0.2594	0.2890	0.3038
39	0.0800	0.1159	0.1547	0.1973	0.2273	0.2239	0.2594	0.2890	0.3038
40.5	0.0800	0.1159	0.1547	0.1973	0.2273	0.2239	0.2594	0.2890	0.3038
42	0.0734	0.1067	0.1434	0.1854	0.2182	0.2163	0.2547	0.2868	0.3039
43.5	0.0734	0.1067	0.1434	0.1854	0.2182	0.2163	0.2547	0.2868	0.3039
45	0.0690	0.1006	0.1356	0.1766	0.2104	0.2095	0.2501	0.2834	0.3015
46.5	0.0690	0.1007	0.1359	0.1774	0.2120	0.2116	0.2516	0.2858	0.3045
48	0.0648	0.0948	0.1283	0.1686	0.2038	0.2042	0.2462	0.2816	0.3016
49.5	0.0648	0.0948	0.1283	0.1686	0.2038	0.2042	0.2462	0.2816	0.3016

Table 15.6: Adiabatic Lateral Average Film Cooling Effectiveness for various Tu at VR: 0.64 DR: 1.65

	TU: 5%	TU: 10%	TU: 15%	TU: 20%	TU: 25%
X/D	$\eta_{f\,avg}$	$\eta_{f\,avg}$	$\eta_{f\,avg}$	$\eta_{f\,avg}$	$\eta_{f\,avg}$
0	0.3014	0.3007	0.2999	0.2988	0.2979
1	0.2513	0.2522	0.2539	0.2564	0.2599
2	0.2177	0.2199	0.2239	0.2293	0.2351
3	0.1973	0.2004	0.2055	0.2117	0.2161
4	0.1883	0.1917	0.1966	0.2011	0.2012
5	0.1880	0.1909	0.1942	0.1954	0.1904
6	0.1883	0.1899	0.1904	0.1873	0.1773
7	0.1893	0.1892	0.1866	0.1793	0.1652
8	0.1880	0.1863	0.1812	0.1709	0.1542
9	0.1874	0.1839	0.1761	0.1626	0.1435
10	0.1848	0.1799	0.1703	0.1548	0.1345
11	0.1830	0.1768	0.1654	0.1479	0.1265
12	0.1794	0.1721	0.1593	0.1403	0.1185
13	0.1759	0.1677	0.1538	0.1338	0.1120
14	0.1723	0.1632	0.1482	0.1273	0.1055
15	0.1678	0.1578	0.1418	0.1199	0.0984
16	0.1658	0.1552	0.1385	0.1160	0.0947
17	0.1620	0.1511	0.1340	0.1115	0.0907
18	0.1574	0.1460	0.1282	0.1054	0.0853
19	0.1559	0.1439	0.1253	0.1021	0.0823
20	0.1519	0.1398	0.1209	0.0977	0.0786
21	0.1489	0.1365	0.1174	0.0944	0.0759
22	0.1455	0.1328	0.1131	0.0901	0.0723
23	0.1440	0.1310	0.1109	0.0878	0.0704
24	0.1409	0.1278	0.1075	0.0847	0.0679
25	0.1372	0.1241	0.1037	0.0813	0.0653
26	0.1340	0.1208	0.1002	0.0782	0.0628
27	0.1324	0.1189	0.0980	0.0762	0.0613
28	0.1300	0.1165	0.0955	0.0741	0.0596
29	0.1262	0.1127	0.0915	0.0706	0.0569
30	0.1238	0.1103	0.0891	0.0686	0.0554
31	0.1227	0.1091	0.0879	0.0676	0.0547
32	0.1192	0.1056	0.0842	0.0646	0.0524
33	0.1172	0.1034	0.0821	0.0629	0.0511
34	0.1158	0.1021	0.0808	0.0618	0.0504
35	0.1121	0.0983	0.0770	0.0588	0.0481
36	0.1122	0.0984	0.0770	0.0588	0.0481

37	0.1117	0.0979	0.0765	0.0584	0.0478
38	0.1097	0.0959	0.0746	0.0569	0.0467
39	0.1056	0.0917	0.0705	0.0538	0.0443
40	0.1051	0.0912	0.0701	0.0534	0.0441
41	0.1033	0.0893	0.0683	0.0520	0.0430
42	0.1017	0.0876	0.0667	0.0509	0.0422
43	0.1008	0.0868	0.0659	0.0503	0.0417
44	0.0984	0.0844	0.0638	0.0487	0.0405
45	0.0953	0.0812	0.0609	0.0465	0.0389
46	0.0955	0.0814	0.0611	0.0466	0.0390
47	0.0957	0.0815	0.0612	0.0467	0.0391
48	0.0956	0.0815	0.0611	0.0467	0.0390
49	0.0920	0.0778	0.0578	0.0442	0.0372
50	0.0889	0.0747	0.0551	0.0423	0.0357

Table 15.7: Centerline Adiabatic Film Cooling Effectiveness for various Tu at VR: 0.64 DR: 1.65

	TU: 5%	TU: 10%	TU: 15%	TU: 20%	TU: 25%
X/D	η_f	η_f	η_f	η_f	η_f
0	0.9974	0.9971	0.9951	0.9915	0.9864
1.5	0.7252	0.7294	0.7336	0.7383	0.7388
3	0.5235	0.5319	0.5423	0.5532	0.5537
4.5	0.3119	0.3180	0.3238	0.3264	0.3172
6	0.2791	0.2827	0.2845	0.2817	0.2681
7.5	0.2701	0.2699	0.2653	0.2546	0.2341
9	0.2666	0.2618	0.2504	0.2316	0.2049
10.5	0.2615	0.2527	0.2363	0.2119	0.1819
12	0.2517	0.2394	0.2186	0.1897	0.1586
13.5	0.2517	0.2394	0.2186	0.1897	0.1586
15	0.2360	0.2206	0.1960	0.1639	0.1338
16.5	0.2360	0.2206	0.1960	0.1639	0.1338
18	0.2360	0.2206	0.1960	0.1639	0.1338
19.5	0.2196	0.2022	0.1749	0.1417	0.1142
21	0.2196	0.2022	0.1749	0.1417	0.1142
22.5	0.2034	0.1850	0.1559	0.1233	0.0990
24	0.2034	0.1850	0.1559	0.1233	0.0990
25.5	0.1868	0.1677	0.1375	0.1067	0.0860
27	0.1868	0.1677	0.1375	0.1067	0.0860
28.5	0.1868	0.1677	0.1375	0.1067	0.0860
30	0.1705	0.1511	0.1204	0.0924	0.0751
31.5	0.1705	0.1511	0.1204	0.0924	0.0751
33	0.1705	0.1511	0.1204	0.0924	0.0751
34.5	0.1705	0.1511	0.1204	0.0924	0.0751
36	0.1547	0.1351	0.1046	0.0799	0.0658
37.5	0.1547	0.1351	0.1046	0.0799	0.0658
39	0.1547	0.1351	0.1046	0.0799	0.0658
40.5	0.1547	0.1351	0.1046	0.0799	0.0658
42	0.1434	0.1236	0.0938	0.0716	0.0596
43.5	0.1434	0.1236	0.0938	0.0716	0.0596
45	0.1356	0.1156	0.0865	0.0662	0.0555
46.5	0.1359	0.1159	0.0869	0.0665	0.0558
48	0.1283	0.1081	0.0800	0.0615	0.0519
49.5	0.1283	0.1081	0.0800	0.0615	0.0519

Table 15.8: Adiabatic Lateral Average Film Cooling Effectiveness for various Tu at VR: 0.64 DR: 1.99

	TU: 5%	TU: 10%	TU: 15%	TU: 20%	TU: 25%
X/D	$\eta_{f\,avg}$	$\eta_{f\,avg}$	$\eta_{f\,avg}$	$\eta_{f\,avg}$	$\eta_{f\,avg}$
0	0.3111	0.3111	0.3109	0.3107	0.3109
1	0.2615	0.2630	0.2652	0.2685	0.2733
2	0.2287	0.2316	0.2359	0.2426	0.2503
3	0.2089	0.2128	0.2183	0.2263	0.2336
4	0.2010	0.2052	0.2109	0.2178	0.2215
5	0.2016	0.2054	0.2098	0.2137	0.2128
6	0.2027	0.2053	0.2073	0.2071	0.2009
7	0.2043	0.2054	0.2045	0.2001	0.1894
8	0.2036	0.2031	0.1998	0.1922	0.1783
9	0.2035	0.2013	0.1953	0.1844	0.1675
10	0.2012	0.1976	0.1897	0.1767	0.1579
11	0.1999	0.1948	0.1851	0.1699	0.1494
12	0.1964	0.1902	0.1790	0.1622	0.1406
13	0.1932	0.1859	0.1736	0.1555	0.1333
14	0.1897	0.1814	0.1680	0.1486	0.1260
15	0.1853	0.1760	0.1614	0.1408	0.1179
16	0.1834	0.1734	0.1581	0.1367	0.1136
17	0.1794	0.1691	0.1534	0.1316	0.1088
18	0.1748	0.1639	0.1474	0.1249	0.1025
19	0.1735	0.1618	0.1446	0.1213	0.0989
20	0.1694	0.1574	0.1399	0.1164	0.0944
21	0.1662	0.1540	0.1362	0.1126	0.0911
22	0.1629	0.1502	0.1317	0.1077	0.0867
23	0.1614	0.1484	0.1295	0.1051	0.0844
24	0.1582	0.1450	0.1258	0.1015	0.0813
25	0.1542	0.1410	0.1217	0.0976	0.0780
26	0.1509	0.1375	0.1179	0.0938	0.0749
27	0.1492	0.1356	0.1156	0.0915	0.0729
28	0.1466	0.1330	0.1129	0.0890	0.0709
29	0.1427	0.1289	0.1085	0.0848	0.0675
30	0.1401	0.1263	0.1058	0.0824	0.0656
31	0.1388	0.1251	0.1045	0.0811	0.0646
32	0.1352	0.1213	0.1004	0.0775	0.0617
33	0.1330	0.1191	0.0980	0.0753	0.0601
34	0.1316	0.1177	0.0966	0.0741	0.0591
35	0.1276	0.1136	0.0924	0.0704	0.0562
36	0.1277	0.1137	0.0923	0.0703	0.0562

37	0.1272	0.1131	0.0918	0.0698	0.0558
38	0.1251	0.1110	0.0895	0.0679	0.0544
39	0.1207	0.1066	0.0849	0.0640	0.0514
40	0.1202	0.1060	0.0844	0.0636	0.0510
41	0.1182	0.1040	0.0823	0.0618	0.0497
42	0.1165	0.1023	0.0804	0.0604	0.0486
43	0.1156	0.1013	0.0795	0.0596	0.0481
44	0.1130	0.0988	0.0770	0.0576	0.0465
45	0.1096	0.0954	0.0736	0.0549	0.0445
46	0.1099	0.0956	0.0738	0.0550	0.0446
47	0.1101	0.0958	0.0739	0.0551	0.0446
48	0.1100	0.0957	0.0738	0.0551	0.0446
49	0.1061	0.0917	0.0698	0.0520	0.0423
50	0.1028	0.0884	0.0666	0.0495	0.0404

Table 15.9: Centerline Adiabatic Film Cooling Effectiveness for various Tu at VR: 0.64 DR: 1.99

	TU: 5%	TU: 10%	TU: 15%	TU: 20%	TU: 25%
X/D	η_f	η_f	η_f	η_f	η_f
0	0.9981	0.9980	0.9966	0.9943	0.9908
1.5	0.7340	0.7397	0.7455	0.7533	0.7593
3	0.5342	0.5441	0.5567	0.5717	0.5799
4.5	0.3298	0.3376	0.3459	0.3526	0.3504
6	0.2987	0.3038	0.3082	0.3094	0.3016
7.5	0.2912	0.2928	0.2910	0.2840	0.2682
9	0.2892	0.2863	0.2775	0.2623	0.2387
10.5	0.2850	0.2780	0.2641	0.2429	0.2144
12	0.2760	0.2651	0.2466	0.2203	0.1886
13.5	0.2760	0.2651	0.2466	0.2203	0.1886
15	0.2608	0.2461	0.2237	0.1929	0.1602
16.5	0.2608	0.2461	0.2237	0.1929	0.1602
18	0.2608	0.2461	0.2237	0.1929	0.1602
19.5	0.2444	0.2272	0.2019	0.1684	0.1369
21	0.2444	0.2272	0.2019	0.1684	0.1369
22.5	0.2277	0.2091	0.1819	0.1474	0.1184
24	0.2277	0.2091	0.1819	0.1474	0.1184
25.5	0.2102	0.1908	0.1621	0.1279	0.1021
27	0.2102	0.1908	0.1621	0.1279	0.1021
28.5	0.2102	0.1908	0.1621	0.1279	0.1021
30	0.1930	0.1733	0.1434	0.1106	0.0883
31.5	0.1930	0.1733	0.1434	0.1106	0.0883
33	0.1930	0.1733	0.1434	0.1106	0.0883
34.5	0.1930	0.1733	0.1434	0.1106	0.0883
36	0.1761	0.1562	0.1255	0.0951	0.0763
37.5	0.1761	0.1562	0.1255	0.0951	0.0763
39	0.1761	0.1562	0.1255	0.0951	0.0763
40.5	0.1761	0.1562	0.1255	0.0951	0.0763
42	0.1640	0.1440	0.1129	0.0848	0.0685
43.5	0.1640	0.1440	0.1129	0.0848	0.0685
45	0.1556	0.1354	0.1043	0.0779	0.0634
46.5	0.1560	0.1359	0.1047	0.0782	0.0636
48	0.1479	0.1276	0.0965	0.0719	0.0588
49.5	0.1479	0.1276	0.0965	0.0719	0.0588

Table 15.10: Adiabatic Lateral Average Film Cooling Effectiveness for various DR at VR: 0.64 and TU: 20%

	DR: 1.99	DR: 1.72	DR: 1.49
X/D	$\eta_{f\,avg}$	$\eta_{f\,avg}$	$\eta_{f\,avg}$
0	0.3107	0.3012	0.2907
1	0.2685	0.2588	0.2481
2	0.2426	0.2319	0.2205
3	0.2263	0.2145	0.2021
4	0.2178	0.2044	0.1904
5	0.2137	0.1990	0.1837
6	0.2071	0.1912	0.1748
7	0.2001	0.1833	0.1663
8	0.1922	0.1750	0.1577
9	0.1844	0.1669	0.1492
10	0.1767	0.1591	0.1415
11	0.1699	0.1522	0.1347
12	0.1622	0.1446	0.1274
13	0.1555	0.1381	0.1212
14	0.1486	0.1315	0.1150
15	0.1408	0.1241	0.1081
16	0.1367	0.1201	0.1044
17	0.1316	0.1155	0.1002
18	0.1249	0.1093	0.0946
19	0.1213	0.1059	0.0916
20	0.1164	0.1015	0.0876
21	0.1126	0.0980	0.0846
22	0.1077	0.0936	0.0807
23	0.1051	0.0913	0.0787
24	0.1015	0.0881	0.0759
25	0.0976	0.0846	0.0729
26	0.0938	0.0813	0.0701
27	0.0915	0.0793	0.0684
28	0.0890	0.0771	0.0665
29	0.0848	0.0735	0.0634
30	0.0824	0.0714	0.0617
31	0.0811	0.0703	0.0608
32	0.0775	0.0672	0.0582
33	0.0753	0.0654	0.0567
34	0.0741	0.0643	0.0558
35	0.0704	0.0612	0.0532
36	0.0703	0.0611	0.0531

37	0.0698	0.0607	0.0528
38	0.0679	0.0591	0.0515
39	0.0640	0.0559	0.0488
40	0.0636	0.0555	0.0485
41	0.0618	0.0540	0.0473
42	0.0604	0.0528	0.0463
43	0.0596	0.0522	0.0458
44	0.0576	0.0505	0.0444
45	0.0549	0.0482	0.0426
46	0.0550	0.0484	0.0427
47	0.0551	0.0484	0.0427
48	0.0551	0.0484	0.0427
49	0.0520	0.0458	0.0406
50	0.0495	0.0438	0.0389

Table 15.11: Centerline Adiabatic Film Cooling Effectiveness for various DR at VR: 0.64 and TU: 20%

	DR: 1.99	DR: 1.72	DR: 1.49
X/D	η_f	η_f	η_f
0	0.9943	0.9921	0.9882
1.5	0.7533	0.7417	0.7257
3	0.5717	0.5573	0.5387
4.5	0.3526	0.3317	0.3090
6	0.3094	0.2872	0.2640
7.5	0.2840	0.2604	0.2361
9	0.2623	0.2376	0.2128
10.5	0.2429	0.2180	0.1934
12	0.2203	0.1958	0.1720
13.5	0.2203	0.1958	0.1720
15	0.1929	0.1697	0.1477
16.5	0.1929	0.1697	0.1477
18	0.1929	0.1697	0.1477
19.5	0.1684	0.1470	0.1273
21	0.1684	0.1470	0.1273
22.5	0.1474	0.1282	0.1107
24	0.1474	0.1282	0.1107
25.5	0.1279	0.1110	0.0959
27	0.1279	0.1110	0.0959
28.5	0.1279	0.1110	0.0959
30	0.1106	0.0961	0.0834
31.5	0.1106	0.0961	0.0834
33	0.1106	0.0961	0.0834
34.5	0.1106	0.0961	0.0834
36	0.0951	0.0830	0.0725
37.5	0.0951	0.0830	0.0725
39	0.0951	0.0830	0.0725
40.5	0.0951	0.0830	0.0725
42	0.0848	0.0743	0.0654
43.5	0.0848	0.0743	0.0654
45	0.0779	0.0686	0.0607
46.5	0.0782	0.0689	0.0610
48	0.0719	0.0636	0.0566
49.5	0.0719	0.0636	0.0566

16 Appendix G: Visualization of Simulated Case Study Data

Appendix G-1: Mb = 0.98, Tu = 20%, DR = 1.65 (Baseline)

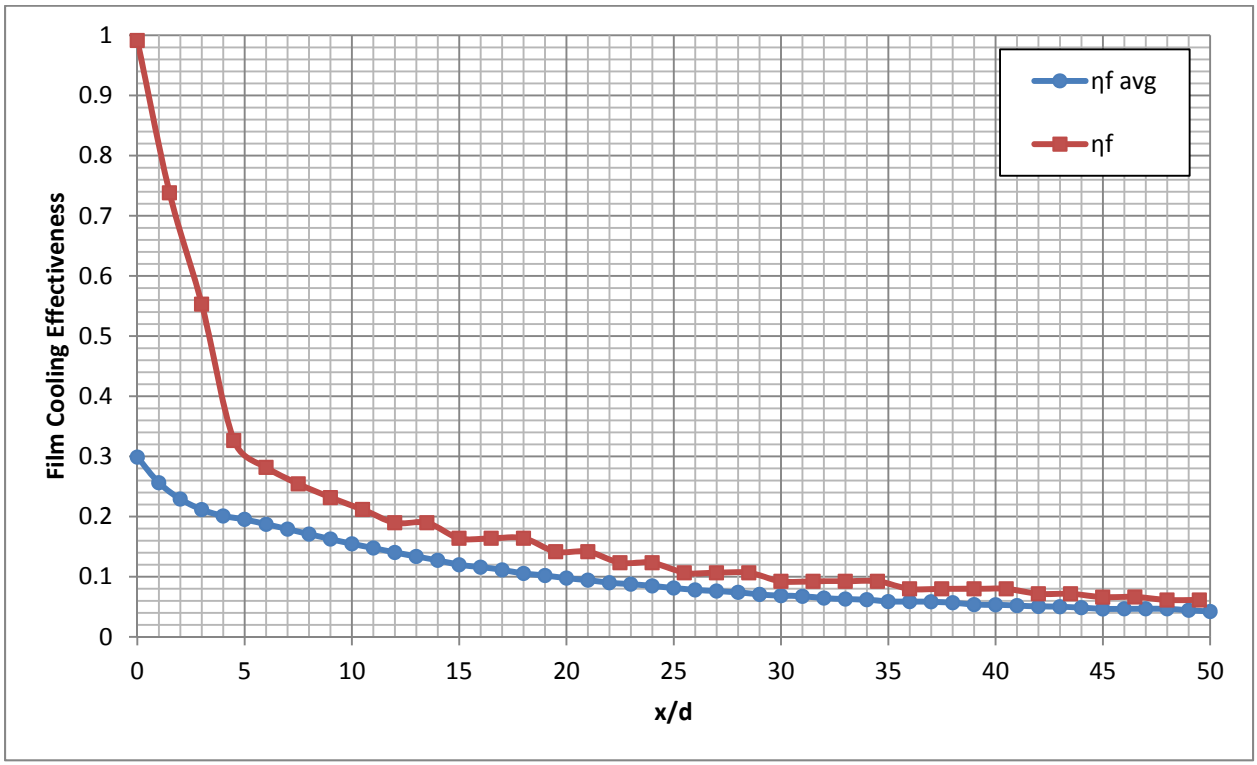

Figure 16.1: Case 1 - Laterally averaged and Centerline adiabatic film cooling effectiveness

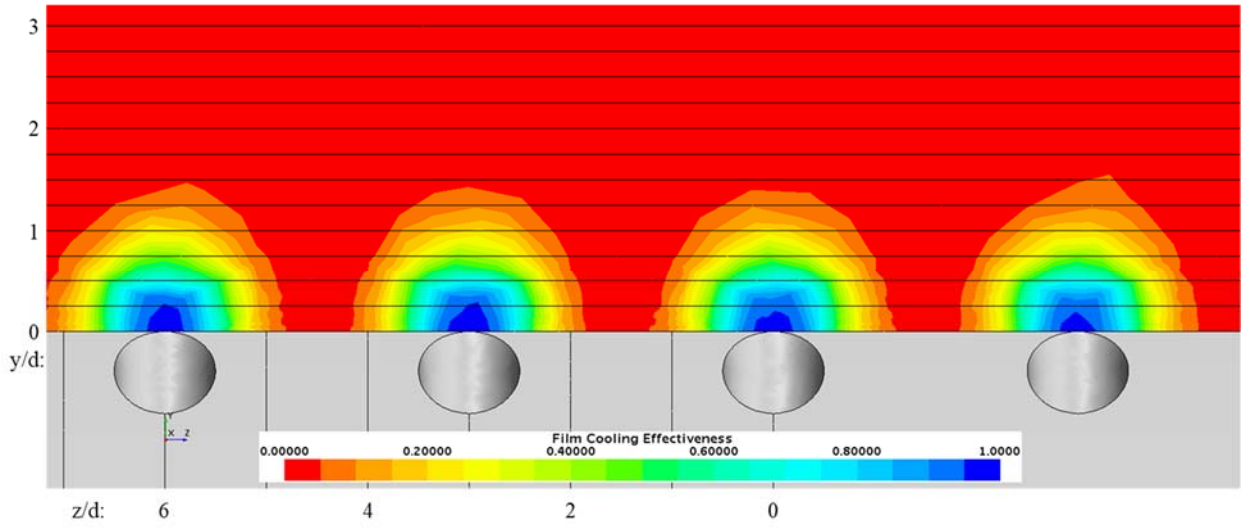

Figure 16.2: Case 1 - Spatial distribution of adiabatic film cooling effectiveness at x/d: 0

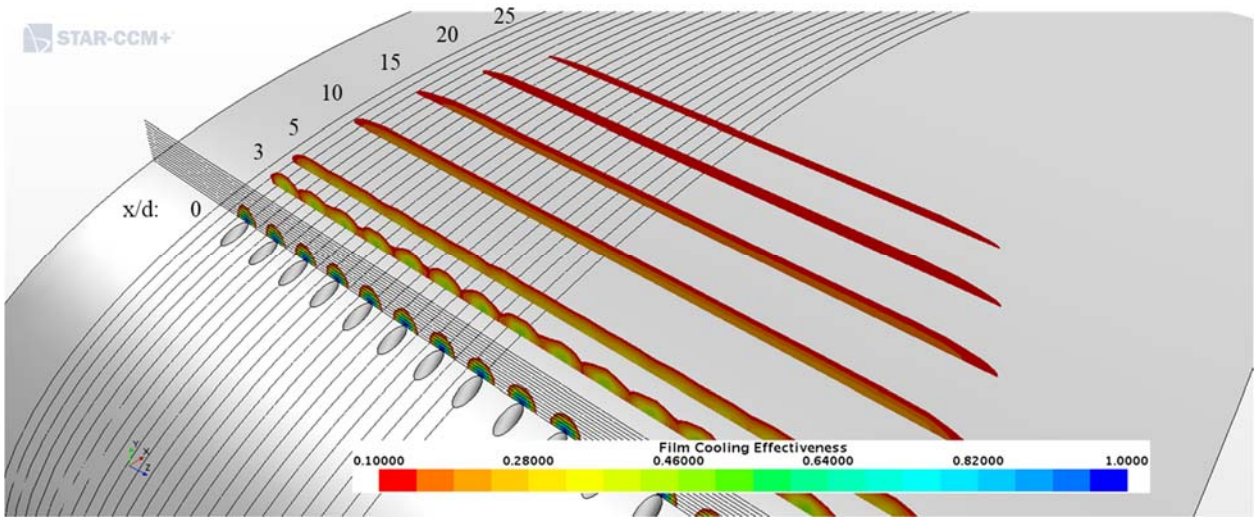

Figure 16.3: Case 1- Streamwise spatial distribution of adiabatic film cooling effectiveness

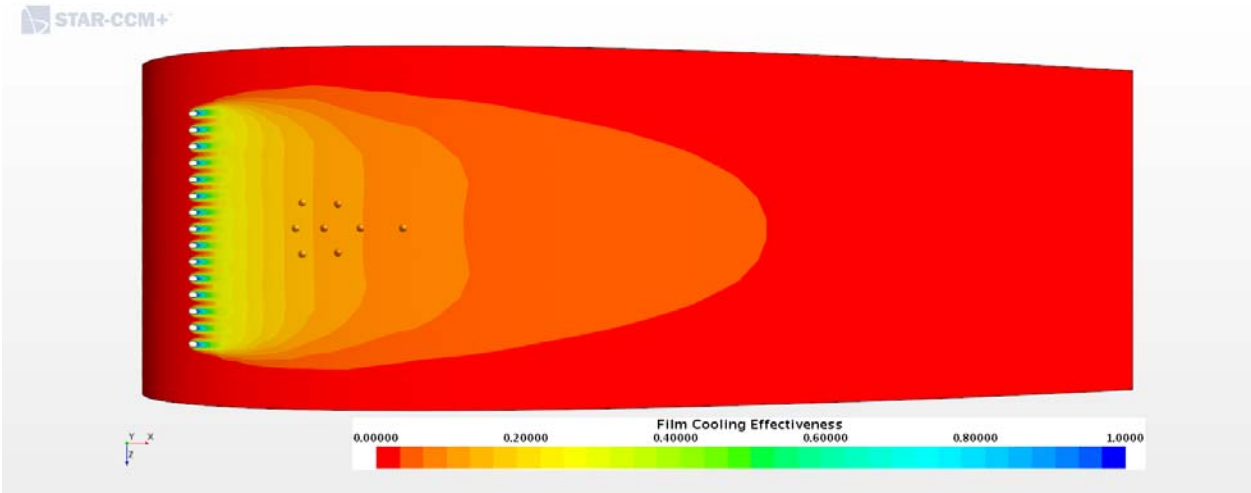

Figure 16.4: Case 1 - Adiabatic Film Cooling Effectiveness on the Suction Surface

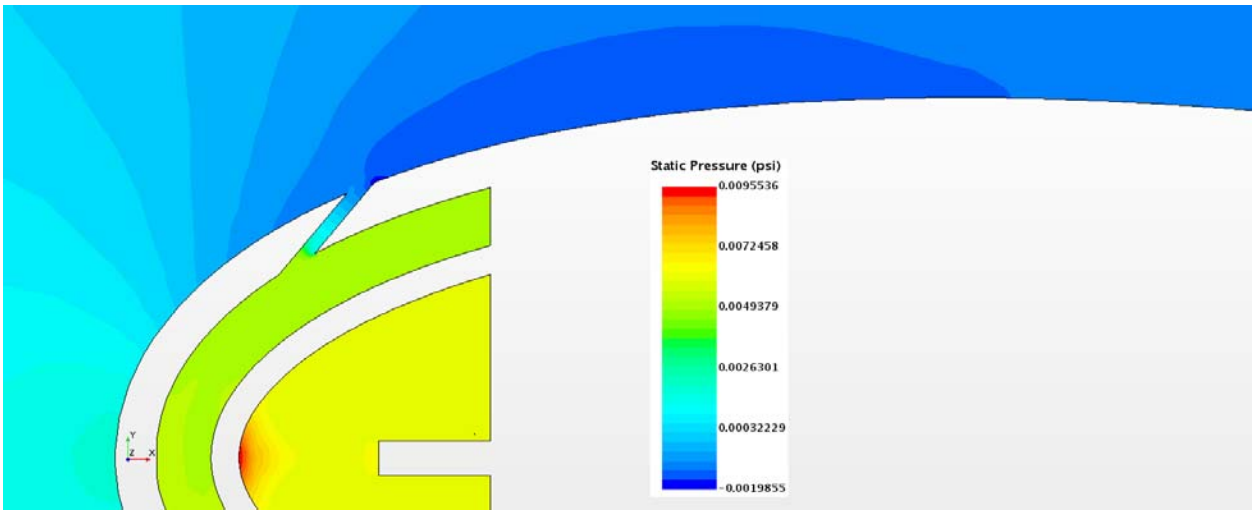

Figure 16.5: Case 1 – Static Pressure profile for center plane

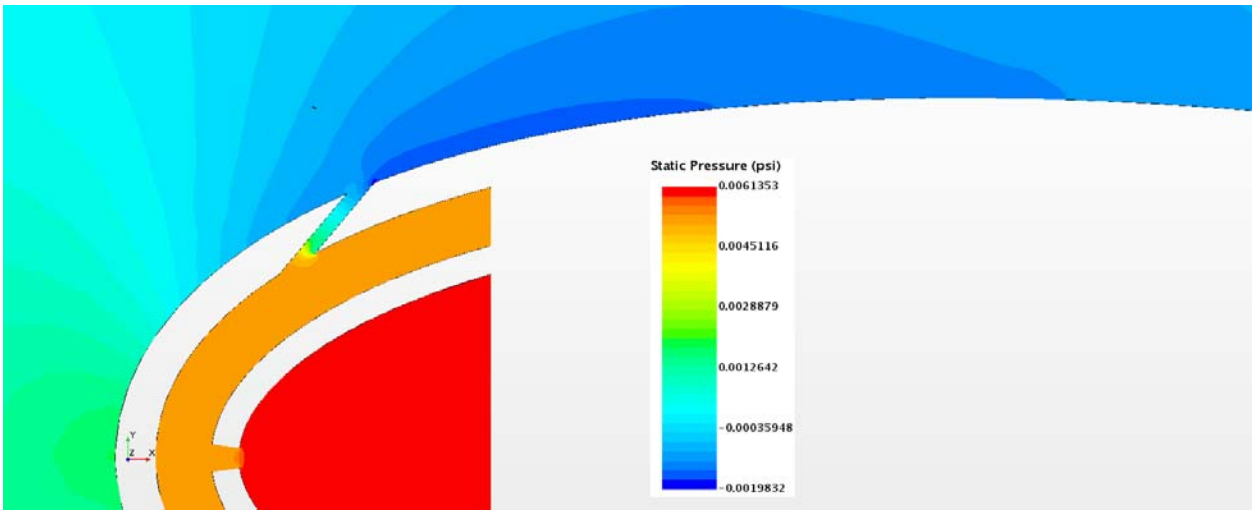

Figure 16.6: Case 1 – Static Pressure profile for off-center plane

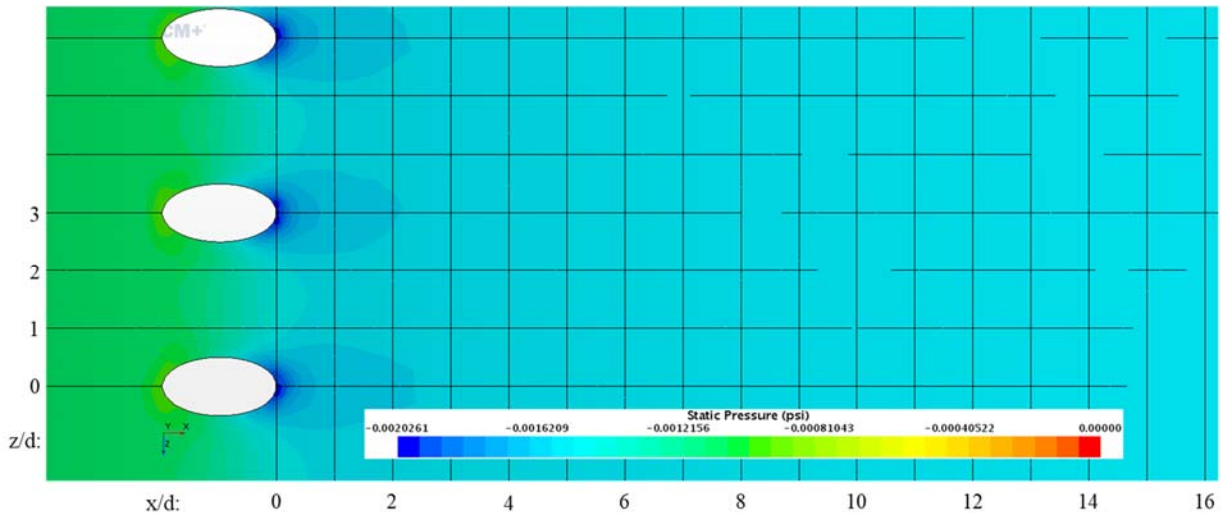

Figure 16.7: Case 1 – Static Pressure distribution for Suction Surface

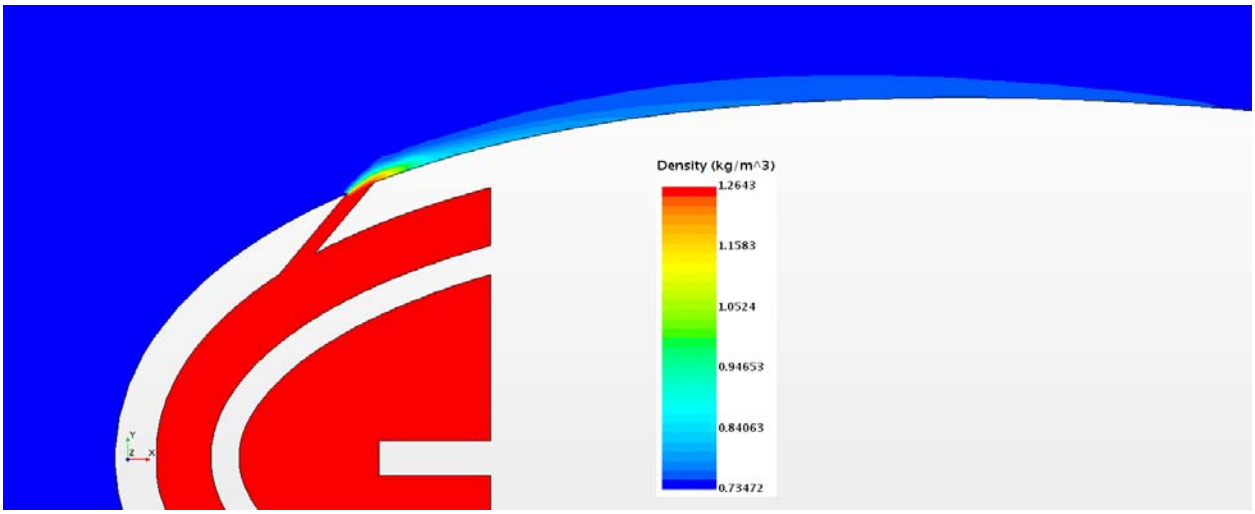

Figure 16.8: Case 1 – Density profile for center plane

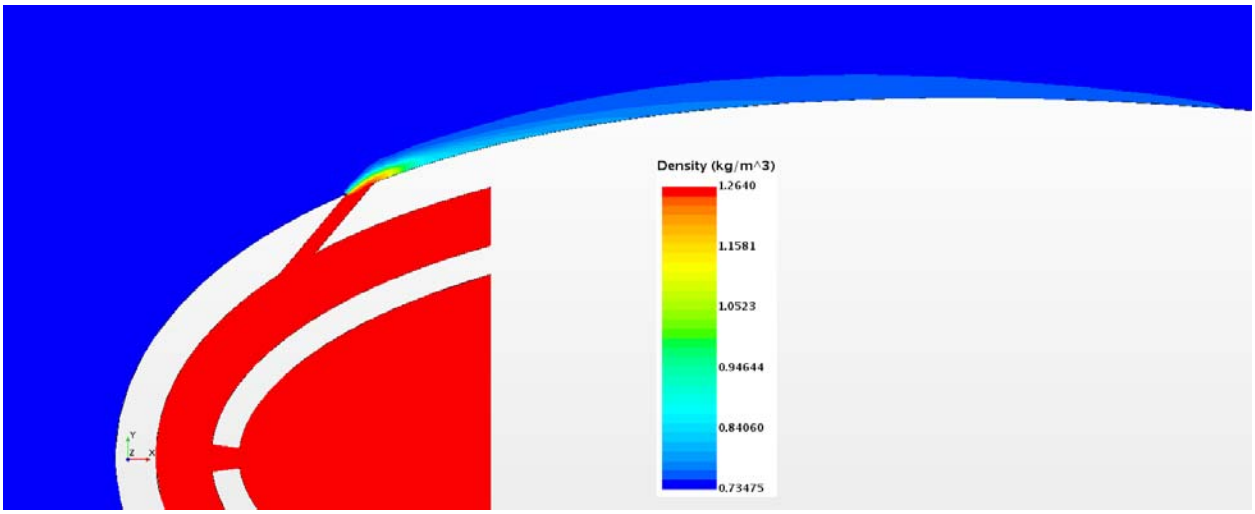

Figure 16.9: Case 1 – Density profile for off-center plane

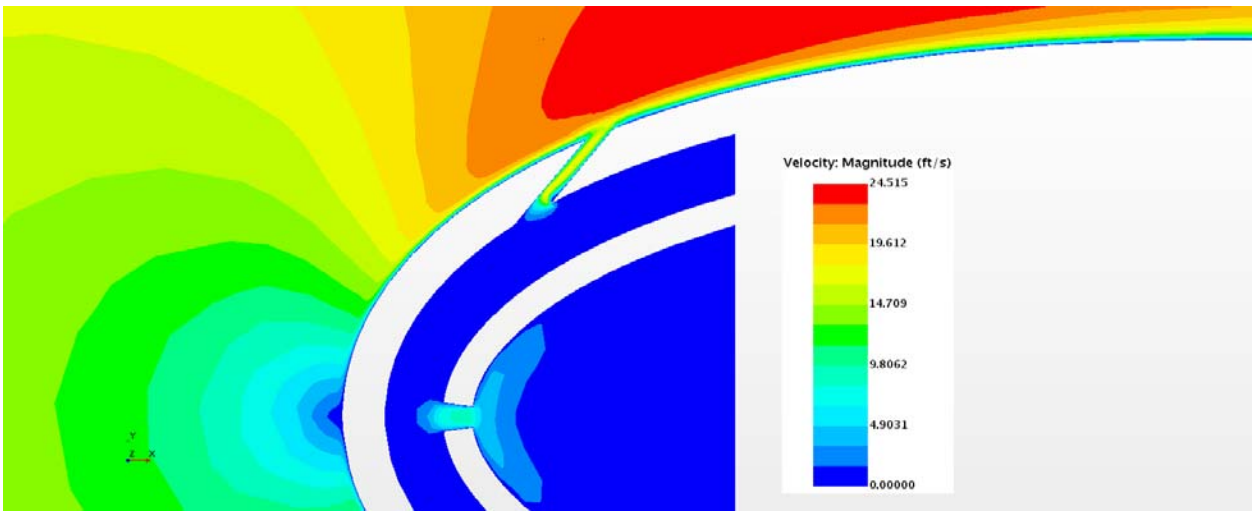

Figure 16.10: Case 1 – Velocity profile for center plane

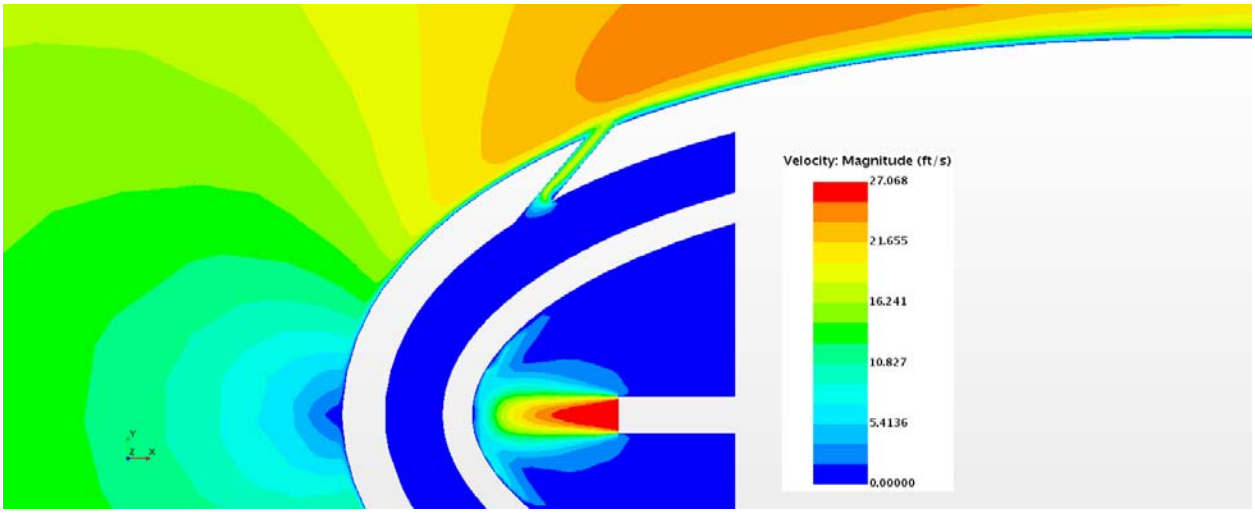

Figure 16.11: Case 1 – Velocity profile for off- center plane

Appendix G-2: M_b = 0.53, Tu = 5%, DR = 1.65

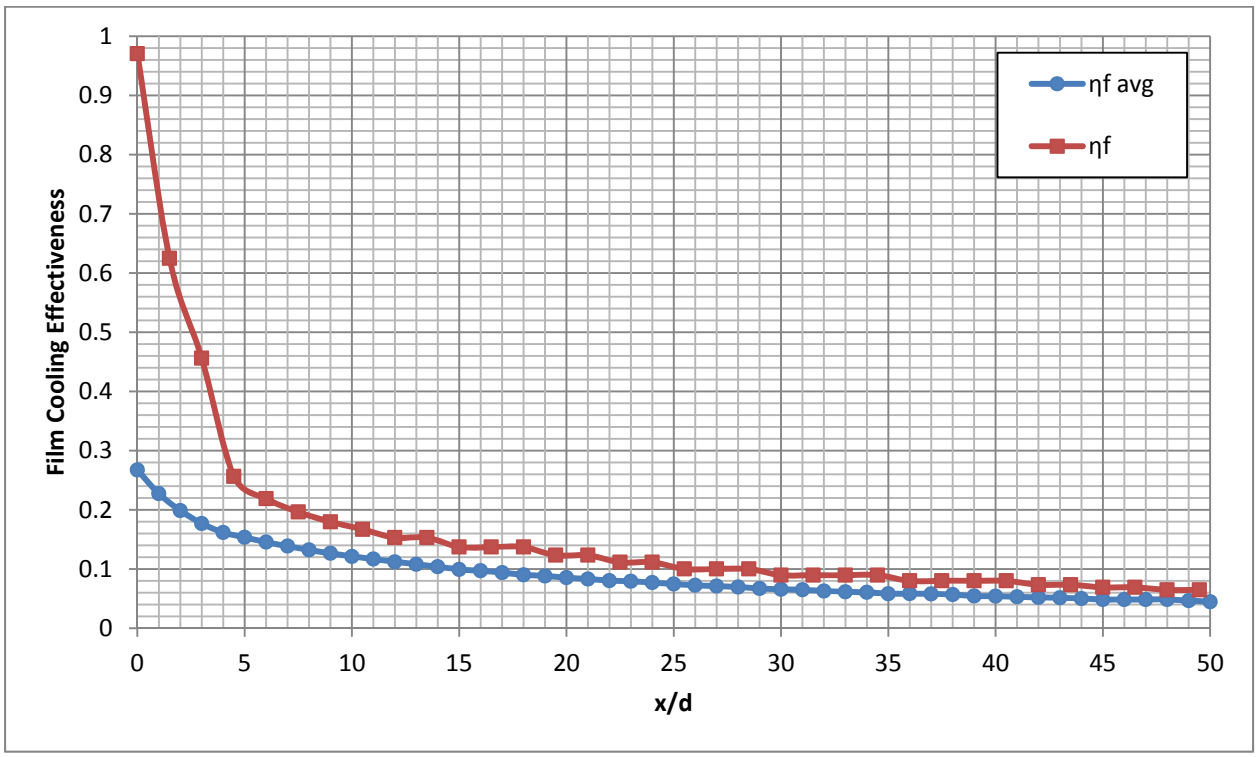

Figure 16.12: Case 2 - Laterally averaged and Centerline adiabatic film cooling effectiveness

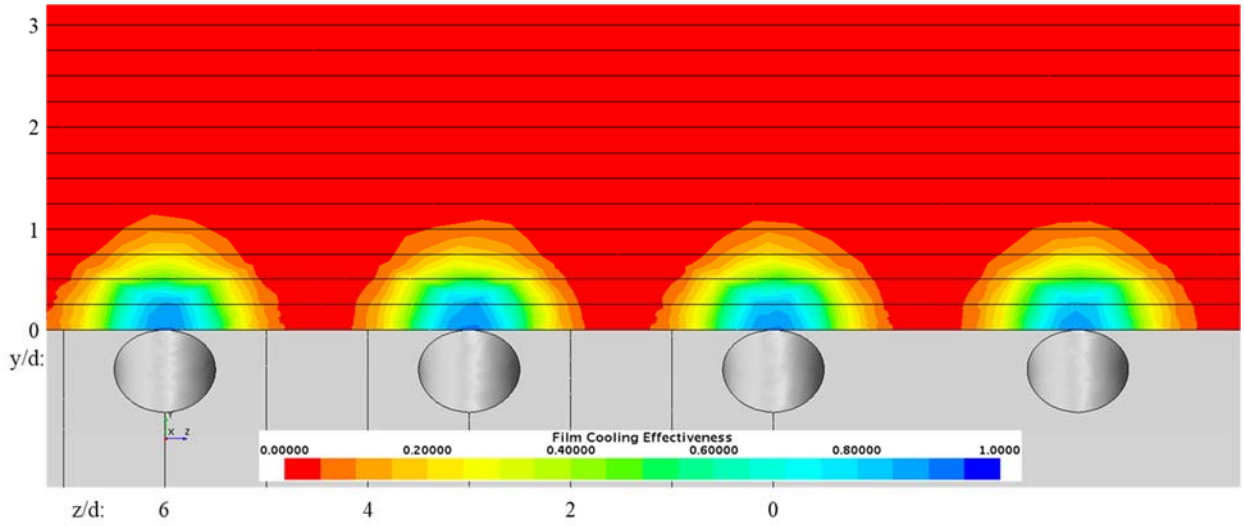

Figure 16.13: Case 2 - Spatial distribution of adiabatic film cooling effectiveness at x/d: 0

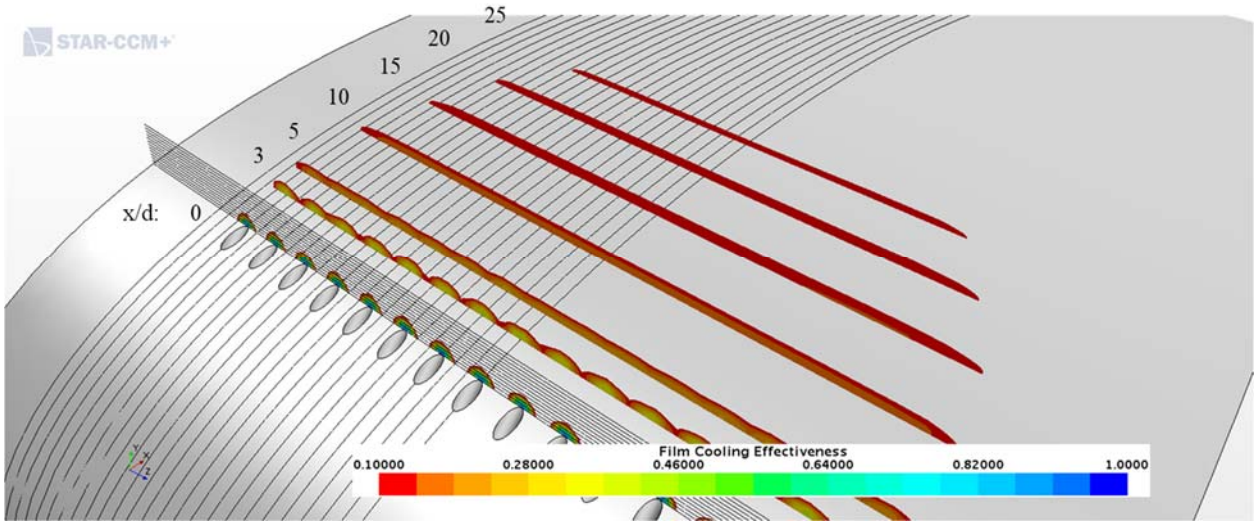

Figure 16.14: Case 2 - Streamwise spatial distribution of adiabatic film cooling effectiveness

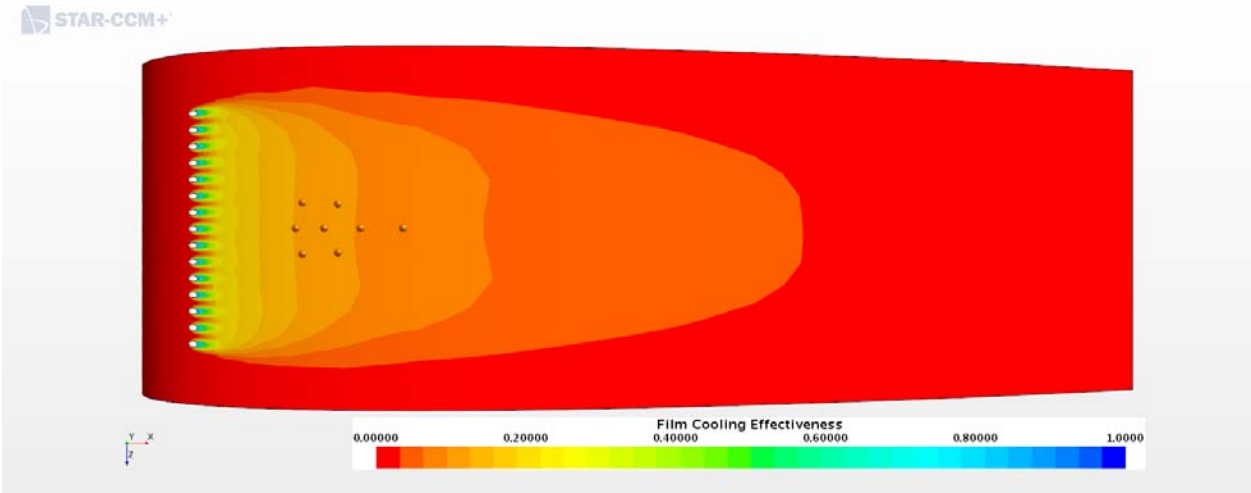

Figure 16.15: Case 2 - Adiabatic Film Cooling Effectiveness on the Suction Surface

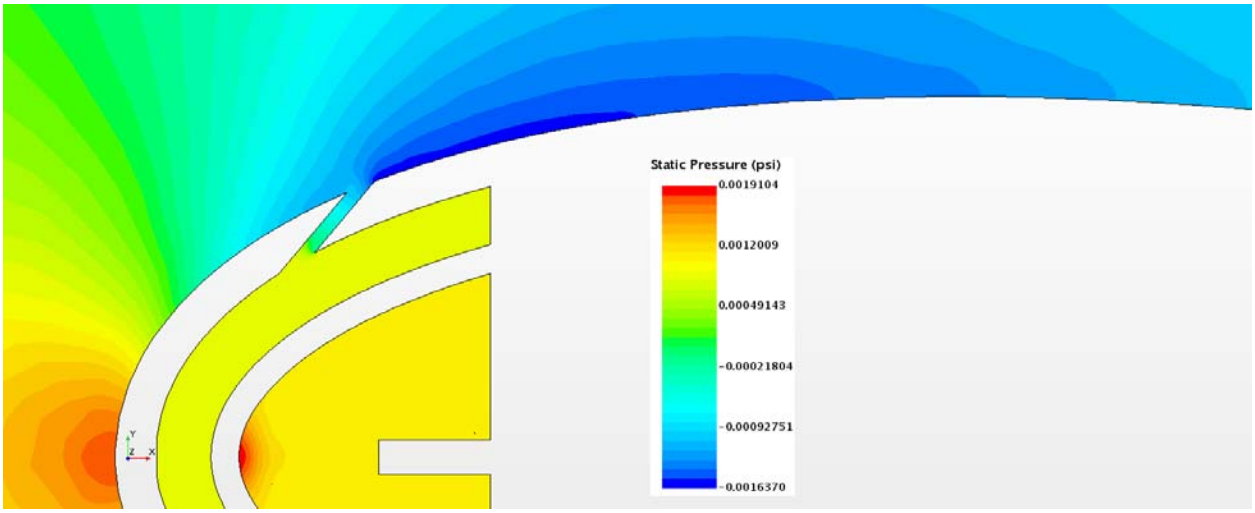

Figure 16.16: Case 2 – Static Pressure profile for center plane

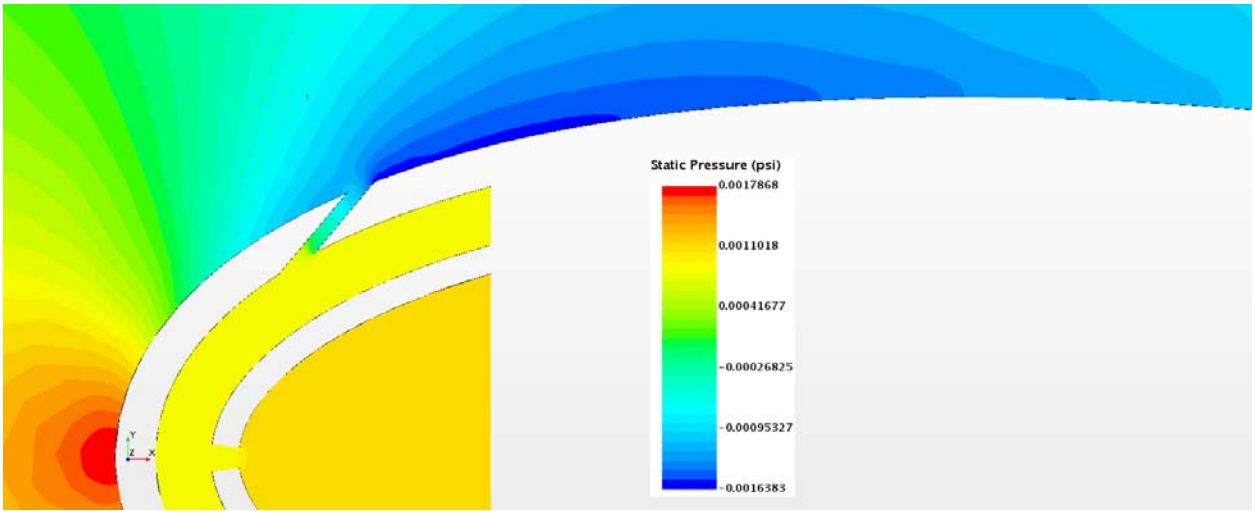

Figure 16.17: Case 2 – Static Pressure profile for off-center plane

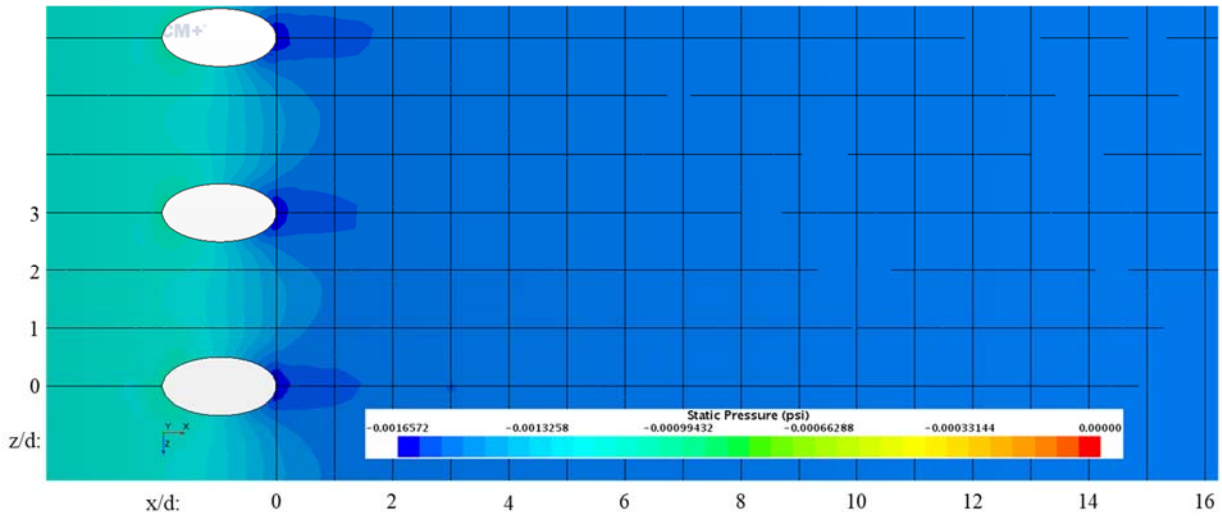

Figure 16.18: Case 2 – Static Pressure distribution for Suction Surface

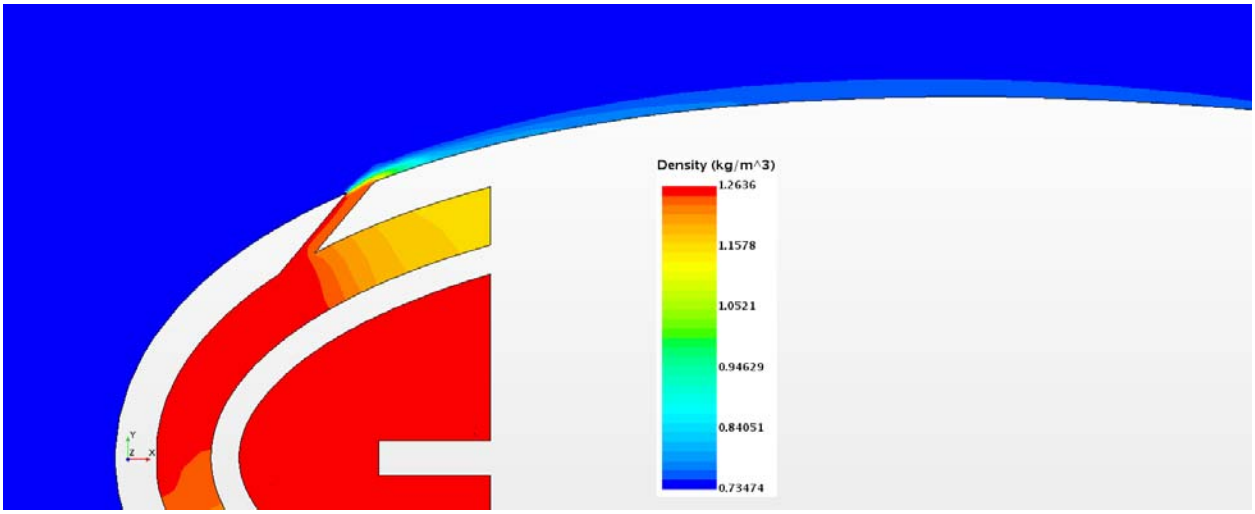

Figure 16.19: Case 2 – Density profile for center plane

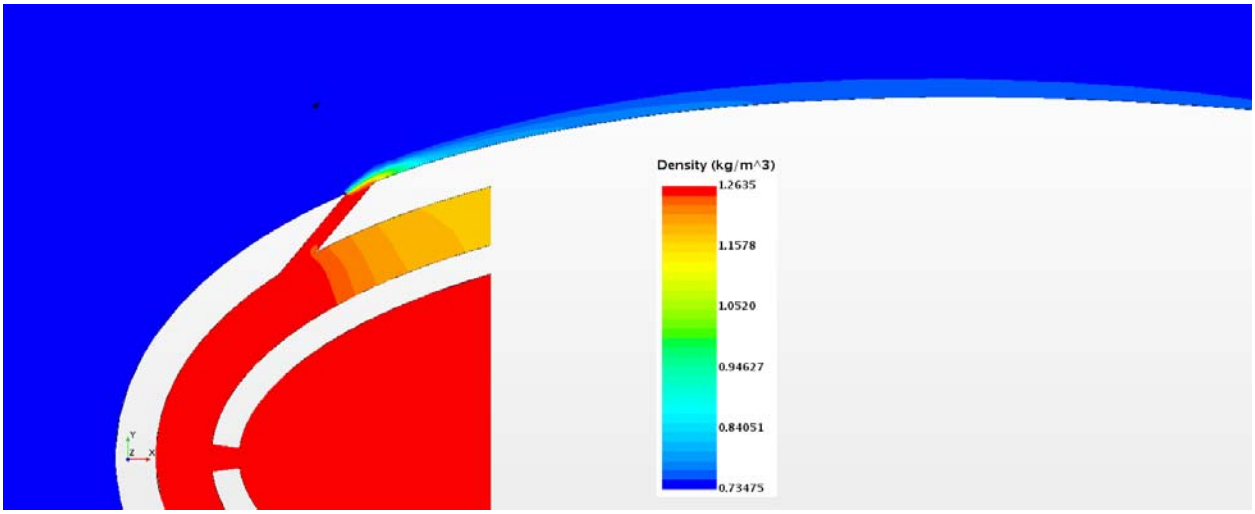

Figure 16.20: Case 2 – Density profile for off-center plane

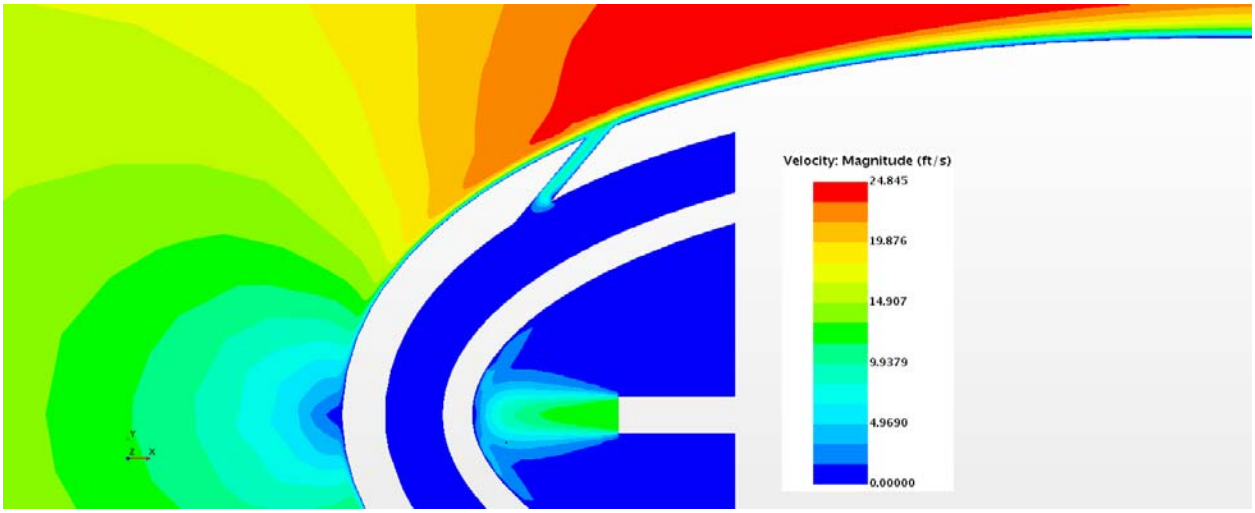

Figure 16.21: Case 2 – Velocity profile for center plane

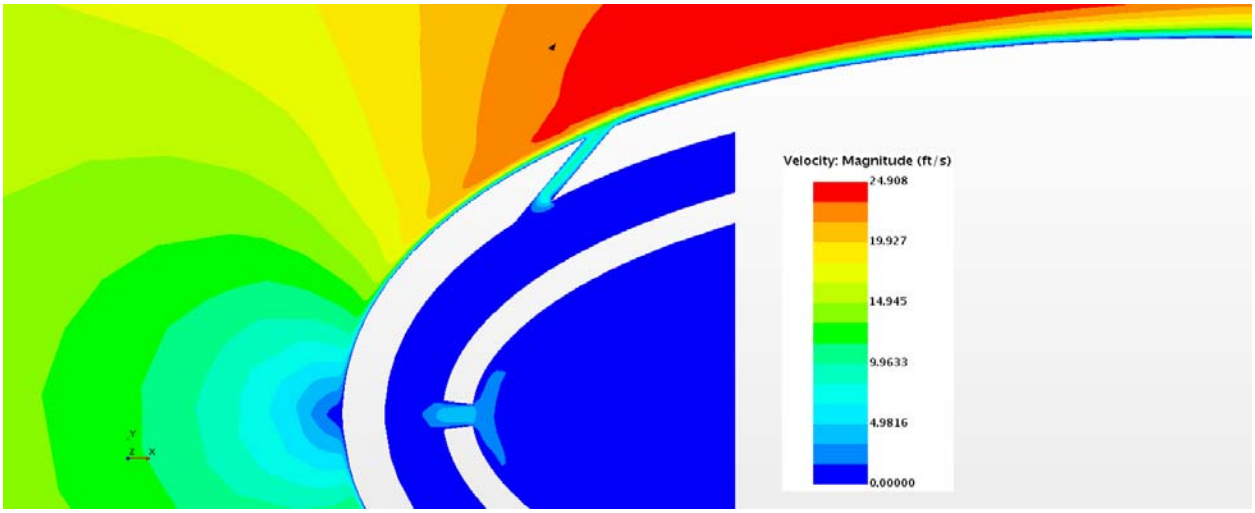

Figure 16.22: Case 2 – Velocity profile for off- center plane

Appendix G-3: M_b = 0.77, Tu = 5%, DR = 1.65

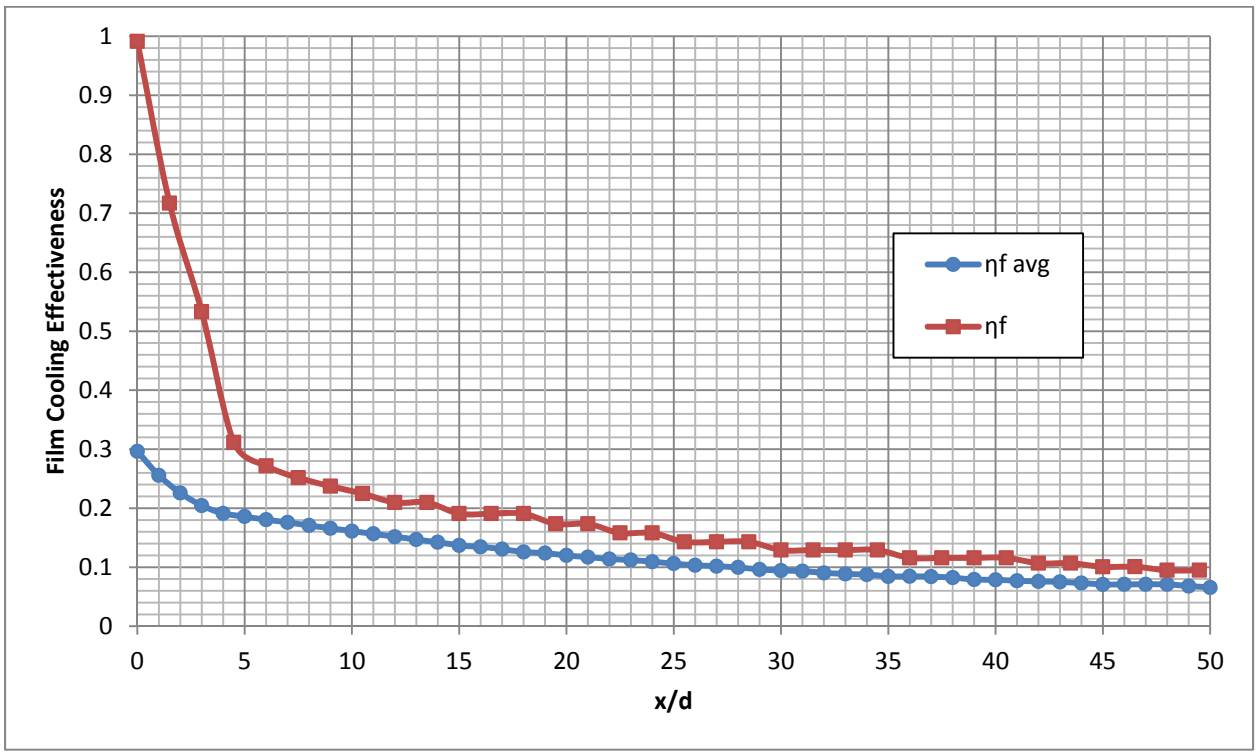

Figure 16.23: Case 3 - Laterally averaged and Centerline adiabatic film cooling effectiveness

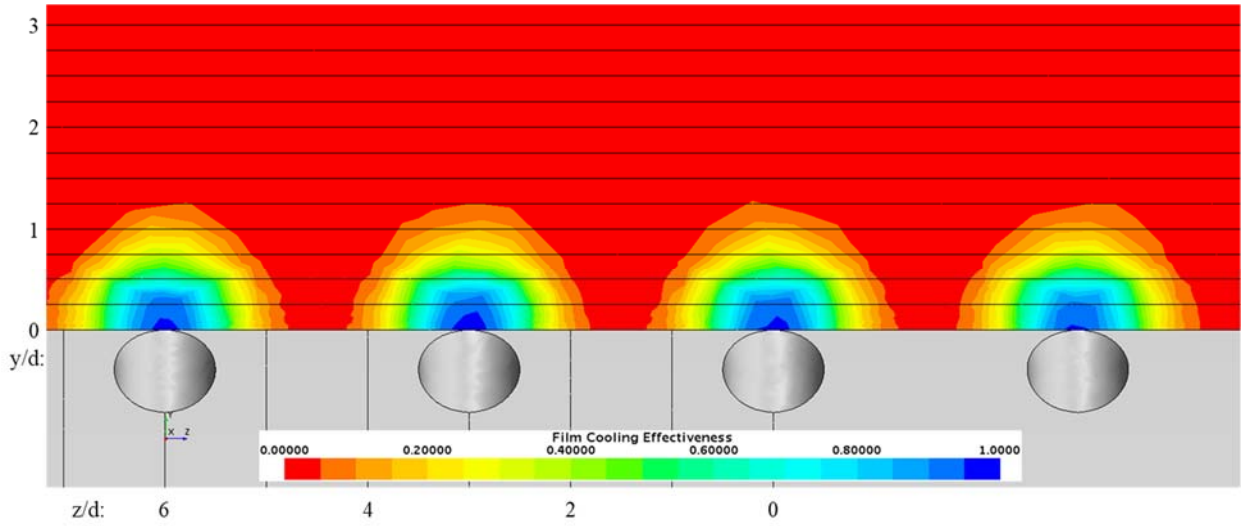

Figure 16.24: Case 3 - Spatial distribution of adiabatic film cooling effectiveness at x/d: 0

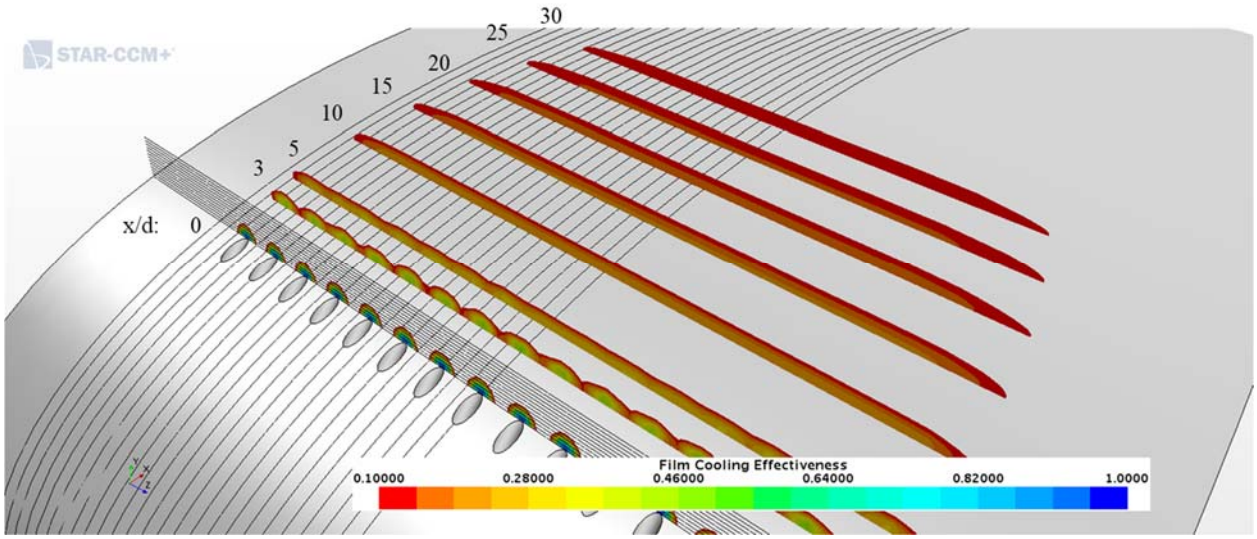

Figure 16.25: Case 3 - Streamwise spatial distribution of adiabatic film cooling effectiveness

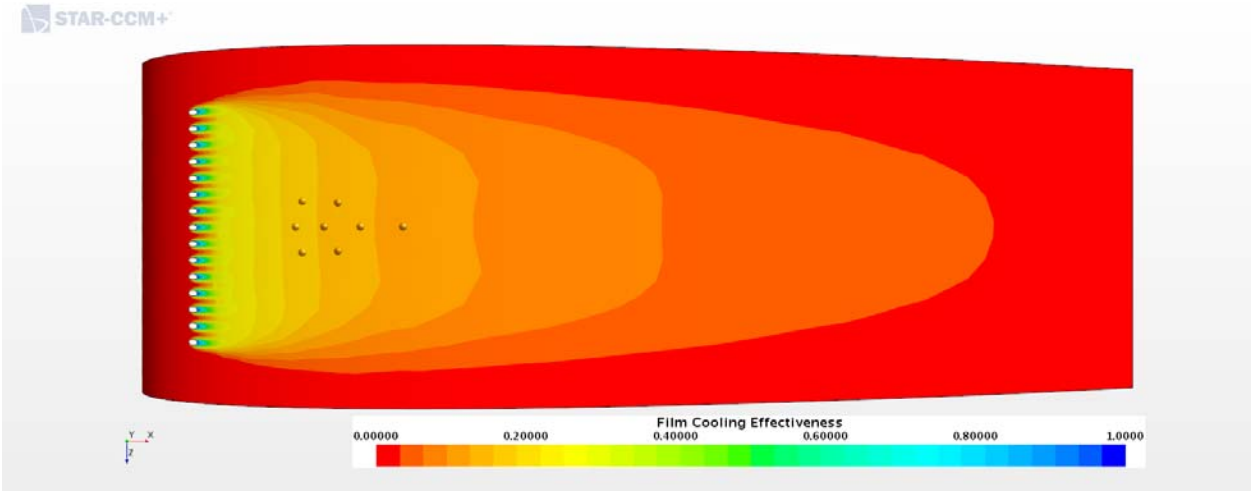

Figure 16.26: Case 3 - Adiabatic Film Cooling Effectiveness on the Suction Surface

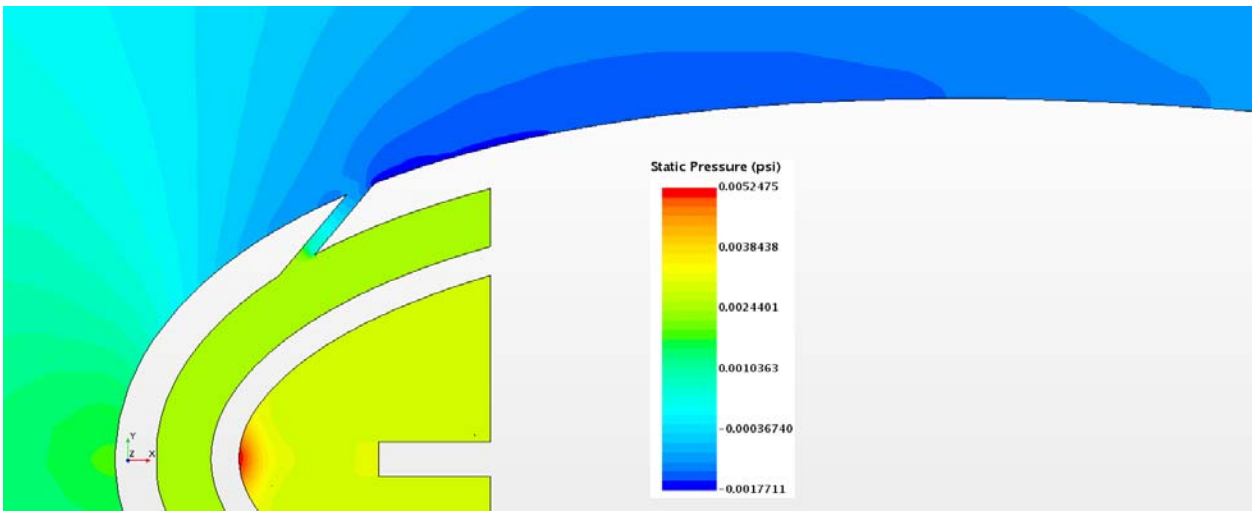

Figure 16.27: Case 3 – Static Pressure profile for center plane

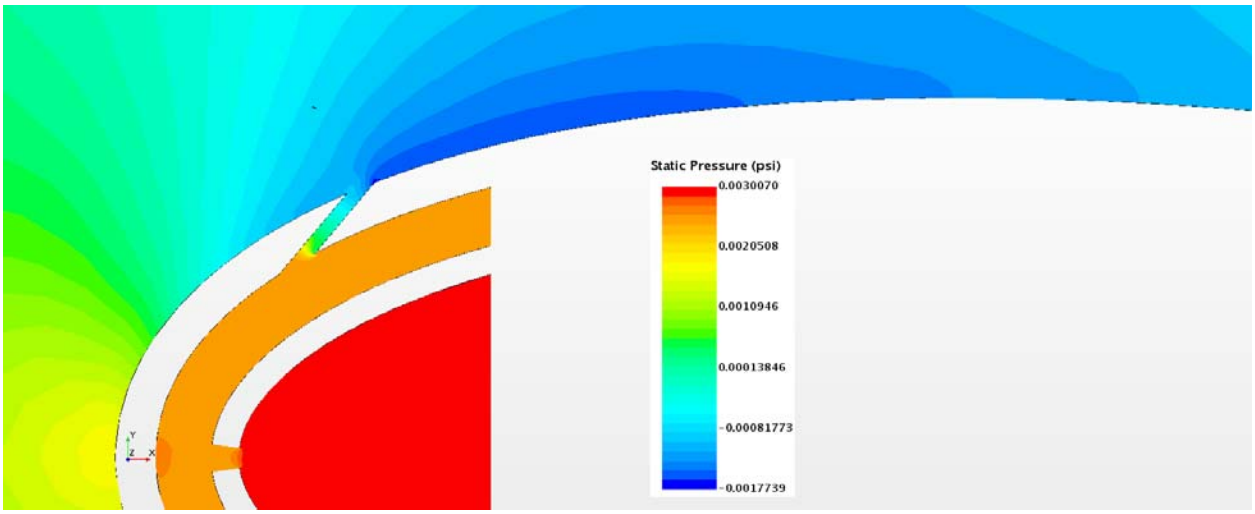

Figure 16.28: Case 3 – Static Pressure profile for off-center plane

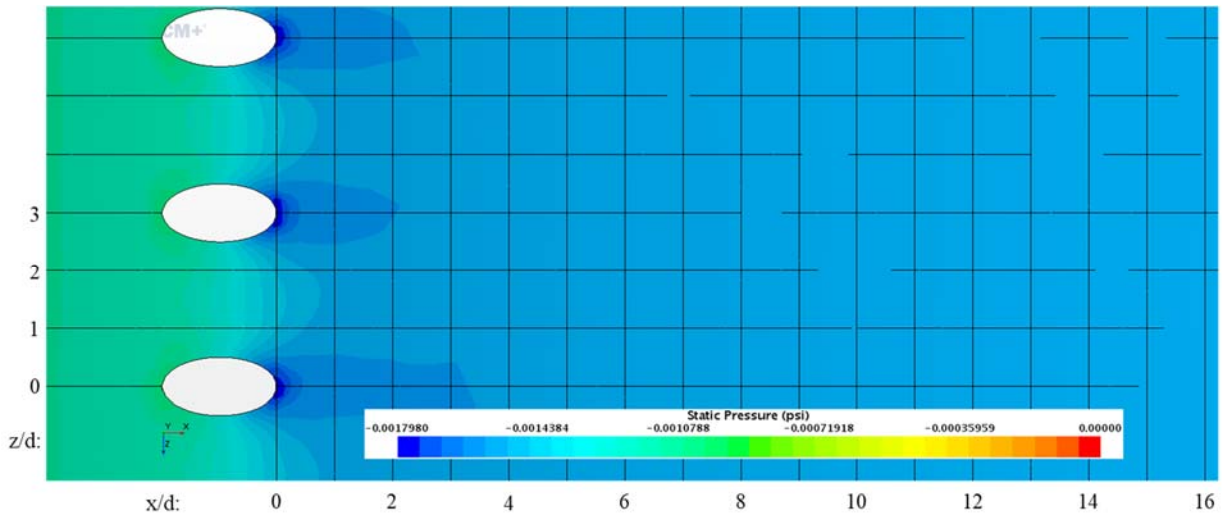

Figure 16.29: Case 3 – Static Pressure distribution for Suction Surface

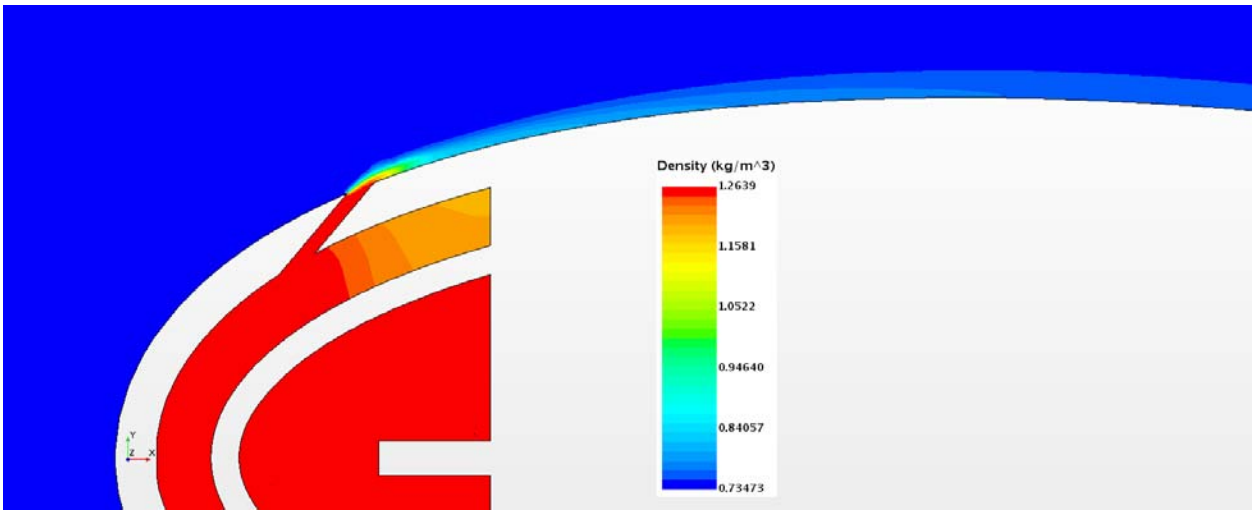

Figure 16.30: Case 3 – Density profile for center plane

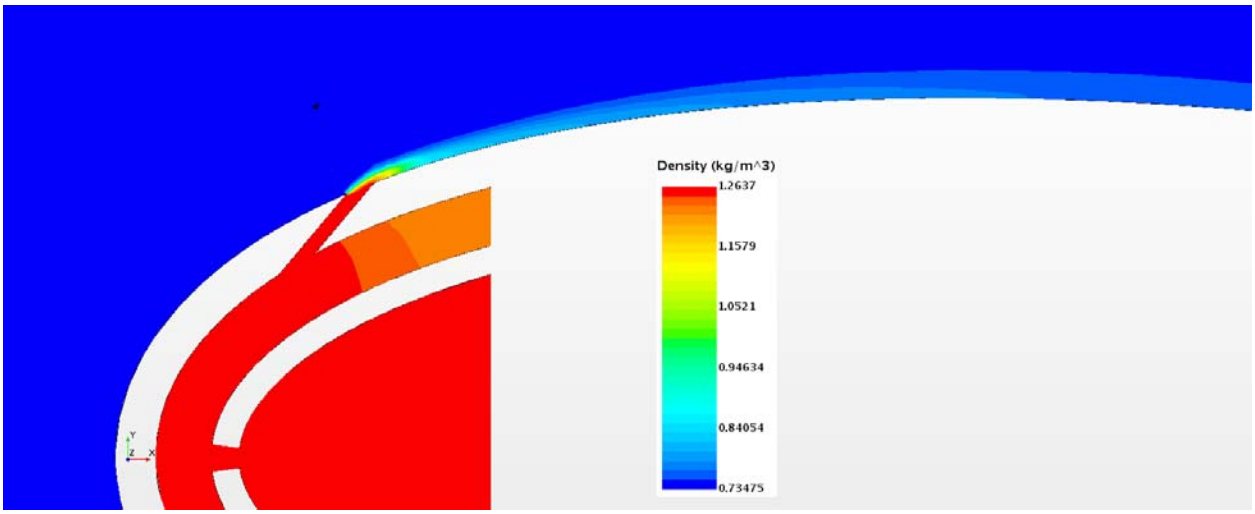

Figure 16.31: Case 3 – Density profile for off-center plane

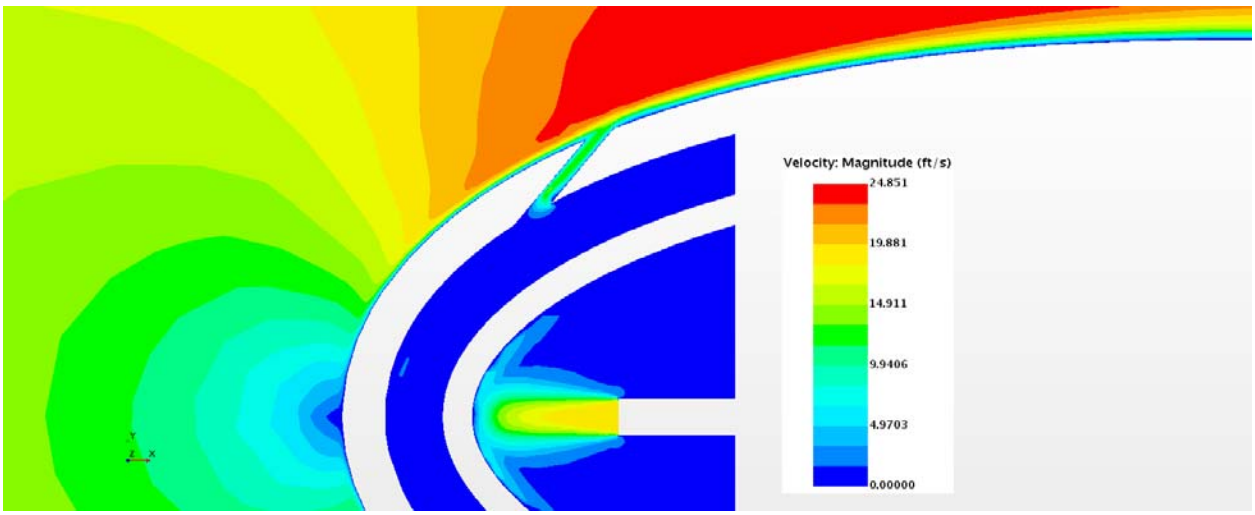

Figure 16.32: Case 3 – Velocity profile for center plane

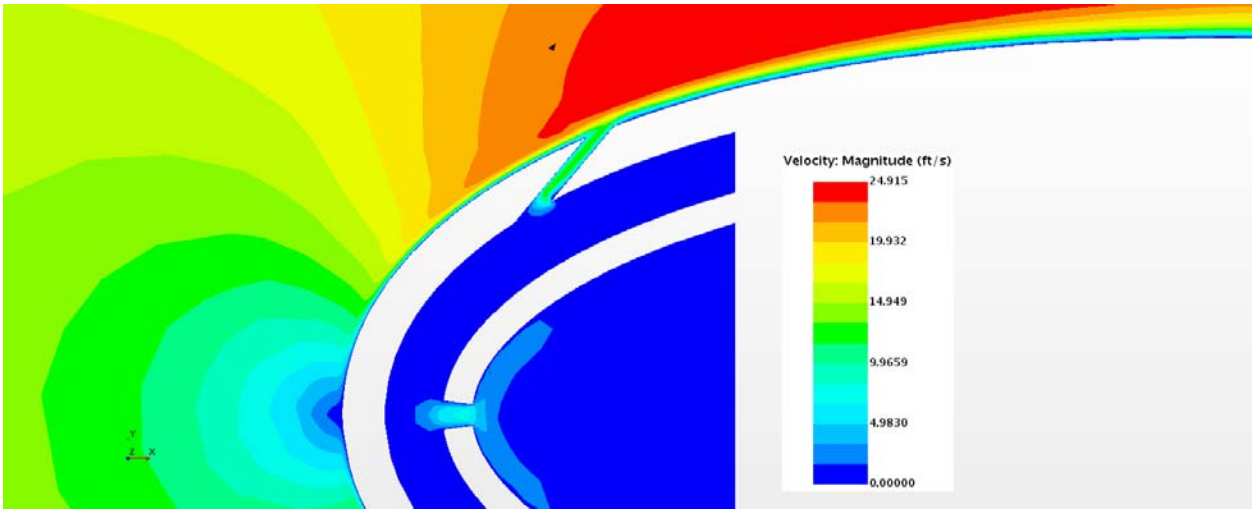

Figure 16.33: Case 3 – Velocity profile for off- center plane

Appendix G-4: M_b = 0.98, Tu = 5%, DR = 1.65

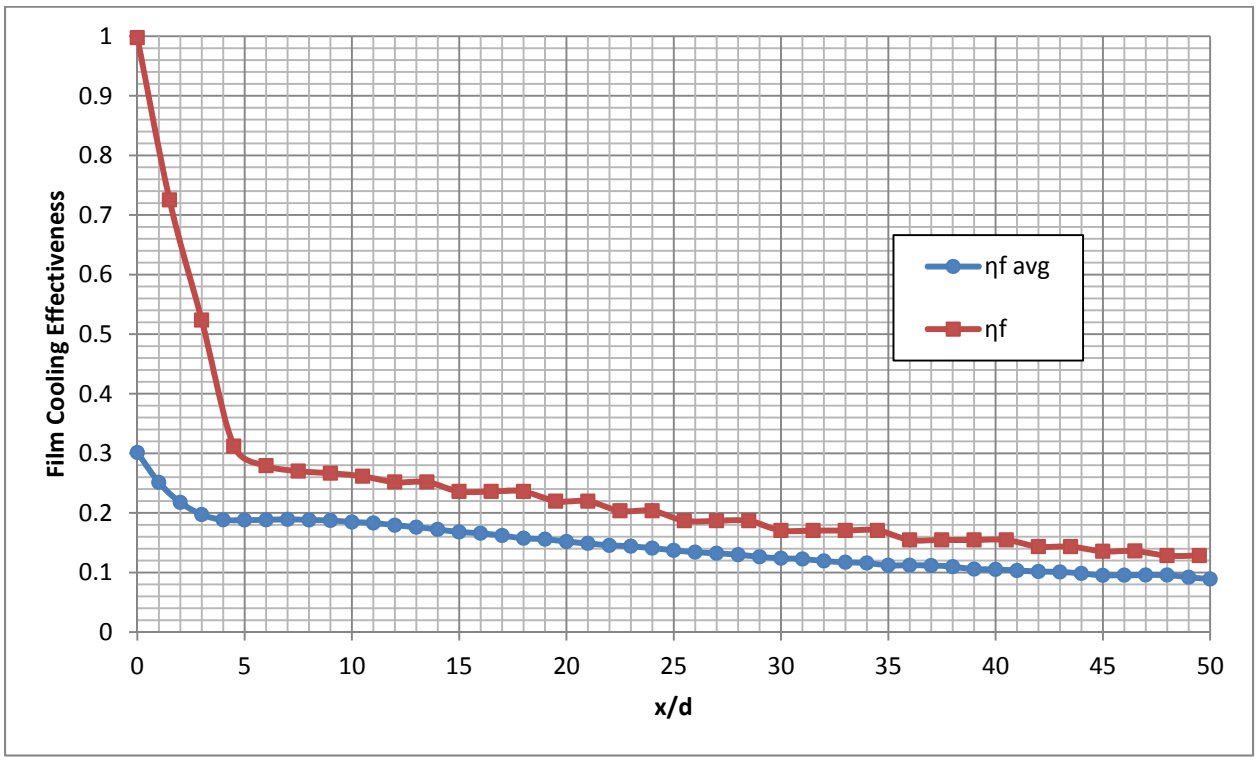

Figure 16.34: Case 4 - Laterally averaged and Centerline adiabatic film cooling effectiveness

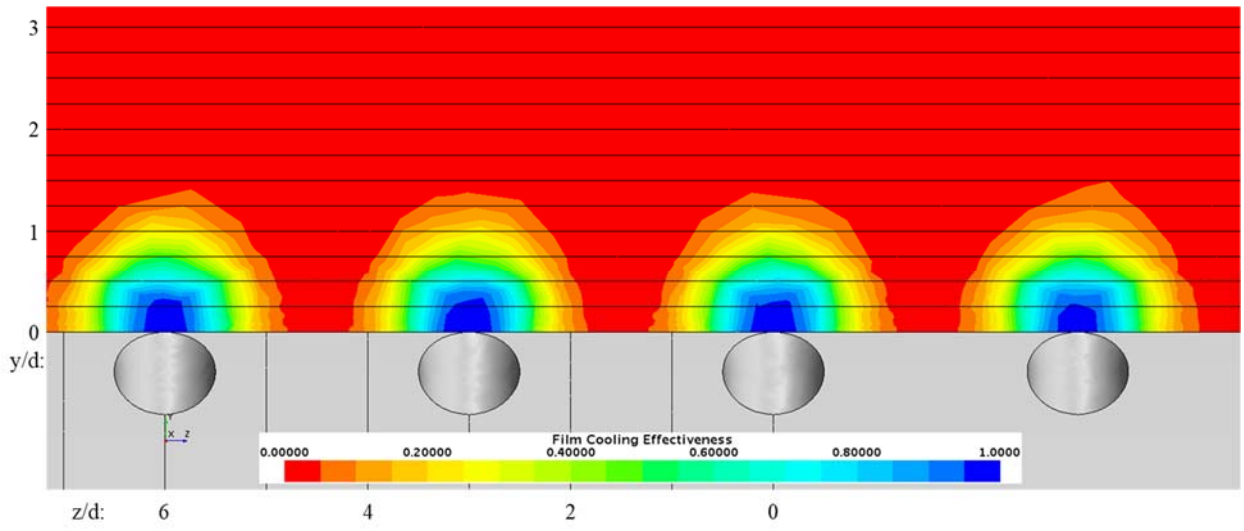

Figure 16.35: Case 4 - Spatial distribution of adiabatic film cooling effectiveness at x/d: 0

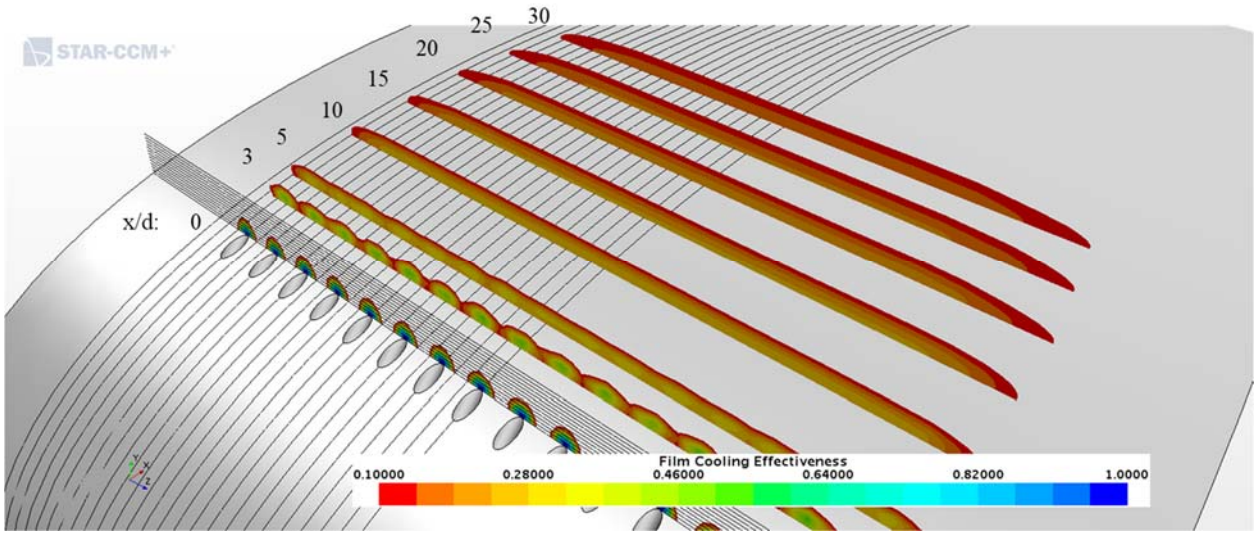

Figure 16.36: Case 4 - Streamwise spatial distribution of adiabatic film cooling effectiveness

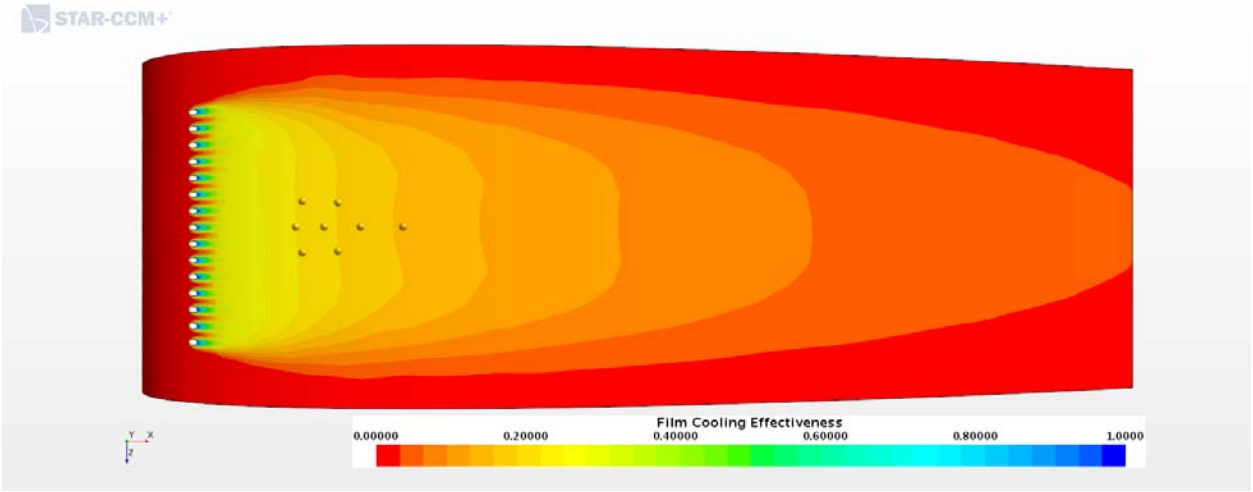

Figure 16.37: Case 4 - Adiabatic Film Cooling Effectiveness on the Suction Surface

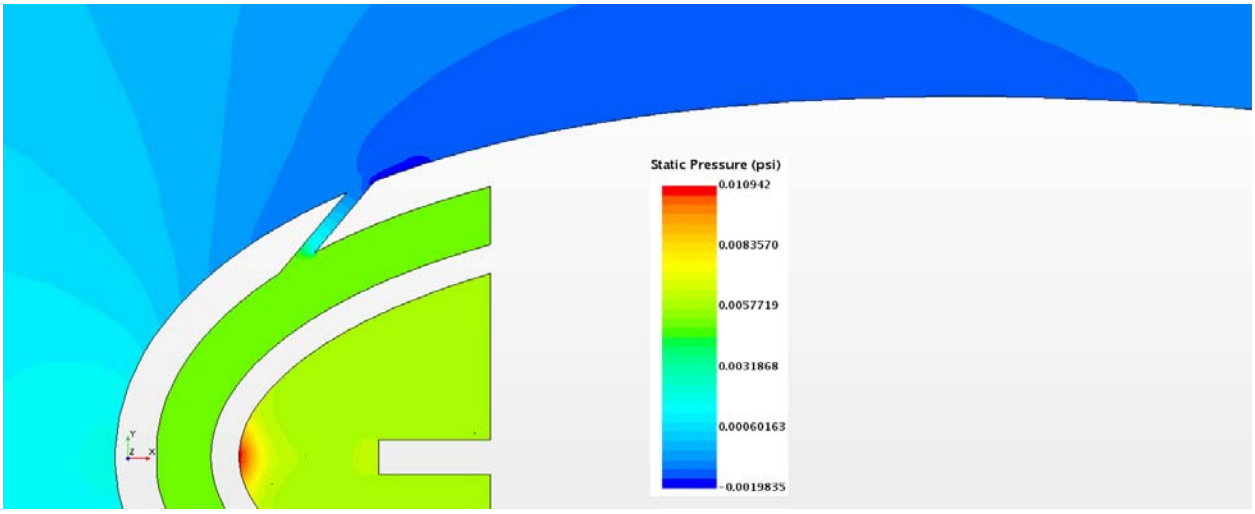

Figure 16.38: Case 4 – Static Pressure profile for center plane

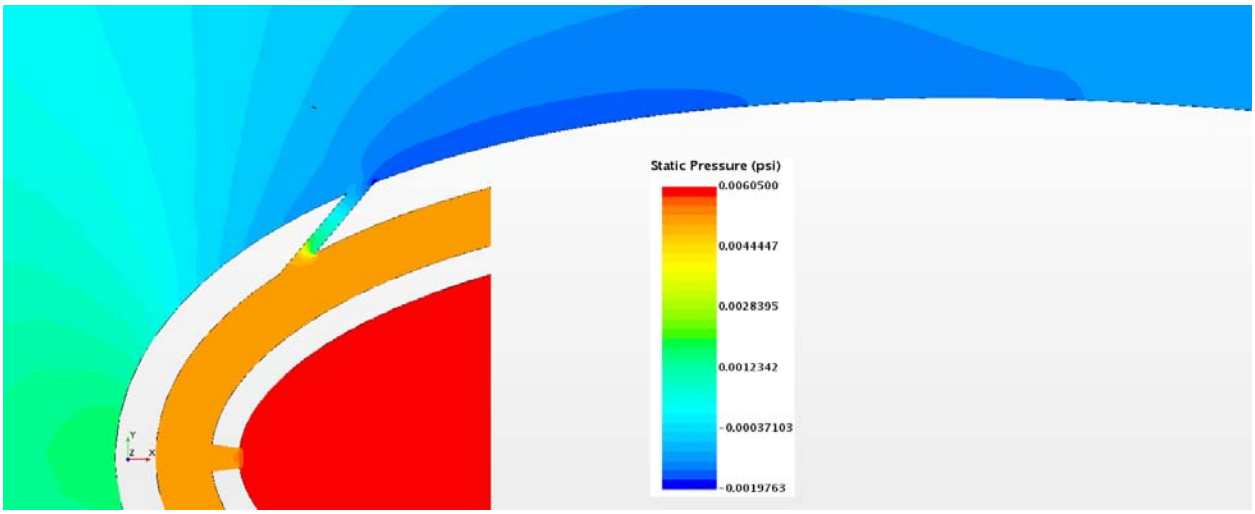

Figure 16.39: Case 4 – Static Pressure profile for off-center plane

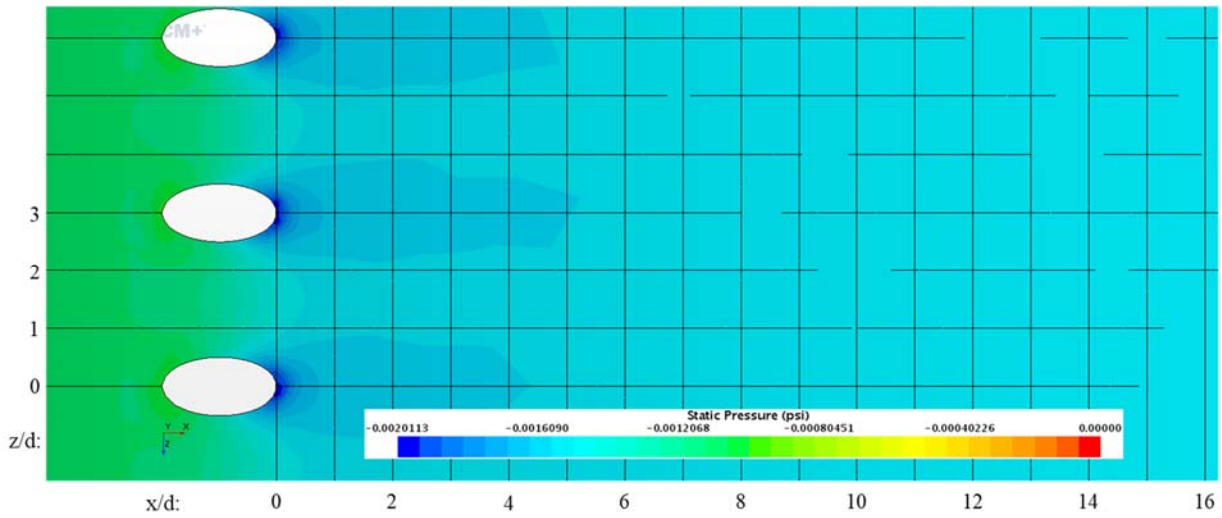

Figure 16.40: Case 4 – Static Pressure distribution for Suction Surface

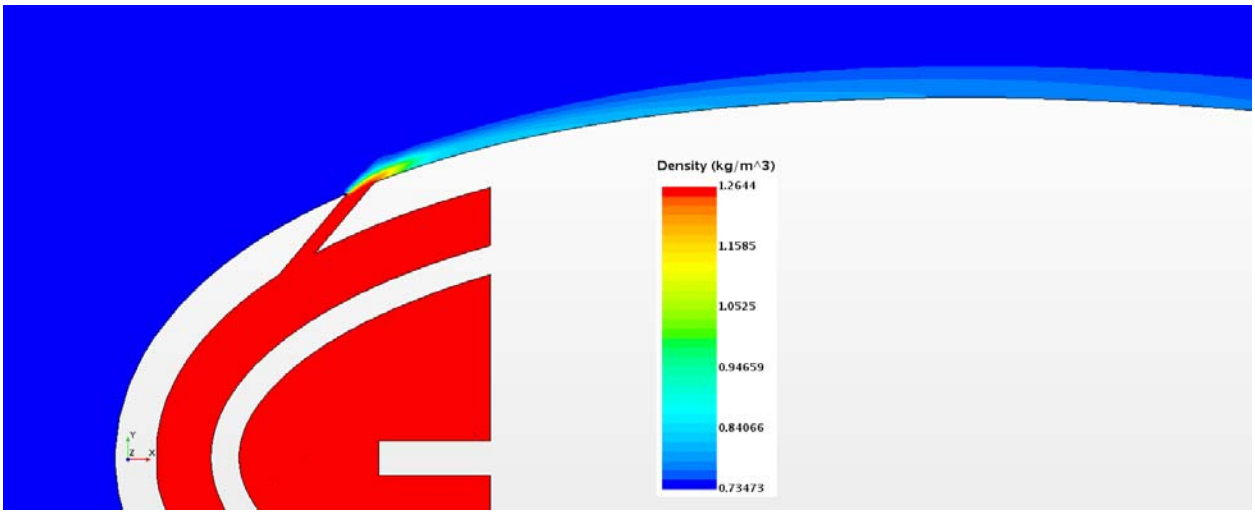

Figure 16.41: Case 4 – Density profile for center plane

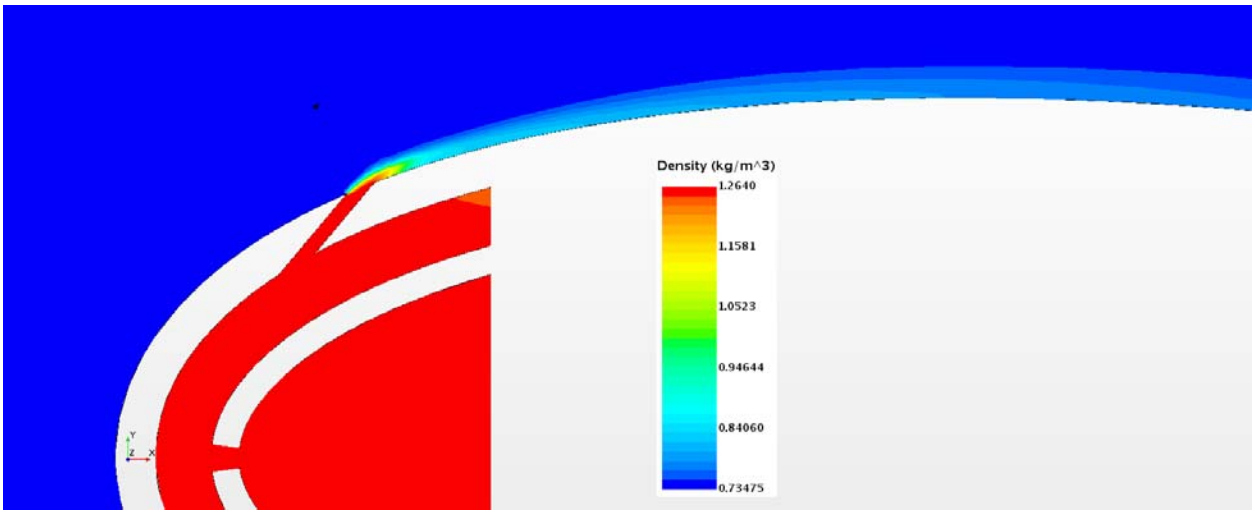

Figure 16.42: Case 4 – Density profile for off-center plane

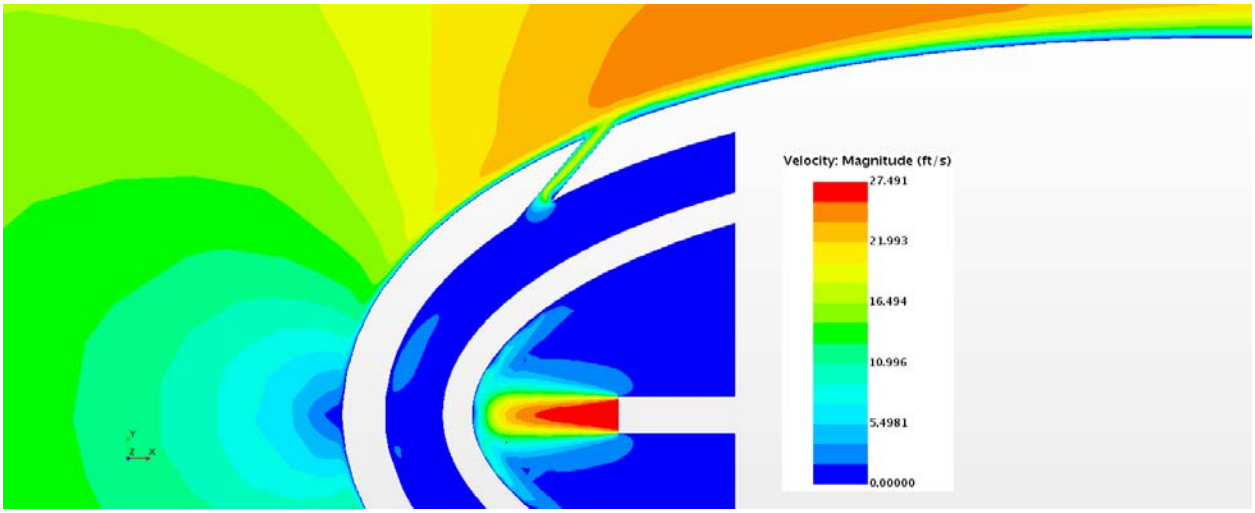

Figure 16.43: Case 4 – Velocity profile for center plane

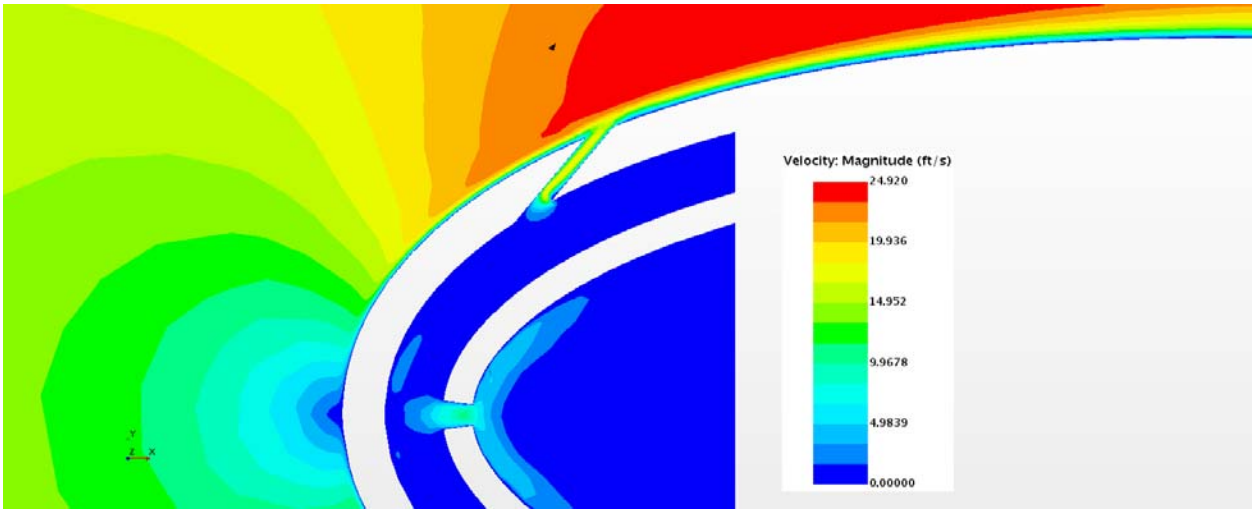

Figure 16.44: Case 4 – Velocity profile for off- center plane

Appendix G-5: M_b = 1.51, Tu = 5%, DR = 1.65

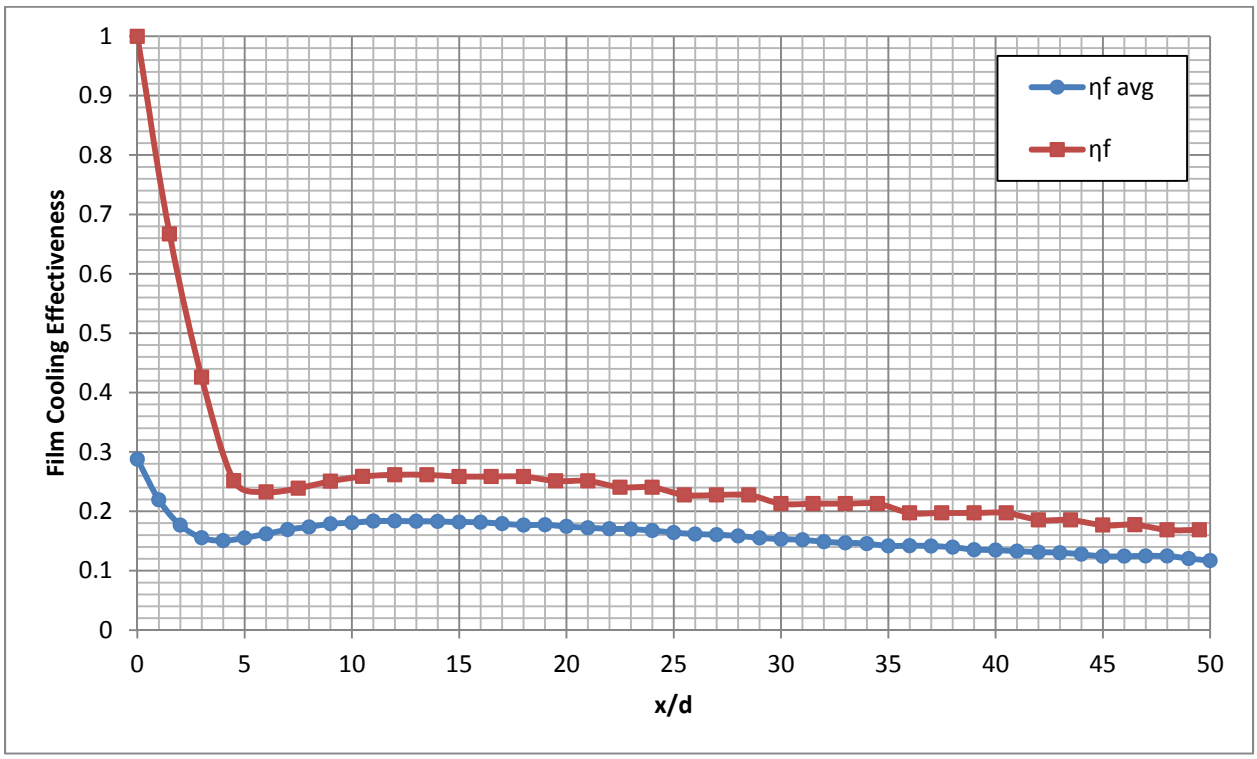

Figure 16.45: Case 5 - Laterally averaged and Centerline adiabatic film cooling effectiveness

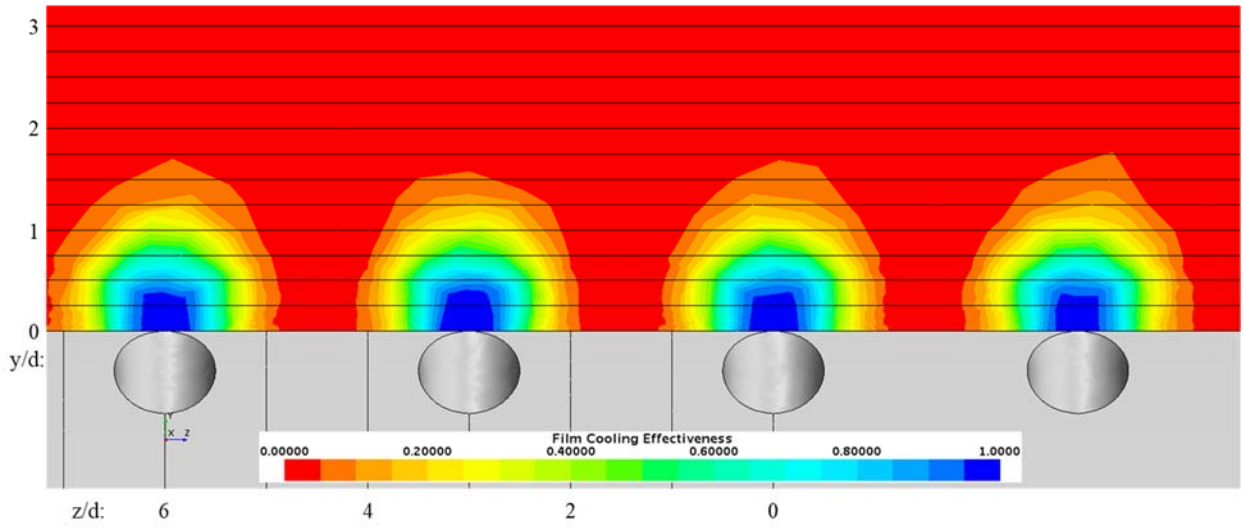

Figure 16.46: Case 5 - Spatial distribution of adiabatic film cooling effectiveness at x/d: 0

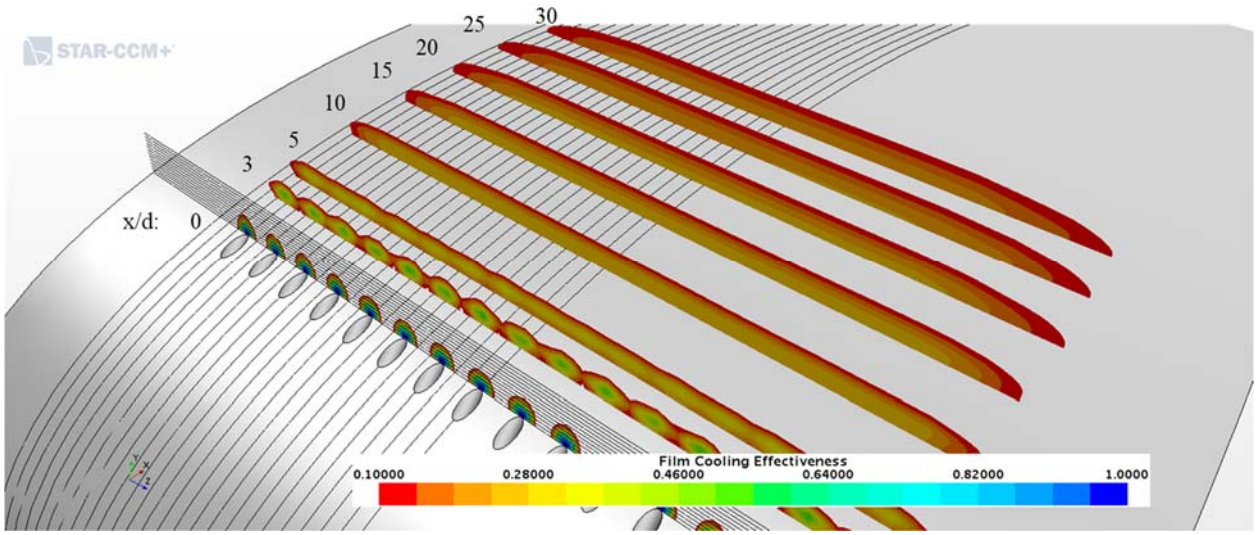

Figure 16.47: Case 5 - Streamwise spatial distribution of adiabatic film cooling effectiveness

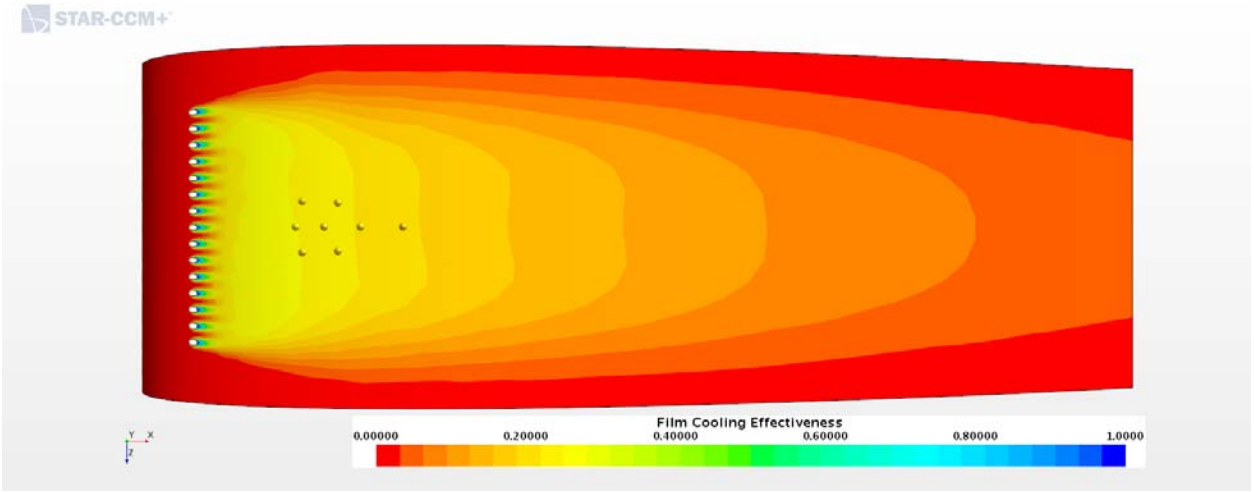

Figure 16.48: Case 5 - Adiabatic Film Cooling Effectiveness on the Suction Surface

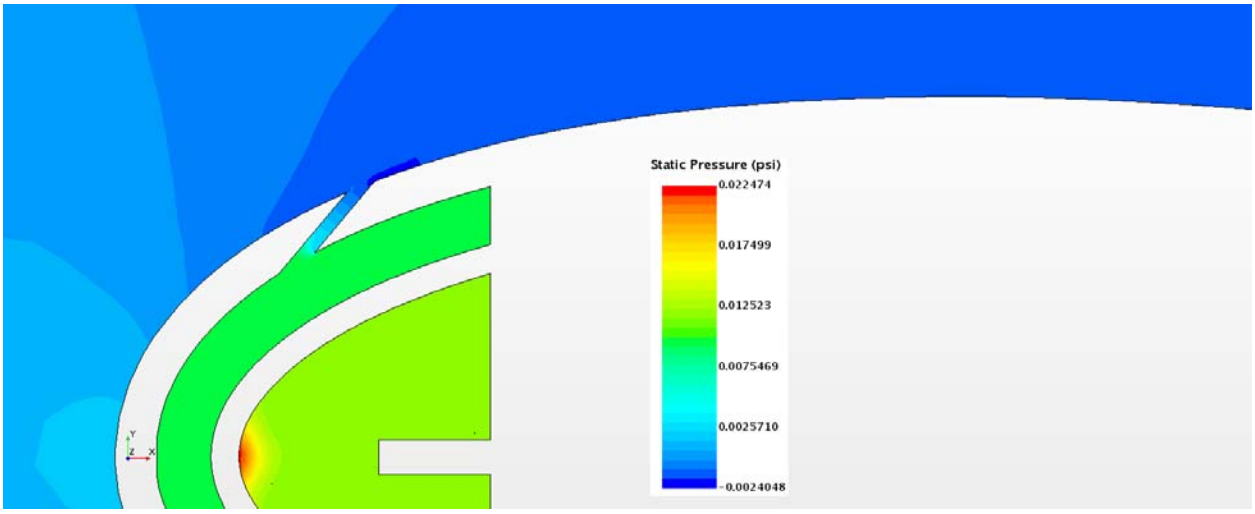

Figure 16.49: Case 5 – Static Pressure profile for center plane

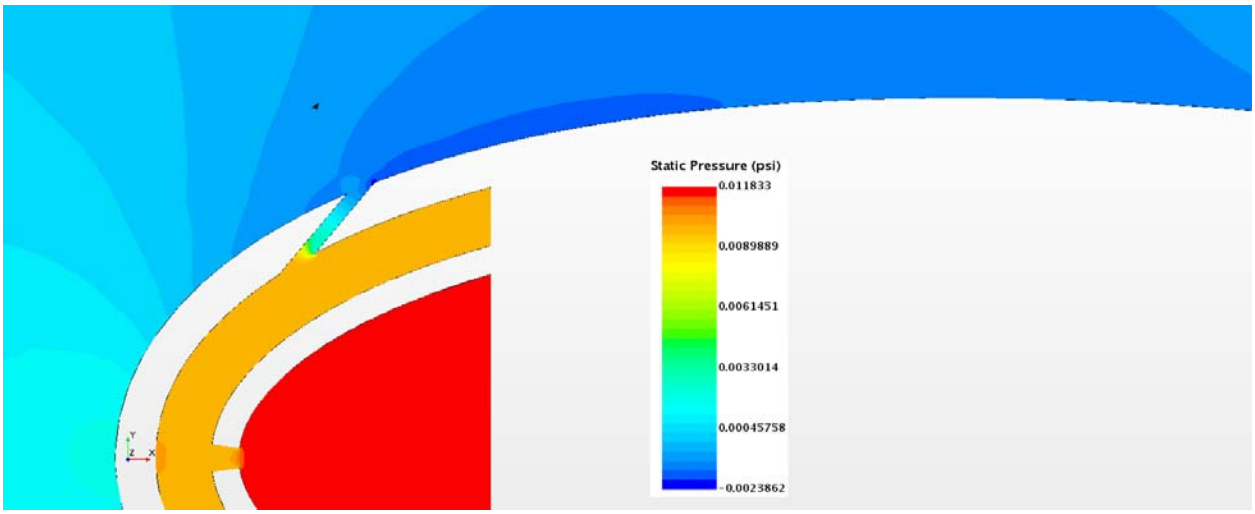

Figure 16.50: Case 5 – Static Pressure profile for off-center plane

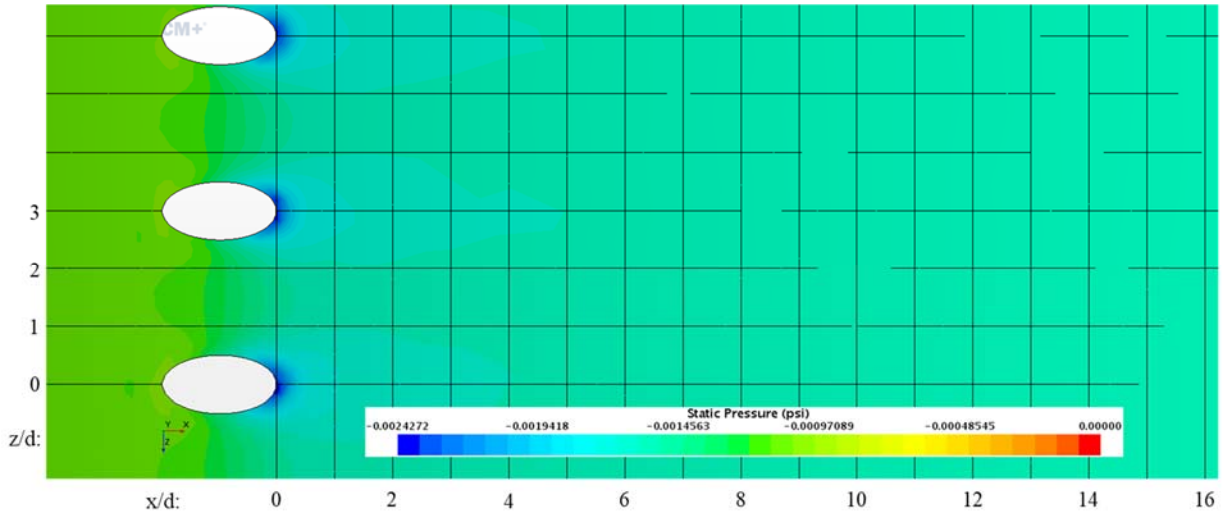

Figure 16.51: Case 5 – Static Pressure distribution for Suction Surface

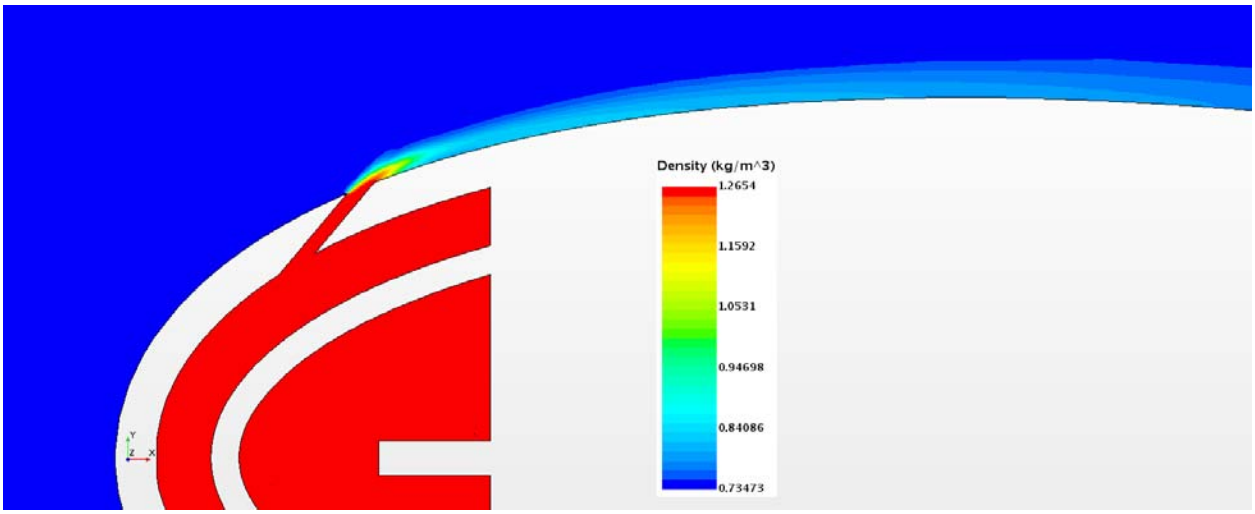

Figure 16.52: Case 5 – Density profile for center plane

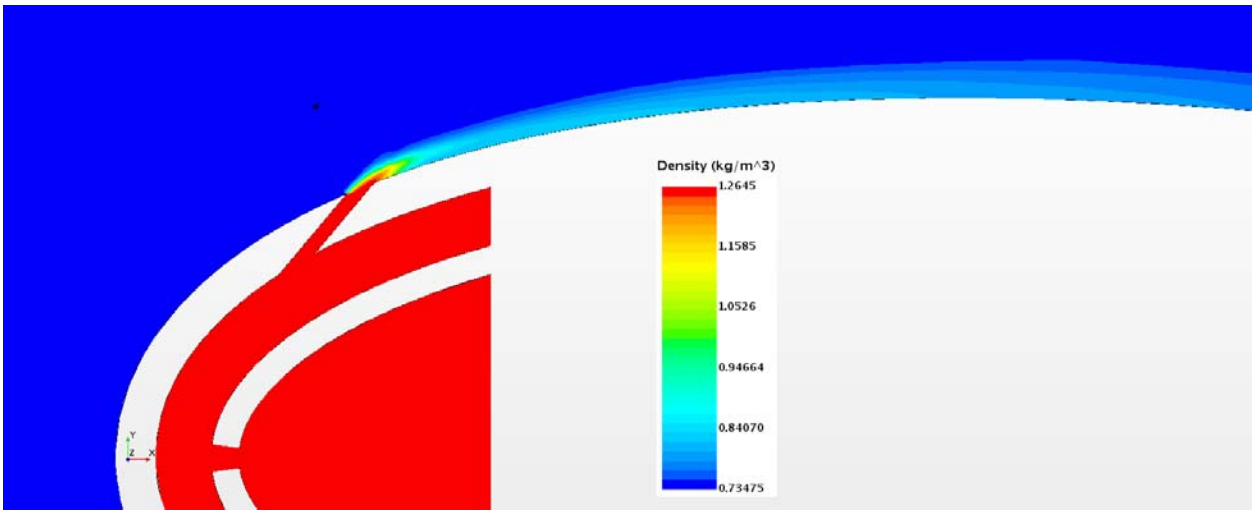

Figure 16.53: Case 5 – Density profile for off-center plane

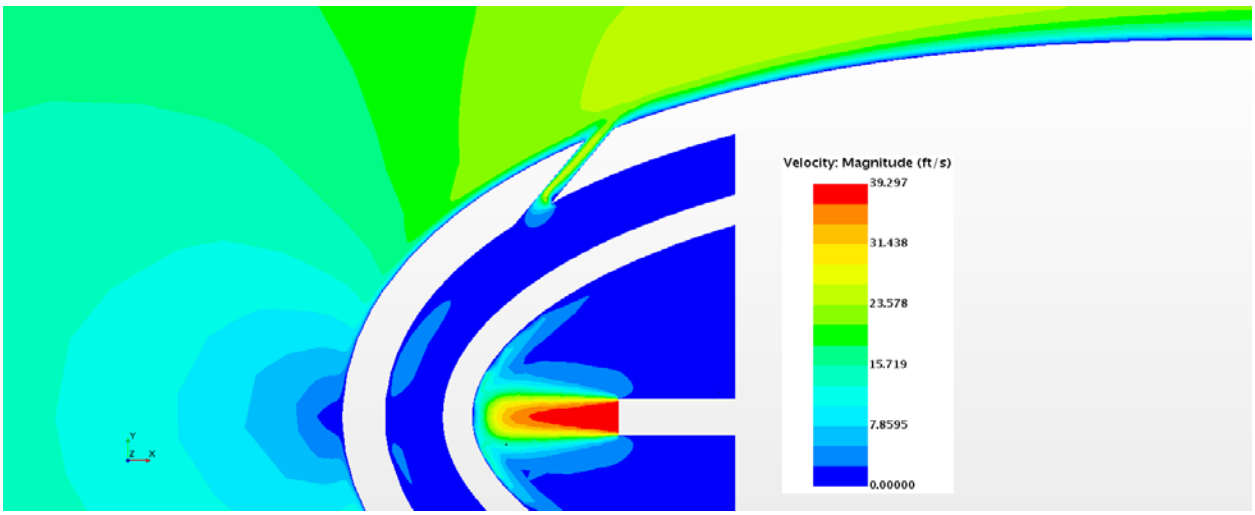

Figure 16.54: Case 5 – Velocity profile for center plane

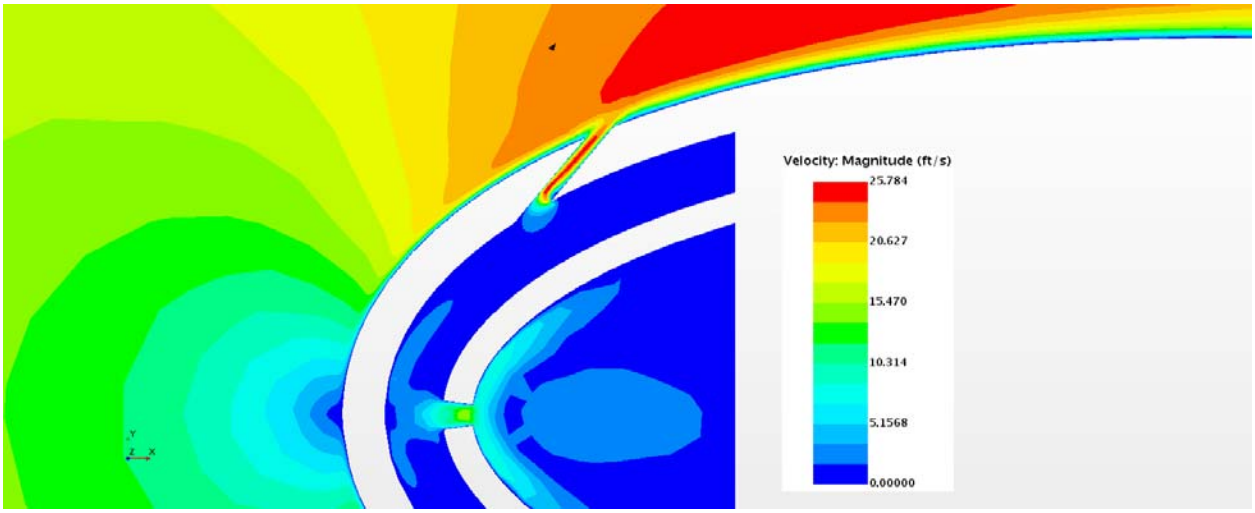

Figure 16.55: Case 5 – Velocity profile for off- center plane

Appendix G-6: M_b = 2.13, Tu = 5%, DR = 1.65

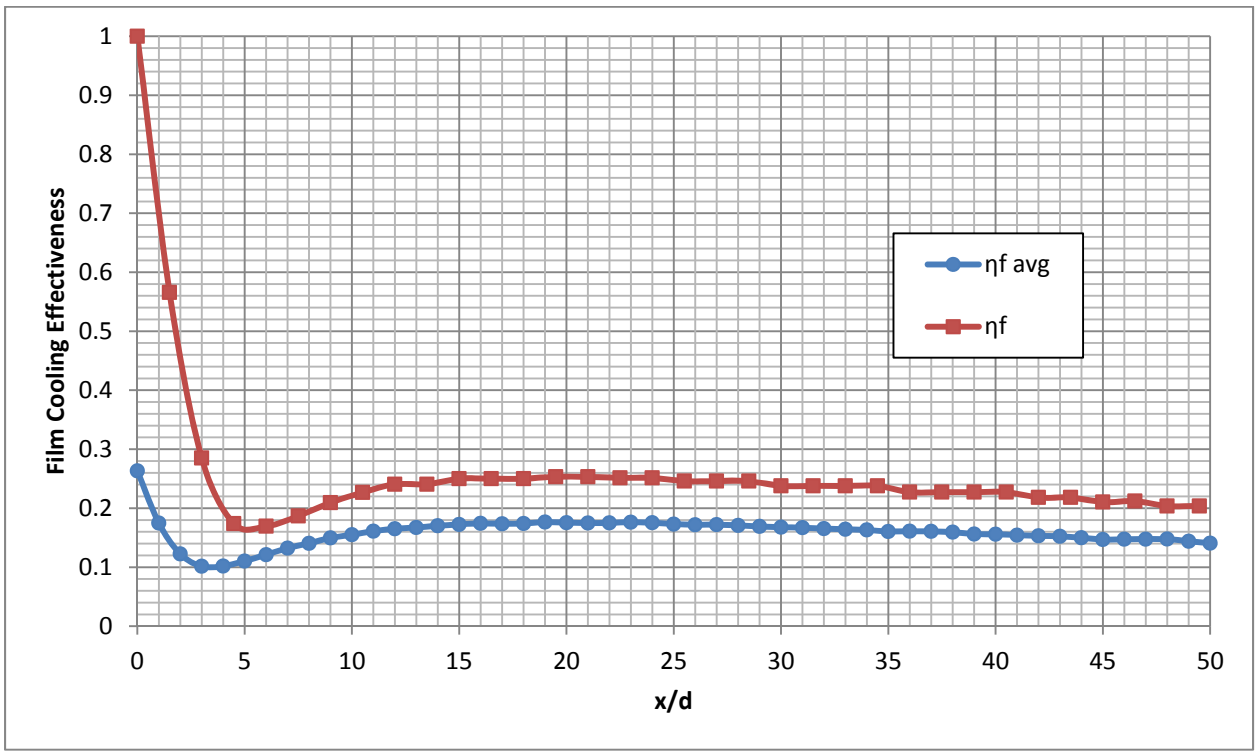

Figure 16.56: Case 6 - Laterally averaged and Centerline adiabatic film cooling effectiveness

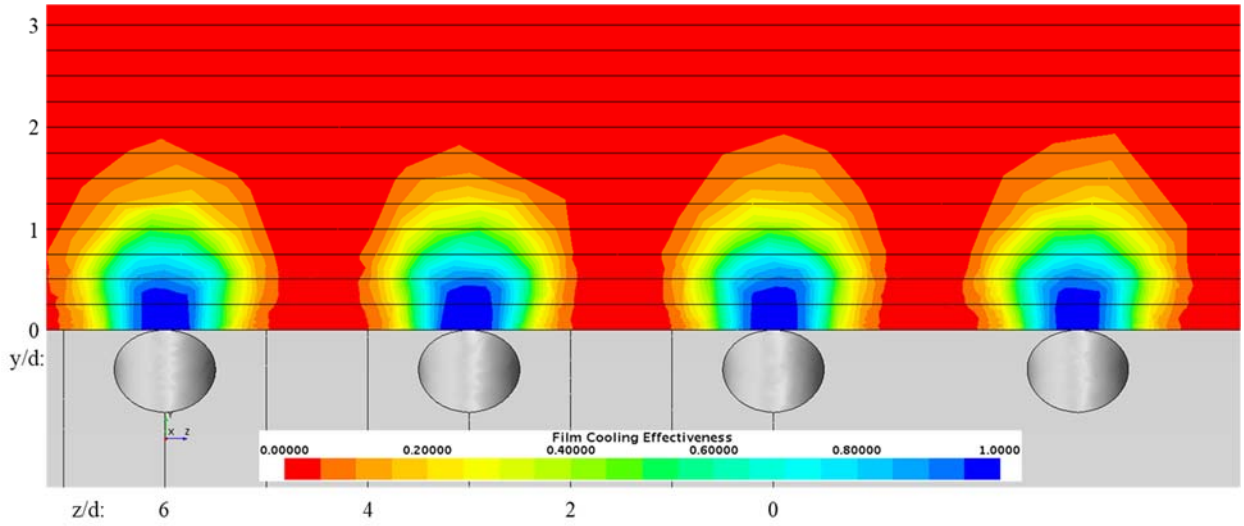

Figure 16.57: Case 6 - Spatial distribution of adiabatic film cooling effectiveness at x/d: 0

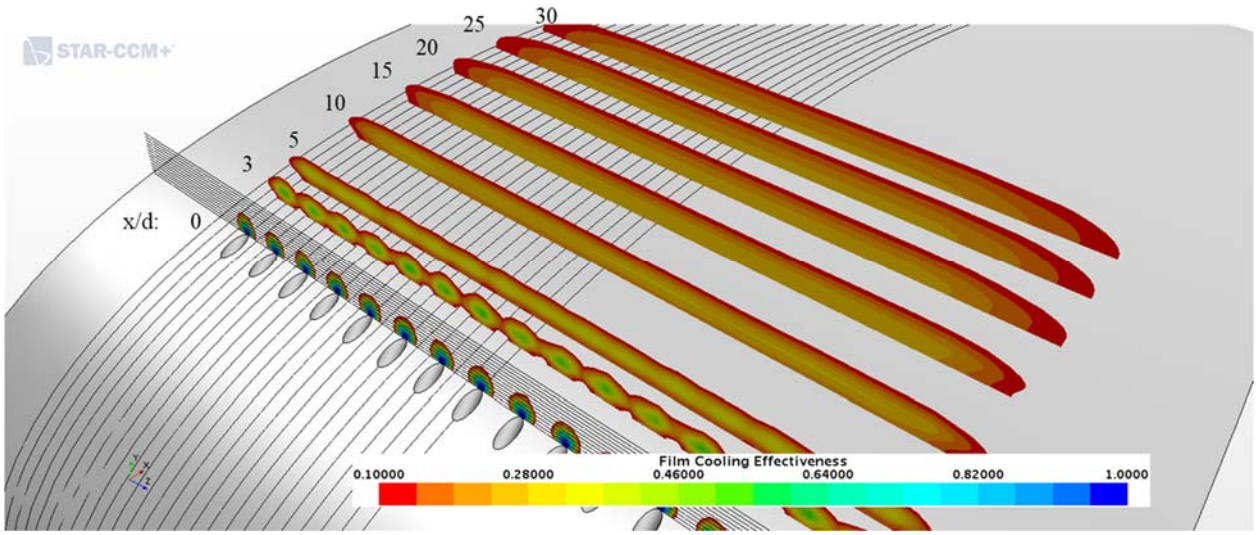

Figure 16.58: Case 6 - Streamwise spatial distribution of adiabatic film cooling effectiveness

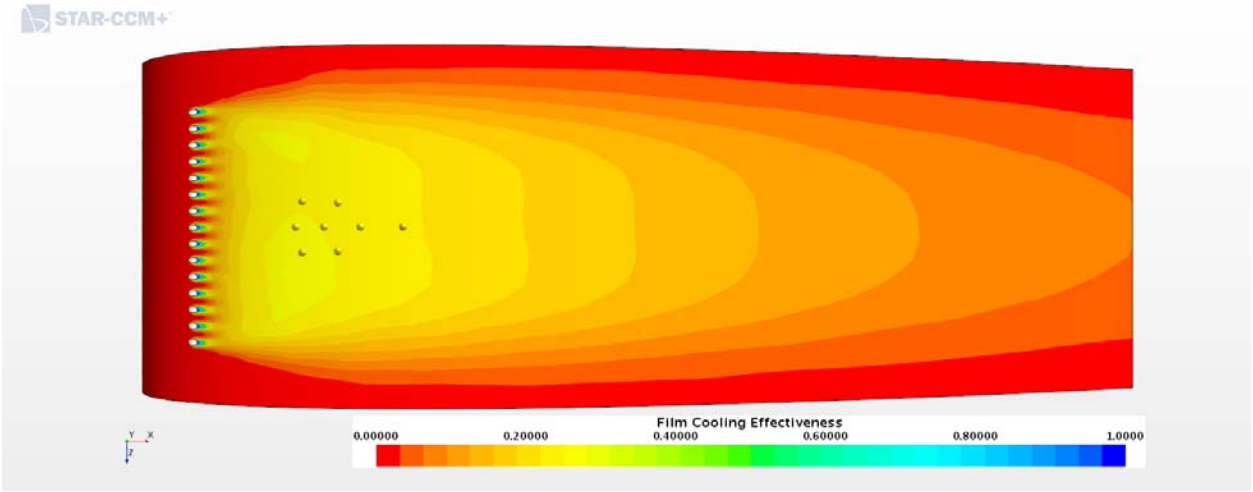

Figure 16.59: Case 6 - Adiabatic Film Cooling Effectiveness on the Suction Surface

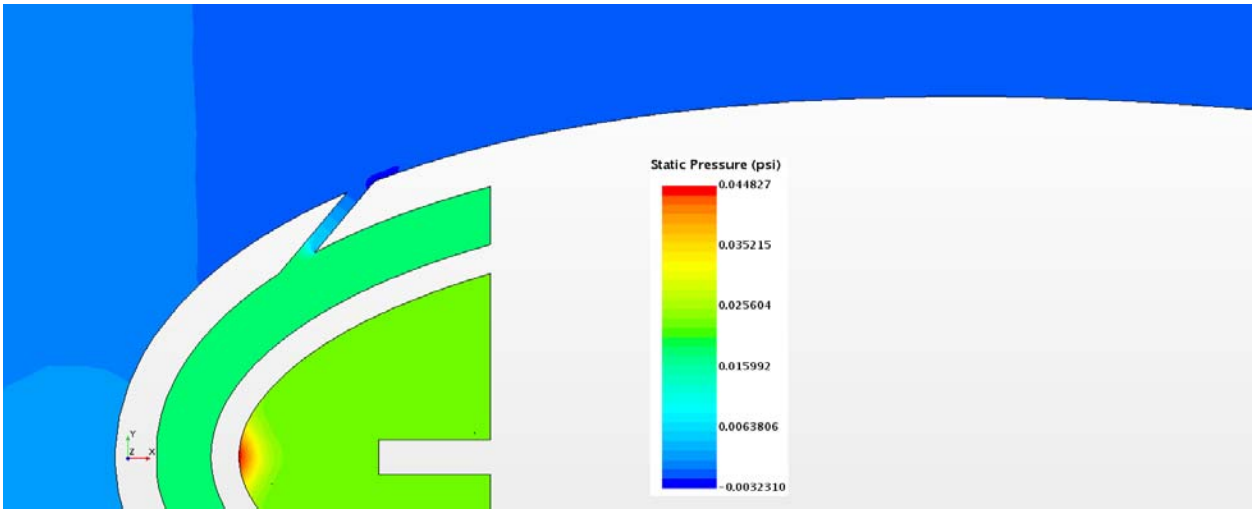

Figure 16.60: Case 6 – Static Pressure profile for center plane

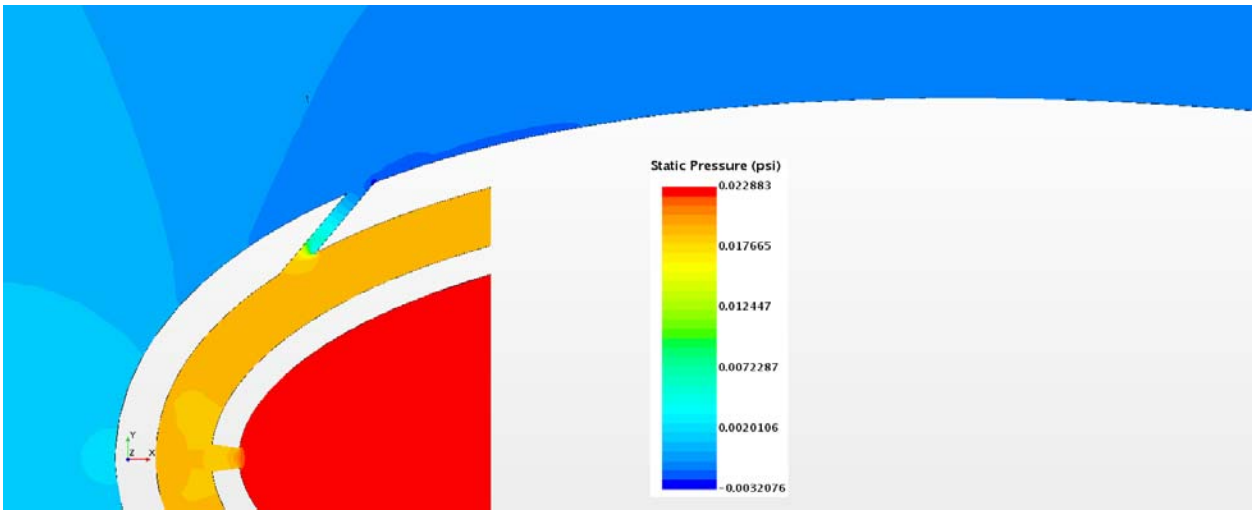

Figure 16.61: Case 6 – Static Pressure profile for off-center plane

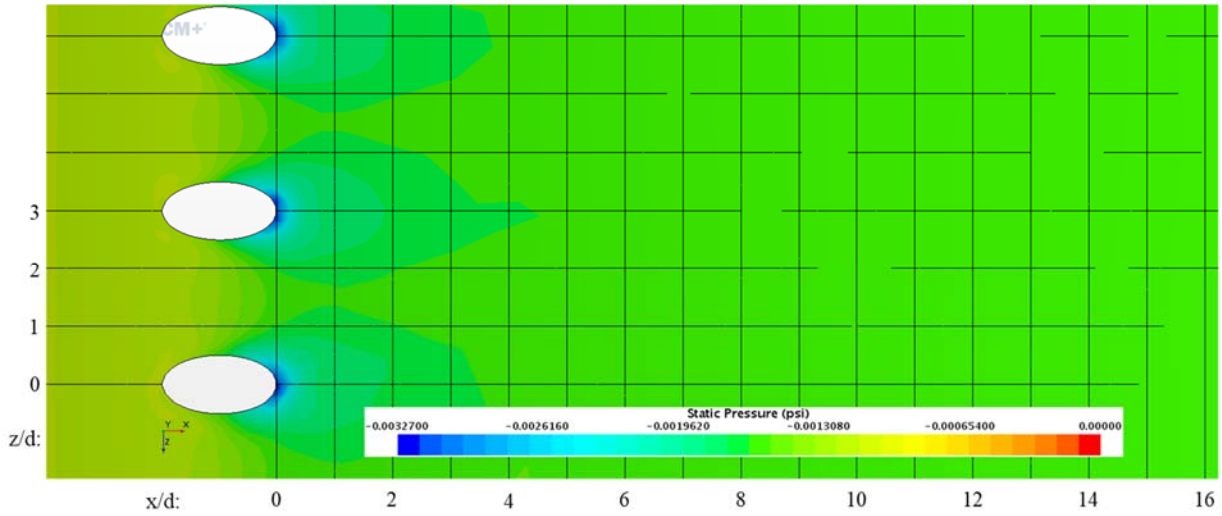

Figure 16.62: Case 6 – Static Pressure distribution for Suction Surface

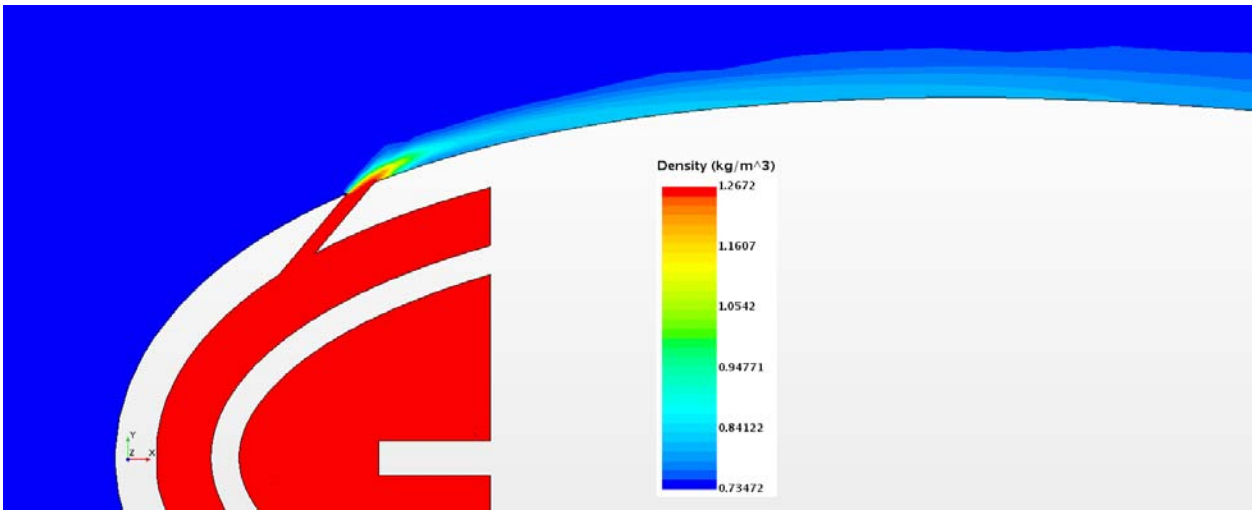

Figure 16.63: Case 6 – Density profile for center plane

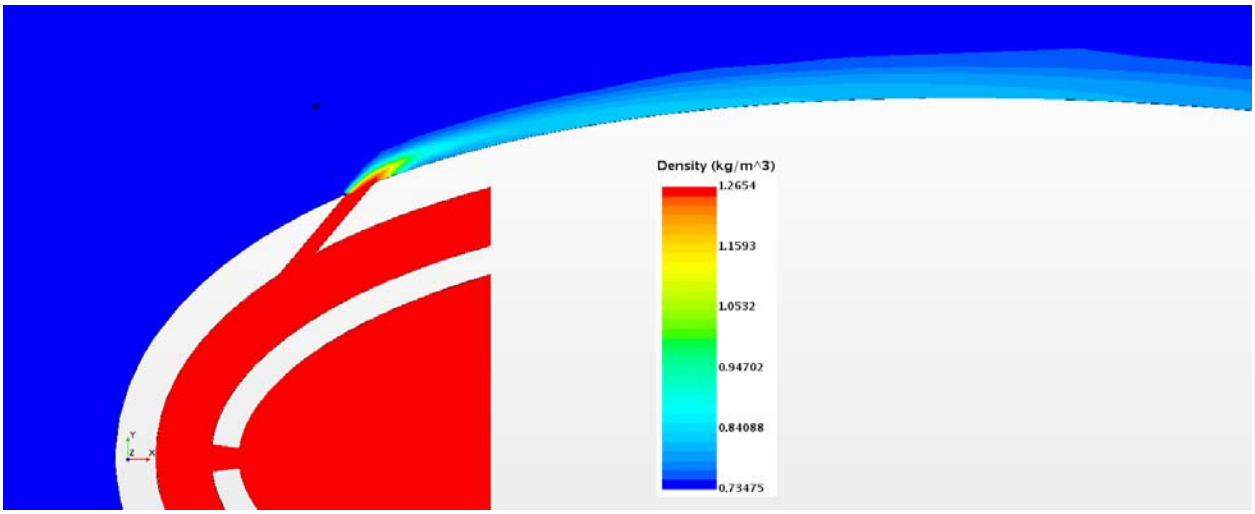

Figure 16.64: Case 6 – Density profile for off-center plane

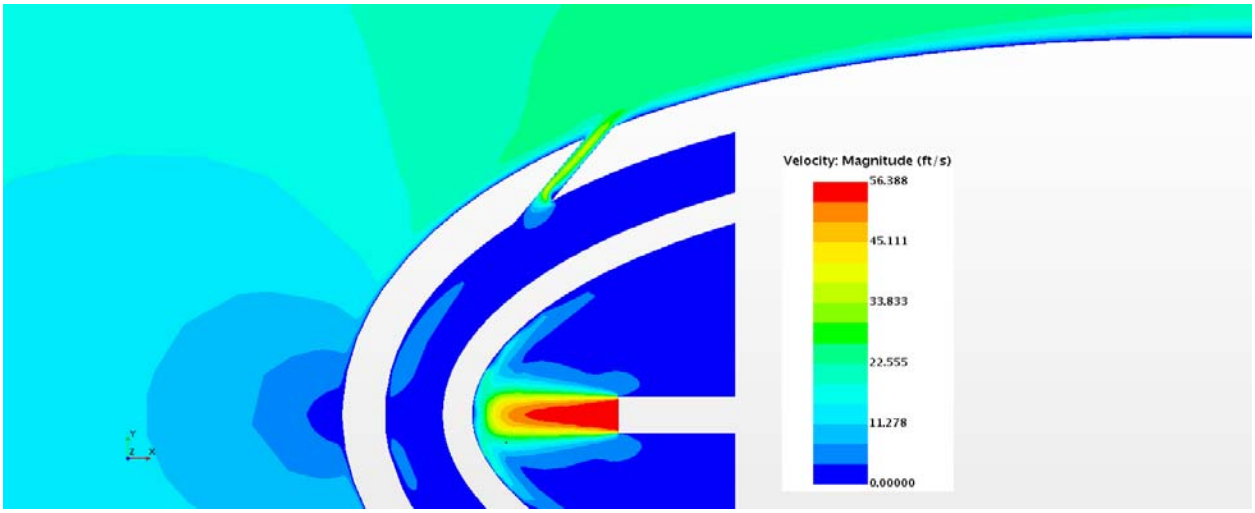

Figure 16.65: Case 6 – Velocity profile for center plane

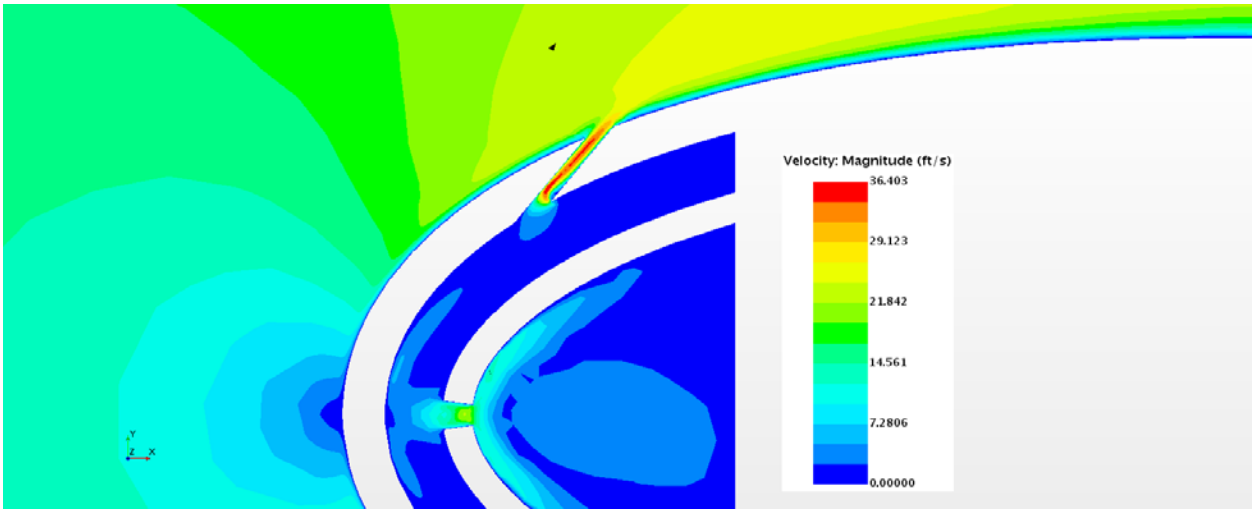

Figure 16.66: Case 6 – Velocity profile for off- center plane

Appendix G-7: M_b = 2.96, Tu = 5%, DR = 1.65

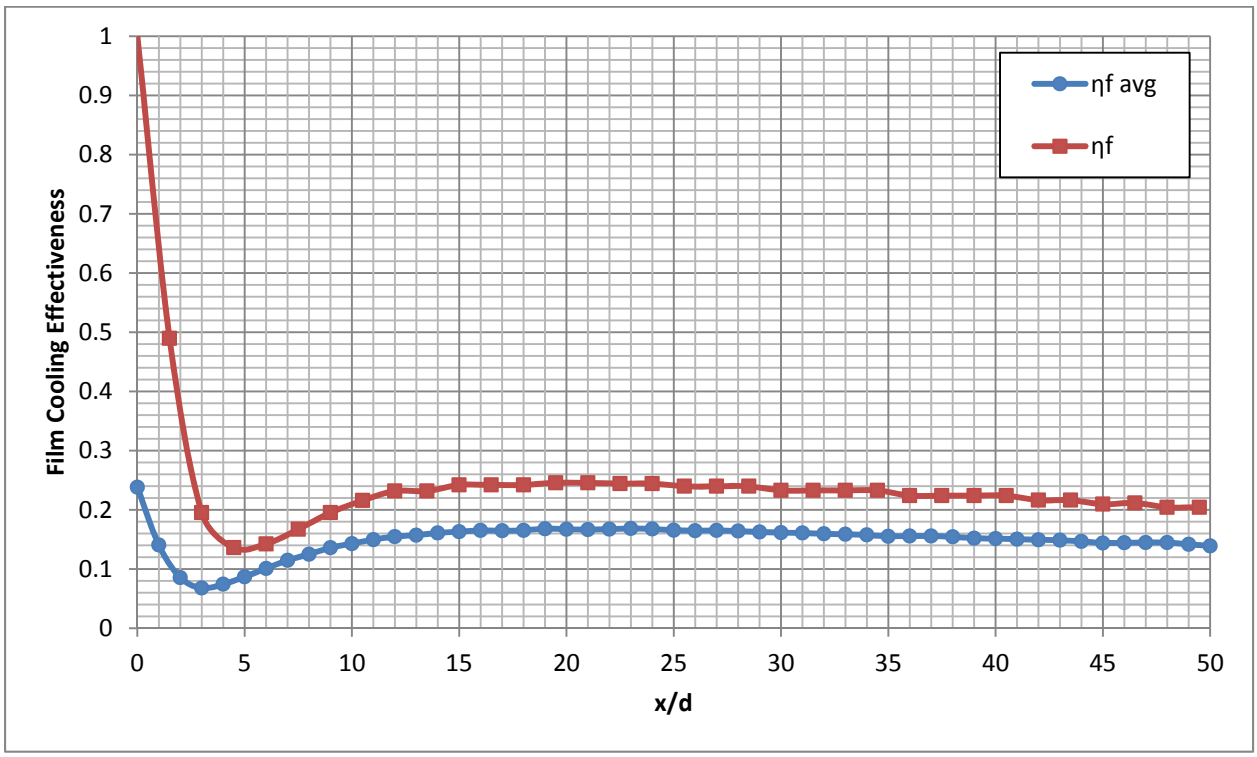

Figure 16.67: Case 7 - Laterally averaged and Centerline adiabatic film cooling effectiveness

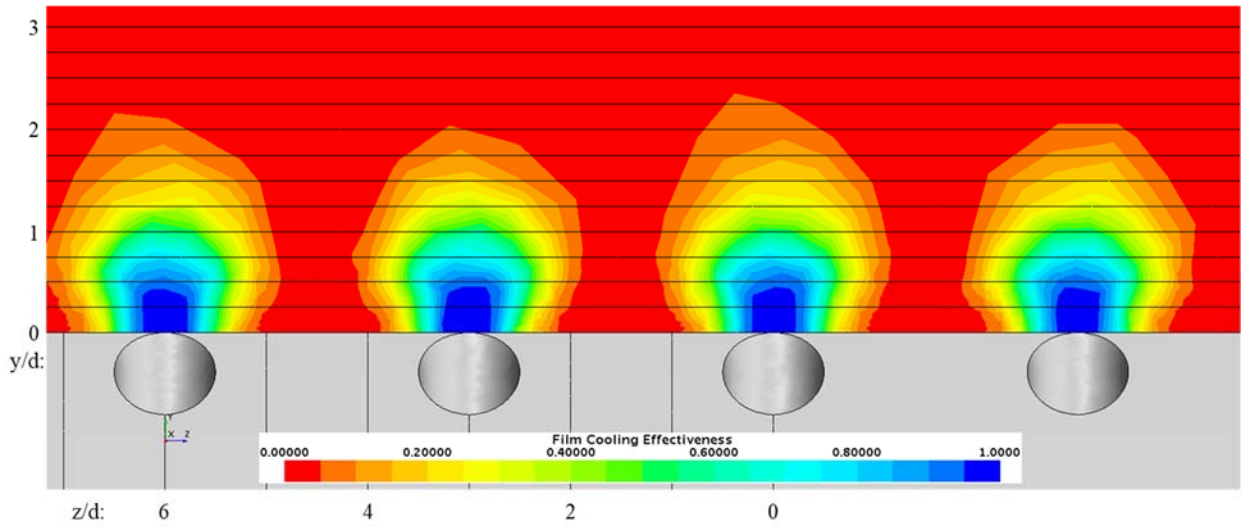

Figure 16.68: Case 7 - Spatial distribution of adiabatic film cooling effectiveness at x/d: 0

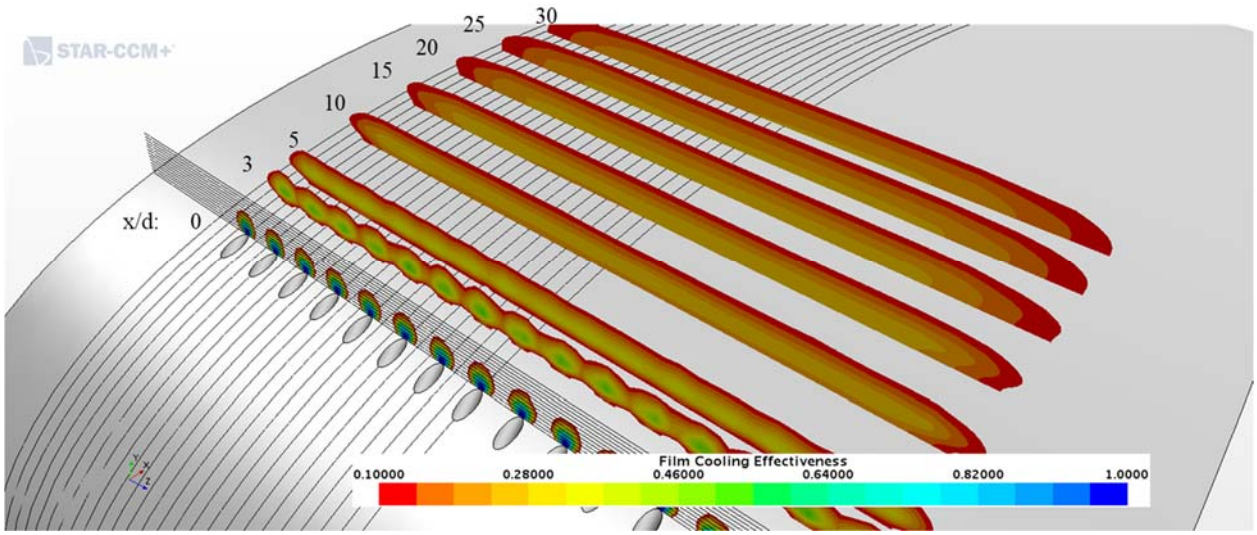

Figure 16.69: Case 7 - Streamwise spatial distribution of adiabatic film cooling effectiveness

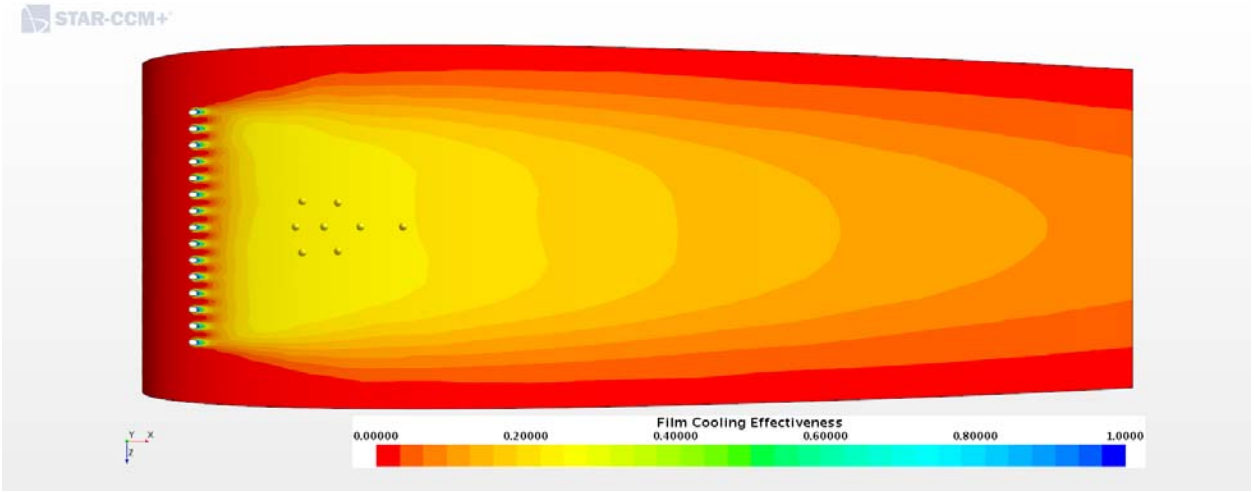

Figure 16.70: Case 7 - Adiabatic Film Cooling Effectiveness on the Suction Surface

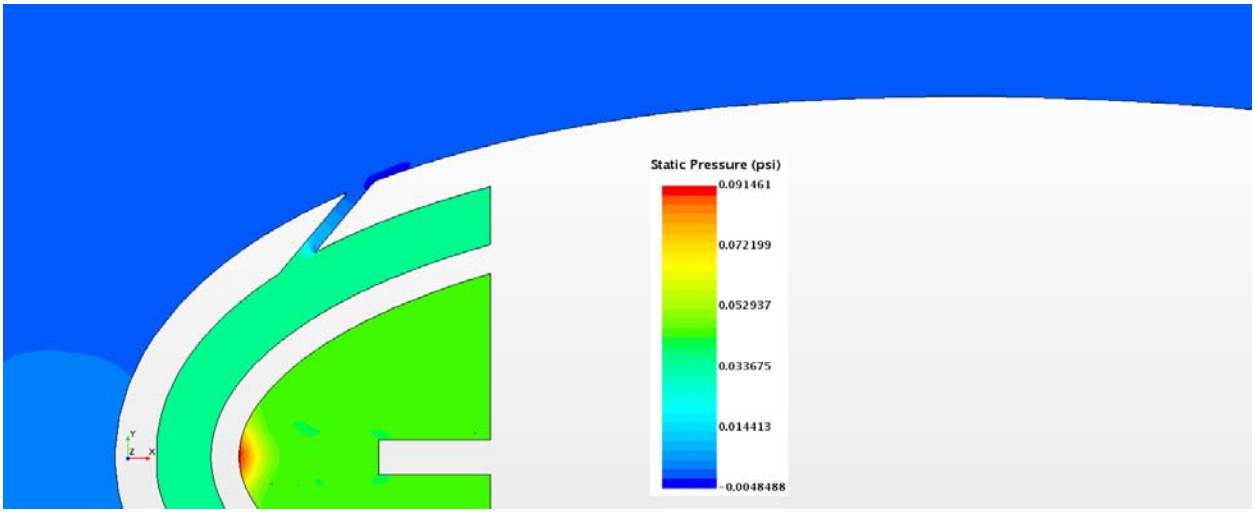

Figure 16.71: Case 7 – Static Pressure profile for center plane

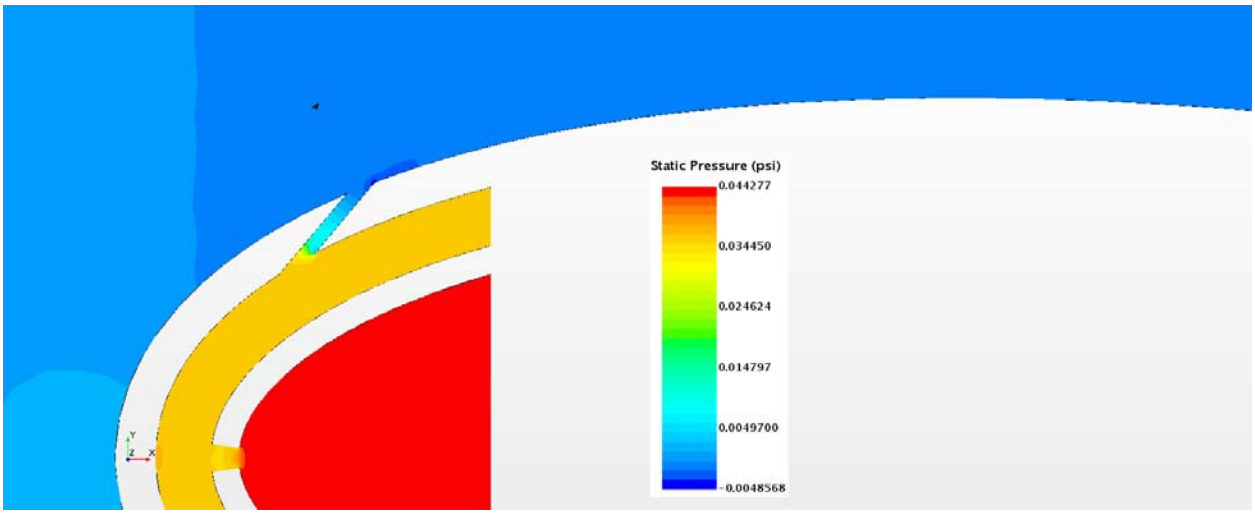

Figure 16.72: Case 7 – Static Pressure profile for off-center plane

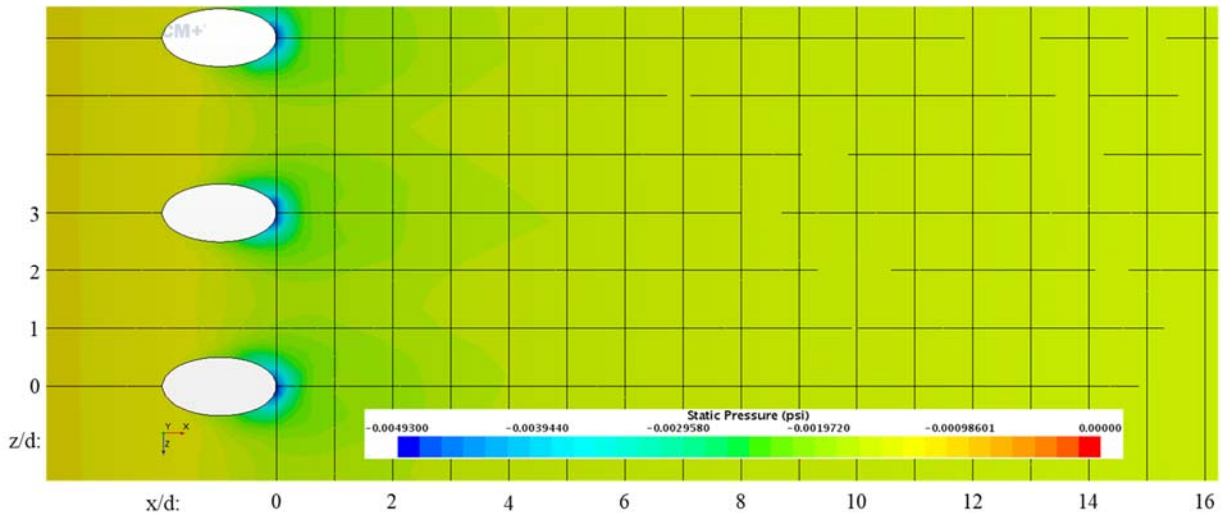

Figure 16.73: Case 7 – Static Pressure distribution for Suction Surface

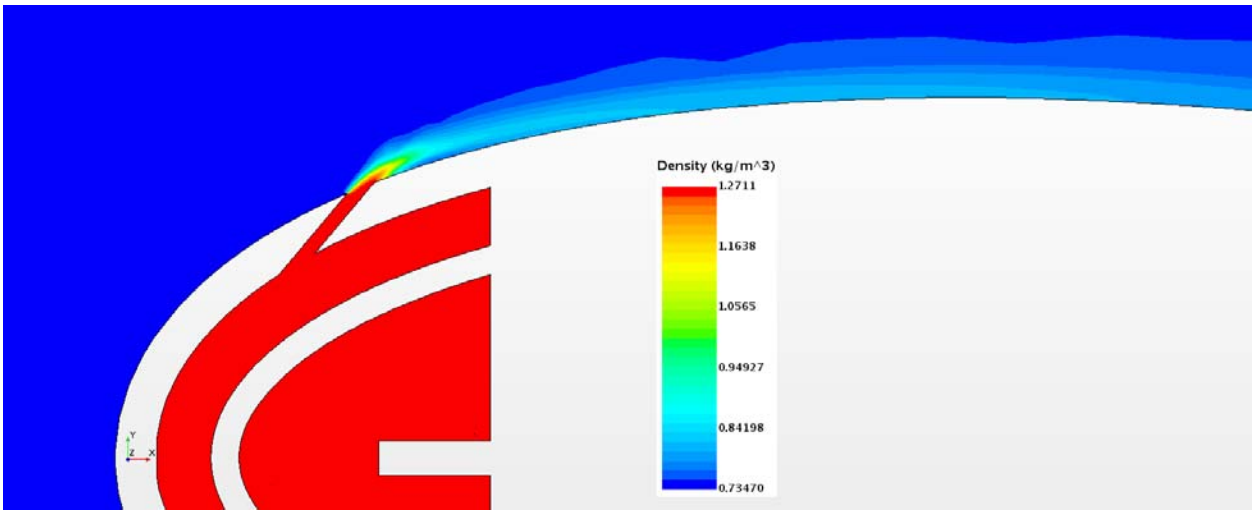

Figure 16.74: Case 7 – Density profile for center plane

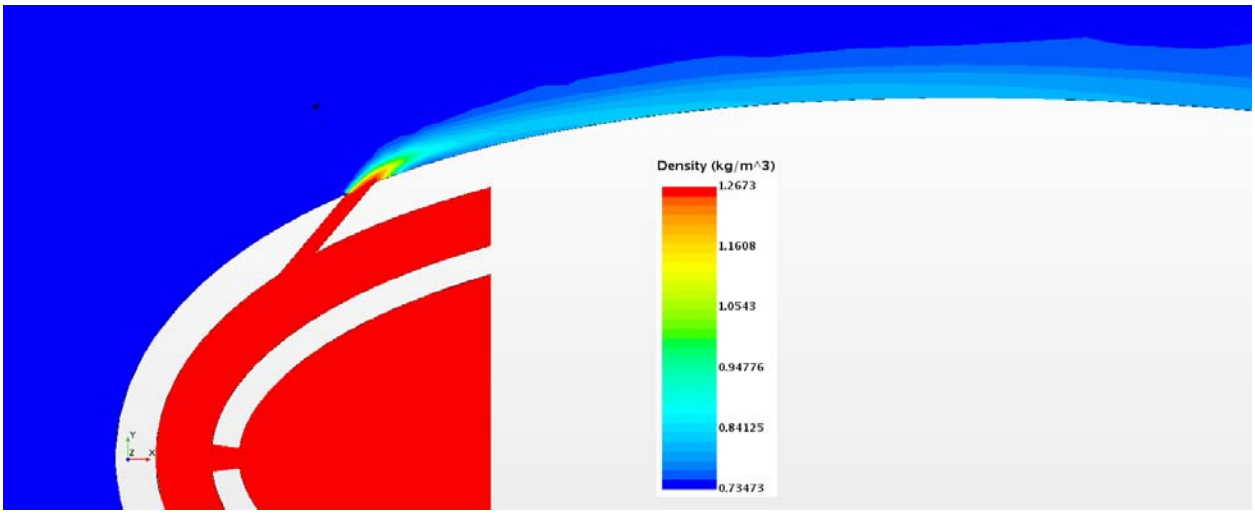

Figure 16.75: Case 7 – Density profile for off-center plane

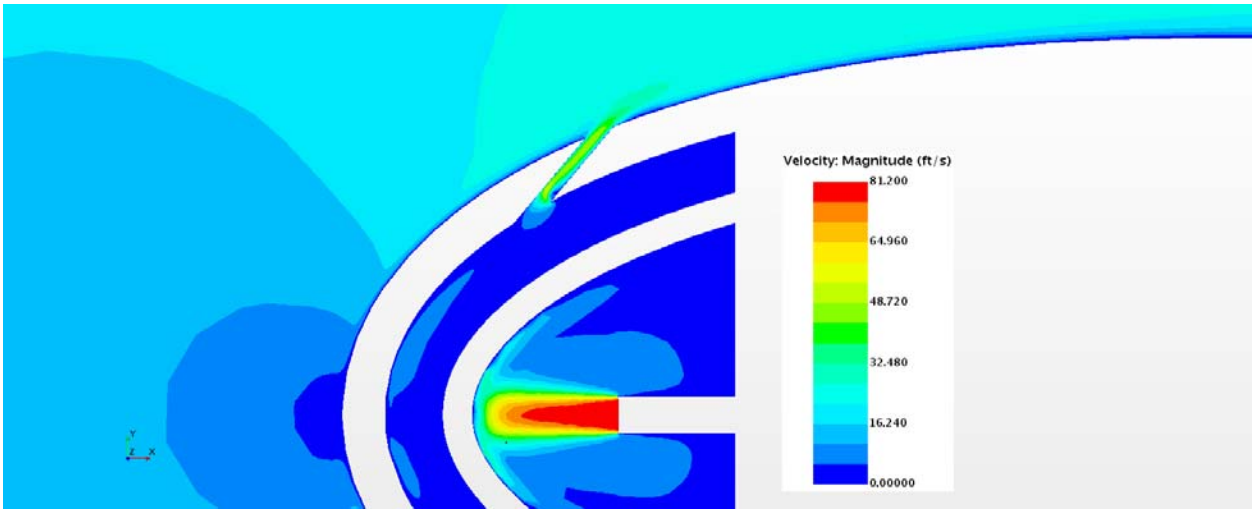

Figure 16.76: Case 7 – Velocity profile for center plane

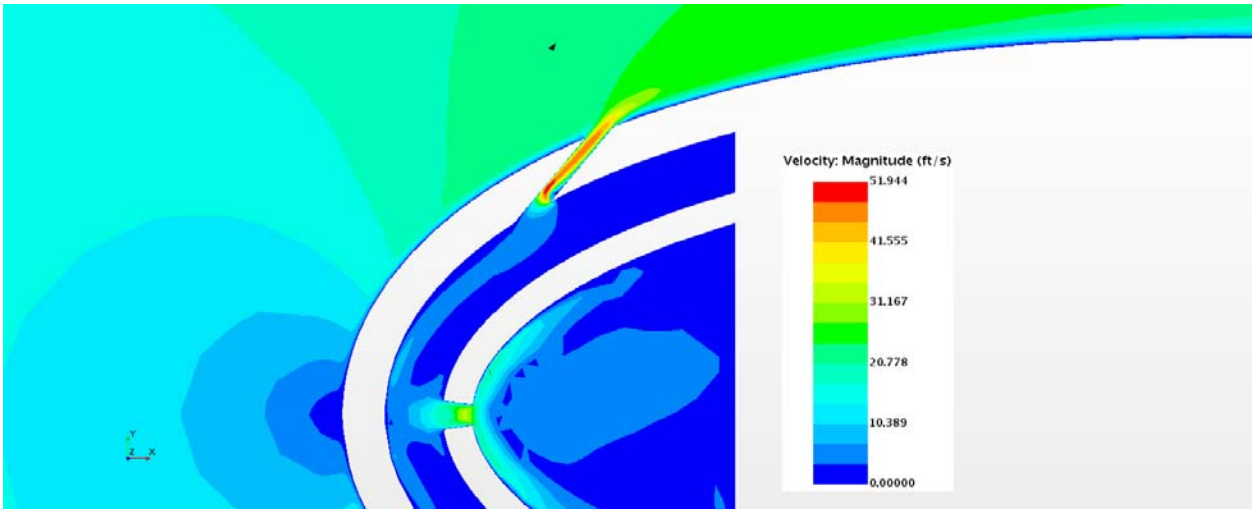

Figure 16.77: Case 7 – Velocity profile for off- center plane

Appendix G-8: M_b = 4.08, Tu = 5%, DR = 1.65

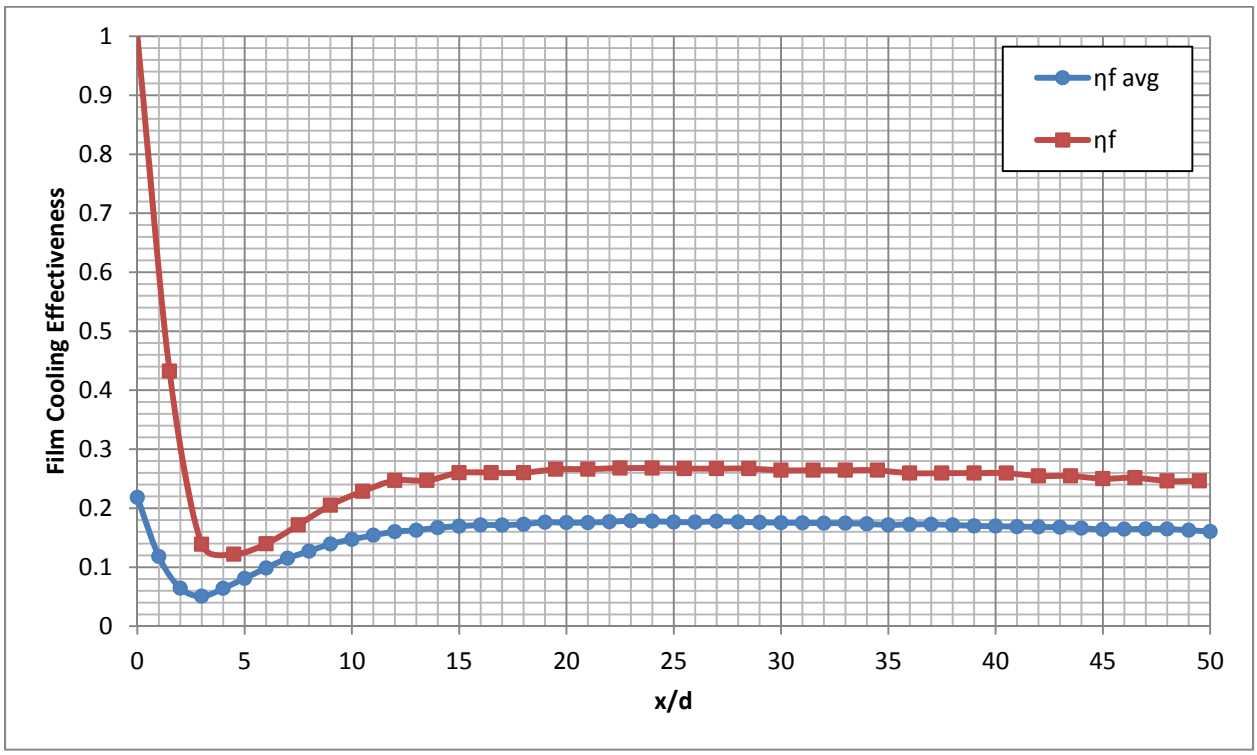

Figure 16.78: Case 8 - Laterally averaged and Centerline adiabatic film cooling effectiveness

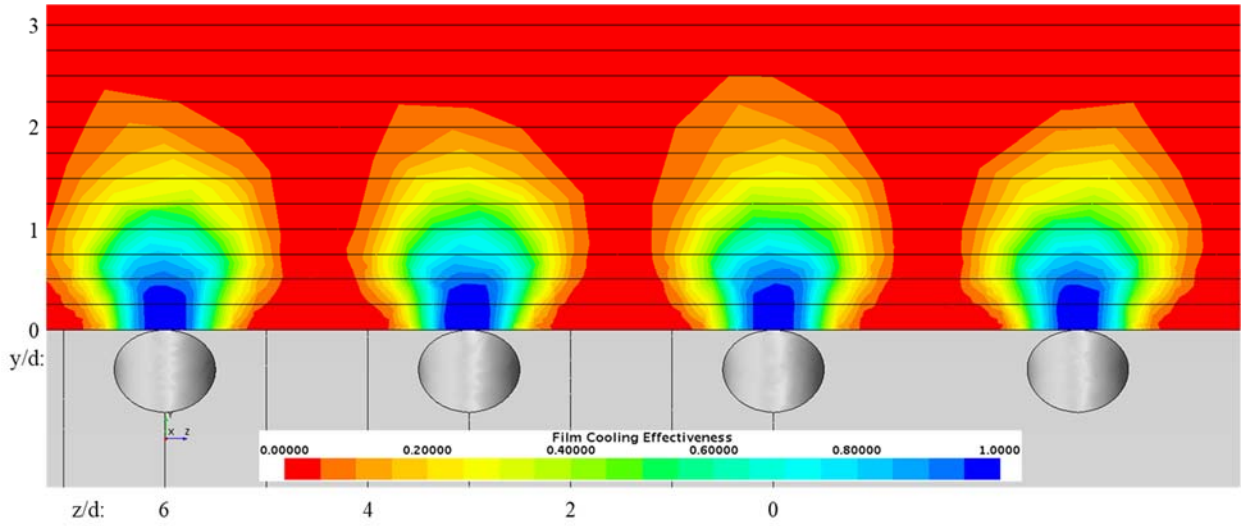

Figure 16.79: Case 8 - Spatial distribution of adiabatic film cooling effectiveness at x/d: 0

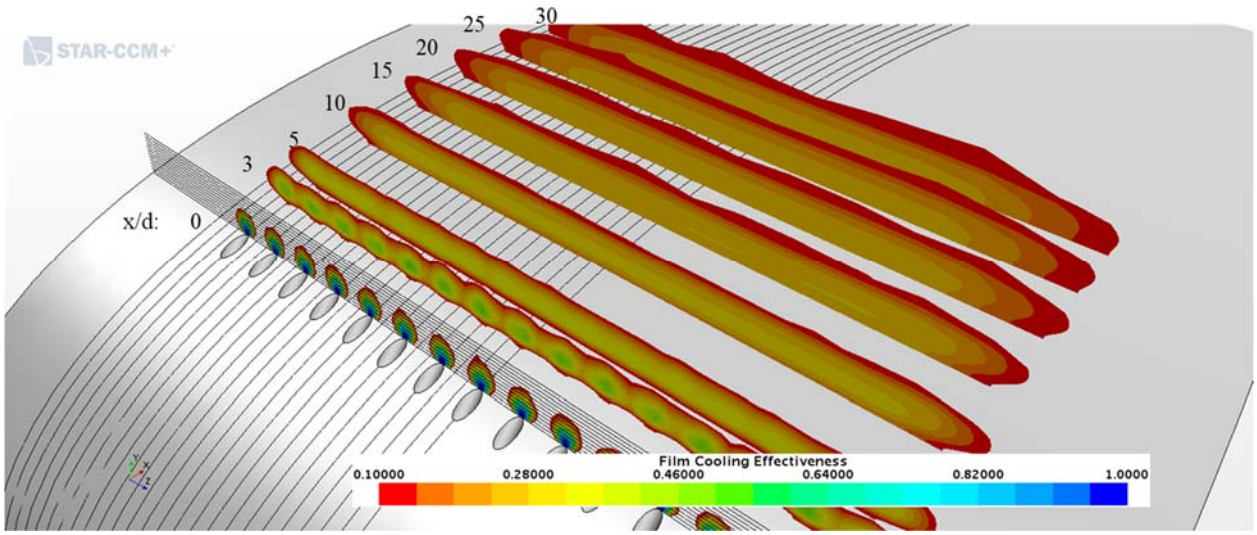

Figure 16.80: Case 8 - Streamwise spatial distribution of adiabatic film cooling effectiveness

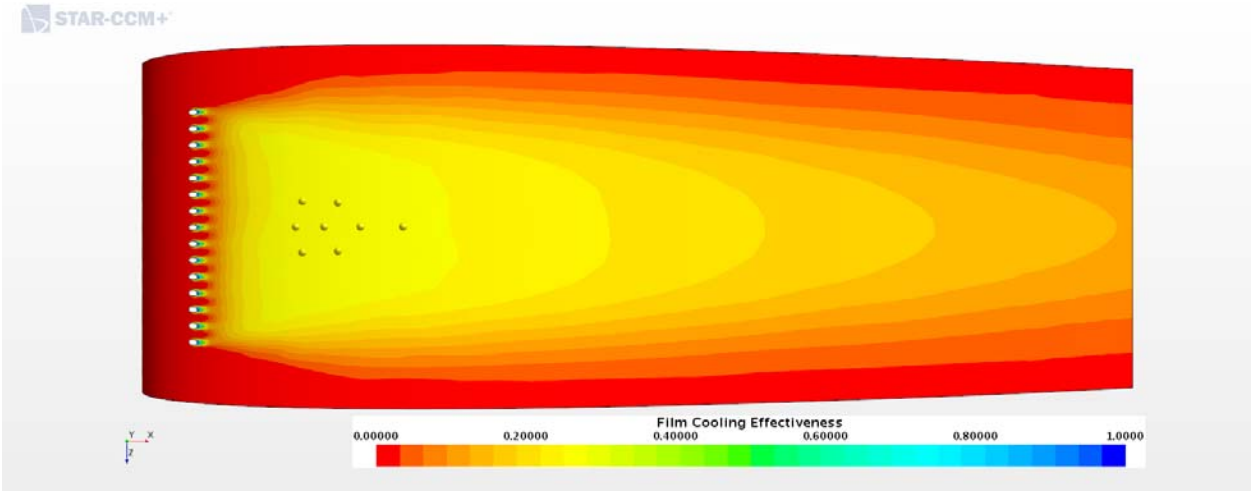

Figure 16.81: Case 8 - Adiabatic Film Cooling Effectiveness on the Suction Surface

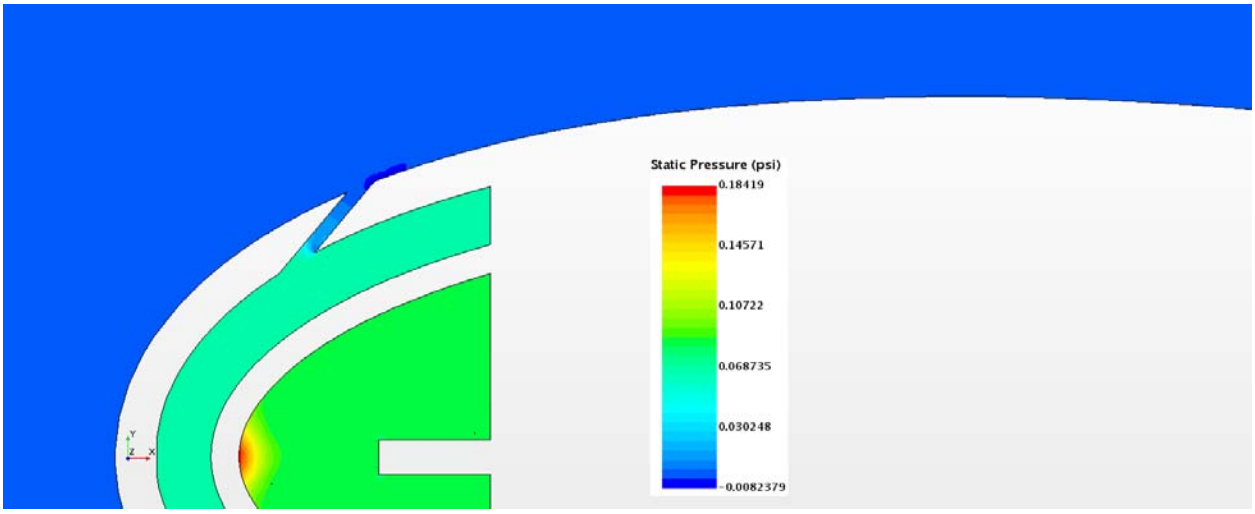

Figure 16.82: Case 8 – Static Pressure profile for center plane

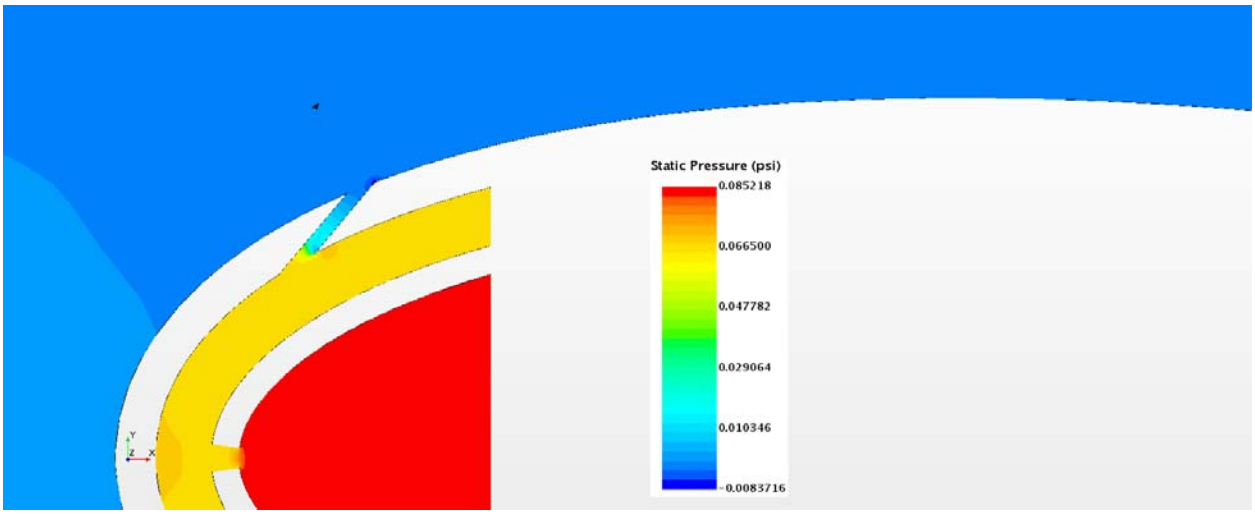

Figure 16.83: Case 8 – Static Pressure profile for off-center plane

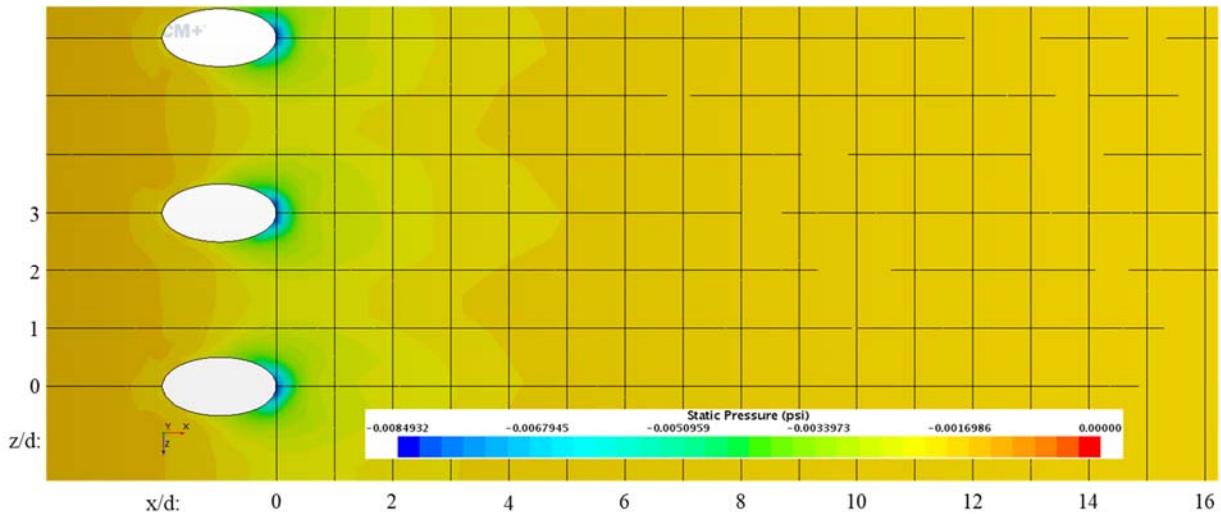

Figure 16.84: Case 8 – Static Pressure distribution for Suction Surface

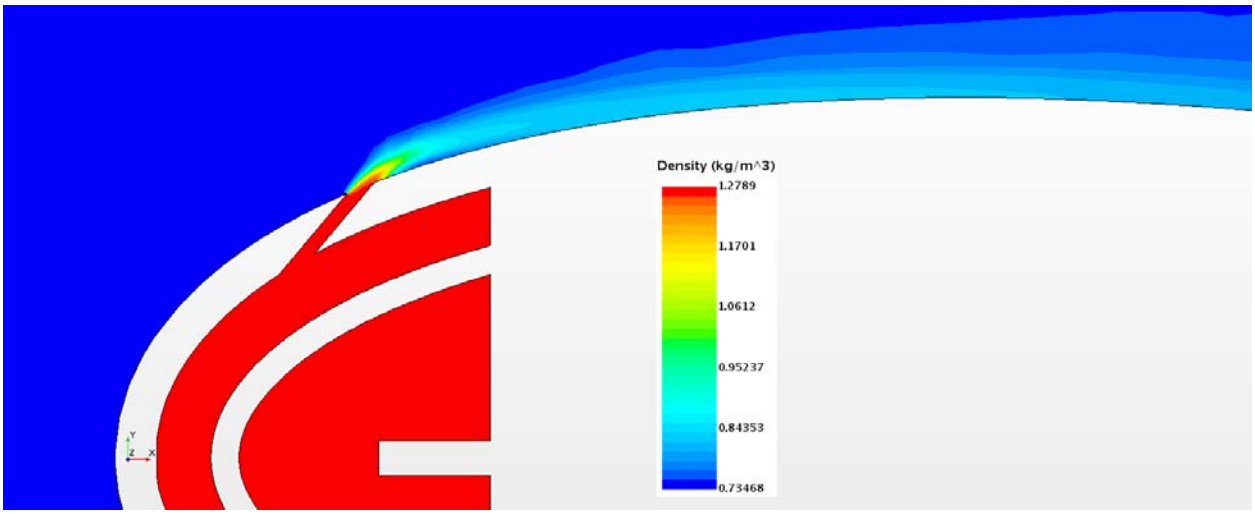

Figure 16.85: Case 8 – Density profile for center plane

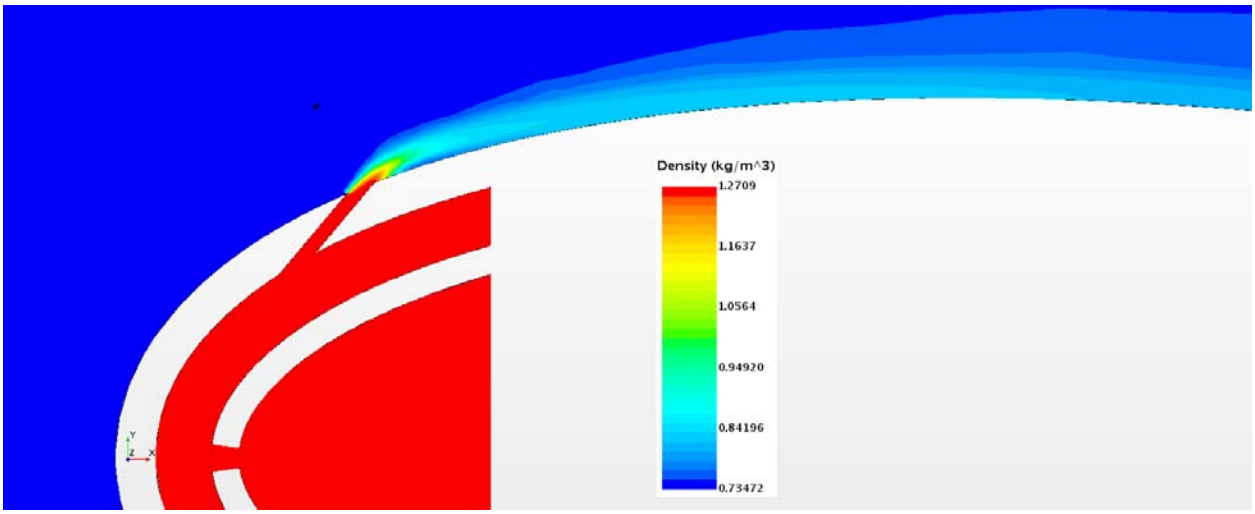

Figure 16.86: Case 8 – Density profile for off-center plane

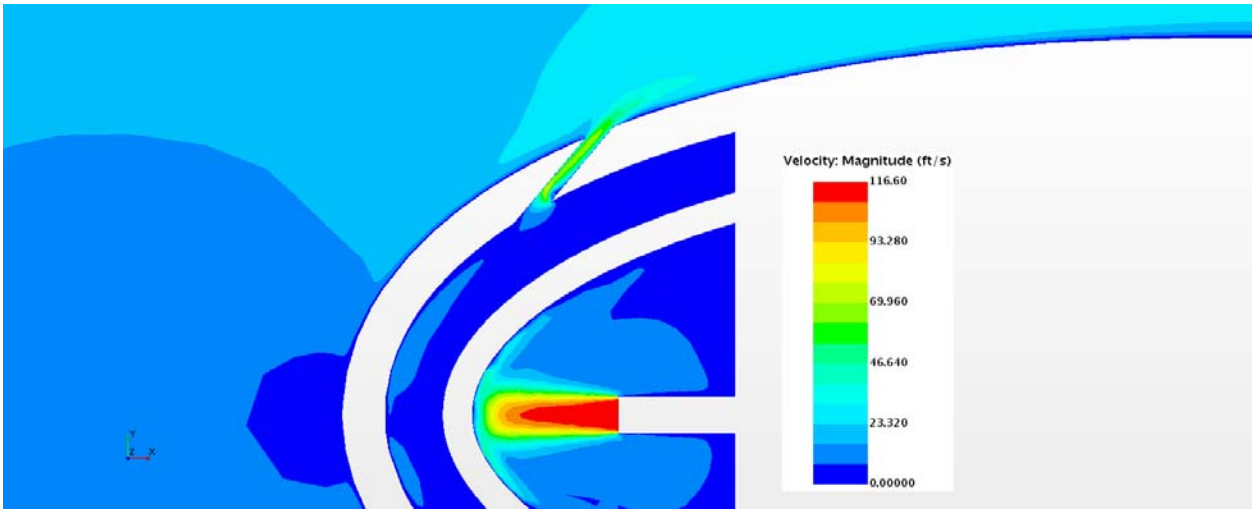

Figure 16.87: Case 8 – Velocity profile for center plane

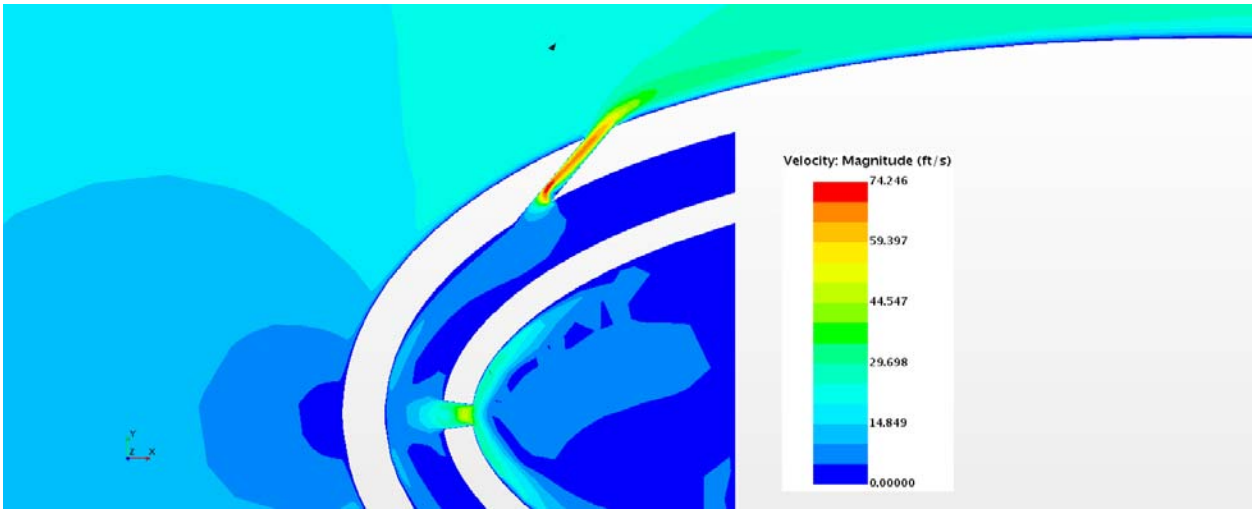

Figure 16.88: Case 8 – Velocity profile for off- center plane

Appendix G-9: M_b = 5.04, Tu = 5%, DR = 1.65

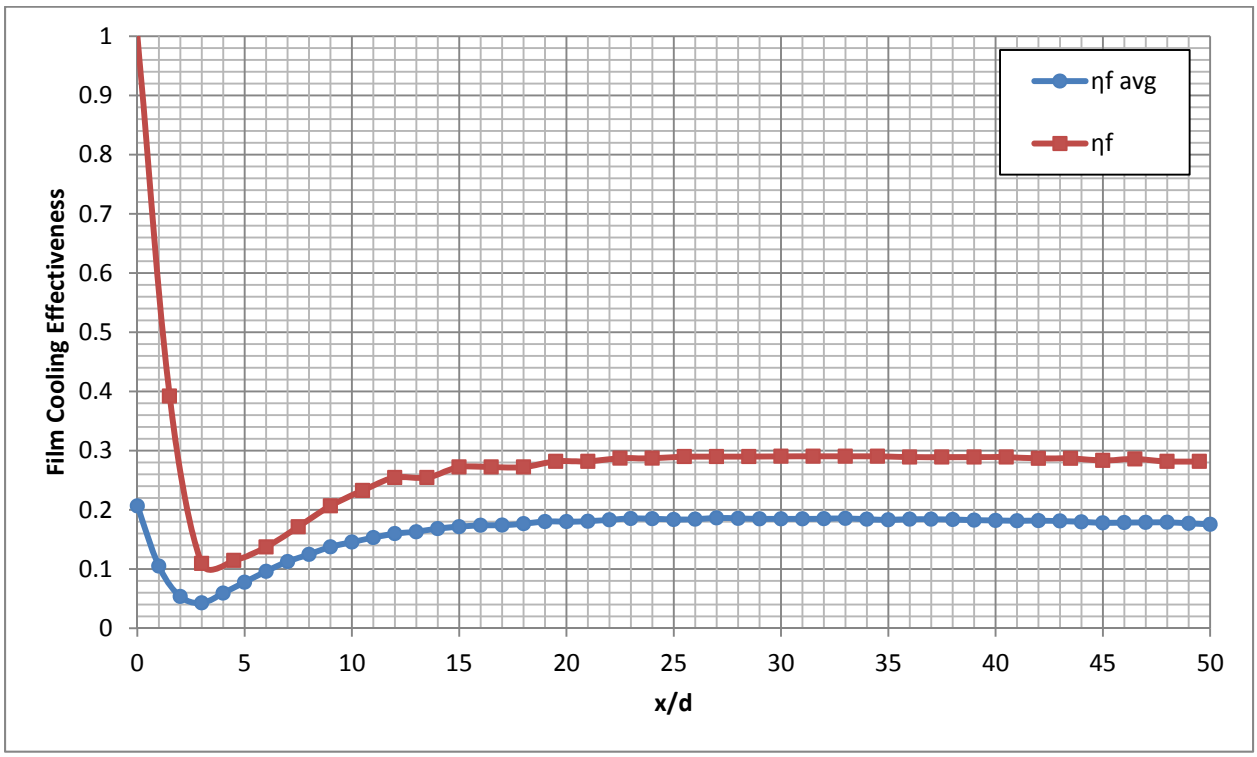

Figure 16.89: Case 9 - Laterally averaged and Centerline adiabatic film cooling effectiveness

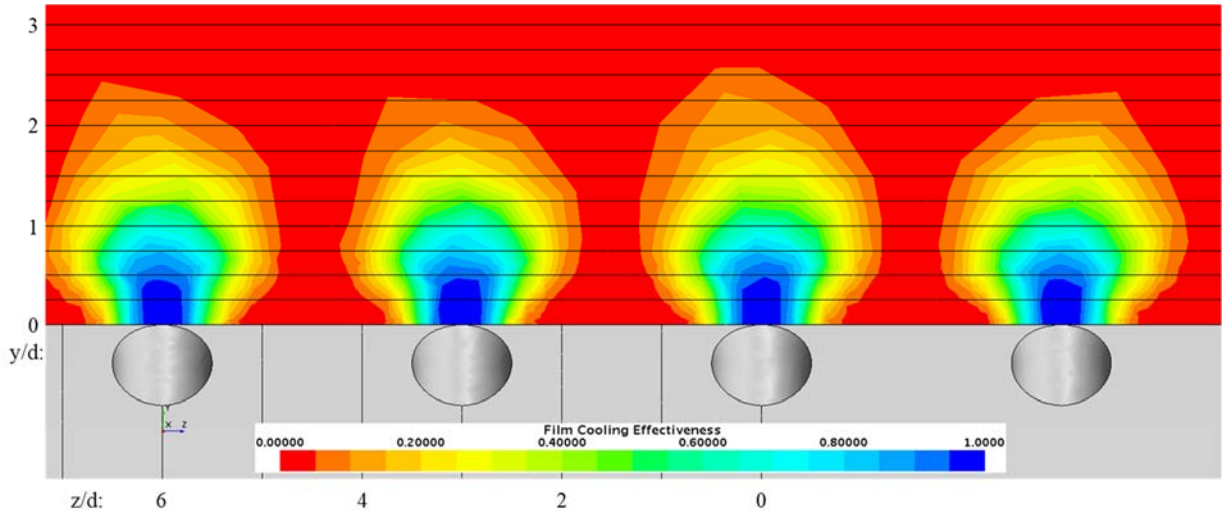

Figure 16.90: Case 9 - Spatial distribution of adiabatic film cooling effectiveness at x/d: 0

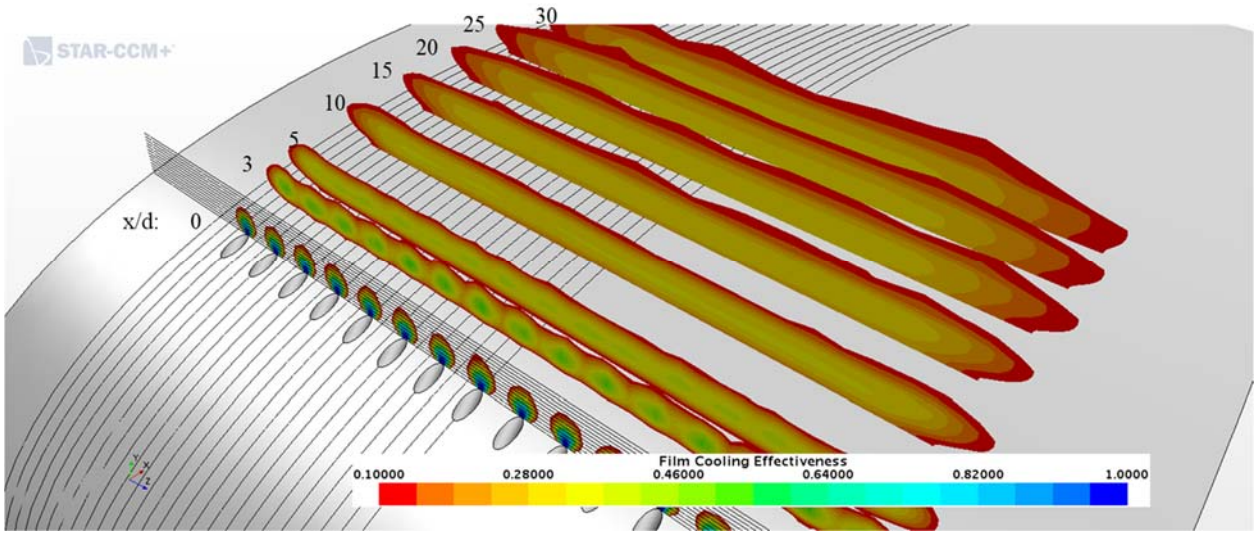

Figure 16.91: Case 9 - Streamwise spatial distribution of adiabatic film cooling effectiveness

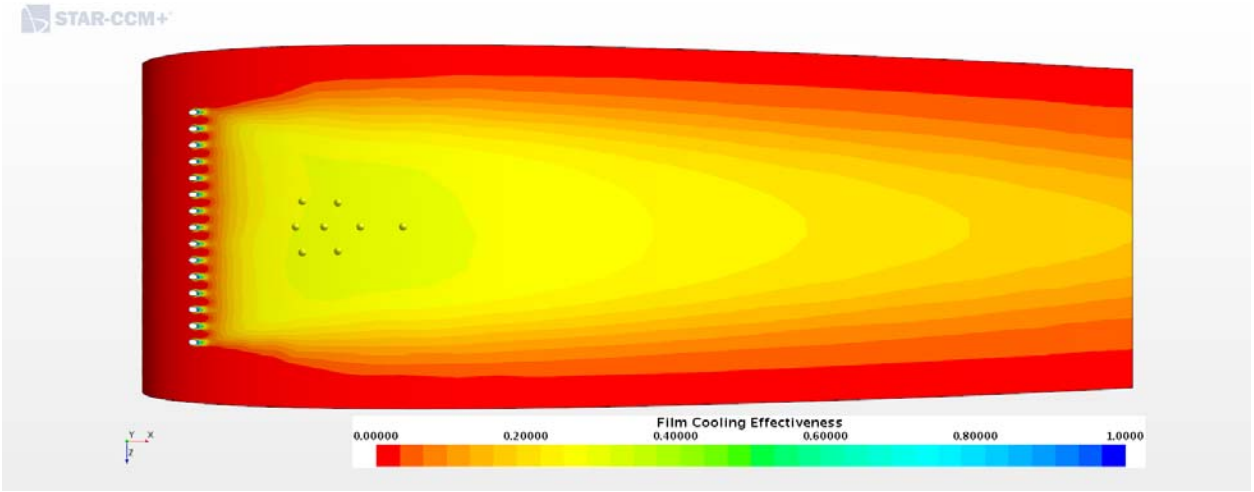

Figure 16.92: Case 9 - Adiabatic Film Cooling Effectiveness on the Suction Surface

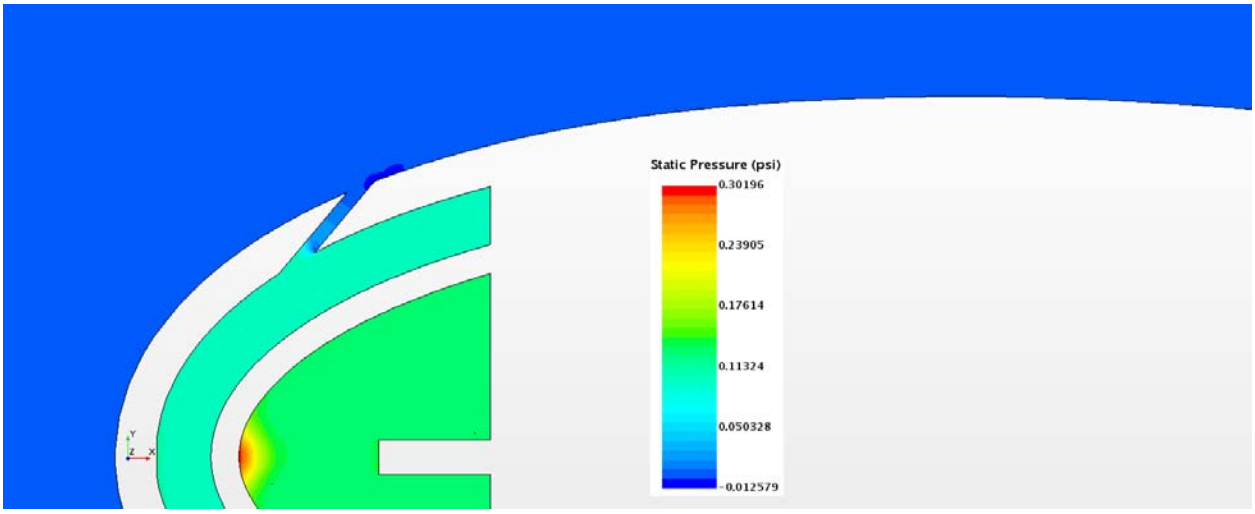

Figure 16.93: Case 9 – Static Pressure profile for center plane

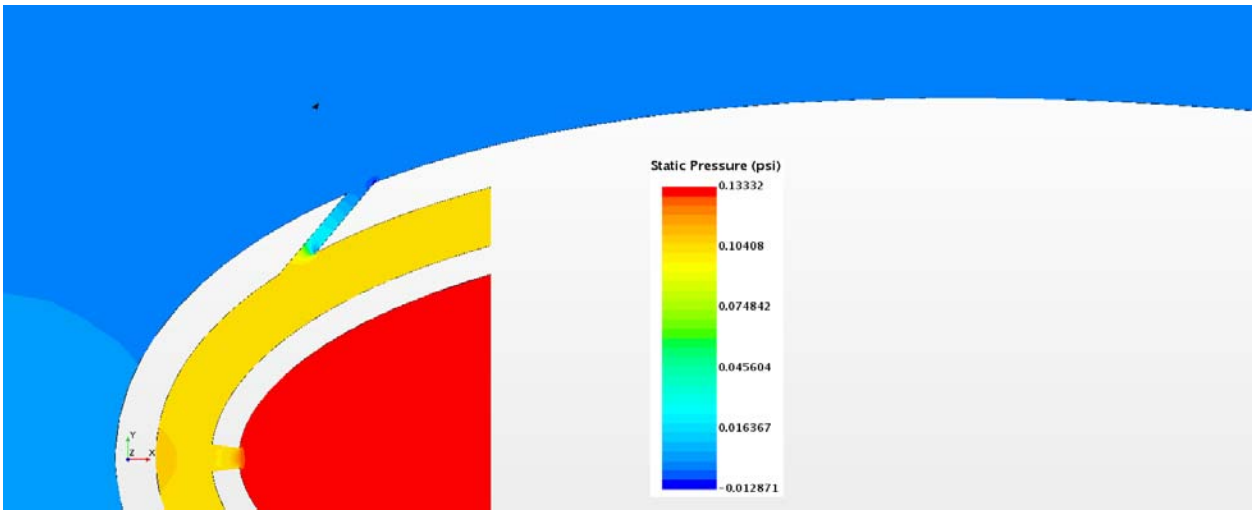

Figure 16.94: Case 9 – Static Pressure profile for off-center plane

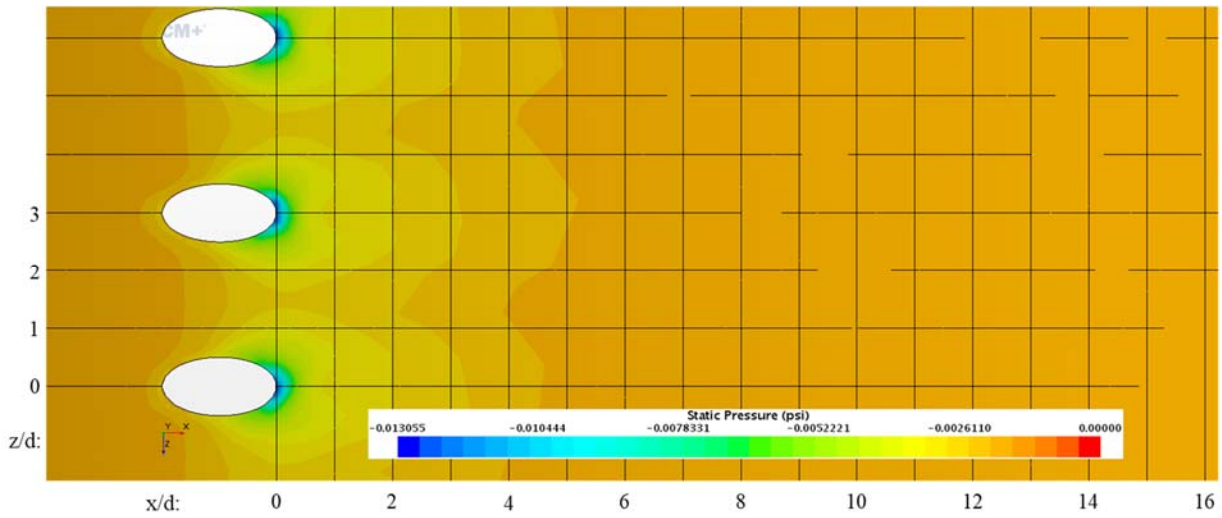

Figure 16.95: Case 9 – Static Pressure distribution for Suction Surface

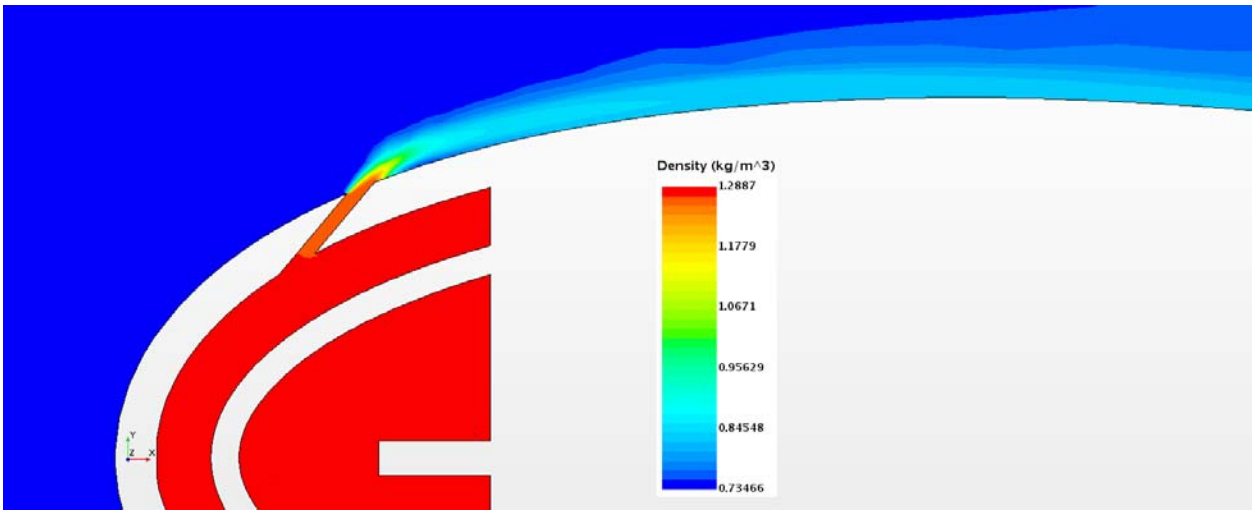

Figure 16.96: Case 9 – Density profile for center plane

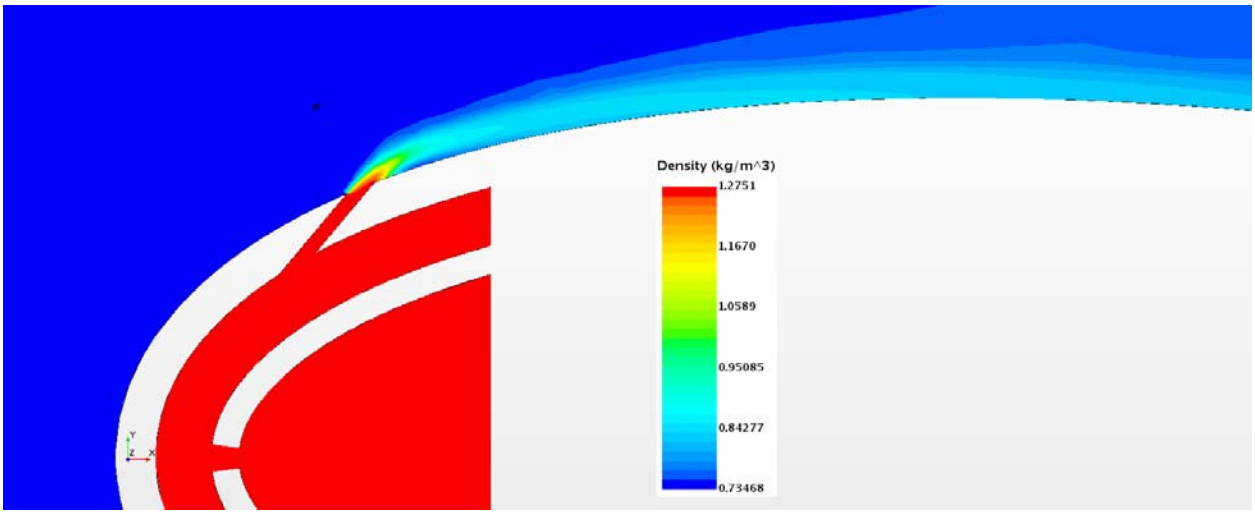

Figure 16.97: Case 9 – Density profile for off-center plane

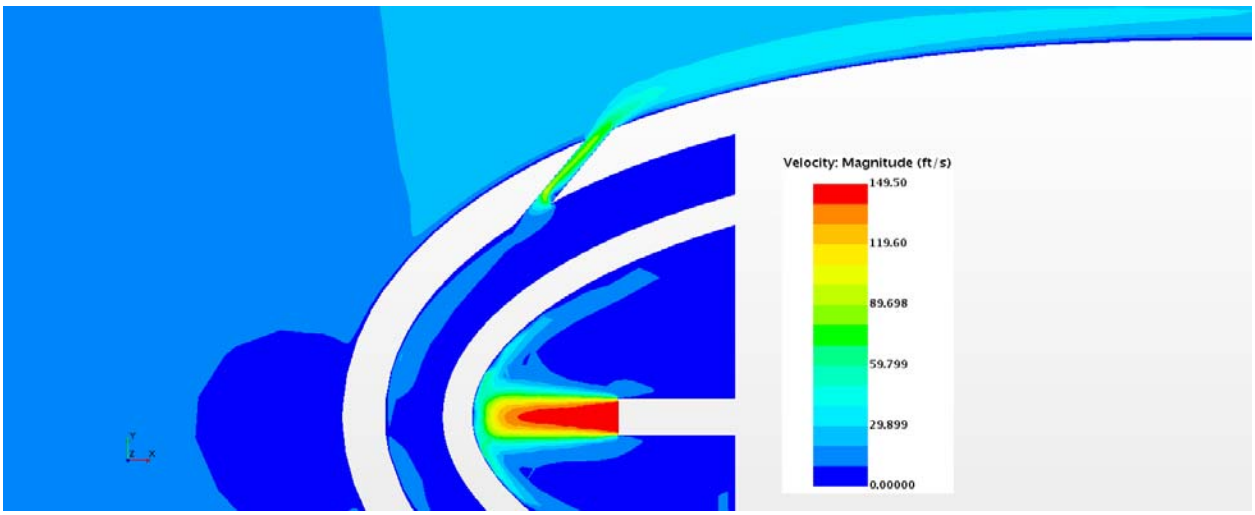

Figure 16.98: Case 9 – Velocity profile for center plane

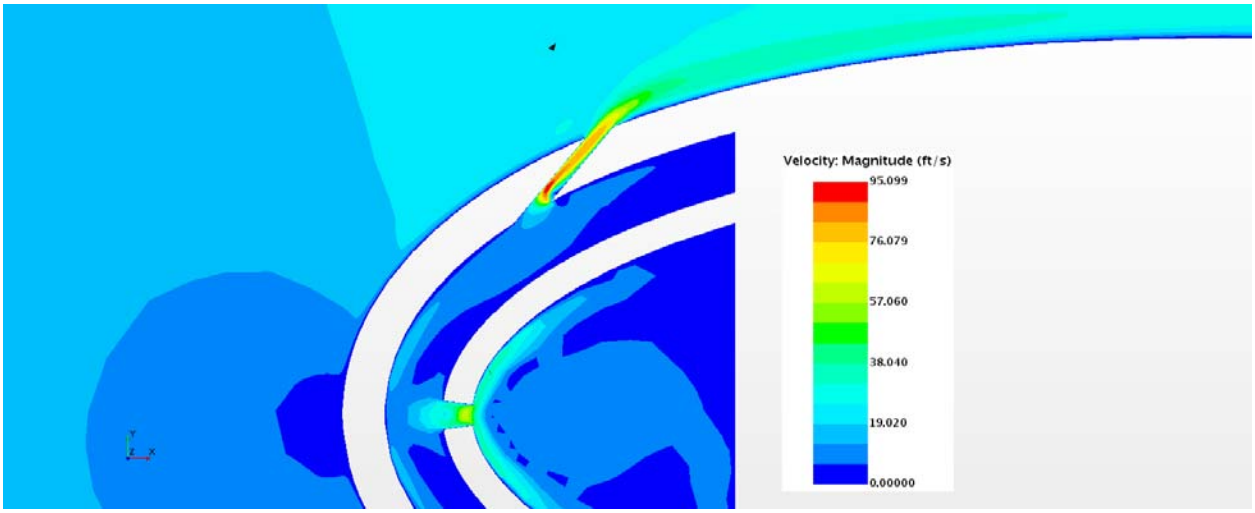

Figure 16.99: Case 9 – Velocity profile for off- center plane

Appendix G-10: M_b = 5.95, Tu = 5%, DR = 1.65

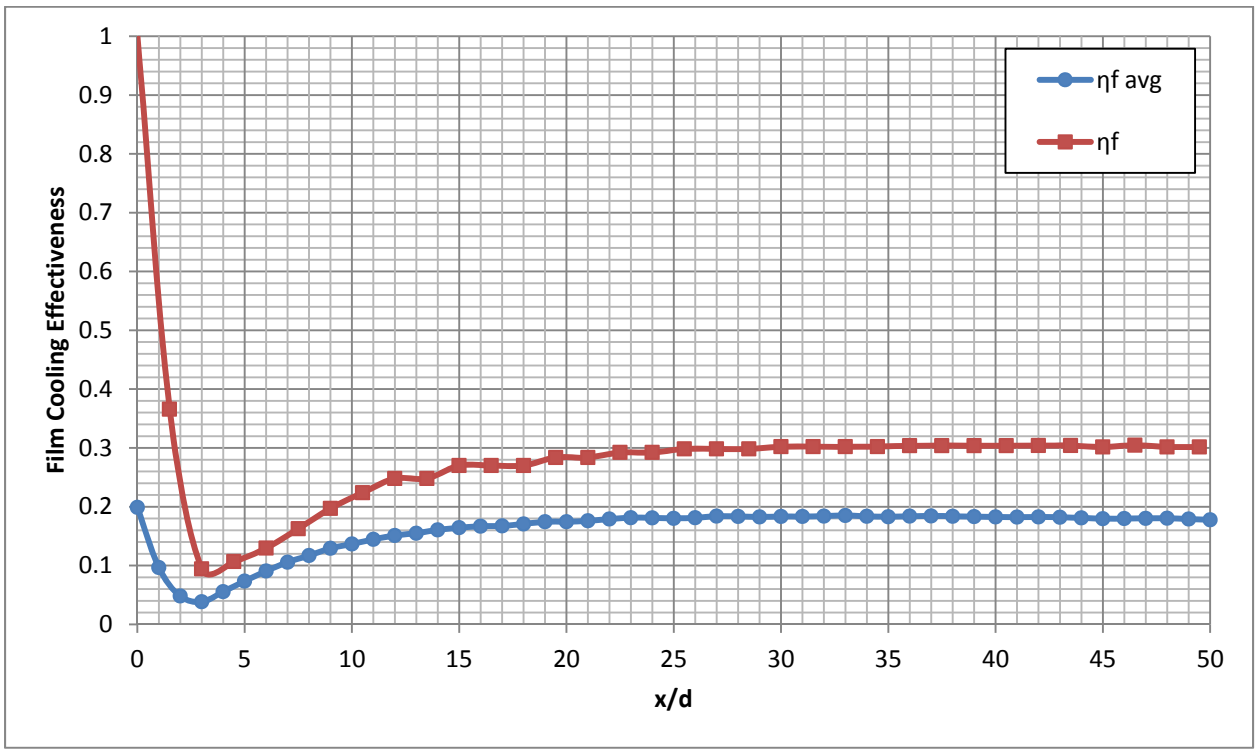

Figure 16.100: Case 10 - Laterally averaged and Centerline adiabatic film cooling effectiveness

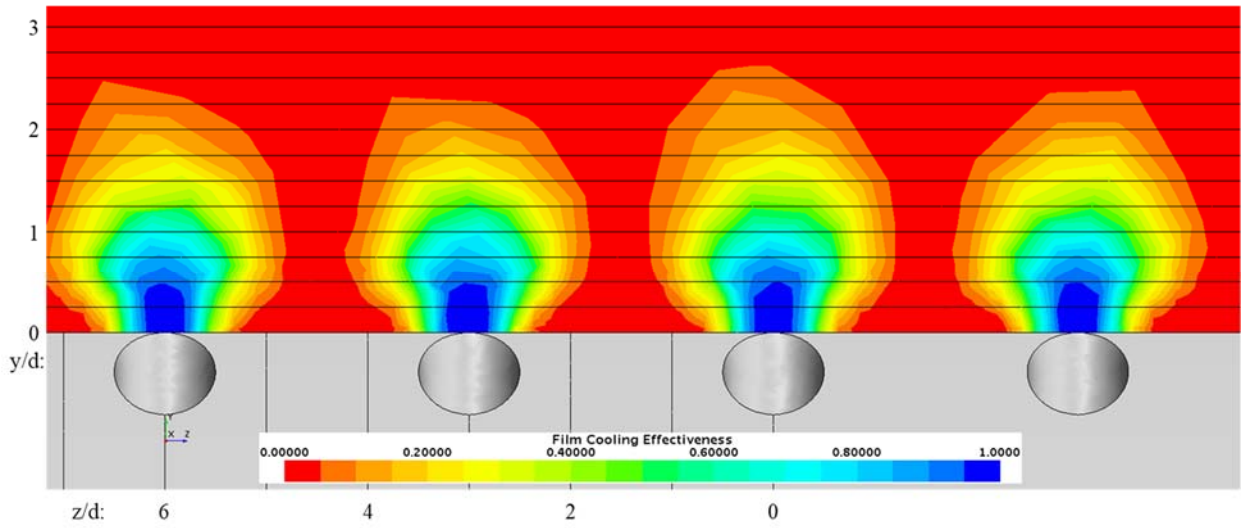

Figure 16.101: Case 10 - Spatial distribution of adiabatic film cooling effectiveness at x/d: 0

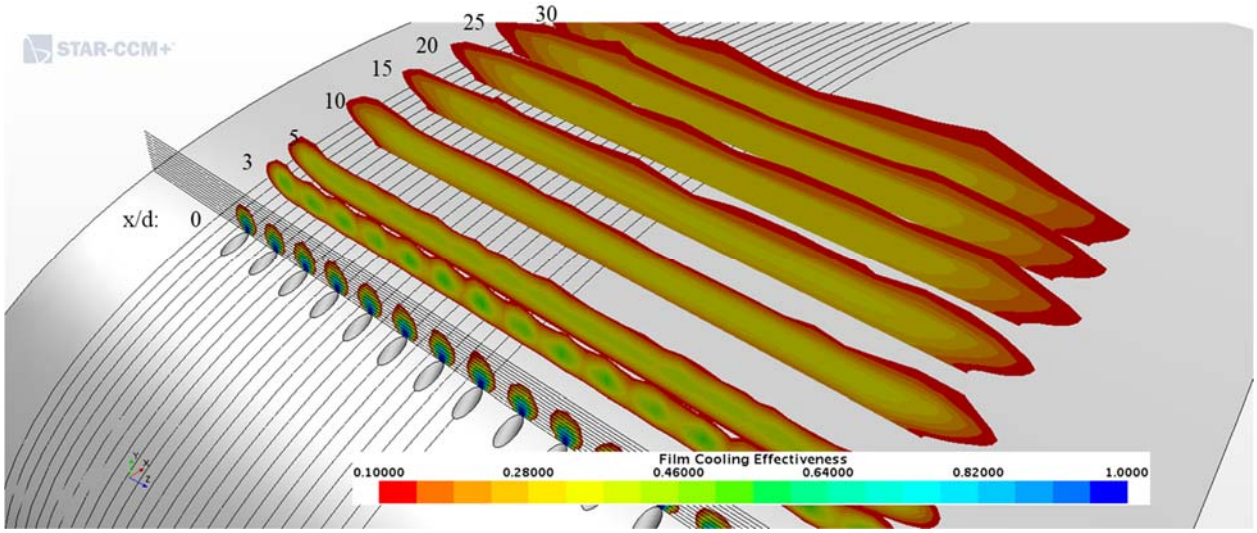

Figure 16.102: Case 10 - Streamwise spatial distribution of adiabatic film cooling effectiveness

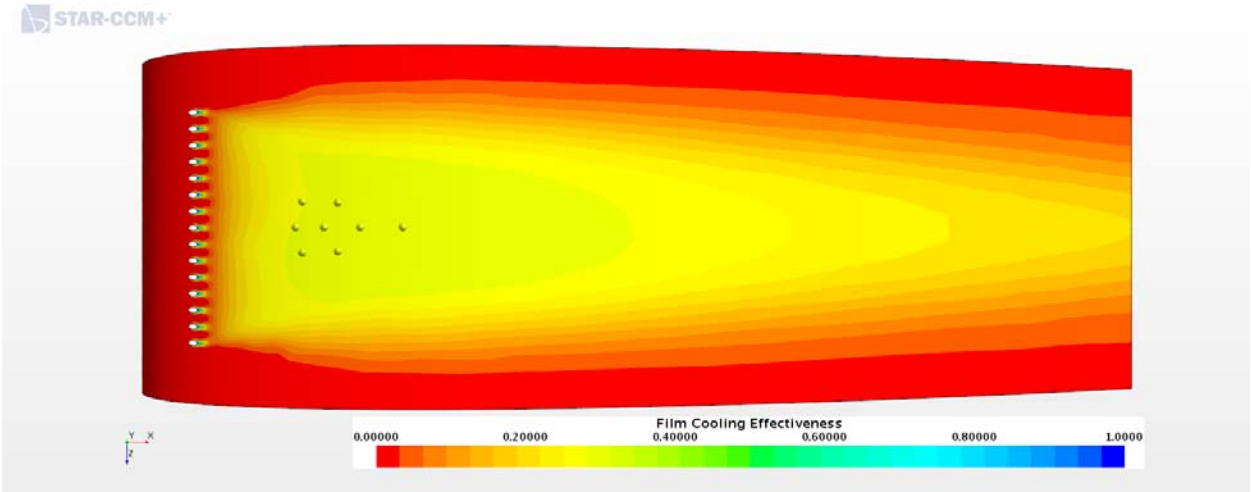

Figure 16.103: Case 10 - Adiabatic Film Cooling Effectiveness on the Suction Surface

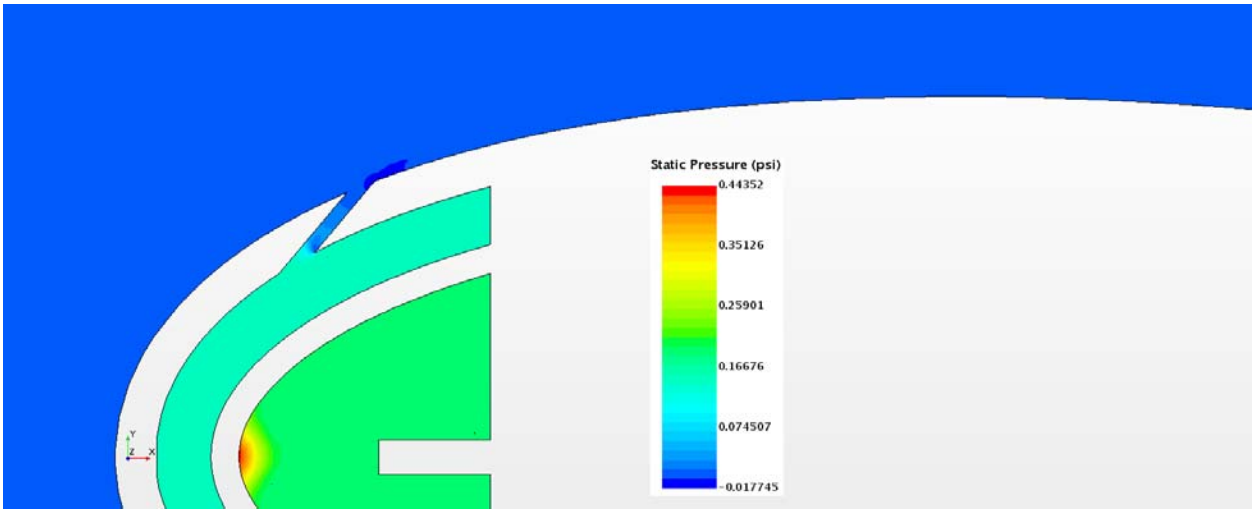

Figure 16.104: Case 10 – Static Pressure profile for center plane

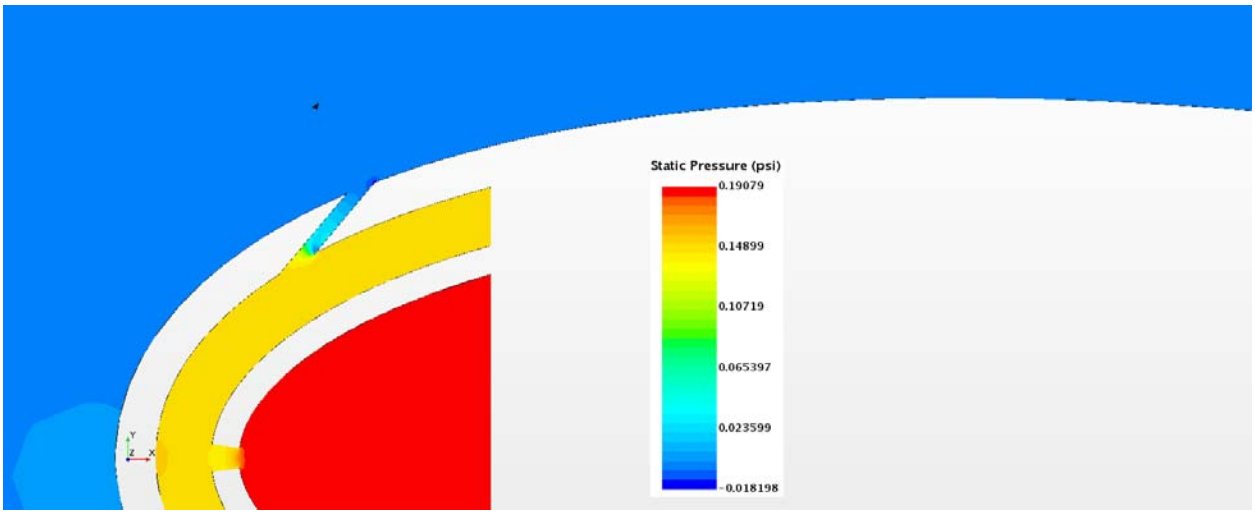

Figure 16.105: Case 10 – Static Pressure profile for off-center plane

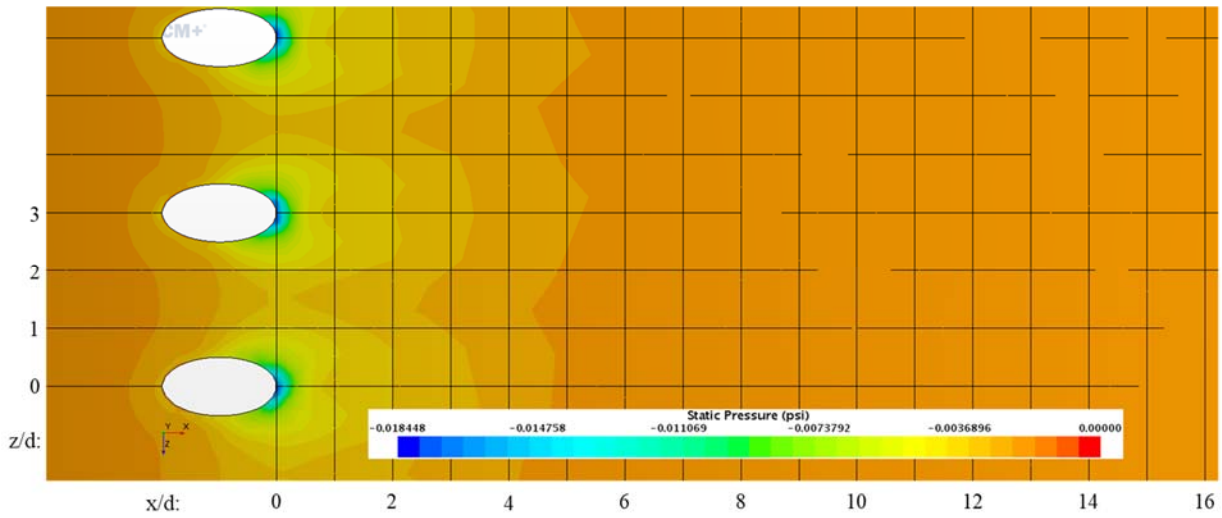

Figure 16.106: Case 10 – Static Pressure distribution for Suction Surface

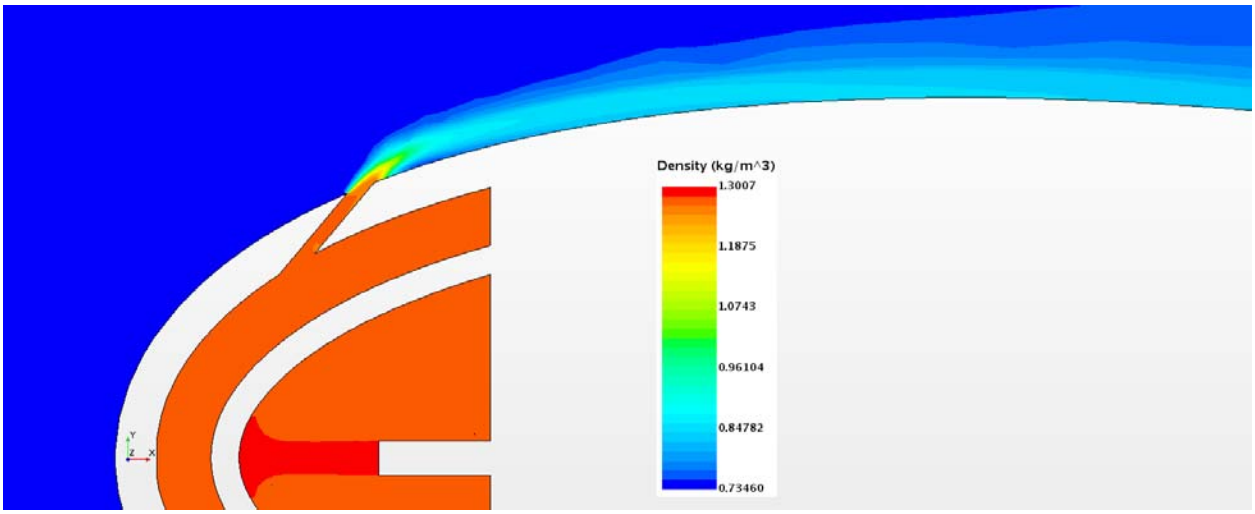

Figure 16.107: Case 10 – Density profile for center plane

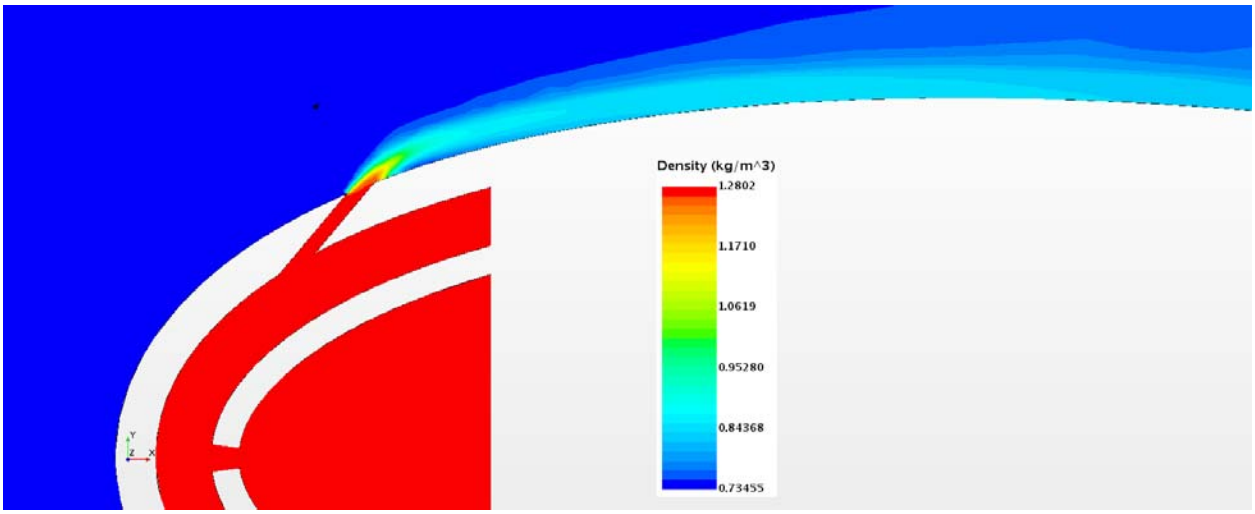

Figure 16.108: Case 10 – Density profile for off-center plane

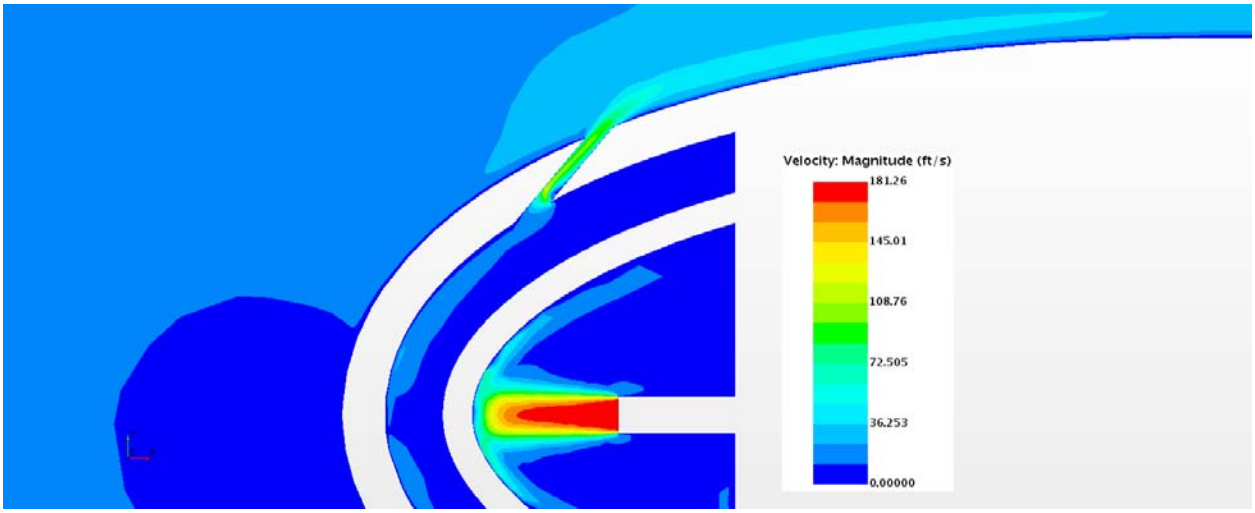

Figure 16.109: Case 10 – Velocity profile for center plane

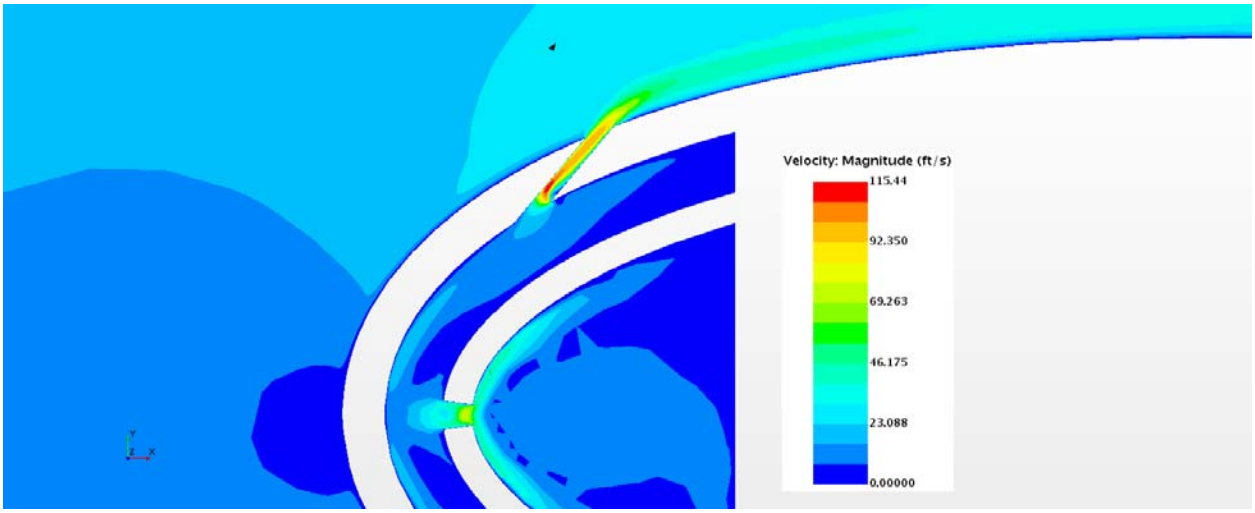

Figure 16.110: Case 10 – Velocity profile for off- center plane

Appendix G-11: M_b = 0.53, Tu = 20%, DR = 1.65

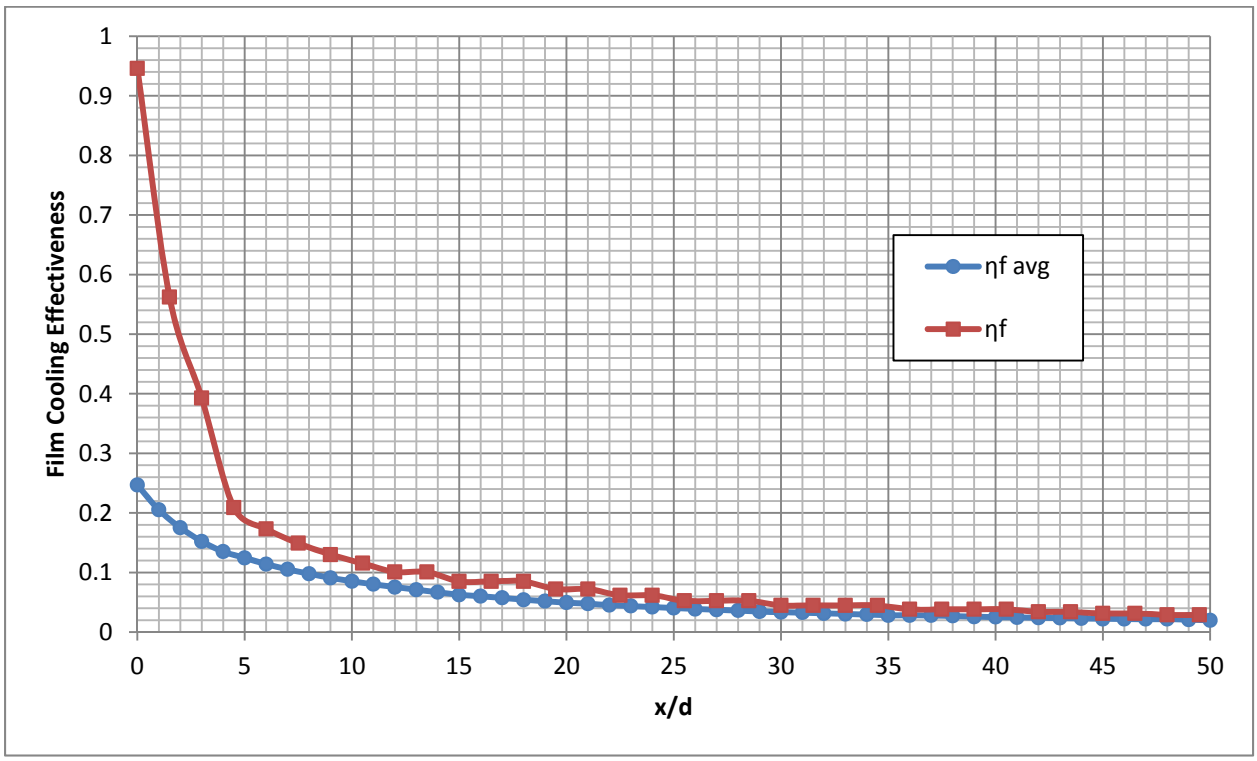

Figure 16.111: Case 11 - Laterally averaged and Centerline adiabatic film cooling effectiveness

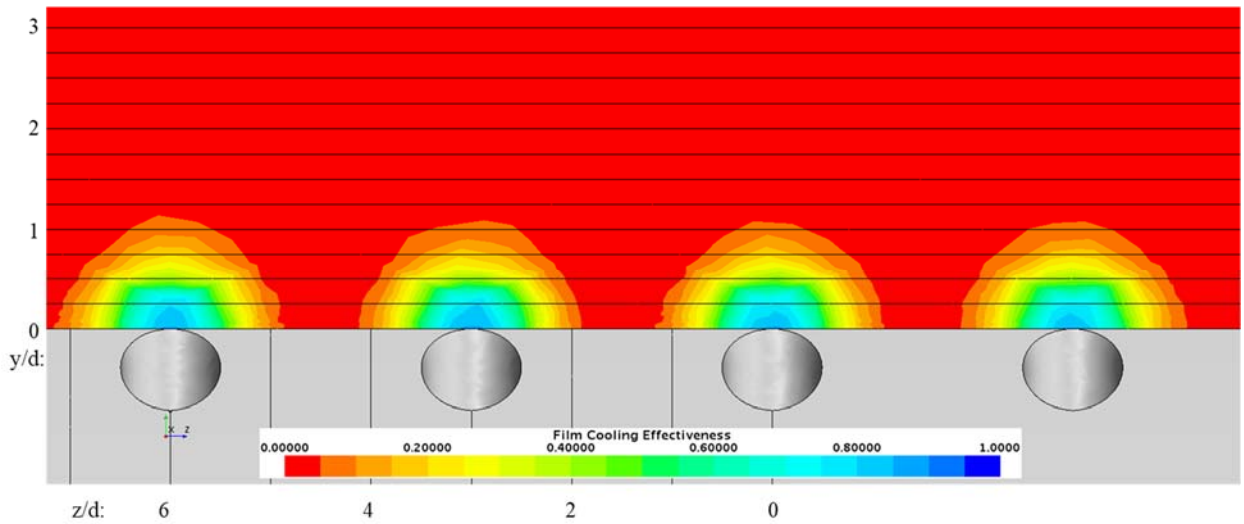

Figure 16.112: Case 11 - Spatial distribution of adiabatic film cooling effectiveness at x/d: 0

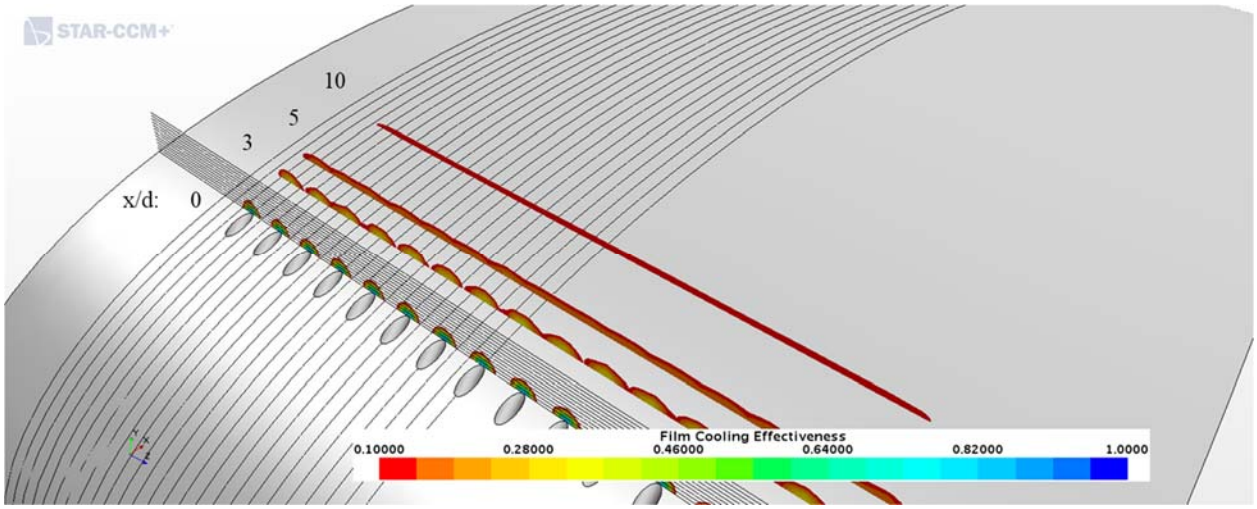

Figure 16.113: Case 11 - Streamwise spatial distribution of adiabatic film cooling effectiveness

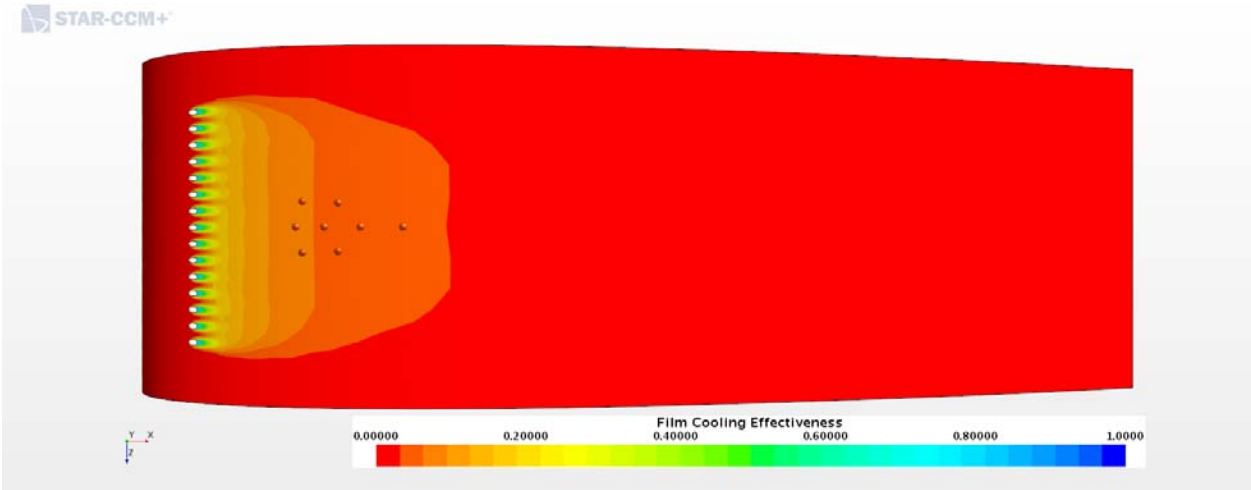

Figure 16.114: Case 11 - Adiabatic Film Cooling Effectiveness on the Suction Surface

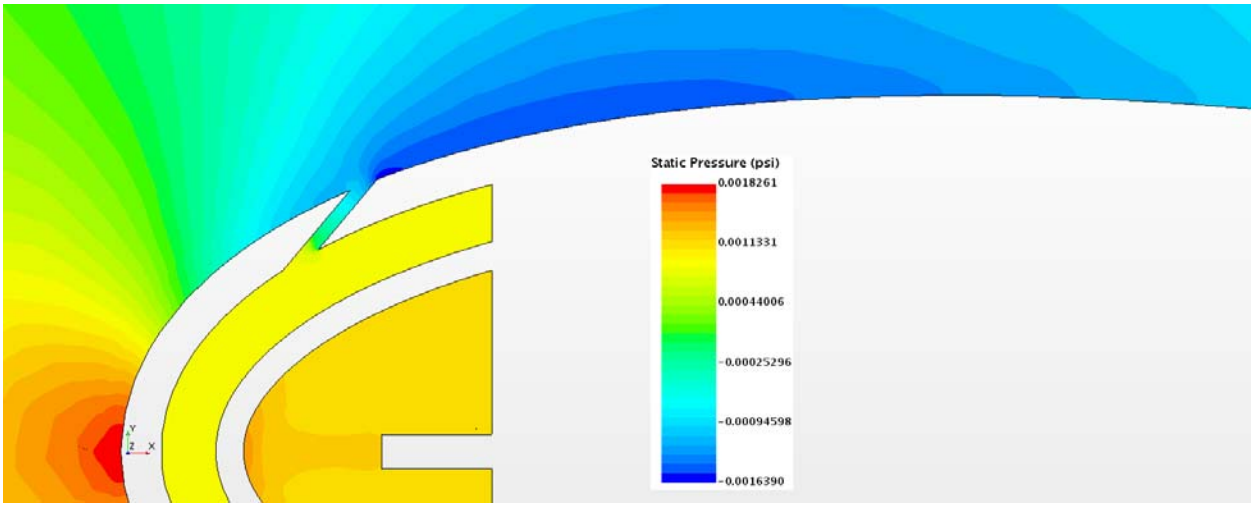

Figure 16.115: Case 11 – Static Pressure profile for center plane

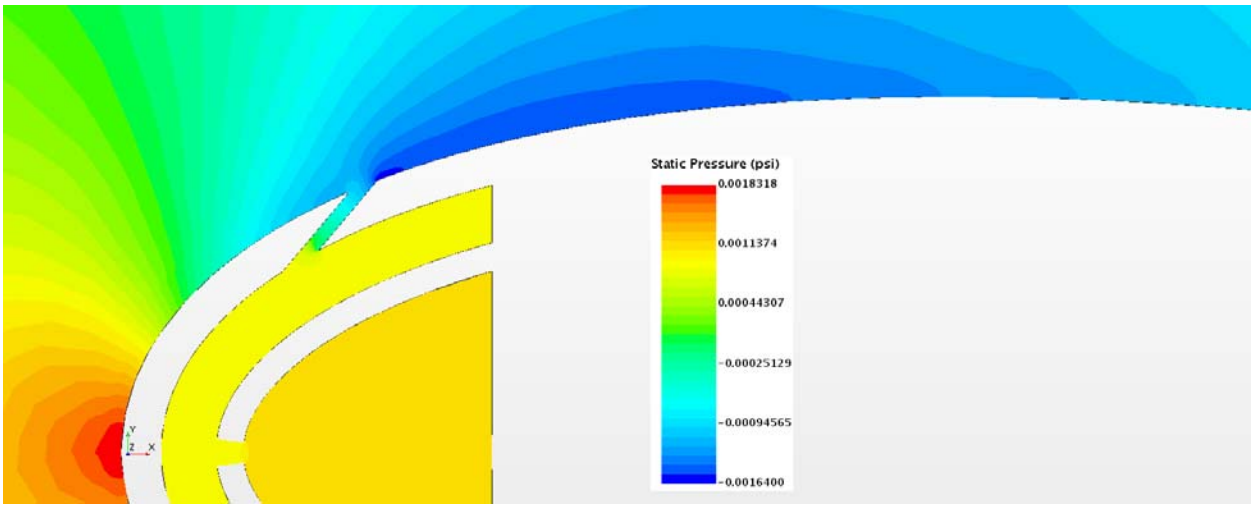

Figure 16.116: Case 11 – Static Pressure profile for off-center plane

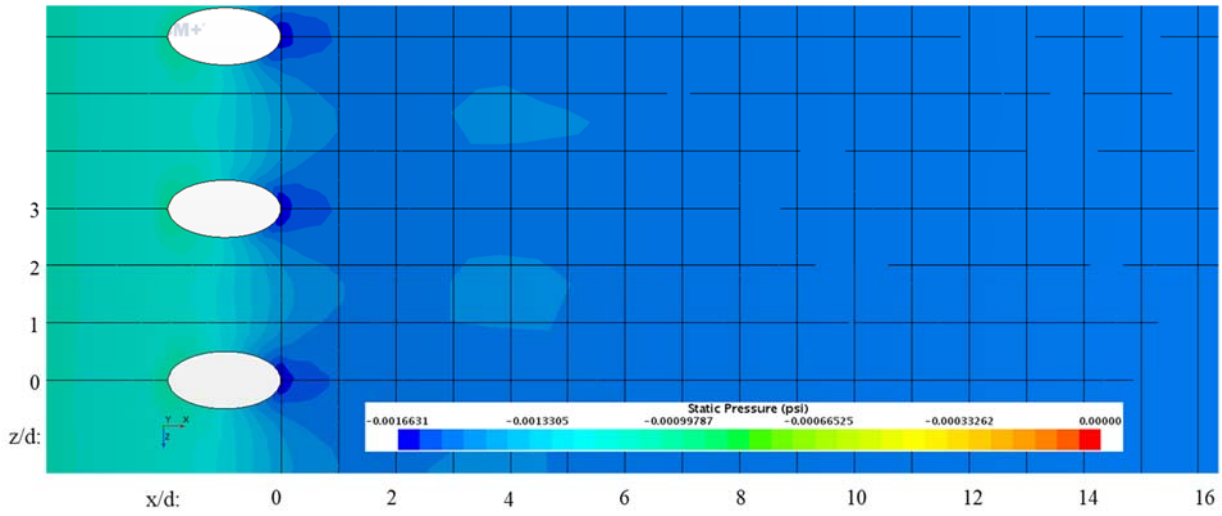

Figure 16.117: Case 11 – Static Pressure distribution for Suction Surface

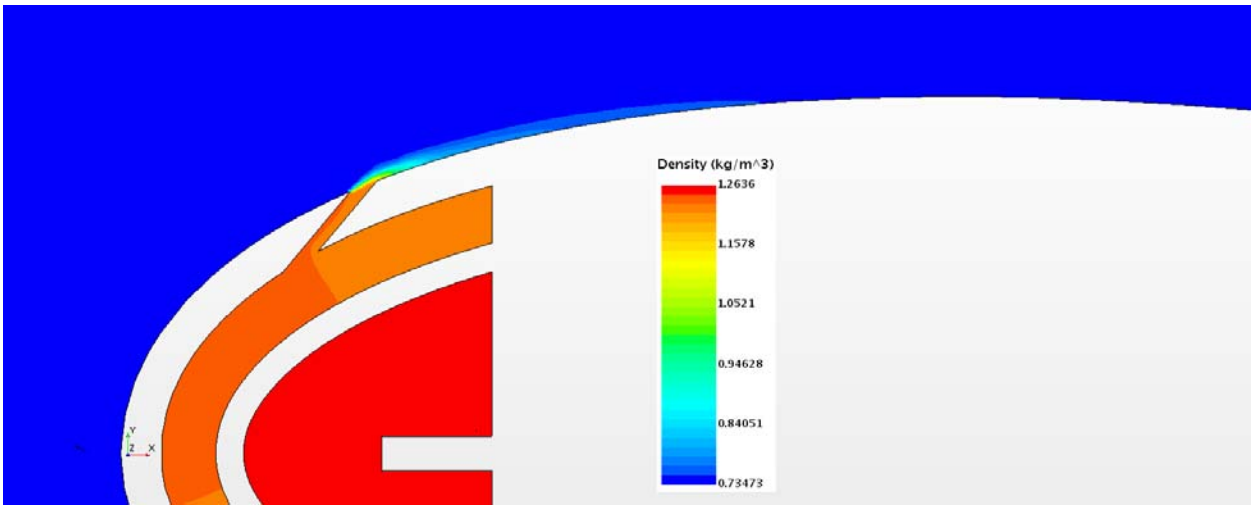

Figure 16.118: Case 11 – Density profile for center plane

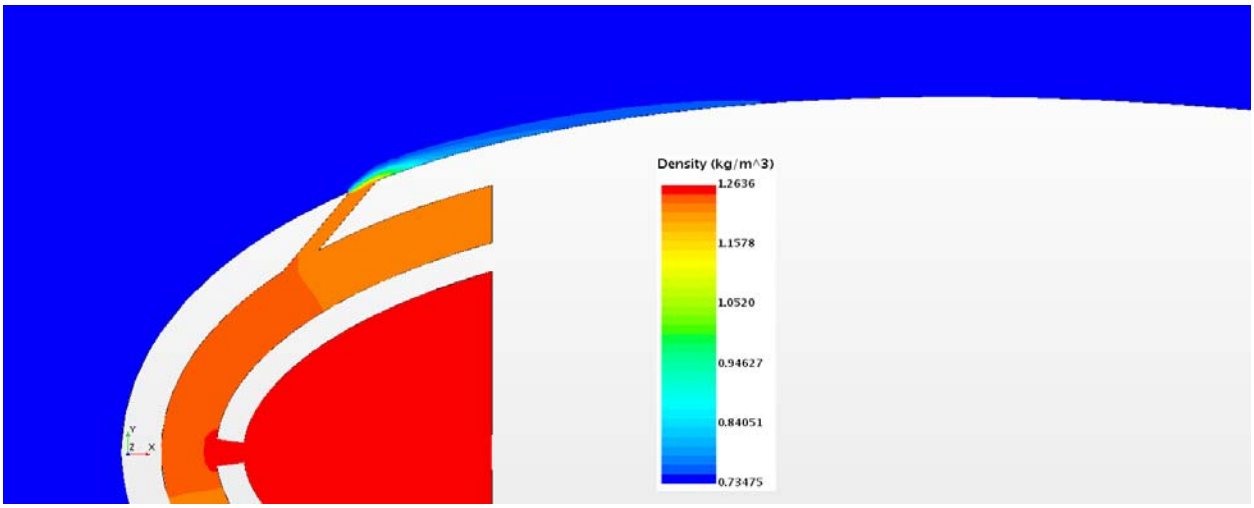

Figure 16.119: Case 11 – Density profile for off-center plane

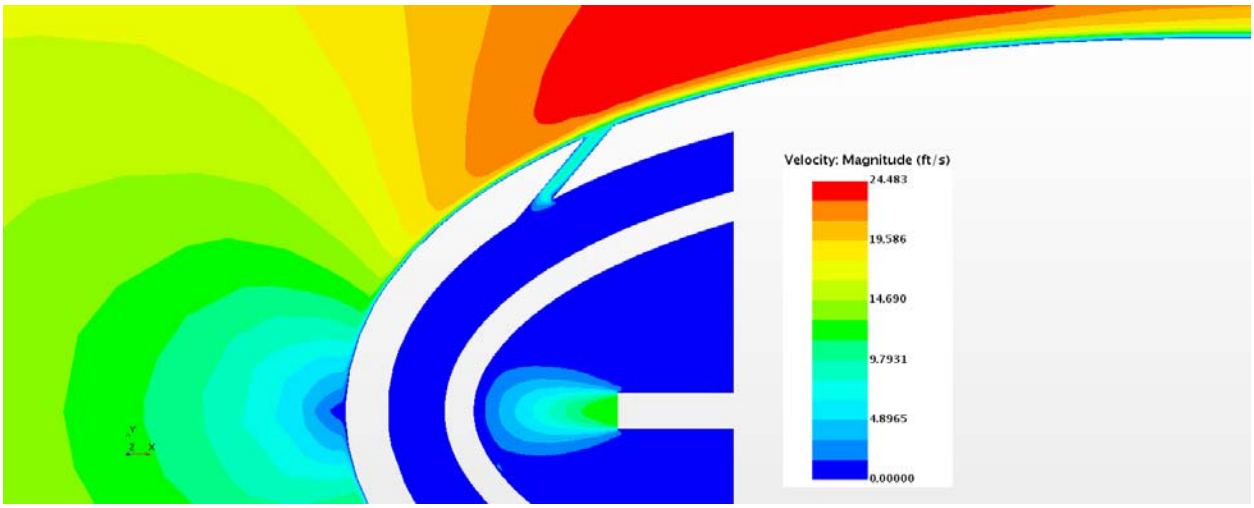

Figure 16.120: Case 11 – Velocity profile for center plane

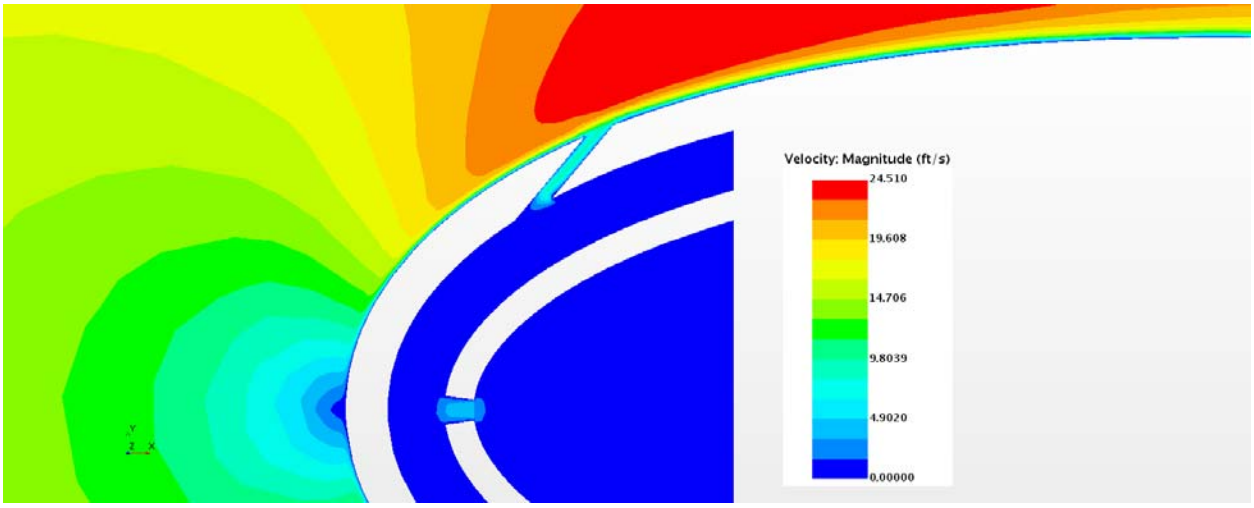

Figure 16.121: Case 11 – Velocity profile for off- center plane

Appendix G-12: M_b = 0.77, Tu = 20%, DR = 1.65

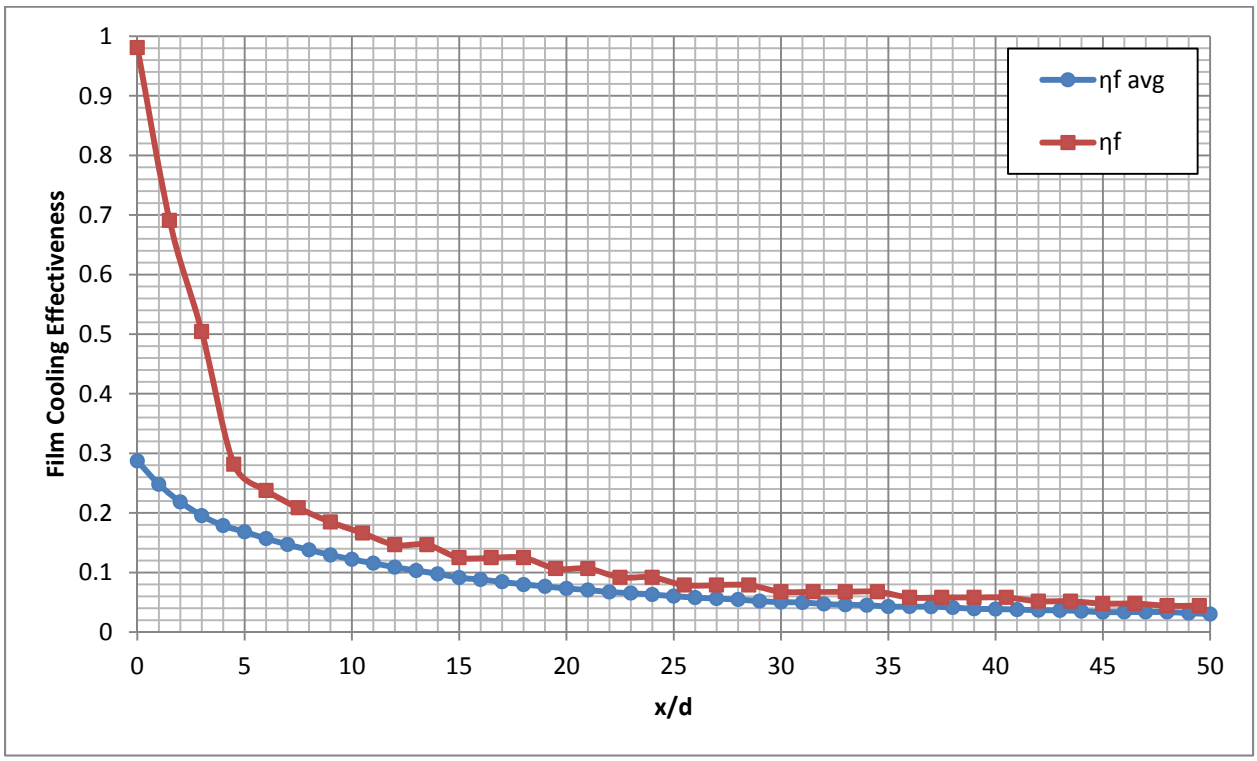

Figure 16.122: Case 12 - Laterally averaged and Centerline adiabatic film cooling effectiveness

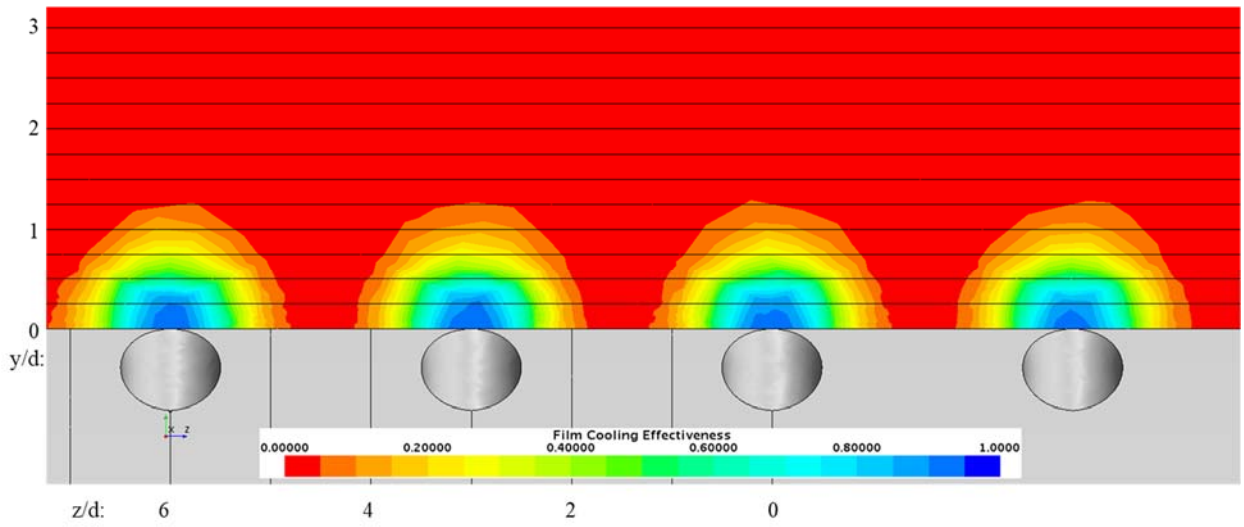

Figure 16.123: Case 12 - Spatial distribution of adiabatic film cooling effectiveness at x/d: 0

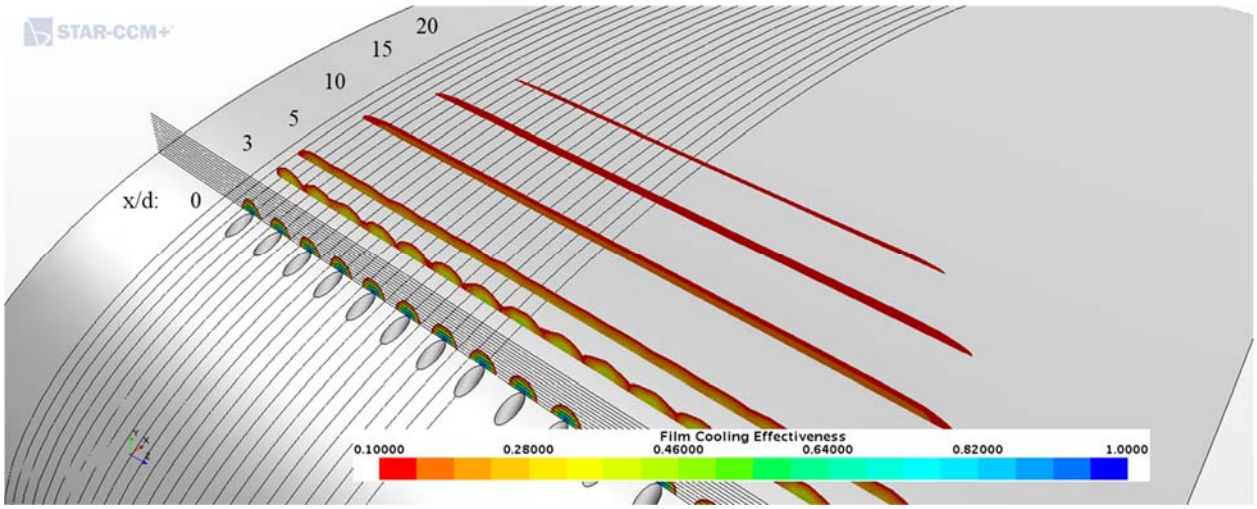

Figure 16.124: Case 12 - Streamwise spatial distribution of adiabatic film cooling effectiveness

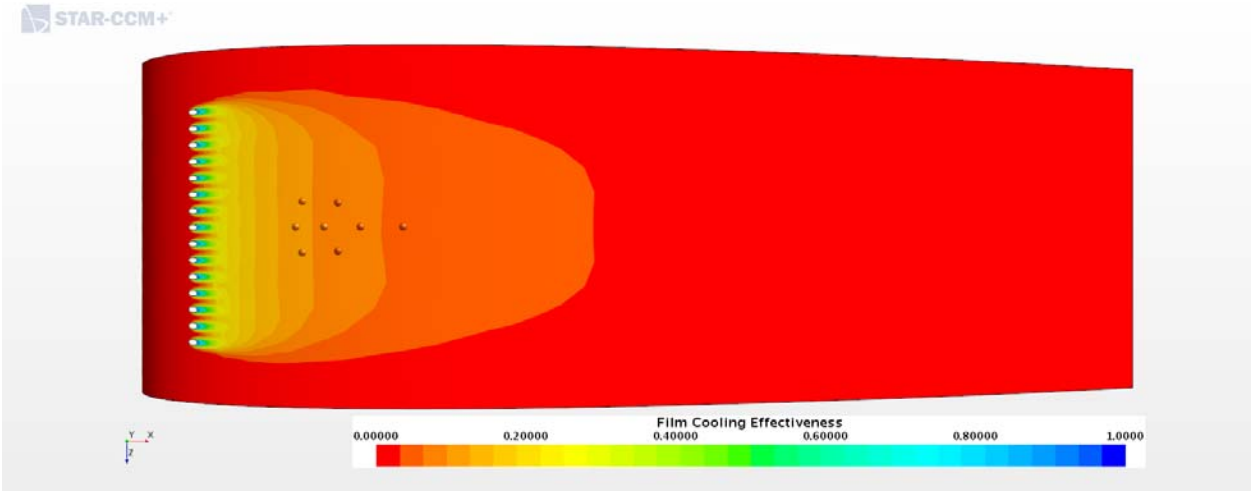

Figure 16.125: Case 12 - Adiabatic Film Cooling Effectiveness on the Suction Surface

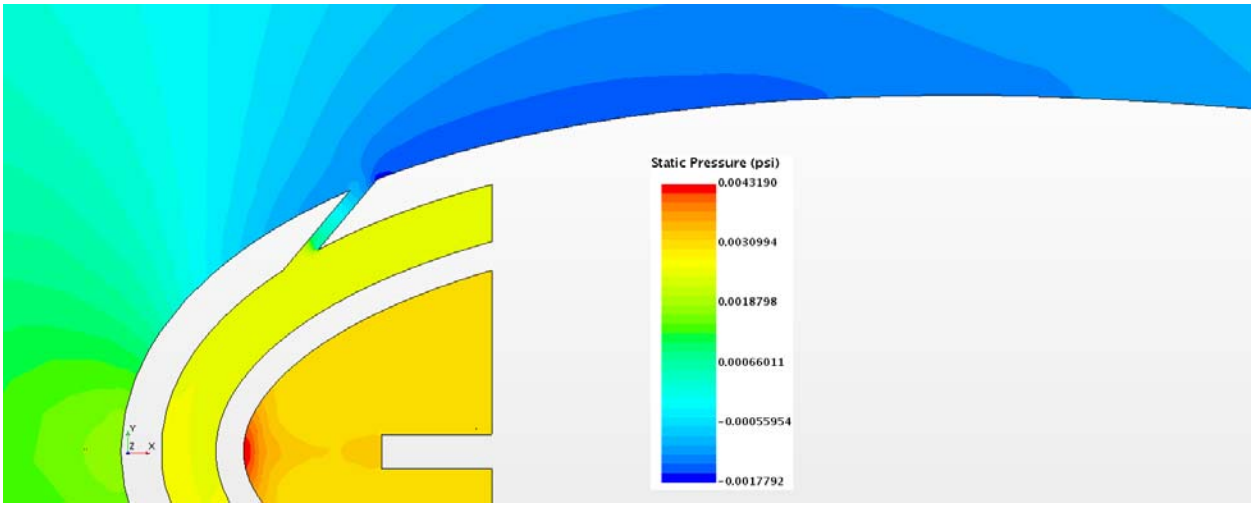

Figure 16.126: Case 12 – Static Pressure profile for center plane

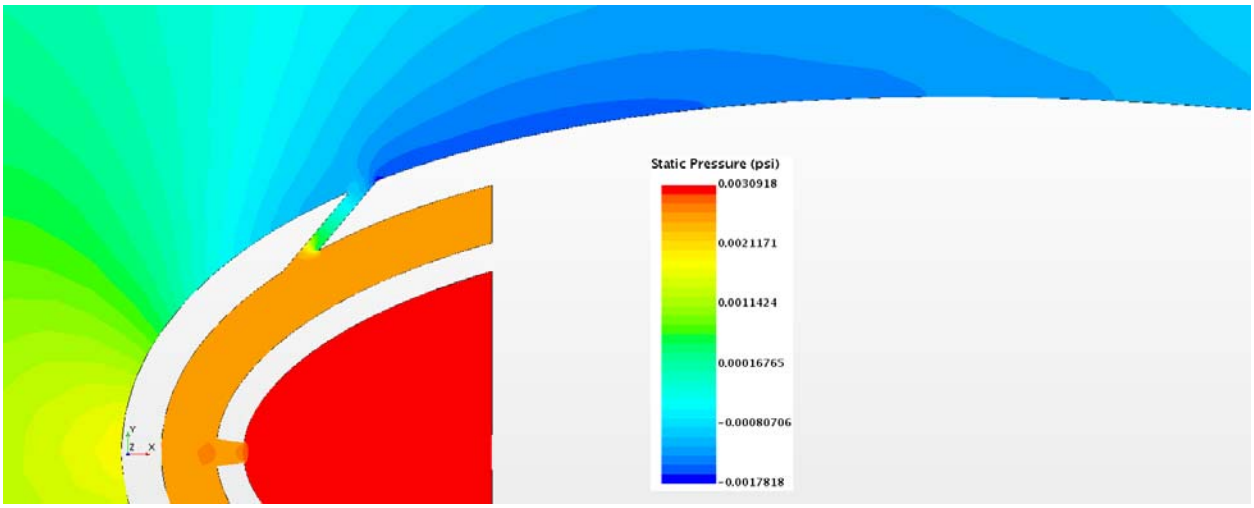

Figure 16.127: Case 12 – Static Pressure profile for off-center plane

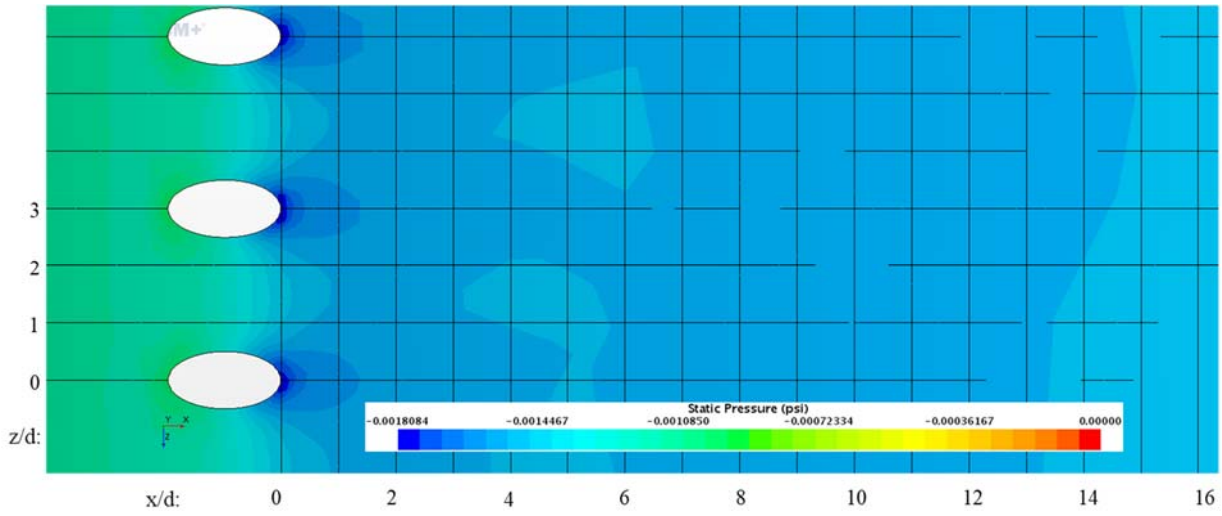

Figure 16.128: Case 12 – Static Pressure distribution for Suction Surface

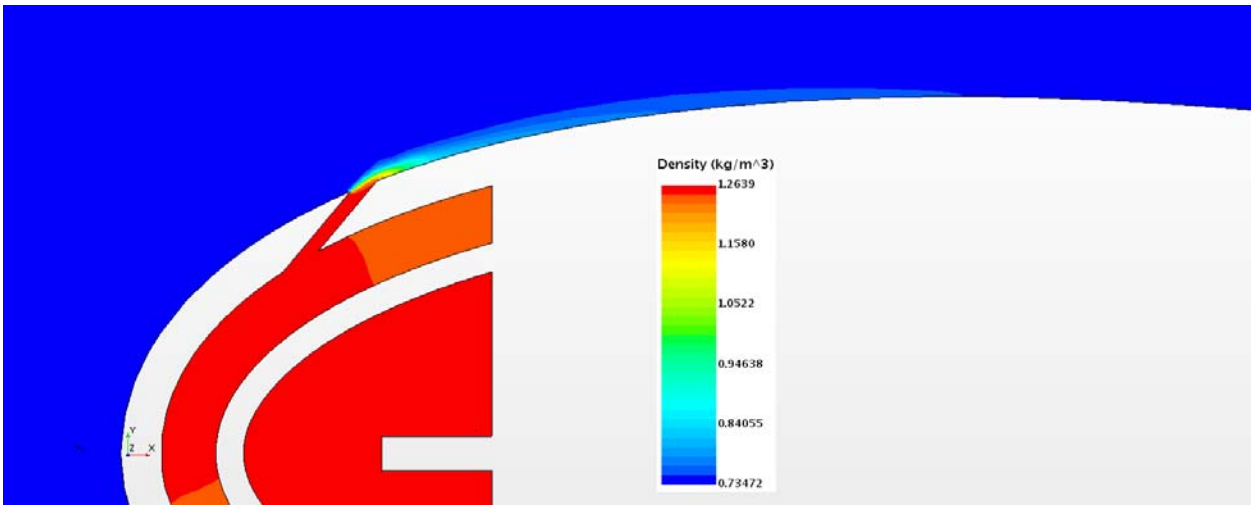

Figure 16.129: Case 12 – Density profile for center plane

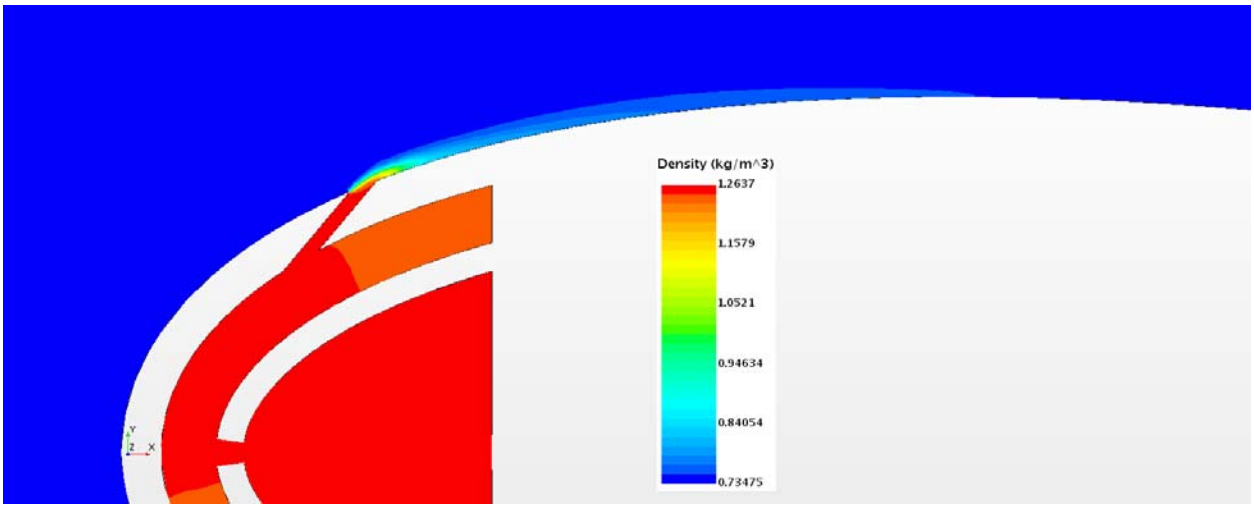

Figure 16.130: Case 12 – Density profile for off-center plane

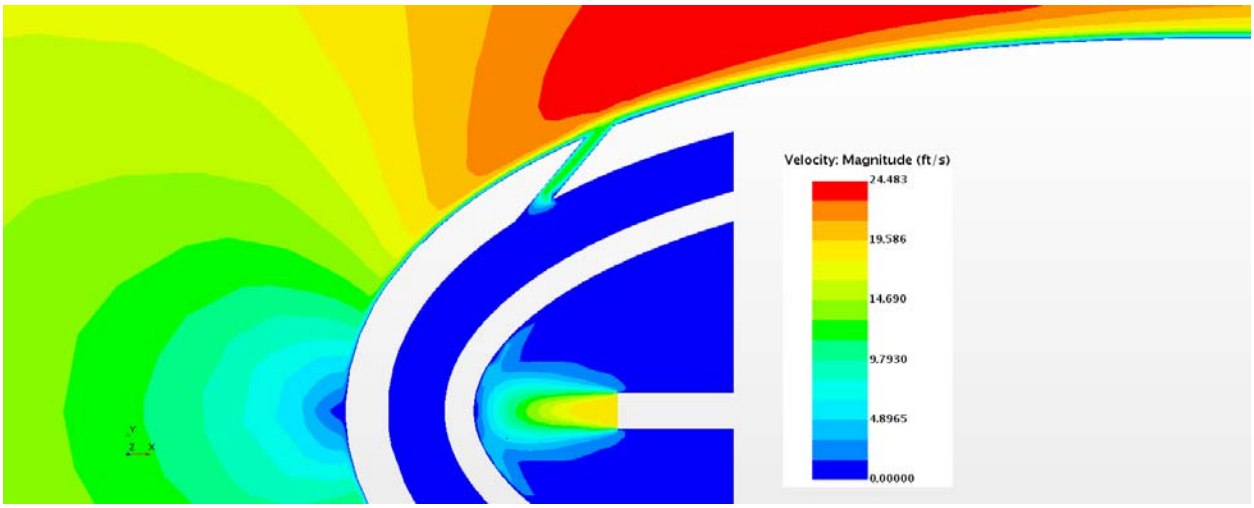

Figure 16.131: Case 12 – Velocity profile for center plane

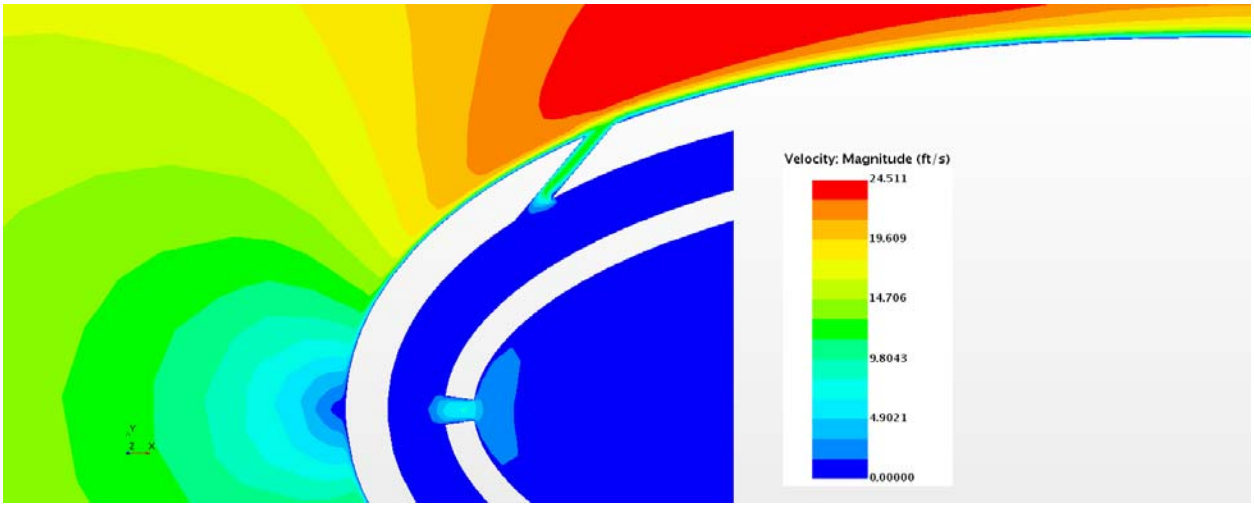

Figure 16.132: Case 12 – Velocity profile for off- center plane

Appendix G-13: M_b = 1.51, Tu = 20%, DR = 1.65

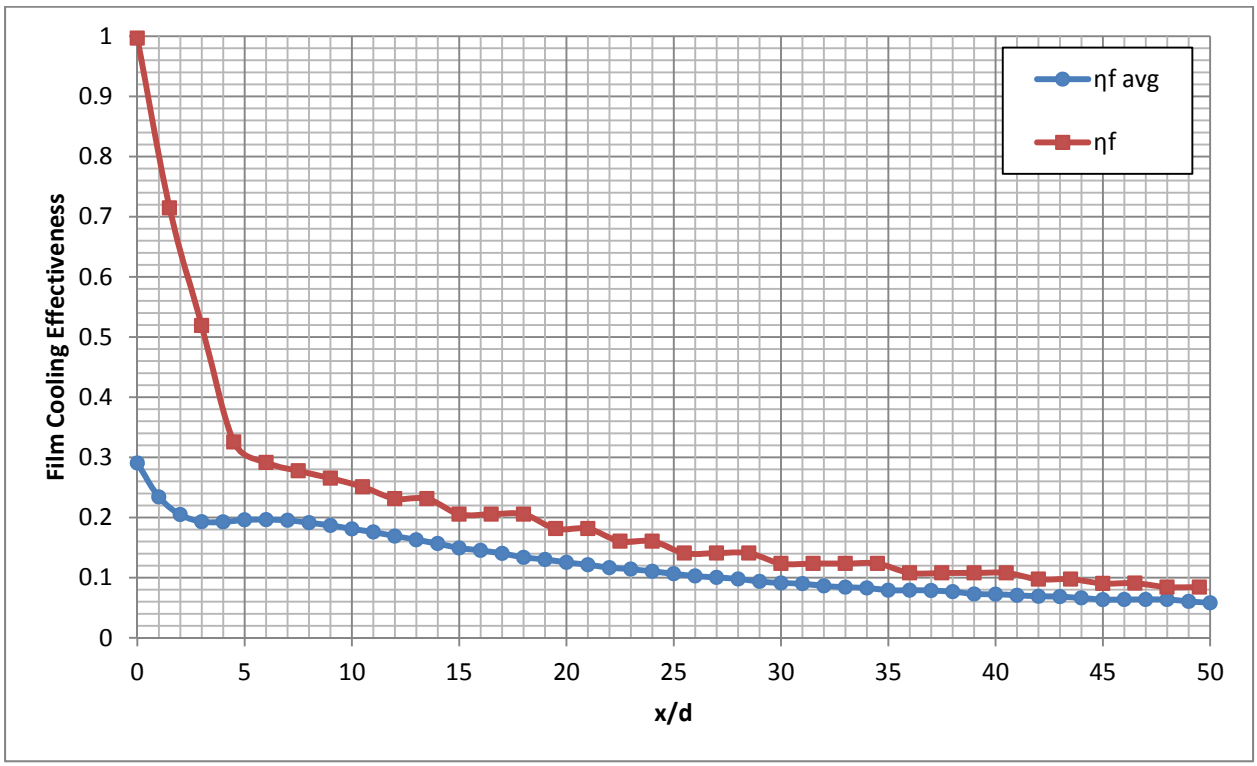

Figure 16.133: Case 13 - Laterally averaged and Centerline adiabatic film cooling effectiveness

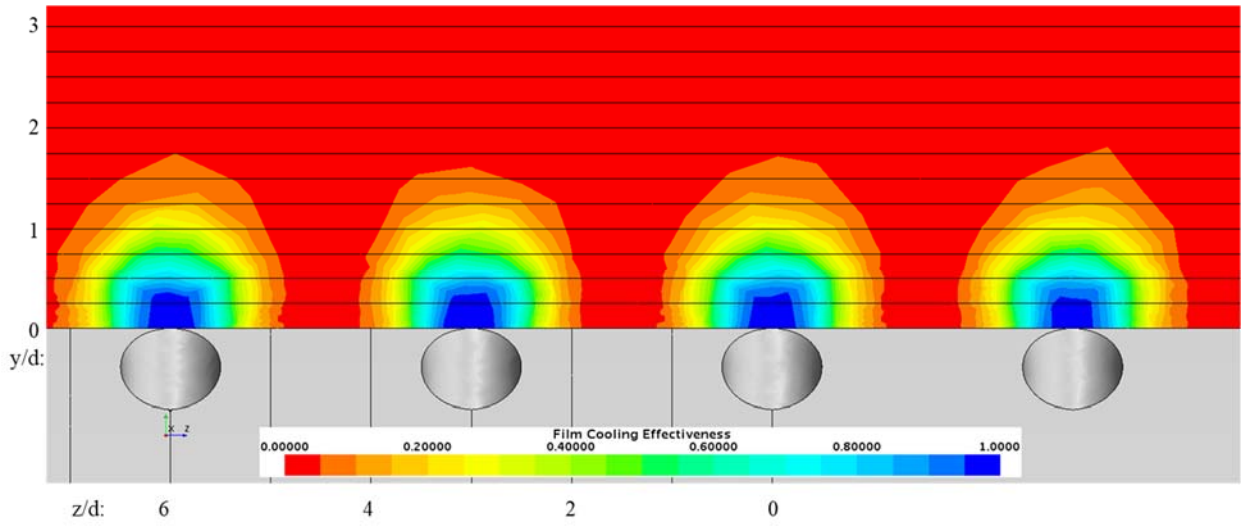

Figure 16.134: Case 13 - Spatial distribution of adiabatic film cooling effectiveness at x/d: 0

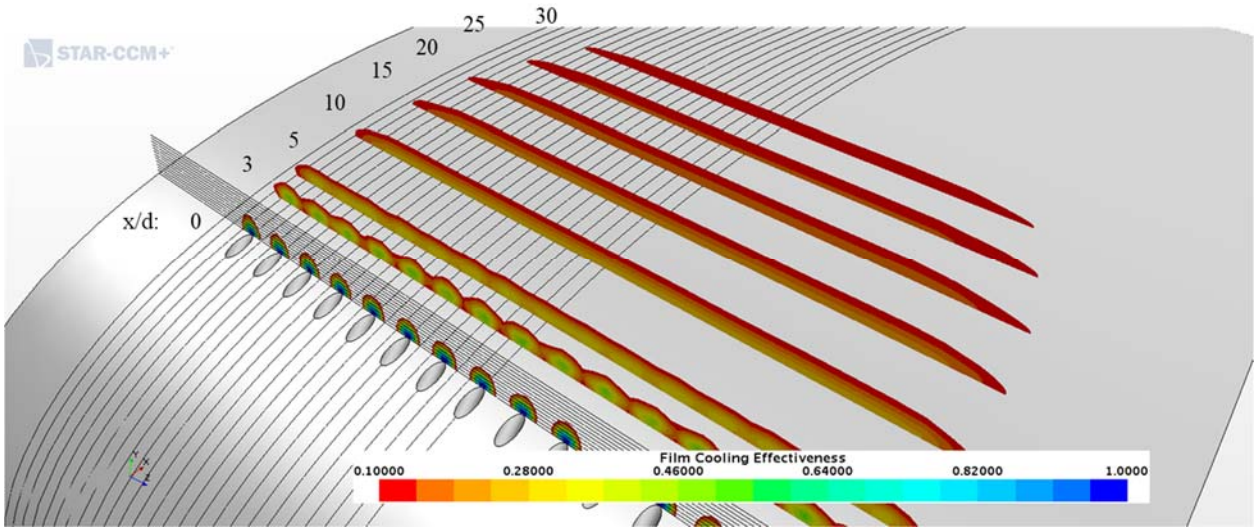

Figure 16.135: Case 13 - Streamwise spatial distribution of adiabatic film cooling effectiveness

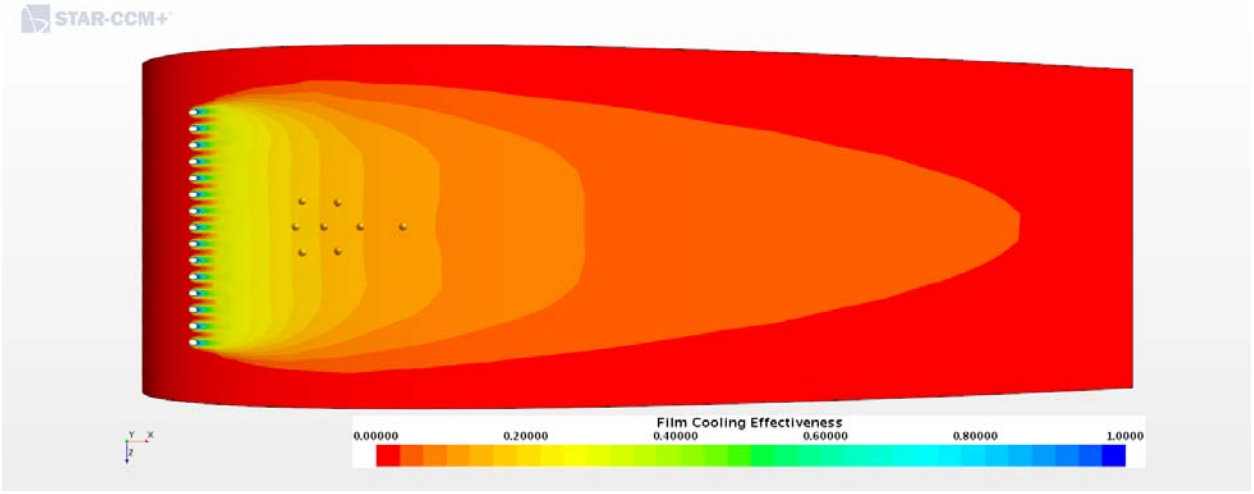

Figure 16.136: Case13 - Adiabatic Film Cooling Effectiveness on the Suction Surface

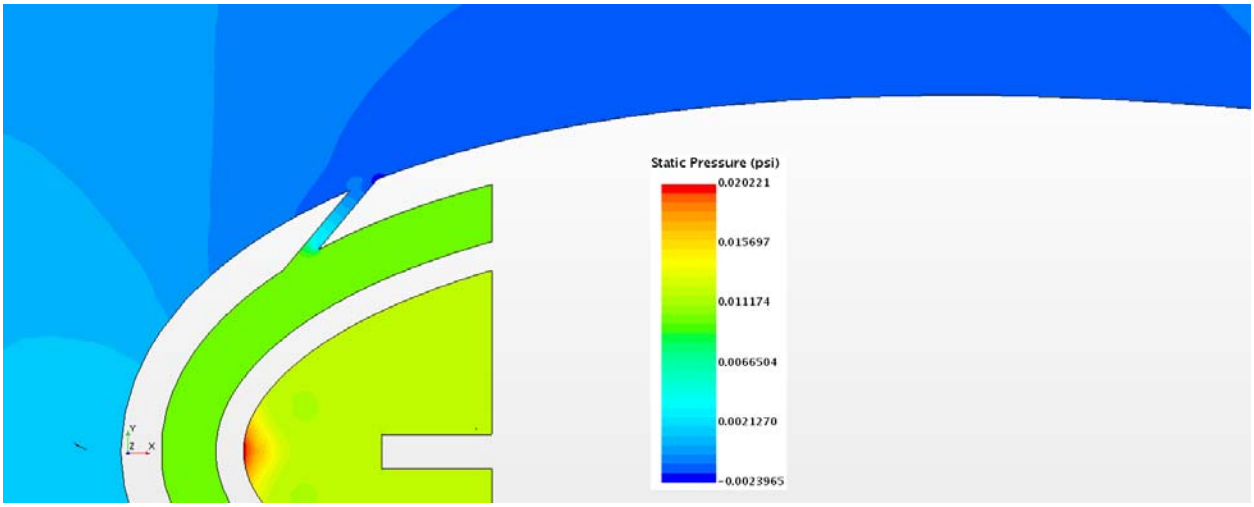

Figure 16.137: Case 13 – Static Pressure profile for center plane

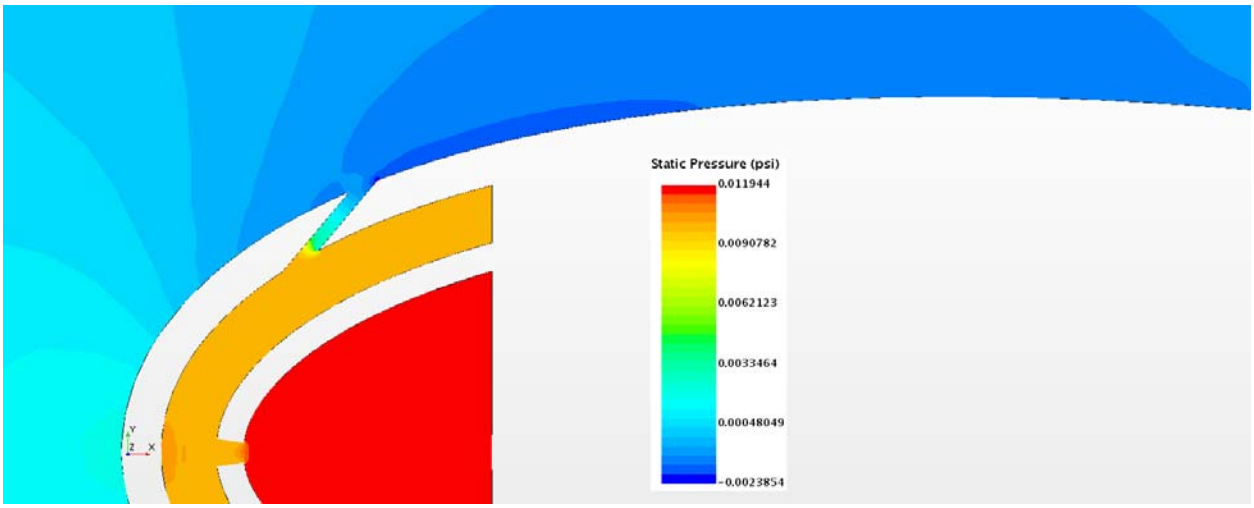

Figure 16.138: Case 13 – Static Pressure profile for off-center plane

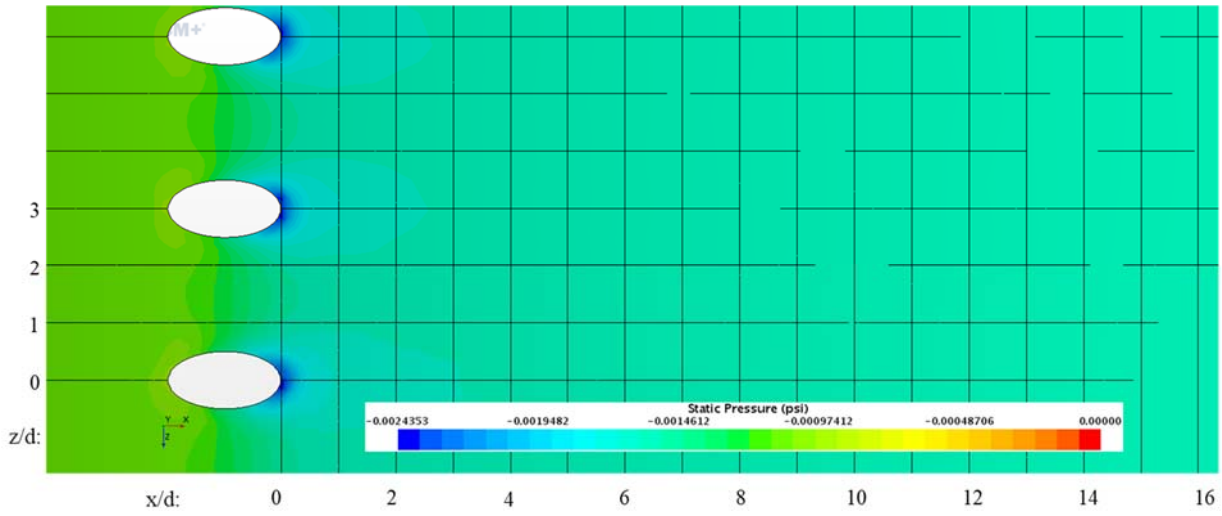

Figure 16.139: Case 13 – Static Pressure distribution for Suction Surface

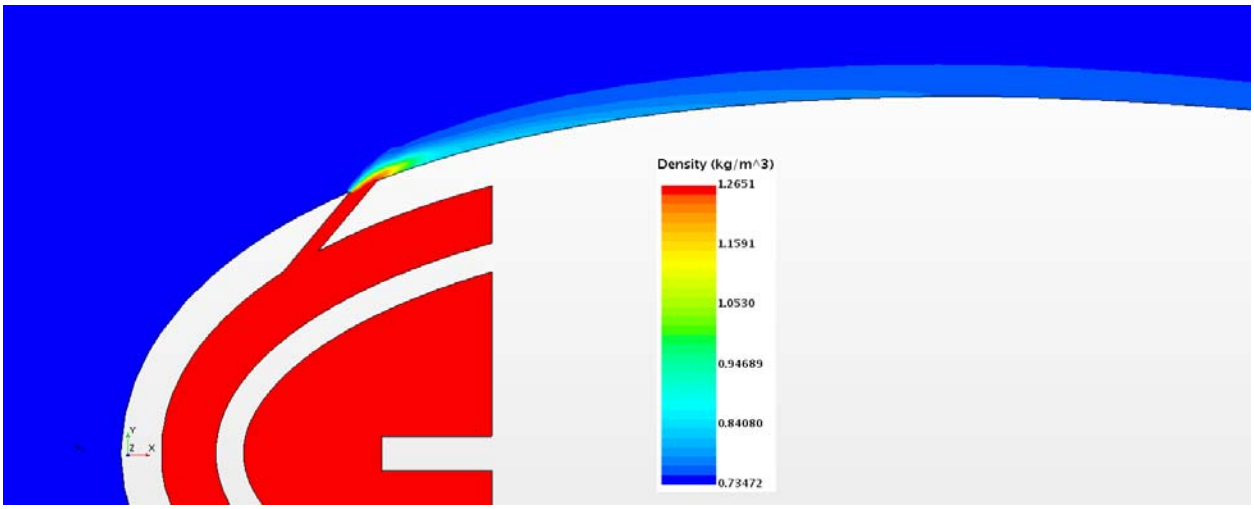

Figure 16.140: Case 13 – Density profile for center plane

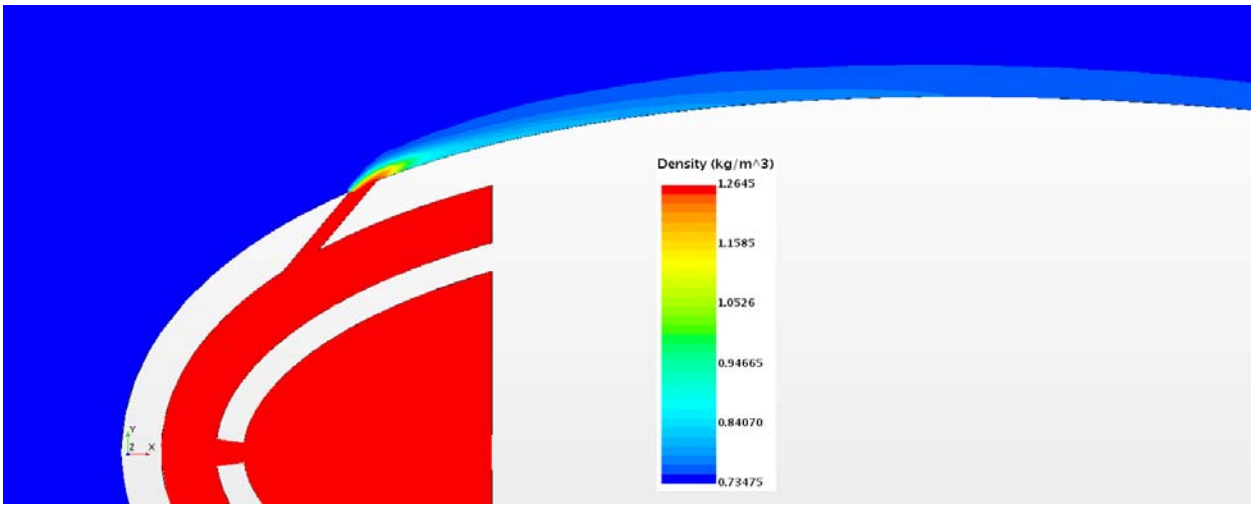

Figure 16.141: Case 13 – Density profile for off-center plane

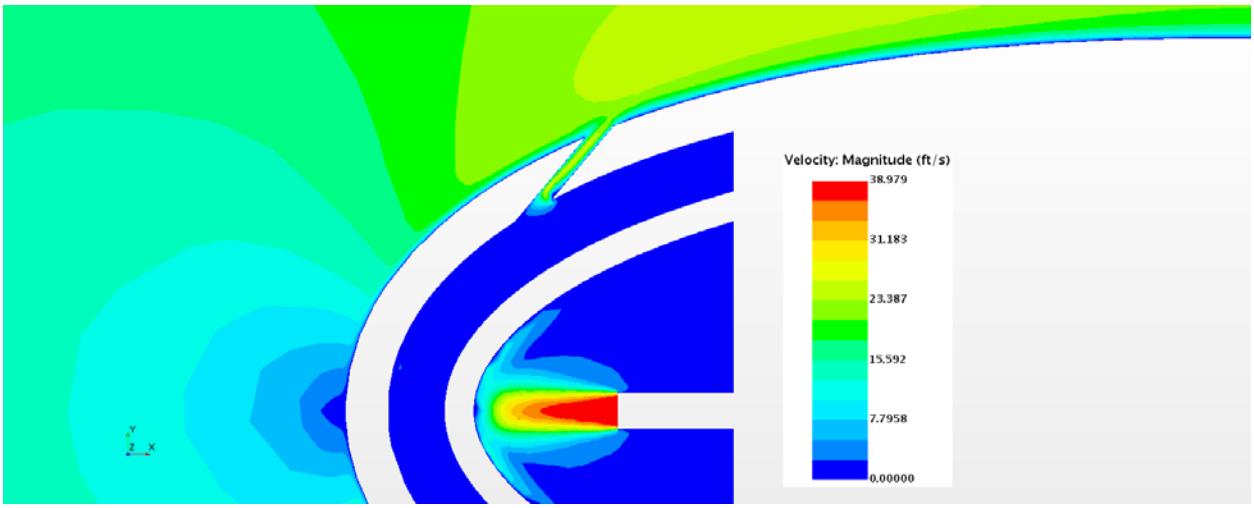

Figure 16.142: Case 13 – Velocity profile for center plane

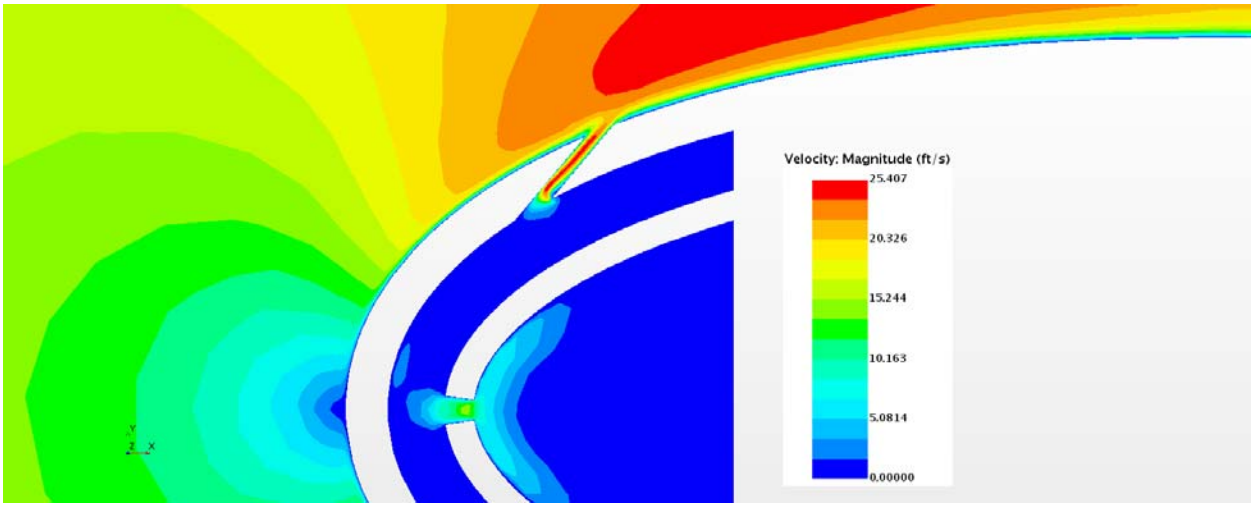

Figure 16.143: Case 13 – Velocity profile for off- center plane

Appendix G-14: M_b = 2.13, Tu = 20%, DR = 1.65

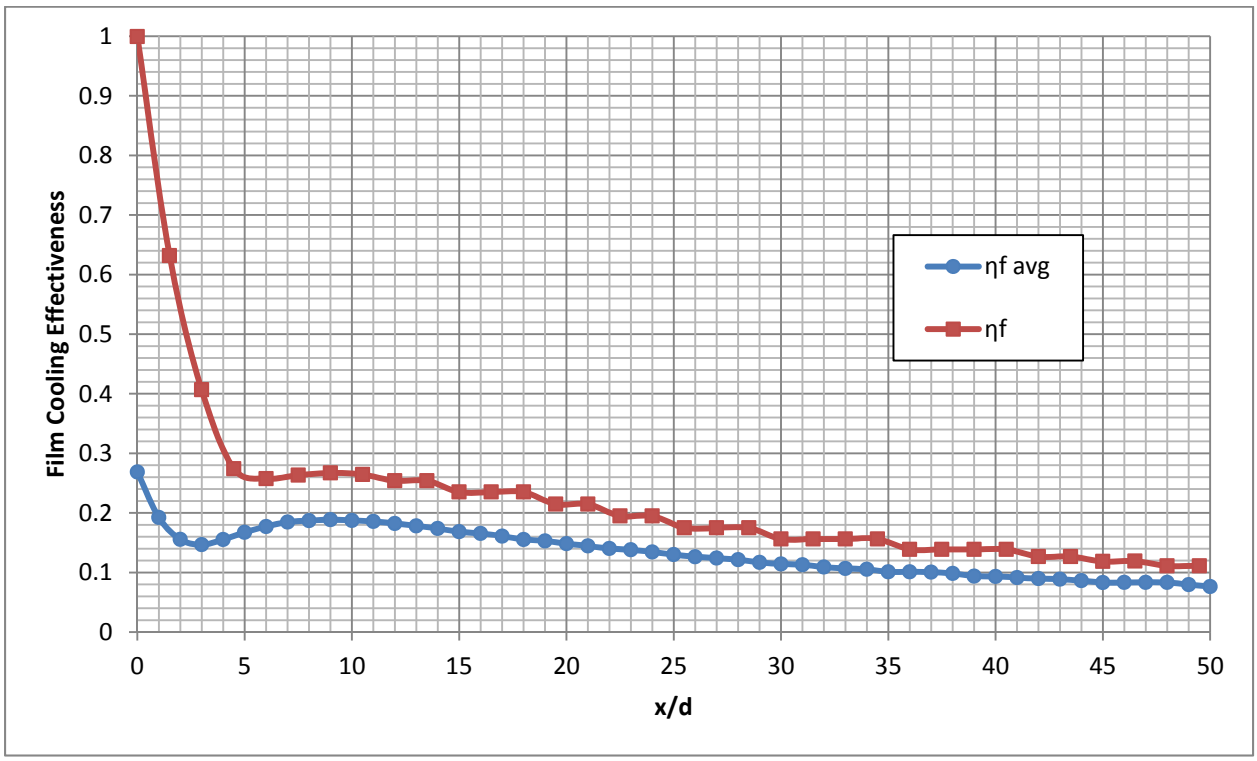

Figure 16.144: Case 14 - Laterally averaged and Centerline adiabatic film cooling effectiveness

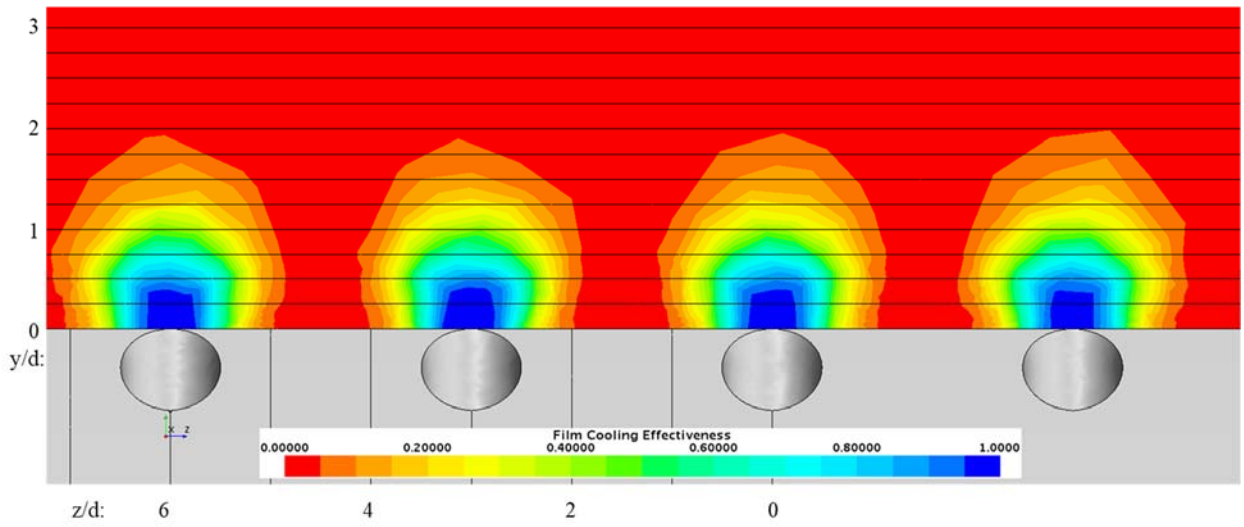

Figure 16.145: Case 14 - Spatial distribution of adiabatic film cooling effectiveness at x/d: 0

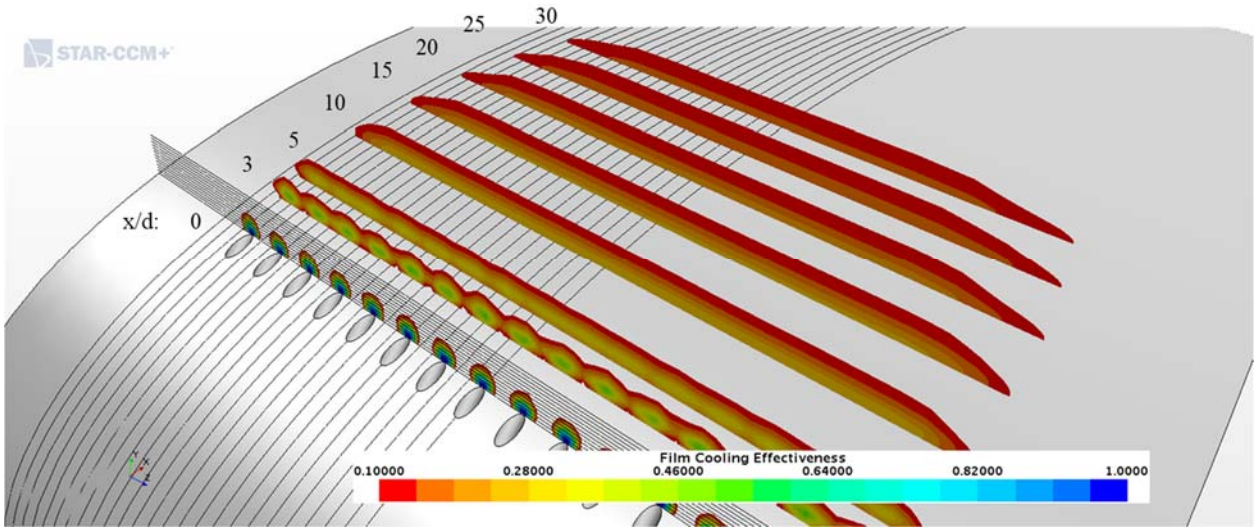

Figure 16.146: Case 14 - Streamwise spatial distribution of adiabatic film cooling effectiveness

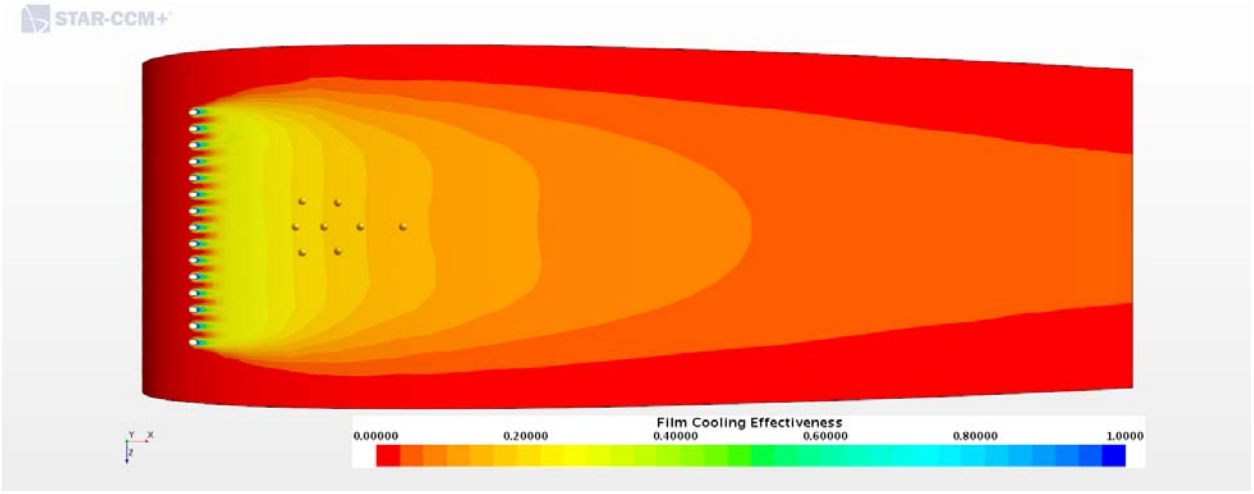

Figure 16.147: Case 14 - Adiabatic Film Cooling Effectiveness on the Suction Surface

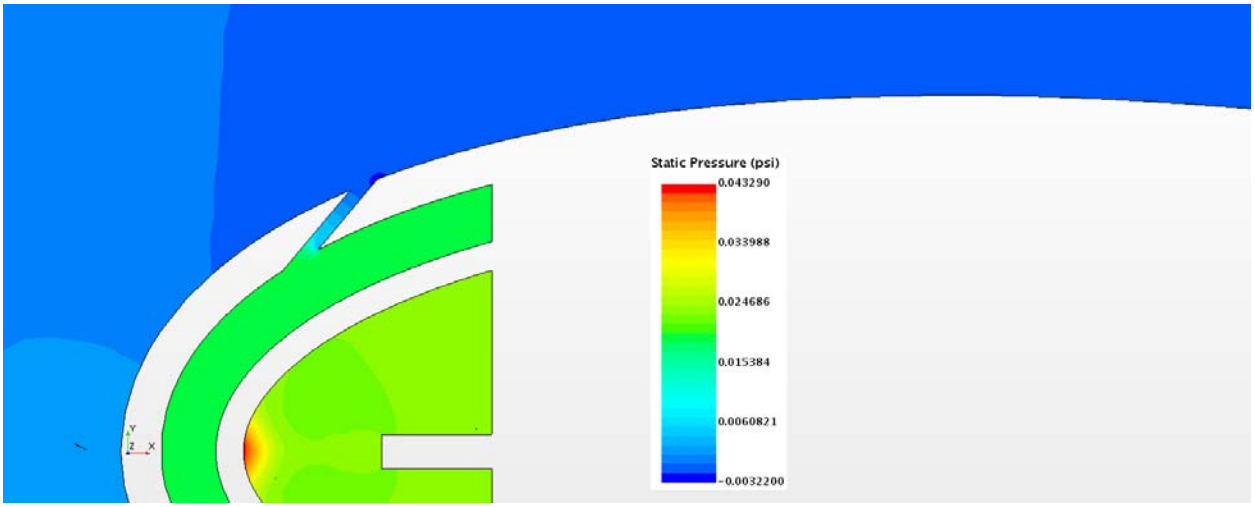

Figure 16.148: Case 14 – Static Pressure profile for center plane

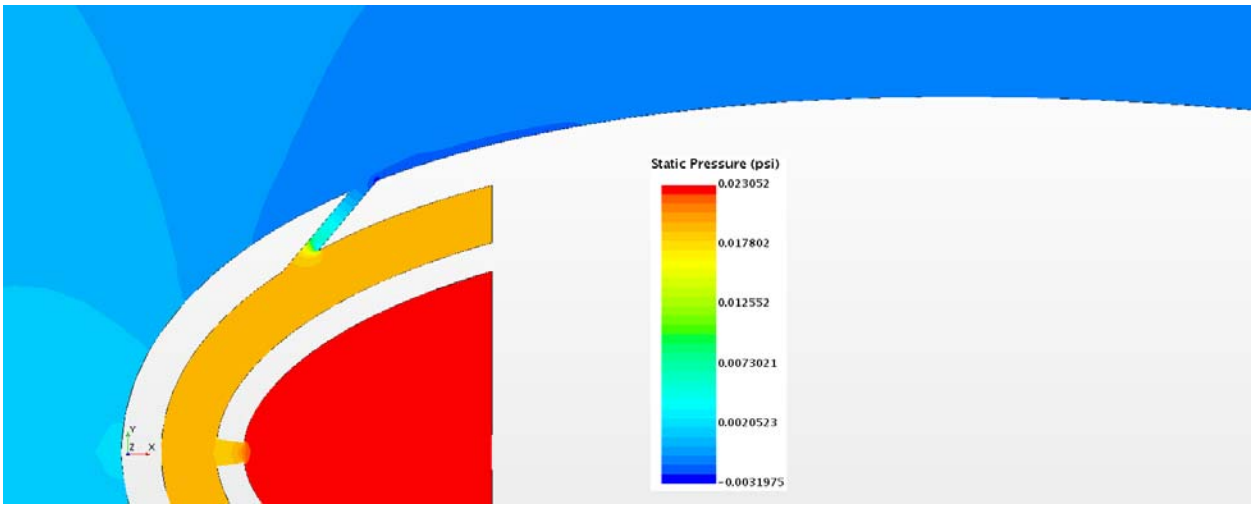

Figure 16.149: Case 14 – Static Pressure profile for off-center plane

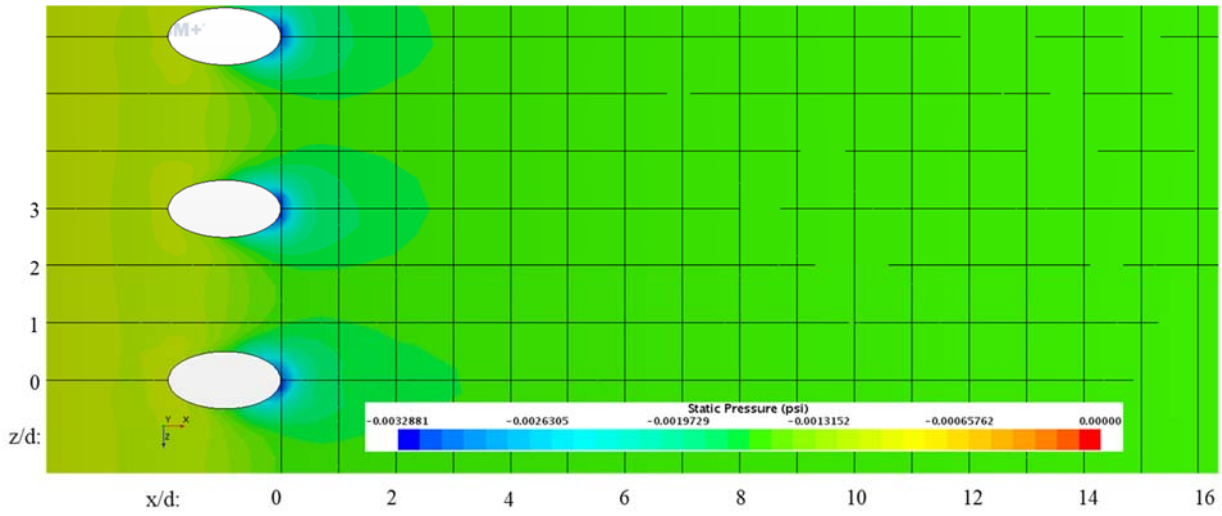

Figure 16.150: Case 14 – Static Pressure distribution for Suction Surface

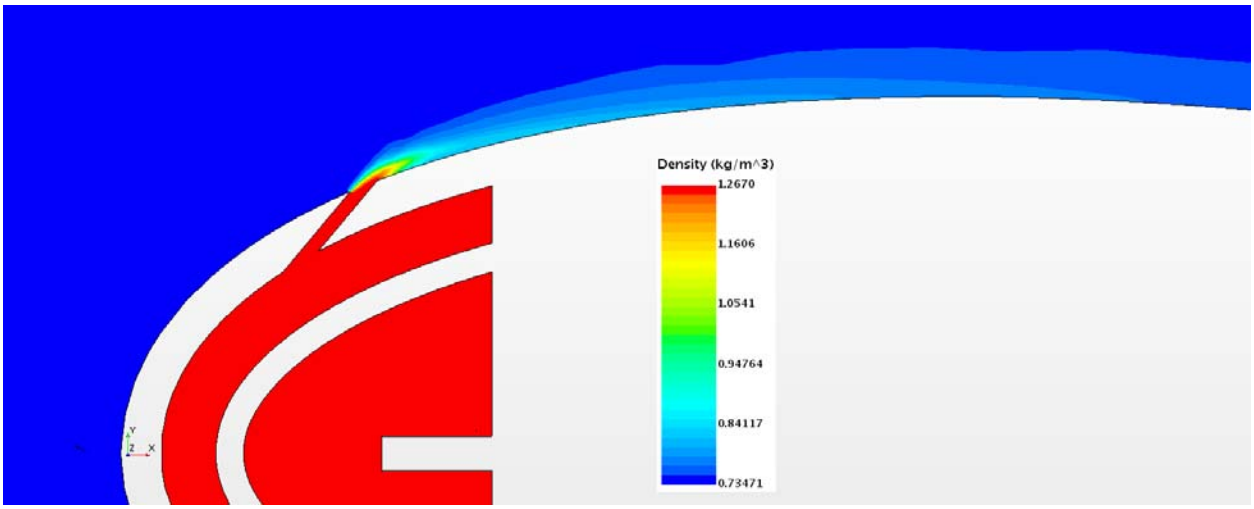

Figure 16.151: Case 14 – Density profile for center plane

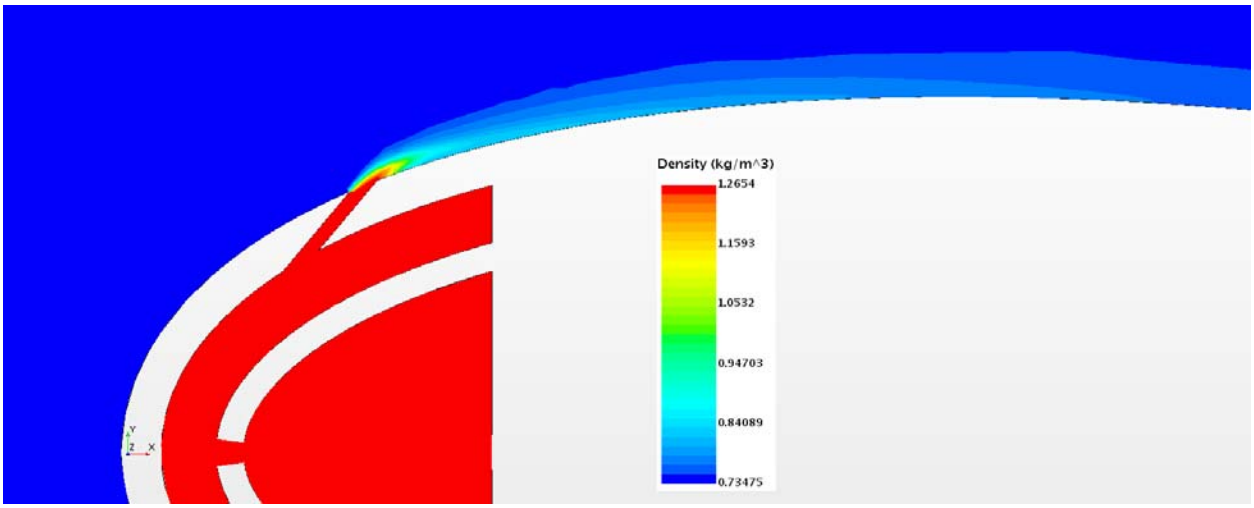

Figure 16.152: Case 14 – Density profile for off-center plane

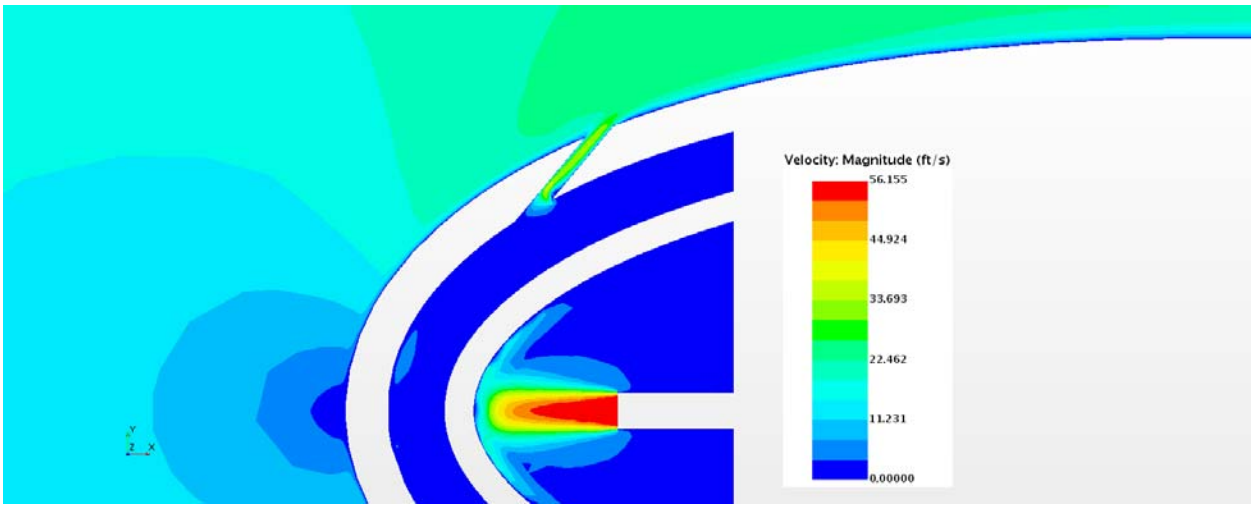

Figure 16.153: Case 14 – Velocity profile for center plane

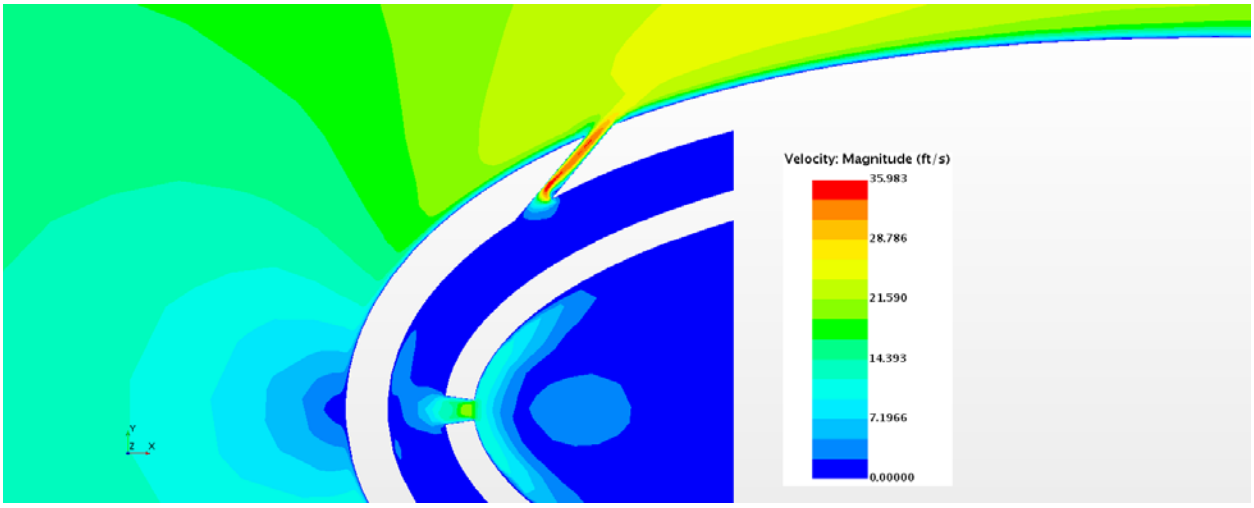

Figure 16.154: Case 14 – Velocity profile for off- center plane

Appendix G-15: M_b = 2.96, Tu = 20%, DR = 1.65

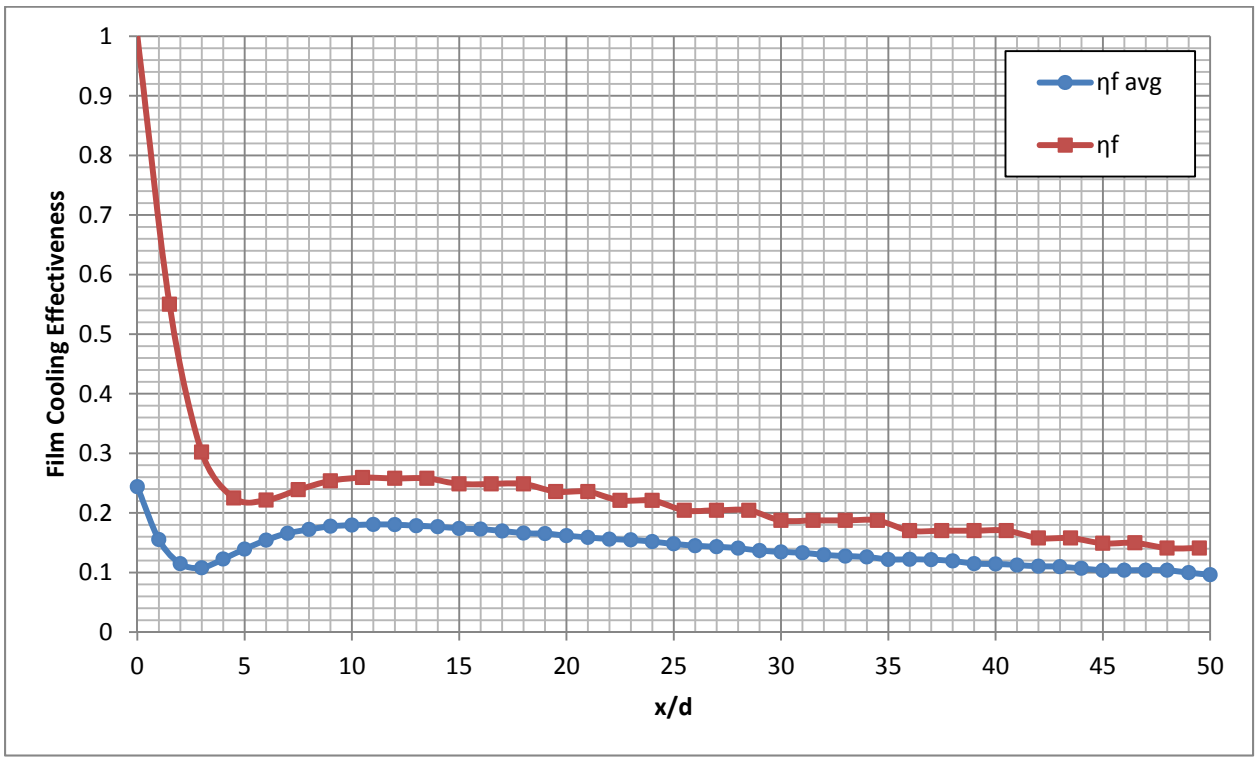

Figure 16.155: Case 15 - Laterally averaged and Centerline adiabatic film cooling effectiveness

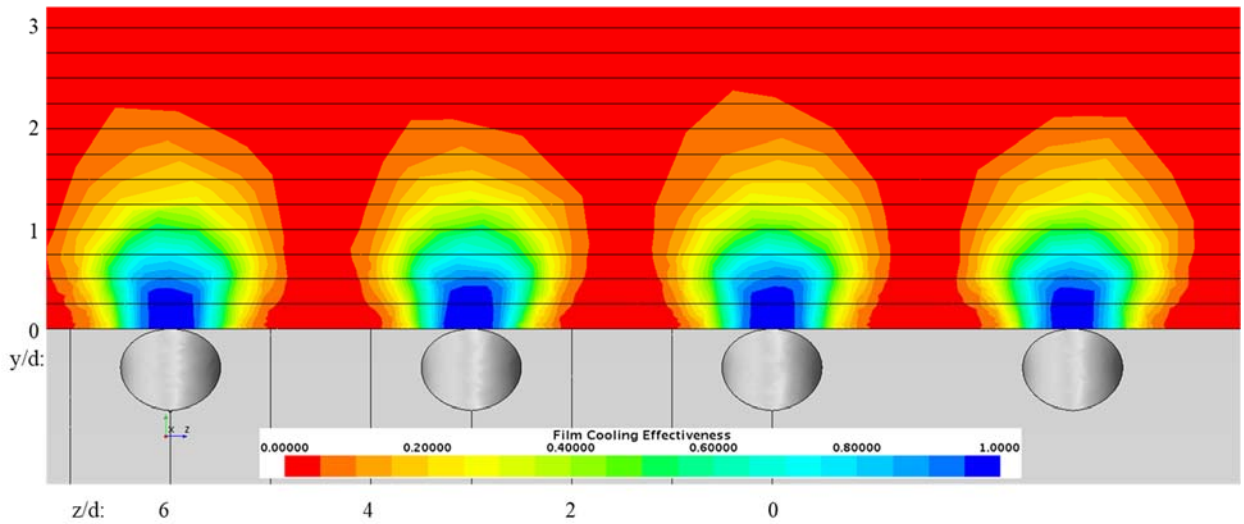

Figure 16.156: Case 15 - Spatial distribution of adiabatic film cooling effectiveness at x/d: 0

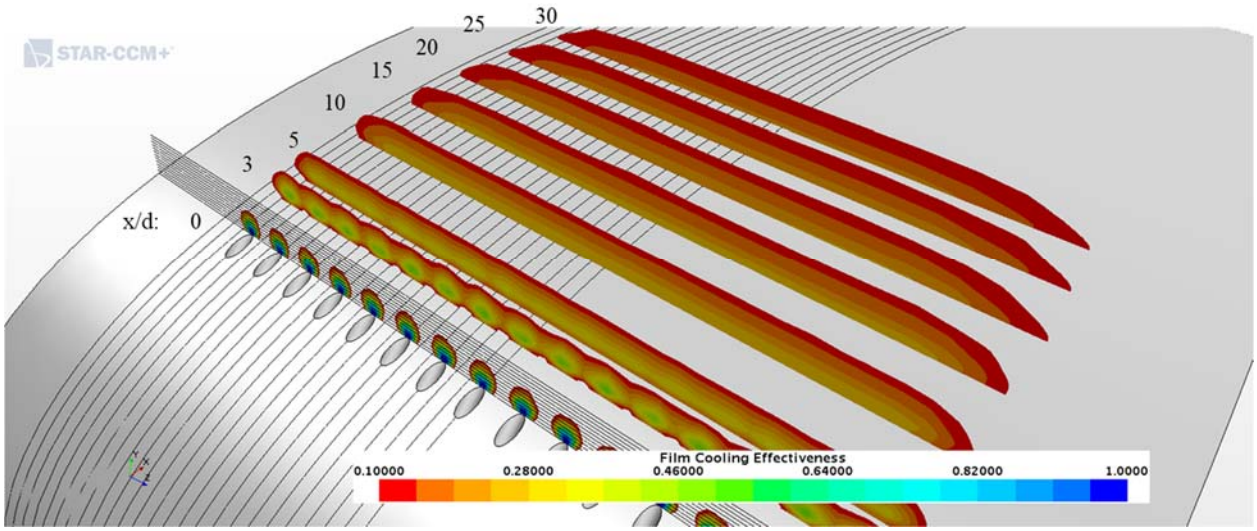

Figure 16.157: Case 15 - Streamwise spatial distribution of adiabatic film cooling effectiveness

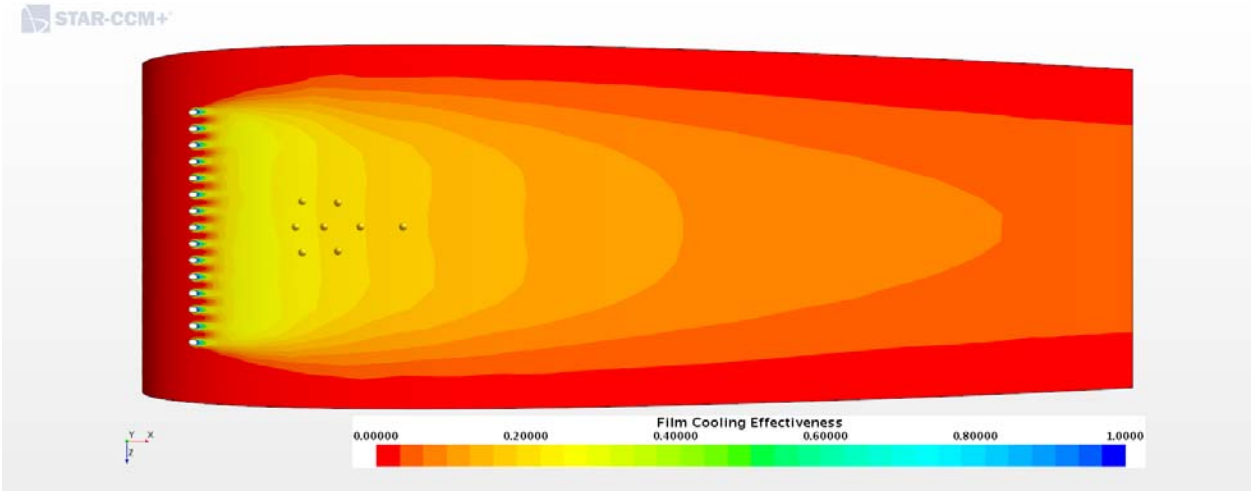

Figure 16.158: Case 15 - Adiabatic Film Cooling Effectiveness on the Suction Surface

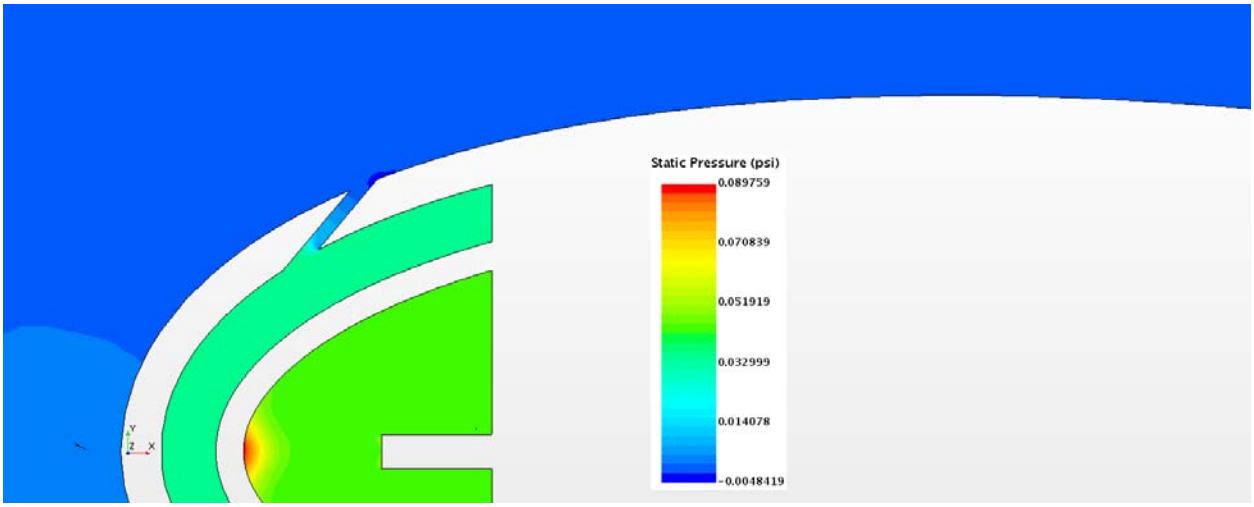

Figure 16.159: Case 15 – Static Pressure profile for center plane

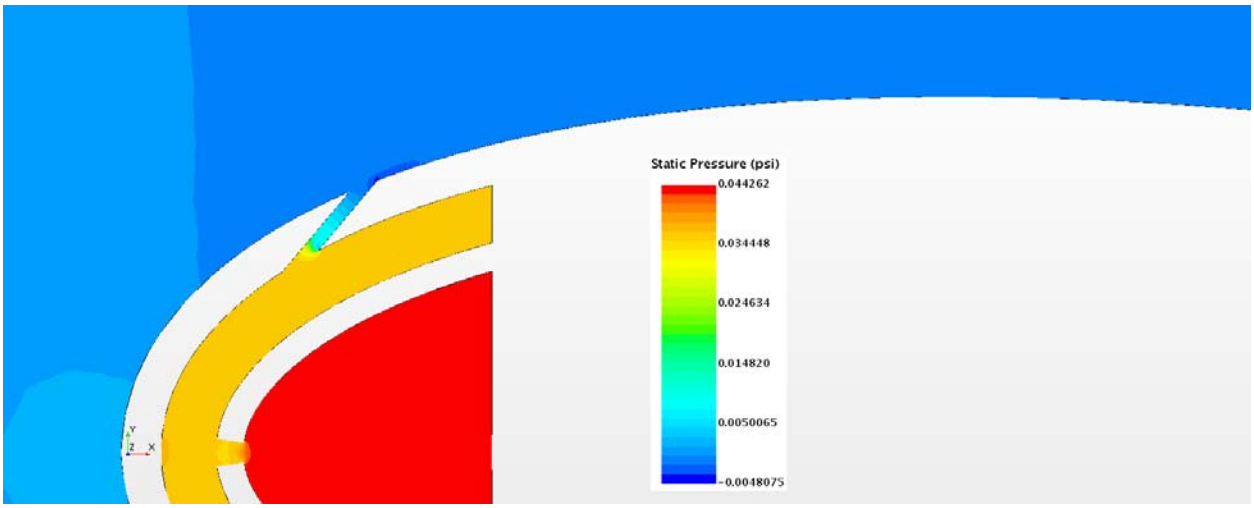

Figure 16.160: Case 15 – Static Pressure profile for off-center plane

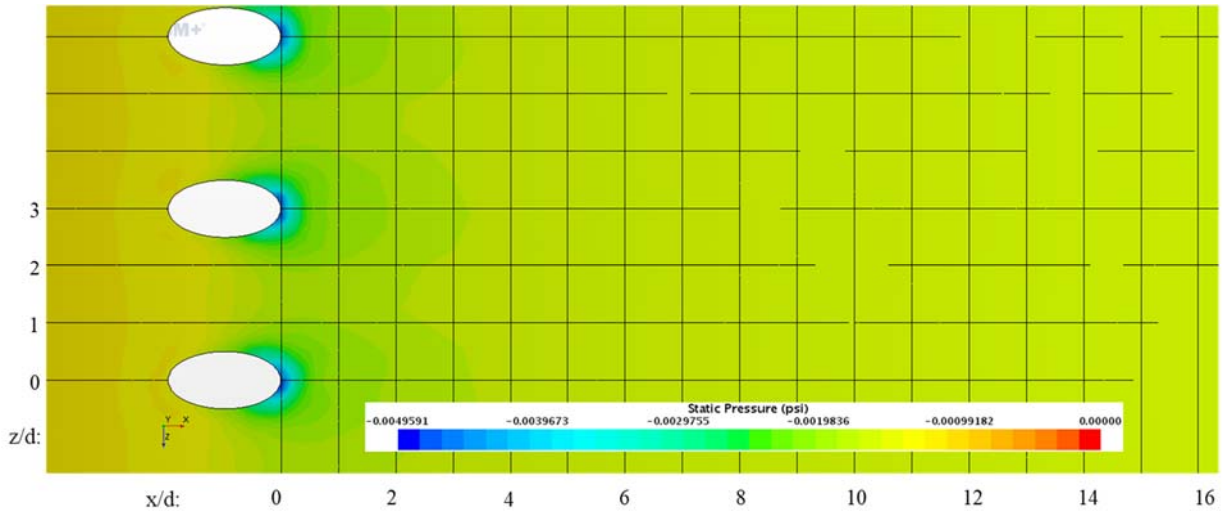

Figure 16.161: Case 15 – Static Pressure distribution for Suction Surface

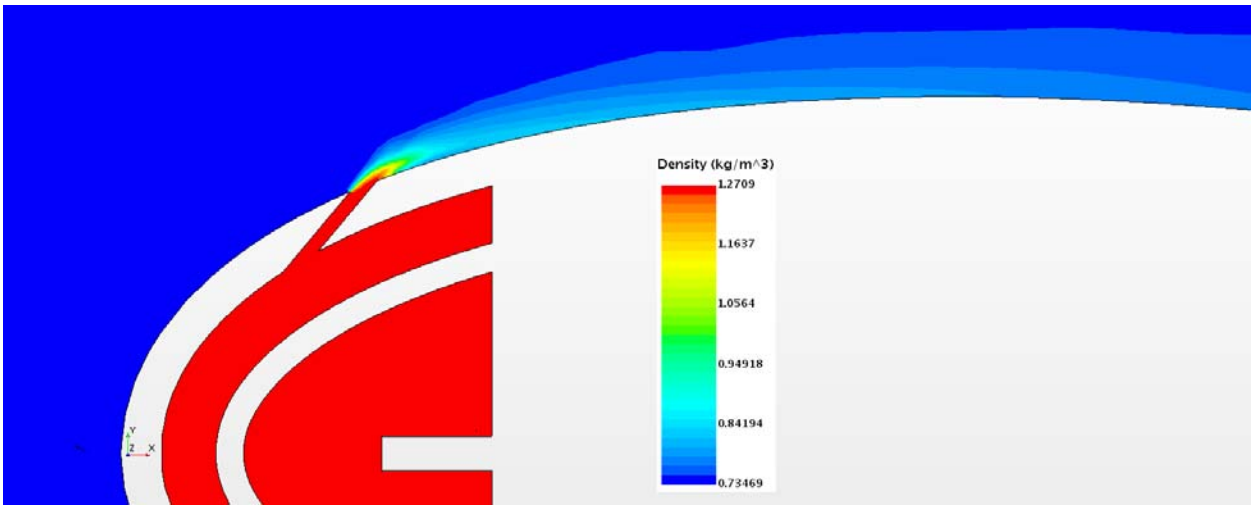

Figure 16.162: Case 15 – Density profile for center plane

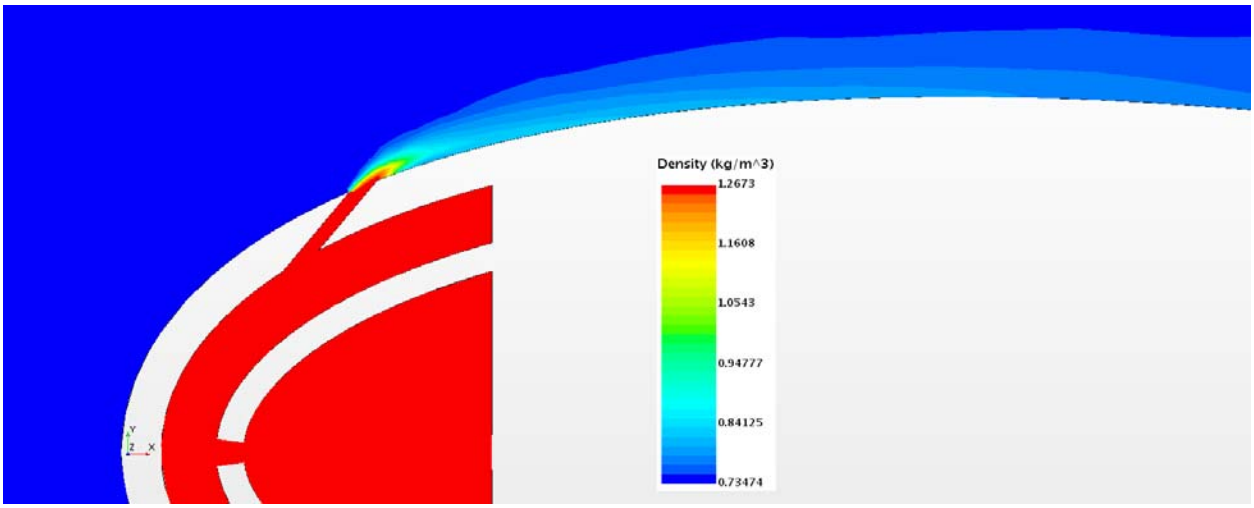

Figure 16.163: Case 15 – Density profile for off-center plane

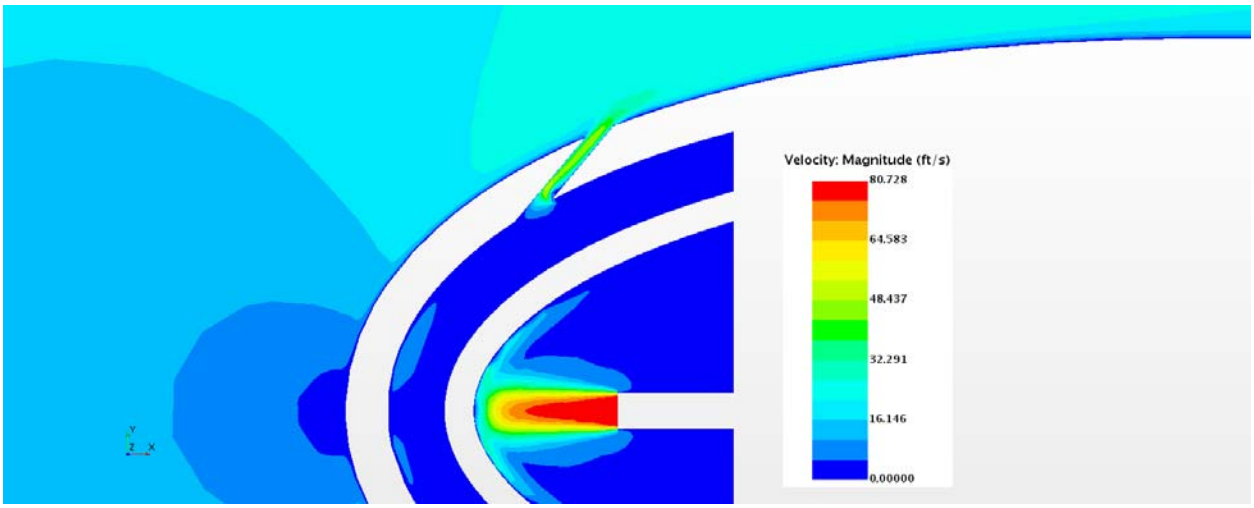

Figure 16.164: Case 15 – Velocity profile for center plane

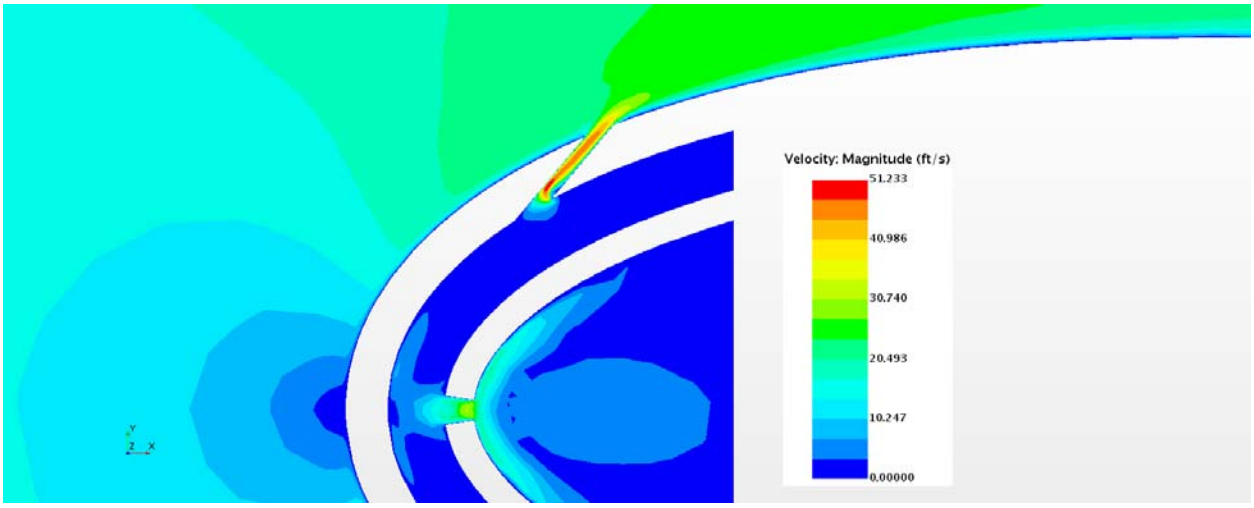

Figure 16.165: Case 15 – Velocity profile for off- center plane

Appendix G-16: M_b = 4.08, Tu = 20%, DR = 1.65

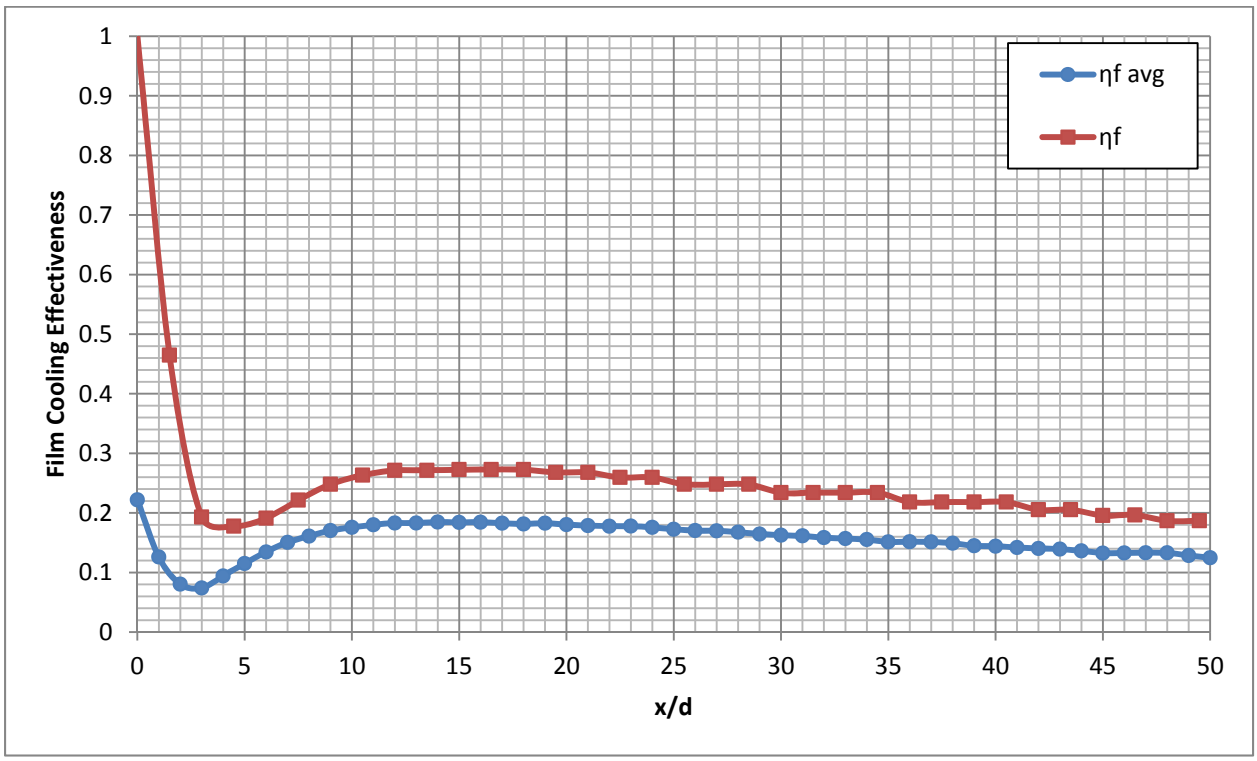

Figure 16.166: Case 16 - Laterally averaged and Centerline adiabatic film cooling effectiveness

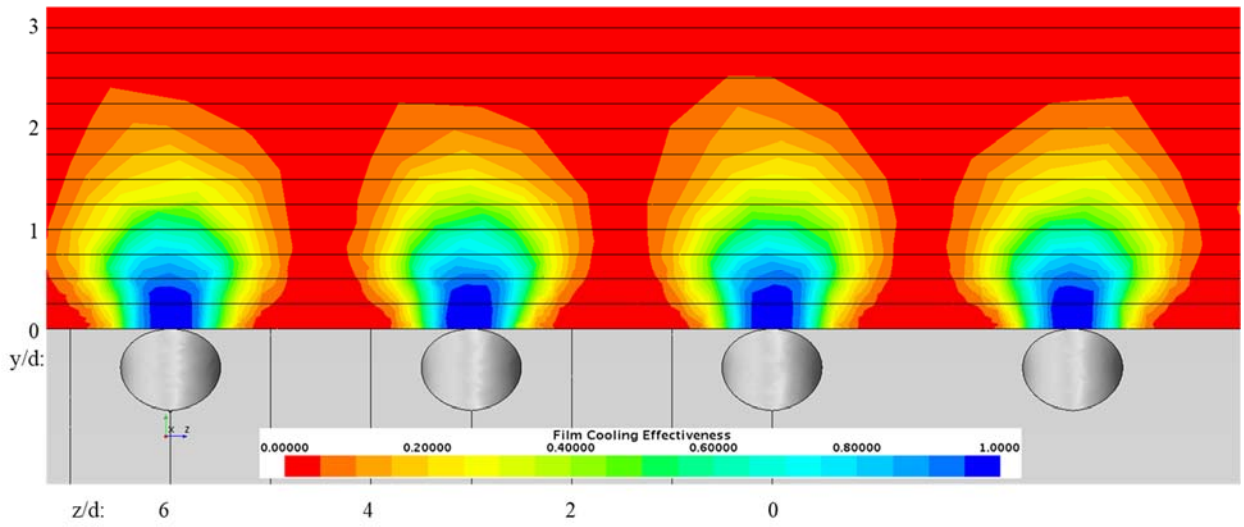

Figure 16.167: Case 16 - Spatial distribution of adiabatic film cooling effectiveness at x/d: 0

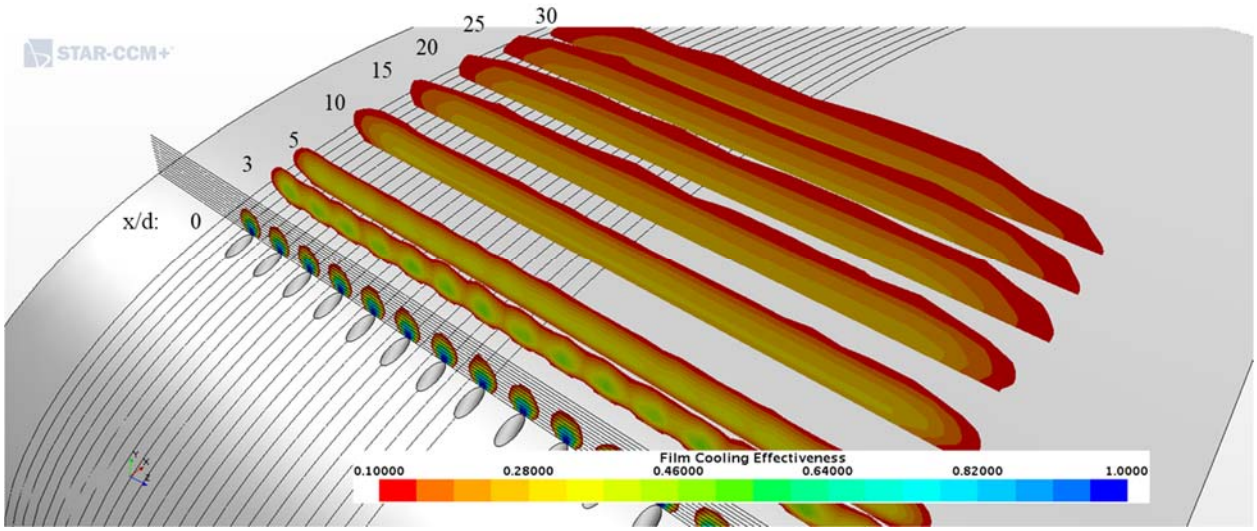

Figure 16.168: Case 16 - Streamwise spatial distribution of adiabatic film cooling effectiveness

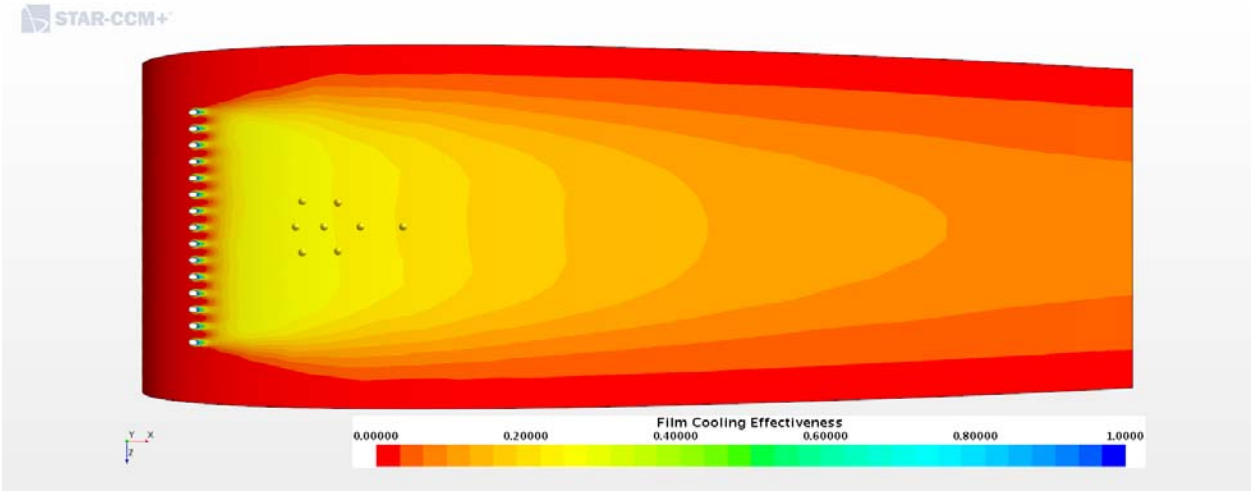

Figure 16.169: Case 16 - Adiabatic Film Cooling Effectiveness on the Suction Surface

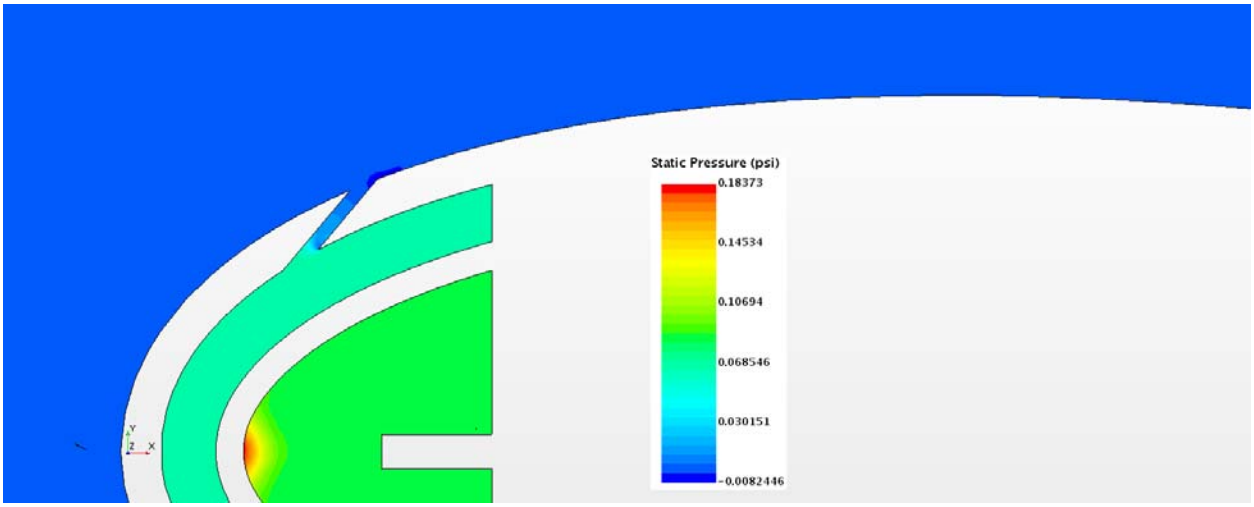

Figure 16.170: Case 16 – Static Pressure profile for center plane

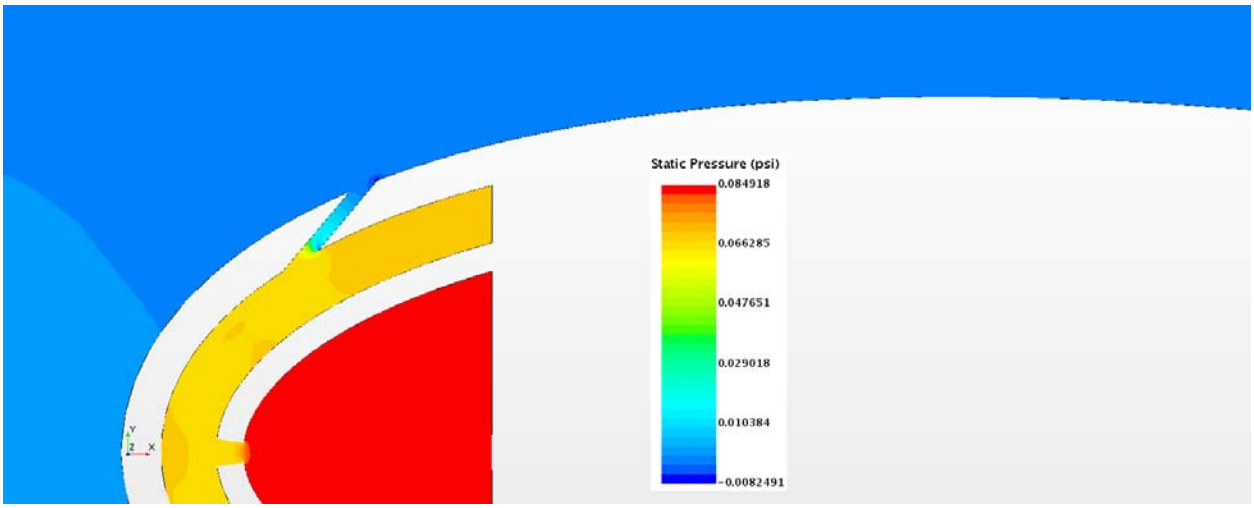

Figure 16.171: Case 16 – Static Pressure profile for off-center plane

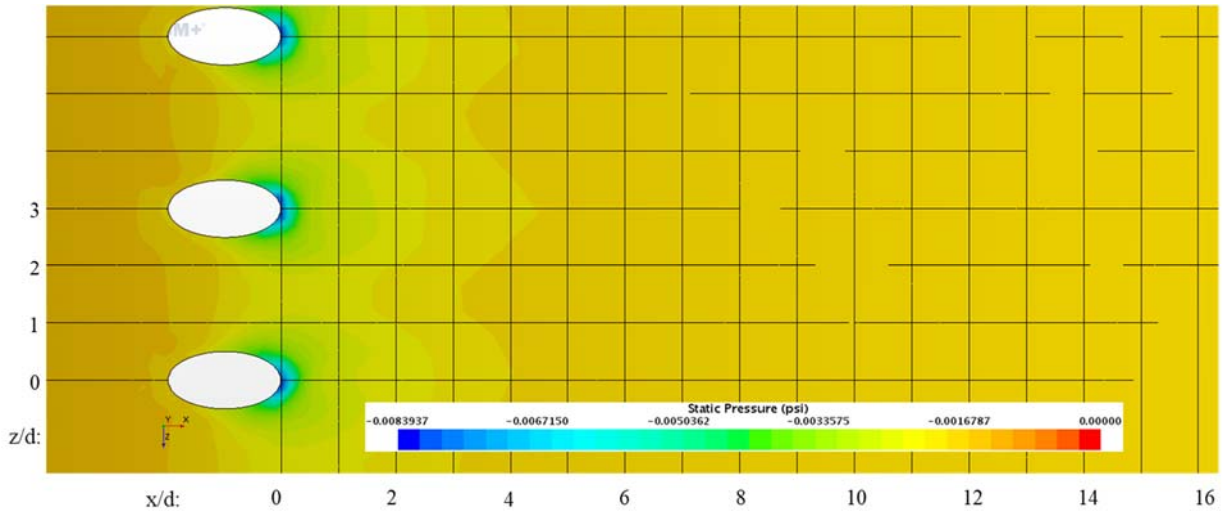

Figure 16.172: Case 16 – Static Pressure distribution for Suction Surface

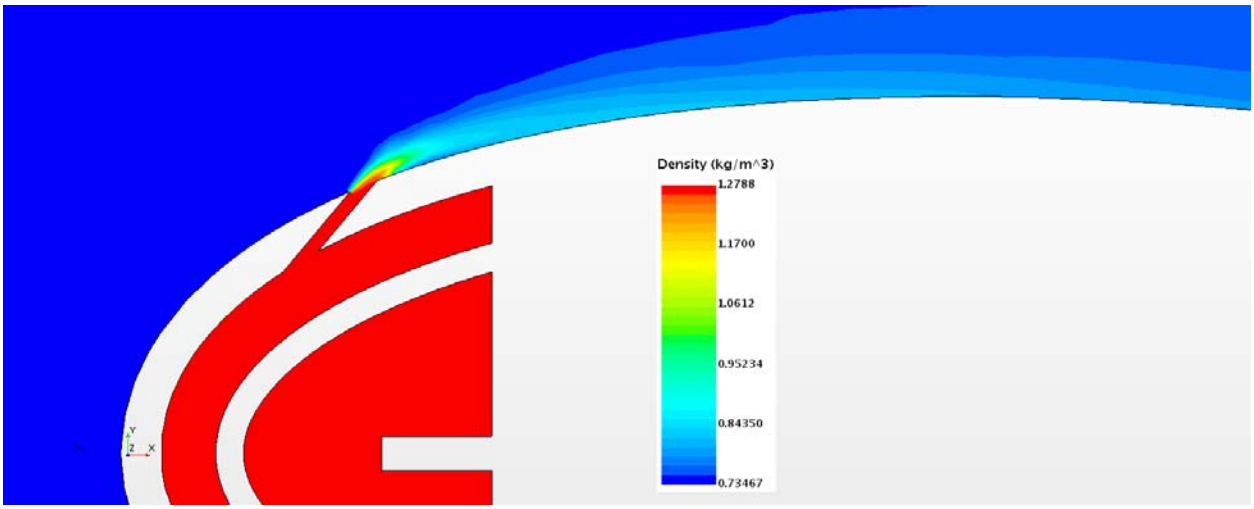

Figure 16.173: Case 16 – Density profile for center plane

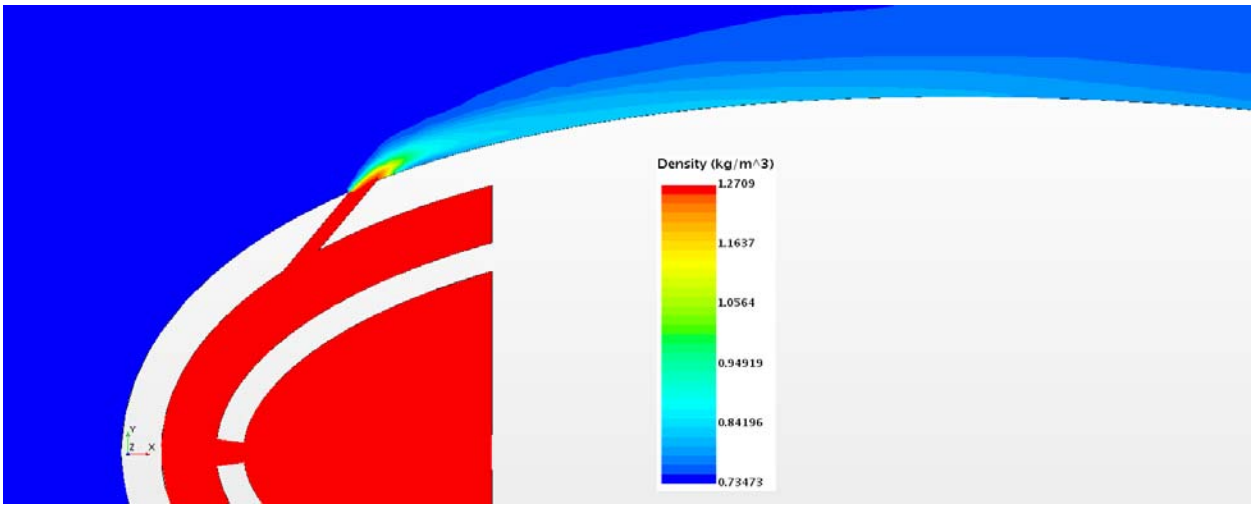

Figure 16.174: Case 16 – Density profile for off-center plane

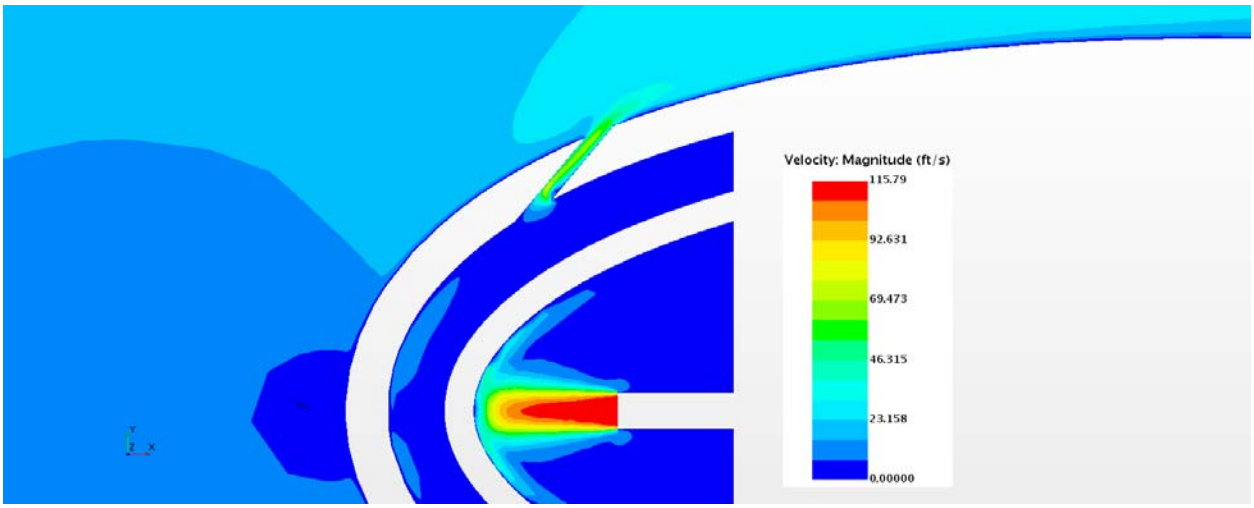

Figure 16.175: Case 16 – Velocity profile for center plane

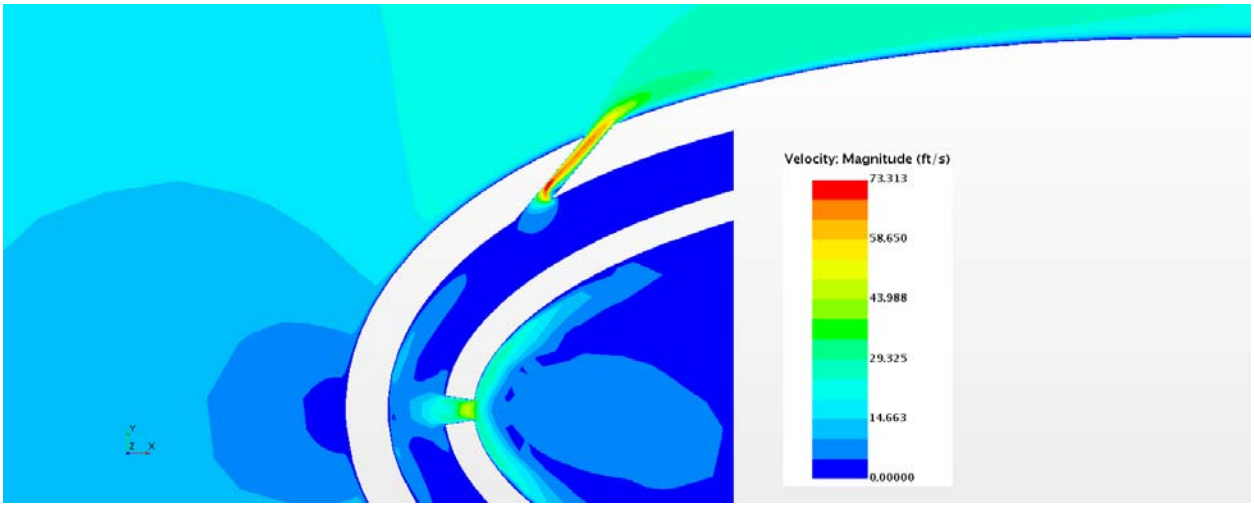

Figure 16.176: Case 16 – Velocity profile for off- center plane

Appendix G-17: M_b = 5.04, Tu = 20%, DR = 1.65

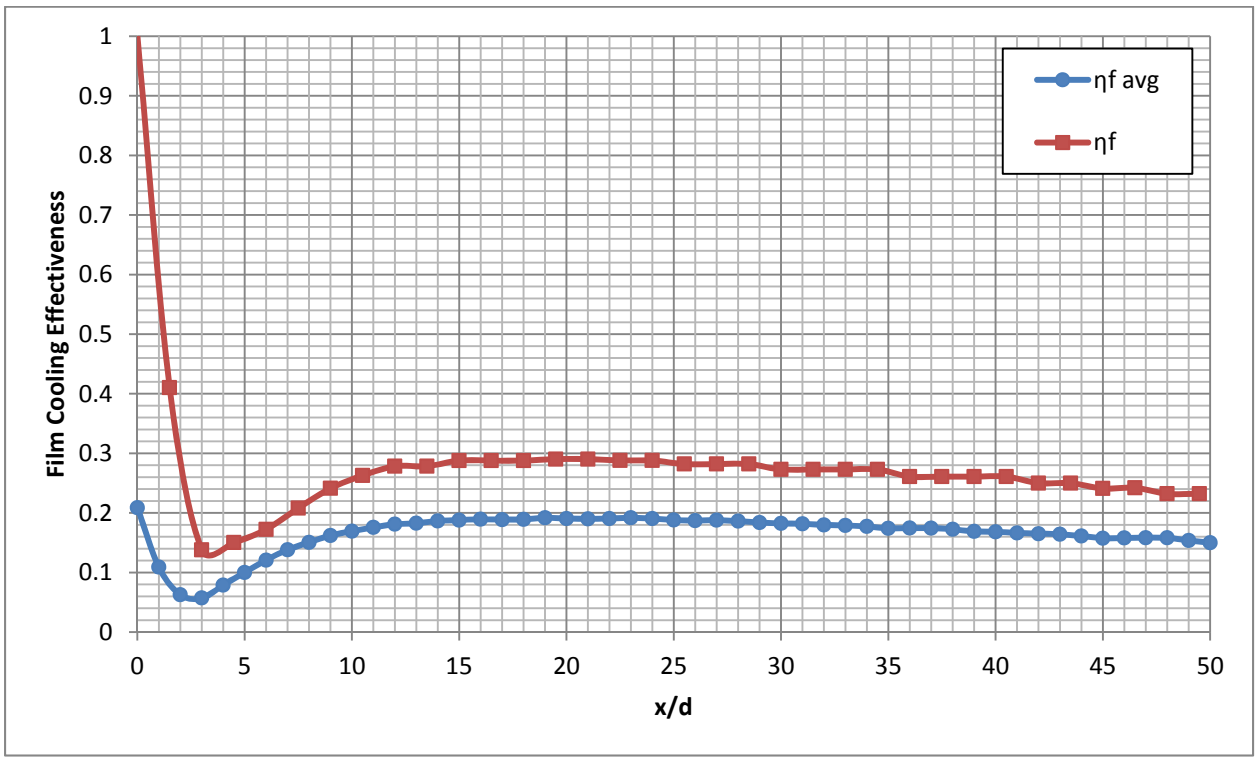

Figure 16.177: Case 17 - Laterally averaged and Centerline adiabatic film cooling effectiveness

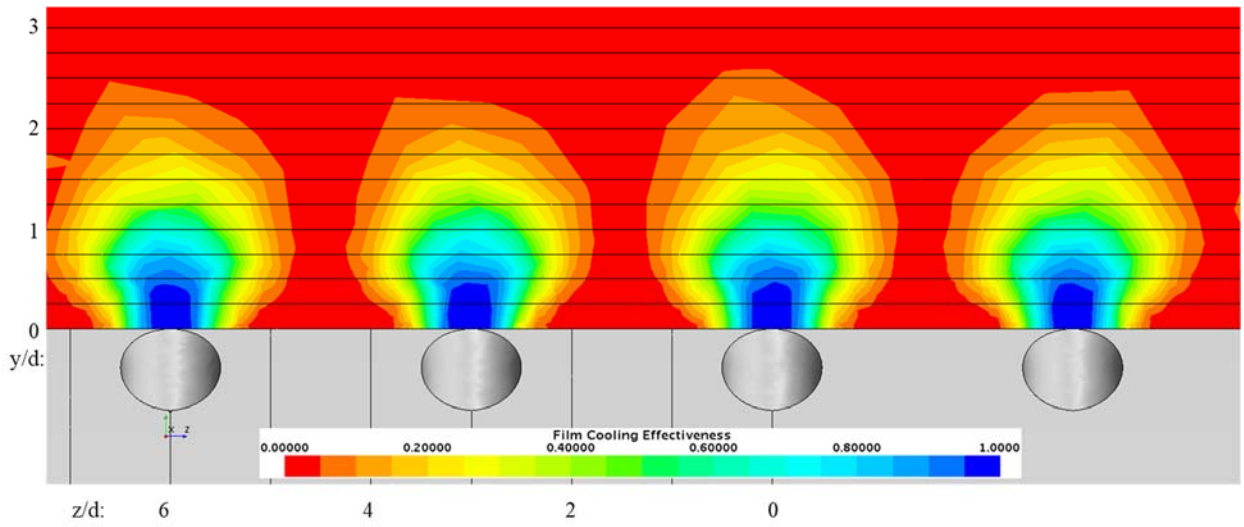

Figure 16.178: Case 17 - Spatial distribution of adiabatic film cooling effectiveness at x/d: 0

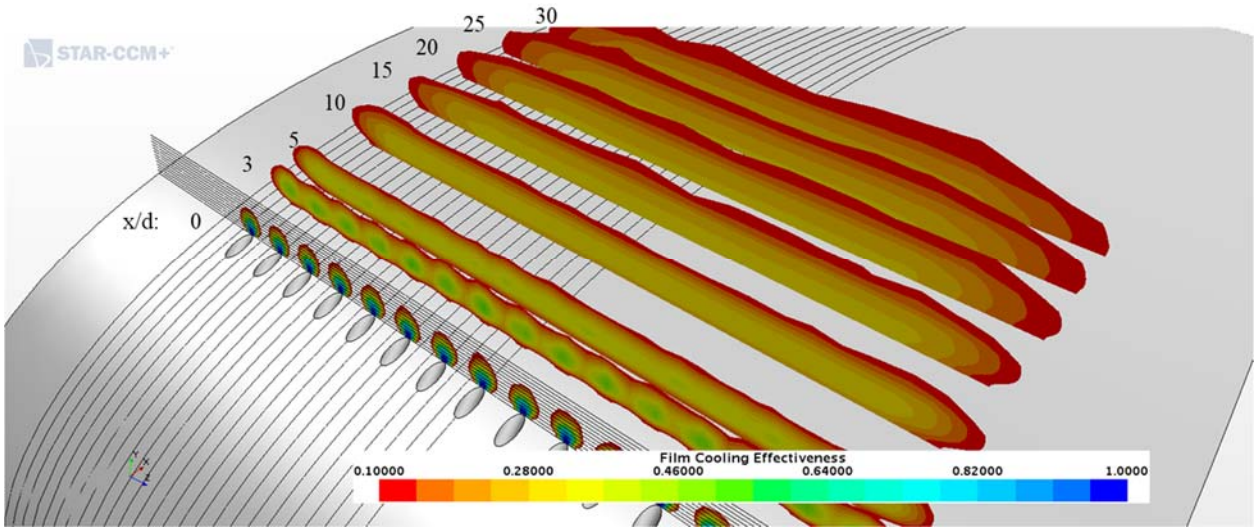

Figure 16.179: Case 17 - Streamwise spatial distribution of adiabatic film cooling effectiveness

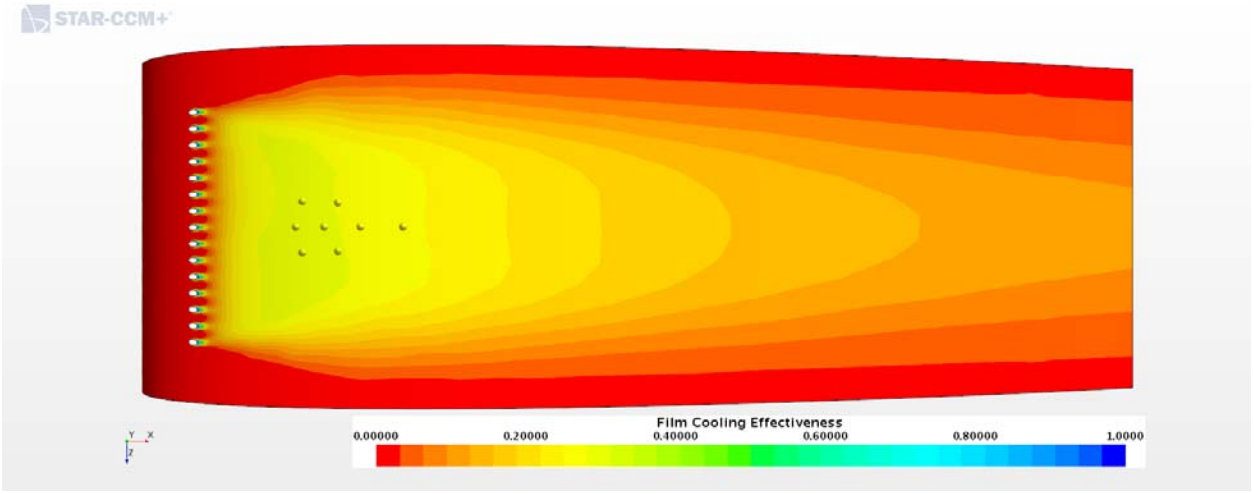

Figure 16.180: Case 17 - Adiabatic Film Cooling Effectiveness on the Suction Surface

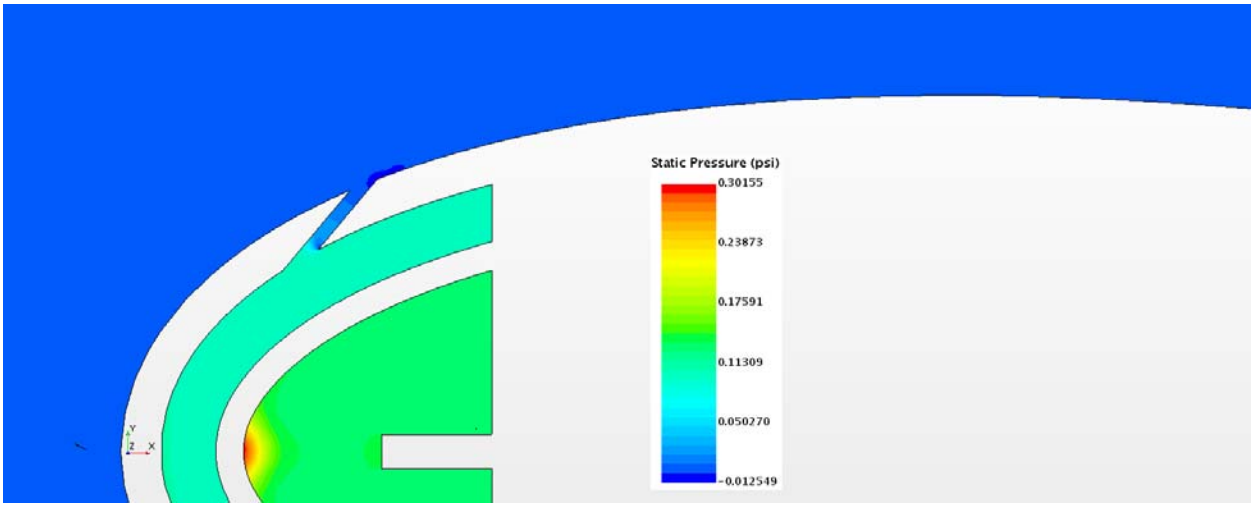

Figure 16.181: Case 17 – Static Pressure profile for center plane

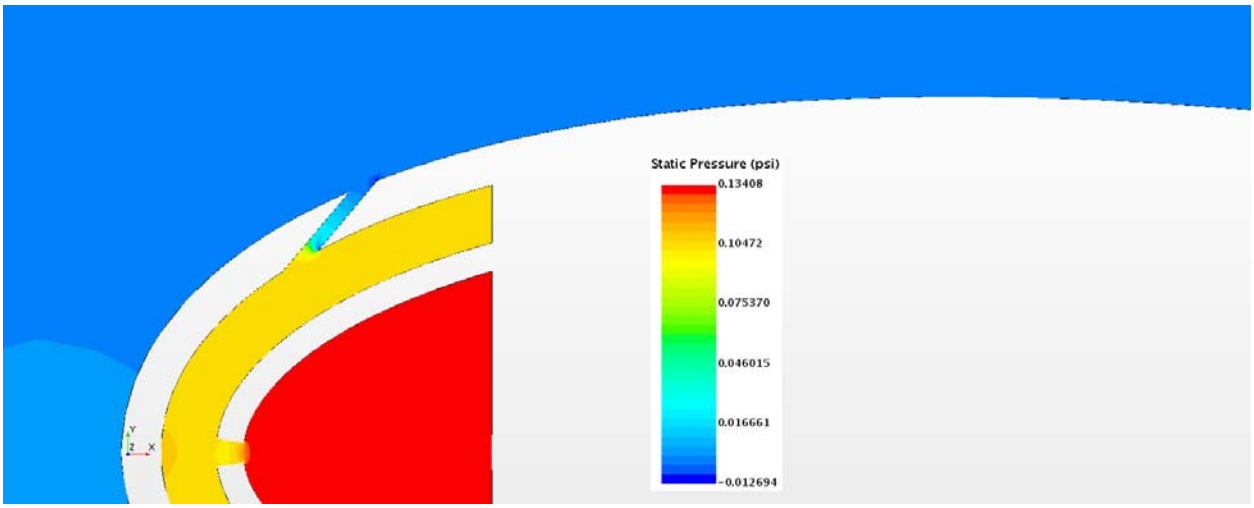

Figure 16.182: Case 17 – Static Pressure profile for off-center plane

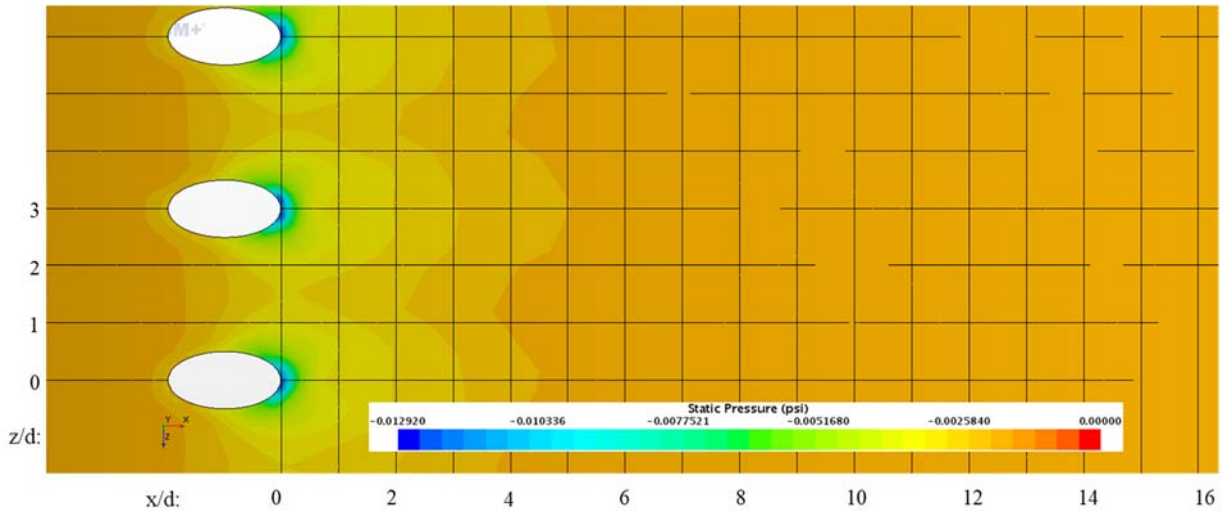

Figure 16.183: Case 17 – Static Pressure distribution for Suction Surface

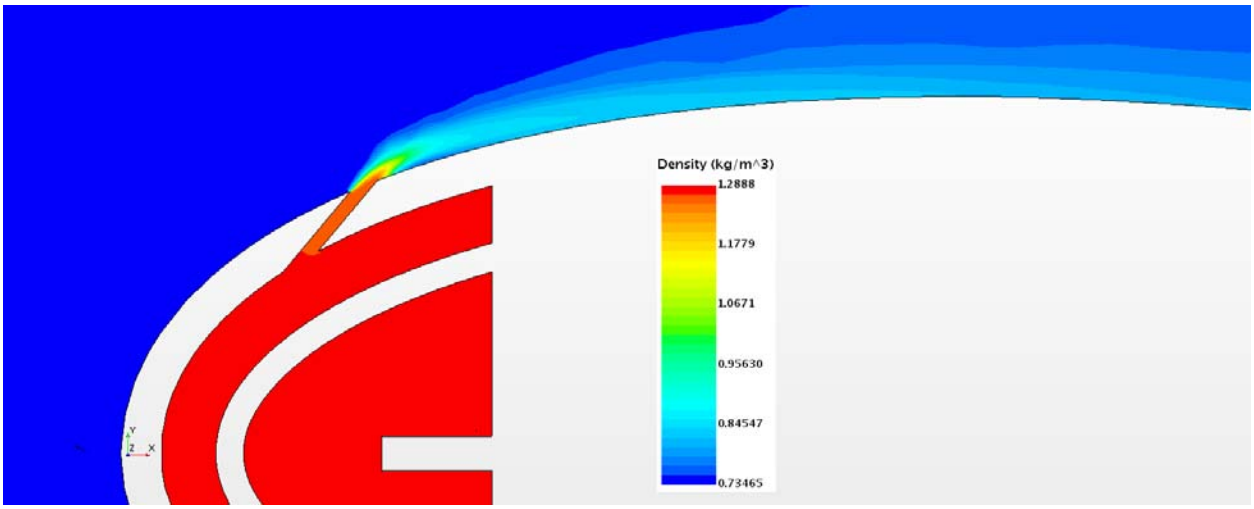

Figure 16.184: Case 17 – Density profile for center plane

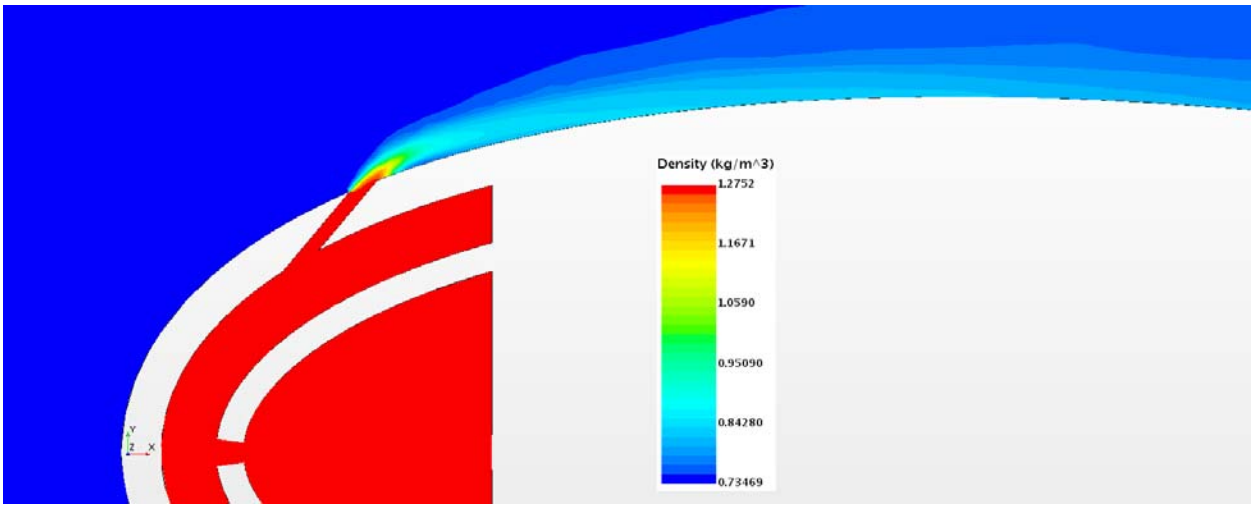

Figure 16.185: Case 17 – Density profile for off-center plane

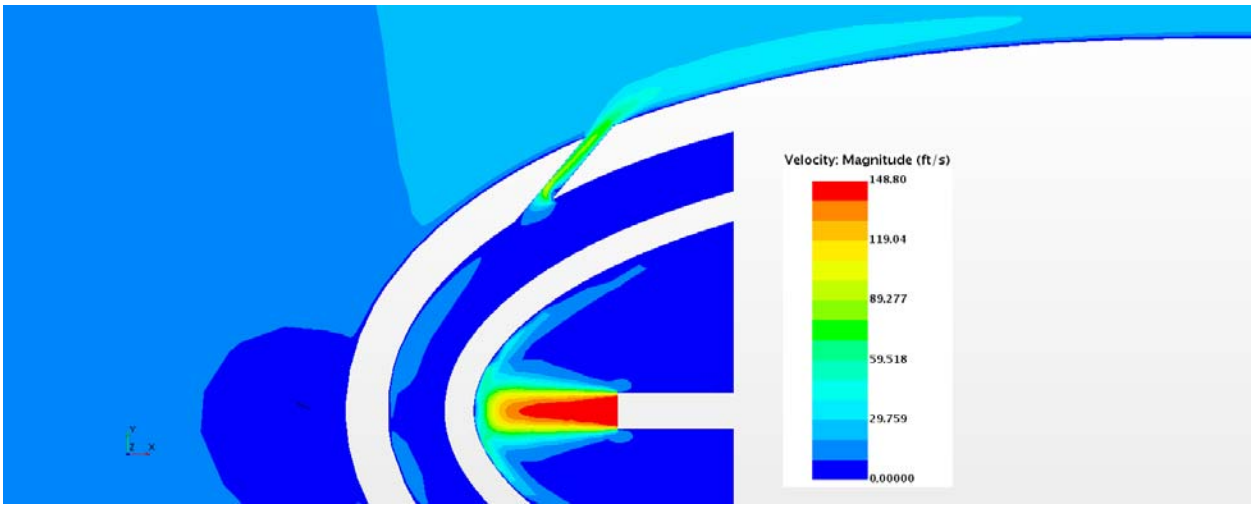

Figure 16.186: Case 17 – Velocity profile for center plane

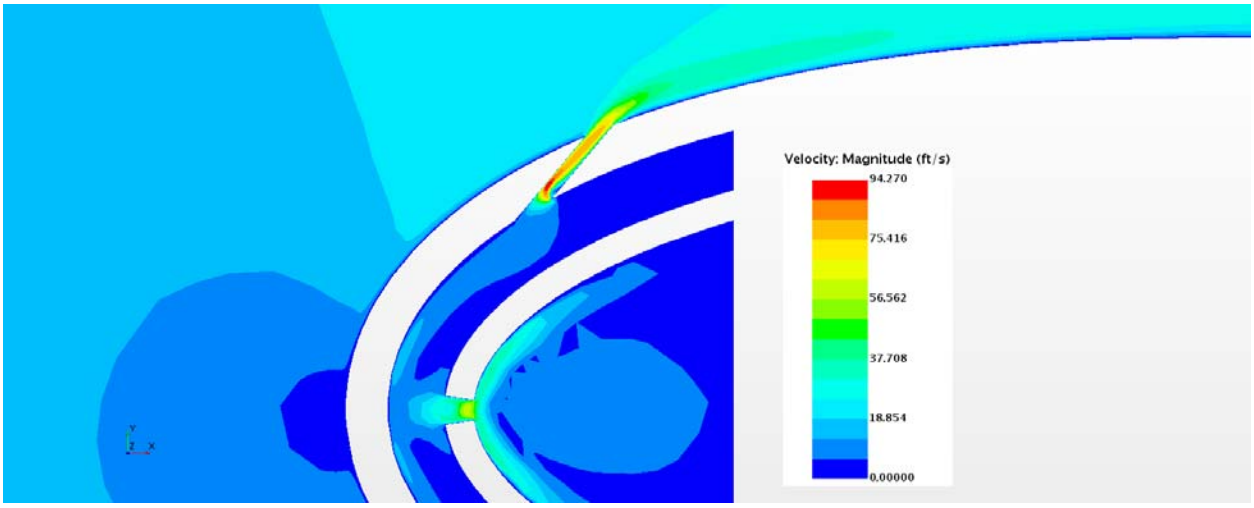

Figure 16.187: Case 17 – Velocity profile for off- center plane

Appendix G-18: M_b = 5.95, Tu = 20%, DR = 1.65

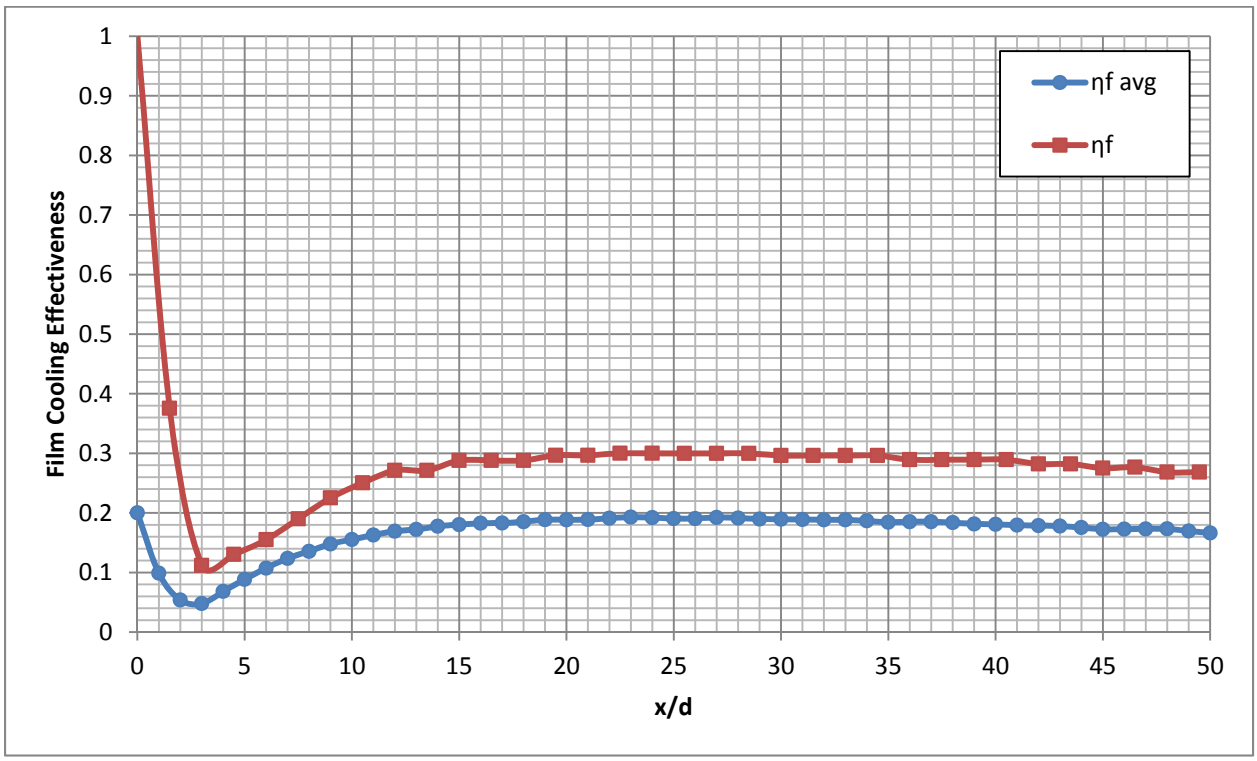

Figure 16.188: Case 18 - Laterally averaged and Centerline adiabatic film cooling effectiveness

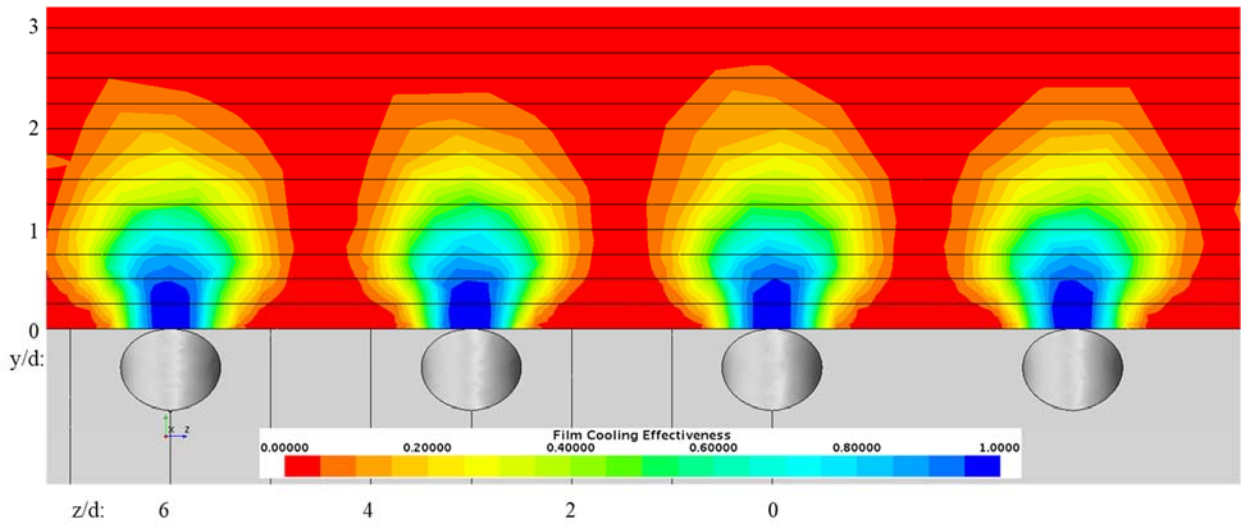

Figure 16.189: Case 18 - Spatial distribution of adiabatic film cooling effectiveness at x/d: 0

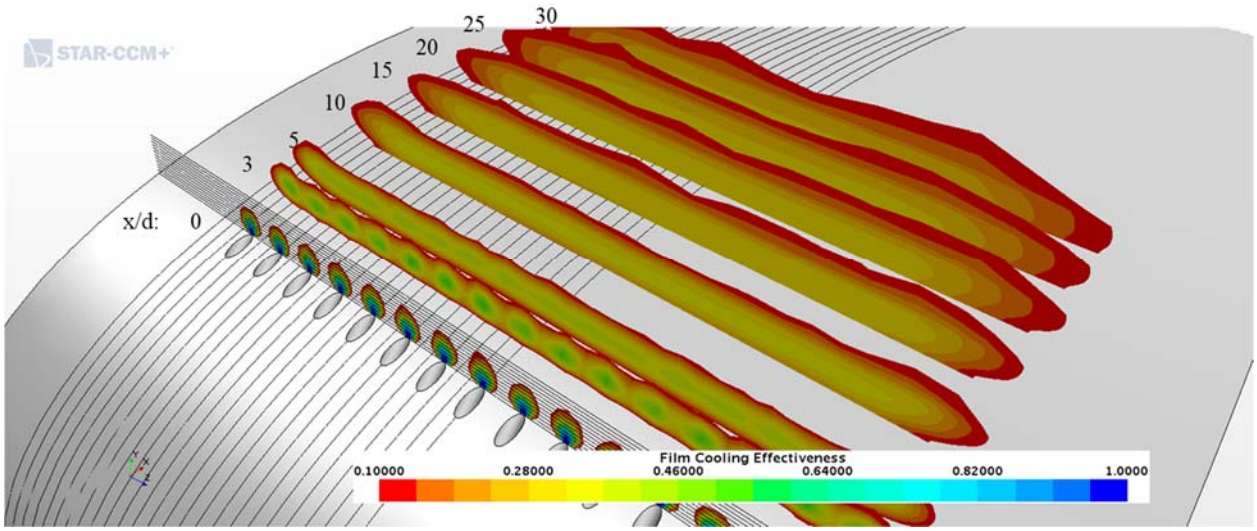

Figure 16.190: Case 18 - Streamwise spatial distribution of adiabatic film cooling effectiveness

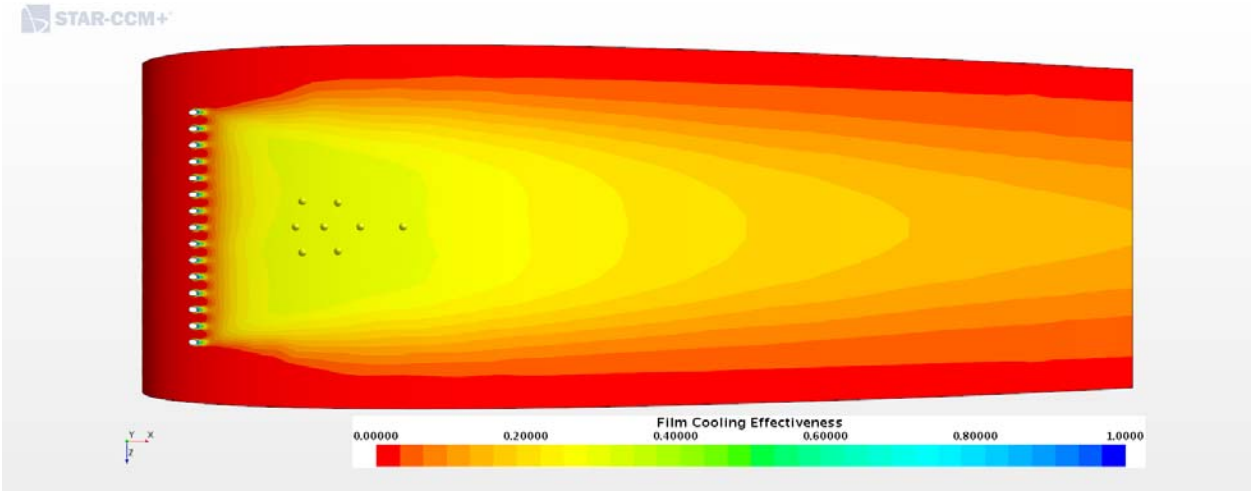

Figure 16.191: Case 18 - Adiabatic Film Cooling Effectiveness on the Suction Surface

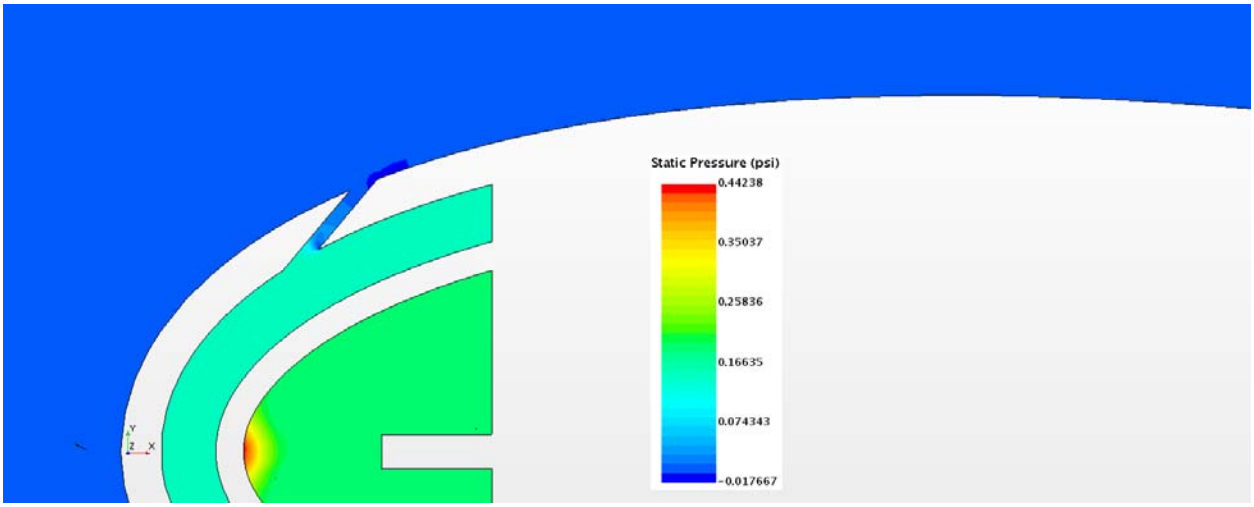

Figure 16.192: Case 18 – Static Pressure profile for center plane

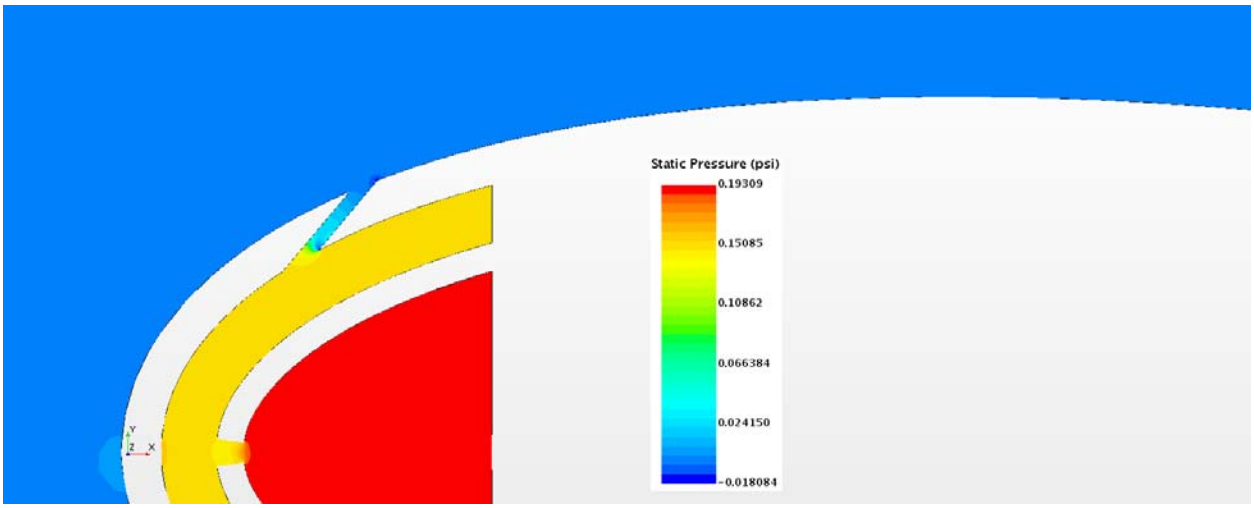

Figure 16.193: Case 18 – Static Pressure profile for off-center plane

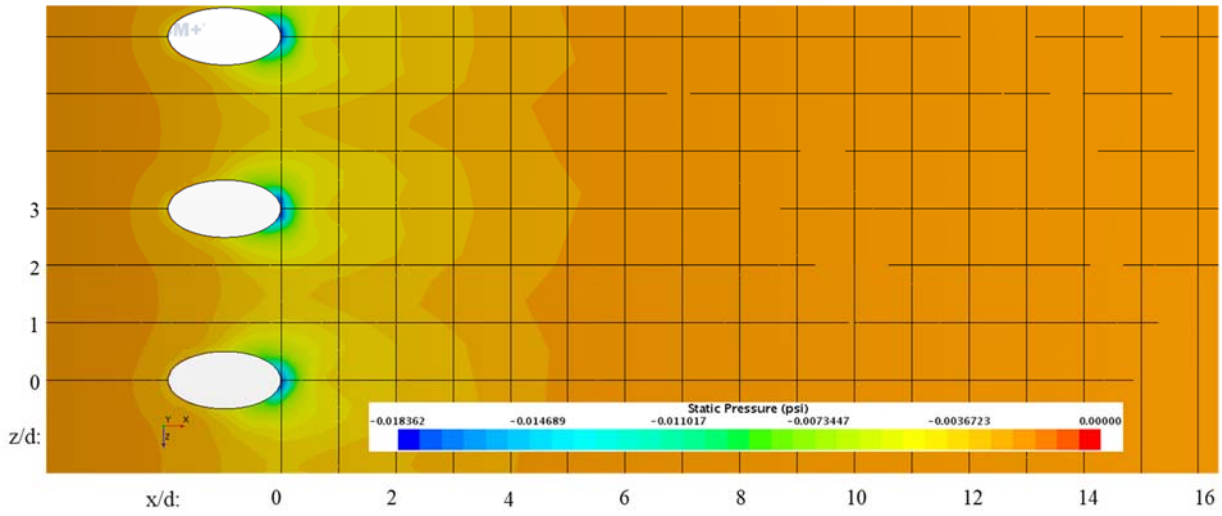

Figure 16.194: Case 18 – Static Pressure distribution for Suction Surface

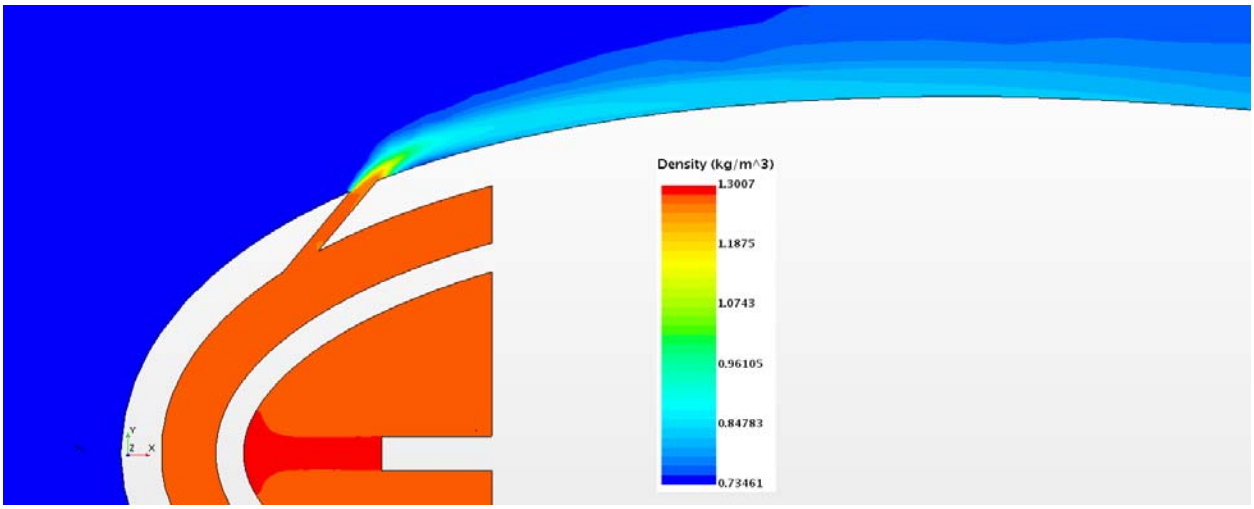

Figure 16.195: Case 18 – Density profile for center plane

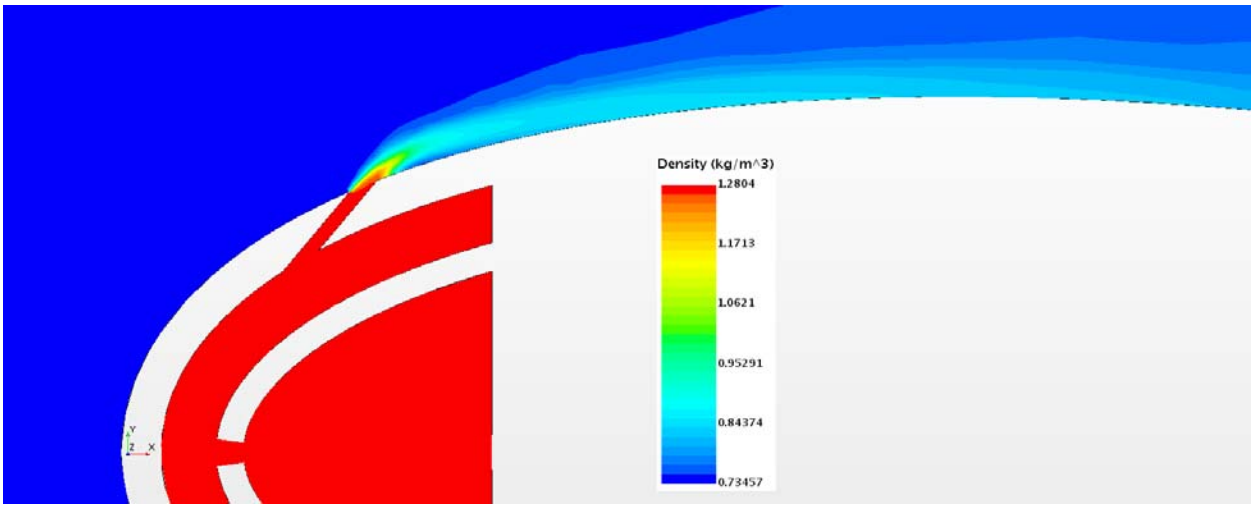

Figure 16.196: Case 18 – Density profile for off-center plane

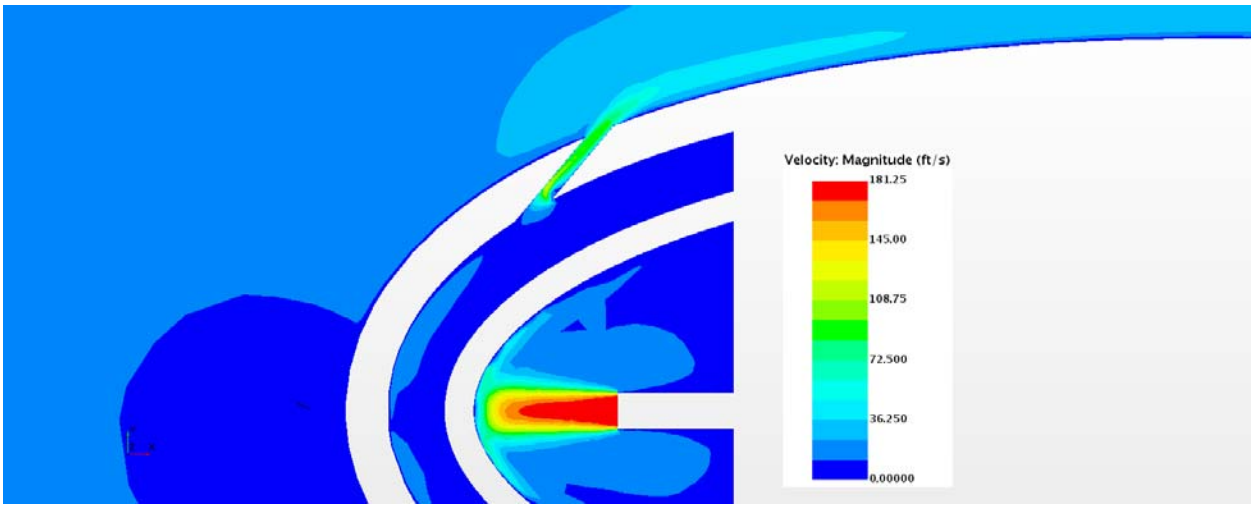

Figure 16.197: Case 18 – Velocity profile for center plane

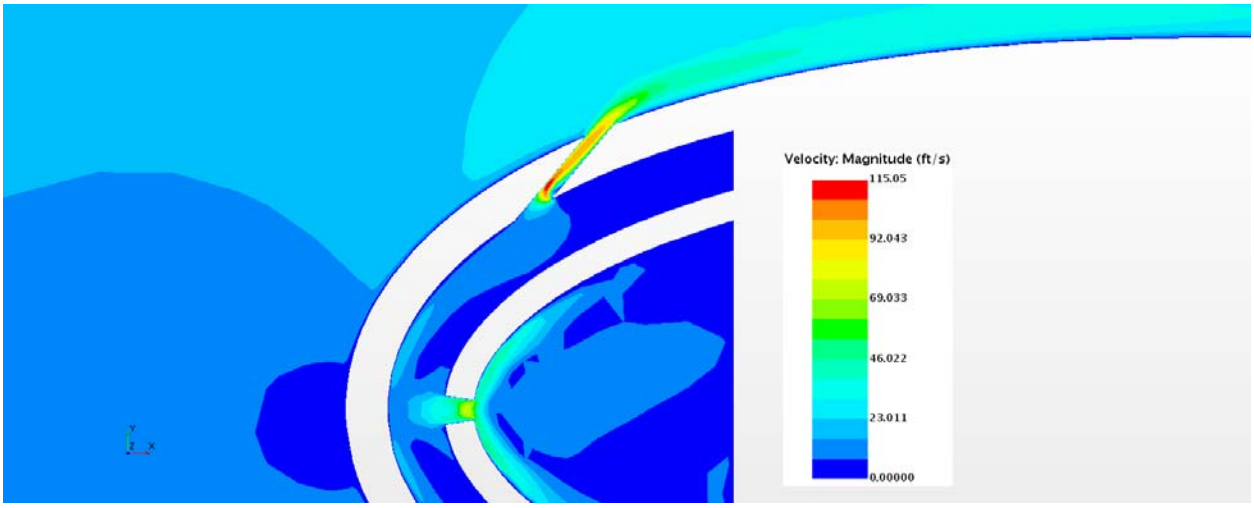

Figure 16.198: Case 18 – Velocity profile for off- center plane

Appendix G-19: M_b = 0.98, Tu = 10%, DR = 1.65

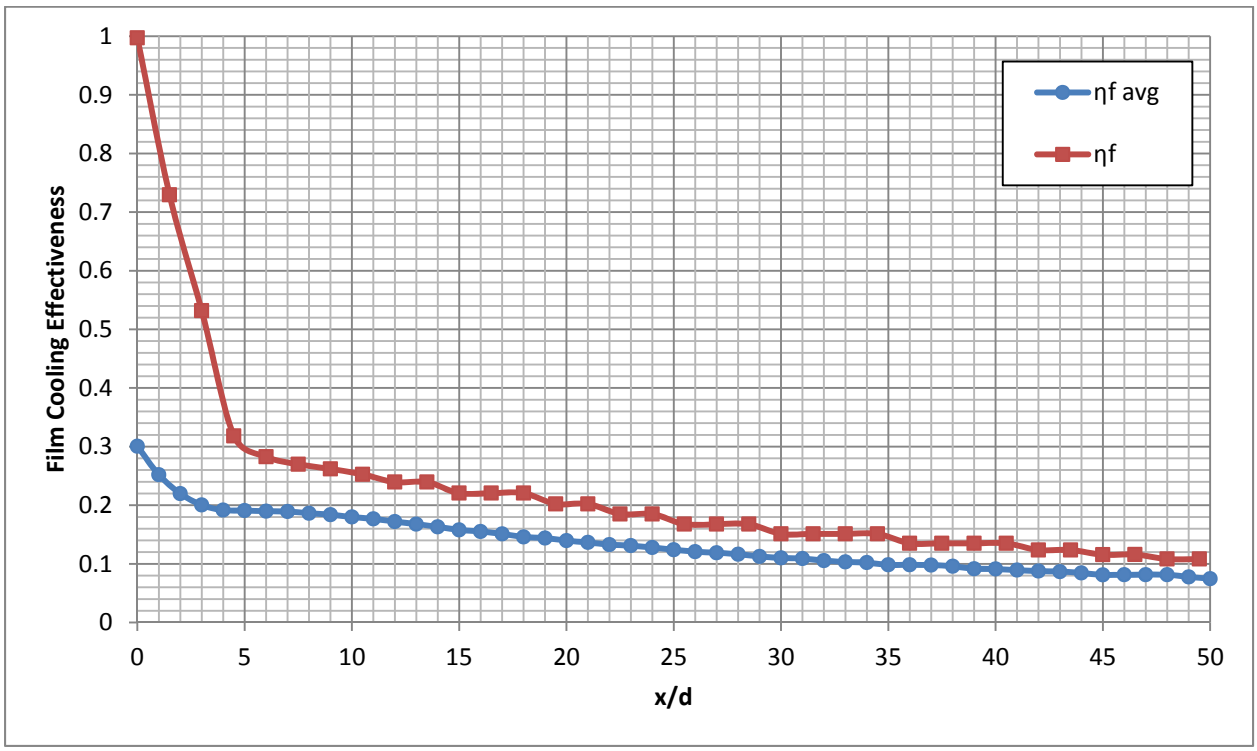

Figure 16.199: Case 19 - Laterally averaged and Centerline adiabatic film cooling effectiveness

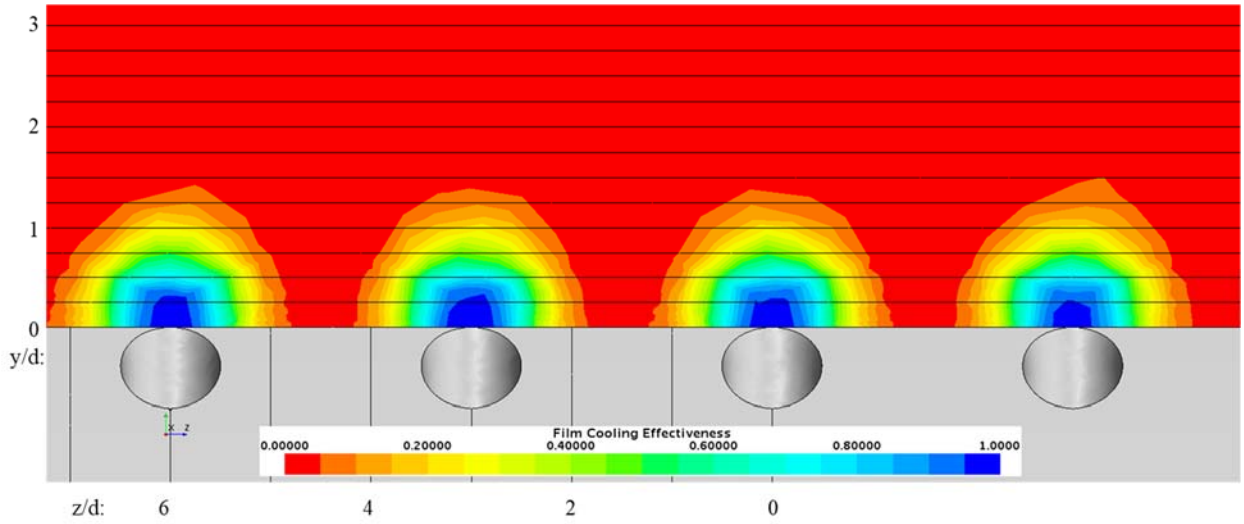

Figure 16.200: Case 19 - Spatial distribution of adiabatic film cooling effectiveness at x/d: 0

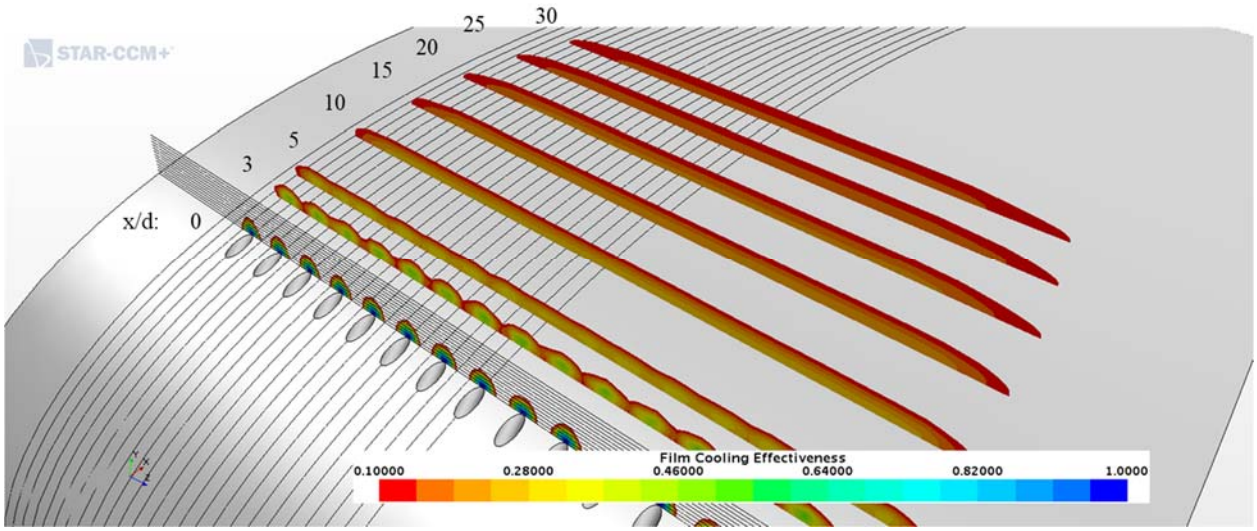

Figure 16.201: Case 19 - Streamwise spatial distribution of adiabatic film cooling effectiveness

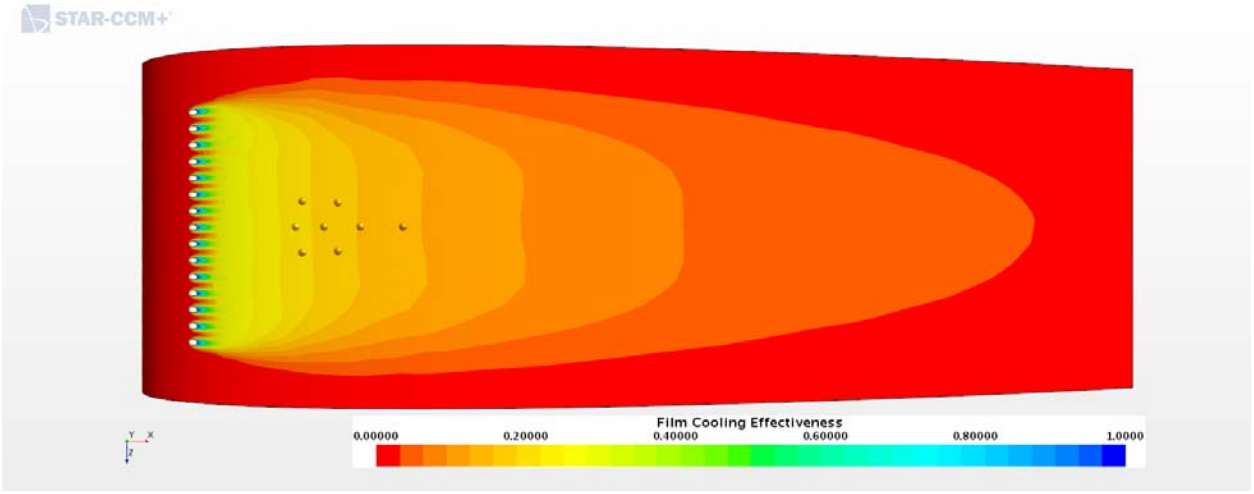

Figure 16.202: Case 19 - Adiabatic Film Cooling Effectiveness on the Suction Surface

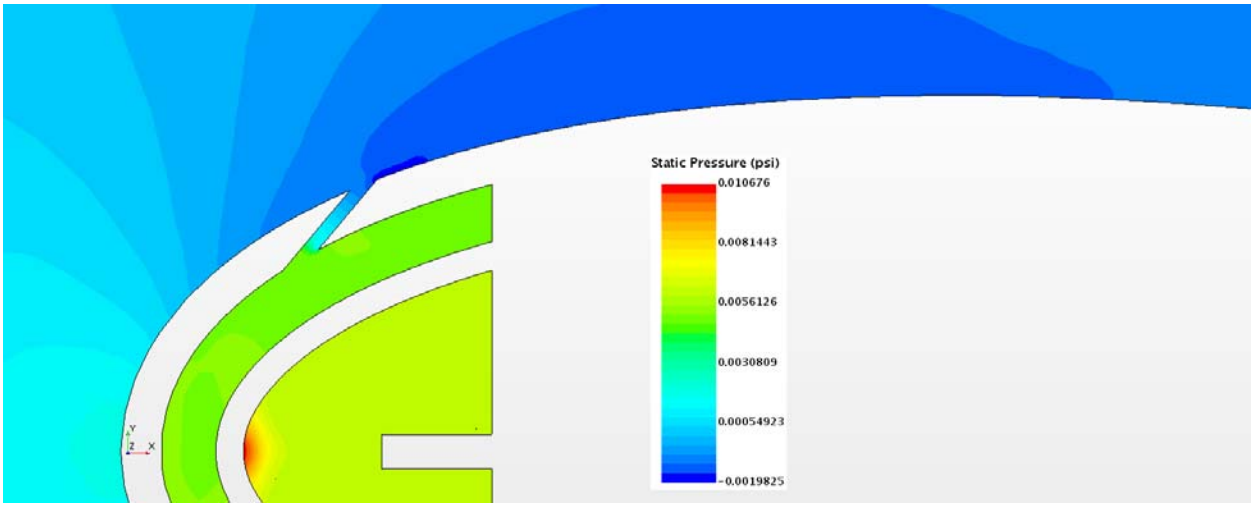

Figure 16.203: Case 19 – Static Pressure profile for center plane

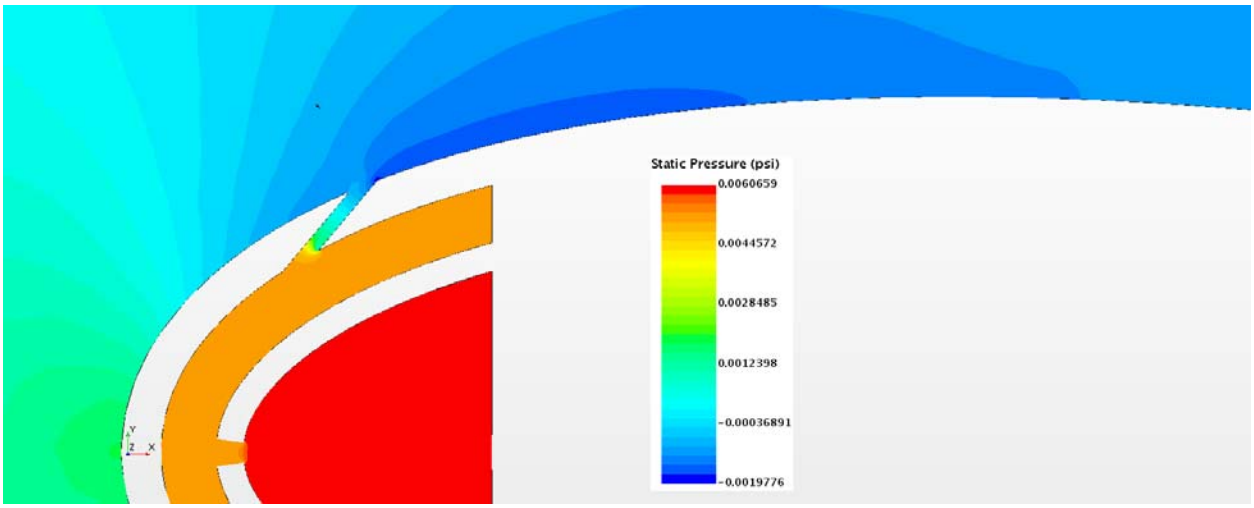

Figure 16.204: Case 19 – Static Pressure profile for off-center plane

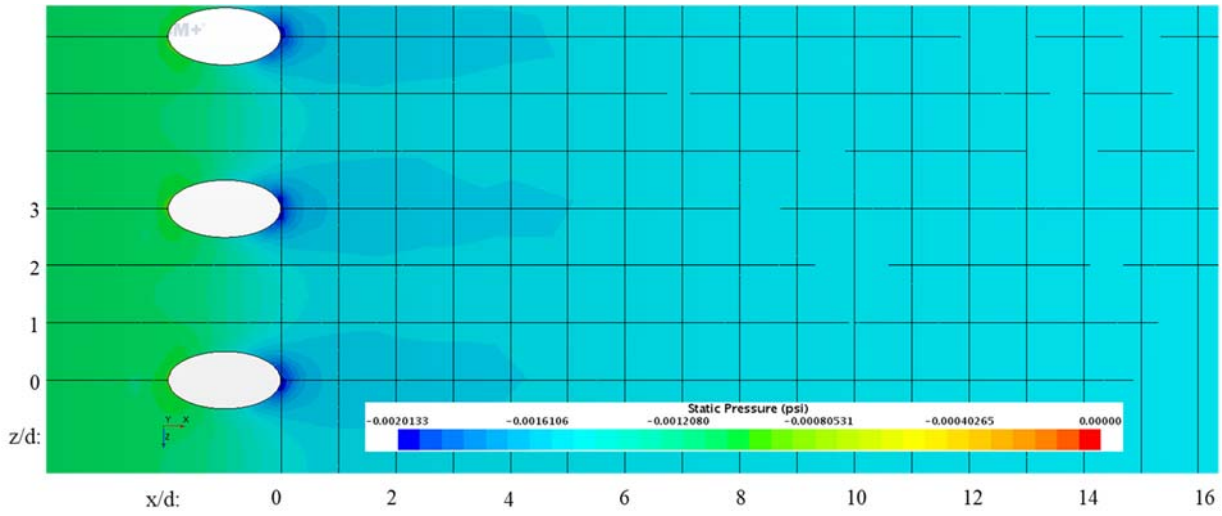

Figure 16.205: Case 19 – Static Pressure distribution for Suction Surface

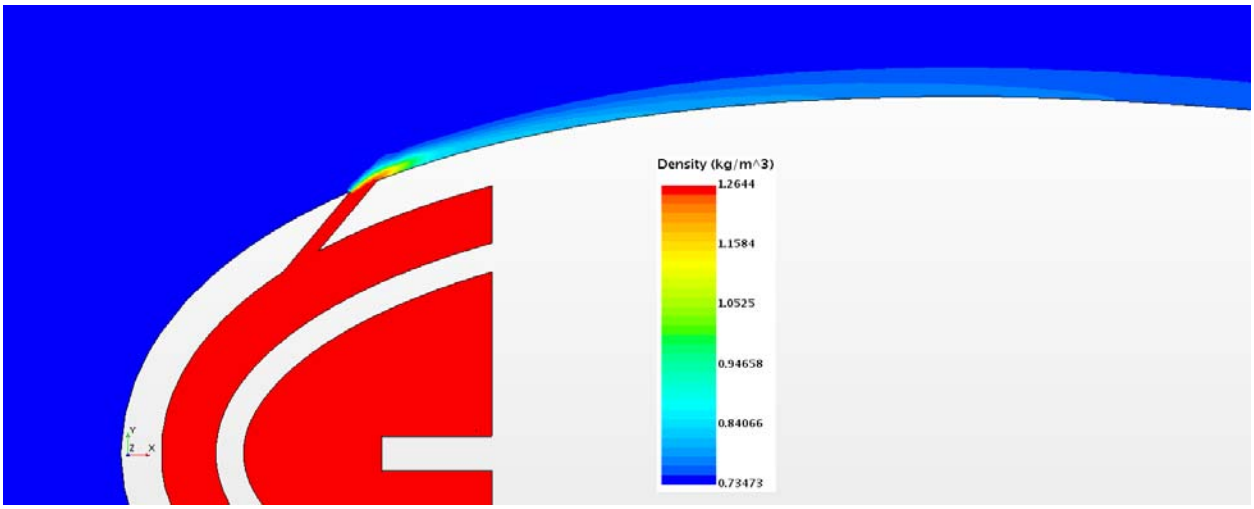

Figure 16.206: Case 19 – Density profile for center plane

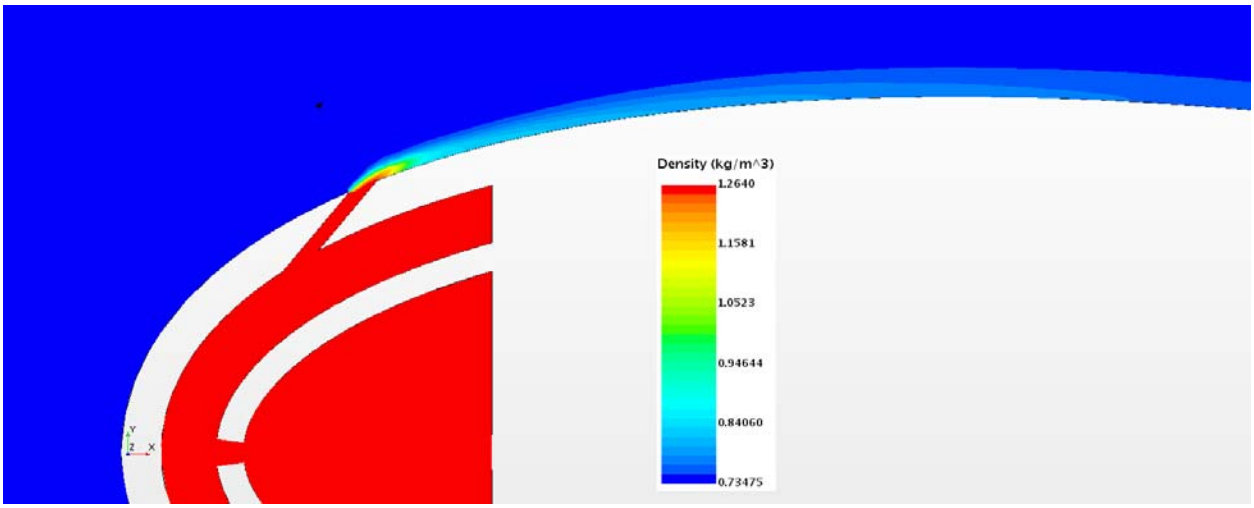

Figure 16.207: Case 19 – Density profile for off-center plane

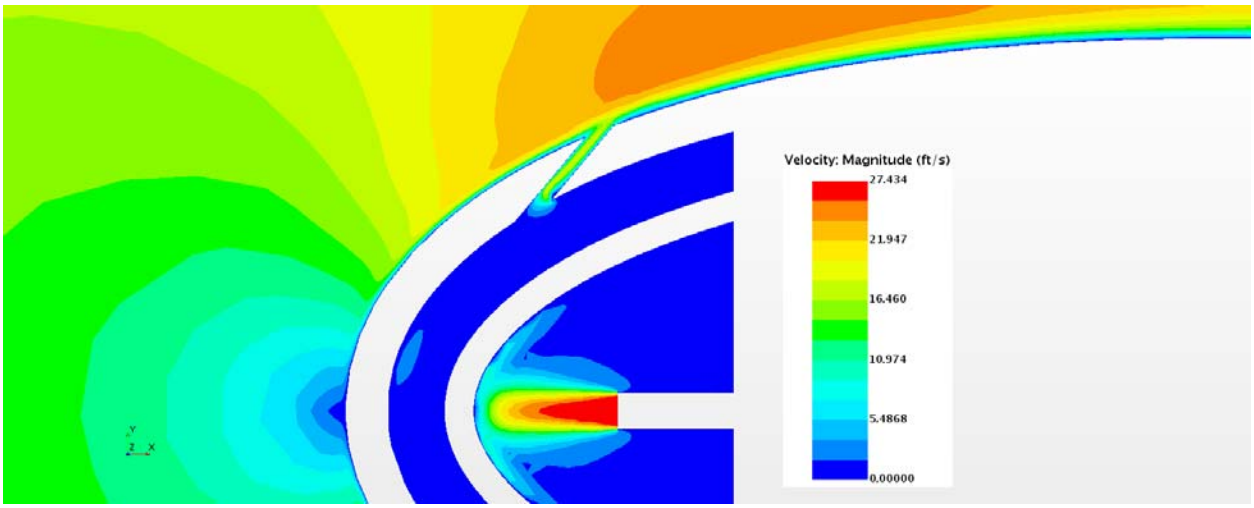

Figure 16.208: Case 19 – Velocity profile for center plane

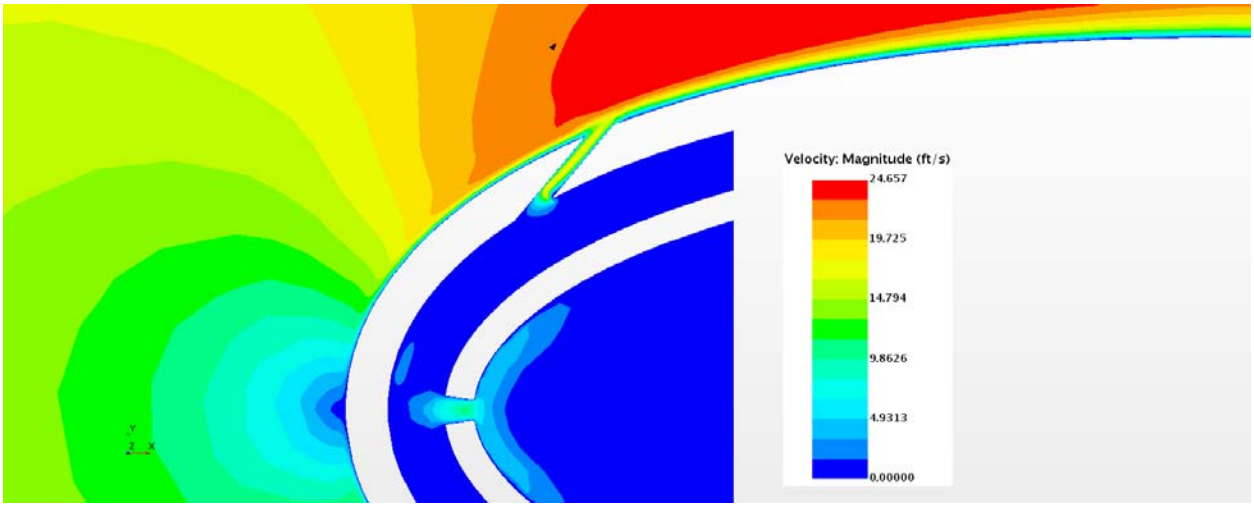

Figure 16.209: Case 19 – Velocity profile for off- center plane

Appendix G-20: M_b = 0.98, Tu = 15%, DR = 1.65

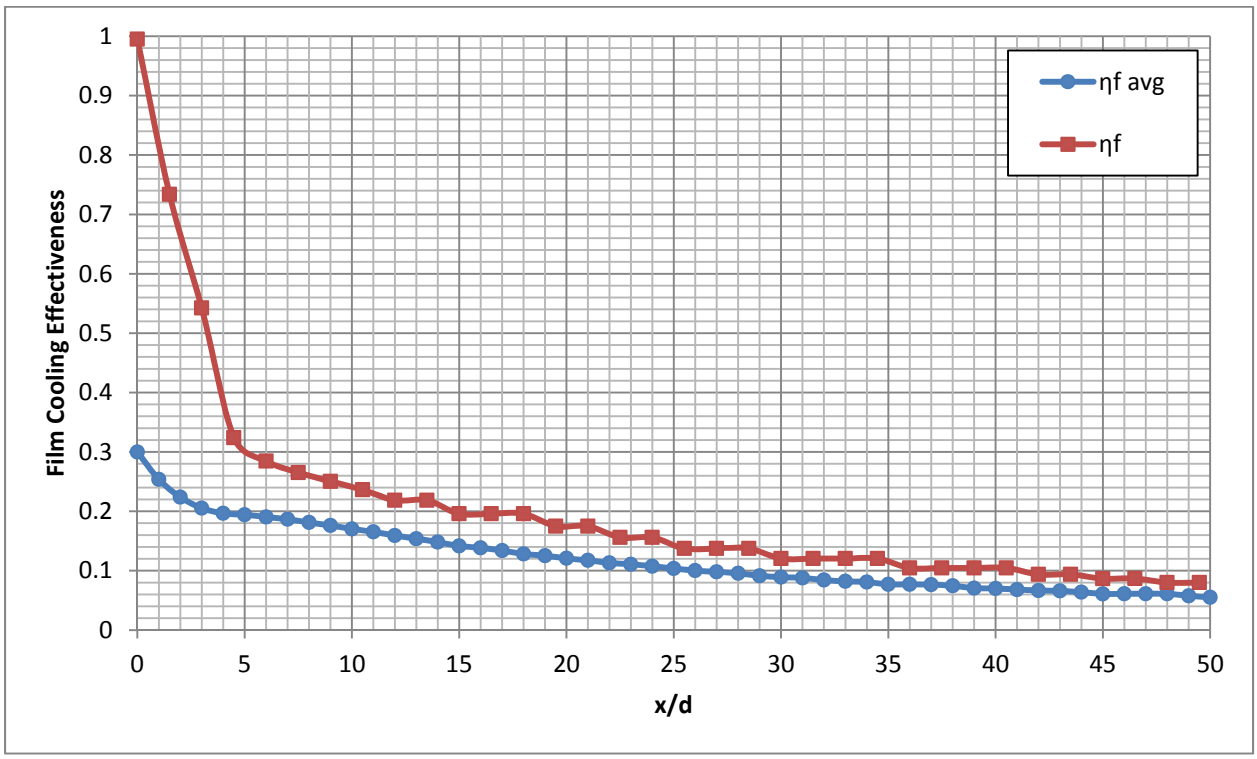

Figure 16.210: Case 20 - Laterally averaged and Centerline adiabatic film cooling effectiveness

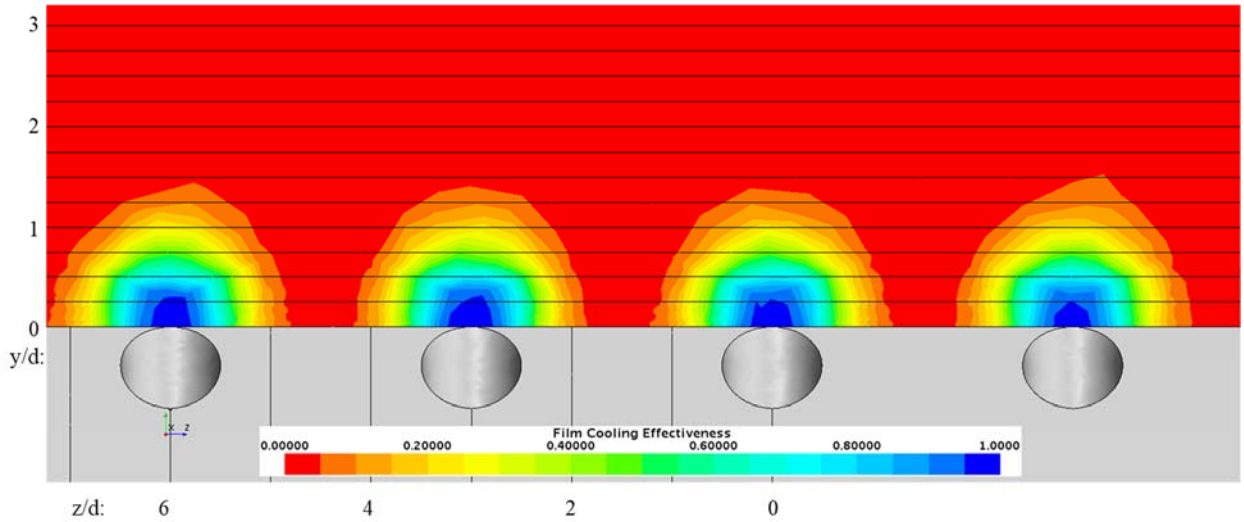

Figure 16.211: Case 20 - Spatial distribution of adiabatic film cooling effectiveness at x/d: 0

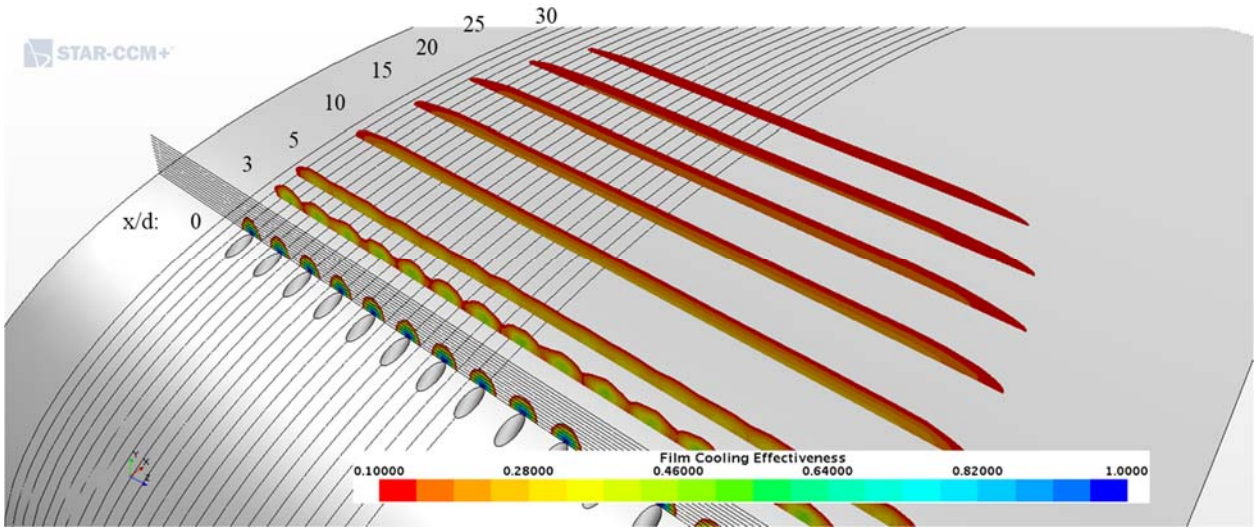

Figure 16.212: Case 20 - Streamwise spatial distribution of adiabatic film cooling effectiveness

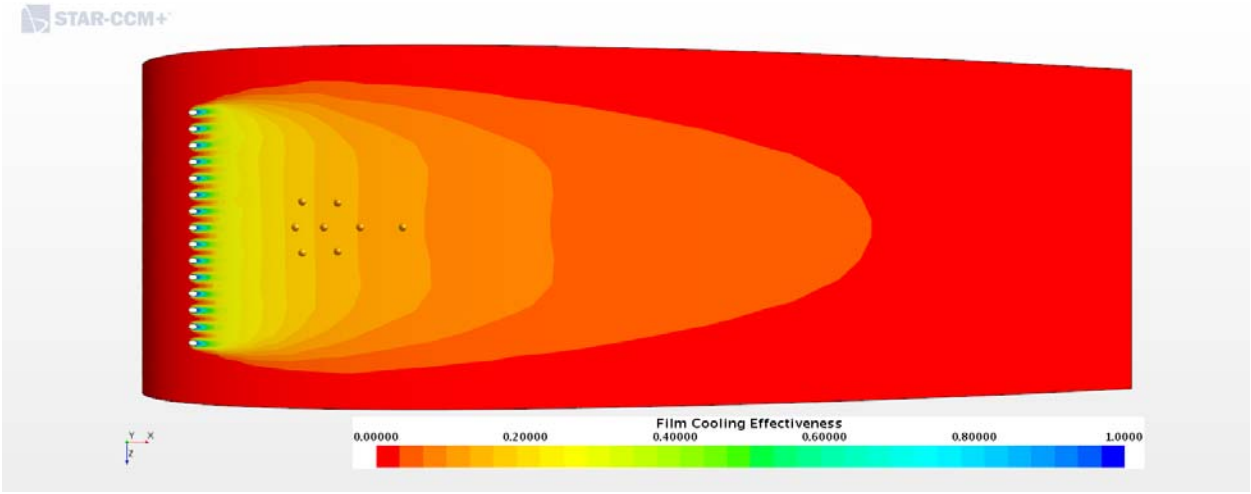

Figure 16.213: Case 20 - Adiabatic Film Cooling Effectiveness on the Suction Surface

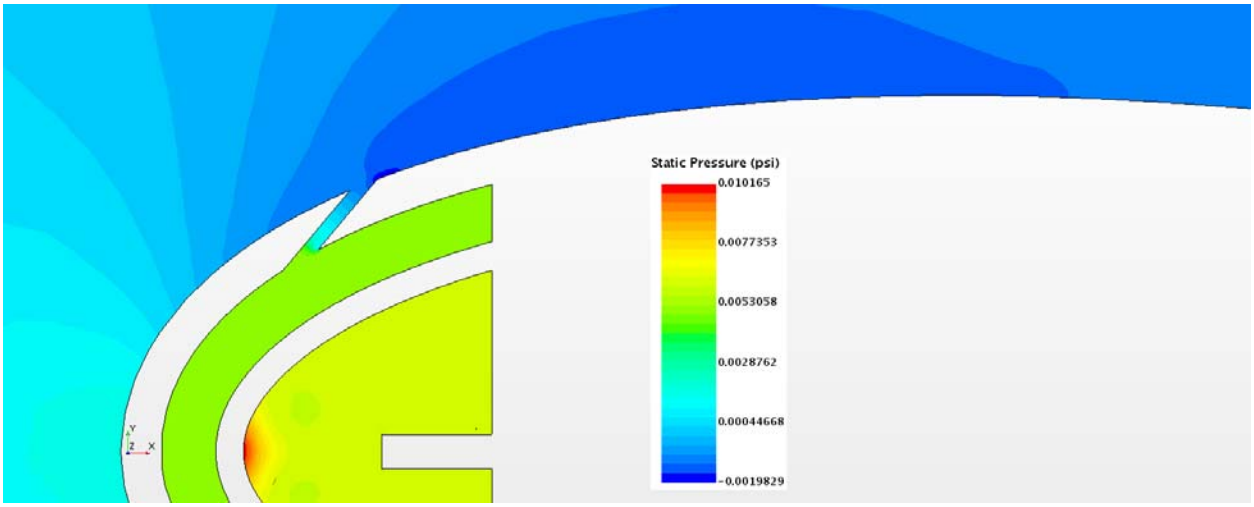

Figure 16.214: Case 20 – Static Pressure profile for center plane

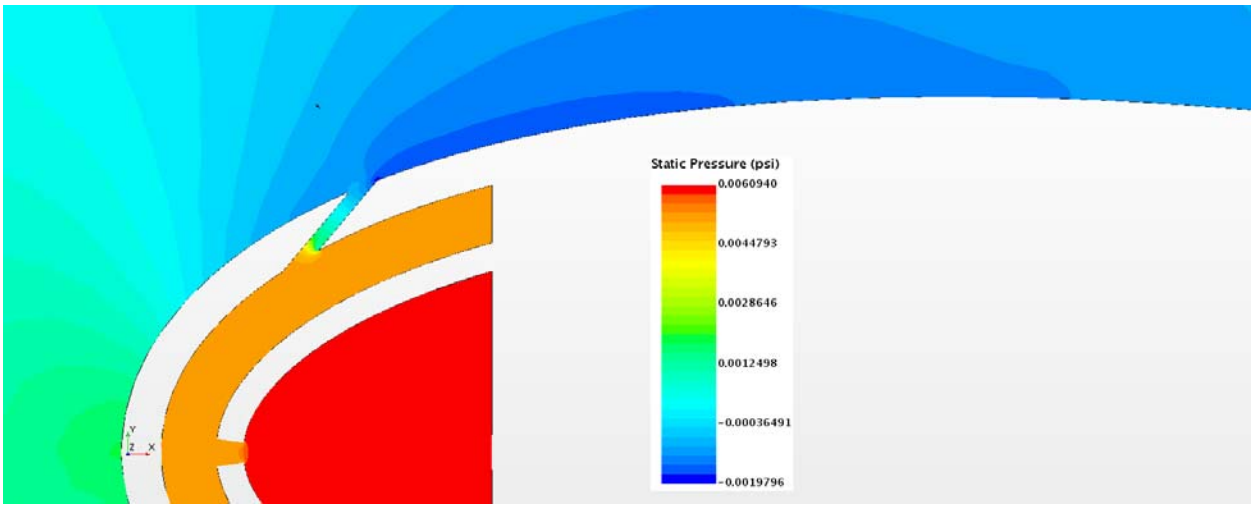

Figure 16.215: Case 20 – Static Pressure profile for off-center plane

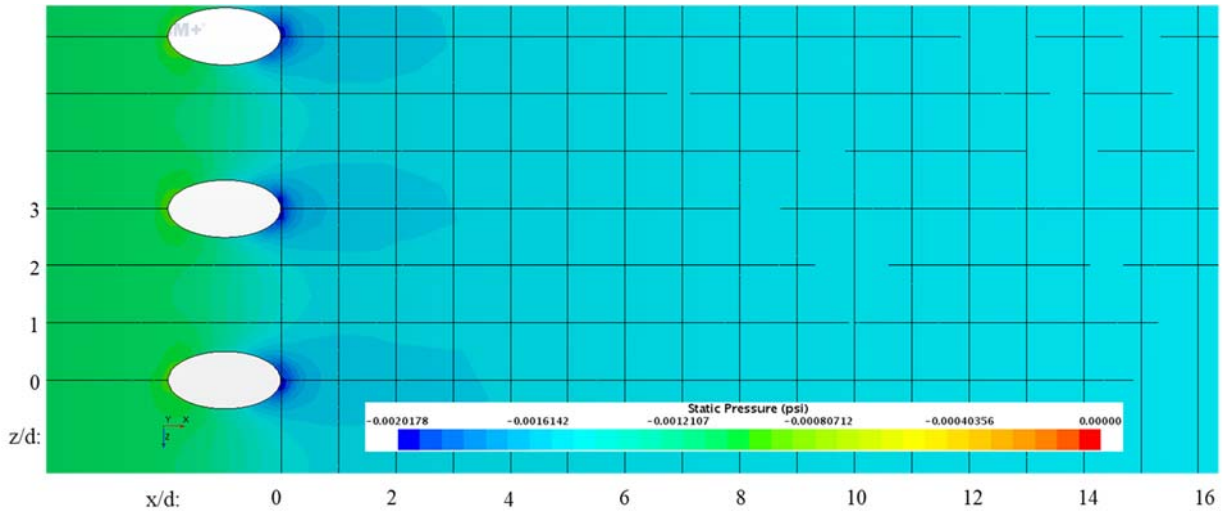

Figure 16.216: Case 20 – Static Pressure distribution for Suction Surface

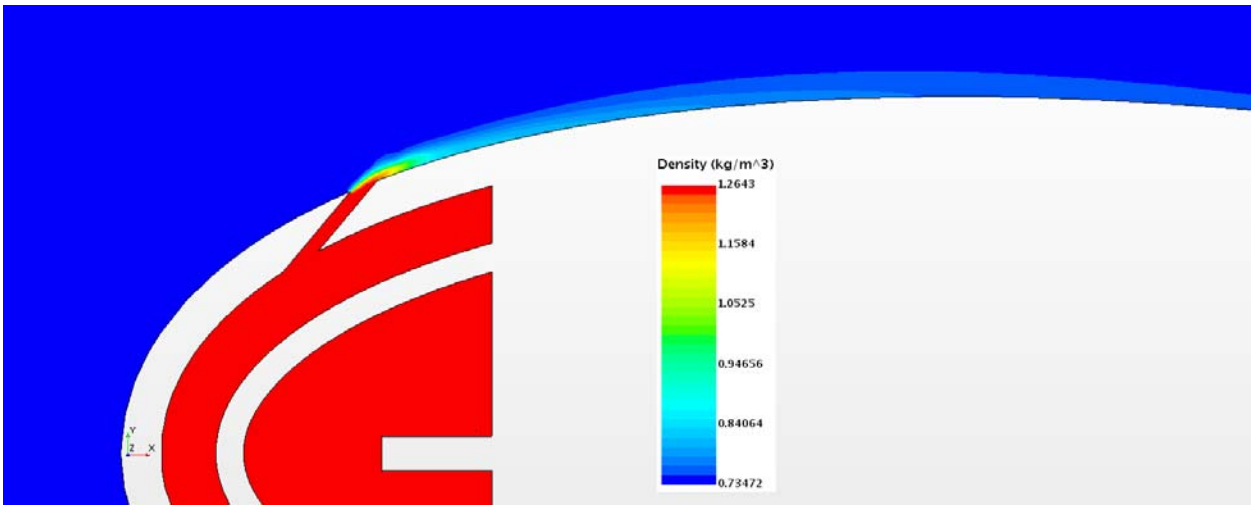

Figure 16.217: Case 20 – Density profile for center plane

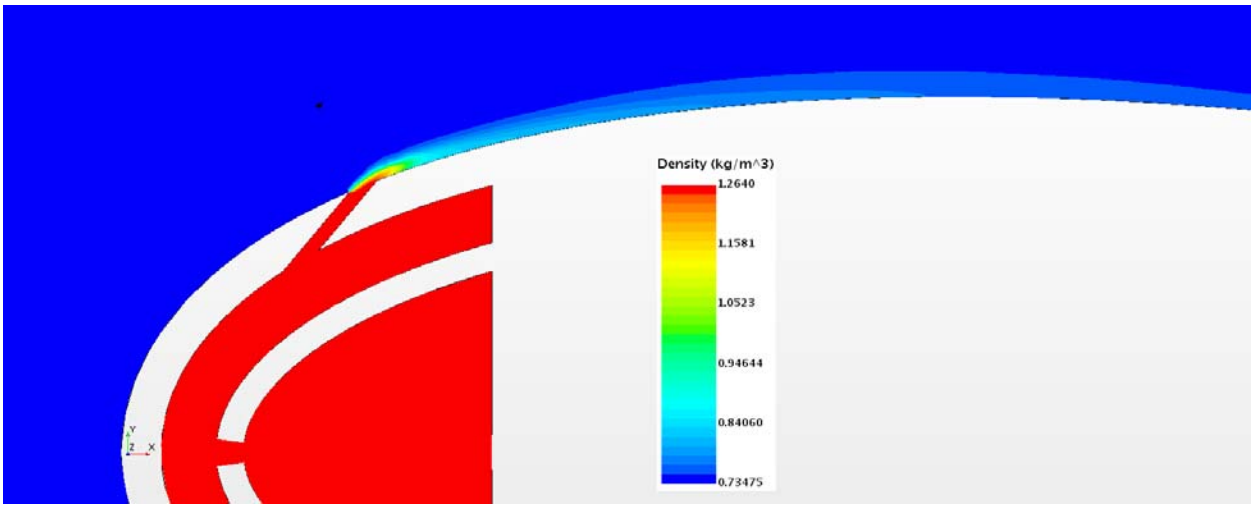

Figure 16.218: Case 20 – Density profile for off-center plane

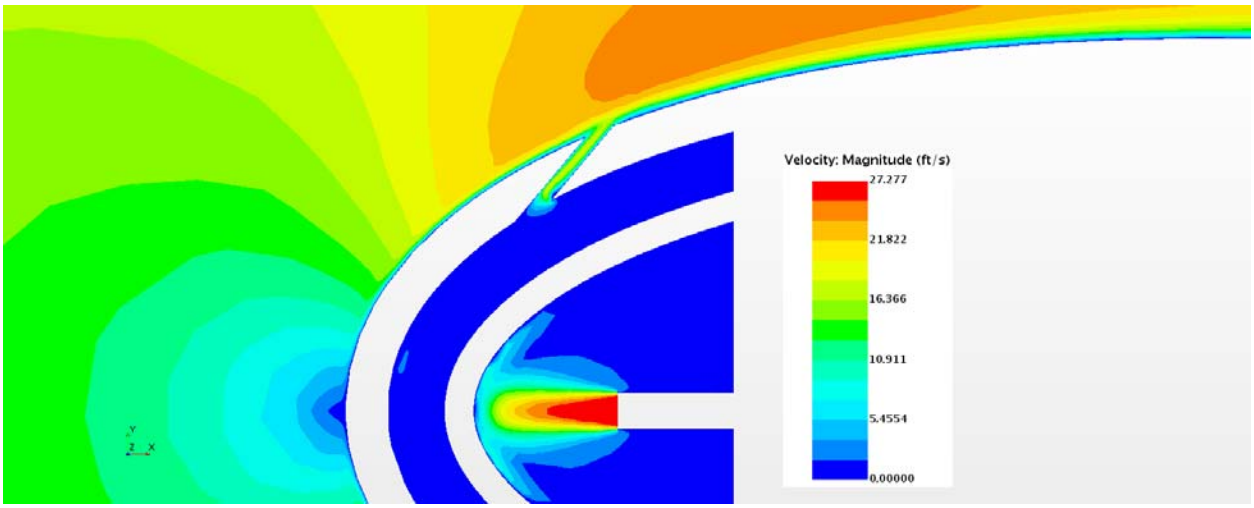

Figure 16.219: Case 20 – Velocity profile for center plane

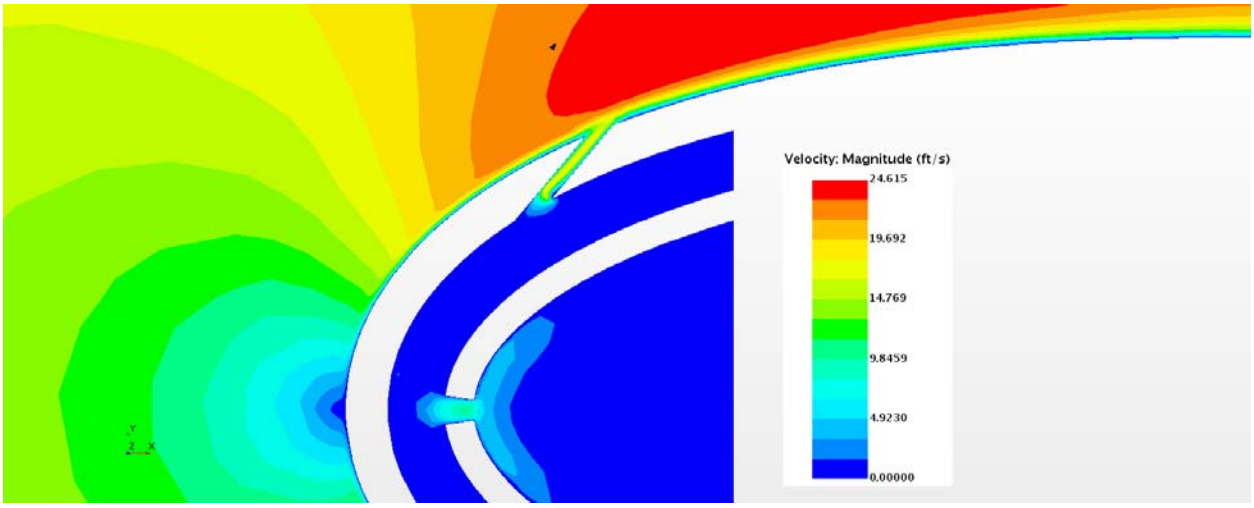

Figure 16.220: Case 20 – Velocity profile for off-center plane

Appendix G-21: M_b = 0.98, Tu = 25%, DR: 1.65

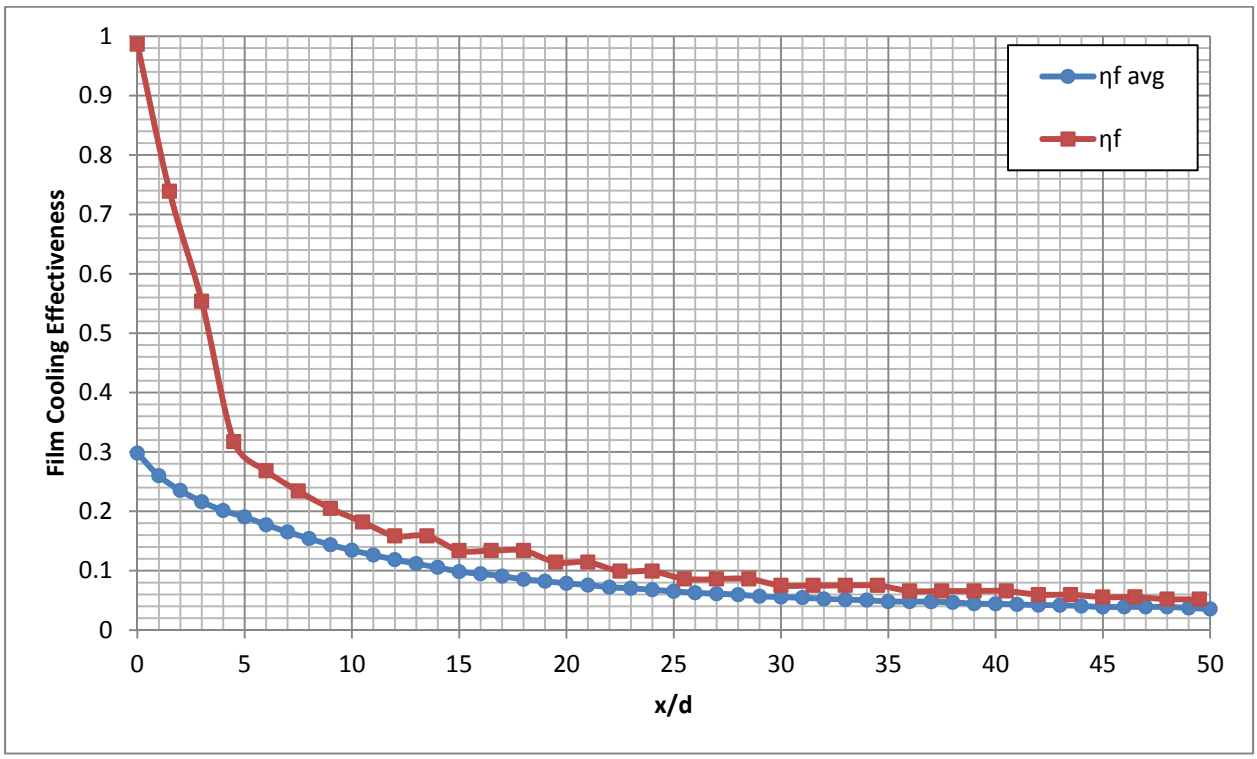

Figure 16.221: Case 21 - Laterally averaged and Centerline adiabatic film cooling effectiveness

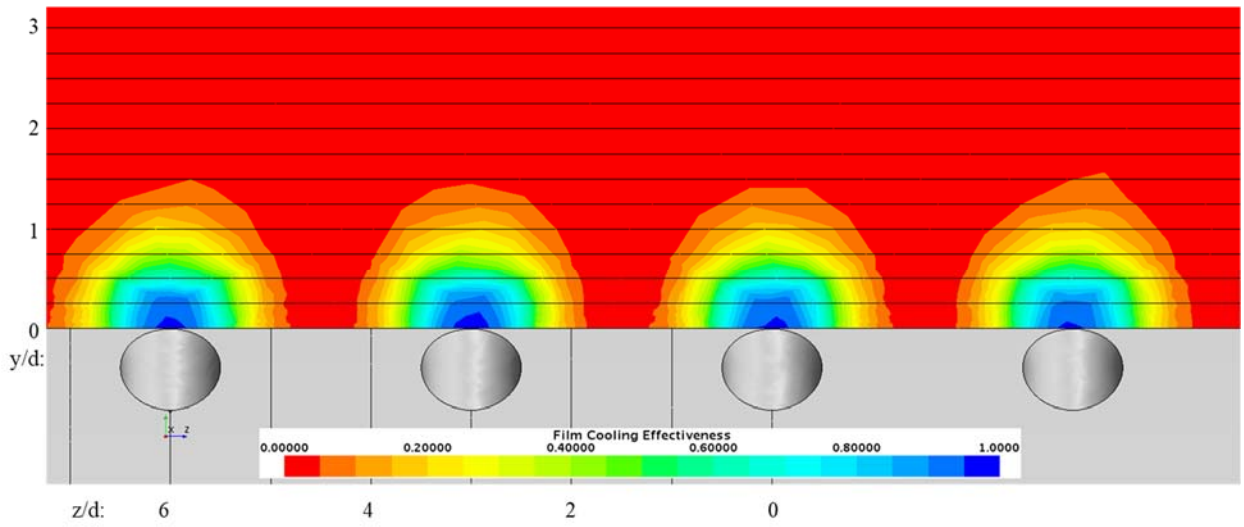

Figure 16.222: Case 21 - Spatial distribution of adiabatic film cooling effectiveness at x/d: 0

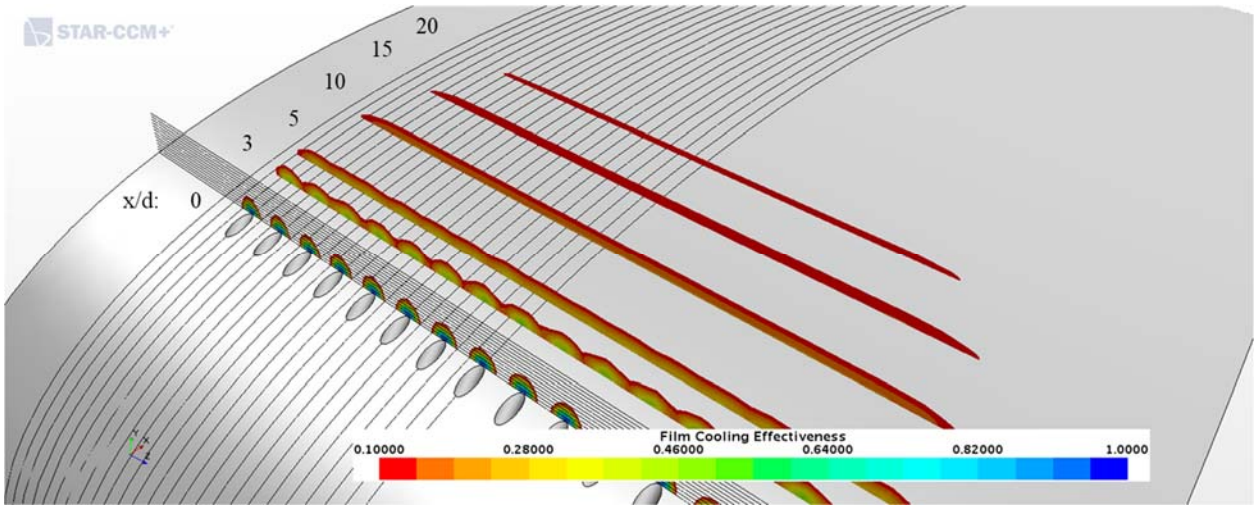

Figure 16.223: Case 21 - Streamwise spatial distribution of adiabatic film cooling effectiveness

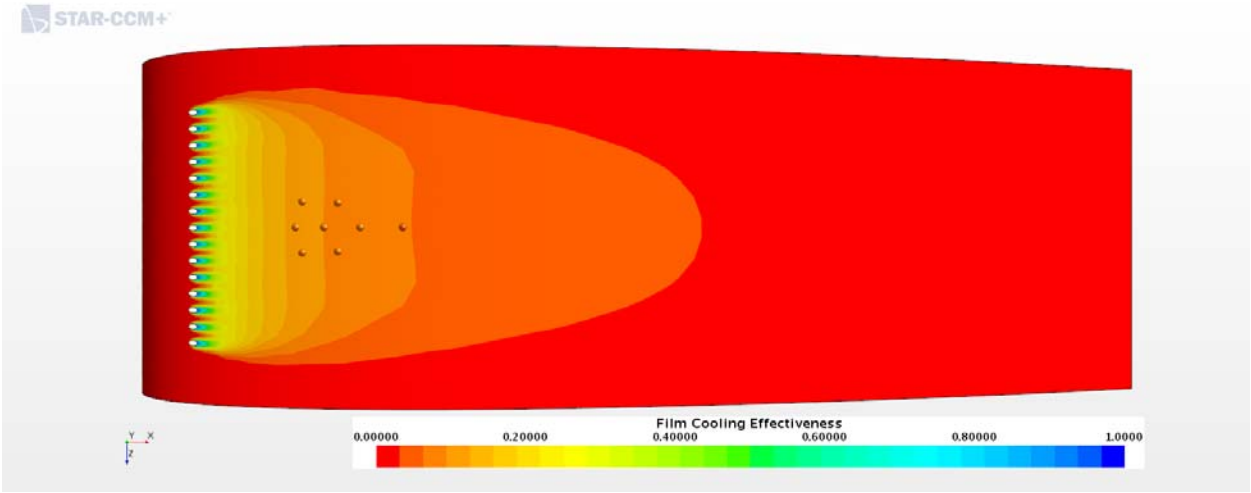

Figure 16.224: Case 21 - Adiabatic Film Cooling Effectiveness on the Suction Surface

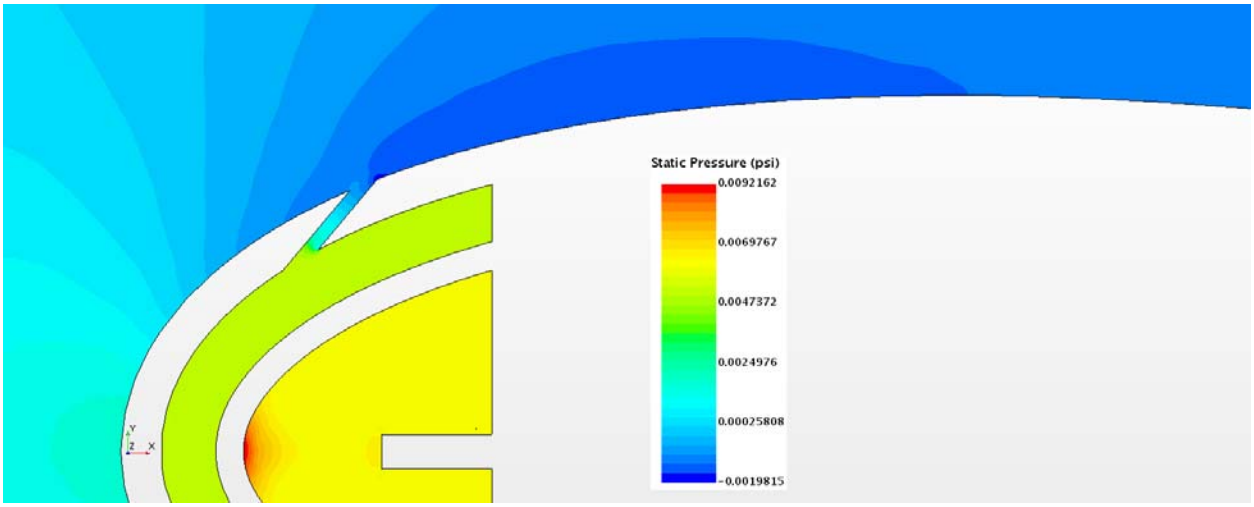

Figure 16.225: Case 21 – Static Pressure profile for center plane

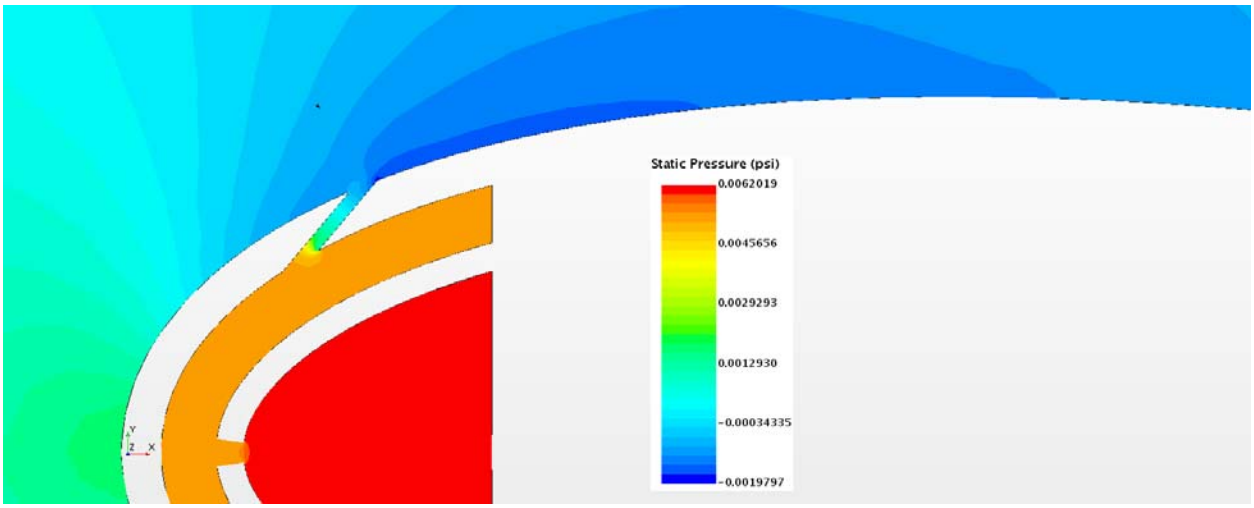

Figure 16.226: Case 21 – Static Pressure profile for off-center plane

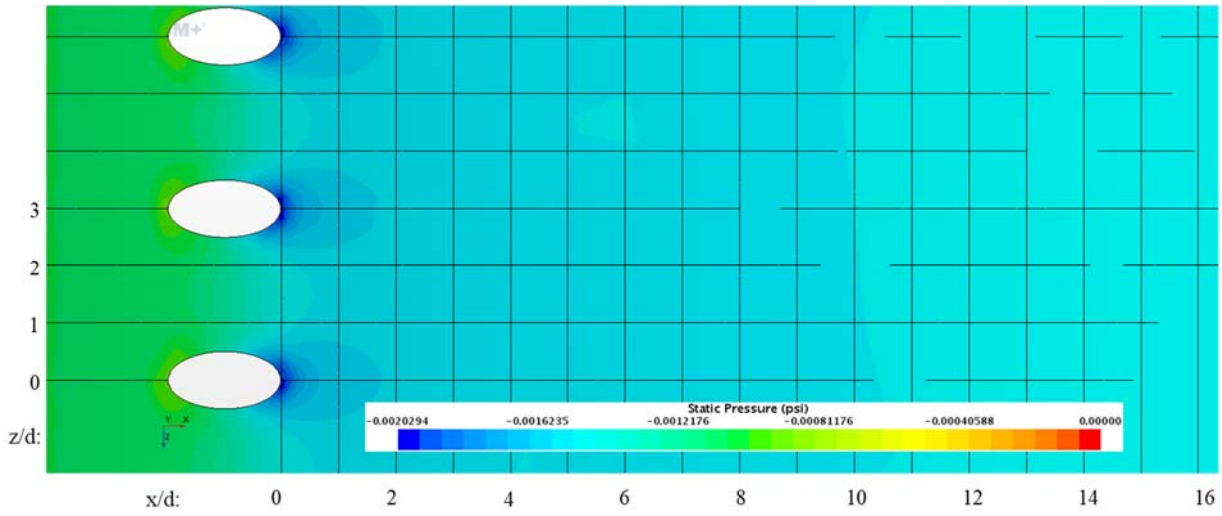

Figure 16.227: Case 21 – Static Pressure distribution for Suction Surface

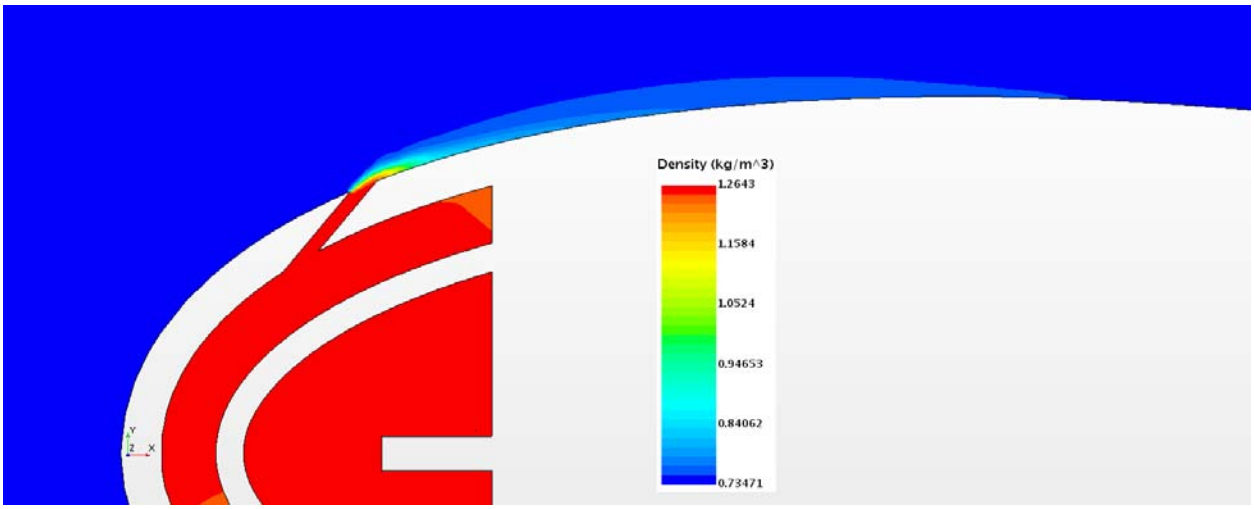

Figure 16.228: Case 21 – Density profile for center plane

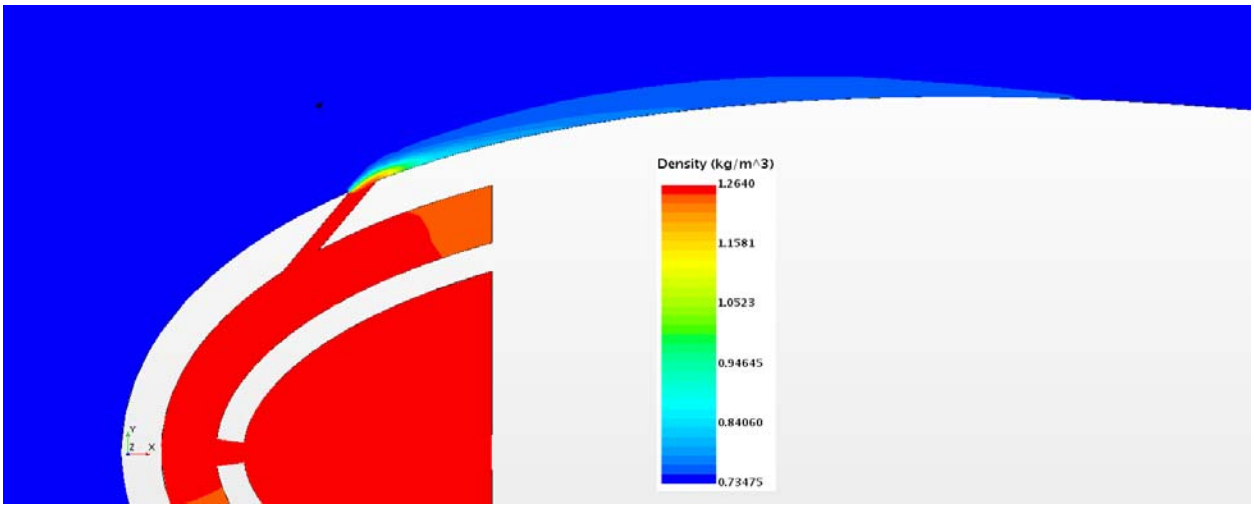

Figure 16.229: Case 21 – Density profile for off-center plane

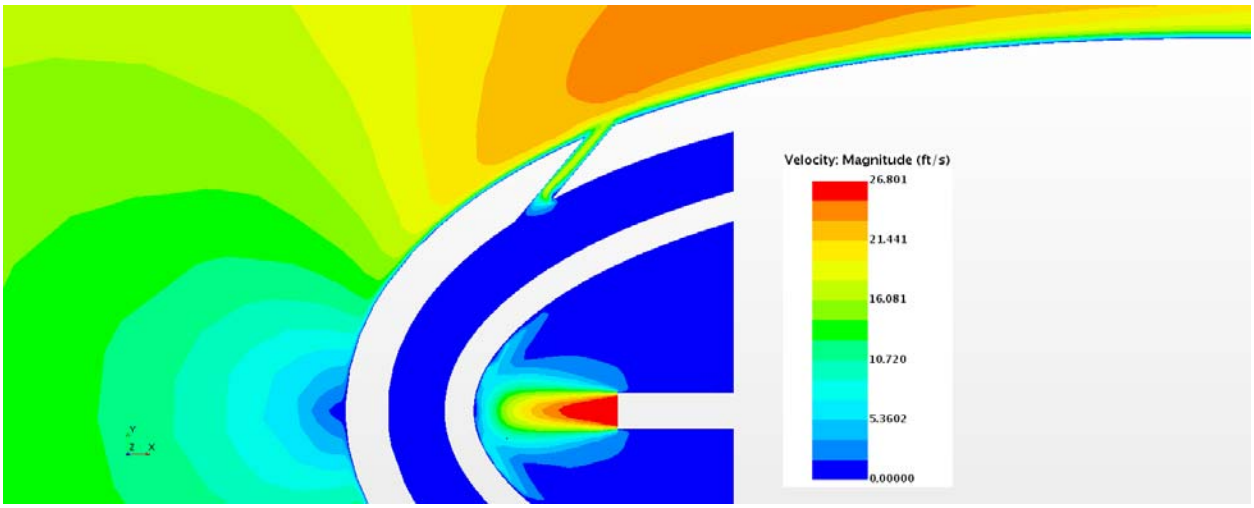

Figure 16.230: Case 21 – Velocity profile for center plane

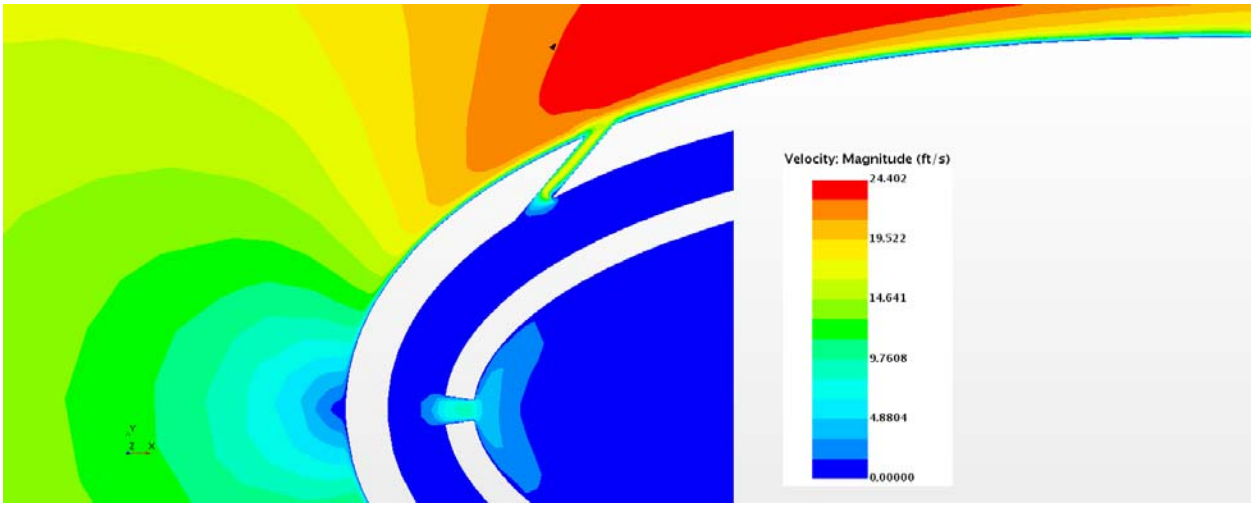

Figure 16.231: Case 21 – Velocity profile for off- center plane

Appendix G-22: M_b = 1.26, Tu = 5%, DR = 1.99

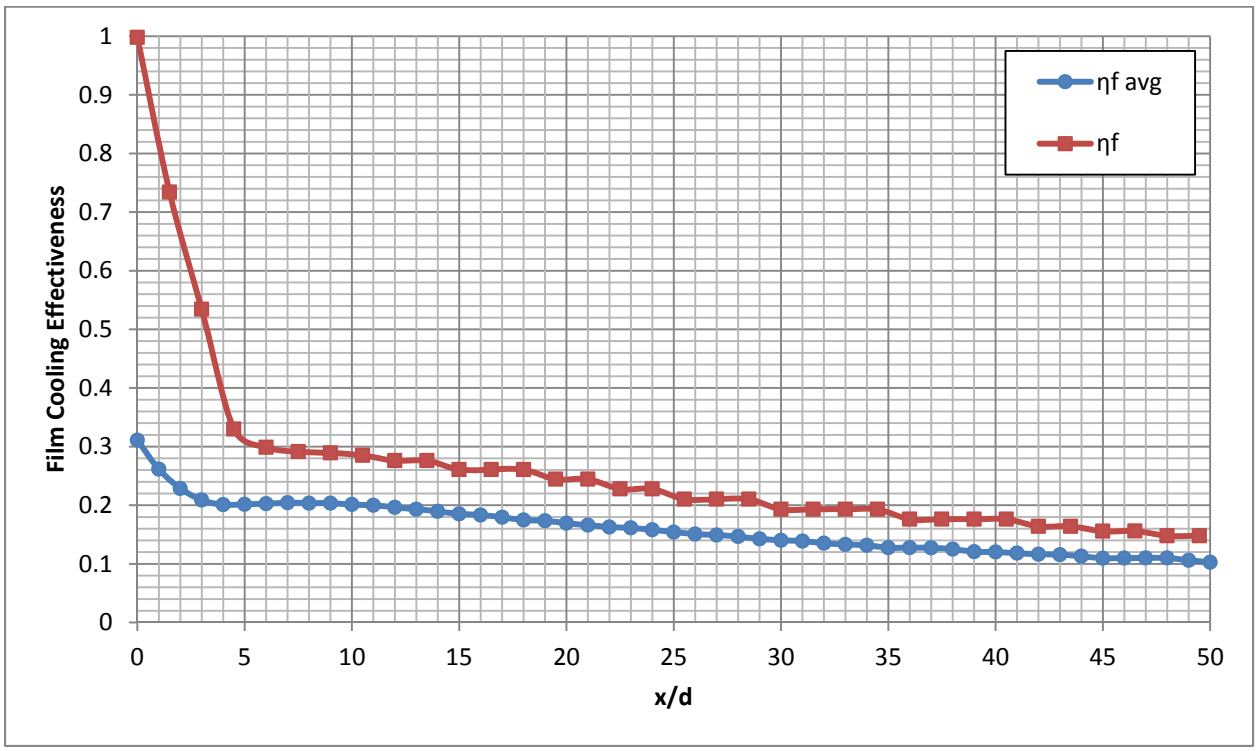

Figure 16.232: Case 22 - Laterally averaged and Centerline adiabatic film cooling effectiveness

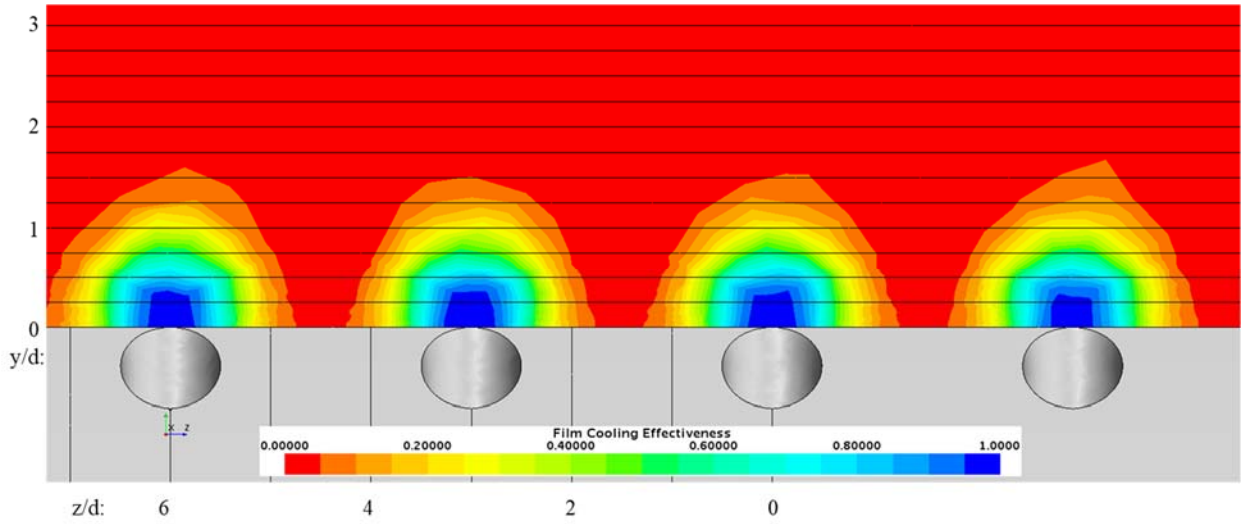

Figure 16.233: Case 22 - Spatial distribution of adiabatic film cooling effectiveness at x/d: 0

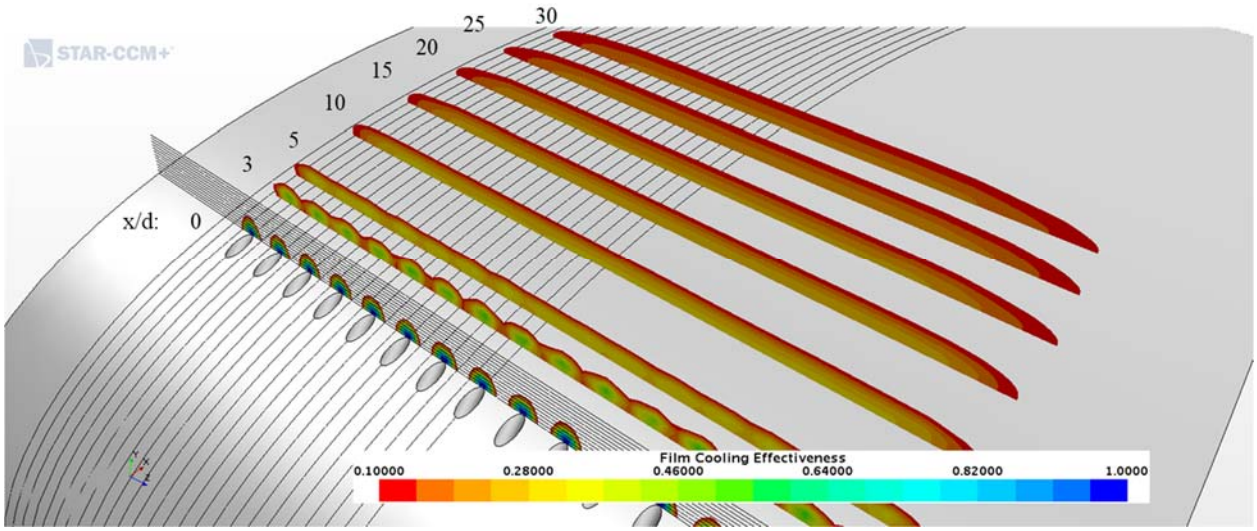

Figure 16.234: Case 22 - Streamwise spatial distribution of adiabatic film cooling effectiveness

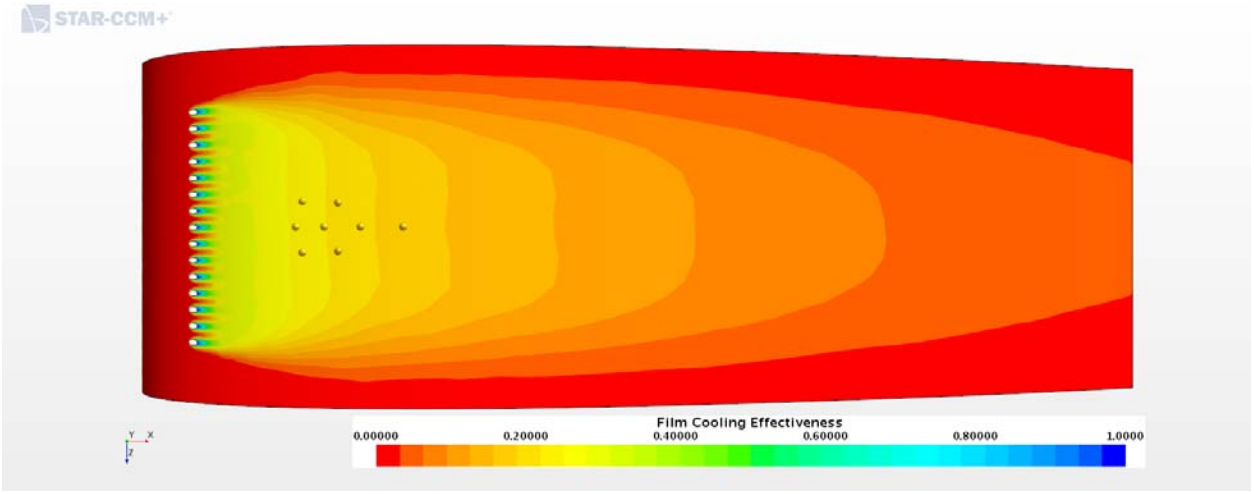

Figure 16.235: Case 22 - Adiabatic Film Cooling Effectiveness on the Suction Surface

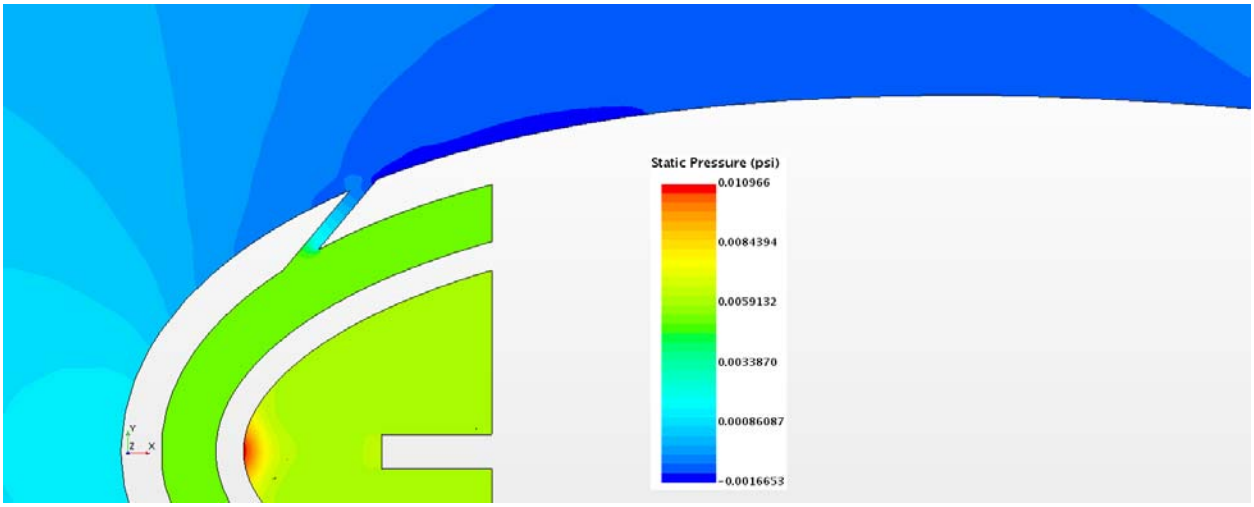

Figure 16.236: Case 22 – Static Pressure profile for center plane

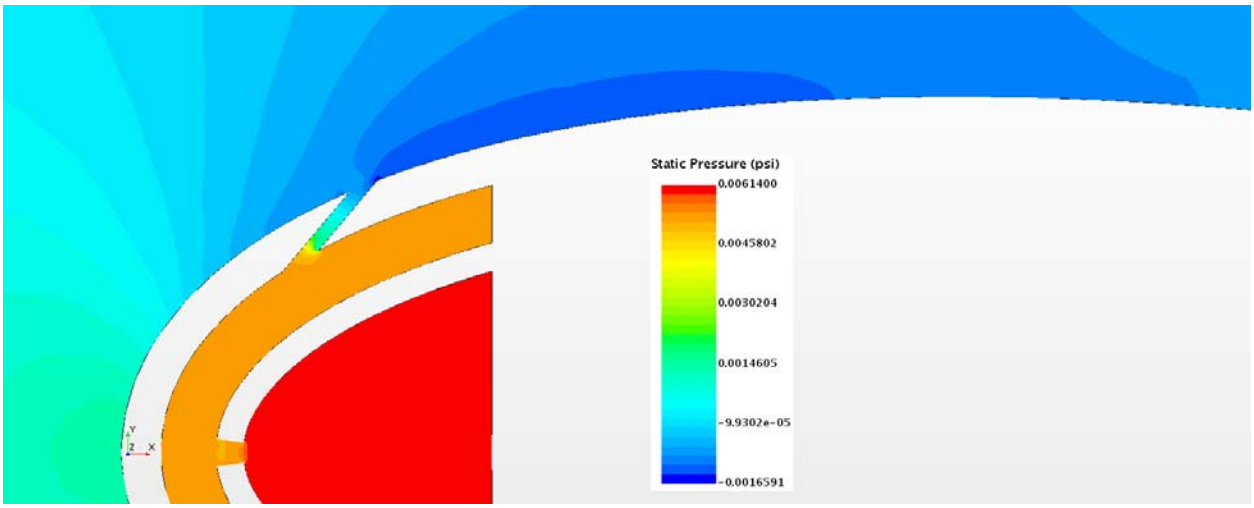

Figure 16.237: Case 22 – Static Pressure profile for off-center plane

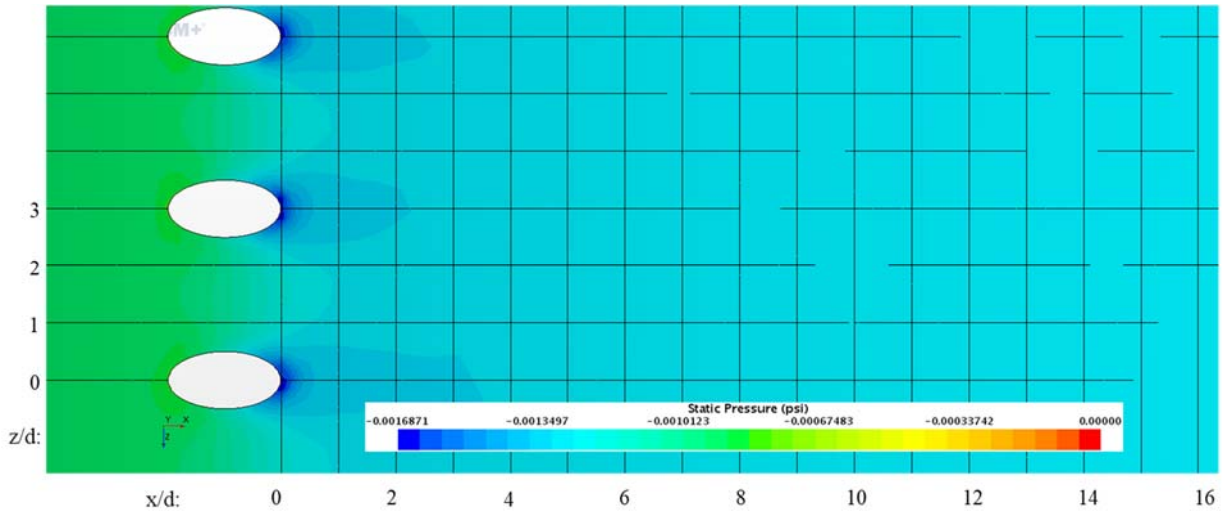

Figure 16.238: Case 22 – Static Pressure distribution for Suction Surface

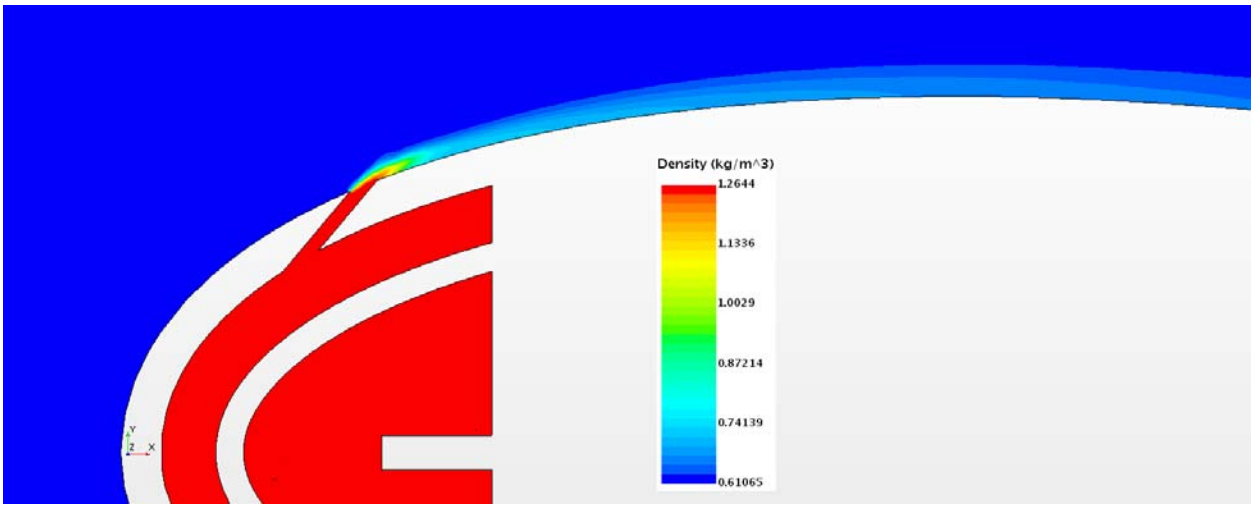

Figure 16.239: Case 22 – Density profile for center plane

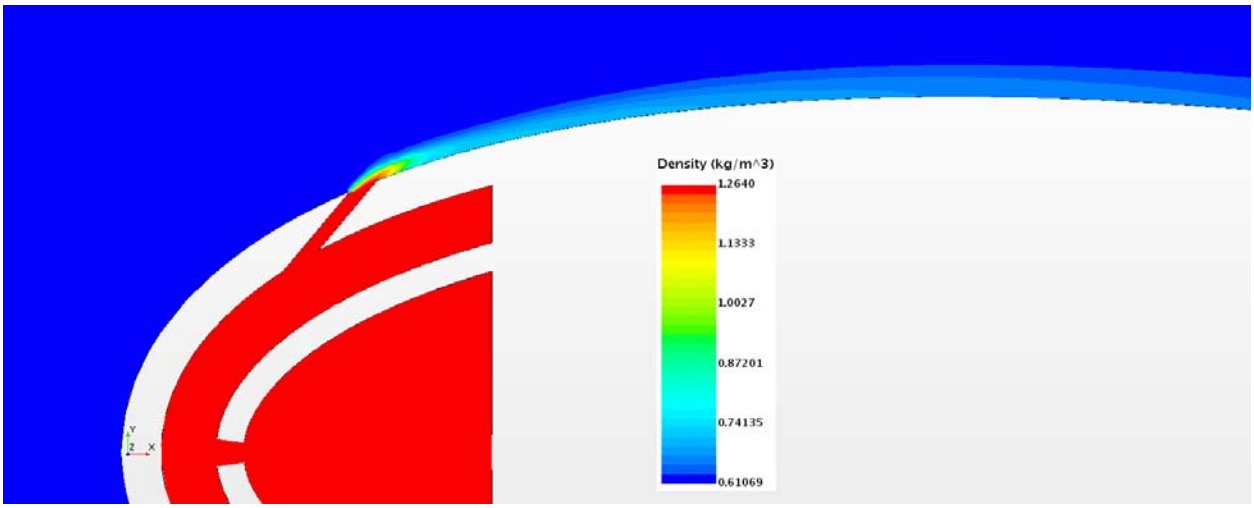

Figure 16.240: Case 22 – Density profile for off-center plane

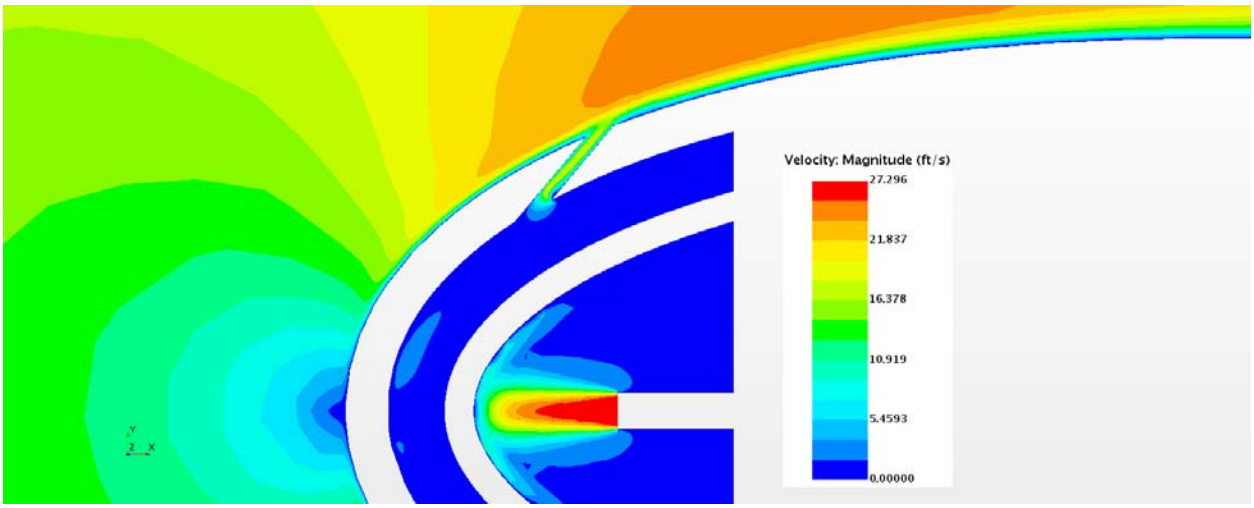

Figure 16.241: Case 22 – Velocity profile for center plane

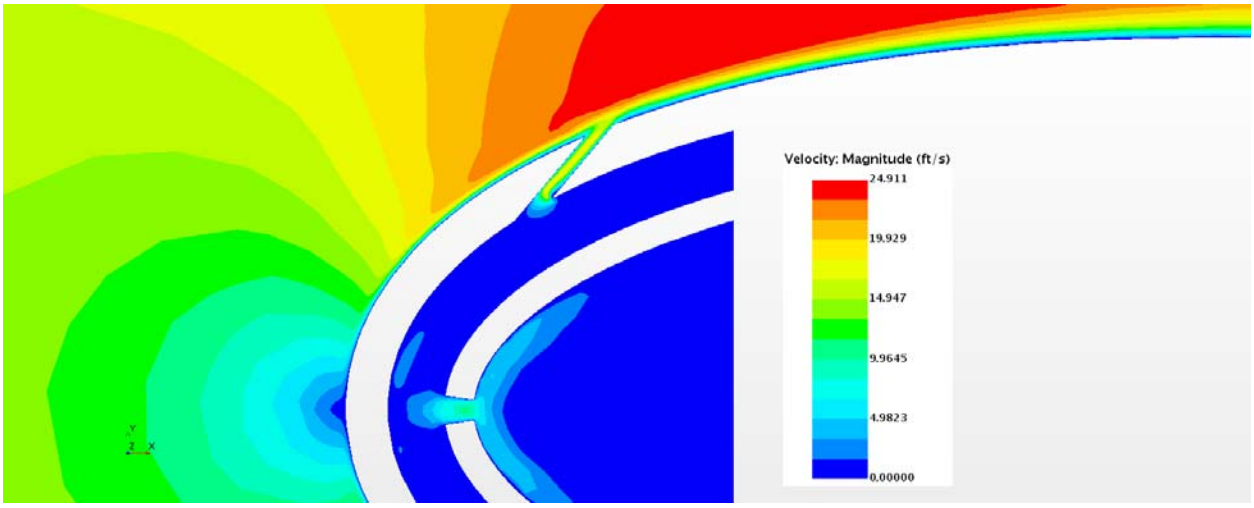

Figure 16.242: Case 22 – Velocity profile for off- center plane

Appendix G-23: M_b = 1.26, Tu: 10%, DR = 1.99

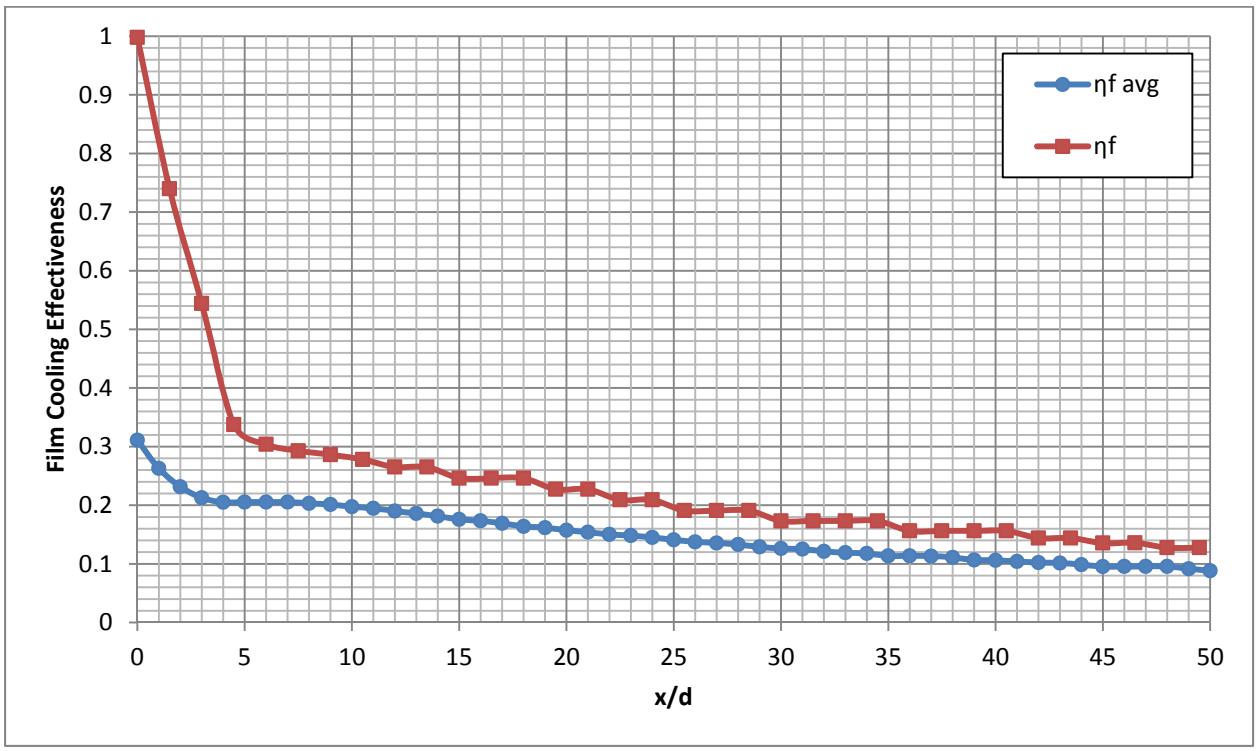

Figure 16.243: Case 23 - Laterally averaged and Centerline adiabatic film cooling effectiveness

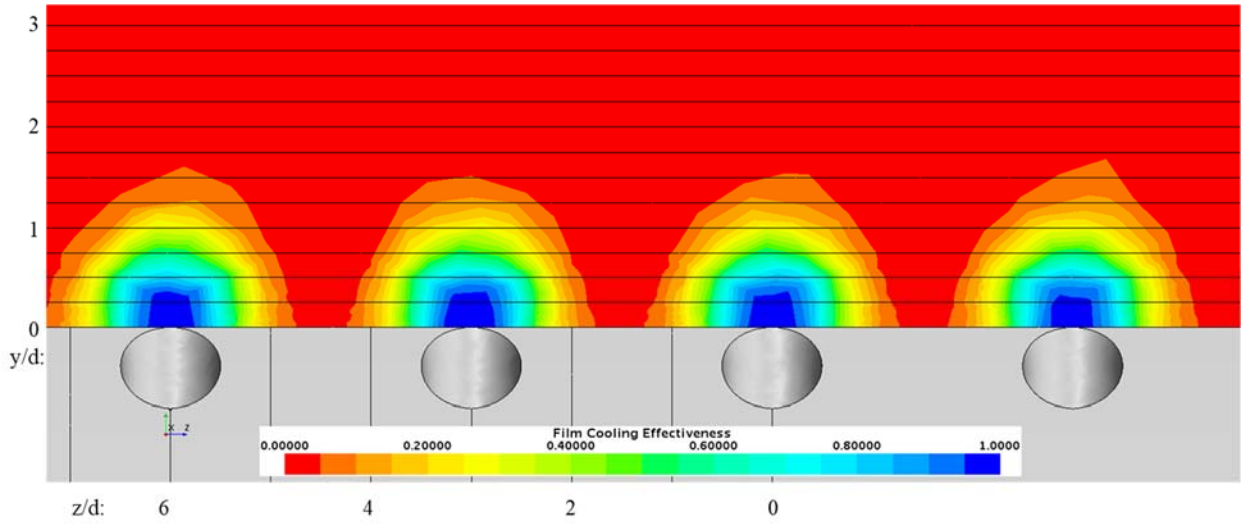

Figure 16.244: Case 23 - Spatial distribution of adiabatic film cooling effectiveness at x/d: 0

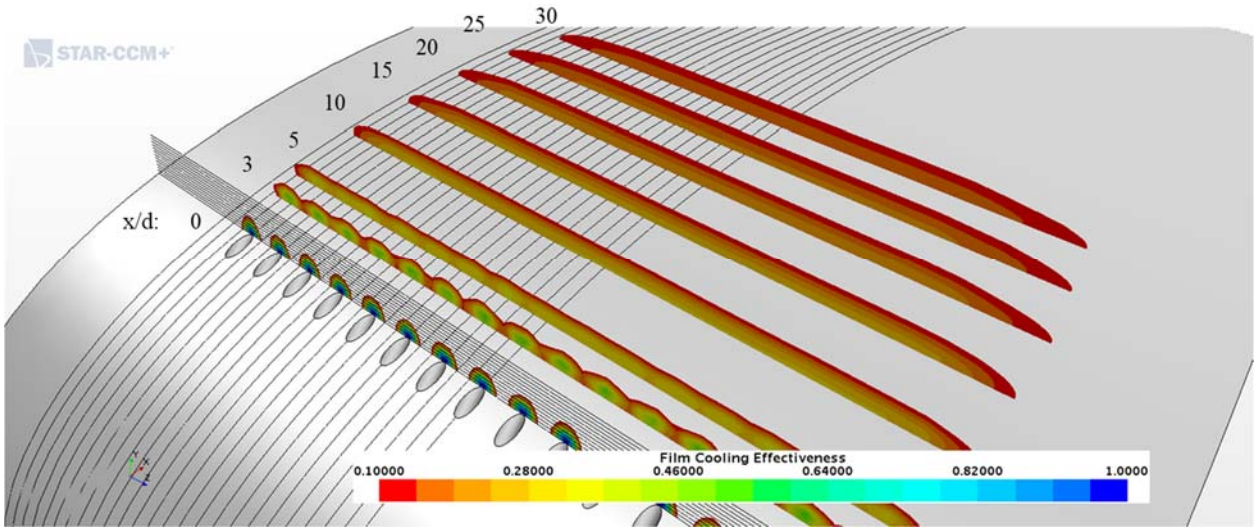

Figure 16.245: Case 23 - Streamwise spatial distribution of adiabatic film cooling effectiveness

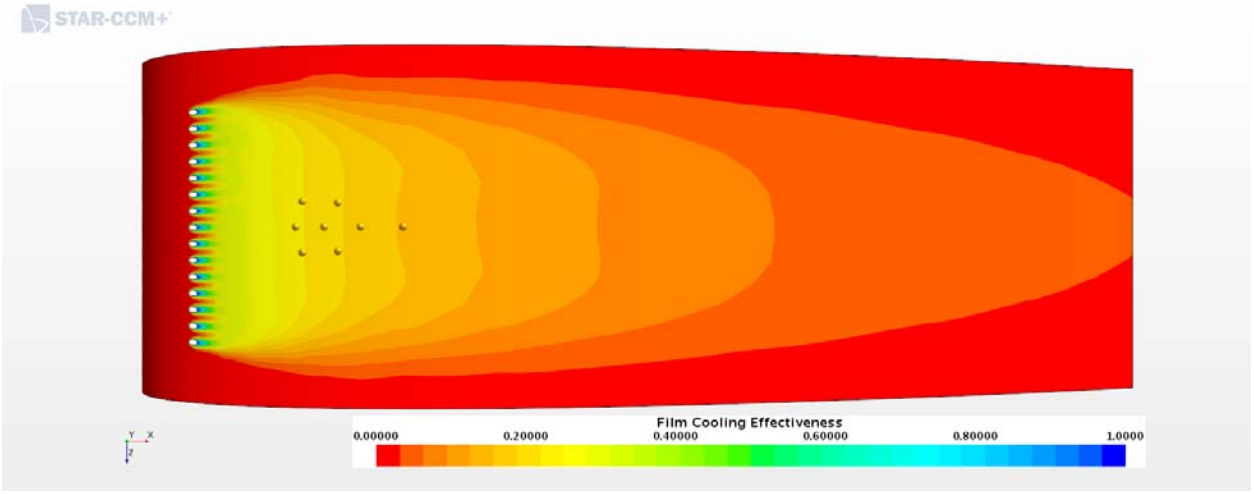

Figure 16.246: Case 23 - Adiabatic Film Cooling Effectiveness on the Suction Surface

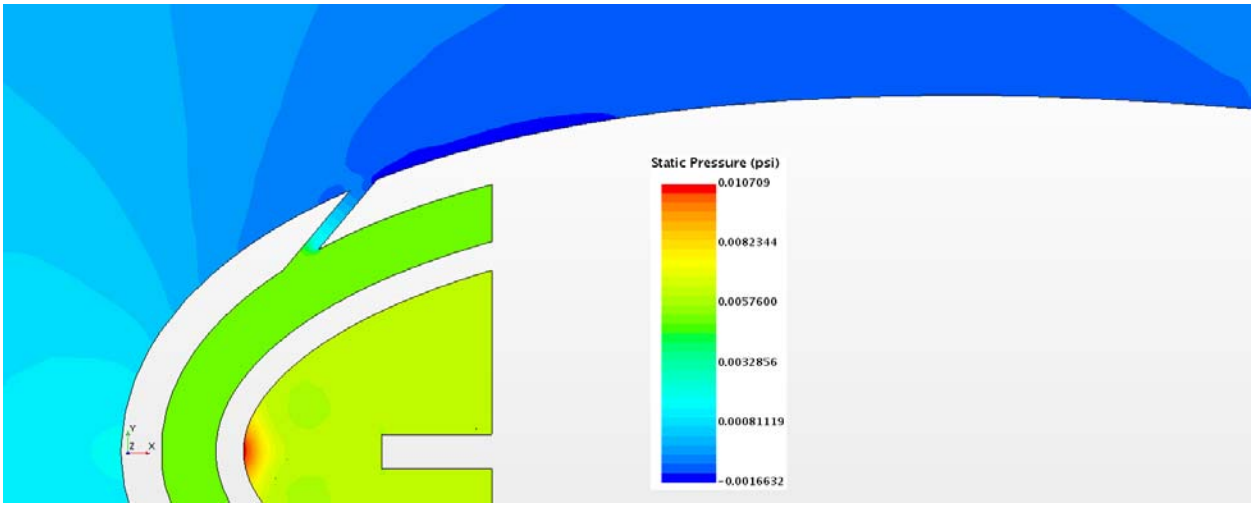

Figure 16.247: Case 23 – Static Pressure profile for center plane

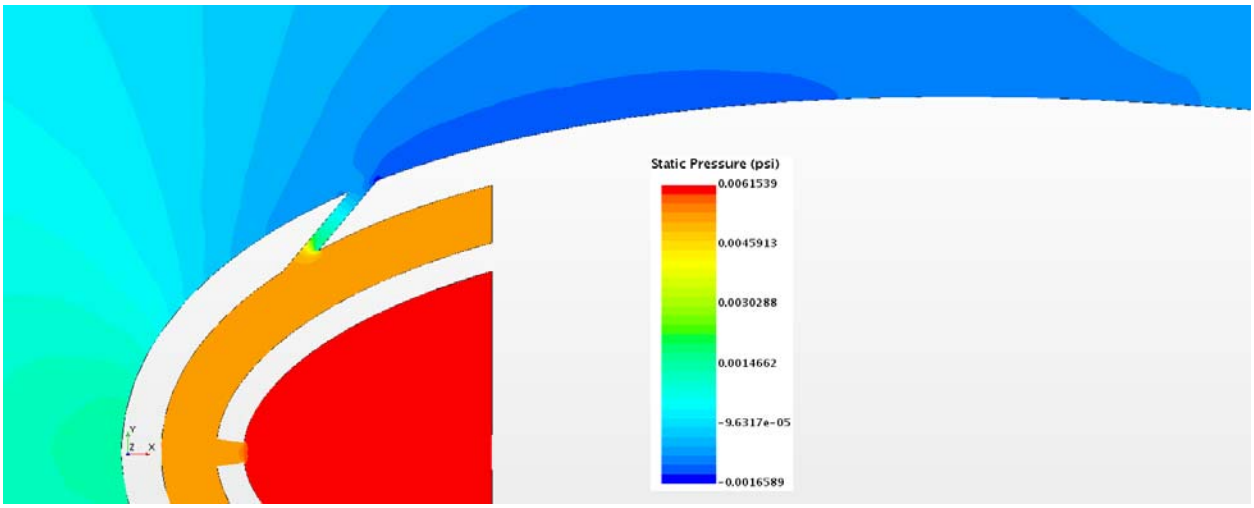

Figure 16.248: Case 23 – Static Pressure profile for off-center plane

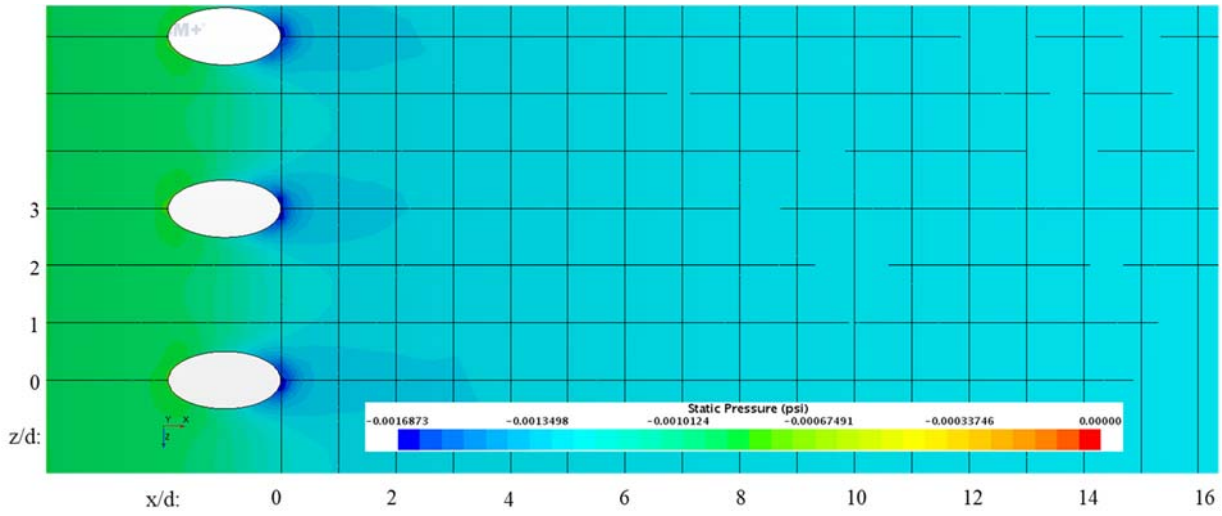

Figure 16.249: Case 23 – Static Pressure distribution for Suction Surface

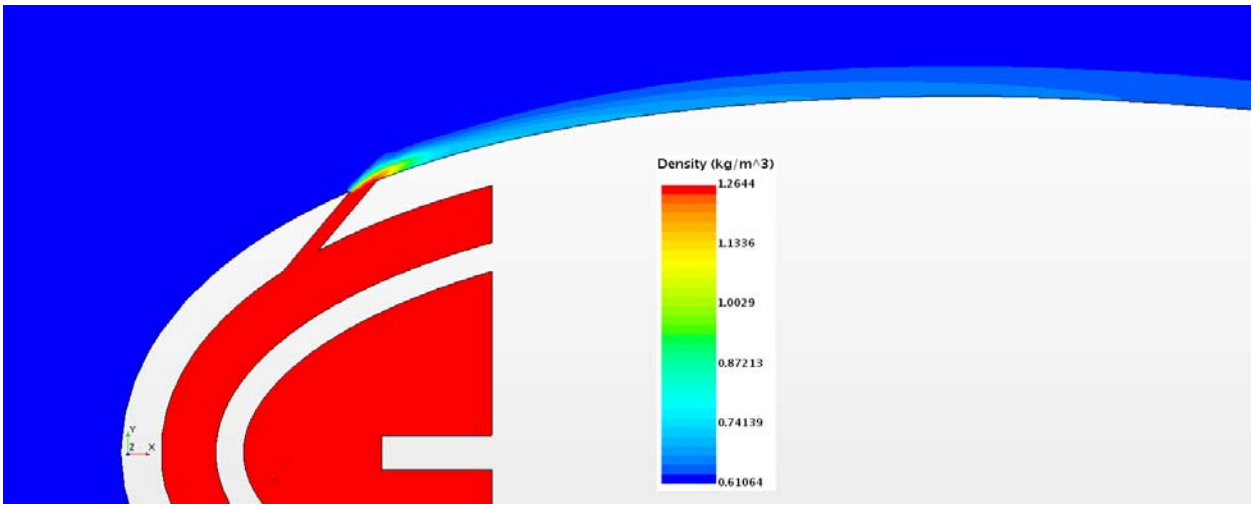

Figure 16.250: Case 23 – Density profile for center plane

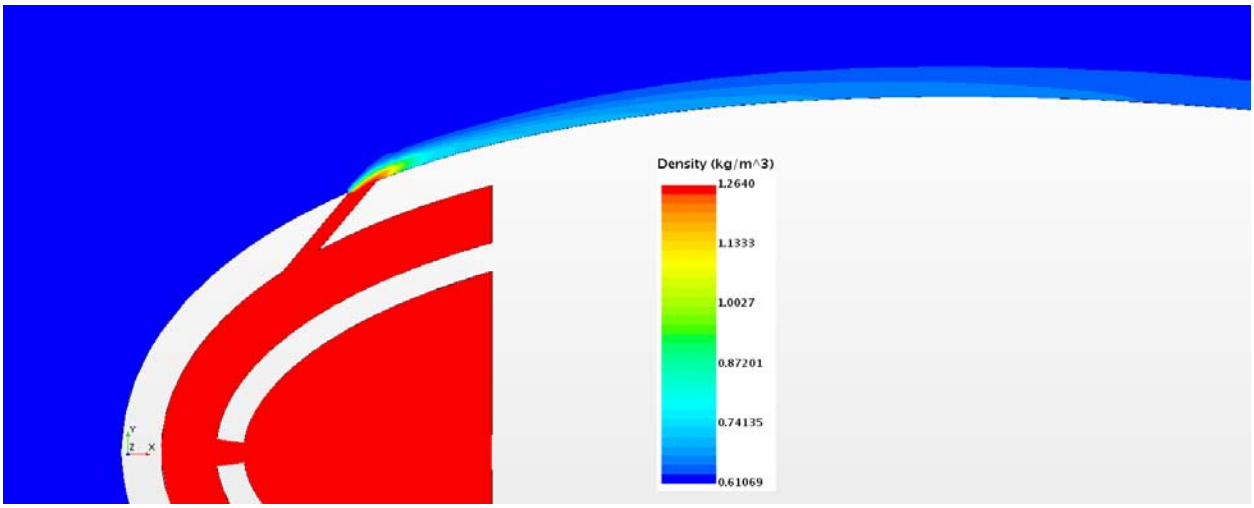

Figure 16.251: Case 23 – Density profile for off-center plane

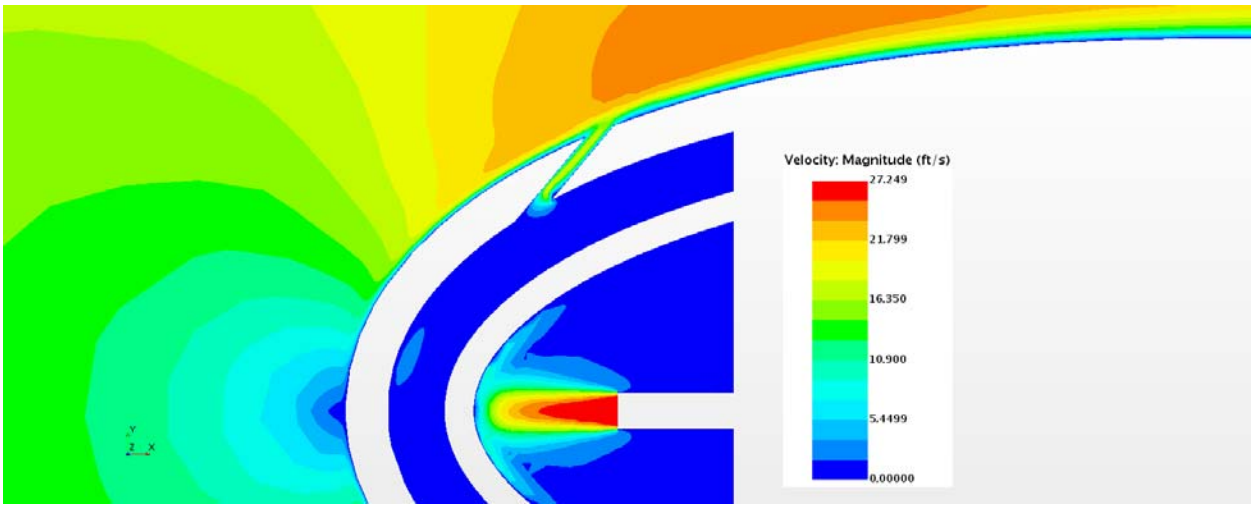

Figure 16.252: Case 23 – Velocity profile for center plane

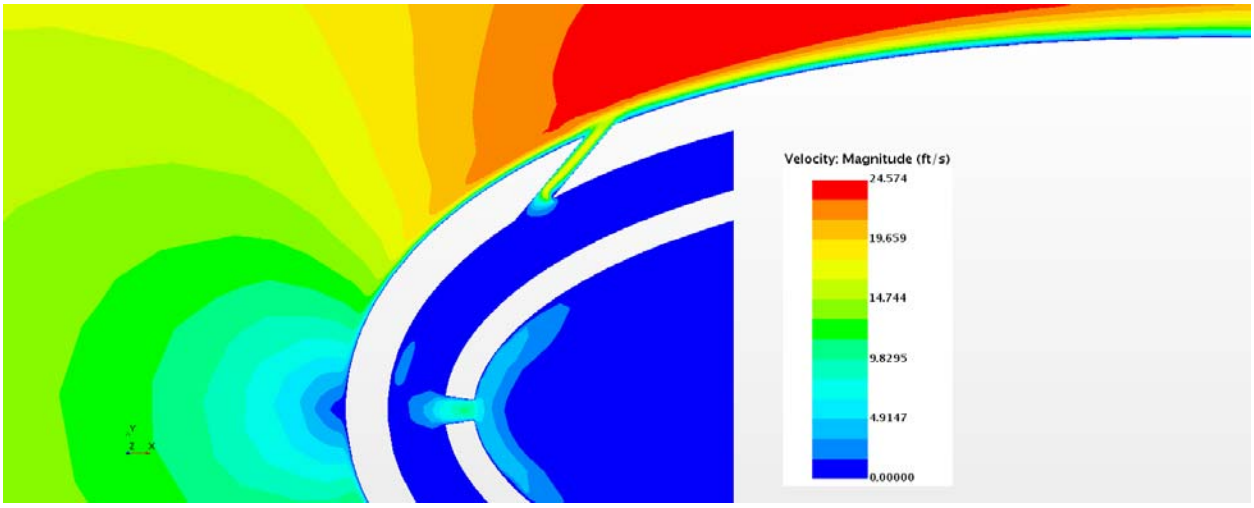

Figure 16.253: Case 23 – Velocity profile for off- center plane

Appendix G-24: M_b = 1.26, Tu = 15%, DR = 1.99

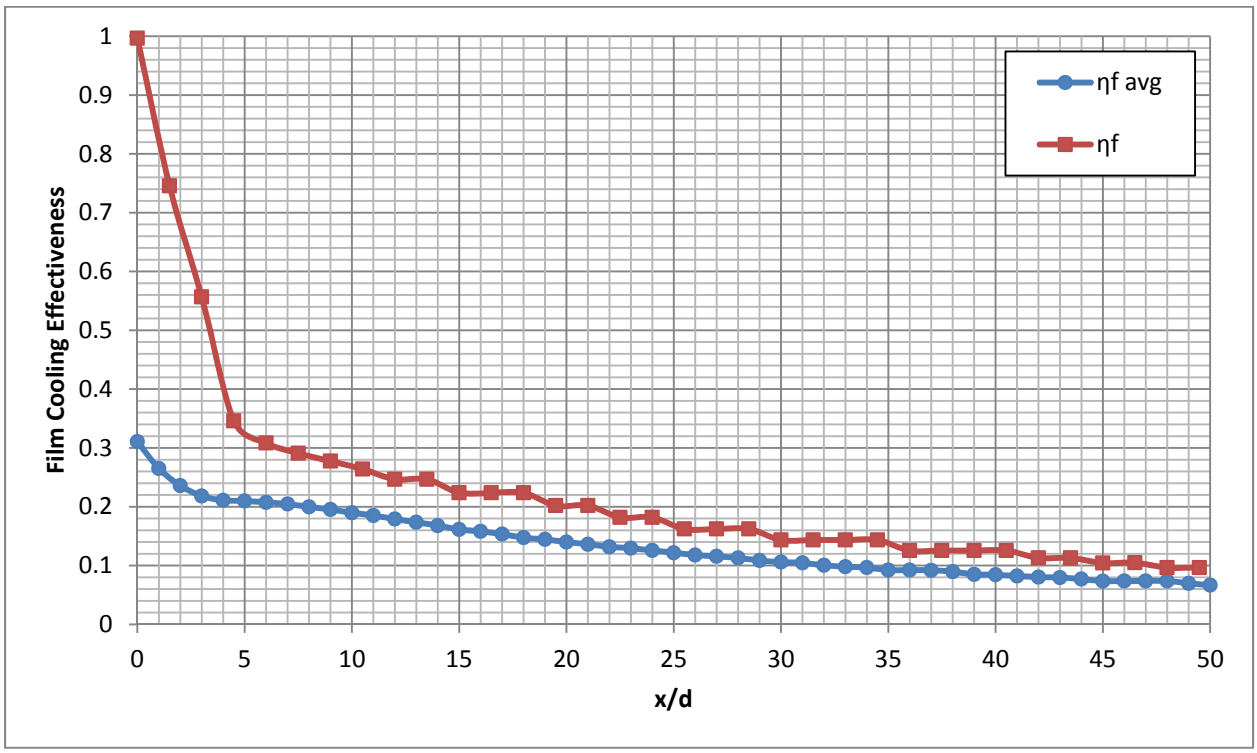

Figure 16.254: Case 24 - Laterally averaged and Centerline adiabatic film cooling effectiveness

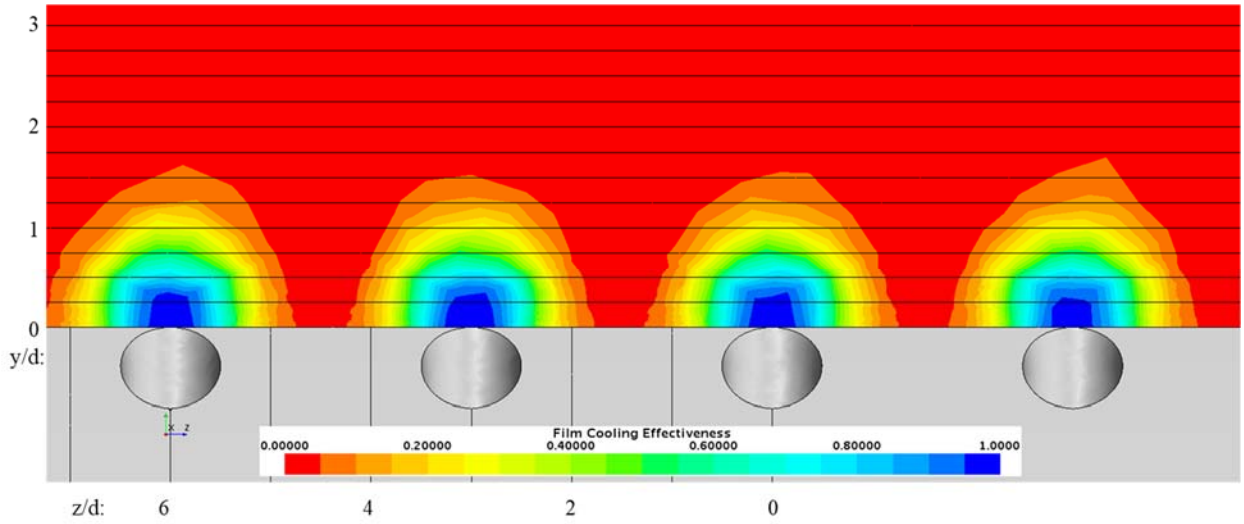

Figure 16.255: Case 24 - Spatial distribution of adiabatic film cooling effectiveness at x/d: 0

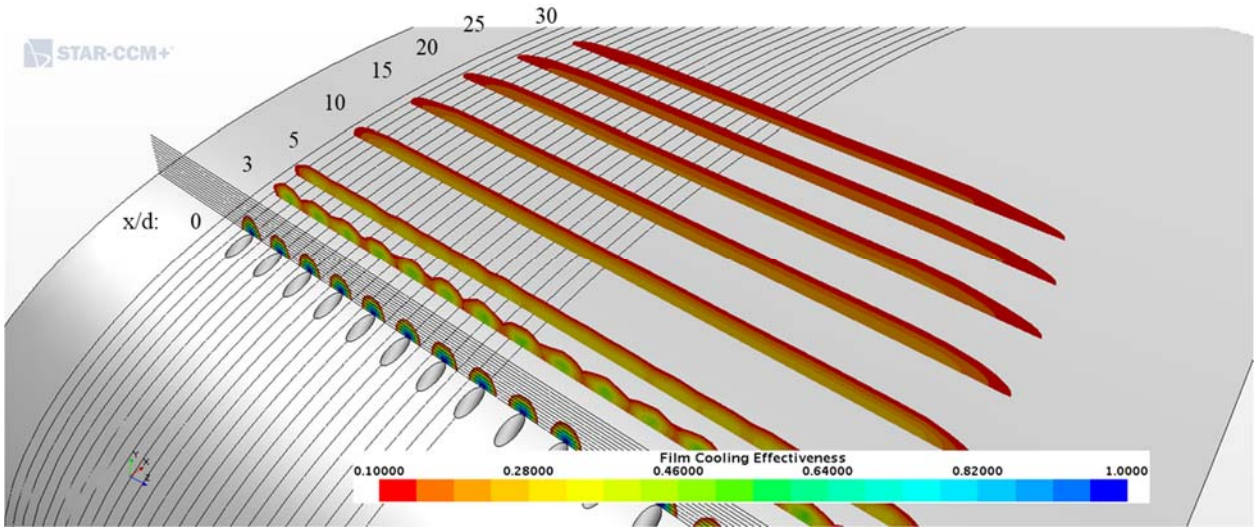

Figure 16.256: Case 24 - Streamwise spatial distribution of adiabatic film cooling effectiveness

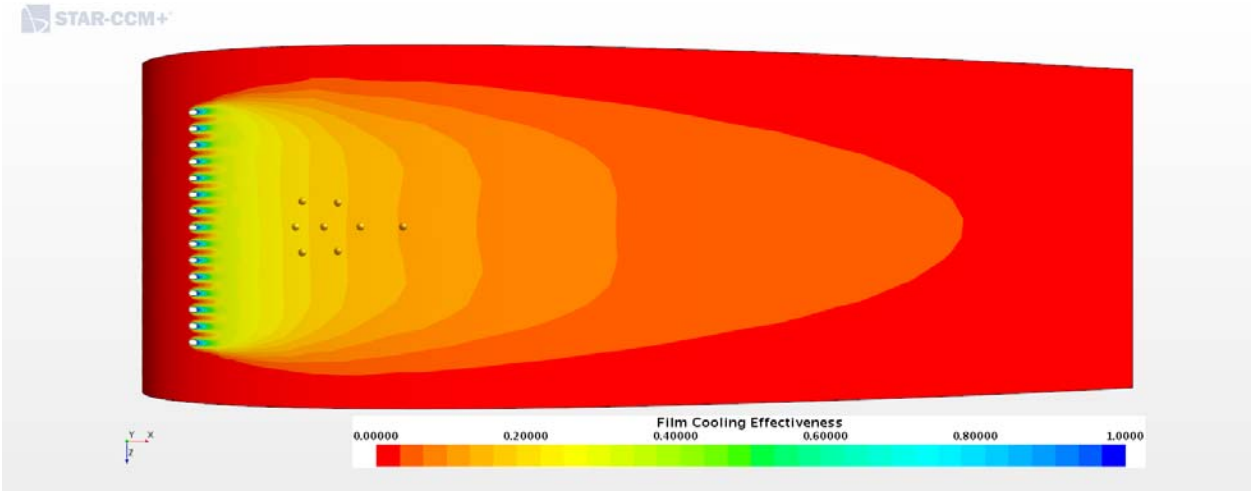

Figure 16.257: Case 24 - Adiabatic Film Cooling Effectiveness on the Suction Surface

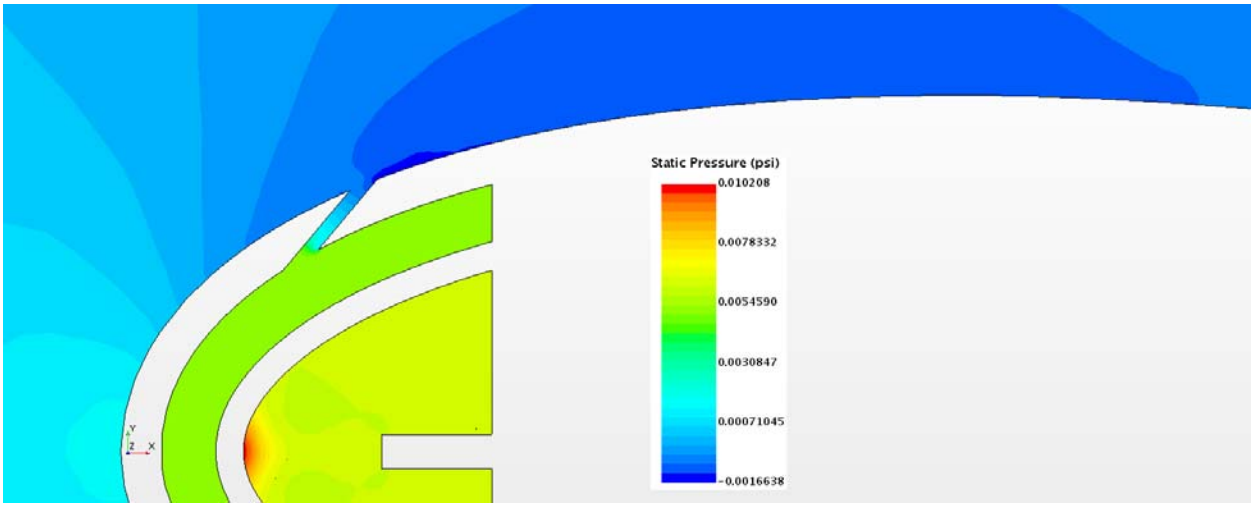

Figure 16.258: Case 24 – Static Pressure profile for center plane

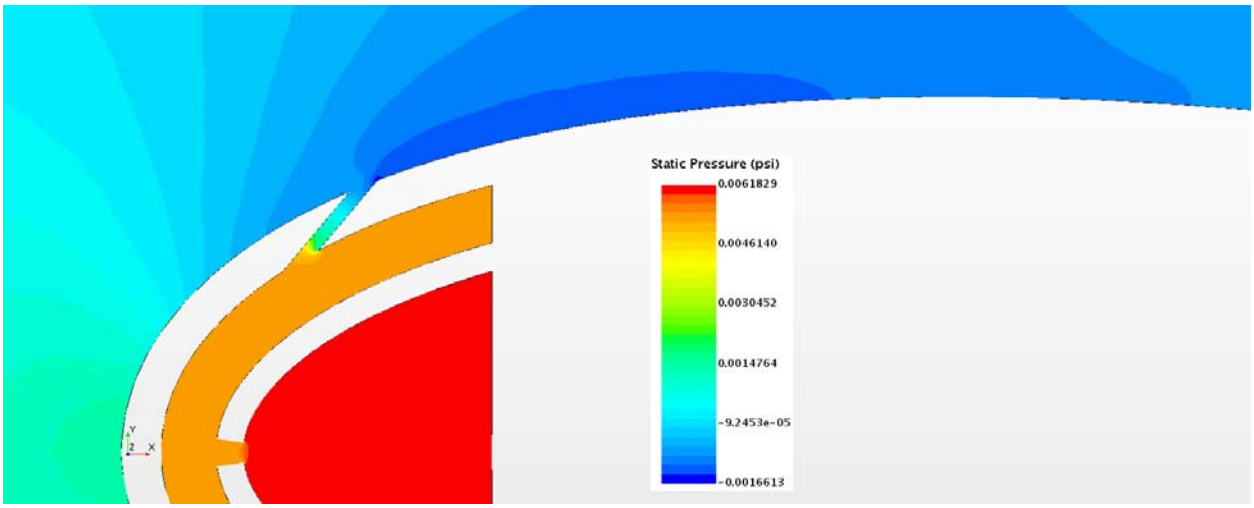

Figure 16.259: Case 24 – Static Pressure profile for off-center plane

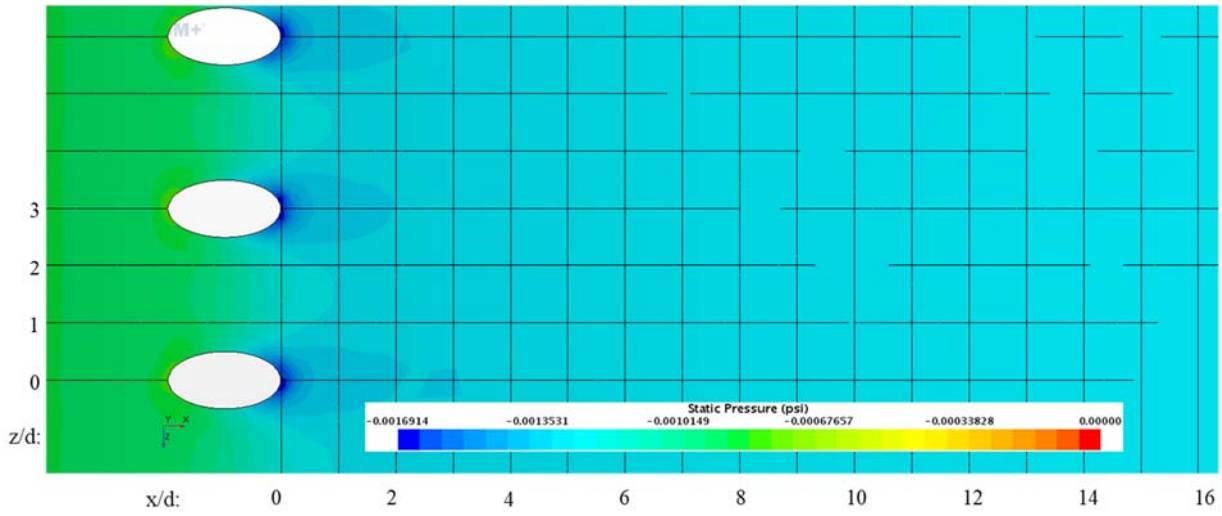

Figure 16.260: Case 24 – Static Pressure distribution for Suction Surface

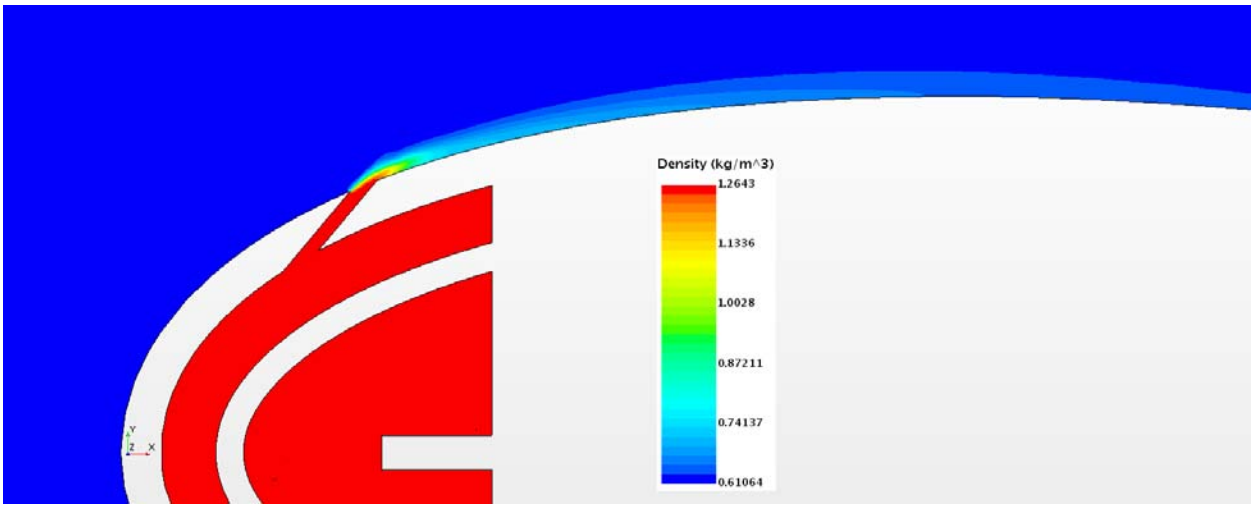

Figure 16.261: Case 24 – Density profile for center plane

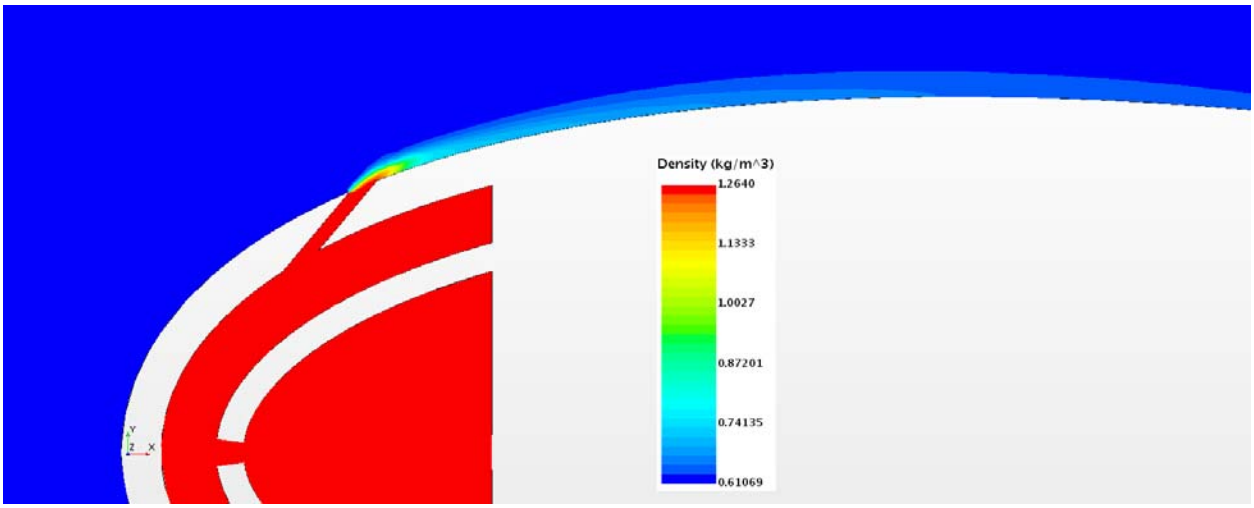

Figure 16.262: Case 24 – Density profile for off-center plane

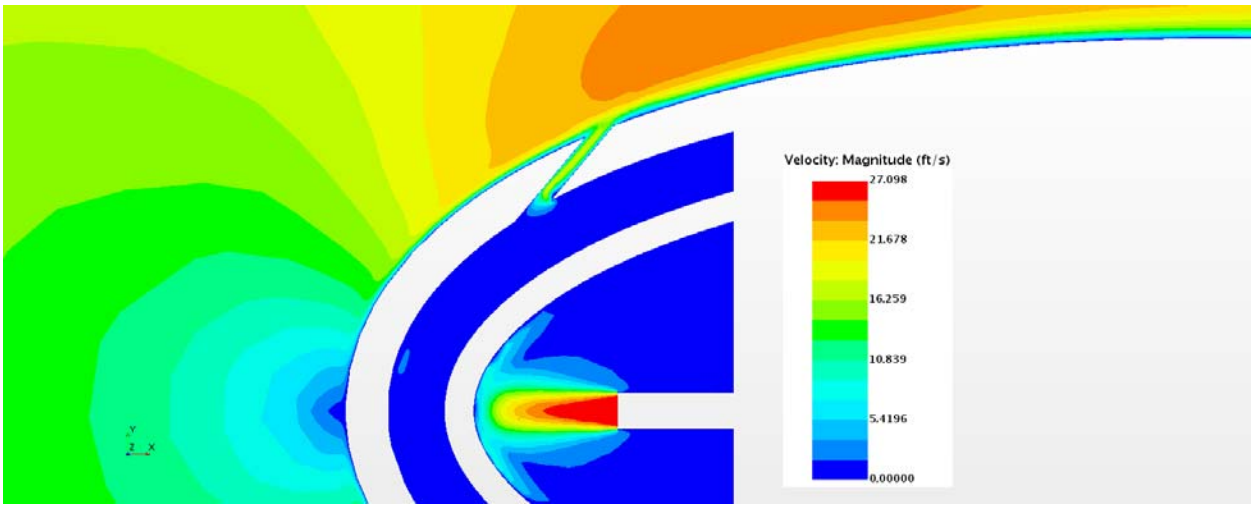

Figure 16.263: Case 24 – Velocity profile for center plane

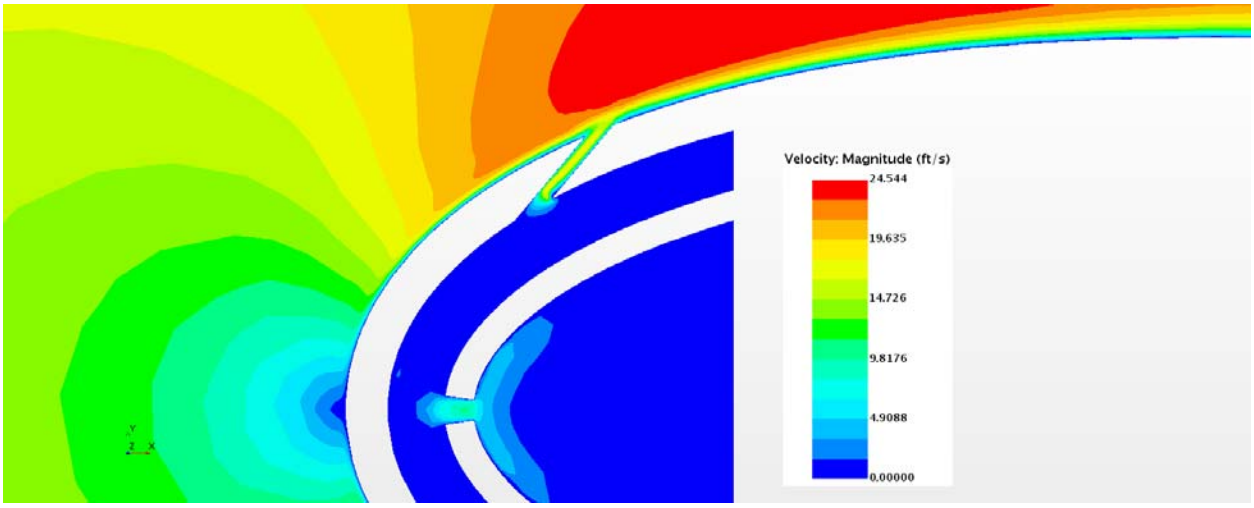

Figure 16.264: Case 24 – Velocity profile for off- center plane

Appendix G-25: M_b = 1.26, Tu = 20%, DR = 1.99

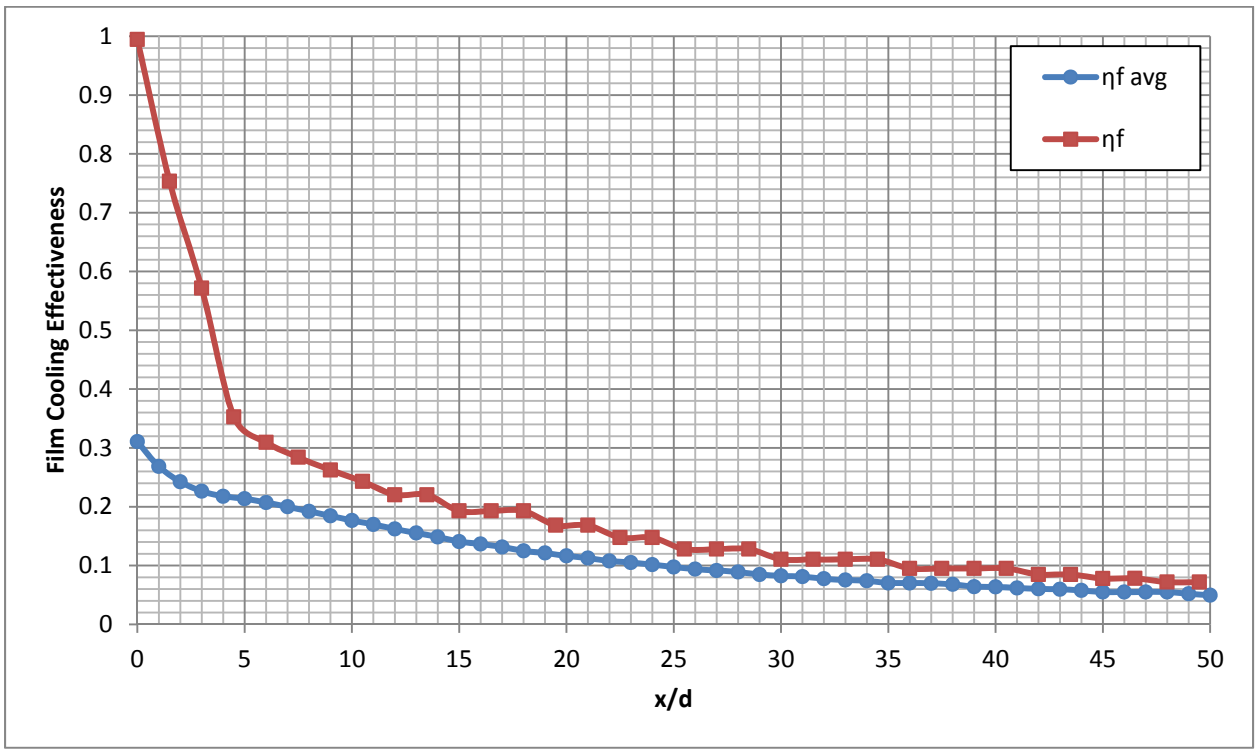

Figure 16.265: Case 25 - Laterally averaged and Centerline adiabatic film cooling effectiveness

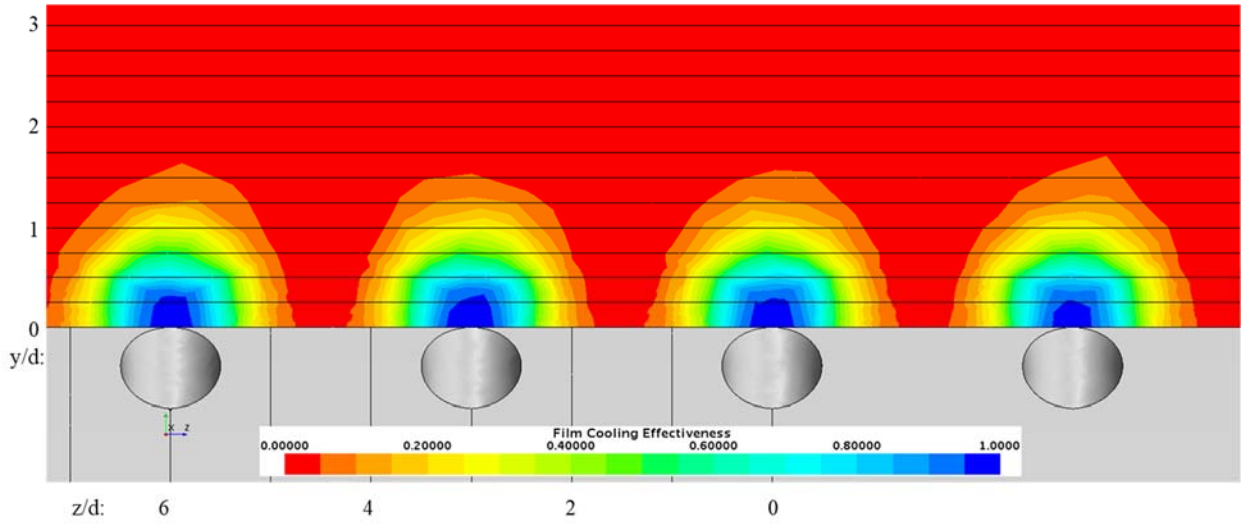

Figure 16.266: Case 25 - Spatial distribution of adiabatic film cooling effectiveness at x/d: 0

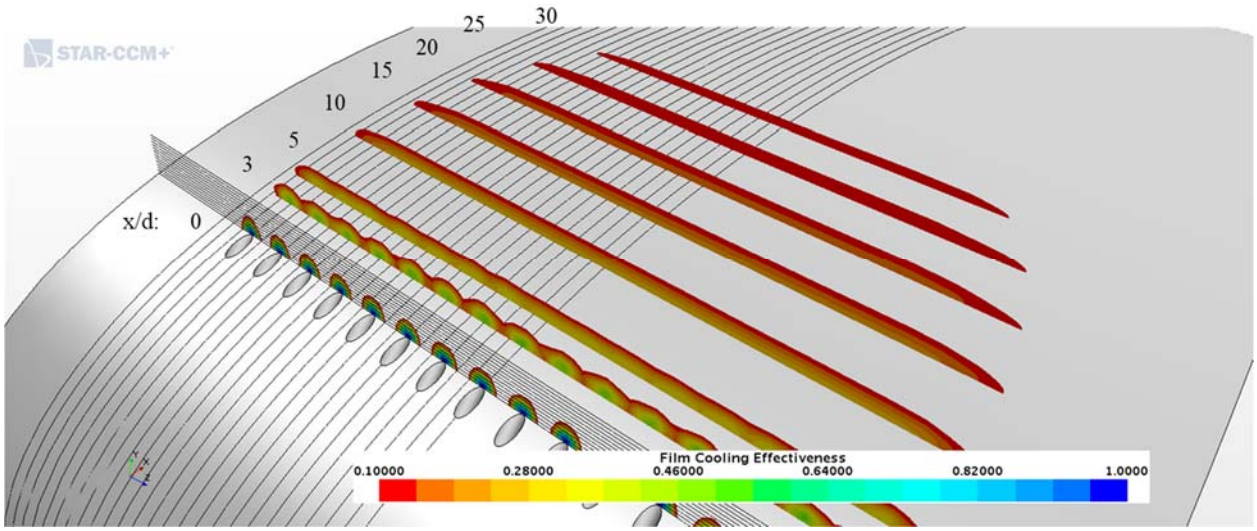

Figure 16.267: Case 25 - Streamwise spatial distribution of adiabatic film cooling effectiveness

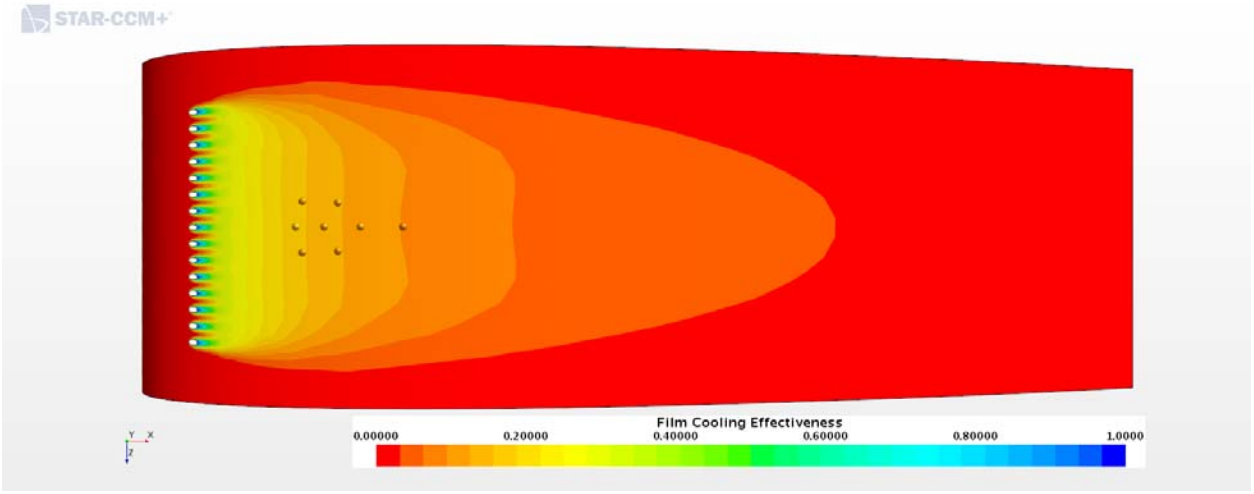

Figure 16.268: Case 25 - Adiabatic Film Cooling Effectiveness on the Suction Surface

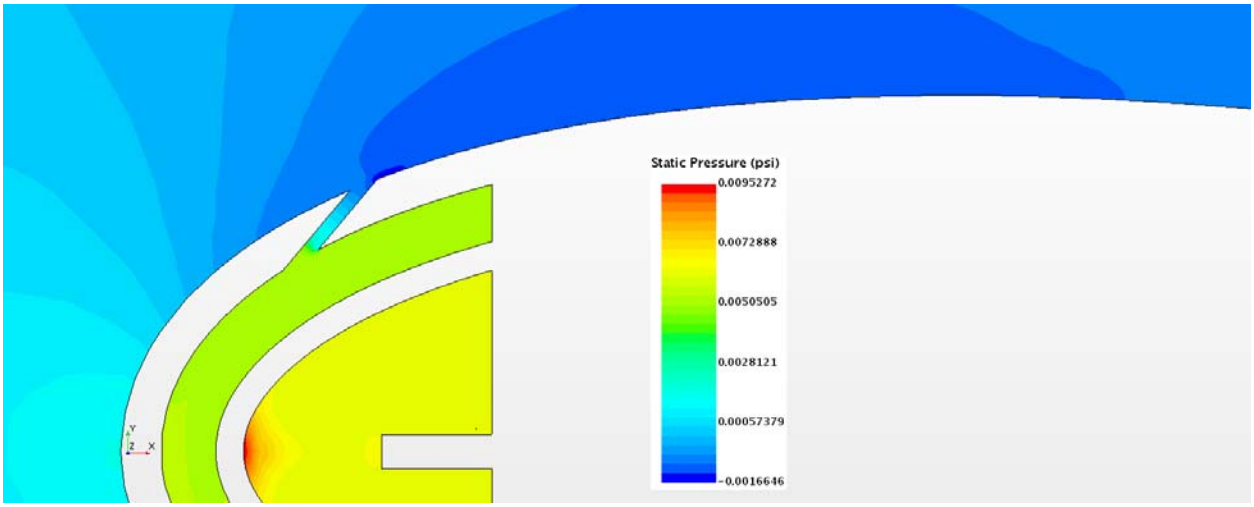

Figure 16.269: Case 25 – Static Pressure profile for center plane

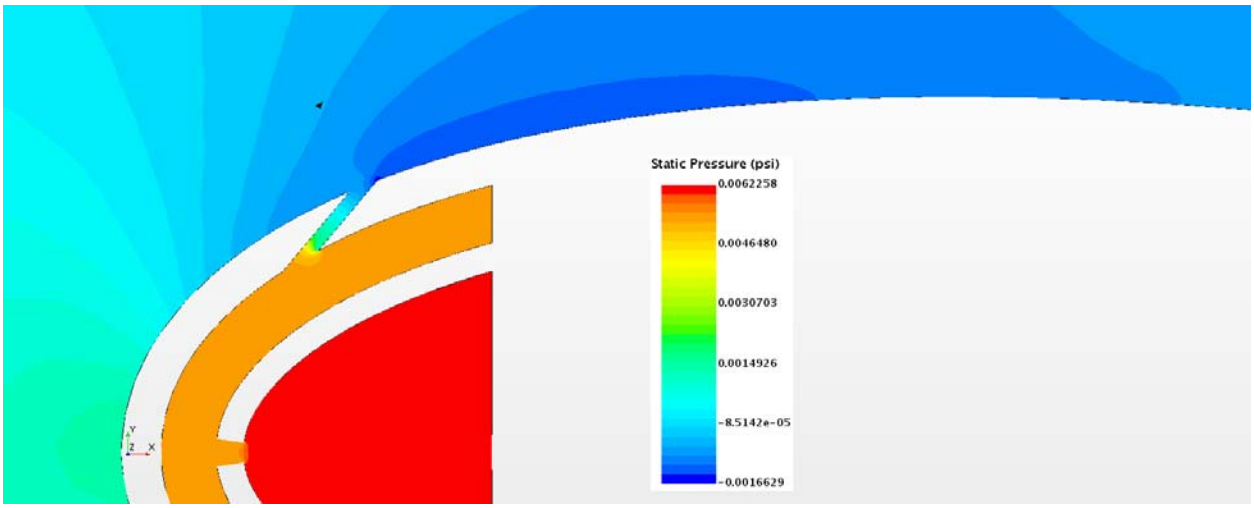

Figure 16.270: Case 25 – Static Pressure profile for off-center plane

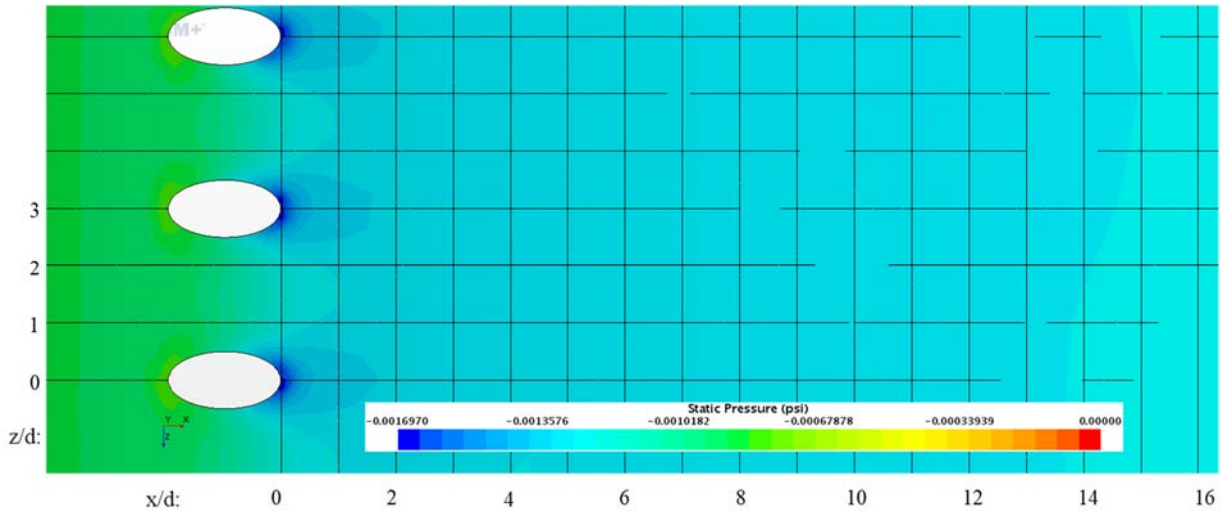

Figure 16.271: Case 25 – Static Pressure distribution for Suction Surface

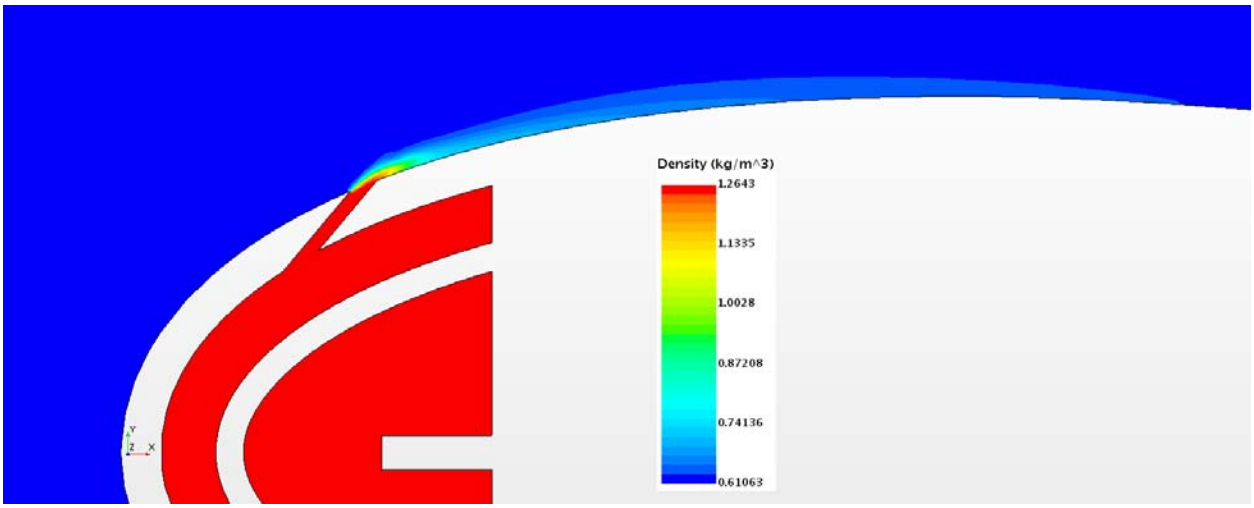

Figure 16.272: Case 25 – Density profile for center plane

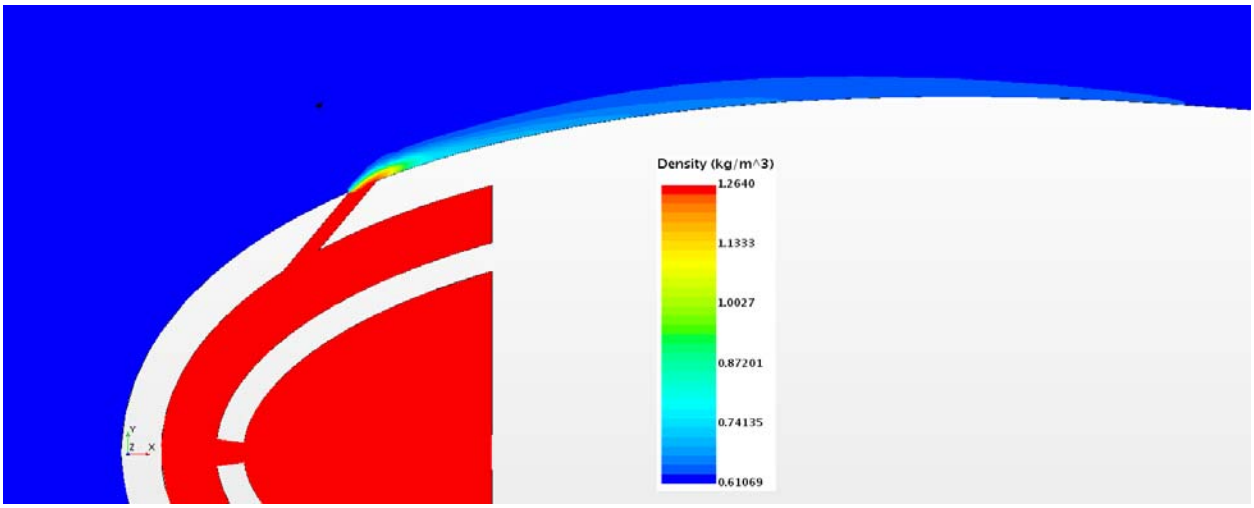

Figure 16.273: Case 25 – Density profile for off-center plane

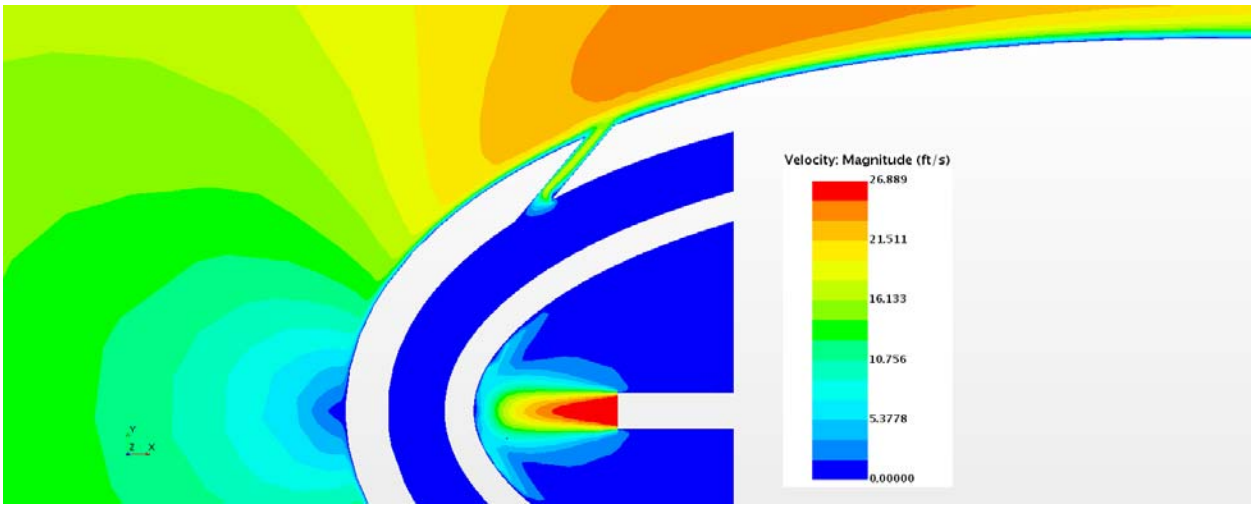

Figure 16.274: Case 25 – Velocity profile for center plane

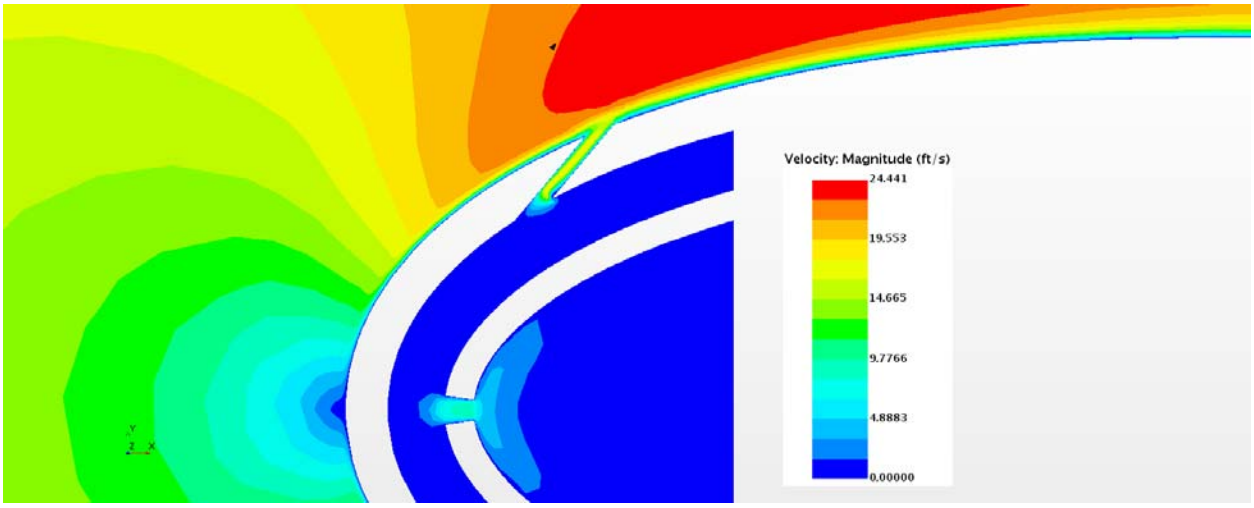

Figure 16.275: Case 25 – Velocity profile for off- center plane

Appendix G-26: M_b = 1.26, Tu = 25%, DR = 1.99

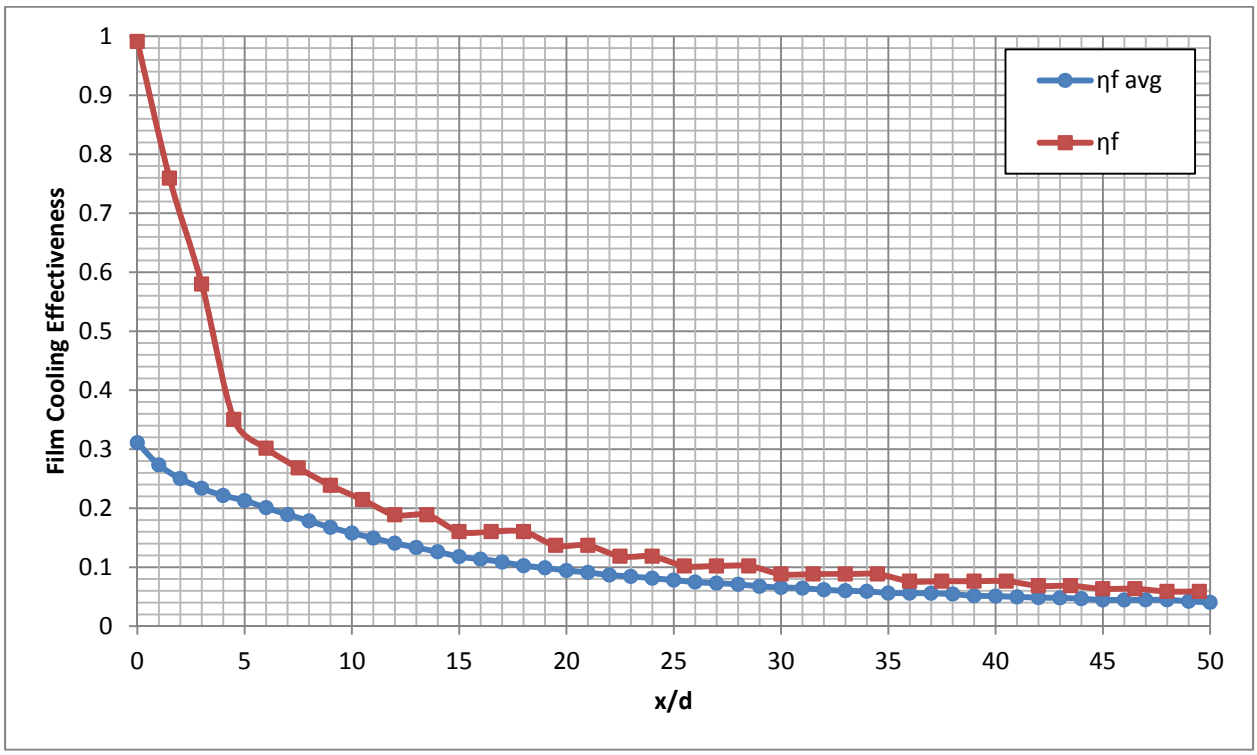

Figure 16.276: Case 26 - Laterally averaged and Centerline adiabatic film cooling effectiveness

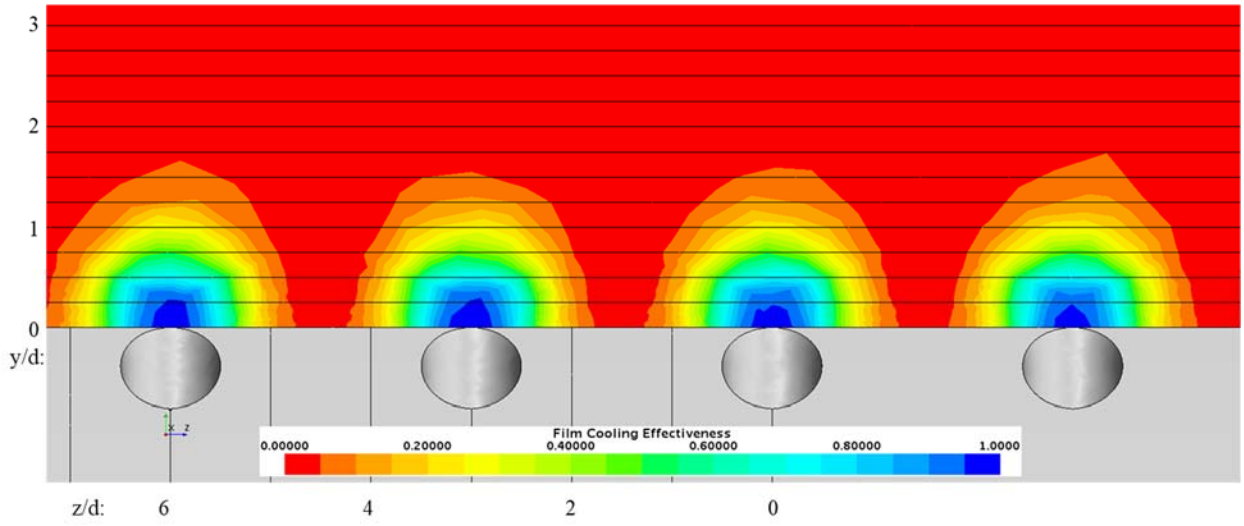

Figure 16.277: Case 26 - Spatial distribution of adiabatic film cooling effectiveness at x/d: 0

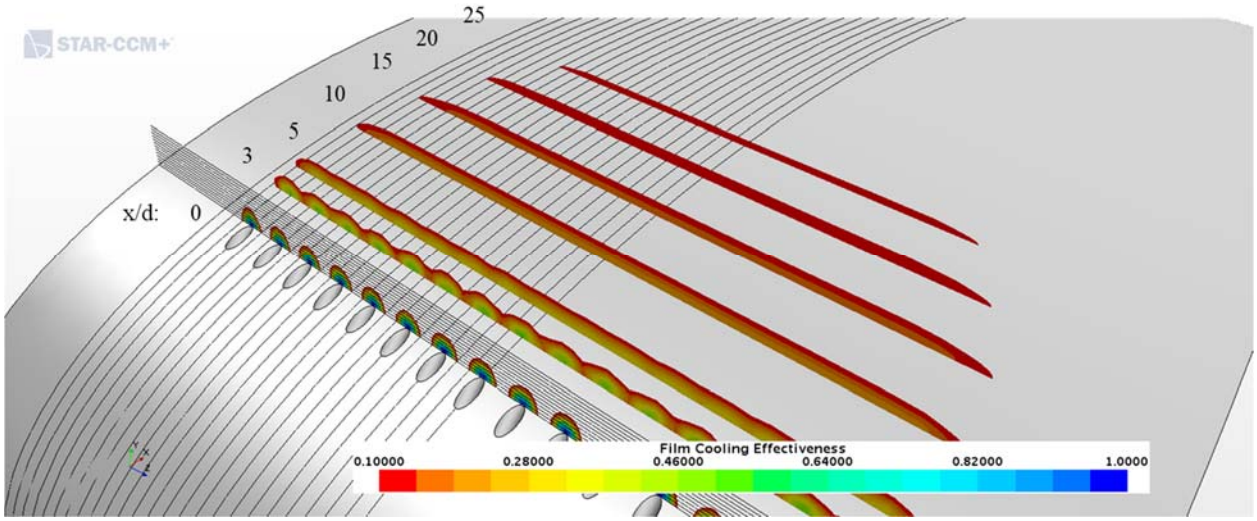

Figure 16.278: Case 26 - Streamwise spatial distribution of adiabatic film cooling effectiveness

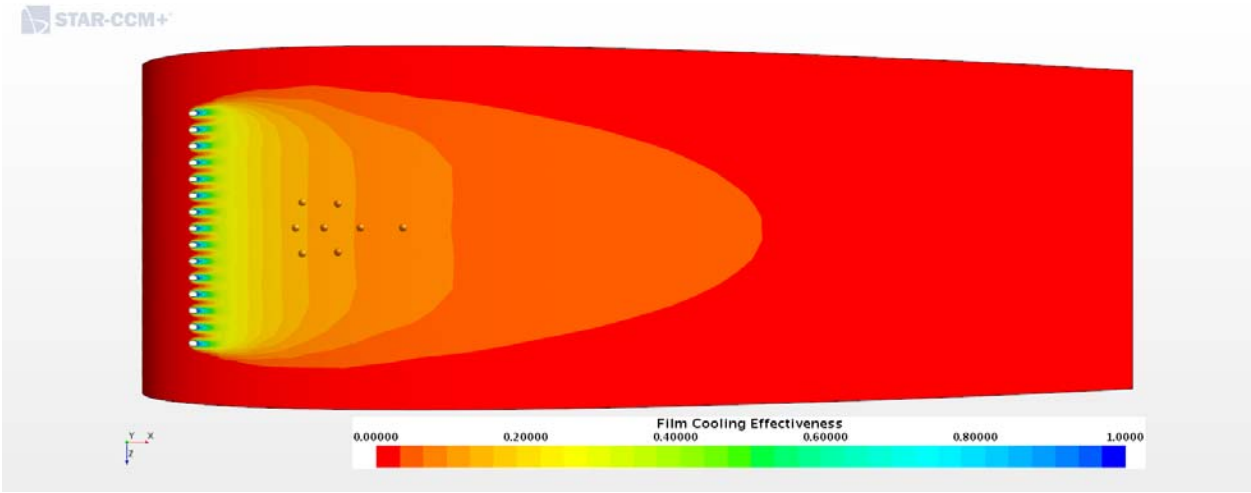

Figure 16.279: Case 26 - Adiabatic Film Cooling Effectiveness on the Suction Surface

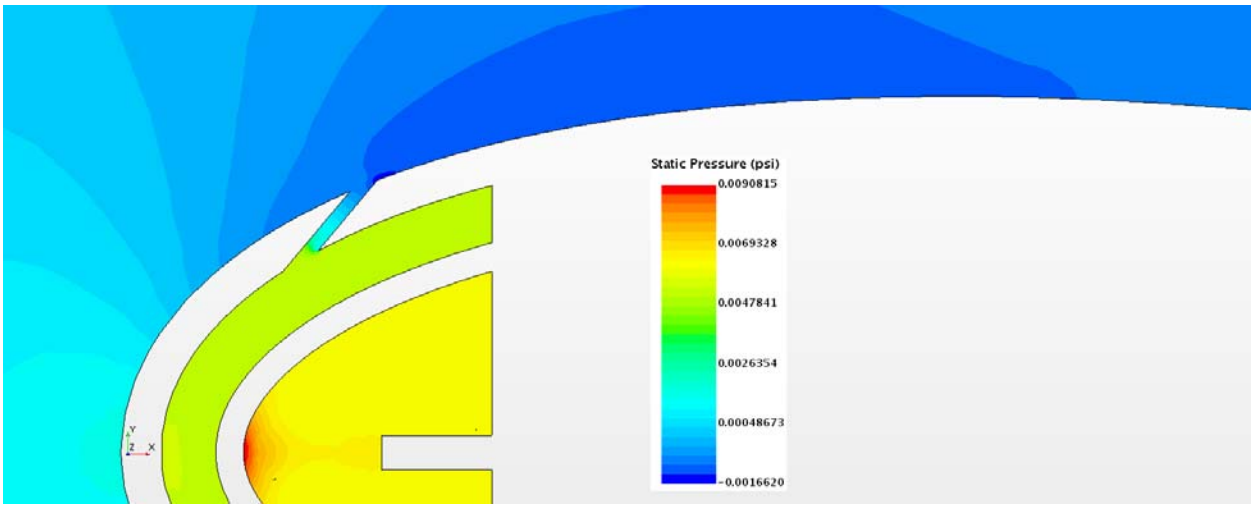

Figure 16.280: Case 26 – Static Pressure profile for center plane

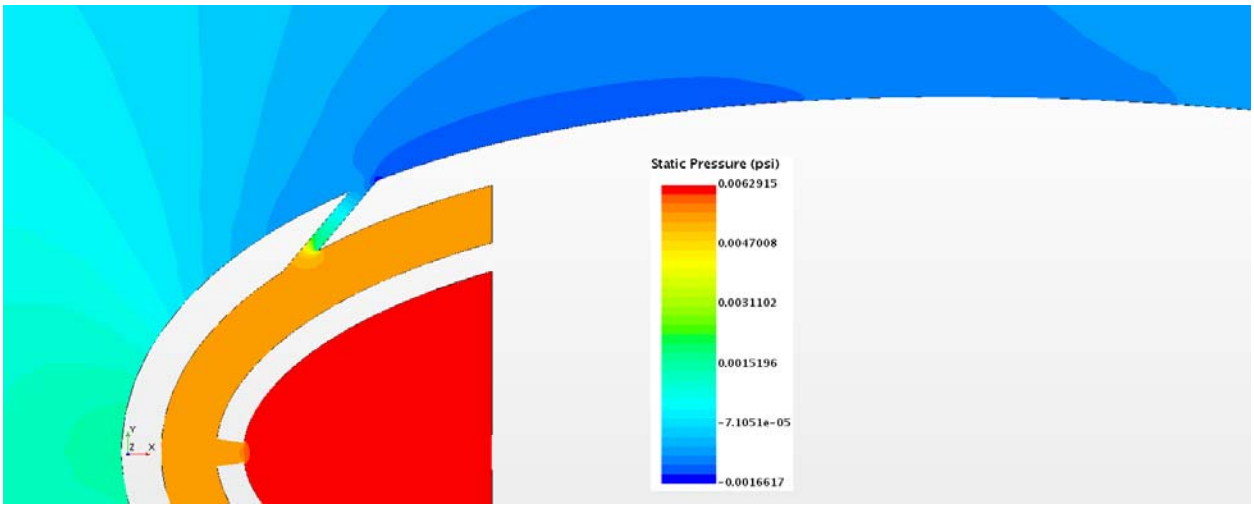

Figure 16.281: Case 26 – Static Pressure profile for off-center plane

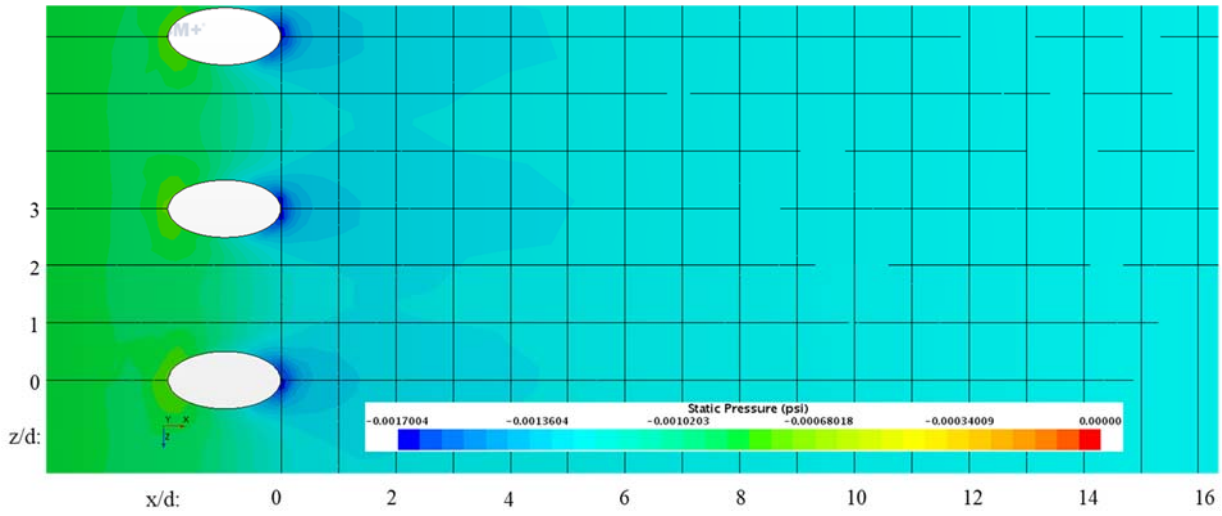

Figure 16.282: Case 26 – Static Pressure distribution for Suction Surface

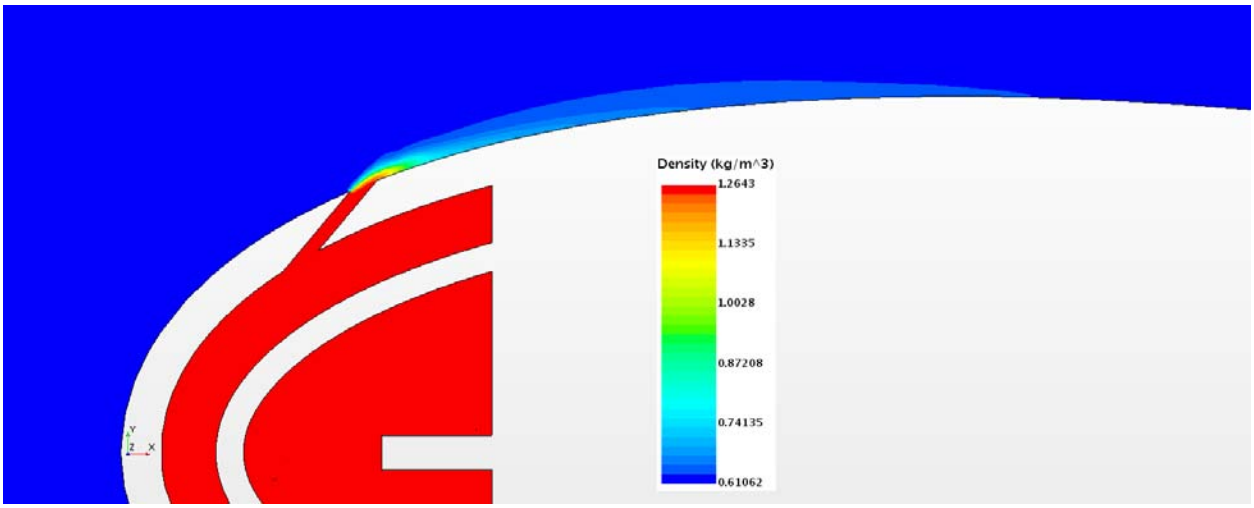

Figure 16.283: Case 26 – Density profile for center plane

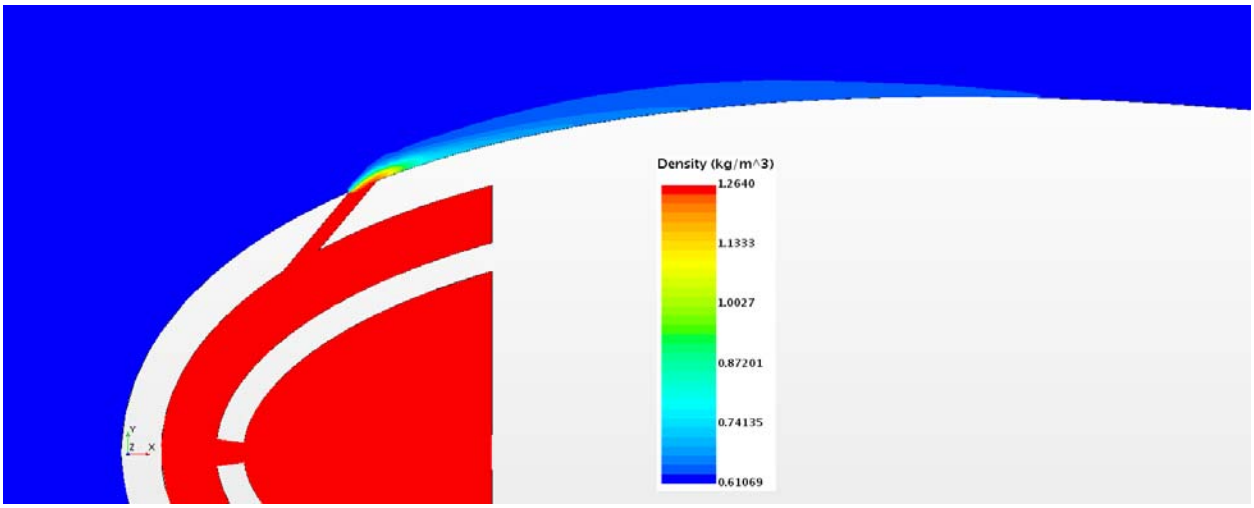

Figure 16.284: Case 26 – Density profile for off-center plane

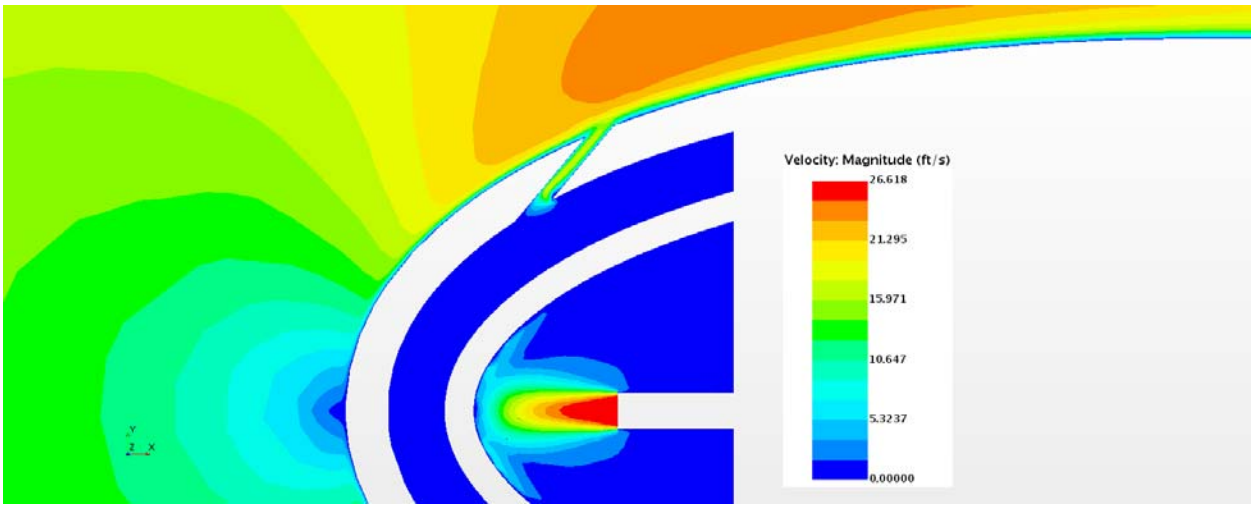

Figure 16.285: Case 26 – Velocity profile for center plane

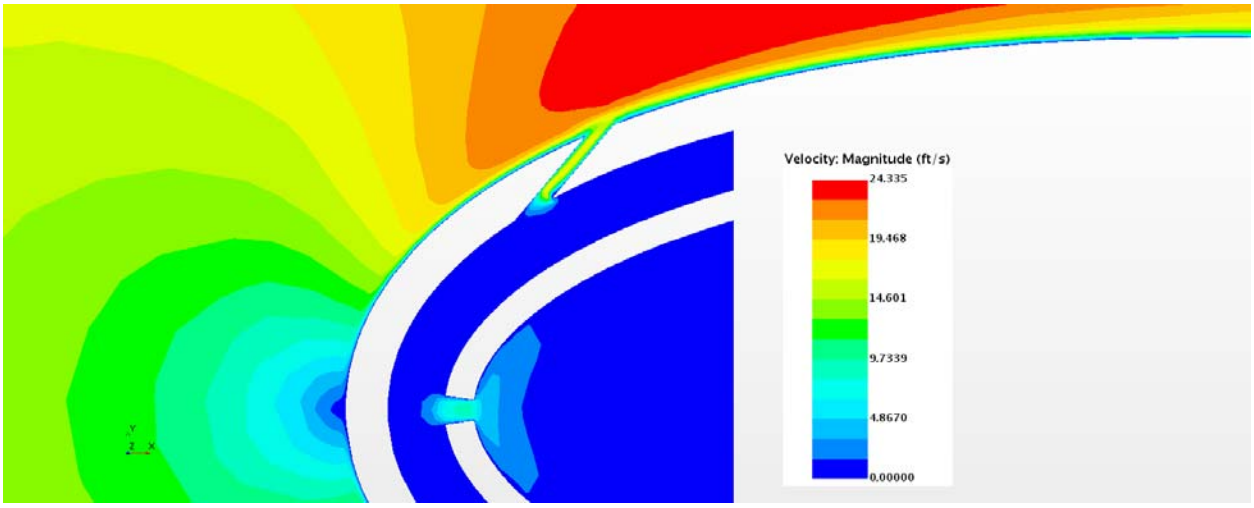

Figure 16.286: Case 26 – Velocity profile for off- center plane

Appendix G-27: M_b = 0.97, Tu = 20%, DR = 1.49

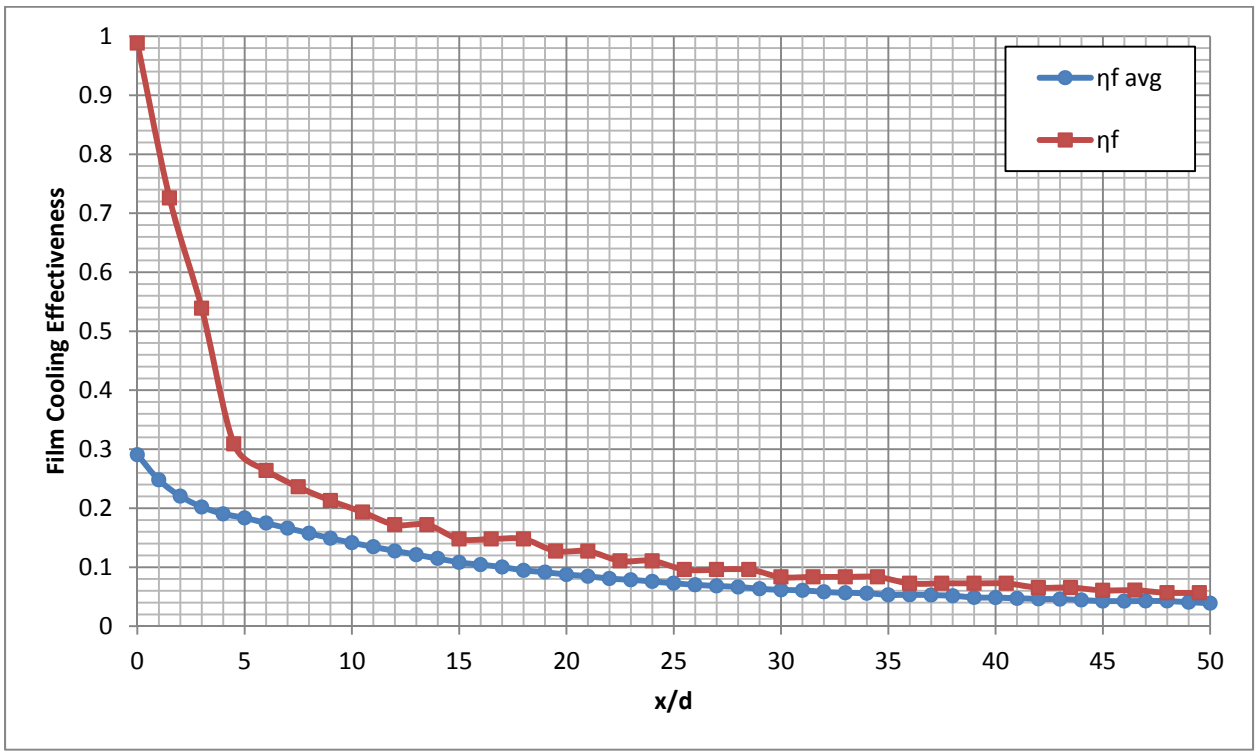

Figure 16.287: Case 27 - Laterally averaged and Centerline adiabatic film cooling effectiveness

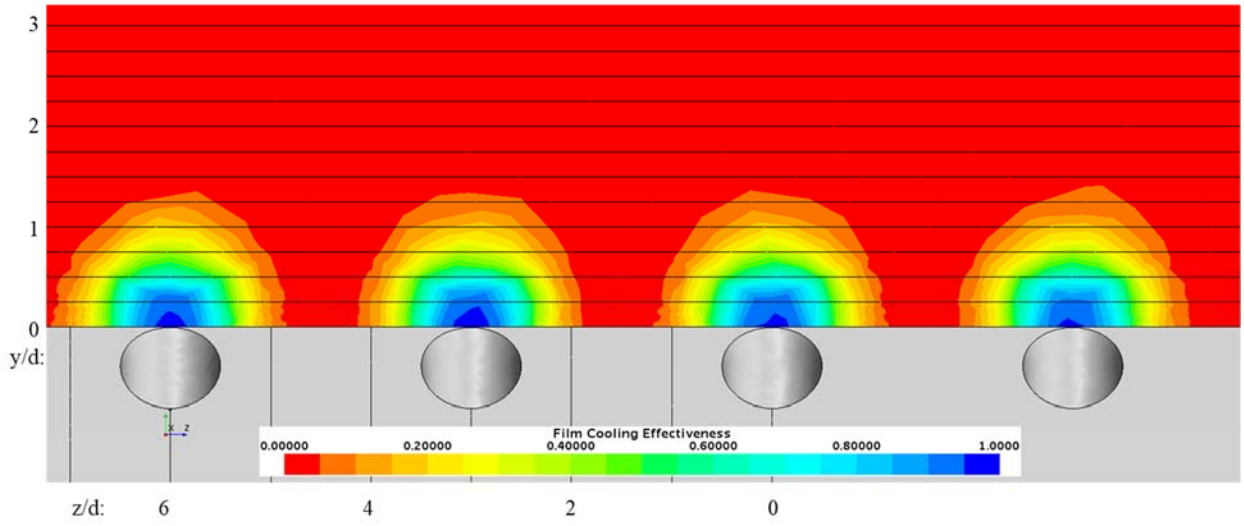

Figure 16.288: Case 27 - Spatial distribution of adiabatic film cooling effectiveness at x/d: 0

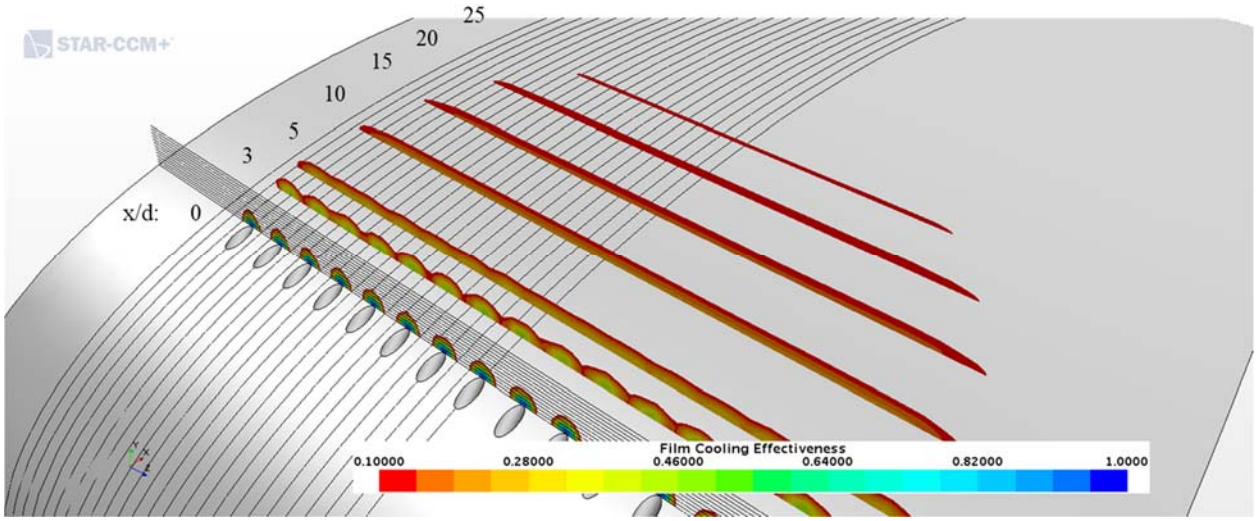

Figure 16.289: Case 27 - Streamwise spatial distribution of adiabatic film cooling effectiveness

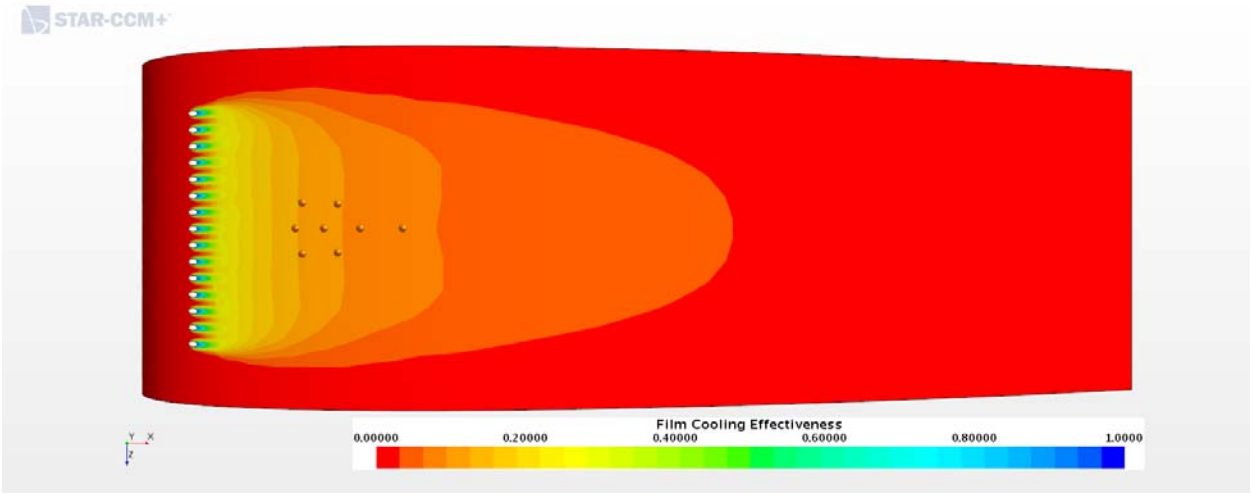

Figure 16.290: Case 27 - Adiabatic Film Cooling Effectiveness on the Suction Surface

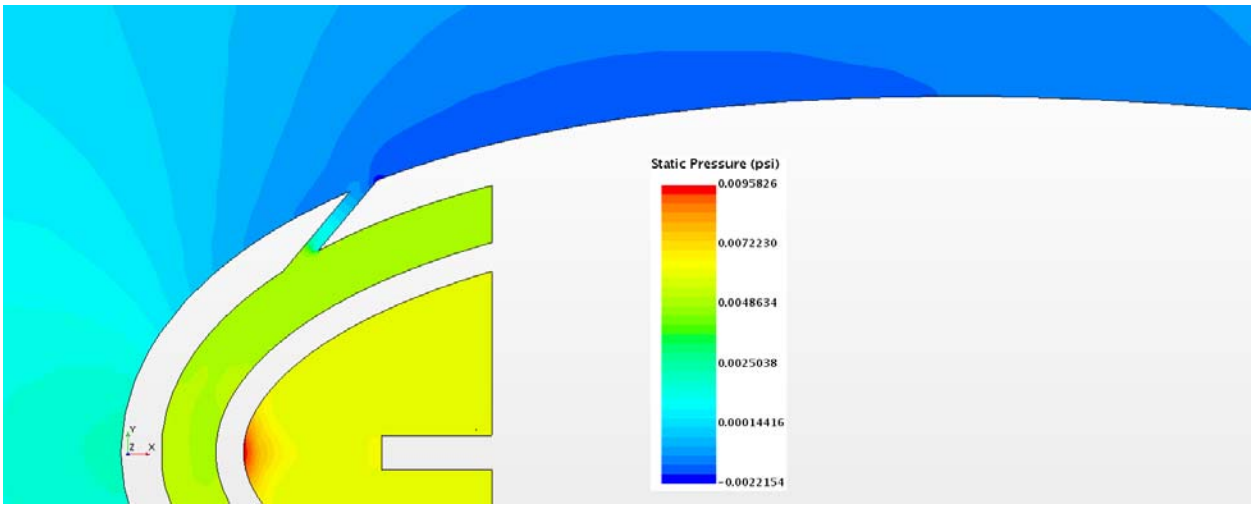

Figure 16.291: Case 27 – Static Pressure profile for center plane

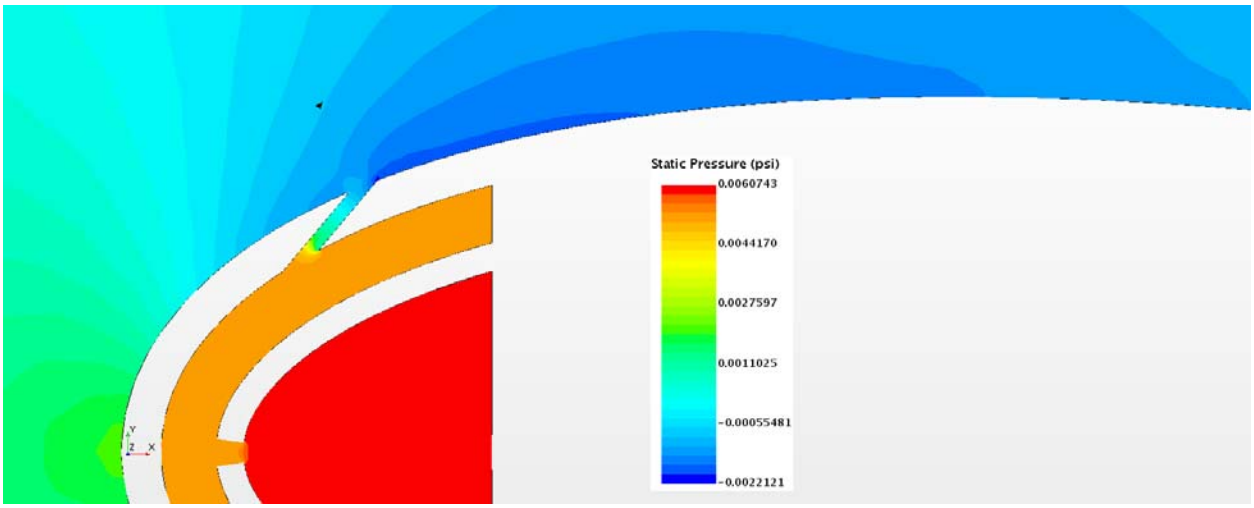

Figure 16.292: Case 27 – Static Pressure profile for off-center plane

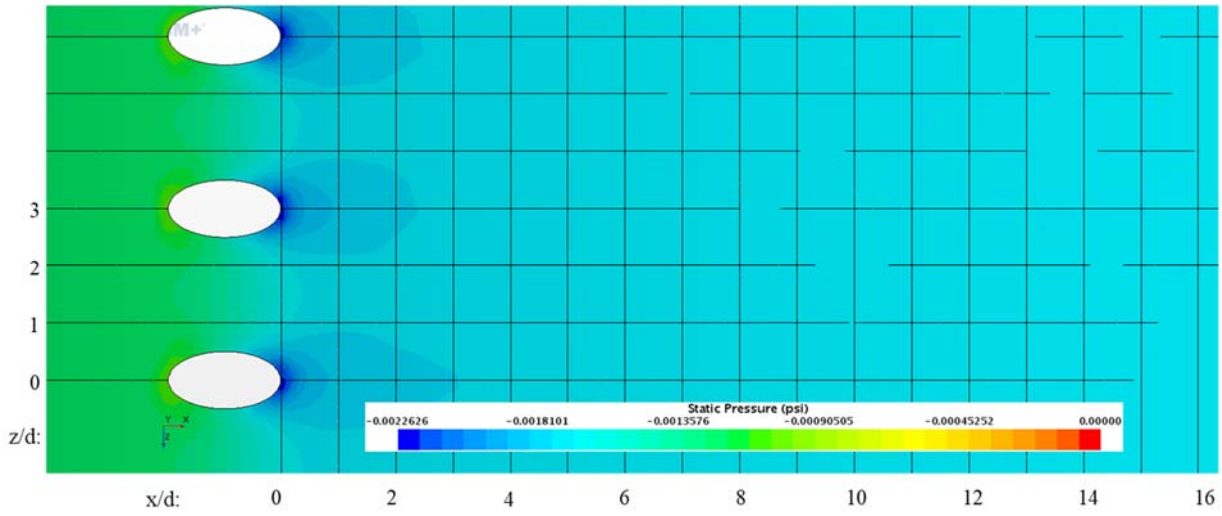

Figure 16.293: Case 27 – Static Pressure distribution for Suction Surface

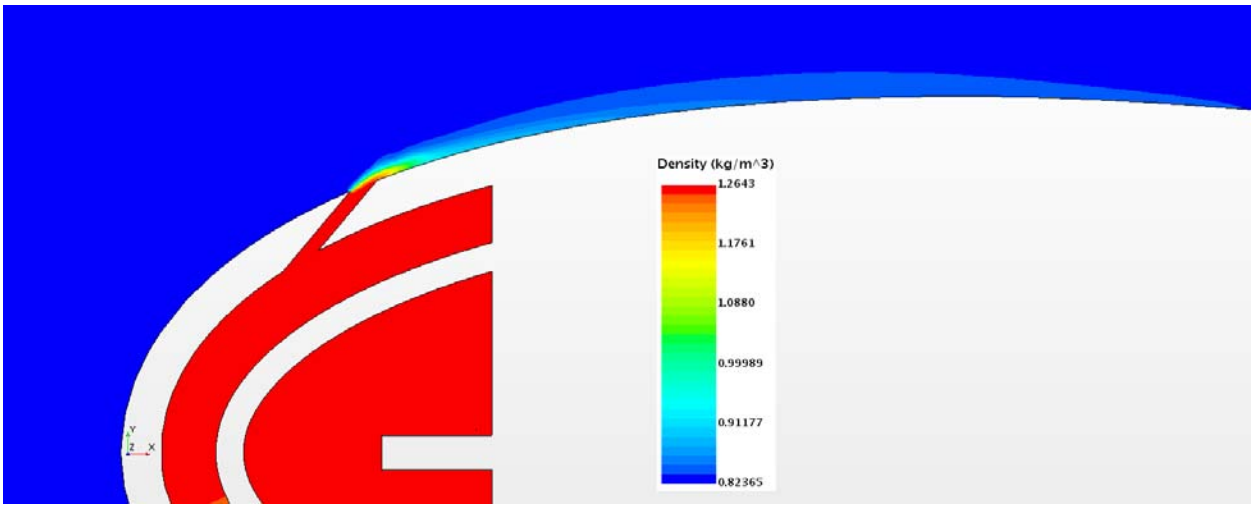

Figure 16.294: Case 27 – Density profile for center plane

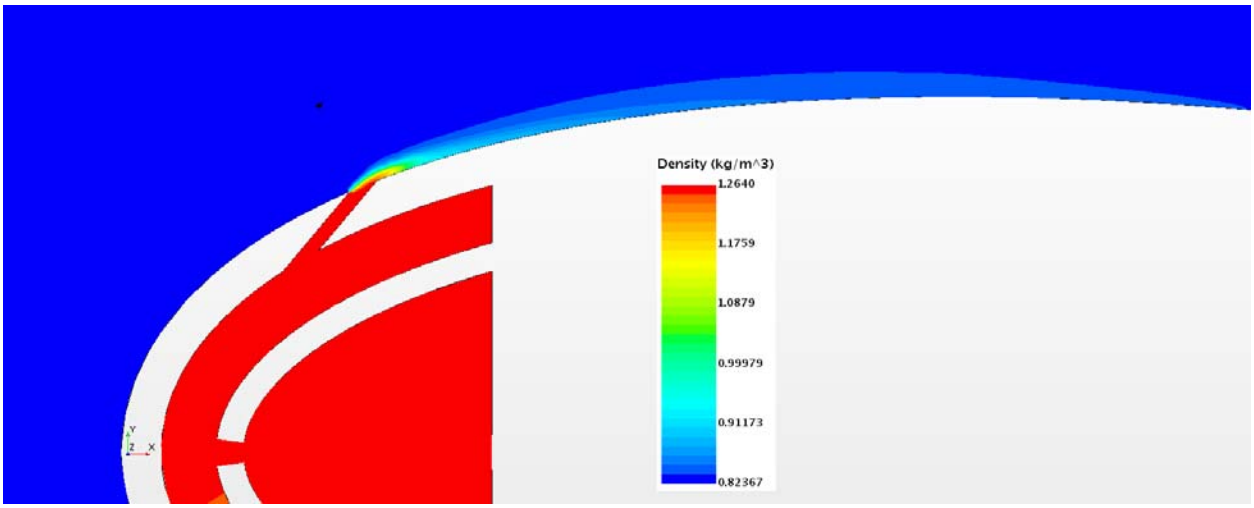

Figure 16.295: Case 27 – Density profile for off-center plane

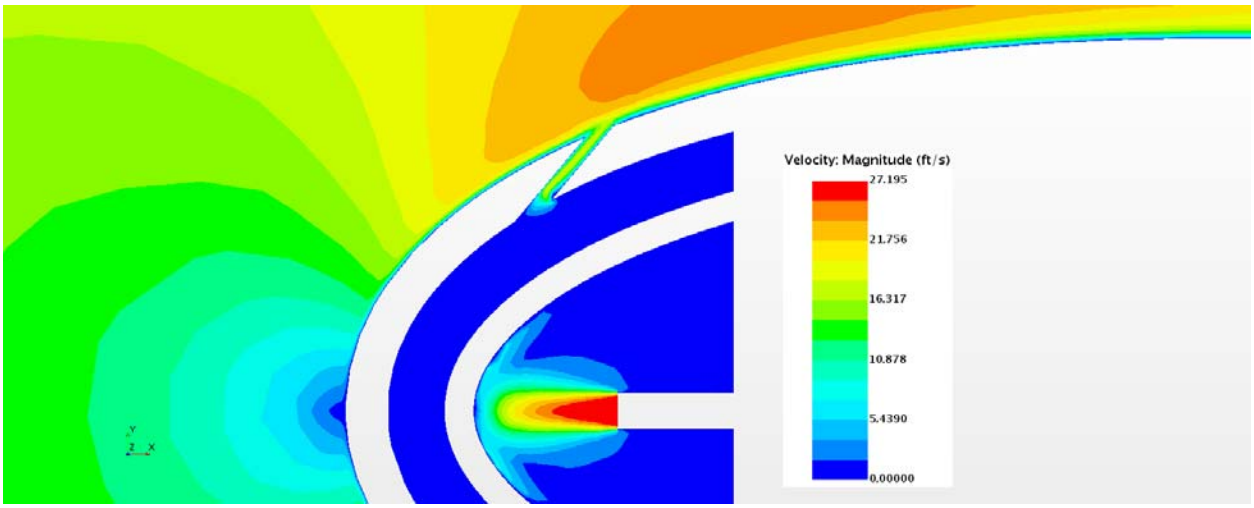

Figure 16.296: Case 27 – Velocity profile for center plane

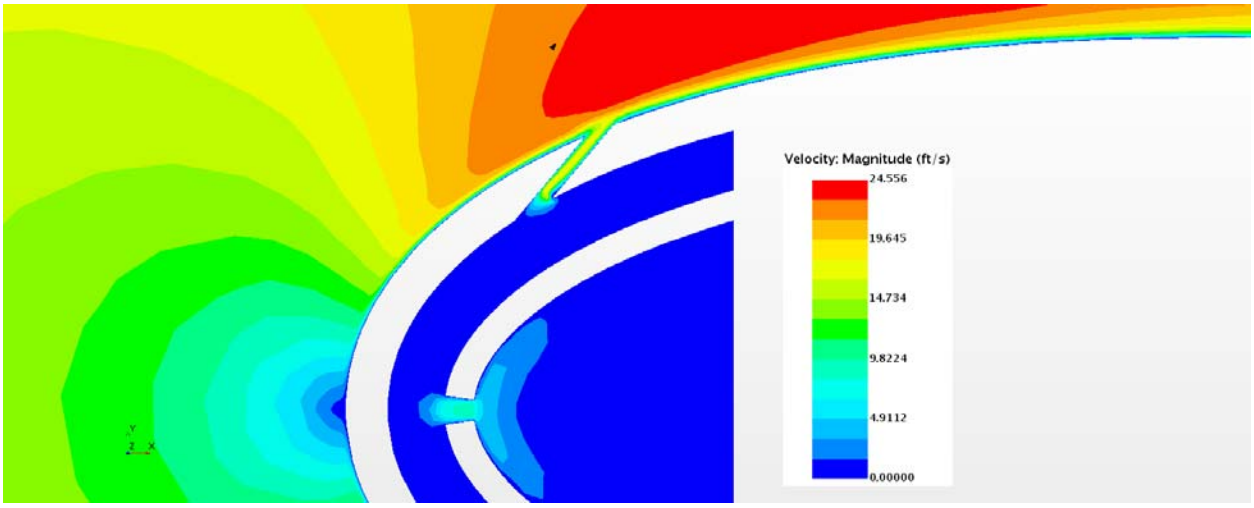

Figure 16.297: Case 27 – Velocity profile for off- center plane

Appendix G-28: M_b = 1.10, Tu = 20%, DR = 1.72

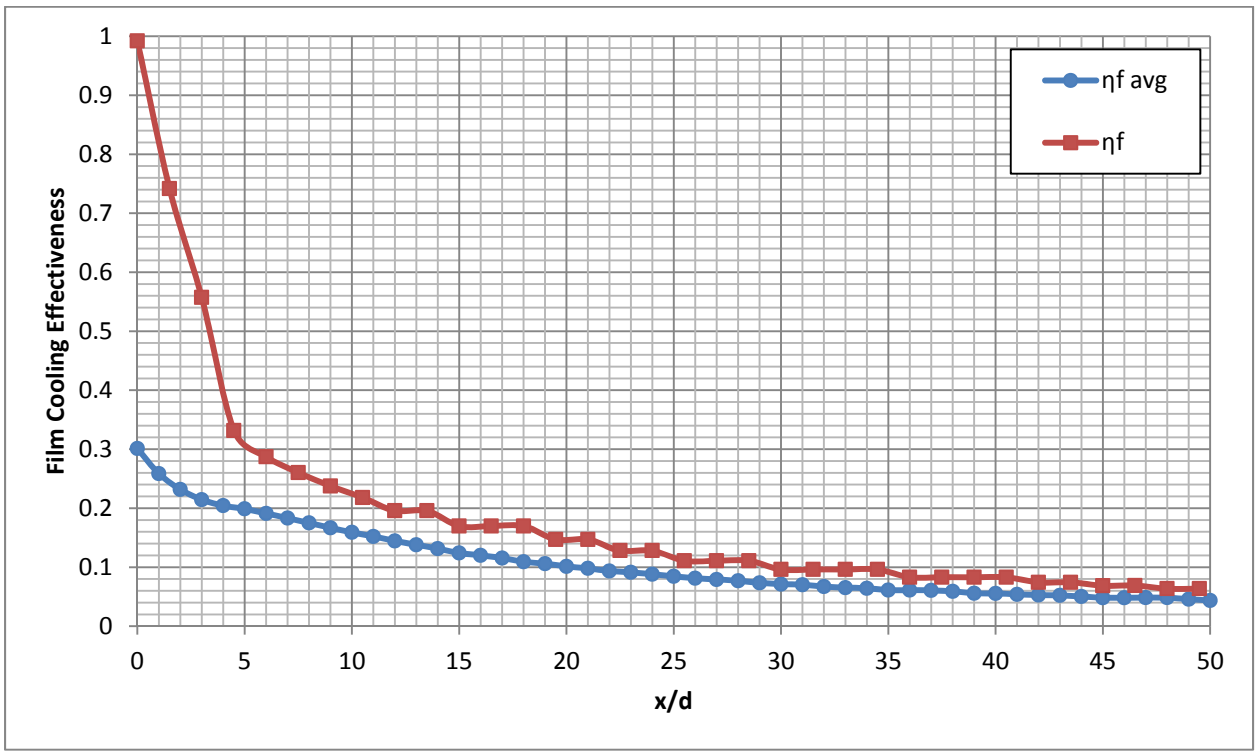

Figure 16.298: Case 28 - Laterally averaged and Centerline adiabatic film cooling effectiveness

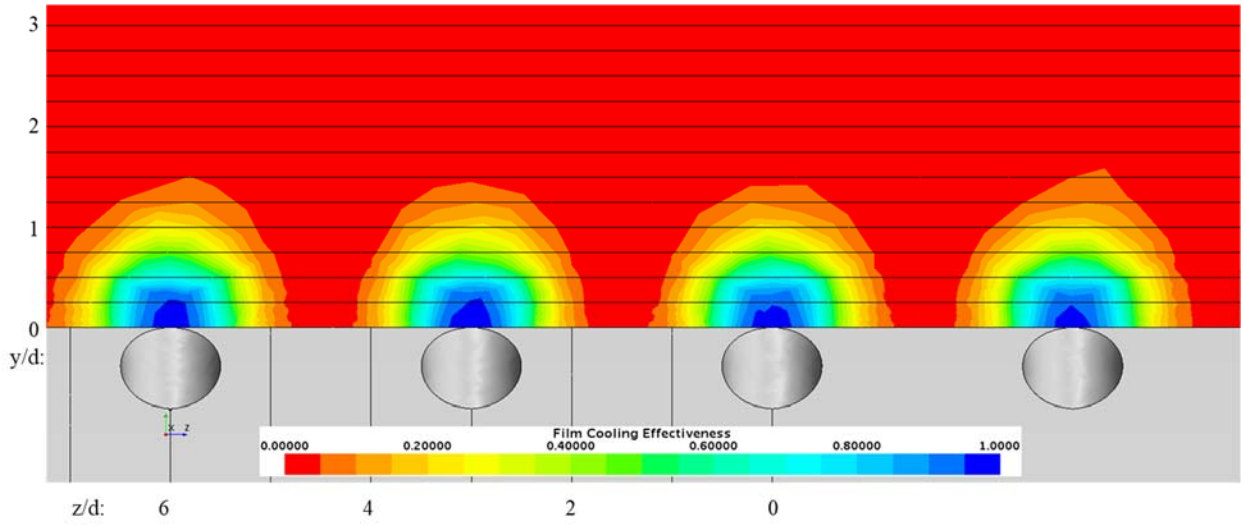

Figure 16.299: Case 28 - Spatial distribution of adiabatic film cooling effectiveness at x/d: 0

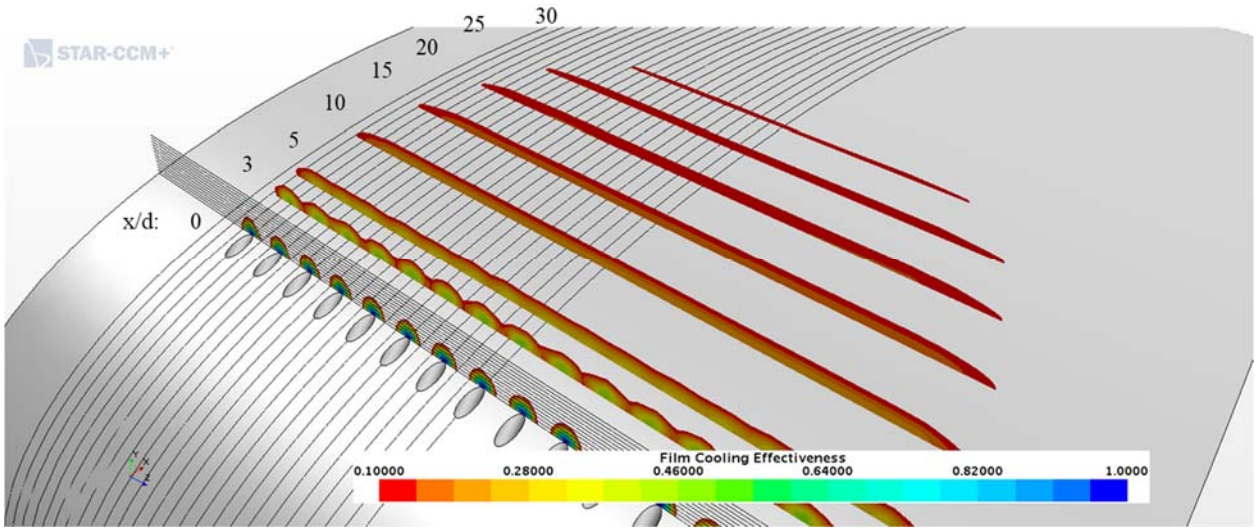

Figure 16.300: Case 28 - Streamwise spatial distribution of adiabatic film cooling effectiveness

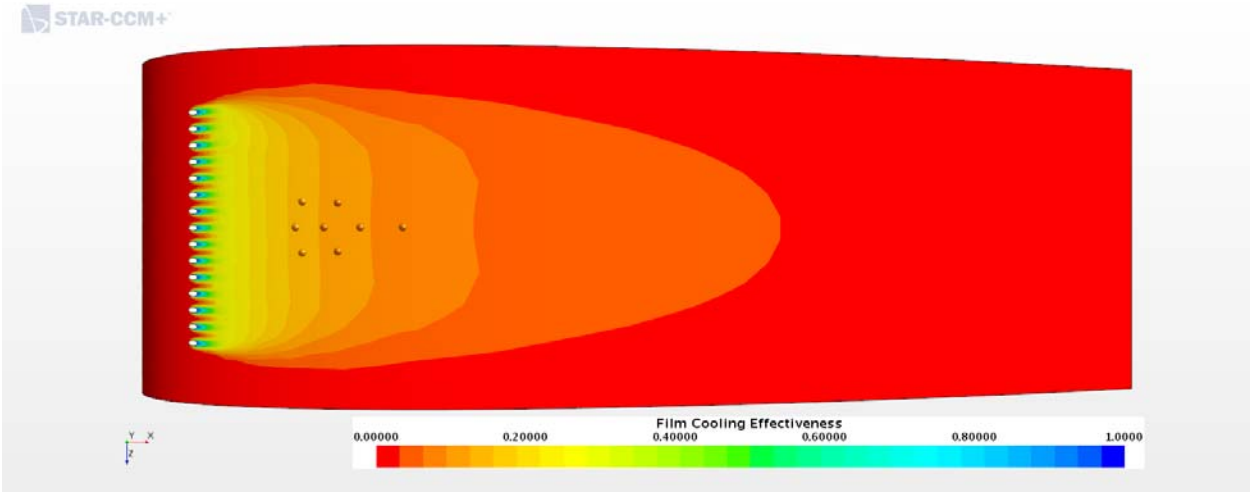

Figure 16.301: Case 28 - Adiabatic Film Cooling Effectiveness on the Suction Surface

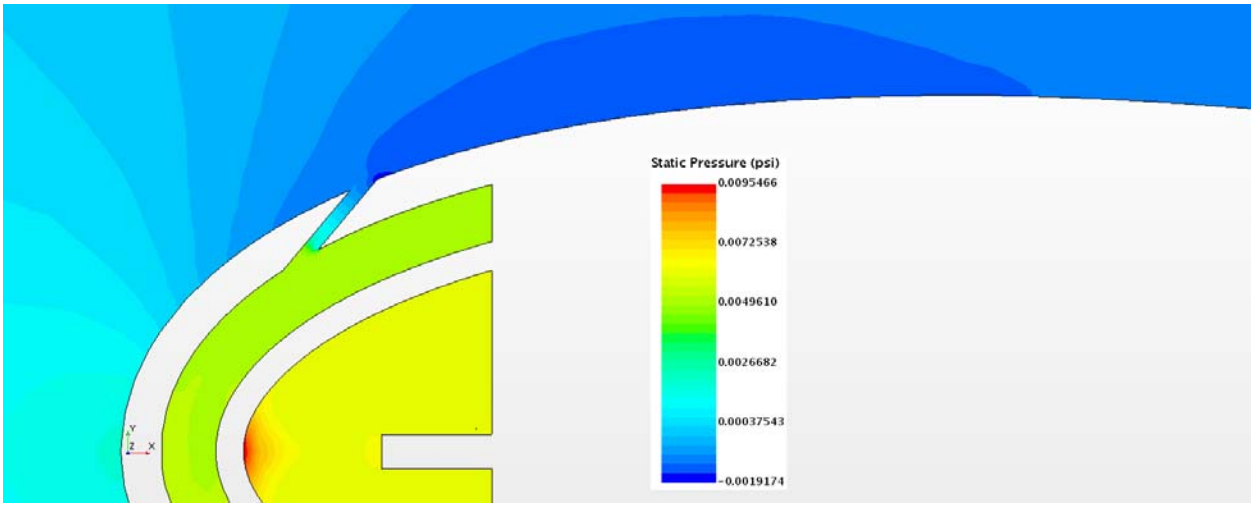

Figure 16.302: Case 28 – Static Pressure profile for center plane

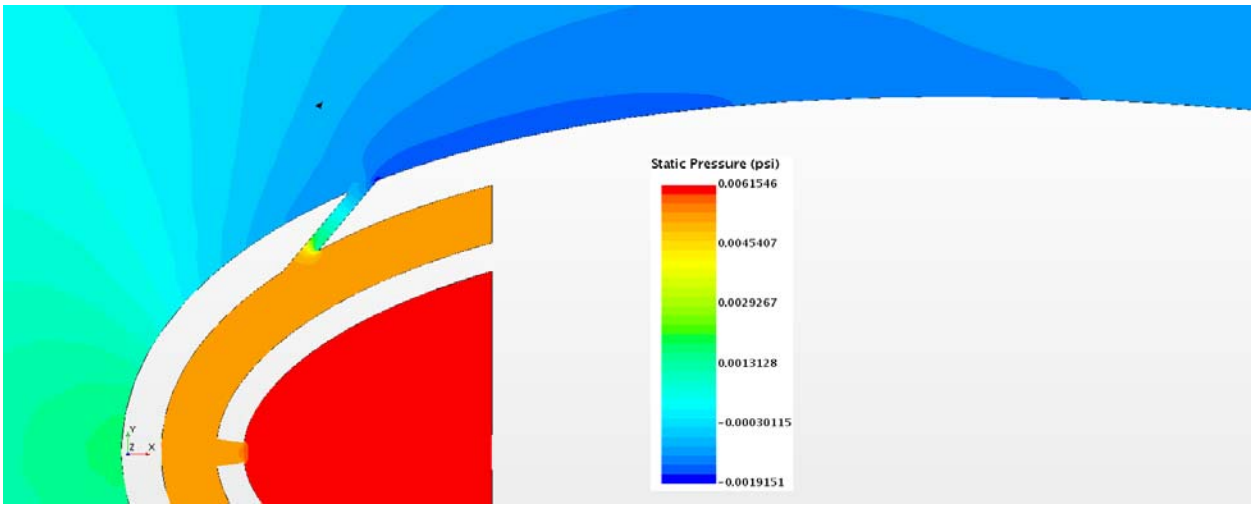

Figure 16.303: Case 28 – Static Pressure profile for off-center plane

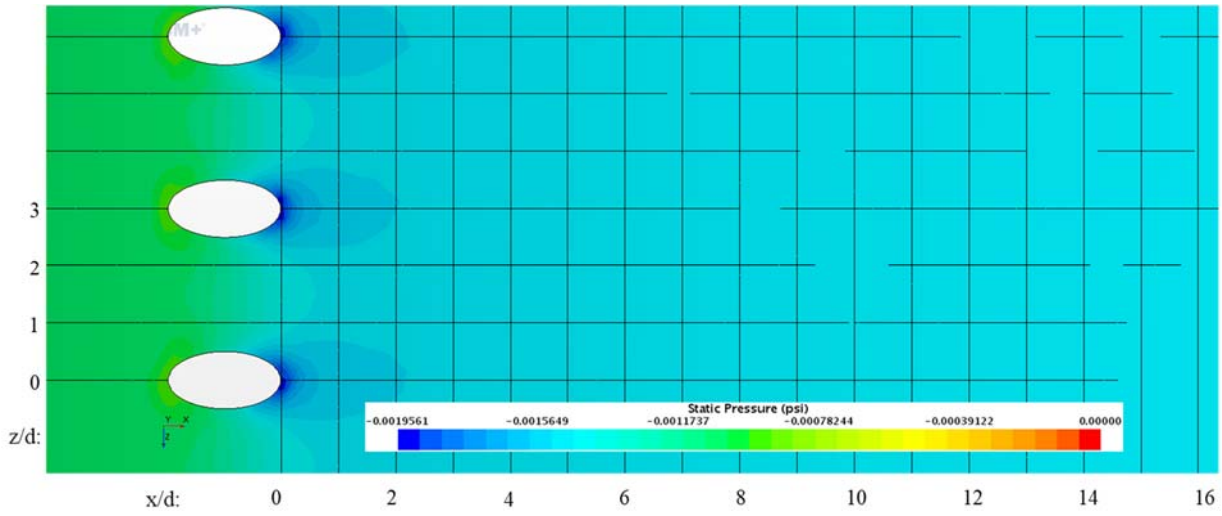

Figure 16.304: Case 28 – Static Pressure distribution for Suction Surface

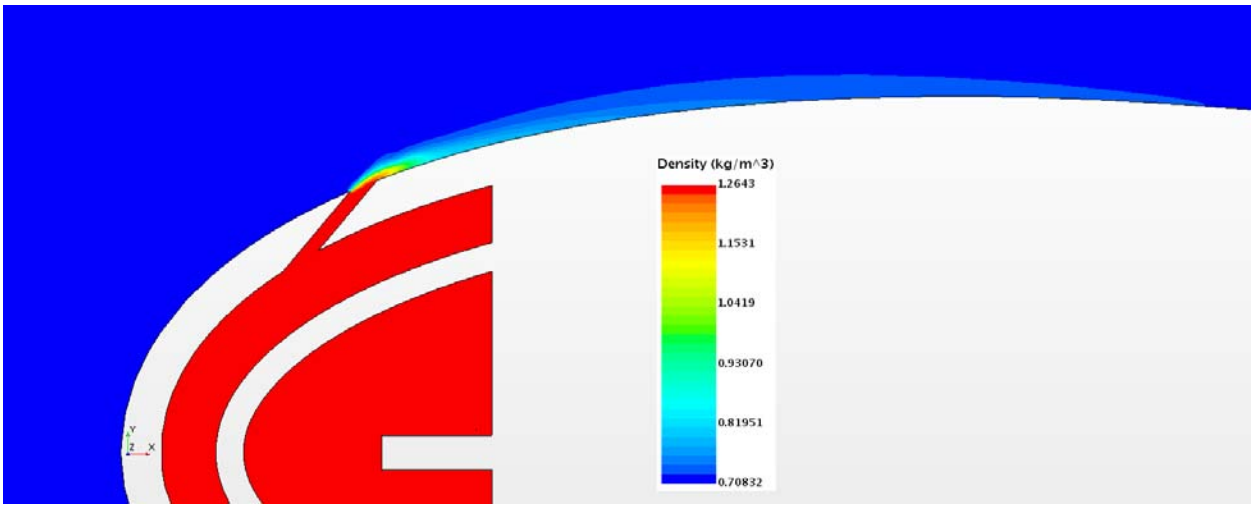

Figure 16.305: Case 28 – Density profile for center plane

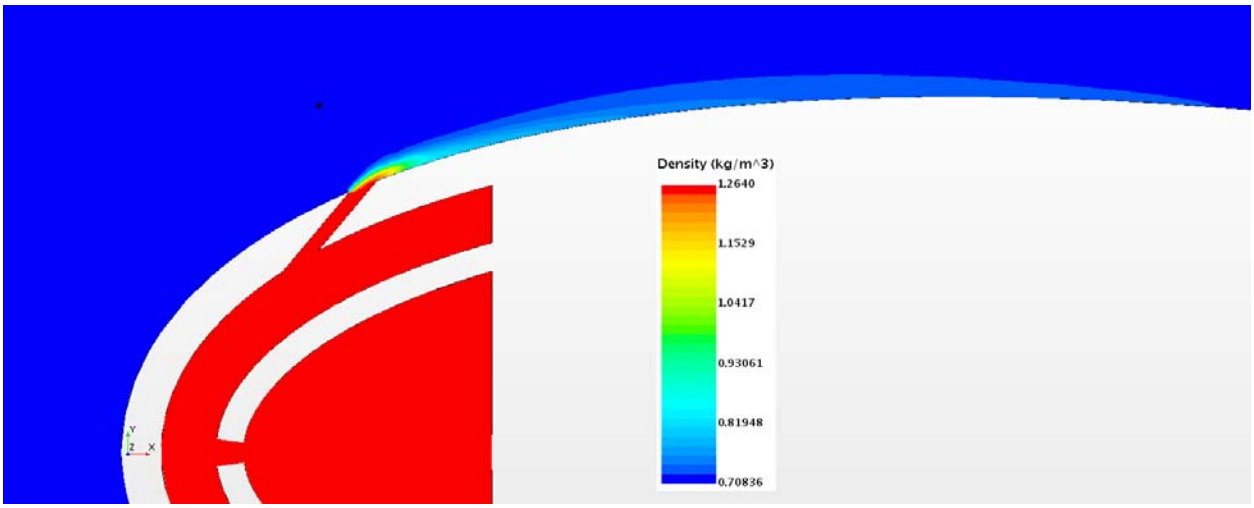

Figure 16.306: Case 28 – Density profile for off-center plane

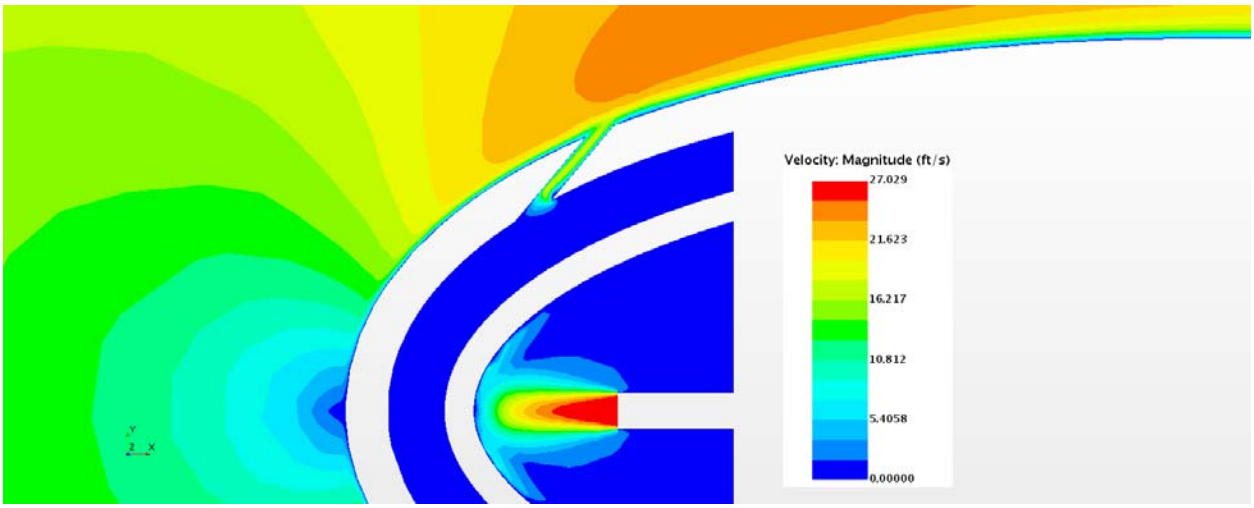

Figure 16.307: Case 28 – Velocity profile for center plane

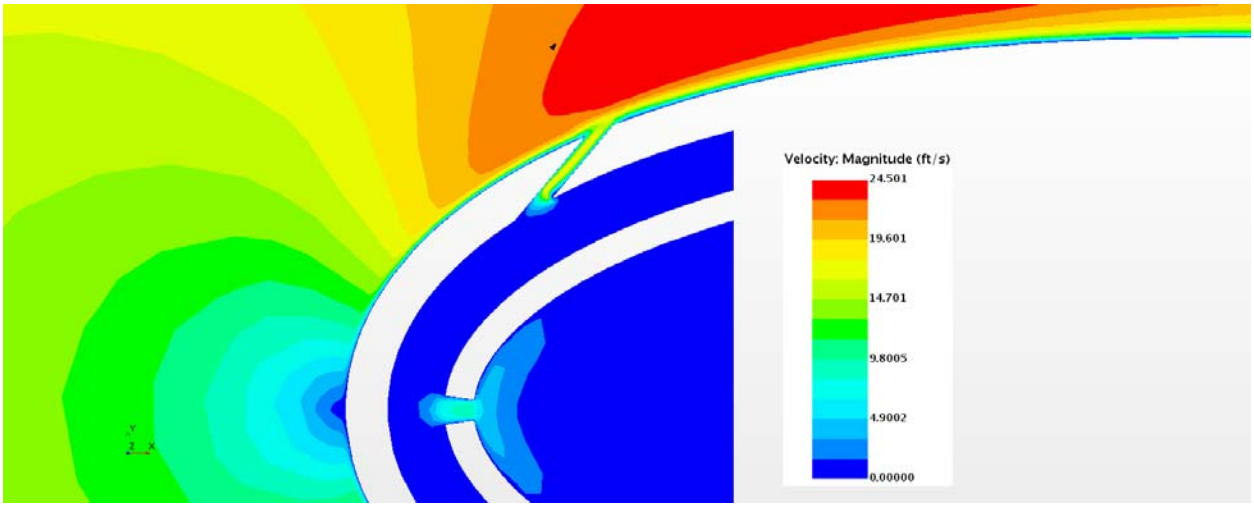

Figure 16.308: Case 28 – Velocity profile for off- center plane